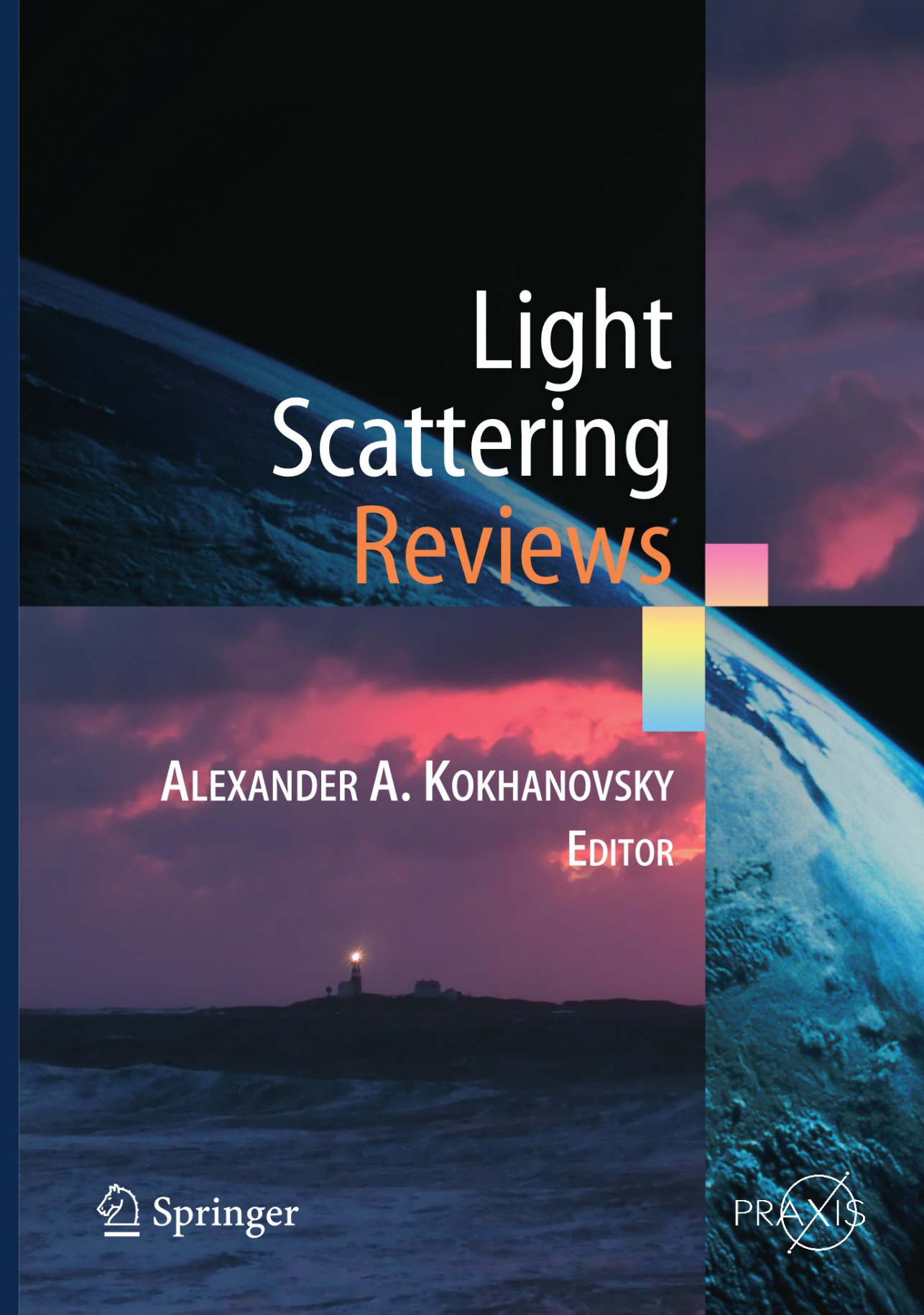
Light
Scattering
Reviews
Alexander A. Kokhanovsky
Editor
Springer
PRAXIS

Light Scattering Reviews

Single and Multiple Light Scattering

Alexander A. Kokhanovsky (Editor)

Light Scattering Reviews

Single and Multiple Light Scattering

Springer

Published in association with
Praxis Publishing
Chichester, UK

Editor
Dr Alexander A. Kokhanovsky
Institute of Environmental Physics
University of Bremen
Bremen
Germany

SPRINGER–PRAXIS BOOKS IN ENVIRONMENTAL SCIENCES
SUBJECT *ADVISORY EDITOR*: John Mason B.Sc., M.Sc., Ph.D.

ISBN 3-540-25315-7 Springer-Verlag Berlin Heidelberg New York

Springer is part of Springer-Science + Business Media (springeronline.com)

Bibliographic information published by Die Deutsche Bibliothek

Die Deutsche Bibliothek lists this publication in the Deutsche Nationalbibliografie; detailed bibliographic data are available from the Internet at http://dnb.ddb.de

Library of Congress Control Number: 2005935704

Printed in Germany

Cover design: Jim Wilkie
Project copy editor: Mike Shardlow
Author-generated LaTex, processed by EDV-Beratung, Germany

Printed on acid-free paper

Contents

List of Contributors

Anatoli G. Borovoi
Institute of Atmospheric Optics
Russian Academy of Sciences
Akademicheskii Prospekt 1
634055 Tomsk
Russia
borovoi@iao.ru

Victor G. Farafonov
St. Petersburg University of Aerocosmic Instrumentation
Bol. Morskaya 67
St. Petersburg 190000
Russia
far@aanet.ru

Evgenii E. Gorodnichev
Theoretical Physics Department
Moscow Engineering Physics Institute
Kashirskoe Shosse 31
115409 Moscow
Russia
gorodn@theor.mephi.ru

Vladimir I. Haltrin
Ocean Optics Section
Code 7333
Naval Research Laboratory
Stennis Space Center
Mississippi 39529-5004
USA
vihaltrin@nrlssc.navy.mil

Vladimir B. Il'in
Astronomical Institute
St. Petersburg University
Universitetskij pr. 28
St. Petersburg 198504
Russia
vi2087@VI2087.spb.edu

Alan R. Jones
Department of Chemical Engineering
Imperial College
London SW7 2BY
UK
a.r.jones@imperial.ac.uk

Alexander A. Kokhanovsky
Institute of Environmental Physics
University of Bremen
Otto Hahn Alee 1
D-28334 Bremen
Germany
alexk@iup.physik.uni-bremen.de

Alexander I. Kuzovlev
Theoretical Physics Department
Moscow Engineering Physics Institute
Kashirskoe Shosse 31
115409 Moscow
Russia
kuzov@theor.mephi.ru

Kuo-Nan Liou
Department of Atmospheric and Oceanic Sciences
University of California
Los Angeles
California 90095-1565
USA
knliou@atmos.uda.edu

Olga Muñoz
Instituto de Astrofísica de Andalucía
Camino Bajo de Huétor 50
Granada 18008
Spain
olga@iaa.es

Dmitrii B. Rogozkin
Theoretical Physics Department
Moscow Engineering Physics Institute
Kashirskoe Shosse 31
115409 Moscow
Russia
rogozkin@theor.mephi.ru

Vladimir V. Rozanov
Institute of Environmental Physics
University of Bremen
Otto Hahn Allee 1
D-28334 Bremen
Germany
rozanov@iup.physik.uni-bremen.de

Subodh K. Sharma
S. N. Bose National Centre for Basic Sciences
Block JD, Sector III
Salt Lake, Kolkata 700098
India
sharma@bose.res.in

Hester Volten
Astronomical Institute 'Anton Pannekoek'
University of Amsterdam
Kruislaan 403
1098 SJ Amsterdam
Netherlands
hvolten@science.uva.nl

Ping Yang
Department of Atmospheric Sciences
Texas A&M University
3150 TAMU
College Station, Texas 77843-3150
USA
pyang@ariel.met.tamu.edu

Notes on the contributors

Anatoli Borovoi received his Ph.D. (candidate of sciences) from Tomsk University in 1967. In his dissertation, he derived the radiative transfer equation from the Maxwell equations and considered certain corrections accounting for spatial correlation of scatterers. Working at the Institute of Atmospheric Optics (Tomsk) from 1969 until now, he headed theoretical and experimental works concerning light propagation in the turbulent atmosphere with precipitation. In his Doctor of Sciences dissertation (1983) he presented a theory of light propagation in random media with large discrete inhomogeneities, the experimental data concerning scattering of laser beams and speckle-optics, and development of certain methods for optical diagnostics of scattering media. His research field includes wave scattering and propagation in random media, radiative transfer, remote sensing and lidar measurements. At present, he is head of the Laboratory for the Theory of Light Scattering, and his recent papers have been devoted to the development of an optical model for cirrus clouds.

Victor Farafonov graduated from St. Petersburg State University, Russia, in 1976. He received his Ph.D. in mathematical physics and his Doctor of Sciences degree in physics and mathematics from the St. Petersburg State University in 1981 and 1991, respectively. He is currently a professor and the head of the Applied Mathematics Department at St. Petersburg University of Aerospace Instrumentation. His research interests are directed to studies of electromagnetic and light scattering and also special functions (e.g., spheroidal wave functions). He has published more than ninety papers in the field of electromagnetic and light scattering theory.

Evgenii E. Gorodnichev graduated from the Theoretical Physics Department of the Moscow Engineering Physics Institute in 1985. He received his Ph.D. in theoretical and mathematical physics from the Moscow Engineering Physics Institute in 1989. His Ph.D. work was devoted to coherent effects at multiple wave scattering from disordered media. He is currently associate professor at the Department of Theoretical Physics of the Moscow Engineering Physics Institute. His principal scientific interests are concerned with multiple scattering of polarized light in random media. He has published over fifty papers on light scattering theory.

Vladimir I. Haltrin joined the ocean optics community in 1976 at the Marine Hydrophysical Institute, Sevastopol, Crimea. He continued working in the same area in the Hydrophysics Branch of the Vavilov State Optical Institute, St. Petersburg, Russia, and later again in the Optics Department of the Marine Hydrophysical Institute. After moving to the USA in 1986, he worked on ocean optics problems at EG&G Washington Analytical Services Center, Lanham, Maryland, and later in the Physics Department of Texas A&M University, College Station, Texas. Since 1994 he has worked at the Ocean Sciences Branch of the Naval Research Laboratory, Stennis Space Center, Mississippi. His interests are in the areas of oceanic and atmospheric optics and in optical remote sensing.

Vladimir B. Il'in graduated from St. Petersburg State University, Russia, in 1977 and received his Ph.D. in astrophysics from St. Petersburg State University in 1989. He is currently a senior research scientist at the Sobolev Astronomical Institute of St. Petersburg State University. His research interests are directed towards light scattering by nonspherical particles, the optics of cosmic dust and the physics of the interstellar medium. He has published more than seventy papers in the field of light scattering theory and its applications in astronomy. Dr Il'in is a member of the European and Euro-Asian Astronomical Societies.

After undergraduate studies in physics at the University College of Swansea, **Alan R. Jones** obtained his Ph.D. in physics from the University of Wales, Aberystwyth, for a study on the scattering of microwaves by gaseous plasma. Following two year's teaching in Virginia and one year at Royal Holloway College, he moved to Imperial College, London. He was awarded the degree of D.Sc. from the University of Wales and was promoted to a professor of the University of London. His research interests have mainly involved light scattering, especially, but not exclusively, by particles relevant to combustion. These have included soot, coal, ash and liquid sprays, but studies have also been undertaken, for example, into detection of fibres in the atmosphere and electrostatic atomization. He has been active in the Combustion Physics Group of the Institute of Physics and in the organization of the International Congresses on Optical Particle Characterization.

Alexander A. Kokhanovsky graduated from the Physical Department of the Belarussian State University, Minsk, Belarus, in 1983. He received his Ph.D. in optical sciences from the B. I. Stepanov Institute of Physics, National Academy of Sciences of Belarus, Minsk, Belarus, in 1991. The Ph.D. work was devoted to modelling the light scattering properties of aerosol media and foams. Alexander Kokhanovsky is currently a member of the SCIAMACHY/ENVISAT algorithm development team (Institute of Environmental Physics, University of Bremen). His research interests are directed towards modelling light propagation and scattering in the terrestrial atmosphere. Dr Kokhanovsky is the author of the books *Light Scattering Media Optics: Problems and Solutions* (Chichester: Springer-Praxis, 1999, 2001, 2004), *Polarization Optics of Random Media* (Berlin: Springer-Praxis, 2003), and *Cloud Optics* (Berlin, Springer, 2006). He has published more than one hundred papers in the field of environmental optics, radiative transfer, and light scattering. Dr Kokhanovsky is a member of the American Geophysical Union and the Belarussian Physical Society.

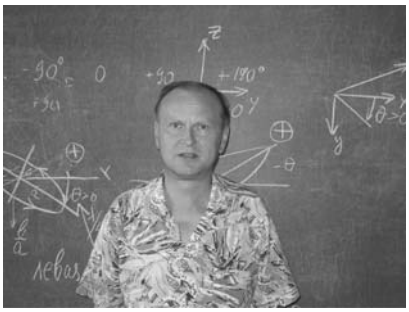

Alexander I. Kuzovlev graduated from the Theoretical Physics Department of the Moscow Engineering Physics Institute in 1983. He received his Ph.D. in theoretical and mathematical physics from the Moscow Engineering Physics Institute in 1988. His Ph.D. work was devoted to the albedo problem of the radiative transfer theory. His principal scientific interests are concerned with radiative transfer. He has published over fifty papers on light scattering theory. He is currently an associate professor at the Department of Theoretical Physics of the Moscow Engineering Physics Institute.

Kuo-Nan Liou received his Ph.D. from New York University in 1970. After a 22-year career at the University of Utah, he became a professor at the University of California, Los Angeles (UCLA) in 1997 where he served as Chair of the Department of Atmospheric and Oceanic Sciences for a number of years and is now a Distinguished Professor of Atmospheric Sciences and Director of the Institute of Radiation and Remote Sensing. Professor Liou is a member of the US National Academy of Engineering and the Academia Sinica. His research fields span light scattering and radiative transfer, remote sensing, and climate studies involving clouds and aerosols. He is the author of a recent text, *An Introduction to Atmospheric Radiation*, second edition, published by Academic Press in 2002.

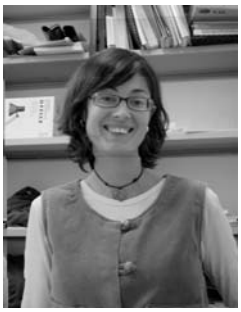

Olga Muñoz received her Ph.D. in physics from the University of Granada, Spain, in 1997. She is currently working at the Astrophysical Institute of Andalucía, CSIC, in Granada. She has a tenure track from the Spanish Ministry of Education and Science. After graduation at the University of Granada she obtained an ESA external fellowship to work for 2.5 years as a postdoctoral researcher at the department of Physics and Astronomy at the Free University in Amsterdam, The Netherlands. Afterwards she went on with her research at the Astrophysical Institute of Andalucía, CSIC. Her research interests cover the areas of radiative transfer in planetary atmospheres. In particular she has specialized in the experimental and theoretical study of the scattering behaviour of irregular mineral dust particles. She has co-authored more than forty peer-reviewed publications.

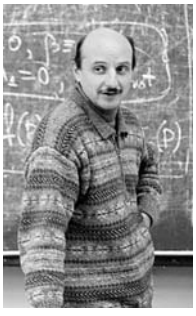

Dmitrii B. Rogozkin graduated from the Theoretical Physics Department of the Moscow Engineering Physics Institute in 1979. He received his Ph.D. in theoretical and mathematical physics and his Doctor of Science degree in theoretical physics both from the Moscow Engineering Physics Institute in 1984 and 1998 respectively. His Ph.D. work was devoted to analytical methods of solving the radiative transfer equation under conditions of anisotropic scattering. His D.Sc. thesis was devoted to interference phenomena in multiple scattering from disordered media. Currently his attention is focused on the study of coherent and polarization phenomena in multiple wave scattering. He has about seventy publications and the monograph *Path-length fluctuations of charged particles* (co-authors: V. S. Remizovich and M. I. Ryazanov). He is currently professor at the Department of Theoretical Physics of the Moscow Engineering Physics Institute.

Vladimir V. Rozanov graduated from the University of St. Petersburg, Russia, in 1973. He received his Ph.D. in physics and mathematics from the University of St. Petersburg, Russia, in 1977. From 1973 until 1991 he was a research scientist at the Department of Atmospheric Physics of the University of St. Petersburg. In 1990–1991 he worked at the Max-Planck Institute of Chemistry, Mainz, Germany. In July 1992 he joined the Institute of Remote Sensing at the University of Bremen, Germany. The main directions of his research are atmospheric radiative transfer and remote sensing of atmospheric parameters (including aerosols, clouds and trace gases) from space-borne spectrometers and radiometers. He is author and co-author of about one hundred papers in peer-reviewed journals.

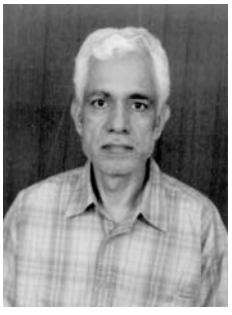

Subodh K. Sharma obtained his Ph.D. in 1977 from Calcutta University, India. He has done teaching and research work at the Birla Institute of Technology and Science, Pilani, India, the Saha Institute of Nuclear Physics, Kolkata, India, the Institute of Wetland Management and Ecological Design, Kolkata, India, University College, Cardiff, UK, and Imperial College, London, UK. He is the author of more than fifty papers relating to scattering problems in optics published in a number of scientific journals. Since 1991, he has been a faculty member at the S.N. Bose National Centre for Basic Sciences, Kolkata, India.

Hester Volten studied both experimental physics and astronomy at the University of Amsterdam, The Netherlands. She continued her studies on the subject at the laboratory of astrophysics in the group of Prof. Joop Hovenier (Department of Physics and Astronomy of the Free University in Amsterdam). She received her Ph.D. in 2001. After that she held a postdoctoral position at the Institute of Molecular and Atomic Physics (AMOLF) in Amsterdam and currently she holds a postdoctoral position at the Astronomical Institute 'Anton Pannekoek' in Amsterdam. She has specialized in laboratory measurements of light scattering by small (irregular) particles relevant to the Earth atmosphere, but also to the atmospheres of other planets and to solar system objects. More about her work and papers can be found in the Amsterdam Light Scattering Database http://www.astro.uva.nl/scatter.

Ping Yang received his Ph.D. in meteorology from the University of Utah in 1995. He is currently an associate professor at the Department of Atmospheric Sciences, Texas A&M University. After graduation from the University of Utah, he remained there for two years, working as a postdoctoral researcher. Later, he was an assistant research scientist at the University of California, Los Angeles, and an associate research scientist in the Goddard Earth Sciences & Technologies Center, University of Maryland Baltimore County. His research interests cover the areas of remote sensing and radiative transfer. He has been actively conducting research in the modelling of the optical and radiative properties of clouds and aerosols, in particular, cirrus clouds, and their applications to space-borne and ground-based remote sensing. He has co-authored more than seventy peer-reviewed publications.

Preface

Light scattering media optics is a special branch of physical optics devoted to studies of light propagation and scattering in inhomogeneous media. The subject has a number of important applications including remote sensing of planetary atmospheres and surfaces, medical diagnostics and image transfer in ocean and atmosphere, to name a few.

Different aspects of light scattering are studied by physicists, chemists, astronomers, biologists, and geophysicists. Often they use very different approaches, methodology, and even journals to present their results. Also different notations are used (see Appendix). However, all light scattering optics (LSO) studies have a single theoretical basis. This is the electromagnetic Maxwell theory. In particular, the vector integro-differential radiative transfer equation (RTE), often used as a way to solve the LSO problem at hand, can be derived from the Maxwell theory under some simplifying assumptions. Parameters of this equation like absorption and scattering coefficients and also the phase function can be either measured directly or calculated using Maxwell equations.

The main problem is to understand how light interacts with inhomogeneous media (e.g., with oceanic water or atmospheric air) and also to develop techniques for monitoring properties of intervening media from the analysis of scattered light.

There are a number of unsolved important physical problems in light scattering media optics. They include, for instance, light scattering by nonspherical scatterers and also light propagation in closely-packed media. The problem of light propagation through inhomogeneous media with sparsely distributed spherical scatterers has been solved in past century resulting in a number important technological and remote sensing advances.

LIGHT SCATTERING REVIEWS aims to facilitate better collaboration and interaction among researchers working with different applications of the phenomenon of light scattering in random media.

This first volume of series is devoted mostly to fundamentals. It composed of three sections: single light scattering, multiple light scattering, and also a small section devoted to applications of light scattering in marine research and combustion.

The first section starts with a paper by Olga Muñoz and Hester Volten presenting experimental studies of intensity and polarization of light scattered by irregularly shaped particles. This is a hot topic of modern light scattering media optics research. Theoreticians must concentrate on the explanation of results

obtained. This could lead to important progress in the field. Three theoretical chapters follow this experimental paper. The first one by Ping Yang and Kuo Nan Liou is devoted to theoretical investigations of light scattering by crystals. In particular, optical properties of ice crystals are the main concern of their work. However, techniques reviewed (e.g., geometrical optics and finite domain difference method) can be also used in other branches of light scattering media optics (e.g., in optics of photo-layers, luminiscent screens, and mineral aerosols). Subodh Sharma concentrates on studies of optical properties of particles immersed in media having refractive index similar to that of scatterers. In this case light scattering occurs mostly in the forward direction and correspondent theoretical derivations considerably simplify. The described theory has a number of important applications in oceanic and medical optics. The section is closed by the theoretical work of Victor Farafonov and Vladimir Ili'n devoted to the review of three most popular methods used in modern light scattering theory, namely: the separation of variables method (SVM), the extended boundary conditions method (EBCM), and the point matching method (PMM). SVM was used successfully for the solution of light scattering by a spherical particle more than one century ago. This solution (so called Lorentz–Mie theory) is widely used in many laboratories world-wide nowadays. Both SVM and EBCM were used in the past to study the optical properties of spheroids and also particles of more complex shapes. Correspondent programs are available over INTERNET. Authors provide valuable hints for the understanding of interrelations and differences between the computational methods. This helps to understand what method is better suited for the problem at hand.

The second section is devoted to multiple light scattering theory. Anatoli Borovoi reviews wave scattering theory. Also he demonstrates how the radiative transfer equation routinely used in studies of multiple light scattering in atmospheric and oceanic optics can be derived from first principles. Alexander Kokhanovsky considers the asymptotic solution of the radiative transfer equation valid for optically thick media (e.g., terrestrial clouds). Corresponding equations have a number of important technological and remote sensing applications. Gorodnichev, Kuzovlev, and Rogozkin consider the problem of polarized light propagation through light scattering media with large particles. The influence of the polarization state on the light beam propagation in a scattering medium is studied in great detail. In conclusion of this section, Vladimir Rozanov introduces the adjoint radiative transfer equation. He shows how this equation (in combination with direct RTE) can be used for the solution of inverse problems of radiative transfer theory.

The last section is devoted to applications. In particular, Alan Jones considers the application of light scattering media in combustion. Vladimir Haltrin concentrates on resent results obtained in marine optics. He gives comprehensive tables of measured *in situ* phase functions. Corresponding tables are of a great importance for a better understanding of image and radiative transfer in oceanic water.

In conclusion, I would like to thank all contributors for the preparation of brilliant work for this first volume of Light Scattering Reviews. This is especially

valued because all authors are actively involved in modern light scattering media optics research and hardly have any time to make substantial reviews as presented here. I also indebted to Clive Horwood, Publisher, for advice, patience, and encouragement.

This work is dedicated to the memory of outstanding Russian mathematician Tatyana A. Germogenova (10.04.1930-27.02.2005), who made extremely valuable contributions to modern radiative transfer theory.

Bremen, Germany
October, 2005

Alexander A. Kokhanovsky

Part I

Single Light Scattering

1 Experimental light scattering matrices from the *Amsterdam Light Scattering Database*

Olga Muñoz and Hester Volten

1.1 Introduction

In recent years a considerable number of experimental single scattering matrices as functions of the scattering angle obtained with the light scattering facility located at the University of Amsterdam [1], [2], have become available for samples of randomly oriented small mineral particles in air with broad ranges of sizes and shapes [3–8]. The particles samples are relevant in particular for astronomy and studies of the Earth atmosphere, but the light scattering results may also be applicable, e.g. in the paper and paint industry, or in the fields of chemistry or biology.

To provide an incentive for further research and applications we have made our experimental data more easily available for the light scattering community by storing them in digital form in a database freely accessible through the Internet in the *Amsterdam Light Scattering Database* (http://www.astro.uva.nl/scatter). The heart of the database is the collection of tables of the measured scattering matrix elements listed as functions of the scattering angle at two different wavelengths [9].

Scattering matrices contain all polarizing properties of the samples of randomly oriented particles and play an important role in radiative transfer processes. If the incident light is unpolarized only a few elements of the scattering matrix (the first column) suffice to fix the flux and state of polarization of the light scattered once by the sample. But the complete scattering matrix is indispensable for accurate multiple scattering calculations, since even unpolarized light becomes polarized after being scattered.

In this chapter we summarize the main concepts of light scattering by mineral aerosols and of the experimental setup located at the University of Amsterdam. Afterward we present the light scattering database and a summary of some of the main results obtained with our measurements until now. All measurements presented in this chapter can be found in the *Amsterdam Light Scattering Database*.

1.2 Light scattering theory

The intensity and state of polarization of a beam of light can be described by a column vector $\mathbf{I} = \{I, Q, U, V\}$, the so-called Stokes vector (see, for example, [10], Sect. 5.12, and [11]). The Stokes parameter I is proportional to the total flux of the beam. The Stokes parameters Q and U describe the state of linear polarization and V describes the state of circular polarization.

The Stokes vector of the incident beam and scattered beam are related by a 4×4 matrix, the so called scattering matrix, for each scattering angle as follows ([10], Sect. 5.22):

$$\begin{pmatrix} I_{\rm sc} \\ Q_{\rm sc} \\ U_{\rm sc} \\ V_{\rm sc} \end{pmatrix} = \frac{\lambda^2}{4\pi^2 D^2} \begin{pmatrix} F_{11} & F_{12} & F_{13} & F_{14} \\ F_{21} & F_{22} & F_{23} & F_{24} \\ F_{31} & F_{32} & F_{33} & F_{34} \\ F_{41} & F_{42} & F_{43} & F_{44} \end{pmatrix} \begin{pmatrix} I_{\rm in} \\ Q_{\rm in} \\ U_{\rm in} \\ V_{\rm in} \end{pmatrix}, \tag{1.1}$$

where the subscripts *in* and *sc* refer to the incident and scattered beams, λ is the wavelength, and D is the distance from the sample to the detector.

The 16 elements of the scattering matrix, F_{ij}, with $i, j = 1$ to 4, depend on the physical properties of the particles, the wavelength of the radiation and the direction of the scattered light, which, for randomly oriented particles, is sufficiently described by means of the scattering angle, θ. When randomly oriented particles and their mirror particles are present in equal numbers in the ensemble the scattering matrix has the simple form [10]:

$$\mathbf{F}(\theta) = \begin{pmatrix} F_{11}(\theta) & F_{12}(\theta) & 0 & 0 \\ F_{12}(\theta) & F_{22}(\theta) & 0 & 0 \\ 0 & 0 & F_{33}(\theta) & F_{34}(\theta) \\ 0 & 0 & -F_{34}(\theta) & F_{44}(\theta) \end{pmatrix}. \tag{1.2}$$

For convenience, we divide all scattering matrix elements (except $F_{11}(\theta)$ itself) by $F_{11}(\theta)$, i.e., we consider $F_{ij}(\theta)/F_{11}(\theta)$, with $i, j = 1$ to 4 except for $i = j = 1$. Further, the values of $F_{11}(\theta)$ are normalized so that they equal one at $\theta = 30$ degrees.

For unpolarized incident light, $F_{11}(\theta)$ is proportional to the flux of the scattered light and is called scattering function or phase function. The ratio $-F_{12}(\theta)/F_{11}(\theta)$ equals the degree of linear polarization of the scattered light if the incident light is unpolarized and $F_{13}(\theta) = 0$. Note further that we must have $|F_{ij}(\theta)/F_{11}(\theta)| \leq 1$ [see, for example, [12]].

1.3 Experimental method

An schematic picture of experimental setup used to measure the scattering matrix elements of the aerosol samples is shown in Fig. 1.1. The setup is similar to that developed by [13] and is a revised and improved version of that described

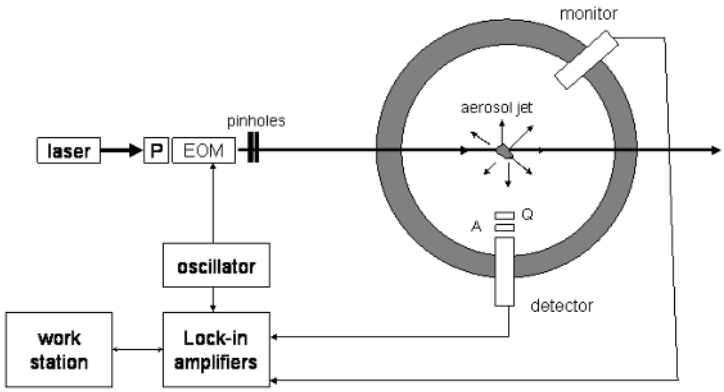

Fig. 1.1. Schematic picture of the experimental setup; P, polarizer; A, polarization analyzer; Q, quarter-wave plate; EOM, electro-optic modulator.

by [14], [15], and [16]. Here we briefly summarize the main characteristics of the setup. A more comprehensive description can be found in [1].

Light from a linearly polarized continuous wave He-Ne laser ($\lambda = 632.8$ nm, 5 mW) or He-Cd laser ($\lambda = 441.6$ nm, 40 mW) passes through a polarizer oriented at an angle γ_P and an electro-optic modulator oriented at an angle γ_M (angles of optical elements are angles between their optical axes and the reference plane, measured counterclockwise when looking in the direction of propagation of the light). The modulated light is subsequently scattered by randomly oriented particles located in a jet stream produced by an aerosol generator. The particles of a particular mineral sample are brought into the jet stream as follows. A compacted mass of powder is loaded into a cylindrical feed stock reservoir. A piston pushes the powder onto a rotating brush at a certain speed. An air stream carries the aerosol particles of the brush through a tube to a nozzle above the scattering volume. In Fig. 1.2 we present a schematic picture of the aerosol

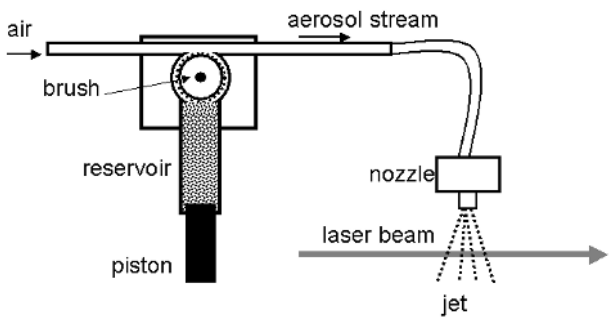

Fig. 1.2. Schematic picture of the aerosol generator. A piston in the cylindrical feed stock reservoir with a diameter of 10 mm pushes powder onto a rotating brush at a certain speed expressed in mm/h. An air stream carries the aerosol particles of the brush through a tube to a nozzle right above the scattering volume.

generator. Thus, no vials, vessels, or cuvettes are needed to contain the sample at the point where the scattering takes place. This is a great advantage, since anything between the particles and the detector decreases the accuracy of the measurements and limits the angular range. The scattered light passes through a quarter-wave plate oriented at an angle γ_Q and an analyzer oriented at an angle γ_A (both optional) and is detected by a photomultiplier tube that moves along a ring in steps of 5 degrees, or less if a higher angular resolution is required. The detector covers a scattering angle range from approximately 3 degrees (nearly forward scattering) to 175 degrees (nearly backward scattering).

The modulator introduces a modulation in time of the polarization of the light before scattering. The modulator in the setup, in combination with lock-in detection, increases the accuracy of the measurements and allows determination of several elements of the scattering matrix from the detector signal. For this purpose, we use the linear Pockels effect, that is, the phenomenon that certain crystals become birefringent when an electric field is applied. In our case, the voltage over the crystal varies sinusoidally in time. Since the response to voltage of the birefringent crystal is also sinusoidal, the resulting phase shift function is a sine of a sine and can be described by Bessel functions of the first kind ($J_K(x)$). If the amplitude ϕ_0 of the varying phase shift is chosen appropriately, the flux reaching the detector is [1].

$$I_{\mathrm{det}}(\theta) = c[DC(\theta) + 2J_1(\phi_0)S(\theta)\sin\omega t + 2J_2(\phi_0)C(\theta)\cos 2\omega t + ...], \qquad (1.3)$$

where $J_1(\phi_0)$ and $J_2(\phi_0)$ are known constants, and c is a constant that depends on the optical arrangement. The modulation angular frequency ω is 1 kHz. The coefficients $DC(\theta)$, $S(\theta)$, and $C(\theta)$ contain elements of the scattering matrix (see Table 1.1) [1, 16].

By using lock-in detection the constant part of the detector signal containing $cDC(\theta)$ and each of the varying parts containing $cS(\theta)$ and $cC(\theta)$ are separated. Subsequently, we divide $cS(\theta)$ and $cC(\theta)$ by $cDC(\theta)$, belonging to the same configuration, which eliminates c for these ratios. A detailed description on how

Table 1.1. Configurations of the orientation angles, γ_P, γ_M, γ_Q, and γ_A of respectively the polarizer, the modulator, the quarter-wave plate, and the analyzer used during the measurements. The coefficients $DC(\theta)$, $S(\theta)$, and $C(\theta)$ correspond to the dc, $\sin\omega t$ and $\cos\omega t$ component of the photomultiplier signal, respectively.

Configuration	γ_P	γ_M	γ_Q	γ_A	$DC(\theta)$	$S(\theta)$	$C(\theta)$
1	0^o	-45^o	–	–	F_{11}	$-F_{14}$	F_{12}
2	0^o	-45^o	–	0^o	$F_{11}+F_{12}$	$-F_{14}-F_{24}$	$F_{12}+F_{22}$
3	0^o	-45^o	–	45^o	$F_{11}-F_{13}$	$-F_{14}-F_{34}$	$F_{12}-F_{23}$
4	0^o	-45^o	0^o	45^o	$F_{11}+F_{14}$	$-F_{14}-F_{44}$	$F_{12}+F_{24}$
5	45^o	0^o	–	–	F_{11}	$-F_{14}$	F_{13}
6	45^o	0^o	–	0^o	$F_{11}+F_{12}$	$-F_{14}-F_{24}$	$F_{13}+F_{23}$
7	45^o	0^o	–	45^o	$F_{11}-F_{13}$	$-F_{14}-F_{34}$	$F_{13}+F_{33}$
8	45^o	0^o	0^o	45^o	$F_{11}+F_{14}$	$-F_{14}-F_{44}$	$F_{13}-F_{34}$

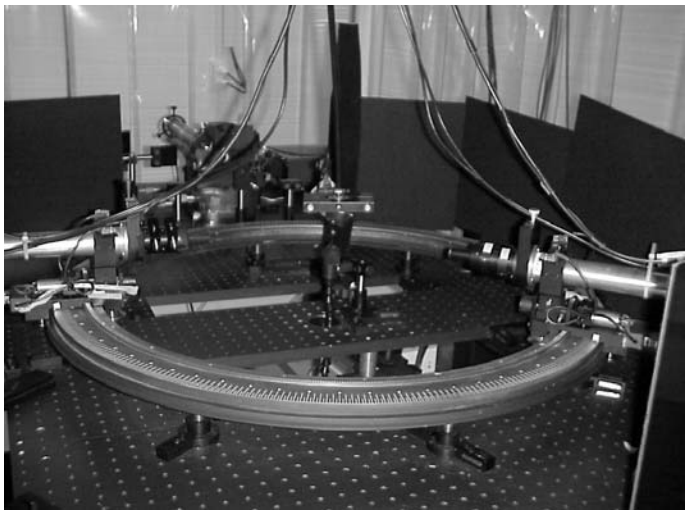

Fig. 1.3. Photograph of the experimental setup.

to obtain the different scattering matrix ratios is given in [1]. In Fig. 1.3 we present a photograph of the experimental setup. On the left we can see the detector that moves along the ring. The detector on the right remains on the same spot and is called the monitor. In the middle we see the nozzle of the aerosol generator, and the bright spot is where the dust particles cross the laser beam from the HeNe laser visible at the back.

1.3.1 Calibration measurements

The alignment of the experimental setup is tested by comparing results of water droplet measurements at 441.6 nm and 632.8 nm to results of Lorenz–Mie calculations [17] for homogeneous spherical particles. The water droplets are produced by a nebulizer. For the Lorenz–Mie calculations we used a lognormal number distribution having $r_{\text{eff}} = 1.1$ μm, $v_{\text{eff}} = 0.25$ (see section 1.4.4 and [18] for the definition of r_{eff} and v_{eff}), and a complex refractive index equal to $1.33 - i0.00$. Since the values for r_{eff} and v_{eff} of the water droplets are not known, they are chosen so that the differences between measured and calculated scattering matrix elements as a function of scattering angle are minimized.

In Fig. 1.4 we present the measured and calculated scattering matrices as functions of the scattering angle for water droplets at 441.6 and 632.8 nm. The results of the $F_{11}(\theta)$ measurements and calculations are plotted on a logarithmic scale. The measured and calculated phase functions are normalized to 1 at 30°. The other elements shown in Fig. 1.4 are normalized to F_{11}. We refrained from showing the four element ratios $F_{13}(\theta)/F_{11}(\theta)$, $F_{14}(\theta)/F_{11}(\theta)$, $F_{23}(\theta)/F_{11}(\theta)$, and $F_{24}(\theta)/F_{11}(\theta)$, since we verified that these ratios do not differ from zero by more than the error bars, as is in accordance with Lorenz–Mie theory.

When the results of the water droplet measurements are compared with the results of Lorenz–Mie calculations (see Fig. 1.4), we find that there is excellent agreement over the entire angle range for most scattering matrix elements. Note that the measured ratios $F_{33}(\theta)/\ F_{11}(\theta)$, and $F_{44}(\theta)/F_{11}(\theta)$ are found to be identical, which is in accordance with Lorenz–Mie theory. The largest systematic deviation from Lorenz–Mie theory, albeit only of a few percent, is found for $F_{22}(\theta)/F_{11}(\theta)$. This may be due to an accumulation of small alignment errors in the experiment [19]. We note that systematic errors, for example due to small inaccuracies in the alignment of the optical elements, are not accounted for in the error bars.

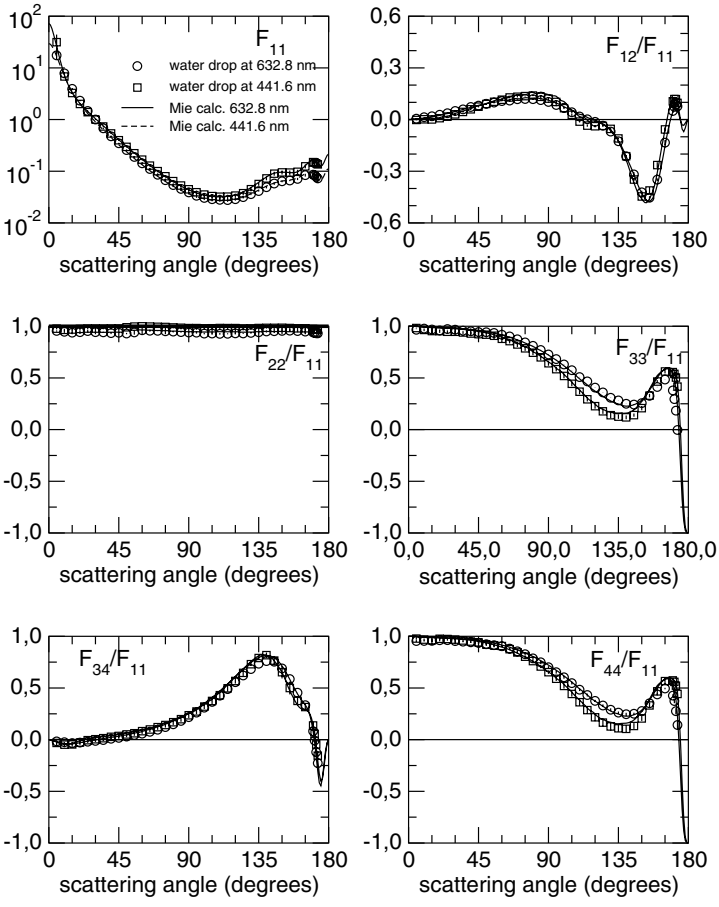

Fig. 1.4. Measured scattering matrix elements as functions of the scattering angle for water droplets. Circles denote the measurements at 632.8 nm, squares those at 441.6 nm, together with their error bars. Solid and dashed lines are results of Lorenz–Mie calculations for 632.8 nm and 441.6 nm, respectively.

1.4 Database

All data in the database have been previously published in scientific journals predominantly in graphical form. The database contains the following data for several samples of mineral aerosols in random orientation:

- Tables and figures of scattering matrix elements as functions of the scattering angle from 5 to 173° at two wavelengths, 441.6 nm and 632.8 nm.
- Tables and figures of size distributions as measured with a laser diffraction method.
- Scanning electron microscope (SEM) images of the particles that are indicative of their shape characteristics.
- Information about the origin, color, composition and/or the complex refractive index of the samples, when available.

We provide information on the accuracy of the data whenever available. We update this database regularly with new measured scattering matrix results.

1.4.1 Samples

As mentioned in the Introduction, the studied samples comprise a wide range in origin, sizes, particle shapes, and composition. Some have been collected from the ground in powdered form such as the volcanic ashes. These were all collected after the eruption at variable distances from their corresponding volcano. Others were obtained by crushing larger rocks (e.g. feldspar, quartz, olivine, allende meteorite particles, Pinatubo volcanic ash). Several samples have been sieved to obtain different size distributions (e.g. olivine) or to remove particles larger than about 100 μm in radius (e.g. Mount St. Helens volcanic ash). Here we use the data concerning the Mount St. Helens volcanic ash to illustrate the contents of the database.

1.4.2 Scanning electron microscope images

To give an indication of the shapes of the particles we provide one or two SEM images in the database per sample. For example, Fig. 1.5 shows two scanning electron microscope images of the Mount St. Helens sample. Such images may for example be compared to images of particles collected directly from the atmosphere or in space [20] or be used for shape analysis, e.g., [21–25]. We like to note that the SEM images per sample in the database are not necessarily representative of the sizes of the particles, mainly because they range over several orders of magnitude, in most cases, so that images with lower magnification will be biased toward showing only larger particles, and vice versa.

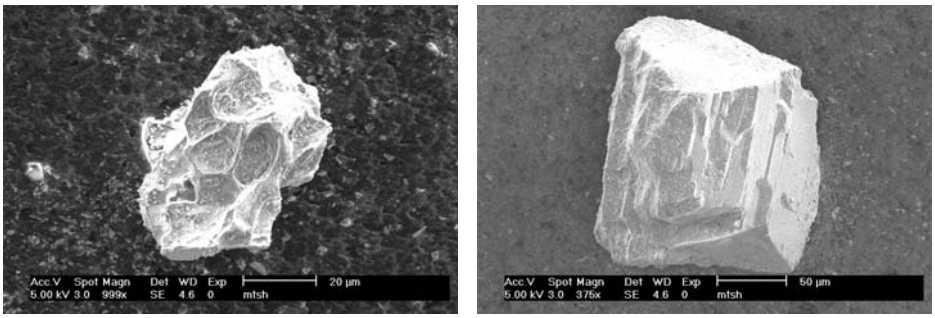

Fig. 1.5. Scanning Electron Microscope Picture of Mount St. Helens. The white bars denote the scale of the pictures.

1.4.3 Particle composition and refractive indices

Samples of natural small particles are often composed of a variety of different minerals. Although the refractive indices at visible wavelengths of these constituent minerals may be known, the refractive index for the mixture may not be easy to derive from these values. For cases where the refractive index is not accurately known, we provide in the database a qualitative estimate of the mineral composition, and an estimate of the real part of the refractive index $\mathrm{Re}(m)$ based on values found in the literature for the constituent minerals. In Table 1.2 we also list estimates of the real parts of the refractive index of all samples mentioned in this chapter. Less information is usually available for the imaginary part of the refractive index $\mathrm{Im}(m)$, because the natural variability within a mineral can be quite large.

For example, the main constituent minerals of the Mount St. Helens sample are silicate glass (SiO_2), and crystallized silicate minerals phases including plagioclase feldspar, pyroxenes, and amphibole. Silicate glasses with compositions between 57% and 78% SiO_2 have real parts of the refractive indices, n, at visible wavelengths which vary inversely from 1.56 at 57% SiO_2 to 1.48 at 77% SiO_2 [26]. Therefore we estimate the real part of the refractive index, n, of our Mount St. Helens sample to be between those values. Based on absorption measurements on ashes from the May 18, 1980, Mount St. Helens eruption performed by Patterson [27], we estimate the imaginary part of the refractive index at red wavelengths to be 0.0018.

1.4.4 Size distributions

Apart from shape and composition, size is a key property in determining the light scattering properties of small particles. For the samples of randomly oriented particles in the database, projected-surface-area distributions have been measured to determine the sizes of the particles using a Fritsch laser particle sizer [28] based on diffraction. This particle sizer provides projected surface-area equivalent distributions $s(r)$, where r is the radius of a projected-surface-area equivalent

Table 1.2. Overview of properties of the aerosol samples used in this chapter.

Sample	r_{eff} (μm)	v_{eff}	$Re(m)$	Color
Mount St. Helens	4.1	9.5	1.5–1.6	light brown
Feldspar	1.0	1.0	1.5–1.6	light pink
Red clay	1.5	1.6	1.5–1.7	red brown
Quartz	2.3	2.3	1.54	white
Pinatubo volcanic ash	3.0	12.3	1.5–1.6	light grey
Loess	3.9	2.6	1.5–1.7	yellow brown
Lokon volcanic ash	7.1	2.6	1.5–1.6	dark brown
Sahara sand	8.2	4.0	1.5–1.7	yellow brown
Fly-ash	3.7	10.9	1.5–1.7	grey brown
Olivine L	3.8	3.7	1.62	white
Olivine M	2.6	5.0	1.62	white
Olivine S	1.3	1.8	1.62	white
Hematite	0.4	0.6	3.0	dark red

sphere. Other distributions can be derived from these projected-surface-area distributions. Number distributions, $n(r)$, are often required for numerical applications and volume distributions $v(r)$, are common in literature about atmospheric particles. To plot these three size distributions in a convenient way a change of variables from r to $\log r$ is often performed, so that three different types of size distributions are formed. In the database as well as in this paper $\log r$ always refers to r expressed in micrometers.

To characterize the sizes of the particles of a sample with a few parameters we may use the effective radius r_{eff} and effective variance v_{eff} defined as follows [18]:

$$r_{\text{eff}} = \frac{\int_0^\infty r\pi r^2 n(r)dr}{\int_0^\infty \pi r^2 n(r)dr}, \tag{1.4}$$

$$v_{\text{eff}} = \frac{\int_0^\infty (r - r_{\text{eff}})^2 \pi r^2 n(r)dr}{r_{\text{eff}}^2 \int_0^\infty \pi r^2 n(r)dr}, \tag{1.5}$$

where $n(r)dr$ is the fraction of the total number of projected surface equivalent spheres with radii in the size range $[r, r+dr]$ per unit volume of space. In Table 1.2 we present the r_{eff} and v_{eff} of all samples mentioned in this chapter.

In Fig. 1.6, we plot examples of the above mentioned size distributions for the Mount St. Helens sample. In this figure, $S(\log r)d(\log r)$ is the relative contribution of projected surface equivalent spheres with radii in the size range from $\log\ r$ to $\log\ r + d(\log r)$ to the total projected-surface-equivalent spheres with

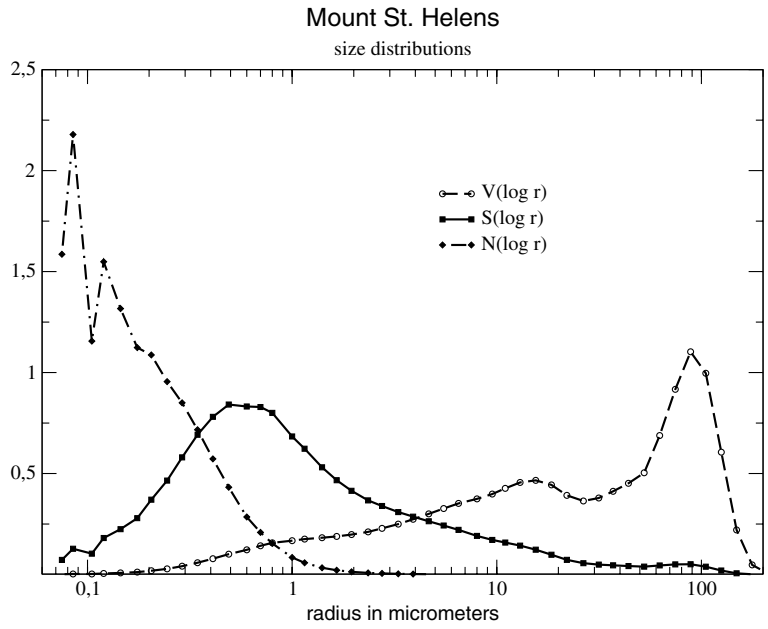

Fig. 1.6. Measured normalized projected-surface distribution $S(\log r)$, and corresponding normalized number $N(\log r)$, and volume distributions $V(\log r)$ of the Mount St. Helens volcanic ash sample. The distributions are plotted as functions of r in a logarithmic scale, where the radius of the projected surface-area-equivalent sphere is expressed in micrometers. The area under each curve equals unity.

radii in the size range from $\log r$ to $\log r + d(\log r)$ to the total projected area of all particles per unit volume. $N(\log r)d(\log r)$ and $V(\log r)d(\log r)$ are the relative number and volume of projected-surface-equivalent spheres with radii in the interval $d\log(r)$. These distributions were deduced from $S(\log r)$.

In the database, we present tables with the normalized size distributions corresponding to the size curves presented in Fig. 1.6 for the Mount St. Helens sample as an example. The number distribution $N(\log r)$, the projected-surface-area distribution $S(\log r)$, and the volume distribution $V(\log r)$ may be converted to, respectively, the number distribution $n(r)$, the projected-surface-area distribution $s(r)$, and the volume distribution $v(r)$, as suggested in the database (see also [9]). We note that some size distribution tables have been published in [29], but there $V(\log r)$ was normalized to 100% instead of 1.

1.4.5 Measurements

For the majority of samples, the measurements have been performed at two different wavelengths: 441.6 and 632.8 nm. In some cases, however, only measurements at one wavelength are available. The main reason for this is that sometimes only a small amount of sample is available for the measurements.

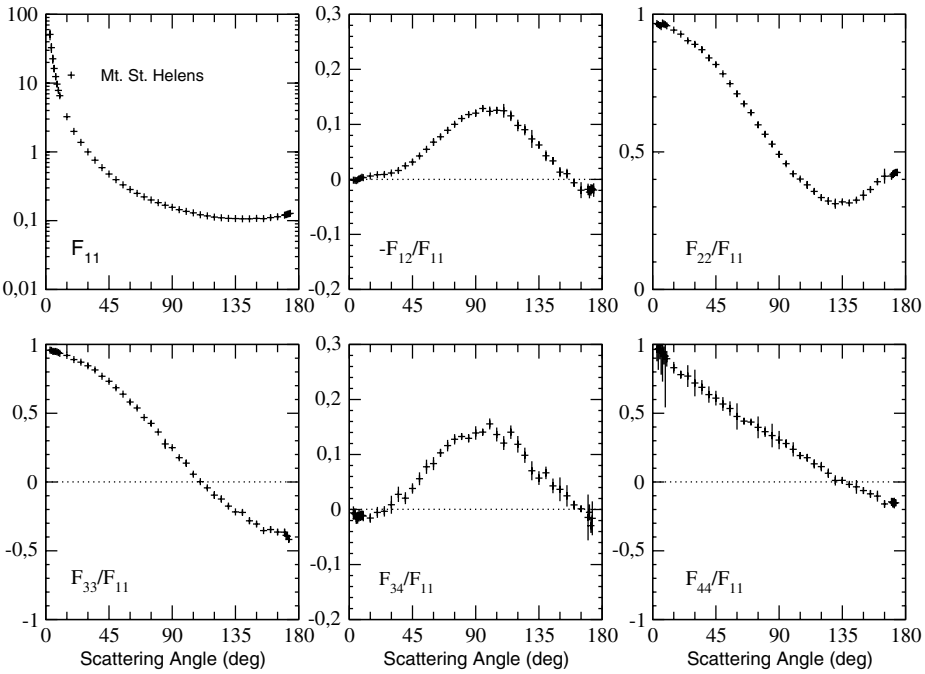

Fig. 1.7. Measured scattering matrix elements as functions of the scattering angle at 632.8 nm for the Mount St. Helens sample. Errors are indicated by bars or are within the size of the symbols.

That is the case for instance for the Mount St. Helens sample. In Fig. 1.7 we present the complete measured scattering matrix as a function of the scattering angle at 632.8 nm, for the Mount St. Helens sample. In the database we also present tables of the scattering matrix elements as they are given in Table 1.3 for the Mount St. Helens sample, corresponding to the curves presented in Fig. 1.7. The measurements are given together with their experimental errors.

All $F_{11}(\theta)$ functions are plotted on a logarithmic scale and are normalized to 1 at 30 degrees. The other elements are shown relative to the corresponding $F_{11}(\theta)$. In all cases we refrained from plotting the four element ratios $F_{13}(\theta)$, $F_{14}(\theta)$, $F_{23}(\theta)$, and $F_{24}(\theta)$, since we verified experimentally that these ratios do not differ from zero more than the error bars. Measurements were performed at intervals of 5 degrees for θ in the range 5 degrees-170 degrees and at intervals of 1 degree for θ from 170 degrees to 173 degrees. The reliability of all measured scattering matrices presented in the database is investigated by applying the Cloude (coherency) matrix as described by [12].

Table 1.3. Measured scattering matrix elements as functions of scattering angle (in degrees), corresponding to curves presented in Fig. 1.7 for the Mount St. Helens sample at 632.8 nm. The calculated uncertainties in the measured values are also given.

θ	F_{11}	$-F_{12}/F_{11}$	F_{22}/F_{11}	F_{33}/F_{11}	F_{34}/F_{11}	F_{44}/F_{11}
3	51.060 ± 9.091	-0.001 ± 0.001	0.967 ± 0.003	0.958 ± 0.002	-0.006 ± 0.012	0.964 ± 0.086
4	32.829 ± 5.377	-0.002 ± 0.001	0.963 ± 0.002	0.957 ± 0.006	-0.008 ± 0.010	0.970 ± 0.155
5	22.560 ± 3.426	-0.002 ± 0.002	0.959 ± 0.004	0.950 ± 0.008	-0.017 ± 0.010	0.958 ± 0.066
6	16.321 ± 2.056	-0.001 ± 0.001	0.955 ± 0.004	0.949 ± 0.016	-0.015 ± 0.011	0.946 ± 0.166
7	12.425 ± 1.409	0.001 ± 0.001	0.968 ± 0.002	0.949 ± 0.007	-0.011 ± 0.010	0.943 ± 0.213
8	9.675 ± 0.908	0.002 ± 0.003	0.965 ± 0.004	0.946 ± 0.003	-0.012 ± 0.009	0.920 ± 0.066
9	7.831 ± 0.541	0.004 ± 0.001	0.963 ± 0.002	0.941 ± 0.010	-0.011 ± 0.009	0.915 ± 0.373
10	6.555 ± 0.450	0.003 ± 0.002	0.958 ± 0.003	0.935 ± 0.007	-0.012 ± 0.009	0.896 ± 0.057
15	3.245 ± 0.091	0.006 ± 0.001	0.943 ± 0.004	0.920 ± 0.007	-0.016 ± 0.009	0.831 ± 0.042
20	1.987 ± 0.017	0.008 ± 0.003	0.928 ± 0.004	0.890 ± 0.006	-0.005 ± 0.010	0.781 ± 0.030
25	1.373 ± 0.011	0.009 ± 0.004	0.904 ± 0.007	0.871 ± 0.010	-0.003 ± 0.010	0.770 ± 0.079
30	1.000 ± 0.000	0.012 ± 0.003	0.891 ± 0.010	0.845 ± 0.016	0.009 ± 0.016	0.720 ± 0.097
35	0.757 ± 0.007	0.016 ± 0.005	0.872 ± 0.011	0.815 ± 0.012	0.028 ± 0.014	0.688 ± 0.053
40	0.590 ± 0.008	0.025 ± 0.005	0.842 ± 0.011	0.769 ± 0.007	0.021 ± 0.011	0.636 ± 0.060
45	0.477 ± 0.007	0.032 ± 0.005	0.818 ± 0.007	0.732 ± 0.009	0.038 ± 0.009	0.610 ± 0.054
50	0.395 ± 0.004	0.043 ± 0.003	0.784 ± 0.004	0.685 ± 0.012	0.056 ± 0.012	0.567 ± 0.050
55	0.331 ± 0.006	0.055 ± 0.003	0.748 ± 0.005	0.639 ± 0.002	0.078 ± 0.013	0.534 ± 0.052
60	0.284 ± 0.006	0.068 ± 0.007	0.711 ± 0.011	0.581 ± 0.015	0.083 ± 0.012	0.476 ± 0.096
65	0.249 ± 0.006	0.078 ± 0.005	0.675 ± 0.008	0.538 ± 0.011	0.103 ± 0.007	0.442 ± 0.022
70	0.222 ± 0.004	0.089 ± 0.006	0.643 ± 0.009	0.469 ± 0.004	0.116 ± 0.010	0.435 ± 0.017
75	0.200 ± 0.006	0.100 ± 0.004	0.598 ± 0.011	0.426 ± 0.018	0.128 ± 0.009	0.397 ± 0.079
80	0.183 ± 0.005	0.111 ± 0.005	0.564 ± 0.010	0.363 ± 0.007	0.133 ± 0.005	0.366 ± 0.039
85	0.168 ± 0.005	0.118 ± 0.005	0.528 ± 0.011	0.277 ± 0.037	0.129 ± 0.008	0.338 ± 0.086
90	0.156 ± 0.004	0.120 ± 0.006	0.491 ± 0.011	0.250 ± 0.010	0.139 ± 0.012	0.305 ± 0.067
95	0.145 ± 0.005	0.129 ± 0.006	0.457 ± 0.008	0.177 ± 0.012	0.141 ± 0.006	0.279 ± 0.033
100	0.136 ± 0.005	0.124 ± 0.009	0.420 ± 0.010	0.137 ± 0.025	0.156 ± 0.010	0.238 ± 0.052
105	0.130 ± 0.004	0.126 ± 0.006	0.401 ± 0.007	0.057 ± 0.016	0.136 ± 0.013	0.192 ± 0.026
110	0.122 ± 0.004	0.125 ± 0.013	0.380 ± 0.014	0.002 ± 0.013	0.121 ± 0.013	0.176 ± 0.029
115	0.118 ± 0.004	0.115 ± 0.010	0.356 ± 0.011	-0.043 ± 0.016	0.141 ± 0.012	0.132 ± 0.034
120	0.113 ± 0.005	0.098 ± 0.011	0.334 ± 0.011	-0.095 ± 0.027	0.119 ± 0.015	0.112 ± 0.034
125	0.110 ± 0.003	0.090 ± 0.010	0.322 ± 0.013	-0.124 ± 0.023	0.099 ± 0.014	0.063 ± 0.035
130	0.108 ± 0.002	0.073 ± 0.016	0.312 ± 0.019	-0.176 ± 0.019	0.070 ± 0.017	0.012 ± 0.038
135	0.107 ± 0.002	0.063 ± 0.007	0.318 ± 0.008	-0.217 ± 0.003	0.057 ± 0.013	0.012 ± 0.024
140	0.106 ± 0.002	0.043 ± 0.010	0.315 ± 0.011	-0.221 ± 0.019	0.067 ± 0.011	-0.018 ± 0.020
145	0.107 ± 0.003	0.034 ± 0.007	0.325 ± 0.008	-0.282 ± 0.022	0.043 ± 0.013	-0.035 ± 0.050
150	0.108 ± 0.004	0.013 ± 0.009	0.342 ± 0.019	-0.306 ± 0.020	0.037 ± 0.022	-0.062 ± 0.023
155	0.107 ± 0.005	0.010 ± 0.009	0.363 ± 0.010	-0.353 ± 0.008	0.025 ± 0.019	-0.086 ± 0.028
160	0.111 ± 0.008	-0.006 ± 0.008	0.392 ± 0.012	-0.346 ± 0.024	0.008 ± 0.008	-0.103 ± 0.040
165	0.114 ± 0.009	-0.020 ± 0.015	0.412 ± 0.027	-0.364 ± 0.022	0.001 ± 0.006	-0.160 ± 0.026
170	0.120 ± 0.009	-0.018 ± 0.010	0.412 ± 0.012	-0.365 ± 0.024	-0.014 ± 0.042	-0.144 ± 0.029
171	0.122 ± 0.010	-0.023 ± 0.011	0.418 ± 0.014	-0.388 ± 0.011	-0.005 ± 0.014	-0.151 ± 0.035
172	0.124 ± 0.011	-0.019 ± 0.010	0.423 ± 0.013	-0.394 ± 0.007	-0.029 ± 0.013	-0.153 ± 0.039
173	0.126 ± 0.011	-0.017 ± 0.008	0.425 ± 0.012	-0.418 ± 0.021	-0.016 ± 0.031	-0.152 ± 0.025

1.5 Applications and examples

From the experimental data it has become clear that particle shape is highly important in determining the overall light scattering behavior of these samples. This has important implications. For example, it confirms that the use of Mie [17] calculations to interpret data involving light scattering by irregular particles in such different media as comets, circumstellar and interstellar matter, or the

Earth atmosphere, is often unlikely to give accurate results (see, for example, [30–34]). In this section we present first a summary of experimental results that show us the typical scattering behavior of irregular compact mineral particles with moderate refractive indices. Also the refractive indices and sizes of the particles play a role in determining the scattering behavior of irregular mineral particles. Some of our experiments have been devoted to distinguishing the size effect on the scattering behavior from the shape and color effects and vice versa. In the last three subsections of this chapter we give a summary of those experiments. All measurements presented in this chapter are included in the *Amsterdam Light Scattering Database*.

1.5.1 Mineral aerosol particles with moderate refractive indices

Volten *et al.* [3] presented measured scattering matrices as functions of the scattering angle for seven distinct irregularly shaped mineral aerosol samples in random orientation. The measurements were performed in the scattering angle range 5–173 degrees and at wavelengths of 441.6 nm and 632.8 nm. The aerosol samples, i.e., feldspar, red clay, quartz, loess, Pinatubo and Lokon volcanic ash, and Sahara sand, represent a broad range in size distributions with effective radii varying between 1.0 and 8.2 μm. In Table 1.2 we present the r_{eff} and v_{eff}

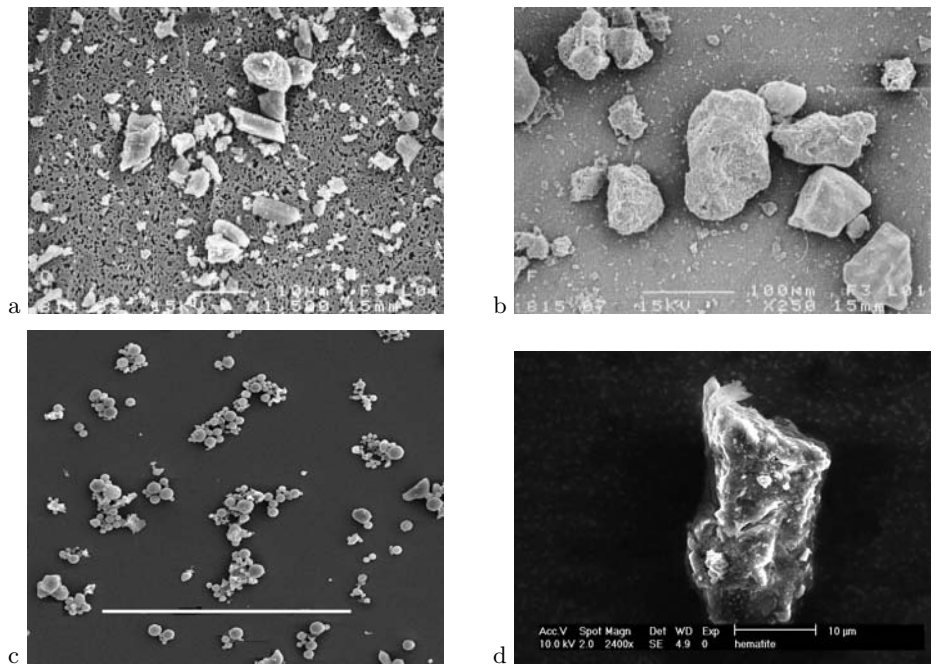

Fig. 1.8. SEM photographs of (a) feldspar, (b) Sahara sand, (c) fly-ash, and (d) hematite White bars in photographs (a) and (d), denote 10 μm, and 100 μm in (b) and (c).

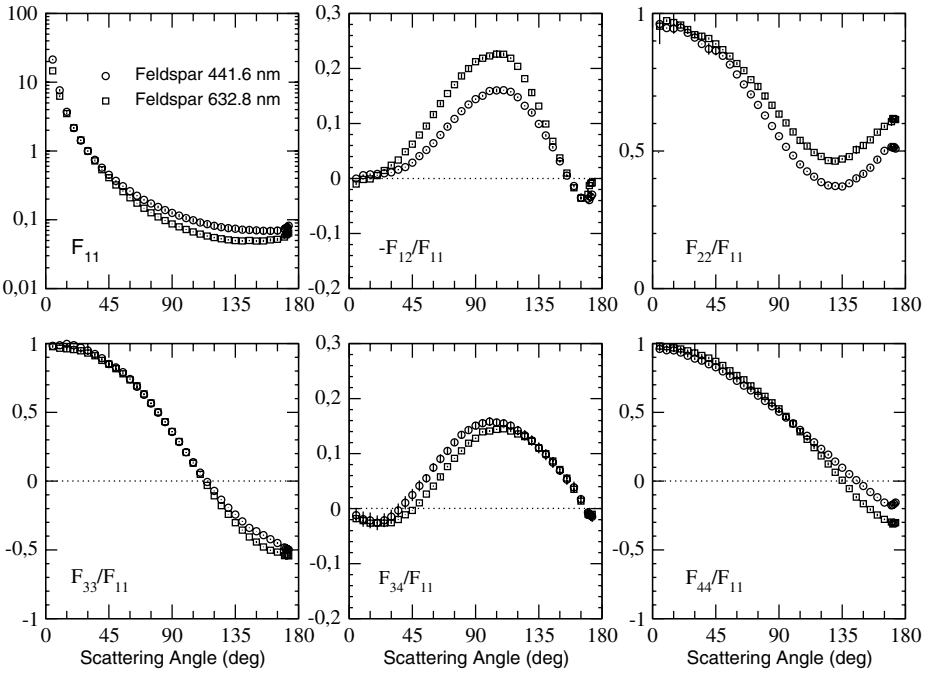

Fig. 1.9. Scattering matrix elements $F_{11}(\theta)$, normalized to 1 at 30 degrees, and element ratios $-F_{12}(\theta)/F_{11}(\theta)$, $F_{22}(\theta)/F_{11}(\theta)$, $F_{33}(\theta)/F_{11}(\theta)$, $F_{34}(\theta)/F_{11}(\theta)$, $F_{44}(\theta)/F_{11}(\theta)$ for feldspar. Circles denote the measurements at 441.6 nm, squares those at 632.8 nm. The measurements are presented together with their error bars.

of the seven samples. Moreover, all samples have moderate real parts of the refractive index ($1.5 \leq n \leq 1.7$) (see Table 1.2). The imaginary parts of the refractive index range between 0 and 10^{-3}. As examples we present in Figs. 1.9 and 1.10 the measured scattering matrix elements $F_{11}(\theta)$, as well as element ratios $-F_{12}(\theta)/F_{11}(\theta)$, $F_{22}(\theta)/F_{11}(\theta)$, $F_{33}(\theta)/F_{11}(\theta)$, $F_{34}(\theta)/F_{11}(\theta)$, $F_{44}(\theta)/F_{11}(\theta)$ for feldspar and Sahara sand, the two samples with the smallest and the largest effective radius, respectively. The measurements have been performed at 441.6 and 632.8 nm. In Fig 1.8 we present SEM pictures of these two samples (top left and right panels). As shown in those images, these type of particles have so-called compact irregular shapes.

In all cases the $F_{11}(\theta)$ curves measured are smooth functions of the scattering angle, showing a steep forward peak and virtually no structure at side-scattering and backscattering angles. The shapes are similar for all aerosol samples and are in agreement with the general behavior exhibited by nonspherical particles [35].

The measured element ratios $-F_{12}(\theta)/F_{11}(\theta)$, which in our case equal the degrees of linear polarization for unpolarized incident light, are all found to be similarly bell-shaped and show a negative branch at very large scattering angles. It is interesting to note that such negative polarization has also been observed in a variety of solar system bodies such as meteorites and comets.

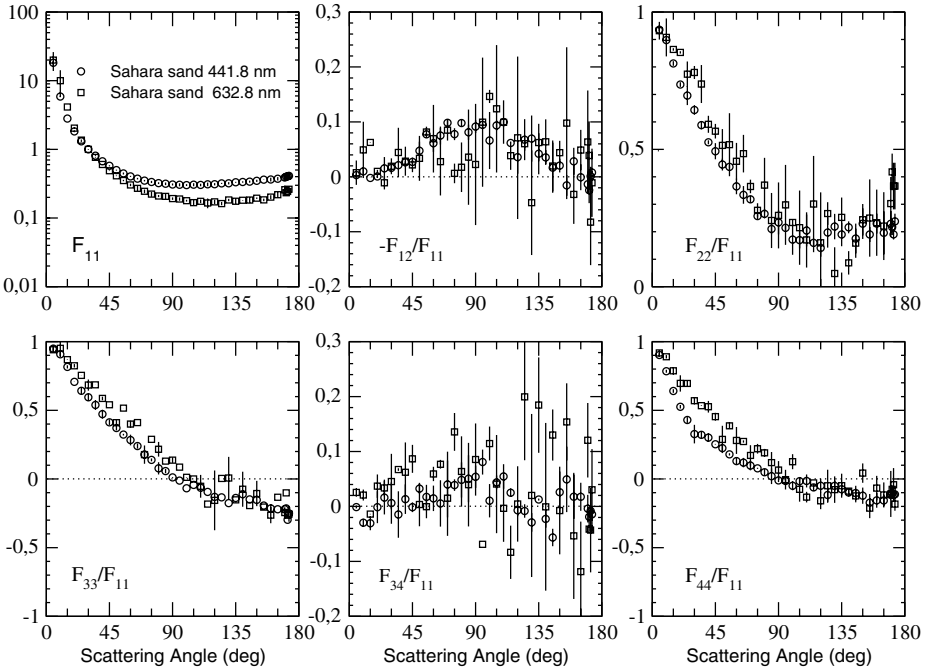

Fig. 1.10. Scattering matrix elements $F_{11}(\theta)$, normalized to 1 at 30 degrees, and element ratios $-F_{12}(\theta)/F_{11}(\theta)$, $F_{22}(\theta)/F_{11}(\theta)$, $F_{33}(\theta)/F_{11}(\theta)$, $F_{34}(\theta)/F_{11}(\theta)$, $F_{44}(\theta)/F_{11}(\theta)$ for Sahara sand. Circles denote the measurements at 441.6 nm, squares those at 632.8 nm. The measurements are presented together with their error bars.

The measured values of $F_{22}(\theta)/F_{11}(\theta)$ for all seven samples decrease smoothly from close to unity in the forward direction to a minimum in the side-scattering range and then increase again toward backscattering angles. Often, $F_{22}(\theta)/F_{11}(\theta)$ is used as a measure of nonsphericity, because this ratio equals unity at all scattering angles for homogeneous optically nonactive spheres. However, for irregular samples, this ratio is affected not only by irregularity but also by particle size and complex refractive index. For instance, the Sahara sand sample, which contains the largest particles, exhibits the deepest minimum, and the feldspar sample, which contains the smallest particles, displays the shallowest minimum of the seven studied samples.

Unlike for homogeneous optically nonactive spheres, $F_{44}(\theta)/F_{11}(\theta)$ and $F_{33}(\theta)/F_{11}(\theta)$ are substantially different from each other. Comparison of these two ratios shows that in most cases, $F_{33}(\theta)/F_{11}(\theta)$ is zero at a smaller scattering angle than $F_{44}(\theta)/F_{11}(\theta)$ and that $F_{33}(\theta)/F_{11}(\theta)$ exhibits in all cases a lower minimum than $F_{44}(\theta)/F_{11}(\theta)$.

The experimentally determined scattering functions and element ratios as functions of the scattering angle for the seven samples of irregular compact mineral particles with moderate refractive indices are generally found to agree well in their overall trends and behavior, independent of the wavelength considered. This similarity in the scattering behavior justified the construction of an av-

erage aerosol scattering matrix for irregular particles with moderate refractive indices. This average was obtained from the seven samples of irregularly shaped mineral particles: feldspar, red clay, quartz, Pinatubo volcanic ash, loess, Lokon volcanic ash, and Sahara sand at both wavelengths (441.6 and 632.8 nm). The aerosol average scattering matrix is displayed in Fig. 1.11 by circles. The area between the highest and lowest measured values are indicated in grey shading. The aerosol average scattering matrix was obtained as follows. First, the average aerosol phase function, $F_{11}(\theta)$ was determined by averaging the 14 phase functions at 441.6 and 632.8 nm presented by Volten *et al.* [3]. Since no scattering cross-sections are available, the phase functions were averaged giving them equal weights. Thus, the normalization to unity at 30 degrees also holds for the average aerosol phase function. Second, each measured element ratio was multiplied with its corresponding normalized phase function. Third, for each pair of indices (i, j) the elements $F_{i,j}$ of the average aerosol scattering matrix were obtained by averaging the 14 corresponding elements. Finally, division by the average aerosol phase function yielded the element ratios of the average aerosol scattering matrix. The resulting average matrix satisfies the Cloude test at each measured scattering angle. The average aerosol scattering matrix may be used for the interpretation of, for example, remote sensing results of the Earth at-

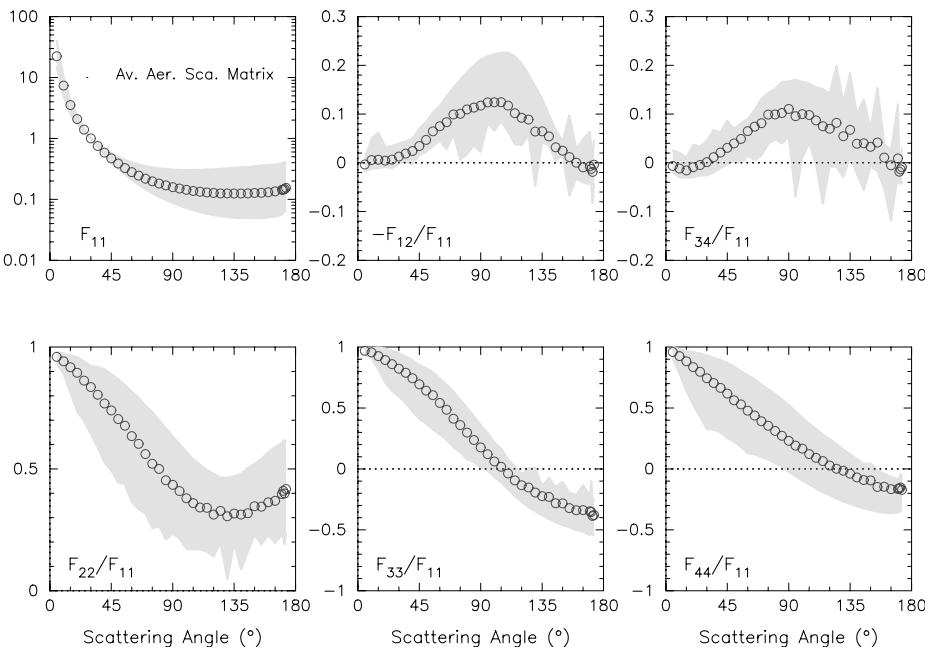

Fig. 1.11. Average aerosol scattering matrix element $F_{11}(\theta)$, normalized to 1 at 30 degrees, and element ratios $-F_{12}(\theta)/F_{11}(\theta)$, $F_{22}(\theta)/F_{11}(\theta)$, $F_{33}(\theta)/F_{11}(\theta)$, $F_{34}(\theta)/F_{11}(\theta)$, $F_{44}(\theta)/F_{11}(\theta)$ averaged over all measurements, i.e., for all aerosol samples at both wavelengths (circles). The domains occupied by the measurements presented here are indicated in grey shading.

mosphere when it is not *a priori* known what is the composition or size of the irregular particles (e.g. desert dust particles) [34].

Expanding on this method, we also devised an average volcanic ash scattering matrix, using scattering matrix elements as functions of the scattering angle of nine volcanic ash samples presented by Muñoz *et al.* [6,7], and Volten *et al.* [3] at a wavelength of 632.8 nm. The randomly oriented particles were taken from seven samples of volcanic ashes corresponding to four different volcanic eruptions: the May 18, 1980, Mount St. Helens eruption; the 1989–1990 Redoubt eruption; and the August 18, and September 17, 1992, Mount Spurr eruption plus measured scattering matrix elements presented by Volten *et al.* [3] for Lokon and Muñoz *et al.* [6] for Pinatubo volcanic ashes. The measured scattering matrix elements for the nine volcanic ash samples at 632.8 nm were found to be confined to rather limited domains when plotted as functions of the scattering angle following the general trends presented by irregular mineral particles. This similarity in the scattering behavior justified the construction of an average scattering matrix for volcanic ash particles as a function of the scattering angle.

In Fig. 1.12 we present the average volcanic scattering matrix element $F_{11}(\theta)$ and element ratios $-F_{12}(\theta)/F_{11}(\theta)$, $F_{22}(\theta)/F_{11}(\theta)$, $F_{33}(\theta)/F_{11}(\theta)$, $F_{34}(\theta)/F_{11}(\theta)$, and $F_{44}(\theta)/F_{11}(\theta)$ together with the domains occupied by the measurements used to obtain the average.

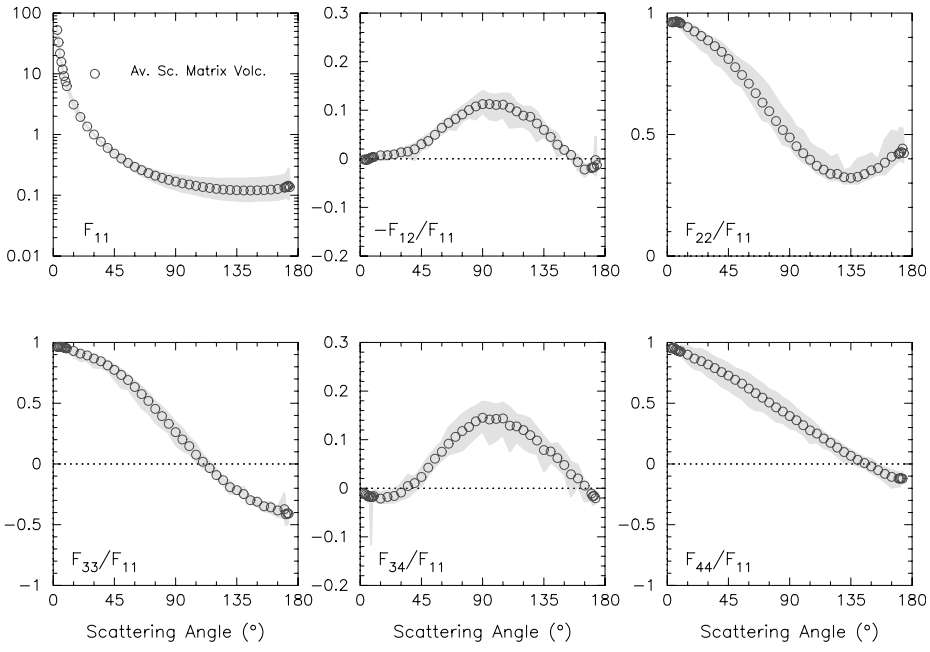

Fig. 1.12. Average volcanic scattering matrix element $F_{11}(\theta)$, and element ratios $-F_{12}(\theta)/F_{11}(\theta)$, $F_{22}(\theta)/F_{11}(\theta)$, $F_{33}(\theta)/F_{11}(\theta)$, $F_{34}(\theta)/F_{11}(\theta)$, $F_{44}(\theta)/F_{11}(\theta)$ (circles). The domains occupied by the measurements used to obtain the average are indicated in grey shading.

Although detailed differences are present in the measured scattering matrices used to construct the average volcanic scattering matrix and it is preferable to take such differences into account in applications involving light scattering by mineral particles, we consider it justified to construct the average for use, for example, in studies of climatic effects of a volcanic eruption when the actual properties of the volcanic ash are not known.

1.5.2 Shape effect

In section 1.5.1 we have considered particles with a more or less compact structure (see Figs 1.5 and 1.8) and moderate refractive indices. In this section we present results for a sample consisting of aggregates of nearly spherical particles: fly ash (see Fig. 1.8, bottom left panel). This sample originates from the inorganic fraction, mainly clays, of the combustion of powdered coal in an electric power plant. Its main components are SiO_2 and Al_2O_3. This sample has a r_{eff} of 3.7 μm and v_{eff} of 10.9 (see Table 1.2).

We present in Fig. 1.13 results of the experimentally determined scattering matrices of fly-ash at 441.6 and 632.8 nm [5]. The fly-ash sample shows quite

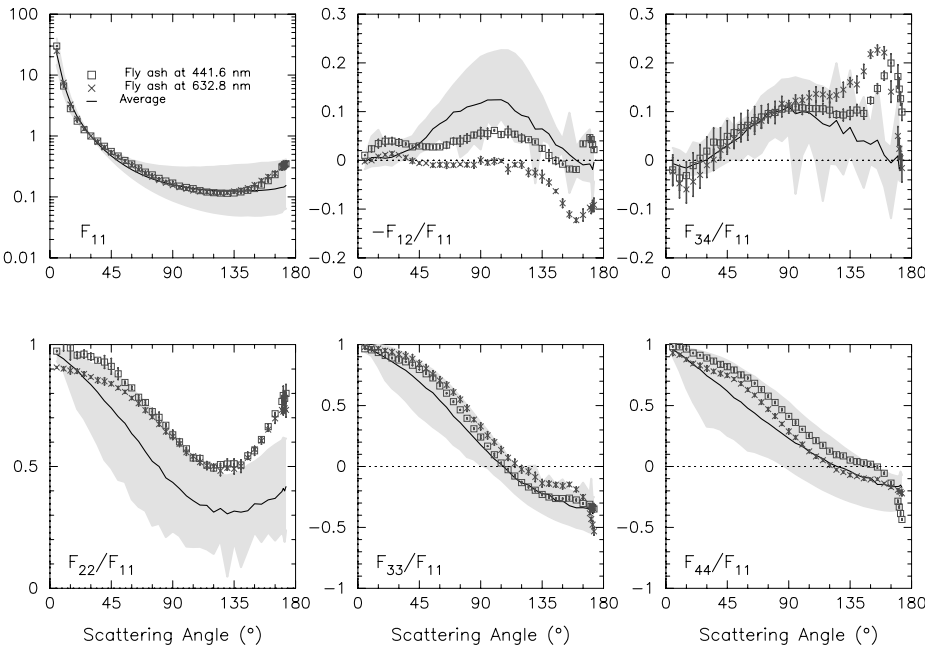

Fig. 1.13. Measured scattering matrix elements $F_{11}(\theta)$, and element ratios $-F_{12}(\theta)/F_{11}(\theta)$, $F_{22}(\theta)/F_{11}(\theta)$, $F_{33}(\theta)/F_{11}(\theta)$, $F_{34}(\theta)/F_{11}(\theta)$, $F_{44}(\theta)/F_{11}(\theta)$ for fly ash at 441.6 and 632.8 nm. The data are shown together with their error bars. In case no errors are shown they are smaller than the symbols. Solid lines correspond to the average aerosol scattering matrix as function of the scattering angle. The domains occupied by the measurements used to obtain the average are indicated in grey shading.

different scattering patterns when compared to the typical scattering behavior of irregular mineral particles with moderate real parts of the refractive index (see, for example [3, 4, 7, 35]). To illustrate this in Fig. 1.13 we show the measured scattering matrix elements for fly-ash together with the experimentally determined average aerosol scattering matrix for irregular compact mineral particles (see section 1.5.1 and [3]). For example, $F_{11}(\theta)$ shows a strong increase at backscattering angles. Furthermore the ratio $-F_{12}(\theta)/F_{11}(\theta)$ which in our case equals the degree of linear polarization for unpolarized incident light, does not show the bellshape presented by compact mineral particles. The degree of linear polarization at 632.8 nm is nearly zero at side-scattering angles and becomes negative at angles larger than about 130°. At 441.6 nm the behavior of $-F_{12}(\theta)/F_{11}(\theta)$ for fly-ash is positive at almost all scattering angles with a strong increase at backscattering positions. The ratio $F_{34}(\theta)/F_{11}(\theta)$ presents a negative branch at small scattering angles, and attains a maximum at about 160°. These matrix elements lie partly outside the domain of the average aerosol scattering matrix for compact irregular mineral particles. Since the main difference between the fly-ash sample and the mineral samples used to construct the average aerosol scattering matrix is related to the shape of its particles (see Table 1.2), we conclude that the characteristic scattering behavior presented by the fly-ash sample is due to the fact that the fly-ash consists of aggregates of more or less spherical particles.

1.5.3 Size effect

Crystalline Mg-rich olivine (forsterite) is one of the main components of cometary dust (see, for example, [36, 37]). We have experimentally obtained the complete scattering matrices (including polarization) as a function of the scattering angle of three Mg-rich olivine samples [5]. Here we present the measurements performed at 632.8 nm. The three samples have been obtained from the same bulk sample. They were prepared so that the measurements could be repeated for different size distributions, i.e., the three samples have the same compositions and shape of the particles, but each of them has a different size distribution. In this way we can distinguish the size effect on the scattering behavior from the composition and shape effects. The sample was ball milled and first sieved with a 125 μm sieve. The portion of the sample that passed through the sieve (particles smaller than 125 μm in diameter) was subsequently sieved in water through a 65 μm sieve. Again the smallest particles (smaller than 65 μm) were subsequently sieved through a 20 μm sieve. In such a way we produced the three olivine samples presented in this section; L ($20 \leq d \leq 65$ μm), M ($d \leq 65$ μm), and S ($d \leq 20$ μm), where d is the width of the sieving grid.

The measured projected-surface-area distributions of our samples are presented in Fig. 1.15. The calculated r_{eff} and v_{eff} of each sample are presented in Table 1.2. According to these measurements the sieving procedure works well for particles larger than about 1 μm. However, we did not succeed in removing all particles with diameters smaller than 20 μm from sample L. It seems like small

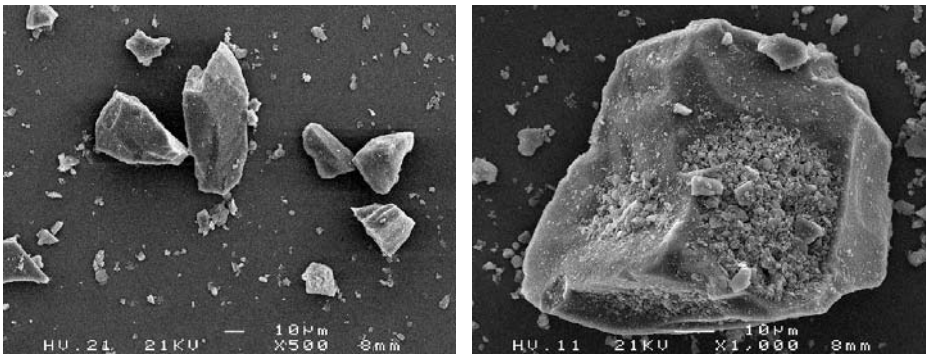

Fig. 1.14. Scanning electron micrograph of the olivine particles. The white bars denote 10 µm.

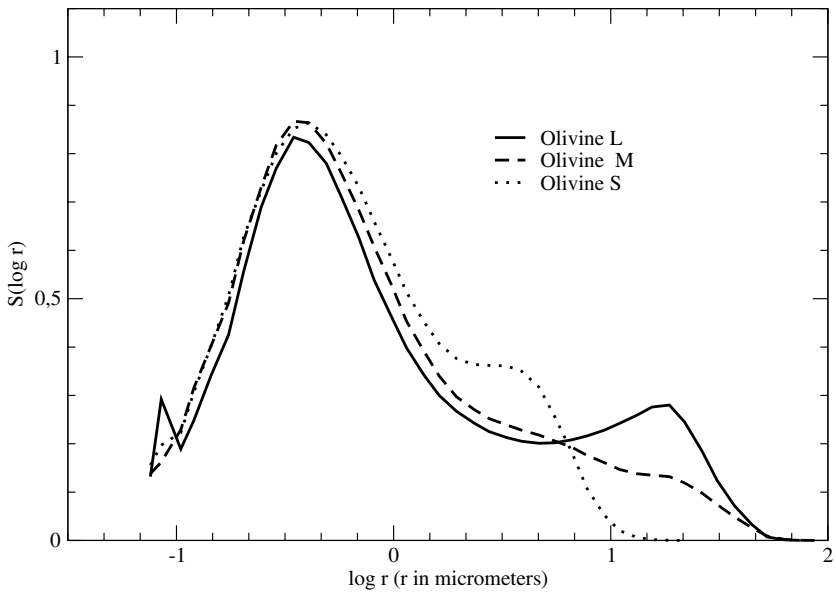

Fig. 1.15. Measured normalized projected-surface distributions $S(\log r)$ of the olivine samples L, M, and S. The distributions are plotted as functions of r in a logarithmic scale, where the radius of the projected surface-area-equivalent sphere is expressed in micrometers. The area under each curve equals unity.

particles remained stuck due to electrostatic forces, for example, on the surface of the larger particles (see Fig. 1.14 right panel).

The exact values of the refractive indices of our samples are unknown. According to the measured optical constants of different types of silicates published so far [38], we estimate the complex refractive index to be around 1.62–i0.00001 (see also Table 1.2).

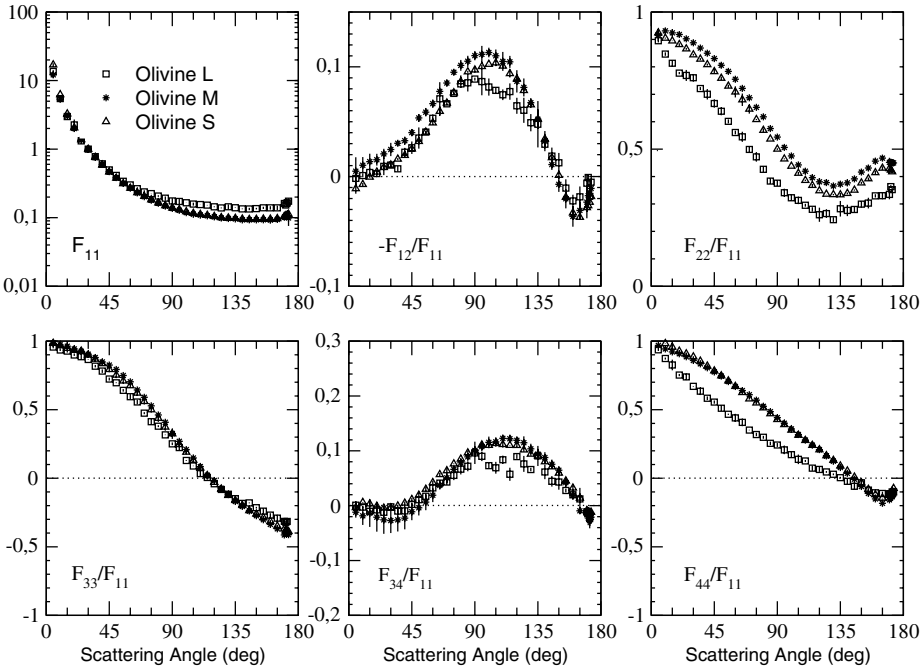

Fig. 1.16. Measured scattering matrix elements as functions of the scattering angle for olivine L (squares), M (stars), and S (triangles) at 632.8 nm. Errors are indicated by bars or are within the size of the symbols.

In Fig. 1.16, we present the complete scattering matrices for the olivine samples L (squares), M (stars), and S (triangles) at 632.8 nm, respectively. The scattering matrix elements for the three olivine samples are very similar to each other and follow the general trends presented by irregular compact mineral particles (see section 1.5.1). The measured phase functions are flat functions of the scattering angle with a strong forward peak and almost no structure at side and backscattering angles. The measured $F_{44}(\theta)/F_{11}(\theta)$ for our olivine irregular particles tends to be larger than $F_{33}(\theta)/F_{11}(\theta)$ for $\theta \geq 80$ degrees. Moreover, $F_{22}(\theta) \neq F_{11}(\theta)$ at all scattering angles, another indication of the nonsphericity of our particles since for spherical particles these to elements are equal to each other at all scattering angles. The measured $-F_{12}(\theta)/F_{11}(\theta)$ curves show the typical bell shape presented by irregular mineral particles.

Despite the high similarity of the scattering matrices for the three olivine samples, we can still see some differences. These differences must be due to the differences in the size distributions since the other physical parameters (i.e. refractive indices, and shapes) are very similar for the three samples. The measured $-F_{12}(\theta)/F_{11}(\theta)$ curves show the highest maximum values for olivine samples M and S, the sample with the smallest $S(\log r)$ beyond 10 micrometers. Moreover, the points for $F_{22}(\theta)/F_{11}(\theta)$ and $F_{44}(\theta)/F_{11}(\theta)$ for olivine samples M and S are practically on top of each other at all scattering angles. The measurements for

$F_{22}(\theta)/F_{11}(\theta)$ and $F_{44}(\theta)/F_{11}(\theta)$ for the olivine L, the sample with the highest $S(\log r)$ beyond 10 micrometers, presents the smallest values at almost all scattering angles.

1.5.4 Color effect

Hematite is believed to be an important component of Martian dust [39, 40] and in addition, it is an important constituent of terrestrial aerosols [41] and [42]. Hematite is a birefringent material with a large real and imaginary part of the refractive index in the visible part of the spectrum. The real part of the refractive index, n at 632.8 nm, has a value 2.9 for the extraordinary and 3.1 for the ordinary axis [41]. The imaginary part, k, ranges between 10^{-2} and 10^{-1} [41]. Our hematite sample has an r_{eff} of 0.4 μm and a v_{eff} of 0.6. In Fig. 1.8, we present a scanning electron microscope (SEM) picture of a hematite particle as an example of the shape of this type of particle. In that picture we can see that the hematite particles exhibit very irregular shapes with a layered structure (bottom right panel).

In Fig. 1.17 we show the measured scattering matrix elements as functions of the scattering angle for the hematite sample at 632.8 nm. As usual, the scattering function or phase function, $F_{11}(\theta)$, is shown on a logarithmic scale and is normalized to 1 at 30°. The experimental errors are indicated by error bars. When no error bar is shown, the value of the standard deviation of the mean value is smaller than the plotted symbol. The hematite sample shows quite different scattering patterns compared to the typical scattering behavior of irregular mineral particles with moderate real parts of the refractive index (see, for example, [3,4,7,35]). To illustrate this in Fig. 1.17 we show the measured scattering matrix elements for hematite [8] together with the experimentally determined average aerosol scattering matrix for irregular mineral particles (see section 1.5.1 and [3]).

In Fig. 1.17 we can see that the degree of linear polarization for incident unpolarized light as a function of the scattering angle (i.e. $-F_{12}(\theta)/F_{11}(\theta)$) of the hematite sample differs considerably from the average aerosol curve. It shows a rather low double maximum around 50 and 140 degrees. In contrast, the average aerosol degree of linear polarization shows a characteristic bell shape with a maximum around 90 degrees and a negative branch at large scattering angles. Moreover, the measured $F_{34}(\theta)/F_{11}(\theta)$ for the hematite sample is found to differ appreciably from the average aerosol curve for irregular mineral particles with moderate refractive indices. This ratio has negative values at all measured scattering angles for the hematite, whereas it is positive at almost all scattering angles for the average aerosol $F_{34}(\theta)/F_{11}(\theta)$. In addition, the measurements for the hematite sample show a bimodal function with a primary minimum around 60 degrees and a secondary minimum around 160 degrees.

Differences between the ratios $F_{33}(\theta)/F_{11}(\theta)$ and $F_{44}(\theta)/F_{11}(\theta)$ for hematite particles compared to irregular mineral particles are not so spectacular although they also lie out of the domains of the average aerosol curve at some measured scattering angles. The measured $F_{22}(\theta)/F_{11}(\theta)$ for the hematite sample shows

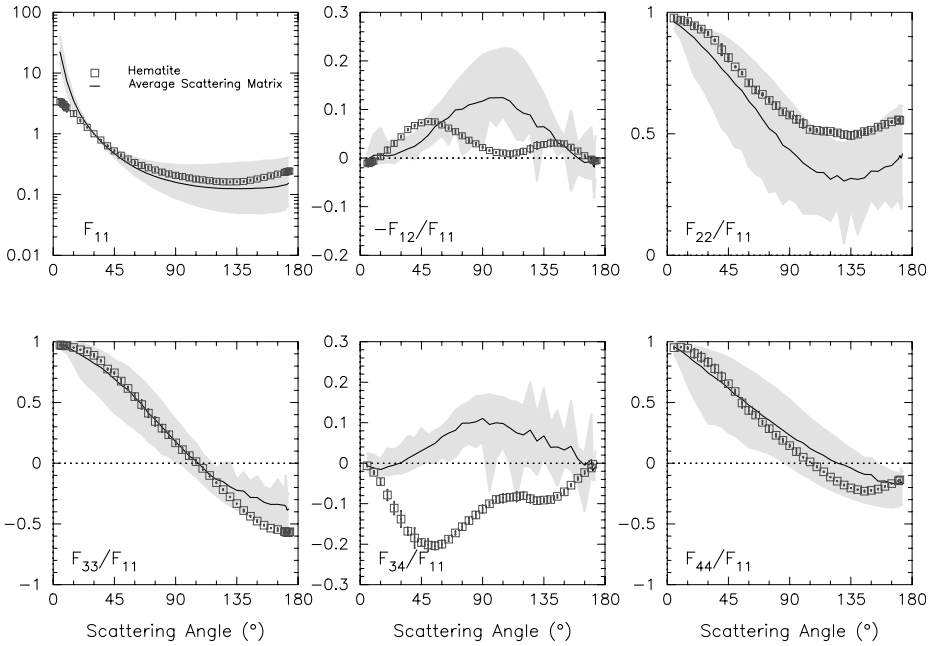

Fig. 1.17. Measured scattering matrix elements $F_{11}(\theta)$, and element ratios $-F_{12}(\theta)/F_{11}(\theta)$, $F_{22}(\theta)/F_{11}(\theta)$, $F_{33}(\theta)/F_{11}(\theta)$, $F_{34}(\theta)/F_{11}(\theta)$, $F_{44}(\theta)/F_{11}(\theta)$ for the hematite sample at 632.8 nm. The data are shown together with their error bars. When error is case no bar is shown then smaller than the symbol. Solid lines correspond to the average aerosol scattering matrix as function of the scattering angle. The domains occupied by the measurements used to obtain the average are indicated in grey shading.

the typical behavior for irregular mineral particles decreasing from almost 1 at angles close to the forward direction to a minimum and then increasing again at back-scattering angles. However, this ratio stays out of the domain of the average aerosol curve at a number of measured scattering angles.

The hematite scattering functions or phase functions, $F_{11}(\theta)$, range over little more than one order of magnitude for the measured angles. In contrast, the average aerosol scattering function ranges over more than two orders of magnitude for the angles covered in the measurements, being strongly peaked toward smaller angles. These differences in the forward scattering peaks are probably due to the differences in sizes between our hematite and the dust samples used to construct the average aerosol scattering matrix (see Table 1.2), since forward scattering peaks depend strongly on the sizes of the particles [31], [43].

Apart from the differences in the forward scattering peaks, we do not think the differences in size between the hematite, on the one hand, and the samples used to obtain the average aerosol scattering matrix, on the other, are strong enough to account for the significant differences observed in almost all scattering matrix elements as functions of the scattering angle (see, for example, [3, 5]).

As mentioned, all samples used to obtain the average aerosol scattering matrix have moderate real parts of the refractive index (see Table 1.2). In contrast, the hematite sample has very high real and imaginary parts of the refractive index. To this we attribute the main differences in scattering behavior of the hematite sample when compared with the average aerosol scattering matrix.

1.6 Conclusions

There are several ways in which the experimental data in the database can be useful. The data can be used in a direct manner, e.g. in comparisons with observations of light that has been scattered only once [4] or to assess results of numerical light scattering methods for nonspherical particles [3,21,44]. Also, the data may be used in an indirect manner. For example, if a method is applied to extrapolate the measured angular distributions of the scattering matrix elements to the full scattering angle range, including forward and backward scattering, the extrapolated functions may serve as input for multiple scattering computations [34,45–49]. Another way to employ the data in an indirect way, is to first find a fit to the experimental results, applying theoretical techniques using parameterized shape distributions. Then the parameterized shape distribution constrained by the fit can be used to obtain the scattering and absorption properties at other scattering angles, wavelengths and/or sizes where experiments are impossible or not practicable, e.g. in the middle and far infrared.

We like to note that a strong point of our measurements is that it provides *complete* scattering matrices as functions of the scattering angle and not one or two elements. This not only facilitates checking of systematic errors in the data, by, for example, applying 'eyeball' tests or the Cloude test (e.g. [12]), but also makes it possible to perform multiple scattering calculations including polarization. Another advantage is that complete scattering matrices may help in obtaining better constraints on the (model) shape parameters.

References

1. Hovenier, J. W., Measuring scattering matrices of small particles at optical wavelengths, in *Light Scattering by Nonspherical Particles,* edited by M. I. Mishchenko, J. W. Hovenier, and L. D. Travis, pp. 355–365, Academic Press, San Diego, CA, 2000.
2. Hovenier, J.W., Volten, H., Muñoz, O., van der Zande, W.J., and Waters, L.B.F.M. Laboratory study of scattering matrices for randomly oriented particles: potentials, problems, and perspectives, *J. Quant. Spectrosc. Radiat. Transfer*, *79–80*, 741, 2003.
3. Volten, H., O. Muñoz, E. Rol, J. F. de Haan, W. Vassen, J. W. Hovenier, K. Muinonen, and T. Nousianen, Scattering matrices of mineral aerosol particles at 441.6 nm and 632.8 nm, *J. Geophys. Res. 106*, 17375, 2001.
4. Muñoz, O., H. Volten, J. F. de Haan, W. Vassen, and J. W. Hovenier, Experimental determination of scattering matrices of olivine and Allende meteorite particles, *Astron. Astrophys., 360,* 777–788, 2000.

5. Muñoz, O., H. Volten, J. de Haan, W. Vassen, and J. W. Hovenier, Experimental determination of scattering matrices of randomly oriented fly ash and clay particles at 442 and 633 nm. *J. Geophys. Res.*, *106*, 22833–22844, 2001.
6. Muñoz O, Volten H, de Haan JF, Vassen W, Hovenier JW. Experimental determination of the phase function and degree of linear polarization of El Chichon and Pinatubo volcanic ashes. *J. Geophys. Res., 107*, 10.1029/2001JD000983, 2002.
7. Muñoz, O., H. Volten, J.W. Hovenier, B. Veihelmann, W.J. van der Zande, L.B.F.M. Waters, and W.I. Rose, Scattering matrices of volcanic ash particles of Mount St. Helens, Redoubt, and Mount Spurr volcanoes, *J. Geophys. Res.*, **109**, 10.1029, 2004JD004684, 2004.
8. Muñoz, O. H. Volten, J.W. Hovenier, M. Min, Y.G. Shkuratov, J.P. Jalava, W.J. van der Zande, and L.B.F.M. Waters, Experimental and computational study of light scattering by irregular particles with extreme refractive indices: hematite and rutile, *Astron. Astrophys.,* in press.
9. Volten, H., O. Muñoz, J. W. Hovenier, J. F. de Haan, W. Vassen, W.J. van der Zande, and L.B.F.M. Waters, WWW scattering matrix database for small mineral particles at 441.6 and 632.8 nm, *J. Quant. Spectrosc. Radiat. Transfer,* **90**, 191–206, 2005.
10. van de Hulst, H. C., *Light Scattering by Small Particles,* John Wiley, New York, 1957.
11. Hovenier, J.W., C. Van der Mee, and H. Domke, Transfer of polarized light in planetary atmospheres, basic concepts and practical methods, Kluwer, Dordrecht, 2004.
12. Hovenier, J.W., and van der Mee, C.V.M., Basic relationships for matrices describing scattering by small particles. In *Light Scattering by Non-Spherical Particles*, ed. M.I. Mishchenko, J.W. Hovenier, and L.D. Travis, Academic, San Diego, 61–85, 2000.
13. Hunt, A. J., and D. R. Huffman, A new polarization-modulation light scattering instrument, *Rev. Sci. Instrum.* 1753–1762, 1973.
14. Stammes, P., Light scattering properties of aerosols and the radiation inside a planetary atmosphere, Ph.D. thesis, Free University, Amsterdam, Netherlands, 1989.
15. Kuik, F., P. Stammes, and J. W. Hovenier, Experimental determination of scattering matrices of water droplets and quartz particles, *Appl. Opt., 30*, 4872–4881, 1991.
16. Kuik, F., Single scattering of light by ensembles of particles with various shapes, Ph.D. thesis, Free University, Amsterdam, Netherlands, 1992.
17. Mie, G., *Beitrage zur Optik Trüber Medien, Speziell Kolloidaler Metalllösungen*, *Ann. Phys., 25,* 337, 1908.
18. Hansen, J. E., and L. D. Travis, Light scattering in planetary atmospheres, *Space Sci. Rev. 16*, 527–610, 1974.
19. Kiphardt, M.M.B., Experimental determination of scattering matrices of ice crystals, Graduation report, Department of Physics and Astronomy, Free University, Amsterdam, 1993.
20. Warren, J.L., Zolensky, M.E., Thomas, K., Dodson, A.L., Watts, L.A., and Wentworth, S. Cosmic Dust Catalog 15. NASA, Houston, 1997.
21. Nousiainen, T., Muinonen, K., and Räisänen, P. Scattering of light by large Saharan dust particles in a modified ray-optics approximation. *J. Geophys. Res.,* 108, 10.1029/2001JD001277, 2003.
22. Hill, S.C., Hill, A.C., Barber, P.W. Light scattering by size/shape distributions of soil particles and spheroids. *Appl. Opt. 23*, 1025–1031, 1984.

23. Jalava, J.P., Taavitsainen, V.M., Lamberg, L., and Haario, H. Determination of particle and crystal size distribution from turbidity spectrum of TiO_2 pigment by means of T-matrix. *J. Quant. Spectrosc. Radiat. Transfer, 60*, 399–409, 1998.
24. Koren, I., Ganor, E., and Joseph, J.H. On the relation between size and shape of desert dust aerosol. *J. Geophys. Res., 106*, 18,047–18,054, 2001.
25. Riley, C., Rose, W.I., and Bluth, G.J.S. Quantitative shape measurements of distal volcanic ash. *J. Geophys. Res., 108*, B10, ECV 8-1, 2003.
26. Williams, H., F.J. Turner, and C.M. Gilbert, *Petrography*, W.H. Freeman, San Francisco (ISBN 0-7167-1376-4), 1982.
27. Patterson, E. M., Measurements of the imaginary part of the refractive index between 300 and 700 nanometers for Mount St. Helens ash, *Science, 211,* 836–838, 1981.
28. Konert, M., and J. Vandenberghe, Comparison of laser grain size analysis with pipette and sieve analysis: a solution for the underestimation of the clay fraction, *Sedimentology, 44,* 523–535, 1997.
29. Volten, H. Light scattering by small planetary particles: an experimental study. Ph.D. thesis, Free University, Amsterdam, 2001.
30. Krotkov, N.A., Flittner, D.E., Krueger, *et al. J. Quant. Spec. Rad. Transfer, 63*, 613, 1999.
31. Mishchenko, M. I., J. W. Hovenier, and L. D. Travis (Eds), *Light Scattering by Nonspherical Particles,* Academic Press, San Diego, CA, 2000a.
32. Dubovik, O., Holben, B. N., Lapyonok, T., Sinyuk, A., Mishchenko, M. I., Yang, P., and Slutsker, I. Non-spherical aerosol retrieval method employing light scattering by spheroids, *Geophys. Res. Lett. 29*, 10, 54-1. ID 1415, 2002.
33. Veihelmann, B., Volten, H., and van der Zande, W.J., Simulations of light reflected by an atmosphere containing irregularly shaped mineral aerosol over the ocean. *Geophys. Res. Lett. 31*, 10.1029/2003GL018229, 2004.
34. Herman, M., J.-L.Deuzé, A. Marchand, B. Roger, and P. Lallart, Aerosol remote sensing from POLDER/ADEOS over the ocean: improved retrieval using a nonspherical particle model. *J. Geophys. Res. 110*, D10S02, 2005.
35. Mishchenko, M.I., Wiscombe, W.J., Hovenier, J.W., and Travis, L.D. Overview of scattering by nonspherical particles, in *Light Scattering by Nonspherical Particles,* edited by M. I. Mishchenko, J. W. Hovenier, and L. D. Travis, pp. 29–60, Academic Press, San Diego, CA, 2000b.
36. Hanner, M.S., Lynch, D.K., and Russell, R.W, The 8-13 micron spectra of comets and the composition of silicate grains, *Astrophys. J., 425*, 274–285, 1994.
37. Colangeli, L., Mennella, V., Di Marino, C., Rotundi, A., and Bussoletti, E., Simulation of the cometary 10μm band by means of laboratory results on silicate grains, *Astron. Astrophys., 293*, 927–934, 1995.
38. Jäger, C., Vladimir B. Il'in, T. Henning, H. Mutschke, D. Fabian, D.A. Semenov, and N. Voshchinnikov, A database of optical constants of cosmic dust analogs. *J. Quant. Spec. Rad. Transfer, 79-80*, 765–774, 2003.
39. Morris R.V., and Lauer, J.V., Matrix effects for reflectivity spectra of dispersed nanophase (superparamagnetic) hematite with application to Martian spectral data, *J. Geophys. Res., 94*, 5101–5109, 1990.
40. Banin, A., Ben-Shlomo, T., Margulies, L., Blake, D. F., Mancinelli, R. L., and Gehring, A. U., The nanosphere iron mineral(s) in Mars soil *J. Geophys. Res., 98*, 20,831–20,853, 1993.

41. Sokolik, I.N., and Toon, O.B. Incorporation of mineralogical composition into models of the radiative properties of mineral aerosol from UV to IR wavelengths 1999, *J. Geophys. Res., 104*, 9423–9444, 1999.
42. Höller, R., Ito, K., Tohno, S., and Kasara, M., Wavelength-dependent aerosol single-scattering albedo: measurements and model calculations for a coastal site near the Sea of Japan during ACE-Asia, *J. Geophys. Res., 108*, D23, 8648, 2003.
43. Mishchenko, M.I., Travis, L.D., Kahn, R.A., and West, R.A., Modelling phase functions for dustlike tropospheric aerosols using a shape mixture of randomly oriented polydisperse spheroids, J. Geophys. Res., *102*, No. D14, 16831–16847, 1997.
44. Kahnert, M., Nousiainen, T., and Veihelman, B., Spherical and spheroidal model particles as an error source in aerosol climate forcing and radiance computations: A case study for feldspar aerosols. *J. Geophys. Res., 110*, D18, CiteID D18S13, 2005.
45. Veihelmann, B., Volten, H., and van der Zande, W.J. Simulations of light reflected by an atmosphere containing irregularly shaped mineral aerosol over the ocean. *Geophys. Res. Lett., 31*, 10.1029/2003GL018229, 2004.
46. Moreno, F., Muñoz, O., Lopez-Moreno, J.J., Molina, A., Ortiz, J.L. A Monte Carlo code to compute energy fluxes in cometary nuclei. *Icarus, 156*, 474–484, 2002.
47. Braak CJ, de Haan JF, van der Mee CVM, Hovenier JW, Travis LD. Parameterized scattering matrices for small particles in planetary atmospheres. *J. Quant. Spectrosc. Radiat. Transfer,* 69, 585-604, 2001.
48. Liu, L., Mishchenko, M.I., Hovenier, J.W., Volten, H., and Muñoz, O. Scattering matrix of quartz aerosols: comparison and combination of laboratory and Lorenz-Mie results. *J. Quant. Spectrosc. Radiat. Transfer, 79-80*, 911–920, 2003.
49. Mishchenko, M.I., Geogdzhaev, I., Liu, L., Ogren, A., Lacis, A., Rossow, W., Hovenier, J.W., Volten, H., and Muñoz, O. Aerosol retrievals from AVHRR radiances: effects of particle nonsphericity and absorption and an updated long-term global climatology of aerosol properties. *J. Quant. Spectrosc. Radiat. Transfer, 79-80*, 953–972, 2003.

2 Light scattering and absorption by nonspherical ice crystals

Ping Yang and Kuo-Nan Liou

2.1 Introduction

The majority of ice crystals in the atmosphere exist in cirrus clouds, clouds that normally reside in the upper troposphere in midlatitudes. In the tropics, ice clouds associated with deep cumulus convections (Houze, 1993) can extend to the lower stratosphere. Ice crystals have also been frequently observed in the polar regions because of low temperatures. The global cirrus cover has been estimated to be about 20% to 25%, but recent analysis using the 15-μm CO_2 satellite channels has shown that their occurrence frequency can be larger than 50% in the tropics (Wylie *et al.*, 1994). The inclusion of the 1.375-μm water vapor absorption channel (Gao and Kaufman, 1995) in the recent Moderate Resolution Imaging Spectroradiometer (MODIS) instrument on Terra and Acqua satellite platforms (King *et al.* 2003) has offered an unprecedented opportunity to detect optically thin cirrus. However, many thin and subvisual cirrus clouds could have been missed from the implementation of various past and current passive satellite detection techniques.

From analysis of the MODIS images acquired from the visible and 1.375-μm channels, it has been shown that most clear-sky pixels identified by the visible channels actually contain thin cirrus (Roskovensky and Liou, 2003; Dessler and Yang, 2003; Meyer *et al.*, 2004). Because of their high location in the atmosphere and the complex microphysical properties of ice crystals within them, cirrus clouds differ significantly from low and middle clouds in terms of their radiative properties. High cirrus clouds reflect a portion of the incoming sunlight, referred to as the solar albedo effect. But at the same time these clouds can also effectively trap a significant amount of the thermal infrared radiation emitted from the surface and lower atmosphere, referred to as the infrared greenhouse effect (Liou, 1992). The intrinsic radiative properties of cirrus clouds determine the competition between the solar albedo and infrared greenhouse effects (Liou, 1986; Stephens *et al.*, 1990), essential to the discussion of the Earth's climate and climate change. Moreover, cirrus clouds are closely related to the water vapor distribution near the upper troposphere and the lower stratosphere (Jensen *et al.*, 1996; Holton and Gettelman, 2001). The important roles of cirrus clouds in

various atmospheric processes have been discussed by Liou (1986, 1992) as well as in a number of recent studies (see Lynch *et al.*, 2002).

Ice crystals in cirrus clouds are almost exclusively nonspherical particles (e.g., Heymsfield and Iaquinta, 2000), ranging from plates, solid and hollow columns, bullet rosettes, and aggregates, to more irregular shapes with various complex surface morphological conditions (e.g., surface roughness). The effect of nonspherical ice crystals within cirrus clouds on their bulk radiative properties is pronounced and must be accounted for in the development of remote sensing techniques and climate analysis. Liou *et al.* (2000) demonstrated that the approximation of nonspherical ice crystals as equivalent ice spheres for the single-scattering and radiative transfer processes can substantially underestimate the albedo of the cirrus. Moreover, the single-scattering properties associated with proper ice crystal morphologies must be used for a correct interpretation of other bulk optical properties of cirrus clouds, particularly, the polarization configuration (Liou and Takano, 2002). Mishchenko *et al.* (1996), Rolland *et al.* (2000), and Yang *et al.* (2001a) also showed strong sensitivity of the cirrus cloud albedo, bidirectional reflectance, and the accuracy of optical thickness retrieval to the ice particle shape assumed. Consequently, it is critically important that the nonsphericity of ice crystals be accurately modeled in radiative transfer computations and remote sensing implementations involving cirrus clouds.

Because of the importance of ubiquitous cirrus clouds in remote sensing and climate research, substantial efforts have been made in the last three decades to understand and determine the fundamental scattering and absorption properties of ice crystals. Early research efforts to account for the nonsphericity of ice crystals in cirrus can be traced back to the studies by Liou (1972a, 1972b) and Stephens (1980a, 1980b) who assumed that these clouds are composed of long circular cylinders. The analytical solution for the scattering of light by an infinite circular cylinder at normal incidence was developed by Lord Rayleigh (1918). Wait (1955), Kerker (1969), and Liou (1972a) extended the solutions for oblique incidence. The single-scattering properties of ice crystals assuming circular-cylinder shape, however, cannot be used to explain a number of optical phenomena associated with cirrus clouds, for example, the well-known 22° halo. The simplest habits (or shapes) of realistic ice crystals are columns and plates with well-defined hexagonal structures. Even for this type of ice crystal, it appears not to be possible to impose an appropriate coordinate system to analytically solve the associated electromagnetic wave equation subjected to the boundary conditions at the surface of a hexagonal particle. The difficulty in conjunction with the application of the variable separation method to complex ice crystal morphologies (e.g., bullet rosettes and aggregates) would be more prominent. This is because proper coordinate systems for the variable separation method can only be defined in cases involving the scattering of light by spheres (Lorenz, 1890; Mie, 1908), spheroids (Oguchi, 1973; Asano and Yamamoto, 1975), and infinite cylinders (Kerker, 1969; Liou, 1972a).

From the late 1970s to the 1990s, the geometric optics method by means of the ray-tracing technique has been extensively used to investigate the single-scattering properties of nonspherical ice crystals (Wendling *et al.*, 1979; Coleman

and Liou, 1981; Cai and Liou, 1982; Takano and Jayaweera, 1985; Takano and Liou, 1989a, 1989b; Macke, 1993; Hess and Wiegner, 1994; Macke *et al.*, 1996a). Note that application of the ray-tracing technique to light scattering by a sphere and a hexagonal column can be traced back to the studies by Liou and Hansen (1971) and Jacobowitz (1971), respectively. The research results from these efforts have been used in various applications in conjunction with the study of cirrus clouds, ranging from remote sensing (e.g. Minnis *et al.*, 1993a, 1993b) to the parameterization of the radiative properties of ice clouds (Ebert and Curry, 1992; Fu and Liou, 1993) for use in climate models.

Recent reviews by Wriedt (1998), Kokhanovsky (1999), Mishchenko *et al.* (2000), Liou (2002), and Kahnert (2003) have enumerated various methods that have been developed for the solution of light scattering by nonspherical particles. These include the T-matrix method (Waterman, 1971; Mishchenko and Travis, 1998), the discrete dipole approximation (Purcell and Pennypacker, 1973; Draine and Flatau, 1994), the finite-difference time domain (FDTD) method (Yee, 1966; Taflove and Brodwin, 1975; Holland, 1977; Kunz and Lee, 1978; Taflove, 1980; Kunz and Simpson, 1981; Umashankar and Taflove, 1982; Taflove, and Umashankar, 1990; Yang and Liou, 1996a; Yang *et al.*, 2000; Sun *et al.*, 1999), and the boundary-element method (Miller, 1988; Kress, 1990; Mano, 2000), and various approximate methods including the geometric optics approximation. Applications of some of these methods to light scattering by ice crystals have been shown to be useful for a better understanding of the optical and radiative properties of cirrus clouds.

In this chapter, we review the progress in the studies of the scattering and absorption properties of nonspherical ice crystals in the Earth's atmosphere from the theoretical and computational perspectives. Specifically, we will highlight the method of geometric optics and the relevant improvements based on which ray-tracing can be performed for large ice crystals with complex geometries and the FDTD numerical method that can be used for the solution of light scattering by small nonspherical and inhomogeneous ice crystals. No originality is claimed in this review; however, we have made an effort to systematically recapture the geometric optics approach and illustrate the basic concepts of the FDTD method and the major numerical steps associated with its application to light scattering and absorption by ice crystals.

2.2 Geometric optics for light scattering by large ice crystals

According to aircraft observations (e.g., Mitchell *et al.*, 1996; McFarquhar *et al.*, 1999) by means of the optical imaging, high resolution video camera, and replicator techniques, the ice crystal size distribution in various types of cirrus clouds ranges from about 10 micrometers to thousands of micrometers. For visible and near-infrared wavelengths, the size parameters (defined as $\pi D/\lambda$ in which D and λ are the particle's characteristic dimension and the incident wavelength, respectively) associated with these particles are large enough that we may apply the

principles of geometric optics in terms of the ray-tracing technique. van de Hulst (1957) and Liou and Hansen (1971) applied this technique to light scattering by spheres. The latter authors also compared the phase function and polarization patterns computed from the geometric ray-tracing method and the Lorenz–Mie theory for polydisperse spheres. The solution from the ray-tracing technique is reasonably accurate when the modal size parameter is larger than 100 for a polydisperse system of spheres. The earliest application of ray-tracing to light scattering by hexagonal ice prisms was first carried out by Jacobowitz (1971). In his study, a sufficiently large number of equally spaced, parallel rays were traced through a hexagonal ice crystal. The external reflection and two refractions after various orders of internal reflections were summed to determine the scattering pattern in the far field. Diffraction contribution to the scattering of the incident radiation in the forward direction can be computed by Kirchhoff's formula. In Jacobowitz's study, hexagonal prisms were assumed to be infinite by long, which is not realistic. To circumvent this shortcoming, Wendling *et al.* (1979) combined the Monte Carlo method and the ray-tracing technique to compute the phase function of finite hexagonal columns. In these early studies, the polarization effect and phase interferences associated with the incident, internal, and scattered rays were not accounted for in the calculation.

Cai and Liou (1982) were the first to include the polarization configuration and phase interferences in ray-tracing to compute the single-scattering properties of hexagonal columns and plates. The theoretical foundation for the 'conventional' geometric ray tracing and the associated computional algorithm developed by Cai and Liou (1982) were later improved and refined by a number of researchers. Takano and Liou (1989a, 1989b) considered the effects of the ice crystal's birefringence property, horizontal orientation, and size spectrum in association with light scattering calculations. The single-scattering properties of ice crystals with horizontally orientation have also been investigated by Rockwitz (1989) and Noel *et al.* (2001). The ray-tracing method has been applied to various complex ice crystal shapes by Takano and Liou (1995), Macke (1993), Macke *et al.* (1996a), Iaquinta *et al.* (1995), Muinonen *et al.* (1997), Peltoniemi *et al.* (1998), and Yang and Liou (1998), and to ice crystals with inclusions (e.g., air bubbles and soots) by Macke *et al.* (1996b) and Macke (2000). Application of the ray-tracing technique implemented with the Monte Carlo method to complex geometries have also been recently reported by Nousiainen *et al.* (2003), and Grynko and Shkuratov (2003). Most recently, Borovoi *et al.* (2002) investigated the scattering characteristics (backscattering features, in particular) of hexagonal ice crystals with arbitrary orientations using the ray-tracing method. Additionally, Borovoi and Grishin (2003) reported an effective ray-tracing algorithm for computing the Jones scattering matrix, and subsequently, the Mueller matrix.

Alternate approaches to the conventional ray-tracing method have been developed by Muinonen (1989) and Yang and Liou (1995, 1996b, and 1997) in which the principles of geometric optics are applied to the computation of the near field either on the surface of or inside the scattering particle. The near field obtained from the ray-tracing technique is then mapped to the far field on the

basis of either a surface-integral- or a volume-integral-based electromagnetic relation. Below we systematically recast the theoretical basis of the conventional ray-tracing technique, and follow with a concise presentation of two versions of the improved geometric optics method for the scattering of light by ice crystals.

The ray-tracing algorithm for the scattering of polarized light by nonspherical ice crystals that was formulated by Cai and Liou (1982) used various specific coordinate systems. To simplify the formulation presented in this chapter, we shall adopt a vector form (Yang and Cai, 1990; Yang and Liou, 1996b, 1997) that is independent of specific coordinate systems. As shown in Fig. 2.1, when the size parameter associated with the scattering particle is large, the incident field can be thought of as consisting of a bundle of localized waves or rays. As articulated in Cai and Liou (1982), the width of localized rays must be much larger than the incident wavelength and yet smaller than the ice crystal size.

Consider an incident ray that passes through point Q_0 and propagates along the incident direction specified by a unit vector $\hat{e}_0^{\mathrm{i}}$. The ray first impinges on the particle surface at point Q_1 where external reflection and refraction occur. For reflection and refraction at this incident point, the directions of the incident, reflected, and refracted rays are denoted by the unit vectors $\hat{e}_1^{\mathrm{i}}$, $\hat{e}_1^{\mathrm{r}}$, and $\hat{e}_1^{\mathrm{t}}$, re-

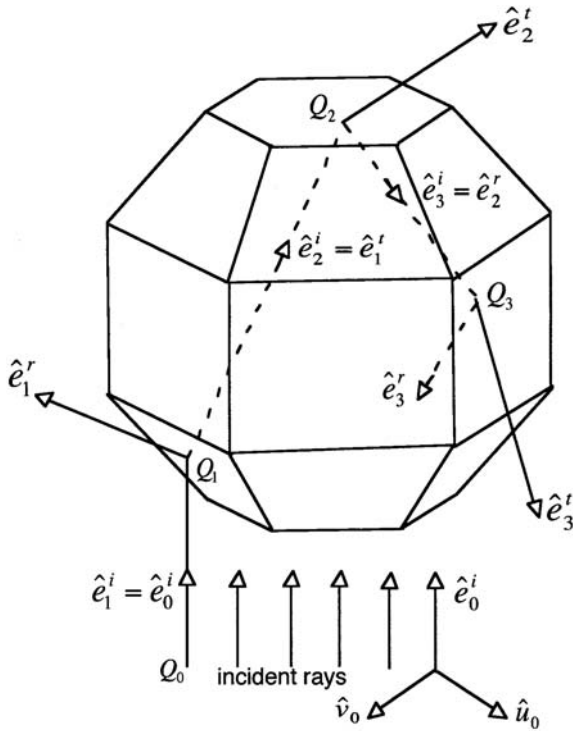

Fig. 2.1. A conceptual diagram for the principle of the ray-tracing technique for computing the single-scattering properties of a particle that is much larger than the incident wavelength.

spectively. The first-order refracted ray then impinges on the next incident point at Q_2 where the first-order internal reflection and the corresponding refraction occur. Note that for the incidence at the point Q_2, the incident direction $\hat{e}_2^{\rm i}$ is the same as that of the first-order refracted ray. Likewise, the subsequent internal reflections and refractions occur at the points $Q_{\rm p}$ in which the order of the ray, p, is larger than 2. The tracing of a ray can be terminated when the energy carried by this ray is practically negligible.

To trace the reflected and refracted rays, let $\hat{n}_{\rm p}$ ($p = 1, 2, 3, \ldots$) be the unit vectors locally normal to the particle surfaces at the incident points $Q_{\rm p}$ ($p = 1, 2, 3, \ldots$) facing the incoming rays, as shown in Fig. 2.2. For the external reflection at the point Q_1, the incident direction $\hat{e}_1^{\rm i}$ and the incident angle $\theta_1^{\rm i}$ are given, respectively, by the following two expressions:

$$\hat{e}_1^{\rm i} = \hat{e}_0^{\rm i}, \tag{2.1}$$

$$\theta_1^{\rm i} = \cos^{-1}(-\hat{n}_1 \cdot \hat{e}_1^{\rm i}), \tag{2.2}$$

where $\hat{e}_0^{\rm i}$ denotes the initial incident direction (Fig. 2.1). Following Snell's law, the directions of the externally reflected ray and the corresponding refracted ray are defined by

$$\hat{e}_1^{\rm r} = \hat{e}_1^{\rm i} + 2\cos\theta_1^{\rm i}\hat{n}_1, \tag{2.3}$$

$$\hat{e}_1^{\rm t} = \hat{e}_1^{\rm i}/m + (\cos\theta_1^{\rm i}/m - \cos\theta_1^{\rm t})\hat{n}_1, \tag{2.4}$$

where m is the refractive index of the scattering particle, and $\theta_1^{\rm t}$ is the refractive angle given by Snell's law as follows:

$$\theta_1^{\rm t} = \sin^{-1}(\sin\theta_1^{\rm i}/m). \tag{2.5}$$

When the refractive index, m, is a complex number, simultaneous absorption and scattering occur and the refracted wave within the particle is an inhomogeneous wave (Born and Wolf, 1959; Bohren and Huffman, 1983). In this case,

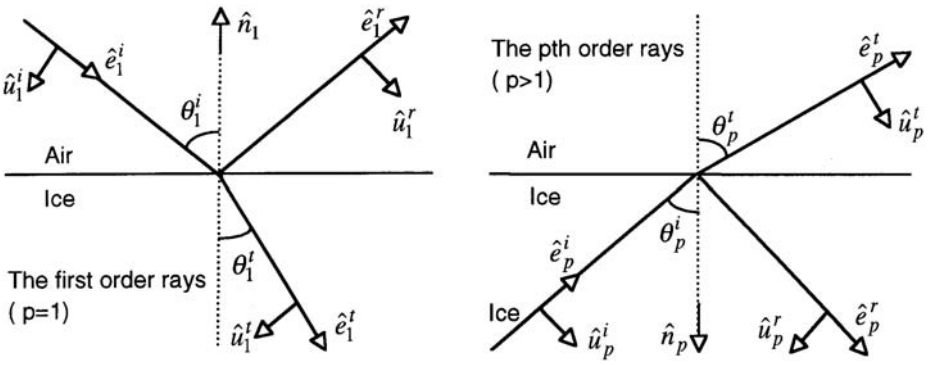

Fig. 2.2. Schematic diagrams for the directions of the incident, reflected and refracted rays. Also shown are the unit vectors for specifying the polarization configuration. Note that $\hat{v}_1$ and $\hat{v}_p$ (not shown in the diagram) point out of the paper.

an adjusted refractive must be used to trace the refracted rays (Yang and Liou, 1995). Note that Born and Wolf (1959) only formulated the Fresnel formula by avoiding the complex refraction angle when absorption occurs. Yang *et al.* (2001b) showed that in general the electric field vector associated with the refracted rays may not be perpendicular to the ray direction and developed an improved scheme for the ray-tracing computation. For practical computations at the visible and near-infrared wavelengths, the real part of the refractive index may be used as an excellent approximation of the adjusted refractive index for tracing the ray directions on the basis of eqs (2.4) and (2.5). The issue associated with the inhomogeneous wave properties within an ice crystal involving complex refractive index will not be elaborated further. Interested readers in this subject may wish to consult with the work of Born and Wolf (1959), Bohren and Huffman (1983), Dupertuis *et al.* (1994), Yang and Liou (1995), Yang *et al.* (2001b), Liou (2002), and Chang *et al.* (2005).

For internal reflection with orders of $p = 2, 3, 4, \ldots$, the incident directions can be defined in a likely manner and are given by the directions of either the first-order refracted rays or internally reflected rays as follows:

$$\hat{e}_2^{\mathrm{i}} = \hat{e}_1^{\mathrm{t}}, \tag{2.6}$$

$$\hat{e}_{\mathrm{p}}^{\mathrm{i}} = \hat{e}_{\mathrm{p}-1}^{\mathrm{r}}, \; p = 3, 4, 5, \ldots \tag{2.7}$$

With some vector algebraic manipulations on the basis of Snell's law, it can be shown that the propagating directions of the pth order reflected and refracted rays are given by

$$\hat{e}_{\mathrm{p}}^{\mathrm{r}} = \hat{e}_{\mathrm{p}}^{\mathrm{i}} + 2\cos\theta_{\mathrm{p}}^{\mathrm{i}}\hat{n}_{\mathrm{p}}, \tag{2.8}$$

$$\hat{e}_{\mathrm{p}}^{\mathrm{t}} = m\hat{e}_{\mathrm{p}}^{\mathrm{i}} + (m\cos\theta_{\mathrm{p}}^{\mathrm{i}} - \cos\theta_{\mathrm{p}}^{\mathrm{t}})\hat{n}_{\mathrm{p}}, \tag{2.9}$$

where the incident and refraction angles, $\theta_{\mathrm{p}}^{\mathrm{i}}$ and $\theta_{\mathrm{p}}^{\mathrm{t}}$, are defined via the following expressions:

$$\theta_{\mathrm{p}}^{\mathrm{i}} = \cos^{-1}(-\hat{n}_{\mathrm{p}} \cdot \hat{e}_{\mathrm{p}}^{\mathrm{i}}), \tag{2.10}$$

$$\theta_{\mathrm{p}}^{\mathrm{t}} = \sin^{-1}(m\sin\theta_{\mathrm{p}}^{\mathrm{i}}). \tag{2.11}$$

The total reflection occurs if the term $m\sin\theta_{\mathrm{p}}^{\mathrm{i}}$ in eq. (2.11) is larger than 1. In this case, a refracted ray should not be expected and the ray-tracing computation should be continued only for the ray associated with total reflection. Equations (2.1)–(2.11) constitute a closed set of equations for tracing the directions of all the reflected and refracted rays associated with a given incident ray.

A localized plane electromagnetic wave is a transverse vector wave. Thus, the vector property or the polarization configuration of the electric fields associated with localized rays in the ray-tracing computation must be accounted for. To include the polarization configuration, we shall define various auxiliary unit vectors. For the incident direction of an initial ray specified by a unit vector $\hat{e}_0^{\mathrm{i}}$, we define two unit vector $\hat{u}_0$ and $\hat{v}_0$ (see Fig. 2.1) that are normal to the incident direction and satisfy the relations as follows:

$$\hat{u}_0 \cdot \hat{v}_0 = 0 \text{ and } \hat{v}_0 \times \hat{u}_0 = \hat{e}_0^{\mathrm{i}}. \tag{2.12}$$

The unit vectors $\hat{v}_0$, $\hat{u}_0$ and $\hat{e}_0^{\mathrm{i}}$ defined in this equation constitute a right-handed coordinate system. To define the initial rays in practice, we may specify the unit vectors $\hat{v}_0$, $\hat{u}_0$ and $\hat{e}_0^{\mathrm{i}}$ to point to the directions along the x-, y- and z-axis of the incident coordinate system. Because the unit vectors $\hat{e}_0^{\mathrm{i}}$, $\hat{u}_0$ and $\hat{v}_0$ are orthogonal to each other, the incident polarization configuration can be specified with respect to $\hat{u}_0$ and $\hat{v}_0$, that is, the incident electric field $\boldsymbol{E}_0^{\mathrm{i}}$ can be written as follows:

$$\boldsymbol{E}_0^{\mathrm{i}} = E_{0u}^{\mathrm{i}} \hat{u}_0 + E_{0v}^{\mathrm{i}} \hat{v}_0. \tag{2.13}$$

Similarly, we may define three pairs of unit vectors, $(\hat{u}_p^{\mathrm{i}}, \hat{v}_p)$, $(\hat{u}_p^{\mathrm{r}}, \hat{v}_p)$, and $(\hat{u}_p^{\mathrm{t}}, \hat{v}_p)$ for the ray directions along $\hat{e}_p^{\mathrm{i}}$, $\hat{e}_p^{\mathrm{r}}$ and $\hat{e}_p^{\mathrm{t}}$ ($p = 1, 2, 3, \ldots$), respectively. The unit vectors $\hat{u}_p^{\mathrm{i}}$, $\hat{u}_p^{\mathrm{r}}$ and $\hat{u}_p^{\mathrm{t}}$ point along the directions shown in Fig. 2.2, if the unit vectors, $\hat{v}_p$, $p = 1, 2, 3, \ldots$, (not shown in Fig. 2.2) are defined as being pointed out of the paper. These vectors can be specified via the following expressions:

$$\hat{v}_p = (\hat{e}_p^{\mathrm{i}} \times \hat{n}_p)/\sin\theta_p^{\mathrm{i}}, \ p = 1, 2, 3, \ldots, \tag{2.14}$$

$$\hat{u}_p^{\mathrm{i,r,t}} = \hat{e}_p^{\mathrm{i,r,t}} \times \hat{v}_p, \ p = 1, 2, 3, \ldots. \tag{2.15}$$

Evidently, the unit vector $\hat{v}_p$ is normal to the incident plane, the plane containing the incident direction and the direction locally normal to the particle surface at the incident point, for the pth-order reflection and refraction. The unit vectors $\hat{u}_p^{\mathrm{i}}$, $\hat{u}_p^{\mathrm{r}}$, and $\hat{u}_p^{\mathrm{t}}$ are parallel to the pth-order incident plane. Note that $\hat{v}_p$ in eq. (2.14) cannot be uniquely specified if $\sin\theta_p^{\mathrm{i}} = 0$. In this case, we select $\hat{v}_p = \hat{v}_{p-1}$. With the aforementioned unit vectors defined, the electric fields associated with the pth-order incident, reflected, and refracted rays can be expressed as follows:

$$\boldsymbol{E}_p^{\mathrm{i,r,t}} = E_{pu}^{\mathrm{i,r,t}} \hat{u}_p^{\mathrm{i,r,t}} + E_{pv}^{\mathrm{i,r,t}} \hat{v}_p. \tag{2.16}$$

Consider now the external reflection and the first-order refraction. In order to apply the Fresnel formulas, the electric field associated with the incident ray impinging on the point Q_1 must be specified with respect to $\hat{u}_1^{\mathrm{i}}$ and $\hat{v}_1$. Also, the electric field associated with the incident ray specified in eq. (2.13) can also be expressed in an alternative form as follows:

$$\boldsymbol{E}_0^{\mathrm{i}} = E_{1u}^{\mathrm{i}} \hat{u}_1^{\mathrm{i}} + E_{1v}^{\mathrm{i}} \hat{v}_1. \tag{2.17}$$

Equations (2.13) and (2.17) for the incident electric vector are related via a rotational matrix in the form

$$\begin{pmatrix} E_{1u}^{\mathrm{i}} \\ E_{1v}^{\mathrm{i}} \end{pmatrix} = \varGamma_1 \begin{pmatrix} E_{0u}^{\mathrm{i}} \\ E_{0v}^{\mathrm{i}} \end{pmatrix}, \tag{2.18}$$

where $\varGamma_1$ is a rotational matrix given by

$$\varGamma_1 = \begin{pmatrix} \hat{u}_1^{\mathrm{i}} \cdot \hat{u}_0 & \hat{u}_1^{\mathrm{i}} \cdot \hat{v}_0 \\ \hat{v}_1 \cdot \hat{u}_0 & \hat{v}_1 \cdot \hat{v}_0 \end{pmatrix}. \tag{2.19}$$

Because the field components on the left-hand side of eq. (2.18) are specified with respect to the incident plane, the Fresnel formulas can be applied. The externally reflected field ($\boldsymbol{E}_1^{\mathrm{r}}$) is given by

$$\boldsymbol{E}_1^{\mathrm{r}} = E_{1u}^{\mathrm{r}}\hat{u}_1^{\mathrm{r}} + E_{1v}^{\mathrm{r}}\hat{v}_1, \tag{2.20}$$

where

$$\begin{pmatrix} E_{1u}^{\mathrm{r}} \\ E_{1v}^{\mathrm{r}} \end{pmatrix} = R_1 \begin{pmatrix} E_{1u}^{\mathrm{i}} \\ E_{1v}^{\mathrm{i}} \end{pmatrix} = R_1 \Gamma_1 \begin{pmatrix} E_{0u}^{\mathrm{i}} \\ E_{0v}^{\mathrm{i}} \end{pmatrix}. \tag{2.21}$$

In eq. (2.21), R_1 is the reflection matrix for the external reflection given by

$$R_1 = \begin{pmatrix} R_{1u} & 0 \\ 0 & R_{1v} \end{pmatrix}. \tag{2.22}$$

The elements of the reflection matrix in eq. (2.22) are given by the Fresnel coefficients (Born and Wolf, 1959) as follows:

$$R_{1u} = \frac{m\cos\theta_1^{\mathrm{i}} - \cos\theta_1^{\mathrm{t}}}{m\cos\theta_1^{\mathrm{i}} + \cos\theta_1^{\mathrm{t}}}, \tag{2.23}$$

$$R_{1v} = \frac{\cos\theta_1^{\mathrm{i}} - m\cos\theta_1^{\mathrm{t}}}{\cos\theta_1^{\mathrm{i}} + m\cos\theta_1^{\mathrm{t}}}. \tag{2.24}$$

Similarly, the electric field associated with the first-order refracted ray is given by

$$\boldsymbol{E}_1^{\mathrm{t}} = E_{1u}^{\mathrm{t}}\hat{u}_1^{\mathrm{t}} + E_{1v}^{\mathrm{t}}\hat{v}_1, \tag{2.25}$$

$$\begin{pmatrix} E_{1u}^{\mathrm{t}} \\ E_{1v}^{\mathrm{t}} \end{pmatrix} = T_1 \begin{pmatrix} E_{1u}^{\mathrm{i}} \\ E_{1v}^{\mathrm{i}} \end{pmatrix} = T_1 \Gamma_1 \begin{pmatrix} E_{0u}^{\mathrm{i}} \\ E_{0v}^{\mathrm{i}} \end{pmatrix}, \tag{2.26}$$

where the refraction matrix T_1 is defined in the form

$$T_1 = \begin{pmatrix} T_{1u} & 0 \\ 0 & T_{1v} \end{pmatrix} = \begin{pmatrix} (1-R_{1u}^2)^{1/2} & 0 \\ 0 & (1-R_{1v}^2)^{1/2} \end{pmatrix}. \tag{2.27}$$

In eq. (2.27), the conservation of the energy carried out by the ray due to a change in the refractive index and ray cross-section in two media is accounted for in the refraction matrix (see eq. (48) in Cai and Liou (1982) and references cited therein).

For the external reflection, the direction along the reflected ray is the scattering direction. Thus, the scattering angle is given by

$$\theta_1^{\mathrm{s}} = \cos^{-1}(\hat{e}_0^{\mathrm{i}} \cdot \hat{e}_1^{\mathrm{r}}). \tag{2.28}$$

The direction that is perpendicular to the scattering plane can be specified by

$$\hat{v}_1^{\mathrm{s}} = \hat{e}_0^{\mathrm{i}} \times \hat{e}_1^{\mathrm{r}} / \sin\theta_1^{\mathrm{s}}. \tag{2.29}$$

If $\sin\theta_1^{\mathrm{s}} = 0$ in eq. (2.29), implying the forward (i.e., $\theta_1^{\mathrm{s}} = 0^\circ$) and backward scattering (i.e., $\theta_1^{\mathrm{s}} = 180^\circ$), the vector $\hat{v}_1^{\mathrm{s}}$ cannot be defined. In this case, we

select $\hat{v}_1^{\rm s} = \hat{v}_0$. After the unit vector $\hat{v}_1^{\rm s}$ is defined, the direction parallel to the scattering plane is given by

$$\hat{u}_1^{\rm s} = \hat{e}_1^{\rm r} \times \hat{v}_1^{\rm s}. \tag{2.30}$$

If we express the electric field associated with the externally reflected ray with respect to two directions parallel and perpendicular to the scattering plane, we have

$$\boldsymbol{E}_1^{\rm r} = E_{1u}^{\rm s}\hat{u}_1^{\rm s} + E_{1v}^{\rm s}\hat{v}_1^{\rm s}. \tag{2.31}$$

From eqs (2.20), (2.21) and (2.31), it follows that

$$\begin{pmatrix} E_{1u}^{\rm s} \\ E_{1v}^{\rm s} \end{pmatrix} = \varGamma_1^{\rm s} R_1 \varGamma_1 \begin{pmatrix} E_{0u}^{\rm i} \\ E_{0v}^{\rm i} \end{pmatrix}, \tag{2.32}$$

where $\varGamma_1^{\rm s}$ is a rational matrix, given by

$$\varGamma_1^{\rm s} = \begin{pmatrix} \hat{u}_1^{\rm s}\cdot\hat{u}_1^{\rm r} & \hat{u}_1^{\rm s}\cdot\hat{v}_1 \\ \hat{v}_1^{\rm s}\cdot\hat{u}_1^{\rm r} & \hat{v}_1^{\rm s}\cdot\hat{v}_1 \end{pmatrix}. \tag{2.33}$$

To obtain the scattering matrix, the incident field must be specified with respect to the directions parallel and perpendicular to the scattering plane, that is, the incident field needs to be in the form

$$\boldsymbol{E}_0^{\rm i} = E_{1su}^{\rm i}(\hat{e}_0^{\rm i} \times \hat{v}_1^{\rm s}) + E_{1sv}^{\rm i}\hat{v}_1^{\rm s}. \tag{2.34}$$

Note that the unit vector $\hat{e}_0^{\rm i} \times \hat{v}_1^{\rm s}$ in eq. (2.34) is parallel to the scattering plane. The expression in eq. (2.34) for the incident field is related to that in eq. (2.13) as follows:

$$\begin{pmatrix} E_{0u}^{\rm i} \\ E_{0v}^{\rm i} \end{pmatrix} = \varGamma_1^{\rm i} \begin{pmatrix} E_{1su}^{\rm i} \\ E_{1sv}^{\rm i} \end{pmatrix}, \tag{2.35}$$

where $\varGamma_1^{\rm i}$ is a 2-D rotational matrix given by

$$\varGamma_1^{\rm i} = \begin{pmatrix} \hat{u}_0\cdot(\hat{e}_0^{\rm i}\times\hat{v}_1^{\rm s}) & \hat{u}_0\cdot\hat{v}_1^{\rm s} \\ \hat{v}_0\cdot(\hat{e}_0^{\rm i}\times\hat{v}_1^{\rm s}) & \hat{v}_0\cdot\hat{v}_1^{\rm s} \end{pmatrix}. \tag{2.36}$$

Thus, we can express the scattered field in eq. (2.32) as follows:

$$\begin{pmatrix} E_{1u}^{\rm s} \\ E_{1v}^{\rm s} \end{pmatrix} = \varGamma_1^{\rm s} R_1 \varGamma_1 \varGamma_1^{\rm i} \begin{pmatrix} E_{1su}^{\rm i} \\ E_{1sv}^{\rm i} \end{pmatrix}. \tag{2.37}$$

Similarly, for the refracted rays with $p = 2$, we have

$$\begin{pmatrix} E_{2u}^{\rm s} \\ E_{2v}^{\rm s} \end{pmatrix} = \varGamma_2^{\rm s} T_2 \varGamma_2 T_1 \varGamma_1 \varGamma_2^{\rm i} \begin{pmatrix} E_{2su}^{\rm i} \\ E_{2sv}^{\rm i} \end{pmatrix}. \tag{2.38}$$

For the orders $p = 3, 4, 5, \ldots$, we have

$$\begin{pmatrix} E_{pu}^{\rm s} \\ E_{pv}^{\rm s} \end{pmatrix} = \varGamma_p^{\rm s} T_p \varGamma_p \cdots R_2 \varGamma_2 T_1 \varGamma_1 \varGamma_p^{\rm i} \begin{pmatrix} E_{psu}^{\rm i} \\ E_{psv} \end{pmatrix}. \tag{2.39}$$

The definitions for $\Gamma_p^{\rm s}$, T_p, Γ_p, R_p, and $\Gamma_p^{\rm i}$ are similar to those for the case with $p = 1$. In this manner, both the incident and scattered electric field vectors are expressed with respect to the scattering plane in eqs (2.37)–(2.39). Thus, the contributions of the emerging or scattered rays to the amplitude scattering matrix can be expressed in the forms

$$A^{(1)} = \begin{pmatrix} A_2^{(1)} & A_3^{(1)} \\ A_4^{(1)} & A_1^{(1)} \end{pmatrix} = \Gamma_1^{\rm s} R_1 \Gamma_1 \Gamma_1^{\rm i}, \text{ for externally reflected rays,} \quad (2.40)$$

$$A^{(2)} = \begin{pmatrix} A_2^{(2)} & A_3^{(2)} \\ A_4^{(2)} & A_1^{(2)} \end{pmatrix} = \begin{matrix} \Gamma_2^{\rm s} T_2 \Gamma_2 T_1 \Gamma_1 \Gamma_2^{\rm i}, \\ \text{for second-order transmitted rays,} \end{matrix} \quad (2.41)$$

$$A^{(3)} = \begin{pmatrix} A_2^{(3)} & A_3^{(3)} \\ A_4^{(3)} & A_1^{(3)} \end{pmatrix} = \begin{matrix} \Gamma_p^{\rm s} T_p \Gamma_p \cdots R_2 \Gamma_2 T_1 \Gamma_1 \Gamma_p^{\rm i}, \\ \text{for } p\text{th } (p > 2)\text{-order transmitted rays.} \end{matrix} \quad (2.42)$$

In the foregoing discussion, we have not accounted for the phase change associated with the optical paths of rays. The rays incident on the scattering particle at different locations must experience phase change due to different paths. Noticing this feature, Cai and Liou (1982) considered the phase interference of the emerging rays in ray-tracing computations. Most follow-on studies reported in the literature essentially ignored the phase shifts associated with raypaths. However, it should be pointed out that the approach developed by Stamnes and Heier (1998) and Chen and Stamnes (1998) can also be used to effectively account for the phase inference of rays. Takano and Jayaweera (1985) showed that the phase interference can be smoothed out when ice crystals are randomly oriented. For practical applications, we normally assume the random orientation condition for ice crystals in radiative transfer computations. If ice crystals are horizontally oriented, the single-scattering properties depend not only on the scattering angle but also on the azimuth of the scattering plane. In this case, the radiative transfer calculation can be quite involved (Takano and Liou, 1989b). In addition to random orientation, the integration over the size spectrum will smooth out the fluctuations produced by phase interferences in the scattering pattern for one size.

For randomly oriented particles, the corresponding phase matrix has only six independent elements (van de Hulst, 1957). Thus, for the pth-order emerging ray, its contribution to the phase matrix is given by the following expression (Takano and Jayaweera, 1985):

$$F^{(\rm p)} = \begin{pmatrix} (M_1^{(\rm p)} + M_2^{(\rm p)} + M_3^{(\rm p)} + M_4^{(\rm p)})/2 & (M_2^{(\rm p)} - M_1^{(\rm p)})/2 & 0 & 0 \\ (M_2^{(\rm p)} - M_1^{(\rm p)})/2 & (M_2^{(\rm p)} - M_3^{(\rm p)} - M_4^{(\rm p)} + M_1^{(\rm p)})/2 & 0 & 0 \\ 0 & 0 & S_{12}^{(\rm p)} + S_{34}^{(\rm p)} & -D_{12}^{(\rm p)} \\ 0 & 0 & D_{21}^{(\rm p)} & S_{12}^{(\rm p)} - S_{34}^{(\rm p)} \end{pmatrix}, \quad (2.43)$$

where the matrix $F^{(\rm p)}$ transforms the incident Stokes parameters to the scattered Stokes parameters associated with the pth-order outgoing localized wave. In eq. (2.43), the phase matrix elements are defined by

$$M_{\mathrm{i}}^{(\mathrm{p})} = |A_{\mathrm{i}}^{(\mathrm{p})}|^2, \tag{2.44}$$

$$S_{ij}^{(\mathrm{p})} = S_{ji}^{(\mathrm{p})} = (A_I^{(\mathrm{p})} A_j^{(\mathrm{p})*} + A_i^{(\mathrm{p})*} A_j^{(\mathrm{p})})/2, \tag{2.45}$$

$$D_{ij}^{(\mathrm{p})} = -D_{ji}^{(\mathrm{p})} = \sqrt{-1}(A_i^{(\mathrm{p})} A_j^{(\mathrm{p})*} - A_i^{(\mathrm{p})} A_j^{(\mathrm{p})})/2, \tag{2.46}$$

where the subscripts i and j range from 1 to 4, and the asterisk indicates complex conjugate. Thus, the scattering matrix associated with the various orders of external reflections and transmissions of all the incident rays is given by

$$F_{\mathrm{ray}} = \sum_{j=1}^{N} \sum_{p=1}^{\infty} \Delta\sigma_j F_j^{(\mathrm{p})} / \sum_{p=1}^{\infty} \Delta\sigma_j, \tag{2.47}$$

where j denotes that the external reflection and the various orders of transmission are associated with the jth initial ray, N is the total number of incident rays, and $\Delta\sigma_j$ is the cross-section of the jth initial ray. To speed up the computation, the foregoing ray-tracing algorithm can be implemented by using the Monte Carlo method. Interested readers may wish to consult with the papers by Wendling *et al.* (1979), Takano and Liou (1995), Macke (1993), and Yang and Liou (1998). More recently, an efficient algorithm for specifying the incident rays in the Monte Carlo ray-tracing technique implemented for convex geometries has been reported by Zhang *et al.* (2004).

In addition to the contributions from the reflected and refracted rays, diffraction also contributes to the scattering of the incident wave. According to Babinet's principle (Born and Wolf, 1959), the diffraction pattern associated with an object is the same as that for an aperture with a shape identical to the projection of the object on a plane normal to the incident direction. The diffraction matrix obtained by the scalar Fraunhofer diffraction theory for a scattering particle has been extensively employed in the previous ray-tracing studies. Yang and Liou (1998) showed that the scattering matrix associated with diffraction is given in the form

$$A_{\mathrm{dif}} = \frac{k^2}{2\pi} D \begin{bmatrix} (\cos\theta + \cos^2\theta)/2 & 0 \\ 0 & (1+\cos\theta)/2 \end{bmatrix}, \tag{2.48}$$

where

$$D = \iint_{\substack{\text{projected} \\ \text{area}}} \exp(-ik\hat{r} \cdot \bar{\xi})\, \mathrm{d}^2\xi. \tag{2.49}$$

From eqs (2.48) and (2.49), the contribution of diffraction to the scattering phase matrix, denoted as F_{dif}, can be evaluated. To sum the contributions due to diffraction and Fresnel rays, proper weighting factors must be accounted for, particularly, in the case when the scattering particle is absorptive.

If the scattering ice crystal is absorptive, i.e., the imaginary refractive index is nonzero, the total absorption can be accounted for by considering the absorption of individual rays. In general, the absorption cross of a particle depends on the polarization configuration of the incident light. However, for randomly oriented particles, their absorption cross-section is the average of the absorption

cross-sections for two orthogonal polarization cases. Consider a case where the polarization of the incident light is specified as follows:

$$(\boldsymbol{E}^{\mathrm{i}}_{0u}, \boldsymbol{E}^{\mathrm{i}}_{0v}) = (1, 0). \tag{2.50}$$

The intensity of the first-order refracted field can be obtained from eq. (2.26) in the form

$$(\boldsymbol{E}^{\mathrm{t}}_{0u}, \boldsymbol{E}^{\mathrm{t}}_{0v})(\boldsymbol{E}^{\mathrm{t}}_{0u}, \boldsymbol{E}^{\mathrm{t}}_{0v})^{*,+}\Big|_{(\boldsymbol{E}^{\mathrm{i}}_{0u}, \boldsymbol{E}^{\mathrm{i}}_{0v})=(1,0)} = (1,0)(T_1\Gamma_1)^{+}(T_1\Gamma_1)^{*}(1,0)^{+}, \tag{2.51}$$

where the superscript symbol + denotes the transpose of a matrix, and $*$ indicates the complex conjugate. The intensity given by eq. (2.51) is essentially the amplitude of the Poyting vector (Born and Wolf, 1959) in which the refractive index and change in the ray cross-section due to refraction have been implicitly accounted for in the refractive matrix given by eq. (2.27). A similar expression can be derived for the case when the polarization of field is given by $(\boldsymbol{E}^{\mathrm{i}}_{0u}, \boldsymbol{E}^{\mathrm{i}}_{0v}) = (0, 1)$. Therefore, the contribution of the first-order refracted rays to the absorption cross-section is given by

$$\begin{aligned}
\sigma_{\mathrm{abs},1} &= \sum_{j=1}^{N} 2^{-1}\Delta\sigma_j \left[1 - \exp(-4\pi m_i d_{j1}/\lambda)\right] \\
&\quad \times \Big[(\boldsymbol{E}^{\mathrm{t}}_{pu}, \boldsymbol{E}^{\mathrm{t}}_{pv})(\boldsymbol{E}^{\mathrm{t}}_{\mathrm{pu}}, \boldsymbol{E}^{\mathrm{t}}_{\mathrm{pv}})^{*,+}\Big|_{(\boldsymbol{E}^{\mathrm{i}}_{0u}, \boldsymbol{E}^{\mathrm{i}}_{0v})=(1,0)} \\
&\qquad + (\boldsymbol{E}^{\mathrm{t}}_{pu}, \boldsymbol{E}^{\mathrm{t}}_{pv})(\boldsymbol{E}^{\mathrm{t}}_{pu}, \boldsymbol{E}^{\mathrm{t}}_{pv})^{*,+}\Big|_{(\boldsymbol{E}^{\mathrm{i}}_{0u}, \boldsymbol{E}^{\mathrm{i}}_{0v})=(1,0)}\Big] \\
&= \sum_{j=1}^{N} 2^{-1}\Delta\sigma_j \left[1 - \exp(-4\pi m_i d_{j1}/\lambda)\right] \\
&\qquad \cdot \left[(1,0)(T_1\Gamma_1)^{+}(T_1\Gamma_1)^{*}(1,0)^{+} + (0,1)(T_1\Gamma_1)^{+}(T_1\Gamma_1)^{*}(1,0)^{+}\right],
\end{aligned} \tag{2.52}$$

where subscript j denotes the jth initial ray, d_{j1} is the distance between the first incident point (i.e., Q_1 in Fig. 2.1) and the second incident point (i.e., Q_2 in Fig. 2.1), $\Delta\sigma_j$ is the cross-section of the jth initial ray, m_i is the imaginary part of the refractive index, and λ is the incident wavelength in a vacuum. Likewise, the contribution by the pth-order reflected rays is

$$\begin{aligned}
\sigma_{\mathrm{abs},p} &= \sum_{j=1}^{N} 2^{-1}\Delta\sigma_j \left[1 - \exp(-4\pi m_i d_{jp}/\lambda)\right] \exp\left(-4\pi m_i \lambda^{-1} \sum_{L=1}^{p-1} d_{jL}\right) \\
&\quad \times \Big[(1,0)(T_p\Gamma_p \cdots R_2\Gamma_2 t_1\Gamma_1)^{+}(T_p\Gamma_p \cdots R_2\Gamma_2 T_1\Gamma_1)^{*}(1,0)^{+} \\
&\quad + (0,1)(T_p\Gamma_p \cdots R_2\Gamma_2 T_1\Gamma_1)^{+}(T_p\Gamma_p \cdots R_2\Gamma_2 T_1\Gamma_1)^{*}(0,1)^{+}\Big],
\end{aligned} \tag{2.53}$$

Thus, the absorption cross-section of the scattering particle can be expressed as follows:

$$\sigma_{\rm abs} = \sum_{p=1}^{\infty} \sigma_{{\rm abs},p}. \tag{2.54}$$

In practice, the summation in eq. (2.54) can be truncated for the terms with $p > 10$, because the amount of the energy carried by the higher-order rays is insignificant. Equations (2.52)–(2.54) provide the explicit formulations for absorption cross-section within the framework of the ray-tracing technique in which the polarization configuration is fully accounted for. In the conventional ray-tracing method, the extinction cross-section is twice the projected area of the scattering particle, that is

$$\sigma_{\rm ext} = 2\sigma_p, \tag{2.55}$$

where σ_p is the particle's projected area on a plane normal to the incident direction. The contribution of diffraction to the extinction cross-section is equal to that associated with the externally reflected rays and the transmitted rays that experience two refractions and various orders of internal reflections.

One of the shortcomings of the conventional ray-tracing method is the production of the delta-transmission associated with the refraction of rays through two parallel faces of the pristine ice crystals. The delta-transmission phenomenon has been discussed in detail by Takano and Liou (1989a) and Mishchenko and Macke (1998). Let the portion of the scattering cross-section associated with the delta-transmission be σ_δ. Then, the scattering cross-section can be separated into three terms as follows:

$$\sigma_{\rm sca} = (\sigma_p - \sigma_{\rm abs} - \sigma_\delta) + \sigma_\delta + \sigma_p, \tag{2.56}$$

The first term $(\sigma_p - \sigma_{\rm abs} - \sigma_\delta)$ corresponds to the contribution from the externally reflected rays and the various transmitted rays excluding the delta-transmitted rays, the second term (σ_δ) denotes the contribution from the delta-transmitted rays, and the third term (σ_p) is associated with diffraction. Let f_δ be the ratio of the delta-transmitted energy to the total scattered energy defined by

$$f_\delta = \sigma_\delta/\sigma_{\rm sca} = \sigma_\delta/(2\sigma_p - \sigma_{\rm abs}) = \sigma_\delta/(\sigma_{\rm ext} - \sigma_{\rm abs}). \tag{2.57}$$

Using the standard notation, the scattered Stokes vector can be expressed as follows:

$$\begin{pmatrix} I_{\rm s} \\ Q_{\rm s} \\ U_{\rm s} \\ V_{\rm s} \end{pmatrix} = \frac{\sigma_{\rm sca}}{k^2 r^2} P \begin{pmatrix} I_{\rm i} \\ Q_{\rm i} \\ U_{\rm i} \\ V_{\rm i} \end{pmatrix}, \tag{2.58}$$

where $(I_{\rm i}, Q_{\rm i}, U_{\rm i}, V_{\rm i})$ and $(I_{\rm s}, Q_{\rm s}, U_{\rm s}, V_{\rm s})$ are the incident and scattered Stokes parameters, respectively, and P is the normalized phase matrix. Based on $F_{\rm ray}$ in eq. (2.47), $F_{\rm dif}$ that is defined on the basis of $A_{\rm dif}$ in eq. (2.48), the expressions in eqs (2.56) and (2.57), and the associated physical meanings of these quantities and expressions, the normalized phase matrix is given by

$$P(\theta) = \frac{[(2\sigma_p - \sigma_{\rm abs})(1-f_\delta) - \sigma_p] a F_{\rm ray} + 2(2\sigma_p - \sigma_{\rm abs}) f_\delta \delta(\cos\theta - 1)\bar{\bar{I}} + \sigma_p b F_{\rm dif}}{2\sigma_p - \sigma_{\rm abs}}$$
$$= 2 f_\delta \delta(\cos\theta - 1)\bar{\bar{I}} + \left[(1-f_\delta) - \frac{1}{2\tilde{\omega}_o}\right] a F_{\rm ray} + \frac{1}{2\tilde{\omega}_o} b F_{\rm dif}, \tag{2.59}$$

where $\tilde{\omega}_0 = \sigma_{\rm sca}/\sigma_{\rm ext}$ is the single scattering albedo. In eq. (2.59) θ is the scattering angle, $\bar{\bar{I}}$ is a unit 4×4 matrix, and the two parameters, a and b, are normalization factors given, respectively, by the following two equations:

$$a = \frac{2}{\int_0^\pi F_{{\rm ray},11}(\theta)\, \sin\theta \, {\rm d}\theta}, \tag{2.60}$$

$$b = \frac{2}{\int_0^\pi F_{{\rm dif},11}(\theta)\, \sin\theta \, {\rm d}\theta}, \tag{2.61}$$

where the subscript 11 indicates the first element of the associated matrix. With the normalization factors given in eqs (2.60) and (2.61), it can be shown that the phase matrix in eq. (2.59) is normalized in the sense that the first phase matrix element P_{11} (i.e., the phase function) satisfies the following normalization condition:

$$\frac{1}{2}\int_0^\pi P_{11}(\theta) \sin\theta \, {\rm d}\theta = 1. \tag{2.62}$$

The conventional ray-tracing technique utilizes the assumption that the energy attenuated by a scattering particle is equally divided into two parts: extinction associated with diffraction and extinction due to Fresnel reflection and refraction. In this case, the extinction efficiency (i.e., the ratio of extinction cross-section to particle projected area) is 2 regardless of the size and shape of the scattering particle, referred to as the optical theorem. In addition, the computation of far field by directly applying the ray-tracing technique leads to the delta-transmission (Takano and Liou, 1989a) in the forward direction, as is evident from the presence of a delta function in eq. (2.59). To overcome these shortcomings, Yang and Liou (1995, 1996a, 1996b, 1997) have developed two improved geometric optics methods.

According to the fundamental theory of classic electrodynamics, the far field can be exactly computed if the tangential components of the electric and magnetic fields on the surface of a scattering particle are known (Jackson, 1998, p. 485) in the form

$$\boldsymbol{E}^{\rm s}(\boldsymbol{r})\big|_{kr\to\infty} = \frac{{\rm e}^{ikr}}{-ikr}\frac{k^2}{4\pi}\hat{r} \times \iint \{\hat{n}_{\rm s} \times \boldsymbol{E}(\boldsymbol{r}') - \hat{r} \times [\hat{n}_{\rm s} \times \mathbf{H}(\boldsymbol{r}')]\}\, {\rm e}^{-ik\hat{r}\cdot\boldsymbol{r}'}\, {\rm d}^2\boldsymbol{r}, \tag{2.63}$$

where the integral domain is the surface of the scattering particle. In essence, eq. (2.63) is derived on the basis of the electromagnetic equivalence theorem (Schelkunoff, 1943). Thus, the geometric ray-tracing technique can be used to compute the near field on the particle's surface, which can be subsequently mapped to the far field on the basis of eq. (2.63). The mapping idea within the framework of the ray-tracing computation was first employed by Muinonen

(1989) who developed an algorithm known as the modified Kirchhoff approximation (MKA) to solve the scattering by nonspherical ice crystals based on an electromagnetic equation similar to eq. (2.63). To simplify numerical computations, a constant extinction efficiency of 2 was assumed in the MKA and the strong forward-scattering maximum was approximated by the Fraunhofer diffraction. Yang and Liou (1995, 1996b) considered the phase interference and the polarization state of the rays in the near-field computation (hereafter, this method is referred to as GOM2). In GOM2, the extinction cross-section is computed from the fundamental extinction formula (van de Hulst, 1957) or the so-called optical theorem (Bohren and Huffman, 1983) given by

$$\sigma_{\rm ext} = \frac{2\pi}{k^2} \,{\rm Re}\left[A_{\parallel}(\hat{e}_0^{\rm i}) + A_{\perp}(\hat{e}_0^{\rm i})\right], \tag{2.64}$$

where $k = 2\pi/\lambda$ in which λ the incident wavelength. $A_{\parallel}(\hat{e}_0^{\rm i})$ and $A_{\perp}(\hat{e}_0^{\rm i})$ are the amplitude scattering matrix elements in the forward scattering direction for parallel and perpendicular polarization configurations, respectively. In eq. (2.64), the symbol, Re, denotes the real part of the associated quantity. In GOM2, the absorption cross-section of an ice crystal is computed via a rigorous electromagnetic relation (Hage *et al.*, 1991) given by

$$\sigma_{\rm abs} = \frac{k\varepsilon_{\rm i}}{|\boldsymbol{E}^{\rm i}|^2} \iiint_v \boldsymbol{E}(\boldsymbol{r}) \cdot \boldsymbol{E}^*(\boldsymbol{r}) \,{\rm d}\boldsymbol{r}, \tag{2.65}$$

where $\varepsilon_{\rm i}$ is the imaginary part of the permittivity, $\boldsymbol{E}^{\rm i}$ is the incident electric vector, and the integration is carried out for the volume of the particle. When eq. (2.65) is applied to the ray-tracing computation, a semi-analytical expression can be derived for the absorption cross-section, as shown by Yang and Liou (1996b).

Similar to the case in eq. (2.63), the far field can be computed if the internal electric field within the scattering particle is known, as is given by the following electrodynamic relation (Saxon, 1973; Goedecke and O'Brien, 1988; Mishchenko *et al.*, 2002):

$$\boldsymbol{E}^{\rm s}(\boldsymbol{r})\big|_{kr\to\infty} = \frac{k^2\,{\rm e}^{ikr}}{4\pi r}(\varepsilon - 1) \iiint_v \{\boldsymbol{E}(\boldsymbol{r}') - \hat{r}[\hat{r} \cdot \boldsymbol{E}(\boldsymbol{r}')]\}\,{\rm e}^{-ik\hat{r}\cdot\boldsymbol{r}'}\,{\rm d}^3r', \tag{2.66}$$

where ε is the permittivity. The advantage of using eq. (2.66) is that only the electric field is involved, whereas both electric and magnetic fields are included in eq. (2.64). In the limit of geometric optics, the incident wave consists of a bundle of rays each of which propagates along a rectilinear path determined by Snell's law. With this assumption, the volume integration in eq. (2.66) can be carried out along the ray paths, and at the same time a semi-analytical solution for the far-field can be derived (Yang and Liou, 1997). This method is referred to as the ray-by-ray integration (RBRI) method in the authors' previous work. Yang and Liou (1997) also showed that RBRI reduces to the anomalous diffraction approximation (ADA) developed by van de Hulst (1957) when the scattering particle is optically tenuous (i.e., the refractive index is close to 1).

The GOM2 and RBRI methods are essentially the same within the context that a hybrid algorithm based on the principles of geometric optics and the near-to-far-field electromagnetic wave theory are employed to compute the single-scattering properties of an ice crystal.

2.3 The finite-difference time domain method

For size parameters less than about 20–40, the geometric optics method breaks down (Yang and Liou, 1995; 1996b; Macke *et al.*, 1995; Mishchenko and Macke, 1999). Although various methods (see Mishchenko *et al.* 2000) have been developed to solve for the single-scattering properties of nonspherical particles, the finite-difference time-domain (FDTD) method pioneered by Yee (1966) is quite attractive for the computation of light scattering and absorption by small nonspherical and inhomogeneous ice crystals. The FDTD method has been known to be a flexible and robust approach for solving various electromagnetic problems. Publications related to the FDTD method in the literature surveyed by Shlager and Schneider (1998) illustrate the popularity of this method. In particular, several books have been entirely devoted to this particular numerical technique for various applications, ranging from the signal propagation in circuits to the study of the electromagnetic hazard in bioscience (Kunz and Luebbers, 1993; Taflove, 1995; Taflove and Hagness, 2000).

The FDTD method can be technically considered as a 'brute force' approach to solve the time-dependent Maxwell curl equations. Unlike the conventional approach of solving Maxwell's equations in the frequency domain in which an electromagnetic scattering process is posed as a boundary-value problem, the FDTD method solves an electromagnetic problem as an initial-value problem. Mathematically, a boundary-value problem is normally more difficult than its initial-value counterpart. To illustrate the basic concept of the FDTD method for those who do not have any experience on this numerical technique, here we first recapture the FDTD solution for the propagation of a plane electromagnetic wave in free space, which is a typical 1-D wave-propagation problem. Then, we outline the other major numerical aspects (namely, the absorbing boundary condition, the transform of the field from the time domain to the frequency domain, and the mapping of the near field to the far field) involved in the implementation of the FDTD technique for computing the scattering properties of dielectric particles. A comprehensive discussion on the 1-D scalar wave equation in the framework of the finite-difference technique has been presented by Umashankar and Taflove (1982), Taflove (1995) and Taflove and Hagness (2000) who also discussed the 1-D electromagnetic wave propagation for the implementation of the incident wave condition in the FDTD numerical computation.

As shown in Fig. 2.3, a wave propagates along the z-axis of a Cartesian coordinate system. The electric and magnetic vectors associated with this wave are specified along the x- and y-axis of the coordinate system. This is a typical 1-D wave propagation problem and the governing equations for the electromagnetic wave can be written as follows:

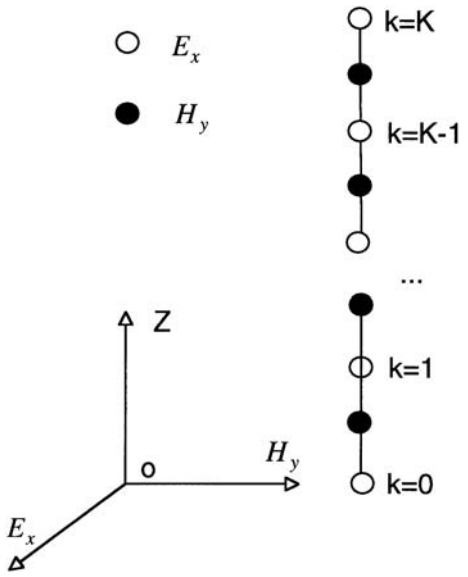

Fig. 2.3. The grid for the one-dimensional finite-difference analog of Maxwell's equations. The propagation of a plane electromagnetic wave is defined as propagating along the z-axis of the coordinate system. The electric and magnetic fields are specified in a staggered manner, i.e., E_x is defined at grid points $k = 0, 1, 2, \ldots, K$ whereas H_y specified at grid points $k = 1/2, 3/2, \ldots, k - 1/2$.

$$\frac{1}{c}\frac{\partial E_x(z,t)}{\partial t} = -\frac{\partial H_y(z,t)}{\partial z}, \tag{2.67}$$

$$-\frac{1}{c}\frac{\partial H_y(z,t)}{\partial t} = \frac{\partial E_x(z,t)}{\partial z}, \tag{2.68}$$

where c is the speed of light in vacuum. To solve variation in the electromagnetic wave, the finite-difference technique is used in the FDTD method, i.e., both electric and magnetic fields are specified in terms of their discrete values in time and space. Following Yee (1966) and Taflove (1995), we define the discrete values of the fields as follows:

$$E^n_{x,k} = E_x(k\,\Delta z,\ n\,\Delta t), \tag{2.69}$$

$$H^{n+1/2}_{y,k+1/2} = H_y\left[(k+1/2)\,\Delta z,\ (n+1/2)\,\Delta t\right], \tag{2.70}$$

where Δz and Δt are the grid size and time increment, respectively, and the indices k and n are integers. The electric and magnetic fields are defined on a stagger grid, i.e., the electric field is specified at grid points with integer indices ($k = 0,\ 1,\ 2,\ \ldots$), whereas the magnetic field is defined at the middle points of adjacent grid points. Similarly, the electric field is defined at time steps $n\,\Delta t$, whereas the magnetic field is defined at time steps $(n+1/2)\,\Delta t$. Using the discrete values of the fields defined in eqs (2.69) and (2.70), the derivatives of the electric and magnetic fields in Maxwell's equations can be expressed in terms of the

standard 'leapfrog' or central difference scheme as follows (Yee, 1966; Taflove, 1995):

$$\left.\frac{\partial E_x(z,t)}{\partial t}\right|_{\substack{z=k\Delta z\\ t=(n+1/2)\Delta t}} \approx \frac{E_x[k\,\Delta z,\ (n+1)\,\Delta t] - E_x[k\,\Delta z,\ n\,\Delta t]}{\Delta t} = \frac{E_{x,k}^{n+1} - E_{x,k}^{n}}{\Delta t}, \tag{2.71}$$

$$\left.\frac{\partial H_y(z,t)}{\partial z}\right|_{\substack{z=k\Delta z\\ t=(n+1/2)\Delta t}} \approx \frac{H_y[(k+1/2)\,\Delta z,\ (n+1/2)\,\Delta t] - H_y[(k-1/2)\,\Delta z,\ (n+1/2)\,\Delta t]}{\Delta z} = \frac{H_{y,k+1/2}^{n+1/2} - H_{y,k-1/2}^{n+1/2}}{\Delta z}, \tag{2.72}$$

Upon substitution of eqs (2.71) and (2.72) into eq. (2.67), the finite-difference analog of eq. (2.67) is given by

$$E_{x,k}^{n+1} = E_{x,k}^{n} + \frac{c\,\Delta t}{\Delta z}\left[H_{y,k-1/2}^{n+1/2} - H_{y,k+1/2}^{n+1/2}\right]. \tag{2.73}$$

Similarly, we can derive the finite difference analog of eq. (2.68) as follows:

$$H_{y,k+1/2}^{n+1/2} = H_{y,k+1/2}^{n-1/2} + \frac{c\,\Delta t}{\Delta z}\left[E_{x,k}^{n} - E_{x,k+1}^{n}\right]. \tag{2.74}$$

The selection of the time increment Δt in the finite analog of Maxwell's equations is not arbitrary because of the stability condition required by the difference equations in numerical computation (Yee, 1966; Taflove and Brodwin, 1975). In the case for 1-D electromagnetic wave, the stability condition requires that $c\,\Delta t/\Delta z \leq 1$.

Equations (2.73) and (2.74) constitute the difference equations for computing variation in the fields. In practice, if the initial values of the fields, say, $E_{x,k}^{1}$ and $H_{y,k+1/2}^{1/2}$ are defined at grid points indicated by indices 0, 1, 2, ... and 1/2, 3/2, 5/2, ..., respectively, this variation can be simulated by a time-marching iteration based on eqs (2.73) and (2.74). However, the computational domain in the numerical simulation must be truncated. For the 1-D case, let the computational domain be the spatial regime bounded by grid point $k = 0$ and $k = K$. From eqs (2.73) and (2.74), the electric fields at $k = 0$ and $k = K$ cannot be computed by these two finite difference equations because $H_{y,-1/2}^{1/2}$ and $H_{y,K+1/2}^{1/2}$ are defined at the locations outside the computational domain. Thus, to update the electric fields at the boundary points, appropriate boundary conditions must be provided. For simplicity in calculating the field values at the boundary grid points, the grid configuration can be specified as follows:

$$c\,\Delta t/\Delta z = 1/2. \tag{2.75}$$

The preceding relation implies that the wave propagates half grid size every time step. Thus, the equations for updating the boundary values can be written as follows:

$$E^n_{x,1/2} = E^{n-1}_{x,1}, \tag{2.76}$$

$$E^{n+1}_{x,0} = E^n_{x,1/2}, \tag{2.77}$$

$$E^n_{x,K-1/2} = E^{n-1}_{x,K-1}, \tag{2.78}$$

$$E^{n+1}_{x,K} = E^n_{x,K-1/2}, \tag{2.79}$$

where $E^n_{x,1/2}$ and $E^n_{x,K-1/2}$ are two auxiliary quantities introduced for updating the electric fields at the two boundary points, respectively. Equations (2.76) and (2.77) constitute the boundary condition for the grid point for $k = 0$, whereas eqs (2.78) and (2.79) constitute the boundary condition for the grid point of $k = K$. Using the finite difference equations (2.73) and (2.74) and the boundary conditions given by eqs (2.76)–(2.79), one can compute variation in the electromagnetic fields within the region between $k = 0$ and K. The computed electromagnetic fields are the same as those in the case where the computational domain is not bounded. Note that if $E^n_{x,0} = 0$ and $E^n_{x,K} = 0$, the boundary grid points constitute the reflecting boundaries. In this case, the electromagnetic wave, when impinges on the boundary grid points, is reflected back to the computational domain and contaminate the numerical simulation. The preceding 1-D finite-difference equations and the associated boundary conditions have been employed to implement the incident wave conditions in various applications of the FDTD technique (e.g., Sullivan *et al.*, 1988).

The discretization of Maxwell's equations in the 3-D case is similar to that in 1-D case. For example, the Maxwell curl equations in the scalar component form for E_x and H_x can be written as follows:

$$\frac{\partial E_x(\boldsymbol{r},t)}{\partial t} = \frac{c}{\varepsilon}\left(\frac{\partial H_z(\boldsymbol{r},t)}{\partial y} - \frac{\partial H_y(\boldsymbol{r},t)}{\partial z}\right), \tag{2.80}$$

$$\frac{\partial H_x(\boldsymbol{r},t)}{\partial t} = -c\left(\frac{\partial E_z(\boldsymbol{r},t)}{\partial y} - \frac{\partial E_y(\boldsymbol{r},t)}{\partial z}\right). \tag{2.81}$$

For simplicity in this discussion, we assume that the permittivity is a real number. Using the standard definitions for the electric and magnetic fields on a grid cell shown in Fig. 2.4 (Yee, 1966), it is straightforward to derive the difference analog of eqs (2.81) and (2.82) on the basis of the central-difference scheme in both time and space as follows:

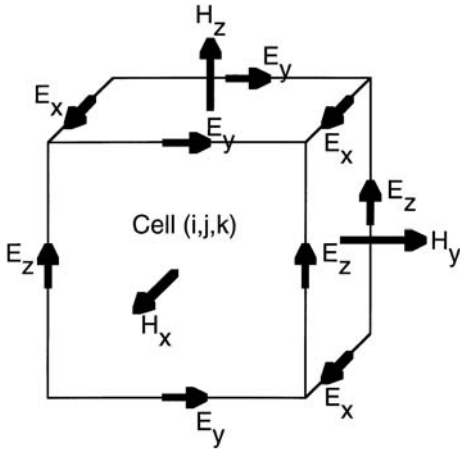

Fig. 2.4. Locations of the electric and magnetic field components on a cubic grid cell, defined by Yee (1966).

$$
\begin{aligned}
E^{n+1}_{x,i,j+1/2,k+1/2} &= E^{n}_{x,i,j+1/2,k+1/2} \\
&\quad + \frac{1}{\varepsilon_{i,j+1/2,k+1/2}} \left[\frac{c\,\Delta t}{\Delta y} (H^{n+1/2}_{z,i,j+1,k+1/2} - H^{n+1/2}_{z,i,j,k+1/2}) \right. \\
&\quad \left. + \frac{c\,\Delta t}{\Delta z} (H^{n+1/2}_{y,i,j+1/2,k} - H^{n+1/2}_{y,i,j+1/2,k+1}) \right], \qquad (2.82)
\end{aligned}
$$

$$
\begin{aligned}
H^{n+1/2}_{x,i+1/2,j,k} &= H^{n-1/2}_{x,i+1/2,j,k} + \left[\frac{c\,\Delta t}{\Delta y} (E^{n}_{z,i+1/2,j-1/2,k} - E^{n}_{z,i+1/2,j+1/2,k}) \right. \\
&\quad \left. + \frac{c\,\Delta t}{\Delta z} (E^{n}_{y,i+1/2,j,k+1/2} - E^{n}_{y,i+1/2,j,k-1/2}) \right]. \qquad (2.83)
\end{aligned}
$$

The finite-difference equations for other components of the electric and magnetic fields can be determined in similar forms. In the 3-D case, the stability condition has been derived by Taflove and Brodwin (1975) given by

$$
c\,\Delta t \le \frac{1}{\sqrt{1/\Delta x^2 + 1/\Delta y^2 + 1/\Delta z^2}}. \qquad (2.84)
$$

In the 3-D case, the boundary condition is a major issue in the FDTD computation because the analytical boundary equations cannot be constructed due to the unknown propagating directions of the outgoing waves. In the past two decades, various numerical techniques (Blaschak and Kriegsmann, 1988; Moore *et al.*, 1988; Berntsen and Hornsleth, 1994) have been developed to update the field values at the boundary grid points. The commonly used approaches are the absorbing boundary condition developed by Mur (1981), the transmitting boundary condition developed by Liao *et al.* (1984), and the perfectly matched layer (PML) boundary condition pioneered by Berenger (1994, 1996). The PML

is particularly efficient and popular in the implementation of the FDTD numerical scheme (e.g., Katz *et al.* 1994). In the following we briefly outline the principle of the PML boundary condition.

The essence of PML is to introduce an artificial absorbing medium within the boundary layers that impose absorption on the partial electromagnetic field components. For implementing the PML absorbing boundary condition, a field component needs to be split into two parts in the forms

$$(E_x, E_y, E_z) = [(E_{xy} + E_{xz}),\ (E_{yx} + E_{yz}),\ (E_{zx} + E_{zy})], \tag{2.85}$$

$$(H_x, H_y, H_z) = [(H_{xy} + E_{xz}),\ (H_{yx} + H_{yz}),\ (H_{zx} + H_{zy})]. \tag{2.86}$$

The PML boundary condition equations for E_z and H_z components at a boundary perpendicular to the x-axis are given by

$$\frac{\exp[-\tau_x(x)t]}{c}\frac{\partial}{\partial t}\{\exp[\tau_x(x)t]E_{zx}\} = \frac{\partial(H_{yx} + H_{yy})}{\partial x}, \tag{2.87}$$

$$\frac{1}{c}\frac{\partial E_{zy}}{\partial t} = -\frac{\partial(H_{xy} + H_{xz})}{\partial y}, \tag{2.88}$$

$$\frac{\exp[-\tau_x(x)t]}{c}\frac{\partial}{\partial t}\{\exp[\tau_x(x)t]H_{zx}\} = -\frac{\partial(E_{yx} + E_{yz})}{\partial x}, \tag{2.89}$$

$$\frac{1}{c}\frac{\partial H_{zy}}{\partial t} = \frac{\partial(E_{xy} + E_{xz})}{\partial z}, \tag{2.90}$$

where $\tau_x(x)$ is defined for the boundary layers near $x = 0$ as follows:

$$\tau_x(x) = \tau_{\max}|(x - \delta x)/\delta x|^p, \tag{2.91}$$

where $\tau_{\max}$ denotes the maximum absorption at $x = 0$, which can be determined by specifying the reflectance of the boundary layers at a normal incidence. In eq. (2.91), δx denotes the thickness of the boundary layer and p is usually selected between 2 and 3 (Lazzi and Gandi, 1996). In numerical computations, the PML boundary condition is applied to outgoing scattered waves. To do so, the FDTD computation is usually divided into an inner domain enclosed by an outer domain. Within the inner domain, the total field (incident plus scattered fields) is simulated, and only outgoing or scattered field is simulated otherwise. In practice, an interface known as the Huygens surface (Merewether *et al.*, 1980) is introduced to connect the fields in the two domains. Note that, to avoid the Huygens surface, an alternative approach for which the scattered field is defined for the entire computational domain has been developed (e.g., Britt, 1989; Yang and Liou, 1995). However, this approach is not computationally efficient, particularly, for the implementation of the FDTD method in the 3-D case.

With the finite difference analog of the Maxwell equations and the absorbing boundary condition, the electromagnetic field within or near a scattering particle (i.e., the near field) in the time domain can be obtained. The corresponding signal in the frequency domain can be obtained via the discrete Fourier transform. For example, if the time series of electric field at a given grid point say,

$E^{n+1}_{x,i,j+1/2,k+1/2}$, are known, the corresponding signal in the frequency domain can be obtained as follows

$$E_{x,i,j+1/2,k+1/2}(k) = \sum_{n=0}^{N} E^{n+1}_{x,i,j+1/2,k+1/2} \exp(i2\pi cn\,\Delta t/\lambda), \tag{2.92}$$

The discrete Fourier transform is more efficient than the fast Fourier transform for application to the FDTD computation, as illustrated by Furse and Gandhi (1995).

After the near field in the frequency domain is obtained, the scattered far field can be obtained from either eq. (2.63) or eq. (2.66). Although these two equations are physically equivalent, the far-field values computed from eqs (2.63) and (2.66) differ in terms of accuracy (Zhai *et al.*, 2004). The near-to-far-field transformation in both the frequency and time domains has been discussed by Taflove and Hagness (2000) and references cited therein.

2.4 Numerical examples

The FDTD technique has been applied to the investigation of the scattering properties of small ice crystals (Yang and Liou, 1995, 1996a; Sun *et al.*, 1999; Sun and Fu, 2000; Yang *et al.*, 2004a) and its accuracy has been extensively studied in reference to the results computed from the 'exact' Lorenz–Mie theory for spheres. Also, Baran *et al.* (2001) compared the FDTD solution and T-matrix results for the single-scattering properties of hexagonal ice crystals. In general, the relative errors of the FDTD solutions are typically less than 1% for computing the extinction and absorption cross-sections and on the order of 10% for computing the phase function if the grid size is less than 1/20 of the wavelength within the scattering particle of interest. The accuracy of the FDTD solution can be further improved if a finer grid size is used, but at the expense of the computational CPU time. In practice, application of the FDTD technique to the light scattering by ice crystals is limited to size parameters less than about 20 because enormous computational efforts are required. Sun *et al.* (1999) applied this method to the solution to the scattering of light by a single ice sphere with a size parameter of 40 at a wavelength at which the refractive index of ice is small. Application of the FDTD technique to the scattering of light by particles with a large refractive index (e.g., the real part of the refractive index is on the order of 8) has been recently reported by Sun and Fu (2000) and Yang *et al.* (2004a). The latter authors also applied this method to complex bullet rosette ice crystals with various branches (Yang *et al.*, 2004a). As an example, Fig. 2.5 shows comparison of the phase matrix elements computed from the FDTD technique and the Lorenz–Mie theory for an ice sphere with a size parameter of 20 at a wavelength of 0.6328 μm. A surface-integral based approach (Zhai *et al.*, 2004) with a grid resolution of $\lambda/\Delta s = 40$ is used to map the near field to far field for the FDTD resolute shown in Fig. 2.5, where λ and Δs are the incident wavelength and grid size, respectively. Excellent agreement between the FDTD

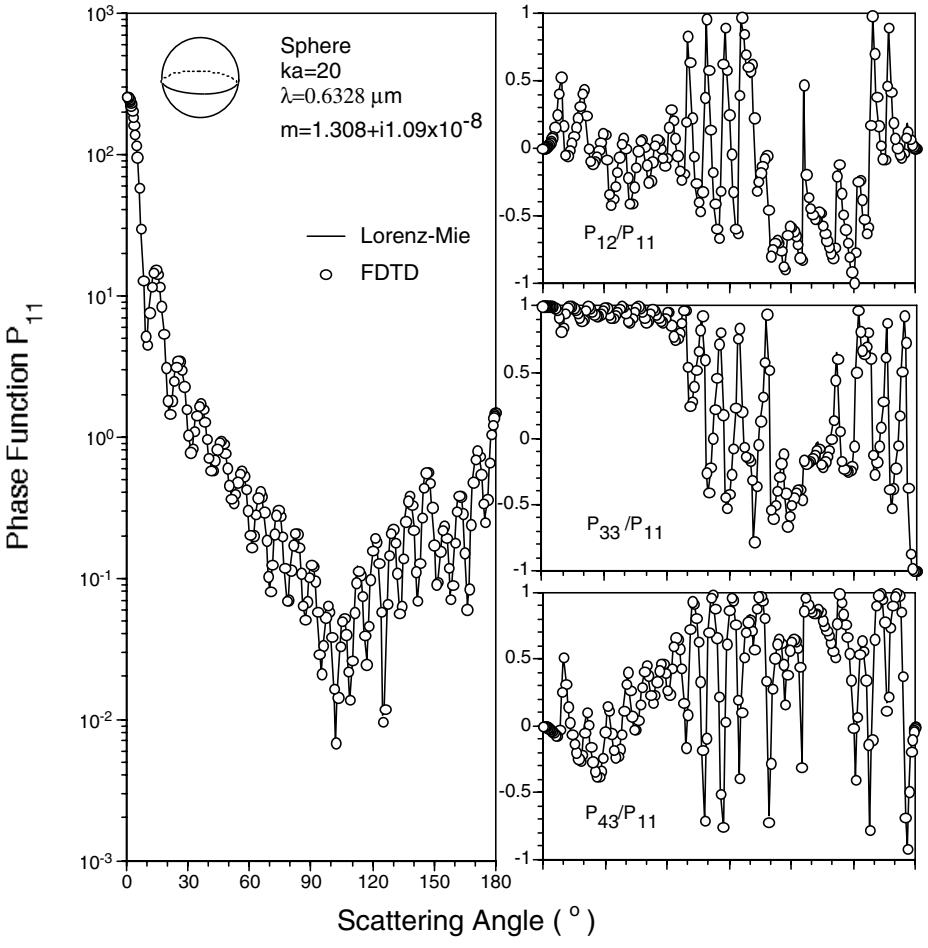

Fig. 2.5. Comparison of the phase matrix elements computed from the Lorenz–Mie theory and the FDTD method for an ice sphere with a size parameter of 20 using a wavelength of 0.6328 μm.

and Lorenz–Mie results is evident. The FDTD solution for the phase function is more accurate than for the other phase matrix elements because former is less sensitive to phase variation in the scattered waves.

It has been commonly assumed that a small quasi-spherical ice crystal may be approximated by an equivalent sphere, defined by (1) the same diameter (D), (2) the same surface area (A), (3) the same volume (V), or (4) the same ratio of V to A. Fig. 2.6 shows comparison of the phase functions computed for these four definitions of spherical equivalence for Platonic solids (i.e., tetrahedron, hexahedron, octahedron, dodecahedron, and icosahedron). It is interesting to note that the study of the Platonic-solid shape has a rich history, which goes back to the beginning of recorded human civilization. For example,

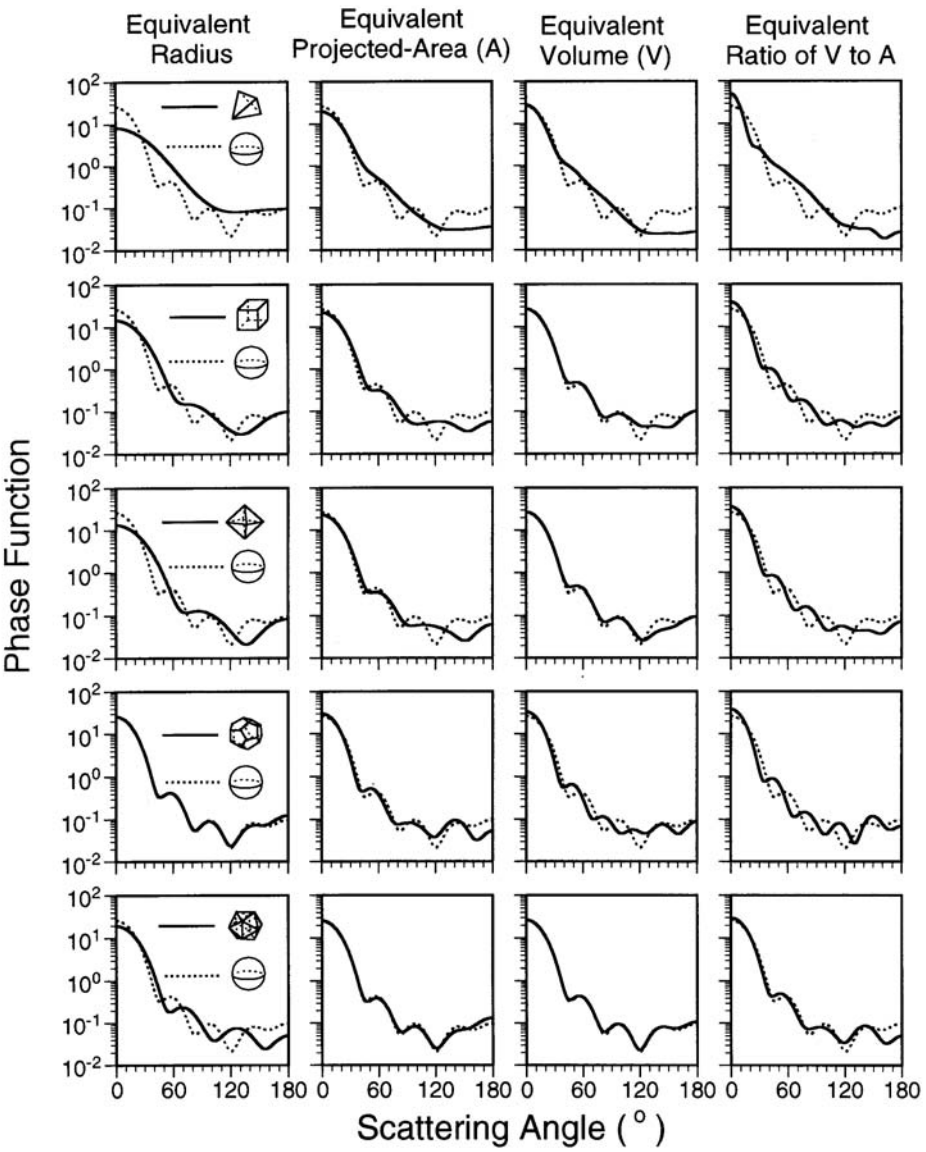

Fig. 2.6. The phase function of an ice sphere with a size parameter of $x = 5$. The wavelength and refractive index are 0.6328 μm and $1.3085 + \text{il}.09 \times 10^{-8}$, respectively. Also shown are the phase functions of the five Platonic shapes with the same radius (the first column), projected area (the second column), volume (the third column) and V/A (the fourth column) as those for the ice sphere (after Yang *et al.*, 2004b).

the polyhedron was extensively used/investigated in ancient Egyptian, Babylonian, Chinese, and Greek cultures associated with the study of architecture, art, mathematics, and even the philosophy regarding the early understanding

of the universe. Historically, it was believed that matter was composed of a few elemental substances combined in different ways. Influenced by Aristotle (384–322 **BC**), ancient wisdom assumed that the basic elements (fire, air, earth, water, and celestial matter) were related to the five regular polyhedra. A review of the history of the study of polyhedron can be found in a monograph by Cromwell (l997) and also in a review article by Field (1979). Although the polyhedron has been studied for millennia from various perspectives, it is still a challenging topic for modern mathematicians. In fact, many mathematical theorems related to the polyhedron have only recently been proved (e.g., Grunbaum, 1967). The numbers of the faces for a tetrahedron, a cube, an octahedron, a dodecahedron, and an icosahedron are 4, 6, 8, 12, and 20, respectively. The faces of a Platonic solid are equilateral polygons with the same number of sides. The number of faces, the number of vertices, and the number of edges of a polyhedron satisfy the famous Euler's theorem (Euler, 1758) that can be expressed as follows:

$$f + v + e = 2, \tag{2.93}$$

where f is the number of polygon faces, v the number of vertices, and e the number of edges. The five platonic solids approach spheres in an orderly manner and, therefore, they are ideal for investigating the asphericity effect on the scattering properties. It is evident from Fig. 2.6 that a systematically optimized definition for 'spherical equivalence' does not exist. It is seen that the 'spherical equivalence' based on the particle dimension leads to the best approximation in the case for dodecahedron, whereas the volume-based 'equivalence' is more accurate than the other three definitions in the case of the icosahedron. It is clear that the extent of nonsphericity of a particle in the context of light scattering computation depends on a specific geometry. This implies that a general optimal 'spherical equivalence' cannot be defined to minimize the errors associated with the spherical approximation for a variety of nonspherical geometries in light scattering computations.

The simplest ice crystal shape can be represented by the pristine column and plate that normally have a basic hexagonal symmetric structure. Using the geometric ray-tracing technique, the scattering properties of hexagonal ice crystals have been extensively investigated in the past. The pristine ice crystal types produce the well-known 22° and 46° halos, as well as a number of fascinating arcs and sundogs that have been observed in cirrus cloud conditions (see for example, Greenler, 1990).

The upper panels of Fig. 2.7 show the nonzero phase matrix elements for randomly oriented hexagonal ice columns at a wavelength of 0.6328 μm. For the scattering of light by large particles with a size parameter on the order of those shown in Fig. 2.7, the conventional and improved geometric optics methods produce about the same results. The peaks at 22° and 46° scattering angles in the phase function are responsible for the halos observed in the atmosphere. The scattering maximum between 150° and 160° is produced by the rays undergoing two internal reflections (Takano and Liou, 1989a). The lower panels in Fig. 2.7

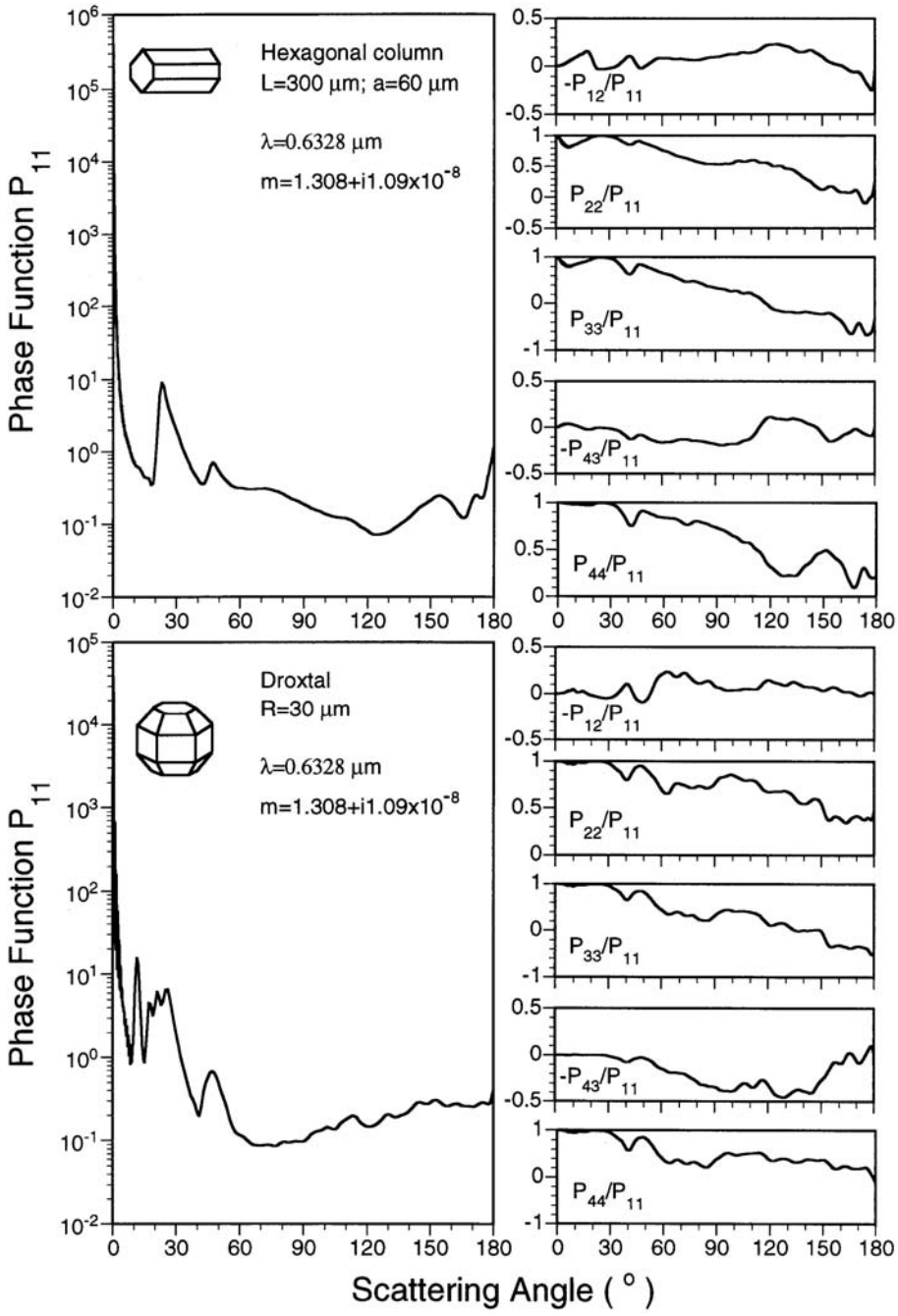

Fig. 2.7. The scattering phase matrix of randomly oriented hexagonal ice columns and droxtal ice crystals computed from the geometric optics method for large size parameters.

show the nonzero phase matrix elements for randomly oriented droxtal, an ice crystal term introduced by Thuman and Robinson (1954) and Ohtake (1970). The droxtal geometry with a 20-face structure has been suggested as a better representation of small quasi-spherical ice crystals observed in ice clouds. It has been speculated that the formation of droxtal ice crystals is associated with the freezing of supercooled water droplets and subsequent growth by water vapor deposition (Zhang *et al.*, 2004). From Fig. 2.7, it is evident that the single-scattering properties of droxtal ice crystals are substantially different from those of well-defined pristine hexagonal ice crystals. For the former, the phase function is quite flat at large scattering angles from 100° to 180°. Additionally, droxtals scatter less energy than hexagonal ice crystals in the scattering directions around 60°. A strong peak at the 11° scattering angle in the phase function of droxtals is produced by rays undergoing two sequential refractions through the trapezoidal and rectangular faces.

Fig. 2.8 illustrates the phase matrix for randomly oriented small hexagonal ice crystals and droxtals computed from FDTD. Based on laboratory and aircraft observations, small ice crystals tend to have unit aspect ratio (Auer and Veal, 1970), i.e., $L/2a \sim 1$ in which L and a are the length and semi-width of an ice crystal, respectively. The pronounced scattering peaks corresponding to halos are not observed in the phase function. However, a scattering maximum is shown for both small hexagons and droxtals that are randomly oriented in space. We also note that the phase function for droxtals shows fluctuations in the side and backscattering directions, which cannot be smoothed out through random orientation averaging. Although the overall geometry of a droxtal is close to a sphere, significant nonsphericity effect is noted from the phase matrix. For a sphere, the ratio P_{22}/P_{11} is one. It has been argued that the deviation of P_{22}/P_{11} from unity is an index of nonsphericity effect (Bohren and Huffman, 1983; Mishchenko *et al.* 2002). From Fig. 2.8, the P_{22}/P_{11} values for droxtals for the scattering angles larger than 60° are substantially deviated from unity, indicating the prominent nonspherecity effect. Yang *et al.* (2003) and Zhang *et al.* (2004) have proposed that small quasi-spherical ice crystals in ice clouds may be approximated as droxtals in light scattering computations.

To compare the single-scattering properties for various ice crystal shapes, Figs. 2.9 and 2.10 show the phase functions for six ice crystal habits with small and large size parameters, respectively. For large aggregates, their surfaces are assumed to be moderately rough in the phase function computation on the basis of the Gram–Charlier distribution (Cox and Munk, 1954) following the method described in Yang and Liou (1998). It is evident from Fig. 2.9 that the scattering of light by small ice crystals does not produce halo peaks. For small plates and columns (the panels in the second row) the phase functions are smooth for scattering angles from 90° to 180°. On the contrary, the overall feature of the phase function for large ice crystals illustrates pronounced peaks, except in the case of aggregates because surface roughness smooths out the scattering peak.

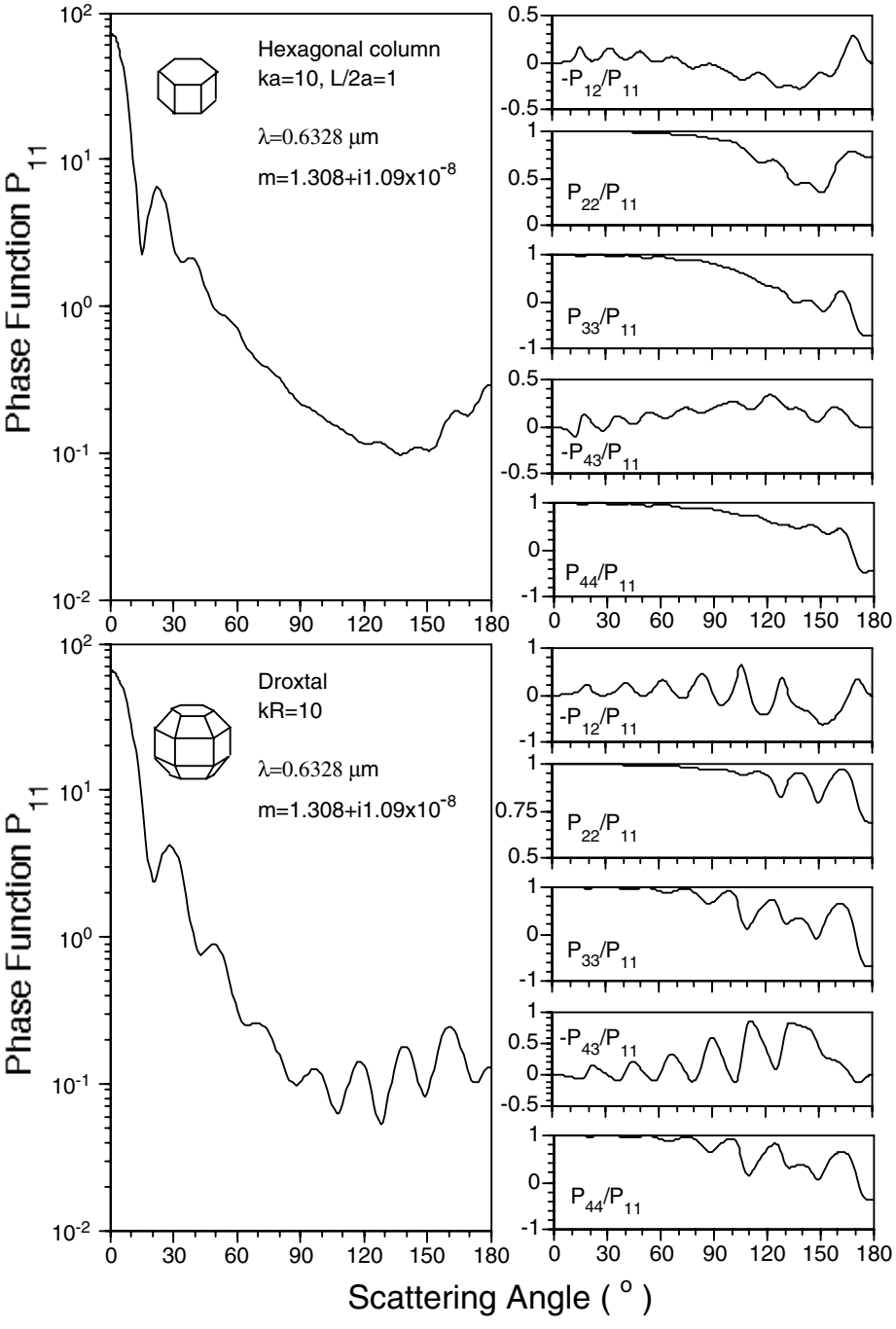

Fig. 2.8. The phase matrix of small compact hexagonal and droxtal ice crystals computed from the FDTD method.

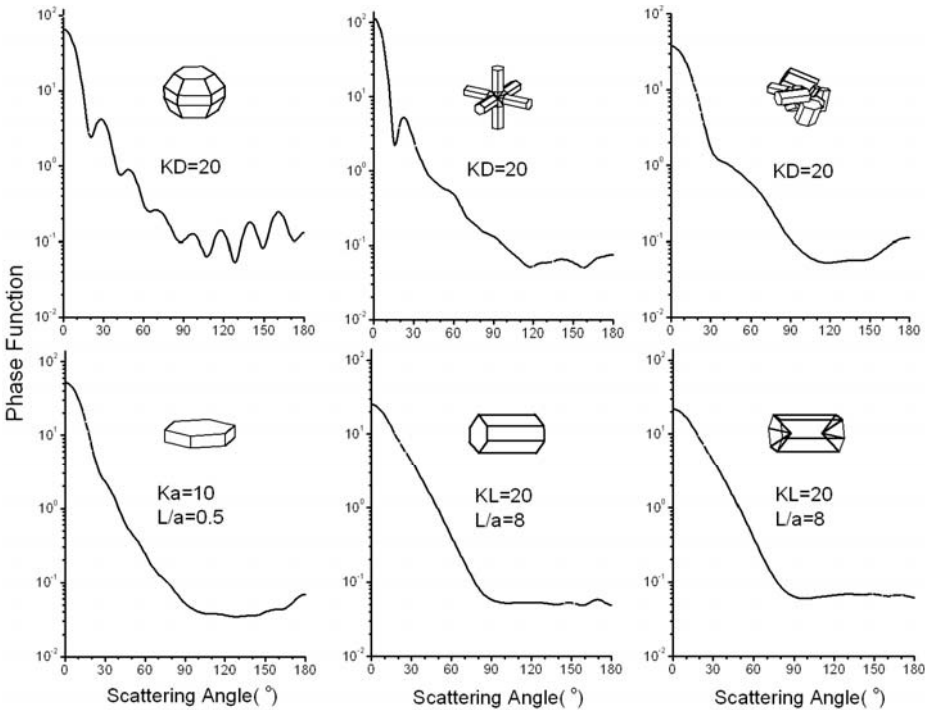

Fig. 2.9. Comparison of the phase functions computed from the FDTD method for ice ice crystal shapes that are commonly observed in ice clouds. The parameter, D, is the maximum dimension for a droxtal, a bullet rosette, or an aggregate ice crystal. For plates and columns, a denotes the half-width and L is the length (for columns) or thickness (for plates). $K = 2\pi/\lambda$ is the wavenumber.

To demonstrate the improvement in GOM2 (Yang and Liou, 1995) as compared to the conventional ray-tracing approach for moderate size parameters, Fig. 2.11 shows the phase function computed by the two methods and FDTD in a 2D case. In the computation, ice crystals were assumed to be infinitely long hexagonal columns with normal incidence. Halo peaks are noticed in the conventional ray-tracing solution, but not in the FDTD result. The scattering patterns produced by the improved geometric optics are similar to those shown in FDTD for both size parameters, but its accuracy is degraded in scattering angles larger than $\sim 100°$.

Fig. 2.12 shows the extinction efficiency and single scattering albedo computed from FDTD, GOM2 based on eq. (2.63), RBRI based on eq. (2.66), and the conventional ray-tracing technique. The limitation of the conventional ray-tracing method is evident in the evaluation of the extinction efficiency, which is equal to 2 regardless of the size parameter. At a size parameter of about 20, the results computed from RBRI, GOM2, and FDTD converge. Owing to the limitations of the geometric optics approximation and computational requirements

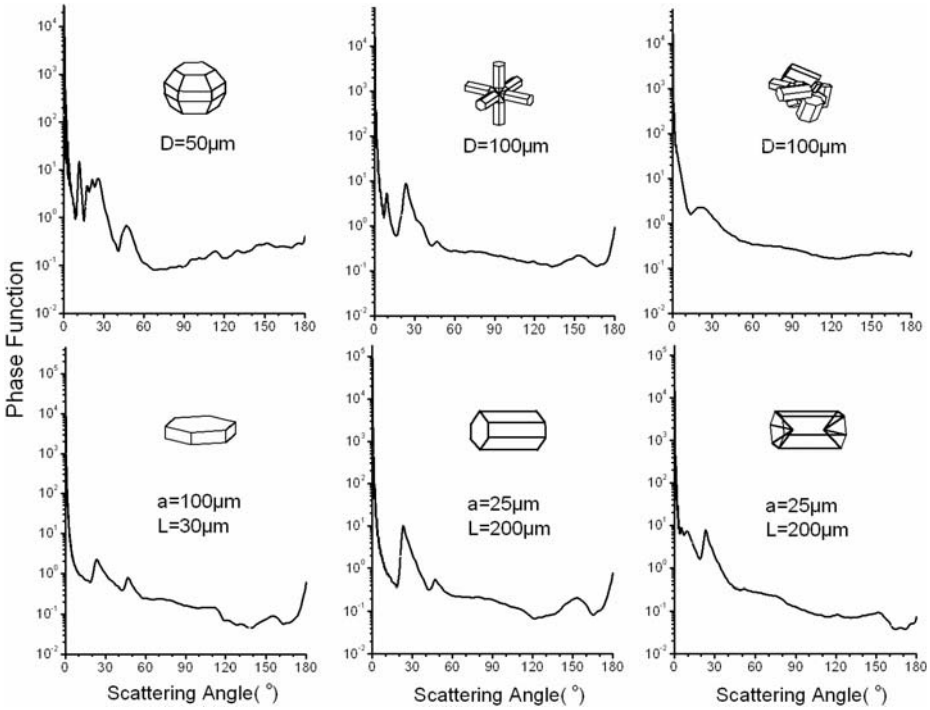

Fig. 2.10. Comparison of the phase functions computed from the geometric optics method for six ice crystal shapes. For aggregates, surface roughness is included in the light scattering computation.

in the FDTD method, they can be applied to large (>20) and small (<20) size parameters, respectively. However, by combining GOM2 and FDTD, calculation of the single-scattering properties for various ice crystal shapes and sizes can be carried out. This is the essence of the unified theory concept developed by Liou *et al.* (2000) in the sense that the accurate FDTD solution can be used for small size parameters and at the same time an approximate geometric optics approach can be applied to large size parameters.

2.5 Summary

In this chapter, we have reviewed the theoretical development and numerical computation for the single-scattering properties of atmospheric ice crystals. Application of two numerical methods, the geometric optics approach and the FDTD technique, to the scattering of light by ice crystals have been highlighted. Specifically, we recaptured the ray-tracing methodology originally developed by Cai and Liou (1982), which is systematically formulated in a vector form in the present presentation. The vector formulation of the ray-tracing procedure is independent of specific coordinate systems and can be implemented in numerical

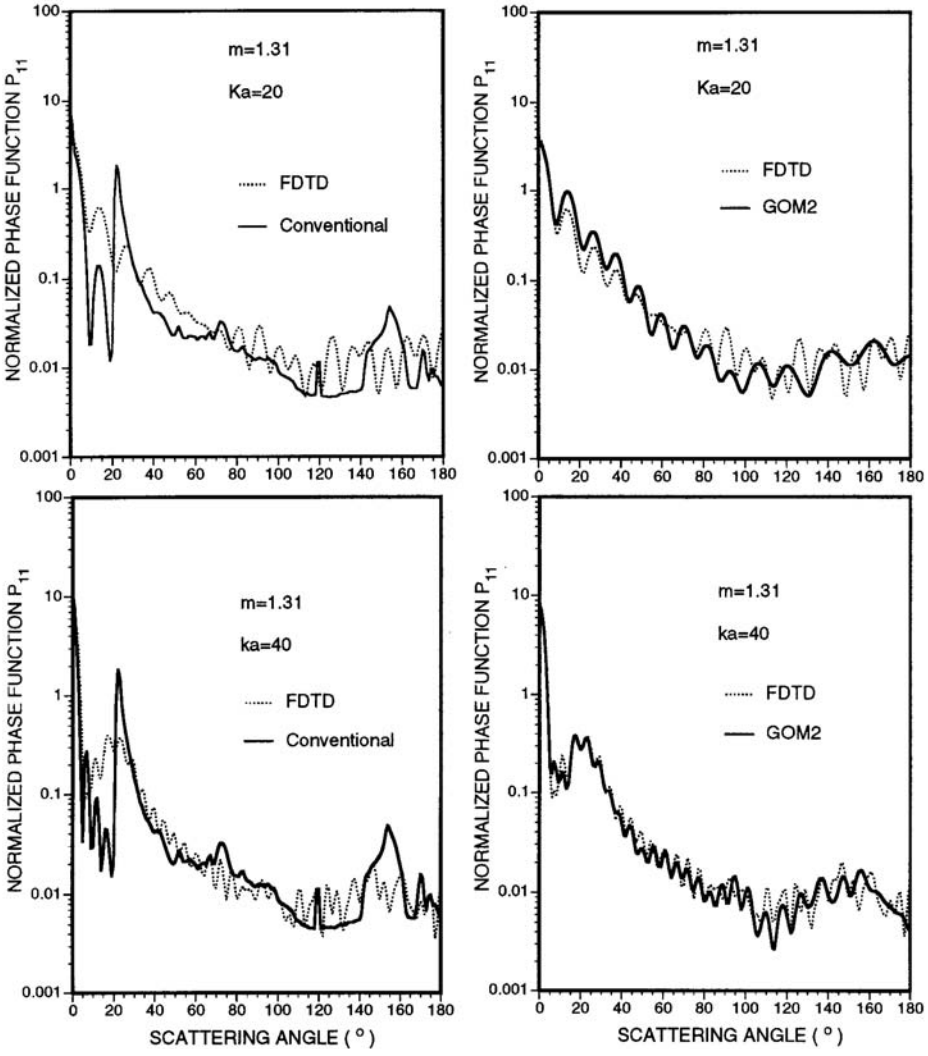

Fig. 2.11. Normalized phase functions computed by the FDTD, conventional ray-tracing, and GOM2 methods for the scattering of light by randomly oriented 2-D hexagonal ice crystals (after Yang and Liou, 1995).

computations effectively. The weightings of diffraction, Fresnel refraction and reflection, and the delta-transmission have been explicitly given in the formulation of the phase matrix. Moreover, the absorption cross-section of ice crystals under the randomly oriented condition is also presented within the framework of the geometric optics approach in which both polarization configurations are accounted for.

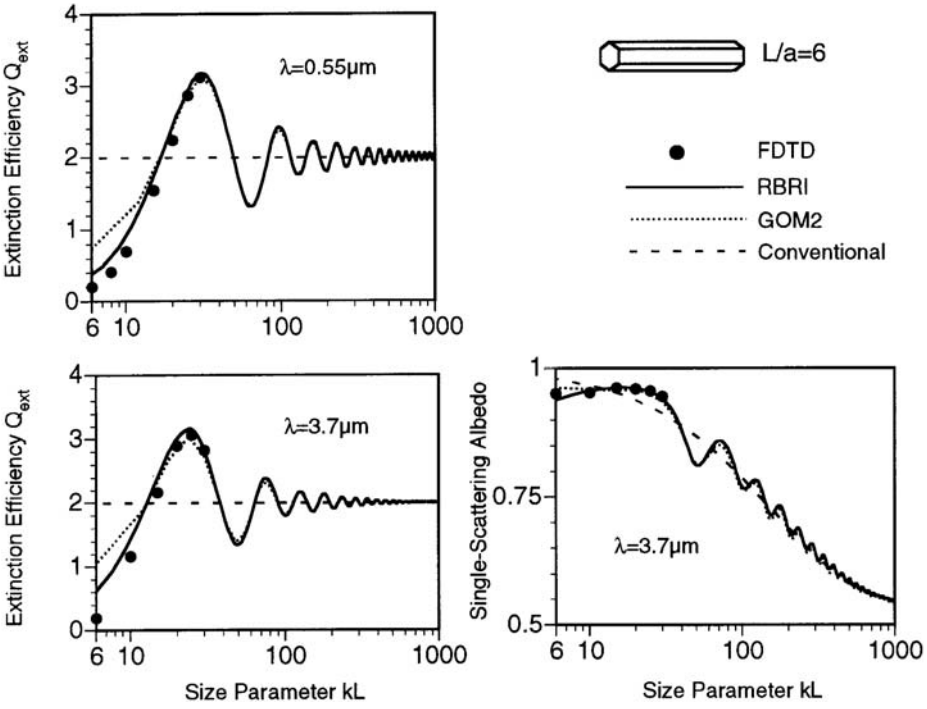

Fig. 2.12. Comparison of the extinction efficiency and the single scattering albedo computed by FDTD, RBRI, GOM2, and the conventional ray-tracing methods at the 0.55-μm and 3.7-μm wavelengths (data taken from Yang and Liou, 1997).

The FDTD techniques pioneered by Yee (1966) and further developed by many others (e.g., Taflove and Hagness (2000) and references cited therein) is an attractive approach to deal with the scattering of light by small ice crystals. We reviewed the basic principle of the FDTD technique by using the 1-D electromagnetic wave propagation process for illustration. The implementation of FDTD in the 3-D case for the scattering of light by ice crystals was outlined, including the discretization of Maxwell's equations on the basis of the difference approximation, the absorption boundary condition for truncating the computational domain, the transform of simulated signals from the time to the frequency domain, and the near field to far field mapping.

Finally, selected numerical results were presented to illustrate the scattering characteristics of large and small ice crystals. The overall feature for the scattering of light by large ice crystals is that the corresponding phase functions normally show strong halo peaks. However, if the surface roughness condition is imposed in the ray-tracing computation, the scattering peaks associated with halos are largely smoothed out. For small ice crystals, the scattering phase functions are generally featureless in the side and backward scattering directions.

Moreover, we revisited some of our previous numerical results to demonstrate certain advantages of the improved geometric optics methods.

Acknowledgments

The authors thank G. Chen, Z. Zhang and P. Zhai for assisting in numerical computation and graphical presentation. During the course of this research, Ping Yang and K. N. Liou were supported by the National Science Foundation under Grants ATM-458131 and ATM-0331550, respectively. Ping Yang would also like to acknowledge support (NAG5-11374) from the NASA Radiation Sciences Program.

References

Asano, S., and G. Yamamoto, 1975: Light scattering by randomly oriented spheroidal particles, *Appl. Opt.* **14**, 29–49.

Auer, A., and D. Veal, 1970: The dimensions of ice crystals in natural clouds. *J. Atmos. Sci.* **27**, 919–926.

Baran, A. J., P. Yang, and S. Havemann, 2001: Calculation of the single-scattering properties of randomly oriented hexagonal ice columns: a comparison of the T-matrix and the finite-difference time-domain methods, *Appl. Opt.* **40**, 4376–4386.

Berenger, B. J., 1994: A perfectly matched layer for the absorption of electromagnetic waves. *J. Comput. Phys.* **114**, 185–200.

Berenger, B. J., 1996: Three-dimensional perfect matched layer for the absorption of electromagnetic wave. *J. Comput. Phys.* **127**, 363–379.

Berntsen, S., and S. N. Hornsleth, 1994: Retarded time absorbing boundary conditions. IEEE Trans. *Antennas Propagat.* **42**, 1059–1064.

Blaschak, J. G., and G. A. Kriegsmann, 1988: A comparative study of absorbing boundary conditions. *J. Comput. Phys.* **77**, 109–139.

Bohren, C. F., and D. R. Huffman, 1983: *Absorption and Scattering of Light by Small Particles.* John Wiley, New York.

Born, M., and E. Wolf, 1959: *Principles of Optics* (Pergamon, Oxford).

Borovoi, A., I. Grishin, E. Naats, and U. Oppel, 2002: Light backscattering by hexagonal ice crystals. *J. Quant. Spectrosc. Radiat. Transfer* **72**, 403–417.

Borovoi, A. G., and I. A. Grishin, 2003: Scattering matrices for large ice crystal particles. *J. Opt. Soc. Am. A* **20**, 2071–2080.

Britt, C. L., 1989: Solution of electromagnetic scattering problems using time domain techniques. *IEEE Trans. Antennas Propagat.* 37, 1181–1191.

Cai, Q., and K. N. Liou, 1982: Polarized light scattering by hexagonal ice crystals: theory. *Appl. Opt.* **21**, 3569–3580.

Chang, P. C., J. G., Walker, K. I. Hopcraft, 2005: Ray tracing in absorbing media. *J. Quant. Spectrosc. Radiative Transfer* **96**, 327–341.

Chen, B., and J. J. Stamnes, 1998: Validity of diffraction tomography based on the first born and the first Rytov approximations. *Appl. Opt.* **37**, 2996–3006.

Coleman, R., and K. N. Liou, 1981: Light scattering by hexagonal ice crystals. *J. Atmos. Sci.* **38**, 1260–1271.

Cox, C., and W. Munk, 1954: Measurement of the roughness of the sea surface from photographs of the sun's glitter. *J. Opt. Amer. Soc.* **44**, 838–850.

Cromwell, P. R., 1997: *Polyhedra*. Cambridge University Press, Cambridge, UK.

Dessler, A. E., and P. Yang, 2003: The distribution of tropical thin cirrus clouds inferred from Terra MODIS data. *J. Climate* **16**, 1241–1247.

Dupertuis, M. A., Proctor, M., and B. Acklin, 1994: Generalization of complex Snell–Descartes and Fresnel laws. *J. Opt. Soc. Am. A* **11**, 1159–1166.

Draine, B. T., and P. J. Flatau, 1994: Discrete-dipole approximation for scattering calculations. *J. Opt. Soc. Am. A* **11**, 1491–1499.

Ebert, E. E. and J. A. Curry, 1992: A parameterization of cirrus cloud optical properties for climate models. J. *Geophys. Res.* **97**, 3831–3836.

Euler, L., 1758: Elementa doctrinae solidorum, novi commentarii academiae. *Scientiarum Petropolitanae* **4**, 109–140.

Field, J. V., 1979: Kepler's star polyhedra, *Vistas in Astronomy* **23**, 109–141.

Fu, Q., and K. N. Liou, 1993: Parameterization of the radiative properties of cirrus clouds. *J. Atmos. Sci.* **50**, 2008–2025.

Furse, C. M., and O. P. Gandhi, 1995: Why the DFT is faster than the FFT for FDTD time-to-frequency domain conversions, *IEEE Microwave Guided Wave Lett.* **5**, 326–328.

Gao, B.-C., and Y. J. Kaufman, 1995: Selection of the 1.375-μm MODIS channels for remote sensing of cirrus clouds and stratospheric aerosols from space. *J. Atmos. Sci.* **52**, 4231–4237.

Goedecke, G. H., and S. G. O'Brien, 1988: Scattering by irregular inhomogeneous particles via the digitized Green's function algorithm. *Appl. Opt.* **27**, 2431–2438.

Greenler, R., 1990: *Rainbows, Halos, and Glories.* Cambridge University Press, New York.

Grunbaum, B., 1967: *Convex Polytopes.* John Wiley, London.

Grynko, Y., and Shkuratov, 2003: Scattering matrix calculated in geometrix optics approximation for semitransparent particles faceted with various shapes. *J. Quant. Spectrosc. Radiat. Transfer* **78**, 319–340.

Hage, J. I., J. M. Greenberg, and R. T. Wang, 1991: Scattering from arbitrary shaped particles: theory and experiment. *Appl. Opt.* **30**, 1141–1152.

Heymsfield, A. J., and J. Iaquinta, 2000: Cirrus crystal terminal velocities. *J. Atmos. Sci.* **57**, 916–938.

Hess, M., and Wiegner, M., 1994: COP: a data library of optical properties of hexagonal ice crystals. *Appl. Opt.* **33**, 7740–7746.

Holland, R., 1977: Threde: a free-field EMP coupling and scattering code. *IEEE Trans. Nuclear Science* **24**, 2416–2421.

Holton, J. R., and A. Gettelman, 2001: Horizontal transport and the dehydration of the stratosphere. *Geophys. Res. Lett.* **28**, 2799–2802.

Houze, R. A. Jr, 1993: *Cloud Dynamics.* Academic Press, San Diego, CA.

Iaquinta, J., H. Isaka, and P. Personne, 1995: Scattering phase function of bullet rosette ice crystals, *J. Atmos. Sci.* **52**, 1401–1413.

Jackson, J. D., 1998: *Classical Electrodynamics*, 3rd edn. John Wiley, New York.

Jacobowitz, H., 1971: A method for computing the transfer of solar radiation through clouds of hexagonal ice crystals. *J. Quant. Spectrosc. Radiat. Transfer* **11**, 691–695.

Jensen, E. J., O. B. Toon, L. Pfister, and H. B. Selkirk, 1996: Dehydration of upper troposphere and lower stratosphere by subvisible cirrus clouds near the tropical tropopause. *Geophys. Res. Lett.* **23**, 825–828.

Kahnert, F. M., 2003: Numerical methods in electromagnetic scattering theory. *J. Quant. Spectrosc. Radiat. Transfer* **79–80**, 775–824.

Katz, D. S., E. T. Thiele, and A. Taflove, 1994: Validation and extension to three dimensions of Berenger PML absorbing boundary condition for FD-TD meshes. *IEEE Microwave Guided Wave Lett.* **4**, 268–270.

Kerker, M., 1969: *The Scattering of Light and Other Electromagnetic Radiation*. Academic Press, New York.

King, M. D., W. P. Menzel, Y. J. Kaufman, D. Tanre, B.-C. Gao, S. Platnick, S. A. Ackerman, L. A. Remer, R. Pincus, and P. A. Hubanks, 2003: Cloud and aerosol properties, precipitable water, and profiles of temperature and humidity from MODIS. *IEEE Trans. Geosci. Remote Sensing* **41**, 442–458.

Kokhanovsky, A., 1999: *Optics of Light Scattering Media*. John Wiley, Chichester, UK.

Kress, R. 1990: Nmerical solution of boundary integral equations in time-harmonic electromagnetic scattering. *Electromagnetics* **10**, 1–20.

Kunz, K. S., and L. Simpson, 1981: A technique for increasing the resolution of finite-difference solutions of the Maxwell's equation. *IEEE Trans. Electromagnetic Campat.* **23**, 419-422.

Kunz, K. S., and K. M. Lee, 1978: A three-dimensional finite-difference solution of the external response of an aircraft to a complex transient EM environment, I: The method and its implementation. *IEEE Trans. Electromagnetic Campat.* **20**, 328–333.

Kunz, K. S., and R. J. Luebbers, 1993: *The Finite Difference Time Domain Method for Electromagnetics*. CRC Press, Boca Raton, FL.

Lazzi, G., and O. P. Gandhi, 1996: On the optimal design of the PML absorbing boundary condition for the FDTD code. *IEEE Trans. Antennas Propagat.* **45**, 914–916.

Liao, Z., H. L. Wong, B. Yang, and Y. Yuan, 1984: A transmitting boundary for transient wave analyses. *Scientia Sinica* **XXVII**, 1063–1076.

Liou, K. N., 1972a: Electromagnetic scattering by arbitrarily oriented ice cylinders. *Appl. Opt.* **11**, 667–674.

Liou, K. N., 1972b: Light scattering by ice clouds in the visible and infrared: a theoretical study. *J. Atmos. Sci.* **29**, 524–536.

Liou, K .N., 1973: Transfer of solar irradiance through cirrus cloud layers. *J. Geophys. Res.* **78**, 1409–1418.

Liou, K. N., 1986: Influence of cirrus clouds on weather and climate process: a global perspective. *Mon. Weather Rev.* **114**, 1167–1199.

Liou, K. N. 1992: *Radiation and Cloud Processes in the Atmosphere*. Oxford University Press, New York.

Liou, K. N. 2002: *An Introduction to Atmospheric Radiation*, 2nd edn. Academic Press, San Diego, CA.

Liou, K. N., and J. E. Hansen, 1971: Intensity and polarization for single scattering by polydisperse spheres: a comparison of ray optics and Mie theory. *J. Atmos. Sci.* **28**, 995–1004.

Liou, K. N., and Y. Takano, 2002: Interpretation of cirrus cloud polarization measurements from radiative transfer theory. *Geophys. Res. Lett.* **29**, 10.1029/2001GL014613,27-1-27-4.

Liou, K. N., Y. Takano, and P. Yang, 2000: Light scattering and radiative transfer by ice crystal clouds: applications to climate research, in *Light Scattering by Nonspherical Particles: Theory, Measurements, and Geophysical Applications*, M. I. Mishchenko, J.W. Hovenier, and L. D. Travis (eds), pp. 417–449. Academic Press, San Diego, CA.

Lord Rayleigh, 1918: The dispersal of light by a dielectric cylinder. *Phil. Mag.* **36**, 365–376.

Lorenz, L. V., 1890, Lysbevaege i og uder en plane lysbolger belyst kulge. *Vidensk. Selk. Skr.* **6**, 1–62.

Lynch, D. K., K. Sassen, D. O'C Starr, and G. Stephens (eds), 2002: *Cirrus.* Oxford University Press, New York.

Macke, A., 1993: Scattering of light by polyhedral ice crystals. *Appl. Opt.* **32**, 2780–2788.

Macke, A., M. I. Mishchenko, K. Muinonen, and B. E. Carlson, 1995: Scattering of light by large nonspherical particles: ray-tracing approximation versus T-matrix method. *Opt. Lett.* **20**, 1934–1936.

Macke, A. J. Mueller, and E. Raschke, 1996a: Single scattering properties of atmospheric ice crystal. *J. Atmos. Sci.* **53**, 2813–2825.

Macke, A., M. I. Mishchenko, and B. Cairns, 1996b: The influence of inclusions on light scattering by large ice particles. *J. Geophys. Res.* **101**, 23311–23316.

Macke, A. 2000: Monte Carlo calculations of light scattering by large particles with multiple internal inclusions, in *Light Scattering By Nonspherical Particles: Theory, Measurements, and Applications*, M. I. Mishchenko, J.W. Hovenier, and L. D. Travis (eds), pp. 309–322. Academic Press, San Diego, CA.

Mano, Y., 2000: Exact solution of electromagnetic scattering by a three-dimensional hexagonal ice column obtained with the boundary-element method. *Appl. Opt.* **39**, 5541–5546.

McFarquhar, G. M., A. J. Heymsfield, A. Macke, J. Iaquinta, and S. M. Aulenbach, 1999: Use of observed ice crystal sizes and shapes to calculate the mean-scattering properties and multispectral radiance; CEPEX April 4 1993 case study. *J. Geophys. Res.* **104**, 31763–31779.

Merewether, D. E., R. Fisher, and F. W. Smith, 1980: On implementing a numeric Huygen's source in a finite difference program to illuminate scattering bodies. *IEEE Trans. Nuclear Sci.* **27**, 1829–1833.

Meyer, K., P. Yang, and B.-C. Gao, 2004: Optical thickness of tropical cirrus clouds derived from the MODIS 0.66 and 1.38-μm channels. *IEEE Trans. Geosci. Remote Sens.* **42**, 833–841.

Mie, G., 1908: Beiträge zur Optik trüber medien, speziell kolloidaler Metalösungen. *Ann. Phy.* **25**, 377–445.

Miller, E. K., 1988, A selective survey of computational electromagnetics. *IEEE Trans. Antennas Propagat.* **36**, 1281–1305

Minnis, P., K. N. Liou and Y. Takano. 1993a: Inference of cirrus cloud properties using satellite-observed visible and infrared radiances. Part I: Parameterization of radiance fields. *J. Atmos. Sci.* **50**, 1279–1304.

Minnis, P., P. W. Heck and D. F. Young. 1993b: Inference of cirrus cloud properties using satellite-observed visible and infrared radiances. Part II: Verification of theoretical cirrus radiative properties. *J. Atmos. Sci.* **50**, 1305–1322.

Mishchenko, M. I., and A. Macke, 1998: Incorporation of physical optics effects and δ-function transmission. *J. Geophys. Res.* **103**, 1799–1805.

Mishchenko, M. I., and A. Macke, 1999: How big should hexagonal ice crystals be to produce halos? *Appl. Opt.* **38**, 1626–1629.

Mishchenko, M. I. and L. D. Travis, 1998: Capabilities and limitations of a current FORTRAN implementation of the T-matrix method for randomly oriented, rotationally symmetry scatterers. *J. Quant. Spectrosc. Radiat. Transfer* **60**, 309–324.

Mishchenko, M. I., W. B. Rossow, A. Macke, and A. A. Lacis, 1996: Sensitivity of cirrus cloud albedo, bidirectional reflectance and optical thickness retrieval accuracy to ice particle shape. *J. Geophys. Res.* **101**, 16973–16985.

Mishchenko, M. I., W. J. Wiscombe, J. W. Hovenier, and L. D. Travis, 2000: Overview of scattering by nonspherical particles, in *Light Scattering by Nonspherical Particles: Theory, Measurements, and Geophysical Applications*, M. I. Mishchenko, J. W. Hovenier, and L. D. Travis (eds), pp. 29–60, Academic Press, San Diago, CA.

Mishchenko, M. I., L. D. Travis, and A. A. Lacis, 2002: *Scattering, Absorption, and Emission of Light by Small Particles*. Cambridge University Press, Cambridge, UK.

Mitchell, D. L., Y. Liu, and A. Macke, 1996: Modeling cirrus clouds. Part II: Treatment of radiative properties. *J. Atmos. Sci.* **53**, 2967–2988.

Moore, T. G., J. G. Blaschak, A. Taflove, and G. A. Kriegsmann, 1988: Theory and application of radiation boundary operators. *IEEE Trans. Antennas Propagat.* **36**, 1797–1812.

Muinonen, K., 1989: Scattering of light by crystals: a modified Kirchhoff approximation. *Appl. Opt.* **28**, 3044–3050.

Muinonen, K., L. Lamberg, P. Fast, and K. Lumme, 1997: Ray optics regime for Gaussian random spheres. *J. Quant. Spectrosc. Radiat. Transfer* **57**, 197–205.

Mur, G., 1981: Absorbing boundary condition for the finite-difference approximation of the time-domain electromagnetic-field equations. *IEEE Trans. Electromagn. Compat.* **23**, 377–382.

Noel, V., H. Chepfer, G. Ledanois and P. H. Flamant, 2001: computation of a single-scattering matrix for nonspherical particles randomlay or horizontally oriented in space. *Appl. Opt.* **40**, 4365–4375.

Nousiainen, T., Muinonen, K., and Raisanen, P., 2003: Scattering of light by large Saharan dust particles in a modified ray optics approximation. *J. Geophys. Res.* **108**, D1, 4025. doi:10.1029/2001JD001277.

Oguchi, T., 1973: Scattering properties of oblate raindrops and cross polarization of radio waves due to rain: calculations at 19.3 and 34.8 GHz. *J. Radio Res. Lab. Jpn.* **20**, 79–118.

Ohtake, T., 1970: Unusual crystal in ice fog. *J. Atmos. Sci.* **27**, 509–511.

Peltoniemi, J. I., Lumme, K., Muinonen, K., and Irvine, W. M., 1998: Scattering of light by stochastically rough particles. *Appl. Opt.* **28**, 4088–4095.

Purcell, E. M. and C. R. Pennypacker, 1973: Scattering and absorption of light by nonspherical dielectric grains. *Astrophys. J.* **186**, 705–714.

Rolland, P., K.N. Liou, M.D. King, S.C. Tsay, and G.M. McFarquhar, 2000: Remote sensing of optical and microphysical properties of cirrus clouds using MODIS channels: methodology and sensitivity to assumptions. *J. Geophys. Res.* **105**, 11,721–11,738.

Rockwitz, K.-D., 1989: Scattering properties of horizontally oriented ice crystal columns in cirrus clouds, *Appl. Opt.* **28**, 4103–41110.

Roskovensky, J.K., and K.N. Liou, 2003: Detection of thin cirrus from 1.38 μm/0.65 μm reflectance ratio combined with 8.6–11 μm brightness temperature difference. *Geophys. Res. Lett.* **30**, 10.1029/2003GL018135, ASC 4-1–4-5.

Saxon, D. S., Lectures on the scattering of light, in *Proceedings of the UCLA International Conference on Radiation and Remote Sensing of the Atmosphere*, J. G. Kuriyan (ed), pp. 227–308. Western Periodicals, North Hollywood, CA.

Schelkunoff, S. A. (1943). *Electromagnetic waves*. D. Von Nostrand, New York.

Shlager, K. L., and J. B. Schneider, 1998: A survey of the finite-difference time domain literature, in *Advances in Computational Electromagnetics*, A. Taflove (ed), pp. 1–62. Artech House, Boston, MA.

Stamnes, J. J., and H. Heier, 1998: Scalar and elctromagnetic diffraction point-spread functions. *Appl. Opt.* **37**, 3612–3622.

Stephens, G. L., 1980a: Radiative properties of cirrus clouds in the infrared region. *J. Atmos. Sci.* **37**, 435–446.

Stephens, G. L., 1980b: Radiative transfer on a linear lattice: Applications to anisotropic ice crystal clouds. *J. Atmos. Sci.* **37**, 2095–2104.

Stephens, G. L., S.-C. Tsay, P. W. Stackhous, and P. J. Flatau, 1990: The relevance of the microphysical and radiative properties of cirrus clouds to climate and climate feedback. *J. Atmos. Sci.* **47**, 1742–1753.

Sullivan, D. M., O. P. Gandhi, and A. Taflove, 1988: Use of the finite-difference time-domain method in calculating EM absorption in man models. *IEEE Trans. Biomedical Engineering* **35**, 179–186.

Sun, W., and Q. Fu, 2000: Finite-difference time-domain solution of light scattering by dielectric particles with large complex refractive indices. *Appl. Opt.* **39**, 5569–5578.

Sun, W., Q. Fu, and Z. Chen, 1999: Finite-difference time-domain solution of light scattering by dielectric particles with perfectly matched layer absorbing boundary conditions. *Appl. Opt.* **38**, 3141–3151.

Taflove, A., 1980: Application of the finite-difference time-domain method to sinusoidal steady-state electromagnetic-penetration problems. *IEEE Trans. Electromagn. Compat.* **22**, 191–202.

Taflove, A., 1995: *Computational Electrodynamics: The Finite-Difference Time-Domain Method*. Artech House, Boston, MA.

Taflove, A. and M. E. Brodwin, 1975: Numerical solution of steady-state eletromagnetic scattering problems using the time-dependent Maxwell's equations. *IEEE Trans. Microwave Theory Tech.* **23**, 623–630.

Taflove, A., and S. C. Hagness (eds.), 2000: *Computational Electromagnetics*, 2nd edn. Artech House, Boston, MA.

Taflove, A., and K. R. Umashankar, 1990: The finite-difference time-domain method for numerical modeling of electromagnetic wave interactions with arbitrary structures. *Progress in Electromagnetic Research (PIER)* **2**, 287–333.

Takano, Y., and K. Jayaweera, 1985: Scattering phase matrix for hexagonal ice crystals computed from ray optics. *Appl. Opt.* **24**, 3254–3263.

Takano, Y., and K. N. Liou, 1989a: Solar radiative transfer in cirrus clouds. Part I. Single-scattering and optical properties of hexagonal ice crystals. *J. Atmos. Sci.* **46**, 3–19.

Takano, Y., and Liou, K. N., 1989b: Radiative transfer in cirrus clouds. II. Theory and computation of multiple scattering in an anisotropic medium. *J. Atmos. Sci.* **46**, 20–36.

Takano, Y., and K. N. Liou, 1995: Radiative transfer in cirrus clouds. III. Light scattering by irregular ice crystals. *J. Atmos. Sci.* **52**, 818–837.

Thuman, W. C., and E. Robinson, 1954: Studies of Alaskan ice-fog particles. *J. Meteor.* **11**, 151–156.

Umashankar, K. and A. Taflove, 1982: A novel method to analyze electromagnetic scattering of complex objects. *IEEE Trans. Electromagn. Compat.* **24**, 397–405.

van de Hulst, H. C., 1957: *Light Scattering by Small Particles*. John Wiley, New York.

Vinh, H., H. Duger, C. P. Van Dam, 1992: Finite-difference methods for computational electromagnetics(CEM). *IEEE AP-S International Symposium Digest* **3**, 1682–1683.

Wait, J. R., 1955: Scattering of a plane wave from a circular dielectric cylinder at oblique incidence. *Can. J. Phys.* **33**, 189–195.

Waterman, P. C., 1971: Symmetry, unitarity, and geometry in electromagnetic scattering, *Phys. Rev.* **D3**, 825–839.

Wendling, P., R. Wendling, and H. K. Weickmann, 1979: Scattering of solar radiation by hexagonal ice crystals. *Appl. Opt.* **18**, 2663–2671.

Wriedt, T., 1998: A review of elastic light scattering theories. *Part. Part. Syst. Charact.* **15**, 67–74.

Wylie, D. P., W. P. Menzel, H. M. Woolf, and K. I. Strabala, 1994: Four years of global cirrus statistics using HIRS. *J. Climate* **7**, 1972–1986.

Yang, P., and Q. Cai, 1990: Light scattering phase matrix for spheroidal and cylindric large particles. *Chinese J. of Atmos. Sci.* **14**, 345–358.

Yang, P., and K. N. Liou, 1995: Light scattering by hexagonal ice crystals: comparison of finite-difference time domain and geometric optics methods. *J. Opt. Soc. Amer. A* **12**, 162–176.

Yang, P., and K. N. Liou, 1996a: Finite-difference time domain method for light scattering by small ice crystals in three-dimensional space. *J. Opt. Soc. Amer. A* **13**, 2072–2085

Yang, P., and K. N. Liou, 1996b: Geometric-optics-integral-equation method for light scattering by nonspherical ice crystals. *Appl. Opt.* **35**, 6568–6584.

Yang, P., and K. N. Liou, 1997: Light scattering by hexagonal ice crystals: solution by a ray-by-ray integration algorithm. *J. Opt. Soc. Amer. A.* **14**, 2278–2288.

Yang, P., and K. N. Liou, 1998: Single-scattering properties of complex ice crystals in terrestrial atmosphere. *Contr. Atmos. Phys.* **71**, 223–248.

Yang, P., K. N. Liou, M. I. Mishchenko, and B.-C. Gao, 2000: An efficient finite-difference time domain scheme for light scattering by dielectric particles: application to aerosols. *Appl. Opt.* **39**, 3727–3737.

Yang, P., B.-C. Gao, B. A. Baum, W. Wiscombe, Y. Hu, S. L. Nasiri, A. Heymsfield, G. McFarquhar, and L. Miloshevich, 2001a: Sensitivity of cirrus bidirectional reflectance in MODIS bands to vertical inhomogeneity of ice crystal habits and size distributions. *J. Geophys. Res.* **106**, 17267–17291.

Yang, P., B.-C. Gao, B. A. Baum, W. Wiscombe, M. I. Mischenko, D. M. Winker, and S. L. Nasiri, 2001b: Asymptotic solutions of optical properties of large particles with strong absorption. *Appl. Opt.* **40**, 1532–1547.

Yang, P., B. A. Baum, A. J. Heymsfield, Y. X. Hu, H.-L. Huang, S.-Chee Tsay, and S. Ackerman, 2003: Single-scattering properties of droxtals. *J. Quant. Spectrosc. Radiat. Transfer* **79–80**, 1159–1180.

Yang, P., G. W. Kattawar, K.N. Liou, and J. Q. Lu, 2004a: Choice of Cartesian grid configurations for applying the finite-difference time domain method to electromagnetic scattering by dielectric particles. *Appl. Opt.* **43**, 4611–4624.

Yang, P., G. W. Kattawar, and W. J. Wiscombe, 2004b: Effect of particle asphericity on single-scattering parameters: comparison between Platonic solids and spheres. *Appl. Opt.* **43**, 4427–4435.

Yee, S. K., 1966: Numerical solution of initial boundary value problems involving Maxwell's equations in isotropic media. *IEEE Trans. Antennas Propagat.* **14**, 302–307.

Yee, S. K., J. S. Chen, and A. H. Chang, 1992: Conformal finite difference time domain (FDTD) with overlapping grids. *IEEE Trans. Antennas Propagat.* **40**, 1068–1075.

Zhai, P., Y.-K. Lee, G. W. Kattawar, and P. Yang, 2004: On the near to far field transformation for the finite-difference time domain (FDTD) application. *Appl. Opt.* **43**, 3738–3746.

Zhang, Z., P. Yang, G. W. Kattawar, S.-C. Tsay. B. A. Baum, H.-L. Huang, Y. X. Hu, A. J. Heymsfield, and J. Reichardt, 2004: Geometrical-optics solution to light scattering by droxtal ice crystals. *Appl. Opt.* **43**, 2490–2499.

3 Light scattering and absorption characteristics of optically soft particles

Subodh K. Sharma

3.1 Introduction

Scattering techniques have been used to infer optical properties of macroscopic particles in various scientific disciplines for many years. To be able to deduce this information about the scatterer it is necessary to have an underlying theory for the analysis of measurements. Unfortunately, the exact analytic solutions are unknown, except in some simplest and most idealized cases. For a number of shapes numerical procedures are a possibility. But in many applications even a numerical approach still proves to be impracticable or even impossible and one needs to resort to approximation methods.

Many particles of interest in nature are such that their refractive index m (relative to the surrounding medium) is close to unity, i.e., $|m-1| \ll 1$. These are called soft scatterers. A number of approximations have been developed for predicting optical properties of such particles. The purpose of this article is to review the situation regarding soft particle scattering and absorption approximations and study their optical characteristics.

Parameters often employed to describe the validity domains in light scattering approximations are the size parameter $x = \pi d/\lambda$ and a parameter $2x|m-1|$ which can be looked upon as a measure of interaction strength. Here λ is the wavelength of the incident radiation and d is the characteristic size of the scatterer (e.g., the diameter of a spherical particle). Two domains may be identified for the purpose of this article. (i) $2x|m-1| \leq 1$ (small phase shifts) and (ii) arbitrary $2x|m-1|$ (arbitrary phase shifts).

3.2 Small phase shifts

3.2.1 Rayleigh–Gans-Debye approximation

If we denote by $\mathbf{E}_i = \mathbf{E_0} \exp(i\mathbf{k}_i.\mathbf{r} - i\omega t)$ as the incident electromagnetic field, the four scattering amplitudes S_1, S_2, S_3 and S_4 at a large distance r from the scatterer may be defined by the following relation

$$\begin{pmatrix} E_{\parallel s} \\ E_{\perp s} \end{pmatrix} = \frac{e^{ik(r-z)}}{-ikz} \begin{pmatrix} S_2 & S_3 \\ S_4 & S_1 \end{pmatrix} \begin{pmatrix} E_{\parallel i} \\ E_{\perp i} \end{pmatrix} \tag{3.1}$$

where $\mathbf{E}_s$ is the scattered electric field. The components $\parallel$ and $\perp$ are defined with respect to the scattering plane which contains the incident wave vector $\mathbf{k}_i$ and the final wave vector $\mathbf{k}_f$. Provision has been made for cross-coupling between polarizations such that $E_{\parallel s}$ may contain both components $E_{\parallel i}$ and $E_{\perp i}$. The same holds for $E_{\perp s}$. For an isotropic scatterer, the scattered vector has the same orientation to the plane of measurement as the incident vector and hence $S_3 = S_4 = 0$.

The Rayleigh–Gans–Debye approximation (RGDA) is designed to work in the domain

$$|m-1| \ll 1, \qquad 2x|m-1| \ll 1, \tag{3.2}$$

where the complex refractive index $m = n + in'$. The four scattering functions defined in (3.1), take the following form in the RGDA

$$\begin{pmatrix} S_2 & S_3 \\ S_4 & S_1 \end{pmatrix} = -ik^3\alpha \begin{pmatrix} \cos\theta & 0 \\ 0 & 1 \end{pmatrix} R(\theta, \phi), \tag{3.3}$$

where θ is the scattering angle (see Fig. 3.1) and α is the isotropic polarizability of the homogeneous scatterer. The shape factor $R(\theta, \phi)$ for a particle of the volume V is

$$R(\theta, \phi) = \frac{1}{V} \int_V e^{i\Delta(\mathbf{r})} dV, \tag{3.4}$$

where $\Delta(\mathbf{r})$ is the phase difference between waves arriving in a given direction after scattering by various volume elements within the scatterer. The generalization to heterogeneous particle can be found in Bohren and Huffman (1983). The shape factor can be easily calculated for most simple shapes (van de Hulst, 1957; Kerker, 1969; Bayvel and Jones, 1981; Kokhanovsky, 1999). For a homogeneous sphere of radius a the shape factor is given by

$$R(qa) = 3(\sin qa - qa\cos qa)/(qa)^3 \tag{3.5}$$

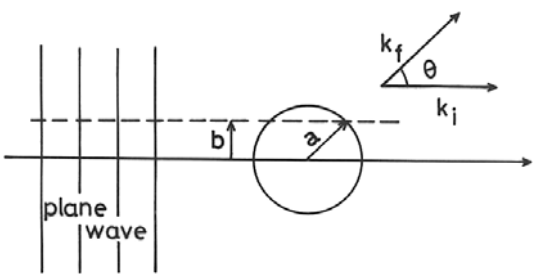

Fig. 3.1. Scattering of a plane wave by a potential in the EA

with $q = |\mathbf{k}_i - \mathbf{k}_f| = 2k\sin(\theta/2)$. Also we have for spherical particles $\alpha = (m-1)V/(2\pi)$. For $\theta = 0$, $S_1(0) = S_2(0) = S(0)$. Further, for a non-absorbing sphere it is clear from (3.3) and (3.5) that $S(0)$ is a purely imaginary number in the RGDA. Thus, the extinction efficiency factor Q_{ext} as calculated from the optical theorem

$$Q_{ext} = (4/x^2)\mathrm{Re}S(0), \tag{3.6}$$

gives $Q_{ext} = 0$, which is obviously a wrong result. The reason for this is that the relation (3.6) is true only for amplitudes that satisfy the unitarity property. The RGDA amplitude does not, and hence Q_{ext} in the RGDA should be calculated as a sum of Q_{abs} and Q_{sca}. The scattering efficiency defined as

$$Q_{sca} = \frac{1}{x^2}\int (|S_1(\theta)|^2 + |S_2(\theta)|^2)\sin\theta d\theta,$$

gives

$$Q_{sca}^{RGDA} = |m-1|^2\phi(x), \tag{3.7}$$

where

$$\phi(x) = \left[\frac{5}{2} + 2x^2 - \frac{\sin u}{u} - \frac{7}{16x^2}(1-\cos u) + \left(\frac{1}{2x^2} - 2\right)(\gamma + \ln(u) - Ci(u))\right],$$

with

$$Ci(u) = -\int_u^\infty \frac{\cos t}{t}dt,$$

$u = 4x$ and $\gamma = 0.577$ as the Euler's constant. The absorption efficiency is

$$Q_{abs}^{RGDA} = \frac{8x}{3}\mathrm{Im}|m-1|, \tag{3.8}$$

and Q_{ext}^{RGDA} may be obtained as sum of (3.7) and (3.8). For $\rho(= 2x(n-1)) \ll 1$, the errors are reasonably small. The approximation for extinction efficiency in the domain $1.0 < m \leq 1.25$ is better than 10% for $x < 1.0$ (Bayvel and Jones, 1981). For a fixed value of m the accuracy decreases as x increases. If $x \gg 1$, (3.7) gives

$$Q_{sca}^{RGDA} = 2x^2|m-1|^2$$

This formula is known as Jobst's approximation (Jobst, 1925).

The scattered intensity for a homogeneous sphere is

$$i(\theta)_{RGDA} = \frac{1}{2}[|S_1(\theta)|^2 + |S_2(\theta)|^2] = \frac{2}{9}x^6|m-1|^2(1+\cos^2\theta)|R(\theta)|^2, \tag{3.9}$$

under unpolarized light illumination conditions. The angular variation of the scattered intensity of optically soft scatterers is reproduced quite accurately by eq. (3.9).

3.2.2 Modified RGDA

Equation (3.9) tells us that the minima of the scattering pattern for a sphere are determined by the zeros of the equation $\tan z = z$. That is, zeros of the scattering pattern are dependent only on the size and not on the refractive index. The zeros z_n, to a good approximation are given by $z_n^2 = (n + 1/2)^2\pi^2 - 2, \quad n = 1, 2, \ldots$. There are however, no zeros of $R(\theta, \phi)$ for any θ unless $x > 2.25$ (Bohren and Huffman, 1983). Shimizu (1983) and Gordon (1985) have examined modifications to the RGDA. Both modifications introduce refractive index dependence in $R(\theta)$. While the modified version of Shimizu changes x to mx, Gordon argues for the substitution $x(1 + m^2 - 2m\cos\theta)^{1/2}$ in place of $x\sin\theta/2$. The modified versions give considerably better agreement with the Mie theory for positions of extrema in the scattering pattern. However, the value of scattered intensity at minima is quite different from the exact results. This discrepancy can be removed by adding an x dependent function $\gamma(x)$ to $R(\theta)$ (Gordon, 1985):

$$R(\theta) = 3(\sin z - z\sin z)/z^3 + \gamma(x).$$

It is found that $\gamma(x) = x^{-3/2}$ provides reasonable agreement with Mie theory up to about $x = 30$ and $1.0 < m < 1.2$. That is, despite the original premise that $\rho < 1$, the modified RGDA gives good results even when $\rho > 1$.

3.2.3 Quasistatic approximation

Another problem with the RGDA is that it does not work well for shapes which strongly differ from the spherical geometry. To overcome this difficulty an approximation known as the quasistatic approximation (QSA) was developed for cylinders by Burberg (1956) and for spheroids by Shatilov (1960). More recently, Voshchinnikov and Farafonov (2000), Farafonov *et al.* (2001) and Posselt *et al.* (2002) have further examined QSA for spheroids, infinite cylinders and multilayered spheroids. In this approximation the field inside the scatterer is represented by the incident plane wave (as in RGDA), while the polarizability of the particle is taken into account as in the Rayleigh approximation. In this sense this approximation is a generalization of the Rayleigh and the RGD approximations. The condition for applicability of the QSA is

$$|m - 1|x_v \ll 1,$$

where, in case of a spheroid, $x_v = 2\pi a_v/\lambda$ (a_v is the radius of a sphere whose volume is equal to that of the spheroid). Numerical results show that the QSA works particularly well for small optically soft particles. In this case it is always preferable to the RGDA. It is found that while the range of applicability of RGDA decreases with growing asphericity, the validity range of QSA remains practically independent of the scatterer shape. In comparison to the RGDA, its range of applicability is nearly always greater if $a/b \geq 3$. Here, a and b are semi-major and semi-minor axes respectively.

Paramanov *et al.*, (1986) have studied the effect of non-sphericity and orientation on scattering of light by soft spheroidal particles. The result shows that in the Rayleigh limit light scattered by randomly oriented spheroids is almost indistinguishable from light scattered by a collection of spheres of equal volume.

3.2.4 Shifrin and Ston approximation

A series representation of $\phi(x)$, particularly useful for polydispersions, has been given by Shifrin and Ston (1976):

$$\phi(x) = \sum_{l=1}^{\infty} (-1)^{l+1} \frac{(4x)^{2l+2}}{(2l+2)} \frac{l^2+l+2}{2(l+2)^2(l+1)}. \tag{3.10}$$

Further, it has been shown that the following approximations derived from (3.10) can be used to within 3% accuracy:

$$\phi(x) \begin{cases} = 1.185x^4(1.0 - 0.4x^2 + 0.096x^4) & x \in [0,1] \\ = 1.92x^4 - 1.084x & x \in [1,2] \\ = 2.112x^2 - 1.456x & x \in [2,12.5] \end{cases}.$$

3.2.5 Walstra approximation

An interpolation formula for a non-absorbing sphere, based on RGDA, has been obtained by Walstra (1964). If for a given x, Q_{ext} is known for $m = a$ and $m = c$, Q_{ext} can be computed for the intermediate value of $m = b$ by

$$Q_{ext}(b) = \frac{(b-1)^2}{c-a} \left[\frac{c-b}{(a-1)^2} Q_{ext}(a) + \frac{b-a}{(c-1)^2} Q_{ext}(c) \right].$$

The results from this formula yield less than 1% error for values of x up to at least 8. The m range considered was $m = 1.025(0.05)1.275$. Walstra (1964) has also given approximate empirical expressions for extinction efficiency. For small particles,

$$Q_{ext}^{WAS} = (1.26m - 0.04)\rho - 2.558(m-1)^{1.273} - 0.843.$$

This gives less than 1% error in the range $1.5 < \rho < 2.5$.

3.3 Potential scattering

Some important work on the development of the theory of light scattering by optically soft particles has been motivated by analogous work in quantum mechanical scattering by drawing an analogy between a potential and the refractive index. It is, therefore, desirable to know how the eikonal approximation (EA) is

derived in potential scattering. Some review articles on the EA in potential scattering include Glauber (1959), Gerjuoy and Thomas (1974), Byron and Joachain (1977), and Gien (1988).

Consider the non-relativistic elastic scattering of a spinless particle of mass M by a local potential $V(\mathbf{r})$ of range a. Let $\mathbf{k}_i$ and $\mathbf{k}_f$ be the incident and scattered wave vectors associated with the particle and let θ be the scattering angle between them. The particle energy E is $\hbar^2k^2/2M$ and $|\mathbf{k}_i| = |\mathbf{k}_f| = k$. Here $\hbar = h/2\pi$, where h is Planck's constant. The problem to be considered is the solution of the Schrödinger equation

$$\Big[(-\hbar^2/2M)\nabla^2 + V(\mathbf{r})\Big]\psi(\mathbf{r}) = E\psi(\mathbf{r}), \tag{3.11}$$

which when substituted in the expression

$$f(\theta) = -\frac{1}{4\pi}\int e^{(-i\mathbf{k}_f.\mathbf{r})}U(\mathbf{r})\psi(\mathbf{r})d\mathbf{r}, \tag{3.12}$$

gives the scattering amplitude. In (3.12), $U(\mathbf{r}) = (2M/\hbar^2)V(\mathbf{r})$. The basic problem, thus, reduces to finding the wave function inside the scattering region. To this end, we consider a trial solution of (3.11) in the form,

$$\psi(\mathbf{r}) = \exp(i\mathbf{k}_i.r)\phi(\mathbf{r}). \tag{3.13}$$

Choosing the z-axis along $\mathbf{k}_i$, substitution of (3.13) in (3.11) gives

$$\Big[\nabla^2 + 2ik\partial/\partial z\Big]\phi(\mathbf{r}) = U(\mathbf{r})\phi(\mathbf{r}). \tag{3.14}$$

Neglecting the term ∇^2 in the left hand side, (3.14) becomes,

$$2ik(\partial/\partial z)\phi(\mathbf{r}) = U(\mathbf{r})\phi(\mathbf{r}), \tag{3.15}$$

which, with the boundary condition $\phi(-\infty) = 1$, gives

$$\psi(\mathbf{b}, z)_{EA} = \exp\left(ikz - \frac{i}{2k}\int_{-\infty}^{z} U(\mathbf{b}, z')dz'\right). \tag{3.16}$$

This is the EA in its simplest form. It can be checked that the assumptions made in arriving at (3.15), namely, $\nabla^2\phi(\mathbf{r}) \ll U(\mathbf{r})\phi(\mathbf{r})$, and $\nabla^2\phi(\mathbf{r}) \ll 2ik\partial\phi(\mathbf{r})/\partial z$ essentially require

$$|U_0|/k^2 \ll 1; \qquad ka \gg 1, \tag{3.17}$$

where $|U_0|$ is the 'strength' of the potential. The physical picture, which emerges from (3.16) may be viewed as follows. A high energy particle passes through the scattering potential at an impact parameter $\mathbf{b}$ in a straight line trajectory (see Fig. 3.1). The presence of the potential introduces a change in the phase of the wave function of the incident particle. Its amplitude and direction of propagation remains unaffected.

The result (3.16) can also be obtained by substituting (3.13) in the integral equation

$$\psi(\mathbf{r}) = \exp(i\mathbf{k}_i.r) - \int G(\mathbf{r}-\mathbf{r}')U(\mathbf{r}')\psi(\mathbf{r}')\mathbf{d}\mathbf{r}' \tag{3.18}$$

and linearizing the Green's function $G(\mathbf{r}-\mathbf{r}')$. The linearized propagator

$$G(\mathbf{r}-\mathbf{r}')_{EA} = (-i/2k)\exp(ik(z-z'))\delta(\mathbf{b}-\mathbf{b}')\Theta(z-z') \tag{3.19}$$

clearly represents a straight line forward propagation. This linearized propagator when substituted in (3.18) gives (3.16).

Substitution of the ψ_{EA} from (3.16) into (3.12) gives,

$$f(\theta)_{EA} = \frac{-1}{4\pi}\int e^{i\left(\mathbf{q}_\perp.\mathbf{b}+2kz\sin^2(\theta/2)\right)}U(\mathbf{b},z)e^{\frac{-i}{2k}\int_{-\infty}^{z}U(\mathbf{b},z')dz'}d\mathbf{b}dz, \tag{3.20}$$

where $\mathbf{q} = \mathbf{k}_i - \mathbf{k}_f$. For small angle scattering $\exp[2ikz\sin^2(\theta/2)] \simeq 1$, and the z-integration can be performed easily giving

$$f(\theta)_{EA} = -\frac{ik}{2\pi}\int e^{i\mathbf{q}_\perp.\mathbf{b}}\left[e^{i\chi(\mathbf{b})_{EA}}-1\right]d\mathbf{b}, \tag{3.21}$$

where

$$\chi(\mathbf{b})_{EA} = -\frac{1}{2k}\int_{-\infty}^{\infty}U(\mathbf{r})dz. \tag{3.22}$$

The amplitude (3.21) is the eikonal amplitude. Strictly speaking though, it is a combination of the EA and an additional small angle approximation. The angular range of the EA is governed by the relations

$$\theta \ll 1/(ka)^{1/2} \quad \text{if} \quad |U_0|a/k < 1, \tag{3.23}$$

and

$$\theta \ll |U_0|^{1/2}/k \quad \text{if} \quad |U_0|a/k > 1. \tag{3.24}$$

If z-axis is chosen along the average momentum direction $\mathbf{k}_n = (\mathbf{k}_i + \mathbf{k}_f)/2$, the scattering amplitude (3.20) reduces to (3.21) even without the small angle approximation. However, $|\mathbf{q}_\perp| = k\sin\theta$ now needs to be replaced by $2k\sin(\theta/2)$. In what follows, it is this amplitude which will be referred to as the EA unless stated otherwise.

Wallace (1971) developed an eikonal expansion in powers of k^{-1} for infinitely often differentiable potentials in which the EA appears as the zeroth-order term. The eikonal amplitude corrected to the first two orders for a spherically symmetric potential may be written as

$$f(q) = -2k\int d\mathbf{b}e^{i\mathbf{q}.\mathbf{b}}\left[f(b)_{EA}^{I,II}-1\right],$$

where f^I_{EA} and f^{II}_{EA} denote first and second order corrections given by

$$f(b)^I_{EA} = e^{i\left(\chi_0(b)+\tau_1(b)\right)}, \quad f(b)^{II}_{EA} = f(b)^I_{EA} e^{i\tau_2(b)-\omega_2(b)},$$

and

$$\tau_1(b) = -\frac{1}{k^3}\left(1+\beta_1\right)\int_0^\infty dz U^2(r), \quad \omega_2(b) = b\chi_0'(b)\nabla^2\chi_0(b)/8k^2,$$

$$\tau_2(b) = -\frac{1}{k^5}\left(1+\frac{5}{3}\beta_1+\frac{1}{3}\beta_2\right)\int_0^\infty dz U^3(r) - \left[b\left(\chi_0'(b)\right)^3/24k^2\right],$$

with $\beta_n = b^n\partial^n/\partial b^n$. Wallace has obtained third-order correction too. It is not given here. The systematic improvement with each increasing order of the eikonal expansion has also been verified by Wallace.

Chen (1984) wrote a modified linearized propagator

$$G(\mathbf{r}-\mathbf{r}')_{EA} = (-i/2\alpha)\exp(i\beta(z-z'))\delta(\mathbf{b}-\mathbf{b}')\Theta(z-z'), \tag{3.25}$$

where the arbitrary parameters α and β are determined in such a way that the dominant real and imaginary parts of the second Born amplitude are correctly reproduced. The resulting approximation, termed as the generalized EA (GEA), has been found to be accurate for angular variation of scattered intensities for Yukawa and Gaussian potentials even at large angles.

3.4 Arbitrary phase shifts

Consider a scalar wave equation for the field $\psi(\mathbf{r})$ propagating through a medium of spatially varying relative refractive index $m(\mathbf{r})$:

$$\nabla^2\psi(\mathbf{r}) + k^2m^2(\mathbf{r})\psi(\mathbf{r}) = 0. \tag{3.26}$$

A comparison of (3.26) with the Schrödinger equation (3.11) shows that

$$U(\mathbf{r}) = \left[1-m^2(\mathbf{r})\right]k^2. \tag{3.27}$$

With this identification, the scalar scattering function, $S(\theta,\phi)$ (related to $f(\theta,\phi)$ via the relation $S(\theta,\phi) = -ikf(\theta,\phi)$), can be written from (3.12) as

$$S(\theta,\phi) = \frac{ik^3}{4\pi}\int d\mathbf{r}e^{-i\mathbf{k}_f\cdot\mathbf{r}}\left[1-m^2(\mathbf{r})\right]\psi(\mathbf{r}). \tag{3.28}$$

Various approximations can be obtained for scattering function by assuming different approximate forms for $\psi(\mathbf{r})$.

3.4.1 Straight line approximations

In the EA, following (3.16) and (3.27), $\psi(\mathbf{r})$ may be approximated as:

$$\psi(\mathbf{r})_{EA} = e^{i\mathbf{k}_i.\mathbf{r}+\frac{k}{2}\int_{-\infty}^{z}(m^2(\mathbf{b},z')-1)dz'}. \tag{3.29}$$

The EA for the scattering function may then be obtained by substituting this expression for $\psi(\mathbf{r})$ in (3.28). The z integration can be easily performed. The result is

$$S(\theta,\phi)_{EA} = k^2 \int d\mathbf{b} e^{i\mathbf{q}.\mathbf{b}}\big[1 - e^{i\chi(\mathbf{b})_{EA}}\big], \tag{3.30}$$

where

$$\chi(\mathbf{b})_{EA} = \frac{k}{2}\int_{-\infty}^{\infty}\big[m^2(\mathbf{r}) - 1\big]dz,$$

with $\mathbf{q}.\mathbf{b} = 2kb\sin(\theta/2)$. The two-dimensional integration in (3.30) is over the projected particle area. The conditions (3.17) for the validity of the EA now translate to

$$|m(\mathbf{r}) - 1| \ll 1, \qquad x \gg 1. \tag{3.31}$$

For complex m ($m(\mathbf{r}) = n(\mathbf{r}) + in'(\mathbf{r})$) the condition $|m(\mathbf{r}) - 1| \ll 1$ is equivalent to two conditions: $|n(\mathbf{r}) - 1| \ll 1$ and $|n'(\mathbf{r})| \ll 1$. This requirement ensures that at boundaries there is negligible deviation of the incident ray and that the energy reflected is negligible. The requirement $x \gg 1$ ensures that the ray travels undeviated through the scatterer as the refractive index varies slowly in a distance of the order of the wavelength. The angular range given by (3.23) and (3.24), now translate to

$$\theta \ll 1/\sqrt{x} \qquad \text{for} \qquad x|m^2 - 1| < 1; \tag{3.32}$$

$$\theta \ll |m^2 - 1|^{1/2} \qquad \text{for} \qquad x|m^2 - 1| > 1. \tag{3.33}$$

Here m may be taken as the maximum value of the refractive index.

An alternative derivation in (3.30) has been given by van de Hulst (1957). The outline of the method is as follows. As a consequence of conditions (3.31), the incident rays are assumed to pass through the particle undeviated. A ray at an impact parameter $\mathbf{b}$ then accumulates a phase shift $\chi(\mathbf{b})_{ADA} = k\int_{-\infty}^{\infty}[m(\mathbf{r}) - 1]dz$. The field not too far beyond the sphere is therefore known. A direct application of Huygens' principle then gives

$$S(\theta,\phi)_{ADA} = -k^2 \int d\mathbf{b} e^{i\mathbf{q}.\mathbf{b}}\big[e^{i\chi(\mathbf{b})_{ADA}} - 1\big]. \tag{3.34}$$

The subscript ADA refers to the anomalous diffraction approximation. The only difference between the EA and the ADA is that the term (m^2-1) in the EA phase

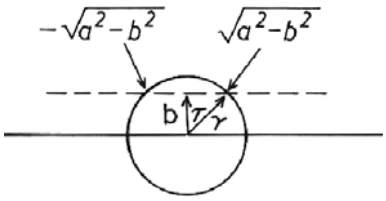

Fig. 3.2. Scattering geometry for a homogeneous sphere

is replaced by $2(m-1)$ in the ADA. Thus, formally both approximations can be treated on the same footing. The approximation has been termed anomalous diffraction approximation because in addition to usual diffraction it takes into account the refraction also.

For a homogeneous sphere of radius a and refractive index $m(\mathbf{r}) = m$, the integration over the azimuthal angle in (3.30) can be easily performed yielding

$$S(\theta)_{EA} = -k^2 \int_0^a bdbJ_0\left(2kbsin(\theta/2)\right)\left[\exp\left(i\chi(b)_{EA}\right) - 1\right]. \tag{3.35}$$

The distance traveled by the ray in the scatterer at an impact parameter b is $2\sqrt{a^2-b^2}$ (see Fig. 3.2). Thus the function $\chi(b)_{EA}$ can be written as

$$\chi(b)_{EA} = x(m^2-1)\sqrt{\left[1-(b^2/a^2)\right]} = \rho^*_{EA}\sqrt{\left[1-(b^2/a^2)\right]}. \tag{3.36}$$

The quantity ρ^*_{EA} is $\rho^*_{EA} \equiv \rho_{EA} + i\tau_{EA}/2$ with

$$\rho_{EA} = x(n^2 - n'^2 - 1), \qquad \tau_{EA} = 4xnn'. \tag{3.37}$$

The quantity ρ^*_{EA} may also expressed as

$$\rho_{EA}(1 + i\tan\beta_{EA}), \tag{3.38}$$

where the absorption parameter, $\tan\beta_{EA} = 2nn'x/\rho_{EA}$, describes amplitude decay due to the absorption. In the ADA one has

$$\rho^*_{ADA} = \rho^* = 2x(m-1) = 2x(n-1) + 2ixn' \tag{3.39}$$

$$\equiv \rho_{ADA} + i\tau_{ADA}/2 \equiv \rho + i\tau/2. \tag{3.40}$$

Clearly as $n \to 1$ and $n' \to 0$ the two approximations tend to the same limit.

For non-forward scattering the integration in (3.35) can be performed for following special cases.

(i) For a completely absorbing sphere, $S(\theta)_{EA} = x^2 J_1(z)/z$, which is nothing but the scattering function in the Fraunhofer diffraction approximation.

(ii) If $x|m^2-1| \ll 1$, one may approximate

$$\exp[i\chi(b)_{EA}] \simeq 1 + i\chi(b)_{EA}. \tag{3.41}$$

The scattering function is then nothing but that from a homogeneous sphere in the RDGA. This is known to be a good approximation if $|m-1| \ll 1$ and $2x|m-1| \leq 1$. Clearly, despite the original premise $x \gg 1$, the EA, in practice, can be a good approximation for arbitrary x as long as condition $|m-1| \ll 1$ is met. As for angular validity, it is clear from (3.32) and (3.33) that for small particles the angular validity of this approximation can be quite large. On the other hand, for large scatterers the angular validity of the EA is restricted to small scattering angles.

(iii) For a non absorbing sphere, it is possible to evaluate $S(\theta)_{EA}$ analytically in terms of known functions by means of a series expansion for $\rho_{EA} < 1$ and $\rho_{EA} > z$ (van de Hulst, 1957).

For forward scattering, the integration in $S(0)$ can be evaluated in a closed form and then using the extinction theorem one obtains

$$Q_{ext}^{EA} = \left[2 - \frac{4\cos\beta_{EA}}{\rho_{EA}}\sin(\rho_{EA}-\beta_{EA})e^{-\rho_{EA}\tan\beta_{EA}} + 4\left(\frac{\cos\beta_{EA}}{\rho_{EA}}\right)^2\cos(2\beta_{EA})\right.$$

$$\left. -4\left(\frac{\cos\beta_{EA}}{\rho_{EA}}\right)^2\cos(\rho_{EA}-2\beta_{EA})e^{-\rho_{EA}\tan\beta_{EA}}\right]. \tag{3.42}$$

The absorption efficiency in the EA is determined by the relation

$$Q_{abs}^{EA} = (1/\pi a^2)\int d\mathbf{b}\big[1-\exp(-\mathrm{Im}\chi_{EA})\big]$$

which for a homogeneous sphere gives

$$Q_{abs}^{EA} = 1 + 2e^{-\tau_{EA}}/\tau_{EA} + 4(e^{-\tau_{EA}}-1)/\tau_{EA}^2.$$

When $\tau_{EA} \gg 1$, absorption efficiency is close to 1. That is, all the rays incident on the sphere are absorbed. In addition, an equal amount of light is diffracted (scattered) resulting in the so-called extinction paradox. It can be easily verified that the extinction efficiency will be dominated by absorption efficiency if ρ_{EA} and τ_{EA} are of the same order and less than unity.

3.4.1.1 The EA scattering function from the Mie solutions

The Mie solutions describe the scattering of light by a homogeneous sphere of arbitrary size and refractive index. Two scattering functions $S_1(\theta)$ and $S_2(\theta)$, corresponding to perpendicular and parallel polarizations respectively are:

$$S_1(\theta) = \sum_{l=1}^{\infty}\frac{2l+1}{l(l+1)}\left[a_l\pi_l(\cos\theta) + b_l\tau_l(\cos\theta)\right], \tag{3.43}$$

$$S_2(\theta) = \sum_{l=1}^{\infty} \frac{2l+1}{l(l+1)} \left[a_l \tau_l(\cos\theta) + b_l \pi_l(\cos\theta)\right], \tag{3.44}$$

where

$$\pi_l(\cos\theta) = dP_l(\cos\theta)/d(\cos\theta),$$

$$\tau_l(\cos\theta) = \cos\theta \pi_l(\cos\theta) - \sin\theta \; d\pi_l(\cos\theta)/d(\cos\theta),$$

with $P_l(\cos\theta)$ as the Legendre polynomial. The scattering coefficients are

$$a_l = (1 - e^{2i\alpha_l})/2 \qquad b_l = (1 - e^{2i\beta_l})/2,$$

where

$$\tan\alpha_l = [u_l'(mx)u_l(x) - mu_l(mx)u_l'(x)]/[u_l'(mx)v_l(x) - mu_l(mx)v_l'(x)],$$

$$\tan\beta_l = [mu_l'(mx)u_l(x) - u_l(mx)u_l'(x)]/[mu_l'(mx)v_l(x) - u_l(mx)v_l'(x)],$$

with $u_l(z) = zj_l(z)$ and $v_l(z) = zn_l(z)$. It can be shown (Bourrely *et al.*, 1991) that in the limit $x \to \infty$, $|mx| \to \infty$ and $n'^2 x/n \ll 1$,

$$e^{2i\alpha_l} = e^{-2i(xf - x'f')}[1 + r_\perp e^{2n'x} e^{-2ix'f'}]/[1 - r_\perp e^{-2n'x} e^{2ix'f'}], \tag{3.45}$$

$$e^{2i\beta_l} = e^{-2i(xf - x'f')}[1 + r_\parallel e^{2n'x} e^{-2ix'f'}]/[1 - r_\parallel e^{-2n'x} e^{2ix'f'}], \tag{3.46}$$

$$f = \cos\gamma - \left[\gamma - (\pi/2)\right]\sin\gamma, \qquad f' = \cos\gamma' - \left[\gamma' - (\pi/2)\right]\sin\gamma', \tag{3.47}$$

and $x' = nx$. The reflection coefficients $r_\parallel$ and $r_\perp$ are

$$r_\parallel(\gamma) = \frac{m\cos\gamma - \cos\gamma'}{m\cos\gamma + \cos\gamma'}; \quad r_\perp(\gamma) = \frac{\cos\gamma - m\cos\gamma'}{\cos\gamma + m\cos\gamma'},$$

and the angle of incidence γ (see Fig. 3.2) is related to γ' as

$$2x\sin\gamma = 2x'\sin\gamma' = (2l+1). \tag{3.48}$$

The expressions (3.45) and (3.46) are generalizations of corresponding expressions for a non-absorbing homogeneous sphere ($n' = 0$) derived in most books on light scattering (see for example, Newton (1966) or van de Hulst (1957)).

Employing (3.47) and (3.48), $(xf - x'f')$ in the limit $n \to 1$ gives $xf - x'f' = -x(n^2 - 1)\cos\gamma/2$. For large x and small scattering angles ($\theta \ll 1/x$) one can approximate,

$$\pi_l(\cos\theta) \simeq \tau_l(\cos\theta) \simeq l(l+1)J_0\big((l + (1/2))\theta\big)/2,$$

and

$$\sum_{l=1}^{l=\infty} \simeq x \int_0^{\pi/2} \cos\gamma \; d\gamma.$$

In addition, if $n \to 1$, $r_\parallel$ and $r_\perp$ go to zero. It is then straightforward to see that (3.43) as well as (3.44) reduce to $S(\theta)_{EA}$.

3.4.1.2 Relationship between the anomalous diffraction approximation and the eikonal approximation

An expansion of $xf - x'f'$ to order $(n^2-1)^3$ gives (Sharma, 1992)

$$-2i(xf - x'f') = i(n^2-1)x\cos\gamma\big[1-(n^2-1)\big(1-\tan^2\gamma\big)/4$$

$$+(n^2-1)^2\big(1-2\tan^2\gamma\big)/8-(n^2-1)^2\tan^4\gamma/24\big]. \tag{3.49}$$

The first term on the right-hand side of (3.49) is the EA phase. It is instructive to compare (3.49) with the Wallace phase defined in section 3. When translated to optical scattering it gives:

$$i(n^2-1)x\cos\gamma\left[1-\frac{(n^2-1)}{4}\left(1-\tan^2\gamma\right)+\frac{(n^2-1)^2}{8}\left(1-2\tan^2\gamma\right)\right], \tag{3.50}$$

to order $(n^2-1)^3$. The first term is obviously the EA phase. The first-order correction in (3.49) is identical to the first-order correction of Wallace. But the second order correction agrees only partially.

Regrouping the terms, we can rewrite (3.49) as

$$-2i(xf - x'f') = 2i\left[\frac{1}{2}(n^2-1)-\frac{1}{8}(n^2-1)^2+\frac{1}{16}(n^2-1)^3\right]x\cos\gamma$$

$$-\frac{i}{4}x(n^2-1)^2\frac{\sin^2\gamma}{\cos\gamma}-\frac{i}{4}x(n^2-1)^3\tan\gamma-\frac{i}{24}x(n^2-1)^3\sin\gamma\tan^3\gamma. \tag{3.51}$$

If the term in the square bracket is approximated as $\big[[1+(n^2-1)]^{1/2}-1\big] \simeq (n-1)$, the equation (3.51) becomes

$$-2i(xf - x'f') = 2ix(n-1)\cos\gamma + ix(n^2-1)^2\tan\gamma\sin\gamma/4$$

$$-ix(n^2-1)^3\tan\gamma\sin\gamma/4 - ix(n^2-1)^3\tan^3\gamma\sin\gamma/24. \tag{3.52}$$

The first term on the right-hand side of this equation is the ADA phase. Note that the corrections tend to zero as either $|n-1| \to 0$ or as $\gamma \to 0$. This equation also tells us that the ADA is valid in the domain $\sin^2\gamma/\cos\gamma \ll 1/\rho|n-1|$. This means that as $n \to 1$ for fixed ρ, the domain of γ values over which this approximation is valid increases and hence the ADA improves. Thus, while it is true that the validity of the ADA phase improves as $n \to 1$, nevertheless it is also true that its validity is not limited to $|n-1| \ll 1$. For $\gamma = 0$ the approximation of phase is valid for arbitrary n.

It is clear from the above discussion that the domain of γ values where the phase approximation is good is quite small if the condition $|n-1| \ll 1$ is not satisfied. But the very fact that the phase approximation is good near $\gamma = 0$ is

significant. This is because the main contribution of the refraction term to near forward scattering comes from the region near $\gamma = 0$ (see, for example, van de Hulst, 1957). Contributions to $\theta = 0$ from non-central and non-grazing rays are of little importance and may therefore be ignored. Since $-r_\perp = r_\parallel = (n-1)/(n+1)$ for near central incidence, it may be concluded that ADA should be a good approximation if $|n-1|^2 \ll |n+1|^2$. This explains why the ADA is a reasonably good approximation even for n as large as 2.

The derivation of the EA from the Mie theory here is limited to weakly absorbing spherical particles. However, this is not a real limitation because similar conclusions can be derived from (3.50) which is not restricted to a weakly absorbing sphere.

3.4.1.3 Modifications to the EA

When translated to optical scattering, the first-order corrected scattering function of the Wallace can be written as (Sharma *et al.*, 1982)

$$S(\theta) = x^2 \int_0^{\pi/2} J_0(z \sin\gamma) \left[1 - e^{i\chi_0 + i\tau_1}\right] \cos\gamma \sin\gamma d\gamma, \tag{3.53}$$

where

$$\tau_1 = -x(m^2-1)^2 \cos\gamma(1 - \tan^2\gamma)\cos\gamma/4.$$

At $\gamma = \pi/2$, the correction to the eikonal phase diverges. This is essentially a consequence of the sharp cut-off at the boundary of the scatterer. The eikonal expansion, derived for infinitely often differentiable potentials, thus need not hold even at the zeroth-order level for optical scattering. But, because numerical calculations using exact electromagnetic scattering theory confirm that the EA is a good approximation, it is customary to ignore mathematical problems associated with the discontinuous behavior at the boundaries. Thus one may consider only that part of the correction term which is free of the divergence problem. Two approximate forms which are free of this problem in the domain

$$x|m^2 - 1|^2/4 \ll 1 \tag{3.54}$$

are

$$S(\theta)_{FCI} = x^2 \int J_0(z \sin\gamma) \left[1 - e^{i\chi_0}(1 + i\tau_1)\right] \sin\gamma \cos\gamma d\gamma; \tag{3.55}$$

and

$$S(\theta)_{FCII} = x^2 \int_0^{\pi/2} J_0(z \sin\gamma) \left[1 - e^{2ix(m-1)\cos\gamma}\left(1 + \frac{ix(m^2-1)}{4\cos\gamma} sin^2\gamma\right)\right] \times \sin\gamma \cos\gamma d\gamma. \tag{3.56}$$

The form (3.56) is essentially a modified form of the ADA based on (3.52). Subscript FC stands for first-order correction. For forward scattering, (3.55) as well as (3.56) can be evaluated analytically to yield

$$S(0)_{FCI} = m^2 S(0)_{EA} + x^2(m^2-1)\left[e^{-ix(m^2-1)} - 1\right]/4, \tag{3.57}$$

$$S(0)_{FCII} = C(m)S(0)_{ADA}, \tag{3.58}$$

with

$$C(m) = 1 + 0.25(m+1)^2(m-1)(2-m^2). \tag{3.59}$$

The correction (3.58) preserves the simplicity of the unmodified approximation.

A generalized EA (GEA) and a modified form of the GEA (MGEA) have been examined by Chen (1989), and Chen and Smith (1992). The scattering functions in the GEA and the MGEA employ a parametrized propagator (eq. (3.25)). The parameters are determined on the basis of following two criteria:

(i) The change in phase in propagation through the medium is $2k(m-1)\sqrt{a^2-b^2}$ in the GEA and $2k(m-\cos\theta/2)\sqrt{a^2-b^2}$ in the MGEA.
(ii) The edge effects due to the sharp boundary are recovered.

The scattering function in the GEA then takes the following form,

$$S(\theta)_{GEA} = (ik/4\pi)(1-\delta)S_B - (m^2-1)\alpha_0\delta^2\ k^2 I, \tag{3.60}$$

where the first Born term, S_B, is given by

$$S_B(\theta) = -4x^2(m^2-1)a\int_0^{\pi/2} \sin^2\gamma\cos\gamma J_0(z\sin\gamma)d\gamma,$$

and

$$I = a^2\int_0^{\pi/2} J_0(z\sin\gamma)\left[e^{i\rho^*_{GEA}\cos\gamma} - 1\right]\cos\gamma\sin\gamma d\gamma.$$

The function ρ^*_{GEA} is $\rho^*_{GEA} = x(m^2-1)/\alpha_0\delta$, where

$$\delta = (m+1)/2\alpha_0; \quad \alpha_0 = \frac{m+1}{2} - \frac{3i}{8}\left[\frac{1}{x} - \frac{2}{\rho^*_{GEA}}\left(\frac{a_1}{x^{2/3}} - \frac{a_2}{x^{4/3}}\right)\right],$$

and $a_1 = 2 + 2.4i, a_2 = 2 + 6i$. For $\theta = 0$ (3.60) gives

$$S(0)_{GEA} = -i\alpha_0\delta x^2(1-\delta)/3 + (\alpha_0/2)\delta^2 x^2\left[1 + (2i/\rho^*_{GEA})e^{i\rho^*_{GEA}}\right.$$

$$\left. +(2/\rho^{*2}_{GEA})\left(1 - e^{i\rho^*_{GEA}}\right)\right]. \tag{3.61}$$

Equation (3.61) reduces to the EA for $\delta = 1$ and $\alpha_0 = 1$.

The GEA assumes, in the calculation of the phase shift, that the light passes undeviated through the medium. The MGEA corrects it by assuming that the light inside the medium travels along a straight line in the average direction of incident and scattered light. It is assumed that the light scattered suffers a deviation $\theta/2$ at each boundary. If $Z(b)$ is the distance traveled inside the medium

along a straight line in the z direction, the phase accumulated is $2knZ(b)$. When there is no medium, the distance traveled by the ray is $Z(b)\cos(\theta/2)$. Thus, the phase shift becomes $2k(m-\cos\theta/2)\sqrt{(a^2-b^2)}$ and the modified relation between α_0 and δ is $\delta = (m^2-1)/\big[2\alpha_0[m-\cos(\theta/2)]\big]$, and $\rho^*_{MGEA} = x[m^2-1]/\alpha_0\delta$. For a large sphere (LS), that is for $\rho^*_{MGEA} \gg 1$, the integrals in (3.60) can be evaluated analytically leading to (Chen, 1993),

$$S(\theta)^{LS}_{MGEA} = (m^2-1)x^3\big[-i(1-\delta)j_1(z)/z + \delta J_1(z)/(z\rho^*_{MGEA})$$

$$+(\delta/y^2)\big(ie^{iy} + (1-e^{iy})/y\big)\big], \tag{3.62}$$

where $y = [z^2 + \rho^2_{MGEA}*]^{1/2}$, and α_0 is redefined as $\alpha_0 = (m+1)/2 - (3i)/8x$.

From the point of view of extending the angular domain of the validity of the EA, Perrin and Chiappetta (1985) have proposed a modification of the EA which is referred to as the eikonal picture (EP). The explicit small angle approximation made for arriving at the two-dimensional scattering amplitude is not made here. Thus, the scattering function in the EP is

$$S(\theta)_{EP} = -\frac{ik^3}{2}\int d\mathbf{b}dze^{i\mathbf{q}.\mathbf{b}}[m^2(\mathbf{b},z)-1]$$

$$\times\exp\left[2ikz\sin^2(\theta/2) + \frac{ik}{2}\int_{-\infty}^{z(\mathbf{b})}[m^2(\mathbf{b},z')-1]dz'\right].$$

For a homogeneous sphere z integration in $S(\theta)_{EP}$ can be performed giving

$$S(\theta)_{EP} = -k^3(m^2-1)\int_0^a bdbJ_0(kb\sin\theta)$$

$$\times\Big[\frac{e^{i[q_z+k(m^2-1)]\sqrt{a^2-b^2}} - e^{-iq_z\sqrt{a^2-b^2}}}{2q_z + k(m^2-1)}\Big]. \tag{3.63}$$

It can be seen from (3.63) that when $\mathrm{Im}|m^2-1|$ is negligible and $4\sin^2(\theta/2) + \mathrm{Re}|m^2-1| = 0$, resonances are produced. But these resonances are spurious. An alternative form in which (3.63) is sometimes, expressed is

$$S(\theta)_{EP} = \frac{ix^2(m^2-1)}{U}\int_0^1 ydyJ_0(yx\sin\theta)\sin(Ux\sqrt{1-y^2})e^{iUx\sqrt{1-y^2}}, \tag{3.64}$$

where

$$U = [2q_z + k(m^2-1)]/2k, \tag{3.65}$$

and as before $q_z = 2k\sin^2(\theta/2)$. Equation (3.64) may be contrasted with the scattering function in the WKB (Wentzel–Kramers–Brillouin) approximation (Klett and Sutherland, 1992; Shepelevich *et al.*, 1999):

$$S(\theta)_{WKB} = ix^2(m^2-1)/(m-\cos\theta) \times \int_0^1 ydyJ_0(yx\sin\theta)\sin[(m-\cos\theta)x)\sqrt{1-y^2}]e^{i(m-\cos\theta)x\sqrt{1-y^2}}. \quad (3.66)$$

Note that if (m^2-1) is replaced by $2(m-1)$ in (3.65), U is nothing but $(m-\cos\theta)$. Equation (3.66) is then same as (3.64).

When the refractive index satisfies the condition $\mathrm{Im}(mx) \geq 1$, it is easy to see that the first term in the square bracket in (3.63) may be neglected and the scattering function can be written as,

$$S(\theta)_{EP}^{mod} = k^2 r(\theta)\int_0^a bdbJ_0(kb\sin\theta)e^{2ik\sin^2(\theta/2)\sqrt{a^2-b^2}}, \quad (3.67)$$

where $r(\theta) = k(m^2-1)/(2q_z+k(m^2-1))$. The superscript *mod* indicates modified EP. For θ close to 0 deg, (3.67) leads to diffractive scattering. For θ close to 180 deg, (3.67) gives correct geometrical optics result (Bourrely *et al.*, 1996) if $r(\theta) = r_\perp(\theta)$. With this replacement in (3.67), the formula reproduces two main components of the scattering pattern and is valid in the forward and the backward scattering directions.

Klett and Sutherland (1992) have examined a two wave WKB approximation. It is obtained by approximating $\psi(\mathbf{r})$ in (3.28) as

$$\psi(\mathbf{r}) = e^{ik(m-1)\sqrt{a^2-b^2}}\left(e^{ikmz} - Re^{ikm(2\sqrt{a^2-b^2}-z)}\right), \quad (3.68)$$

where $R = 1-[m/(1+m)]$. The first term in the bracket is the usual WKB approximation. The second term allows for reflection from the back face of the particle. For unpolarized light the phase function in this approximation is

$$p(\theta) = \frac{2(1+\cos^2\theta)|H_1+\exp(i\rho_1)RH_2|^2}{\int_0^\pi(1+\cos^2\theta)|H_1+\exp(i\rho_1)RH_2|^2\sin\theta d\theta}, \quad (3.69)$$

where

$$H_1(\theta) = \int_0^1 ydyJ_0(yx\sin\theta)\sin[x(m-\cos\theta)\sqrt{1-y^2}]\exp[ix(m-1)\sqrt{1-y^2}],$$

$H_2(\theta) = H_1(\pi-\theta)$, and $\rho_1 = 2mx$. The single wave WKB approximation is obtained by setting $H_2 = 0$ in equation (3.69).

For the extinction efficiency, although it has been noted that the EA as well as the ADA lead to the correct $x \to \infty$ limit, the rate of approach to this limit is much faster than predicted by Mie theory. This difference can be attributed to the effect at the edge of the particle. This edge effect is included as an additional term in the extinction formula (Ackerman and Stephens, 1987)

$$Q_{ext}^{AS} = Q_{ext}^{ADA} + Q_{edge}; \quad (3.70)$$

$$Q_{edge} = 2x^{-2/3}. \quad (3.71)$$

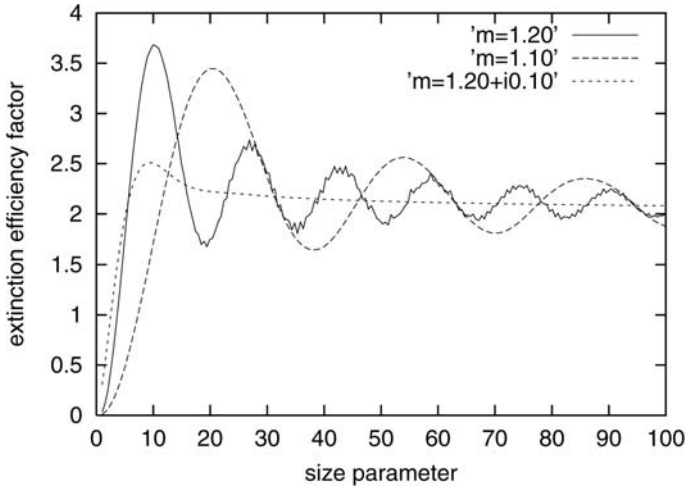

Fig. 3.3. Typical variations of extinction efficiency factor with size parameter

The superscript AS stands for Ackerman and Stephens. The edge correction is essentially a wave optics correction to the geometrical optics result. That is, the edge correction (3.71) applies only to large particles. A more general edge correction also includes a term describing interference of the surface waves that give rise to the ripple structure in the extinction efficiency curve. But this ripple structure is not of much interest in problems relating to scattering by a collection of particles because of averaging effects and also for particles where the condition $(n-1) \ll 1$ is well satisfied. Three typical variations of Mie extinction efficiency factor with x are shown in Fig. 3.3. Note that the extinction efficiency factor approaches 2 as $x \to \infty$ and the ripple structure disappears as $n \to 1$.

Approaching the problem from a different perspective an empirical recipe to improve the accuracy of Q_{ext}^{ADA} has been given by Klett (1984):

$$Q_{ext}^{K} = \mathcal{D} Q_{ext}^{ADA}; \qquad \mathcal{D} = 1.1 + (n - 1.2)/3. \tag{3.72}$$

The $\mathcal{D}$ values obtained from (3.72) agree reasonably well with $C(m)$ values obtained from (3.59).

An empirical formula for the extinction efficiency of a large dielectric sphere has been given by Walstra (1964). The result is

$$Q_{ext}^{WA} = 2 - \frac{16m^2 \sin\rho}{(m+1)^2\rho} + 4\frac{1 - m\cos\rho}{\rho^2} + 7.53\frac{z-m}{z+m}x^{-0.772}, \tag{3.73}$$

where $z = \left[(m^2-1)(6x/\pi)^{(2/3)}+1\right]^{1/2}$. This gives values correct to within 1% for $\rho > 2.4$, $1 < m \leq 1.25$. Even for higher values of m the formula is useful provided $x > \pi/4(\cot^{-1} m)^3$. If $m \to 1$, $Q_{ext}^{WA} \to Q_{ext}^{ADA}$ and if $x \to \infty$, $Q_{ext}^{WA} \to 2$ as

expected. A semi-empirical formula for $S(0)$ was also derived by Walstra (1964) on the same lines. The result is

$$S(0)_{WA} = \frac{1}{2}x^2 - i\frac{2m^2 x\exp(-i\rho)}{(m+1)^2(m-1)} + \frac{1-m\exp(-i\rho)}{4(m-1)^2}$$

$$+(1.88-1.05i)\frac{z-m}{z+m}x^{1.228}.$$

This result is expected to be correct to within 1% for $\rho > 3,\ 1 < m \leq 1.25$.

3.4.1.4 Numerical comparisons of variants of the EA and the ADA

The percent errors for a homogeneous sphere in the EA and the ADA are shown in Table 3.1. The percent error has been defined as

$$\text{percent error} = \left[i(0)_{exact} - i(0)_{approximate}\right] \times 100/i(0)_{exact}. \tag{3.74}$$

The comparison shows that the EA is superior to the ADA in the domain $x \geq 1.0$ and $\rho_{EA} \leq 4.0$. This observation is important because it relates to intermediate size particles. For higher values of ρ_{EA} the ADA gives more consistent results. On the other hand, for smaller particles the Rayleigh or the RGDA approximations are more useful. It is interesting to note that the value of $\rho_{EA} \simeq 4$ corresponds to the first maxima in the extinction curve.

As expected, the EA improves as $n \to 1$. But as x increases for a fixed n, the EA results do not improve continuously. The errors oscillate around the correct value. The reasons advanced to explain this behavior are the following. (i) The condition $x \gg 1$ is essentially a consequence of the requirement that n varies slowly over a distance of order of wavelength. For a homogeneous sphere

Table 3.1. Percent error in various approximation methods in $i(0)$ for a homogeneous sphere of refractive index 1.05

x	ρ	$\rho(m^2-1)/4$	EA	FCI	ADA	FCII	MFCI
1.0	0.1025	2.63×10^{-3}	−3.07	−8.43	1.88	−7.59	0.13
3.0	0.3075	7.88×10^{-3}	1.37	−3.79	6.09	−2.97	−0.69
5.0	0.5125	1.31×10^{-2}	2.58	−2.56	7.20	−1.76	−0.68
10.0	1.025	2.63×10^{-2}	3.67	−1.65	8.04	−0.84	−0.70
20.0	2.05	5.25×10^{-2}	4.90	−1.37	8.35	−0.50	−0.89
30.0	3.075	7.88×10^{-2}	6.60	−1.33	8.45	−0.39	−1.01
40.0	4.10	1.05×10^{-1}	9.11	−1.31	8.55	−0.28	−1.07
50.0	5.125	1.31×10^{-1}	12.65	−1.19	8.65	−0.17	−1.0
60.0	6.15	1.58×10^{-1}	16.65	−0.89	8.67	−0.14	−0.73
70.0	7.175	1.84×10^{-1}	15.17	−0.67	8.10	−0.77	−0.54
80.0	8.20	2.10×10^{-1}	8.20	−0.67	6.80	−2.20	−1.94
90.0	9.225	2.35×10^{-1}	−2.60	−3.44	6.65	−2.36	
100.0	10.25	2.63×10^{-1}	2.98	−3.73	7.04	−1.93	

Table 3.2. Percent error in various approximation methods in Q_{ext} for a homogeneous sphere of refractive index 1.05

x	ρ	$\rho(m^2-1)/4$	EA	FCI	ADA	FCII
1.0	0.1025	2.63×10^{-3}	−155.26	−155.26	−143.03	−154.48
3.0	0.3075	7.88×10^{-3}	−23.41	−23.44	−17.48	−23.02
5.0	0.5125	1.31×10^{-2}	−9.47	−9.55	−4.32	−9.23
10.0	1.025	2.63×10^{-2}	−2.47	−2.77	2.19	−2.42
20.0	2.05	5.25×10^{-2}	0.34	−0.88	4.04	−0.48
30.0	3.075	7.88×10^{-2}	2.15	−0.62	4.36	−0.15
40.0	4.10	1.05×10^{-1}	4.33	−0.60	4.42	−0.09
50.0	5.125	1.31×10^{-1}	6.85	−0.66	4.34	−0.17
60.0	6.15	1.58×10^{-1}	8.65	−0.66	4.13	−0.34
70.0	7.175	1.84×10^{-1}	6.69	−0.65	3.79	−0.75
80.0	8.20	2.10×10^{-1}	0.89	−0.87	3.57	−1.00
90.0	9.225	2.35×10^{-1}	−1.19	−1.33	3.64	−0.90
100.0	10.25	2.63×10^{-1}	−1.22	−1.68	3.71	−0.83

n is constant. Thus, increasing x need not result in increased accuracy. (ii) The requirement of the slow variation of the refractive index is not satisfied at the boundary, where there is a sharp cut-off.

Table 3.2 shows the percent error in the extinction efficiency factor. In comparison to $i(0)$, all approximations work better for Q_{ext} when $x \geq 5.0$. For smaller values of x, the performance of the EA as well as the ADA is not good. This is because, for small values of x neither the EA nor the ADA accurately reproduces the real part of the forward scattering function. In fact, it is this real part of the scattering function, which is directly proportional to the extinction efficiency via the extinction theorem (3.6).

Inclusion of corrections improve the results considerably. The modified approximations are found to work extremely well in the domain $x \geq 5.0$ and $\rho_{EA}|n^2 - 1|/4 < 1$ (Sharma, 1993). Tables 3.1 and 3.2 show a significant improvement for $i(0)$ as well as for Q_{ext}. In particular $S(\theta)_{FCII}$ is found to give very good predictions. Results do not improve, rather they deteriorate, for $x \leq 5$. This is because the effect of neglect of the vector nature is significant here. Unfortunately it is difficult to correct the EA systematically for this type of error. However, the difficulties associated with the region $x \leq 5$ may be removed for $i(0)$ for non-absorbing homogeneous spheres by introducing an empirical multiplicative factor. Sharma *et al.* (1982) define a modified amplitude as

$$i(0)_{MFCI} = A(x, n) i(0)_{FCI}.$$

The multiplicative factor $A(x, n) = 1 - 4(n-1)/x(n^2+1) + (n-1)/x^2(n^2+2)$ is not unique and has been arrived by noting that $A(x, n)$ should be approximately equal to $i(0)_{Mie}/i(0)_{scalar}$. The results in Table 3.1 show that this dramatically improves the FCI results in the domain $x \leq 5$.

Not many numerical studies of the accuracy of the angular variation of $i(\theta)$ have been performed. Whilst Chen (1988, 1989) and Chen and Smith (1992) have compared the angular scattering patterns of the EA, the ADA and the GEA with exact results, Perrin and Chiappetta (1985) and Sharma *et al.* (1988) have examined the EP and the EA against exact results. The following conclusions emerge from these studies:

(i) The EA works to within 25% error for $x \geq 1$, $1 \leq n \leq 1.2$ and $\theta \leq 10.0$.
(ii) The GEA greatly improves the EA results. More importantly, it appears to work very well for n as large as 4.0. However, the success is only for scattering angles up to $\sim 5^0$. Its improved variant, the MGEA, is found to work well for the perpendicular polarization. It accurately predicts positions of minima and maxima for θ up to 60^0, $x \geq 5.0$,$n \leq 4$ and $n' \leq 0.5$.
(iii) The simplified version of the GEA, given in (3.62), is found to work as well as the GEA for $x > 10$.
(iv) For a non-absorbing dielectric sphere the positions of maxima and minima in the angular scattering pattern are determined more accurately in the EP but the errors at the minima in the EP are much larger compared to those obtained when the EA is used. As n' increases the EP appears to qualify as an all angle approximation. The modified EP (eq. (3.67)) is in much better agreement with the Mie theory for scattering angles greater than 40^o. The model is valid for $x \geq 10.0$.

Jones *et al.* (1996) have generated error contour charts for the two-wave WKB approximation for a sphere in the domain $1.0 < n < 1.5$ and $0 < x < 20.0$. The results showed that the two-wave WKB approximation was superior to both the RGDA and the single-wave WKB models.

3.4.1.5 Backscattering in the EA

Although the EA has been derived as a near forward scattering approximation, it can also serve as a useful basis to describe the backward scattering if the conditions (3.31) for the validity of the EA are satisfied. Saxon and Schiff (1957) assume that the backscattering is due to a single hard scattering event. When translated to optical scattering this gives

$$S(\pi)_{SS} = -i(1-m^2)x\left[e^{2ixm^2} + e^{-2ix}\right]/8. \tag{3.75}$$

A comparison of $i(\pi)_{SS}$ with the exact result for a non-absorbing sphere of $n = 1.05$ show that it is in good agreement with exact results except at those values of x for which the scattered intensity has a minimum. Interestingly, the positions of minima are reproduced quite accurately.

The contributions of the two and three hard scattering events respectively (in the sense of Born series) give (Sharma and Somerford, 1994)

$$S(\pi)^I_{SS} = \frac{x(m^2-1)^2}{8}\sqrt{x\pi/\sqrt{2}}\; e^{2ix\sqrt{2}+\frac{3ix}{\sqrt{2}}(m^2-1)-\frac{i\pi}{4}}, \tag{3.76}$$

and

$$S(\pi)_{SS}^{II} = -ix(m^2-1)^3\sqrt{6\pi x}e^{3ix+2ix(m^2-1)-\frac{i\pi}{4}}. \tag{3.77}$$

If the medium is highly absorbing the main contribution comes from (3.75). In contrast, for a non-absorbing dielectric sphere $|S(\pi)_{SS}|^2/|S(\pi)_{SS}^I|^2 = x(n^2-1)^2$, and the contribution from two hard scattering events becomes important and may even dominate if $x > 1/|n^2-1|^2$. The deep minima predicted by $i(\pi)_{SS}$ now get filled up to give values closer to the exact values.

The positions of minima in the scattering pattern, determined by (3.75), are given by $x(n^2+1) = p\pi$, where p is an integer. The separation between two successive minima for a given n is thus

$$\Delta x = \pi/(n^2+1). \tag{3.78}$$

Predicted separation has been found to be in good agreement with the actual separation. Clearly, (3.78) could be a useful relation for diagnostic purposes.

The backscatter efficiency defined as

$$Q_{back} = \frac{1}{x^2}\left|\sum_l (2l+1)(-1)^l(a_l - b_l)\right|^2,$$

gives in the two wave WKB approximation (Klett and Sutherland, 1992):

$$Q_{back} = (4x^2/\pi)(|m-1|^2/|m+1|^2)|I_1 + \exp(i\rho_1)I_2|^2, \tag{3.79}$$

where

$$I_1 = \left[i/\rho_1^2 - (i+\rho_1)e^{i\rho_1}/\rho_1^2 - i/\rho_2^2 + (i-\rho_2)e^{-i\rho_2}/\rho_2^2\right]/2;$$
$$I_2 = i\left[(i\rho_3 - 1)e^{i\rho_3}/\rho_3^2 + 1/\rho_3^2 + 1/2\right]/2,$$

with $\rho_1 = 2xm$, $\rho_2 = 2x$ and $\rho_3 = 2x(m-1)$. Numerical comparisons show that for the moderately soft case $[m = (1.33, 0)]$, (3.79) agrees with the exact values to within an order of magnitude.

3.4.1.6 Vector description

Attempts to incorporate the vector nature in the EA description to get access to polarization studies have been made by Perrin and Lamy (1986) and by Bourrely *et al.*, (1991). Starting from Mie scattering functions Bourrely *et al.*, (1991) obtain

$$\begin{aligned} S_1(\theta) \;=\; & S_1^{diff}(\theta)H(\theta_{max}-\theta) + k\int_0^a db\Big[e^{2i\alpha(b)}\cot\theta J_1(kb\sin\theta) \\ & + e^{2i\beta(b)}[kbJ_0(kb\sin\theta) - \cos\theta\cot\theta J_1(kb\sin\theta)]\Big], \end{aligned} \tag{3.80}$$

where $S_1^{diff}(\theta) = \left[(1-\cos\theta)\cot\theta[1-J_0(x\sin\theta)] + xJ_1(x\sin\theta)\right]$, is the diffractive component which is zero for $\theta > \theta_{max} = 180/x$ radians and $\alpha(b)$ and $\beta(b)$ are

as defined in (3.45) and (3.46). The scattering function $S_2(\theta)$ is obtained from (3.80) by permuting $\alpha(b)$ and $\beta(b)$. This approach has been tested numerically against Mie predictions for $x = 150$, $m = 1.3 + i0.01$ and for $x = 500$ and $m = 1.10 + i0.01$. The degree of polarization defined as

$$\mathcal{P}(\theta) = \big[|S_1(\theta)|^2 - |S_2(\theta)|^2\big] / \big[|S_1(\theta)|^2 + |S_2(\theta)|^2\big],$$

is in satisfactory agreement with the Mie theory predictions for $\theta > \theta_{max}$. Agreement is better for particles of larger sizes.

3.4.2 Perelman approximation

Perelman (1978, 1991) successfully summed the Mie series for small angle scattering by implementing the limit $m \to 1$ in the denominators of the scattering coefficients. It is convenient to write Mie scattering coefficients as

$$a_l = \frac{h_{1l}}{h_{1l} + ih_{3l}}, \qquad b_l = \frac{h_{2l}}{h_{2l} + ih_{4l}}, \tag{3.81}$$

where

$$\begin{aligned} h_{1l} &= mu_l(mx)u_l'(x) - u_l'(mx)u_l(x), \qquad & h_{2l} &= u_l(mx)u_l'(x) - mu_l'(mx)u_l(x), \\ h_{3l} &= mu_l(mx)v_l'(x) - u_l'(mx)v_l(x), \qquad & h_{4l} &= u_l(mx)v_l'(x) - mu_l'(mx)v_l(x), \end{aligned}$$

and $u_l(x) = xj_l(x)$ and $v_l(x) = xn_l(x)$ are the Riccati–Bessel functions. In the limit $m \to 1$, the denominators in (3.81) can be approximated as

$$h_{1l} + ih_{3l} \sim h_{2l} + ih_{4l} = i|m|^{-1/2}. \tag{3.82}$$

The summation over l in scattering functions $S_1(\theta)$ and $S_2(\theta)$ can now be carried out for near forward scattering by expanding $\pi_l(\theta)$ and $\tau_l(\theta)$.

The main form of the Perelman approximation (MPA) is obtained by re-expressing the scattering coefficients in the form

$$a_l = h_{1l}(h_{1l} - ih_{3l})/(h_{1l}^2 + h_{3l}^2); \qquad b_l = h_{2l}(h_{2l} - ih_{4l})/(h_{2l}^2 + h_{4l}^2).$$

The MPA then consists in approximating (Perelman, 1991)

$$h_{1l}^2 + h_{3l}^2 \sim h_{2l}^2 + h_{4l}^2 = |m|. \tag{3.83}$$

The resulting series for $S(0)$ can be summed for forward scattering to yield:

$$S(0)_{MPA} = x^2\Big[(m^2+1)^2 + \omega(m,\rho^*) - (\omega(-m,-R))/2m\Big]/8|m|, \tag{3.84}$$

where

$$\omega(m,z) = [a(m) + a_0(m)z^{\,2}]ei(z) - ia_1(m)e_1(z) + a_2(m)e_2(z),$$

$$a(m) = (m^2-1)^2(m^2+1), \qquad a_0(m) = -2(m^2-1)^2(m-1)^2,$$

$$a_1 = (m+1)^2(m^4 - 2m^3 - 2m^2 - 2m + 1), \qquad a_2(m) = -a_0(m) - a_1(m),$$

$$ei(z) = \int_0^z dt\big(1 - \exp(-it)\big)/t,\ e_1(z) = \exp(-iz)/z,$$

$$e_2(z) = \big(1 - \exp(-iz)\big)/z^2,$$

and $R = 2x(m+1)$. The above result holds for all values of $x > 0$ and $m = n + in'$. For non-forward angles, Mie series can still be summed but only for small scattering angles giving:

$$S_k(\mu)_{MPA} = S(0)_{MPA} - (1-\mu)H_k; k = 1, 2, \tag{3.85}$$

where

$$H_1 = -i(m+1)m^2|m|^{-1/2}x^4z^2u_2(z),$$

and

$$H_2 = -i(m+1)m^2|m|^{-1/2}x^4\big[z^2\psi_2(z) + x^2u_1(z)/mz\big].$$

In (3.85) the scattering functions are accurate to order θ^4.

The extinction efficiency factor may be calculated either by first obtaining an approximation to the amplitude and then following it with the use of the optical theorem or by writing the exact analytic form of the extinction efficiency factor and then implementing the approximation. The second approach is generally preferable because one is then not unduly worried about questions relating to the unitarity property. For a homogeneous sphere

$$Q_{ext}^{MIE} = \frac{4}{x^2}\mathrm{Re}S(0) = \frac{2}{x^2}\mathrm{Re}\sum_{l=1}^{l=\infty}\Big[a_l + b_l\Big], \tag{3.86}$$

where the relations $\pi_l(0) = \tau_l(0) = l(l+1)/2$ have been used. Perelman (1978), starting from (3.86), and employing (3.83) has obtained the following expression for the extinction efficiency of a non-absorbing spherical particle:

$$\begin{aligned} Q_{ext}^{MPA} \;=\; & b_1\Big[Q_h(\rho) - \Big(\frac{m-1}{m+1}\Big)^2 Q_h(R)\Big] + b_2\Big[Q_1(\rho) - Q_1(R) - \int_\rho^R \frac{1-\cos t}{t}dt\Big] \\ & + \frac{(m-1)^2}{4m^2x^2}\left[Q_2(R) - Q_2(\rho) + \frac{1}{2}\int_\rho^R \frac{1-\cos t}{t}dt\right] + \frac{1}{2mx^2}Q_3(m,x), \end{aligned} \tag{3.87}$$

where

$$b_1 = \frac{(m+1)^2(m^4+6m^2+1)}{32m^2}, \qquad b_2 = \frac{(m^2+1)(m^2-1)^2}{4m^2},$$

$$Q_1(\omega) = \frac{2(1-\cos\omega)}{\omega^2} + \frac{2\sin\omega}{\omega}, \quad Q_2(\omega) = \frac{3\cos\omega}{8} + \frac{\sin\omega}{8} + \frac{\omega^2}{16},$$

$$Q_3(\omega) = (m-1)^2(\cos R - 1) + (m+1)^2(\cos\rho - 1),$$

and

$$Q_h(\rho) = 2 - 4\sin\rho/\rho + 4(1-\cos\rho)/\rho^2.$$

The extinction efficiency can also be cast in an integral representation (Granovskii and Ston, 1994a, 1994b)

$$Q_{ext}^{MPA} = mx^2(m^2-1)^2 \int_{-1}^{1} dt(1+t^2)g^2(x\omega(t)), \tag{3.88}$$

where $g(\omega) = (\omega\cos\omega - \sin\omega)/\omega^3$ and

$$\omega(t) = (1+m^2-2mt)^{1/2}. \tag{3.89}$$

It can be seen that for m close to 1, (3.88) may be further approximated as

$$Q_{ext}^{MPA} = 4x^4(m-1)^2 \int_{-1}^{1} dt(1+t^2)g^2(x\sqrt{2(1-t)}), \tag{3.90}$$

by substituting $m = 1$ in (3.89). Equation (3.90) is the RGDA in integral representation. We have for absorption efficiency: $Q_{abs}^{MPA} = 4m_2 n|m_1|^2 S(\tau)$, where $S(\tau) = 4((\tau/2)\cosh(\tau/2) - \sinh(\tau/2))/\tau^2$, and m_1, m_2 are the refractive indices inside and outside the particle and $\tau = 4n'x$.

It may be mentioned here that the Mie series has been summed in the Perelman approximation for backscattering too (Perelman, 1985).

3.4.2.1 Some special cases

If $x \ll 1$, (3.87) can be expanded in powers of x. The leading term gives:

$$Q_{ext}^{MPA} = (8/27)m(m^2-1)^2x^4.$$

This differs from the Rayleigh formula only in that $(m^2+1)^2$ in the original Rayleigh formula is replaced by 9.

For $(m-1) \ll 1, \rho \ll 1$, one can put $b_2 = 0$ and the first term in Q_3 also zero. The dependence of the other terms on ρ may be specified as follows:

$$Q_h(\rho) = \frac{(m-1)^2R^2}{8}, \quad Q_1 = 3, \quad \int_0^{\rho} dt(1-cost)/t = 0, \quad Q_2(\rho) = \frac{(m-1)^2}{8},$$

if terms of order higher than $(m-1)^2$ are neglected. Equation (3.87) then reduces to Q_{ext}^{RGDA} given by (3.7).

For $m \to 1, x \to \infty$, ρ finite, various terms of Q_{ext}^{MPA} are of following order:

$$b_1\Big(\frac{m-1}{m+1}\Big)^2 Q_h(R) = O(m-1)^2, \qquad b_2[Q_1(\rho) - Q_1(R)] = O(m-1)/x,$$

$$b_2\int_{\rho}^{R} \frac{1-\cos t}{t}dt = O(m-1)\rho, \qquad \frac{(m^2-1)^2}{4m^2x^2}[Q_2(R) - Q_2(\rho)] = O(m-1)^2$$

$$\frac{(m^2-1)^2}{8m^2x^2}\int_\rho^R \frac{1-\cos t}{t}dt = O(m-1)^2/x, \qquad \frac{1}{2mx^2}Q_3(m,x) = O(x_2).$$

Neglecting the terms of oder $(m-1)$ and terms of relative order x^{-1}, equation (3.87) gives

$$Q_{ext}^{MPA} = b_1 Q_h(\rho) - b_2 \int_\rho^R \frac{1-\cos t}{t}dt. \tag{3.91}$$

It has been shown that (3.91) does improve over the ADA extinction efficiency factor (Perelman, 1978).

By examining the short wavelength asymptotics of the amplitude functions, Perelman and Voshchinnikov (2002) have further improved Q_{ext}^{MPA}:

$$Q_{ext}^{IPA} = \left[1 - \frac{S(m)-2}{S(m)}\exp\left(-\frac{0.01\ \exp(4m)}{u}\right)\right] Q_{ext}^{MPA},$$

where $S(m) = \lim_{x\to\infty} Q_{ext}^{MPA}$, and $u = x/x(m)$. The size parameter $x(m)$ is that value of x, for a given m, for which the error in Q_{ext}^{MPA} is less than 5%. The superscript IPA stands for the improved Perelman approximation.

3.4.2.2 The scalar Perelman approximation

For forward scattering by a homogeneous sphere the scalar scattering function is expressed as the following partial wave sum (Roy and Sharma, 1996):

$$S(0) = \sum_{l=0}^{\infty}(2l+1)b_l.$$

A straightforward calculation using main form of the PA gives,

$$\begin{aligned} S(0)_{SPA} \ &= \ R^2\Big[2 + 4[1-\exp(i\rho)]/\rho^2 + 4i\exp(i\rho)/\rho\Big]/64 \\ &\quad -\rho^2\Big[2 + 4[1-\exp(-iR)]/R^2 - 4i\exp(-iR)/R\Big]/64. \end{aligned} \tag{3.92}$$

where the superscript SPA stands for the scalar Perelman approximation. The first term on the right-hand side of (3.92) is nothing more than the ADA scattering function multiplied by a m dependent factor. The second term on the right-hand side of (3.92) can be obtained from the first term simply by replacing $\rho \leftrightarrow -R$. It is clear that the SPA constitutes considerable simplification over the MPA. In particular, we have

$$Q_{ext}^{SPA} = (m+1)^2\Big[Q_h(\rho) - \rho^2 Q_h(-R)/R^2\Big]/4, \tag{3.93}$$

for a non-absorbing sphere. Numerical comparison of the MPA and the SPA has been performed by Roy and Sharma (1996). On the basis of this comparison they proposed a modified SPA (MSPA):

$$S(0)_{MSPA} = S(0)_{SPA} - \phi(m-1),$$

$$Q_{ext}^{MSPA} = Q_{ext}^{SPA} - \phi(m-1)$$

where

$$\phi(m-1) = \frac{1}{25}(m-1) + 5(m-1)^2 - 12(m-1)^3 - 2(m-1)^4.$$

The MSPA has the simplicity of the SPA and accuracy of the MPA.

3.4.3 Hart and Montroll approximation

The Hart and Montroll approximation (HMA) (Hart and Montroll, 1951; Montroll and Hart, 1951) also consists in approximating denominators of the scattering coefficients. But, while the limit considered in the PA and the MPA is $m \to 1$, the basic assumption underlying the HMA is $l \ll x$. In this limit denominators of a_l and b_l respectively become:

$$h_{1l} + ih_{3l} \sim \frac{i(m+1)m}{2} \exp(-i\rho/2)\big[1 - (-1)^l r \ \exp(2imx)\big] \tag{3.94}$$

and

$$h_{2l} + ih_{4l} \sim \frac{+i(m+1)m}{2} \exp(-i\rho/2)\big[1 + (-1)^l r \ \exp(2imx)\big], \tag{3.95}$$

where $r = (m-1)/(m+1)$. Note that in the limit $m \to 1$, (3.94) and (3.95) reduce to $h_{1l} + ih_{3l} \sim h_{2l} + ih_{4l} = im$. The approximation is then essentially identical with the PA. Hence the above approximation is valid under both sets of conditions namely

$$|m-1| \ll 1, \qquad x \gg l.$$

The resulting infinite series for $S_1(\theta)$ and $S_2(\theta)$ can be summed to yield,

$$S_1(\theta)_{HMA} = \frac{-i\pi(m-1)\exp(i\rho/2)}{m^{1/2}\sin\theta[1 - r^2\exp(4imx)]}\big[F_1(\theta) + r \ \exp(2imx)F_1(\pi-\theta)\big],$$

and

$$S_2(\theta)_{HMA} = \frac{i\pi(m-1)\exp(i\rho/2)}{m^{1/2}\sin\theta[1 - r^2 exp(4imx)]}\big[F_2(\theta) + r \ \exp(2imx)F_2(\pi-\theta)\big],$$

where F_1 and F_2 are given by equations,

$$\begin{pmatrix} F_1 \\ F_2 \end{pmatrix} = \left(\frac{2m}{\pi}\right)^{1/2} \frac{mJ_{3/2}(x\omega(\cos\theta))\sin\theta}{(x\omega(\cos\theta))^{3/2}} \begin{pmatrix} 1 \\ \cos\theta \end{pmatrix},$$

with $\omega(\cos\theta)$ as defined in (3.89). In the corresponding expression for $F_J(\pi-\theta)$, $\omega(\cos\theta)$ is replace by $\omega(-\cos\theta)$. Neglecting terms of relative order r or higher, the extinction efficiency factor in this approximation can be expressed as:

$$Q_{ext}^{HMA} = \frac{\pi x^2 (m-1)^2}{2m}\left[(m^2+6m^2+1)\Delta_1 - \frac{2(m^2-1)}{x^2}\Delta_2 + x^{-4}\Delta_3\right],$$

where

$$\Delta_j = I_j(x(m+1)) - I_j(x(m-1))$$

and I_1, I_2 and I_3 are given by

$$I_1(x) = \frac{1}{2\pi} - \frac{1}{8x}\left[J_{1/2}^2(2x) + J_{3/2}^2(2x)\right], \quad I_2(x) = \frac{1}{\pi}\left[\frac{\sin 4x}{2x} - \frac{\sin^2 2x}{4x^2} - 1 + \phi(4x)\right],$$

$$I_3(x) = \frac{1}{\pi}\left[2x^2 + x\sin 4x - \frac{5}{2}\sin^2 2x + \phi(4x)\right],$$

with $\phi(x) = \int_0^x (1-\cos t)dt/t$. Sharma and Somerford (1996) have calculated Δ_1, Δ_2 and Δ_3 and have shown that

$$Q_{ext}^{HMA} = \frac{4m}{(m+1)^2} Q_{ext}^{MPA}. \tag{3.96}$$

The factor $4m/(m+1)^2$ is very close to 1 for $|m-1| \ll 1$. For example, for $m = 1.05$ and $m = 1.10$ its value is 0.9994 and 0.9975, respectively.

The relationship (3.96) may be understood as follows. The HMA holds for $x \gg l$. The main contribution here comes from the rays near the central ray. In fact, because of this, van de Hulst (1957) has suggested that this approximation might be called 'central-incidence approximation'. Further, it is also known (see, for example, van de Hulst, 1957) that the dominant contribution to the forward scattering for a large particle when $|m-1| \ll 1$ arises from the near-central rays. This is perhaps the reason for the close relationship between the HMA and the MPA for forward scattering and hence for the extinction efficiency.

3.4.4 Evans and Fournier approximation

The Evans and Fournier approximation (EFA)(Evans and Fournier, 1990; Fournier and Evans, 1991) was designed to modify the ADA extinction efficiency factor in such a way that it correctly accounts for the behavior of Q_{ext} over the entire x range. For a homogeneous sphere one obtains:

$$Q_{ext}^{EFA} = Q_{ext}^{R}\left[1 + \left(\frac{Q_{ext}^{R}}{TQ_{ext}^{ADA}}\right)^P\right]^{-1/P}, \tag{3.97}$$

where

$$\begin{aligned} Q_{ext}^{R} &= \frac{24nn'}{F_1(n,n')}x \\ &+ \left[\frac{4nn'}{15} + \frac{20nn'}{3F_2(n,n')} + \frac{4.8nn'[7(n^2+n'^2)^2 + 4(n^2-n'^2-5)]}{F_1^2(n,n')}\right]x^3 \\ &+ \frac{8}{3}\left[\frac{[(n^2+n'^2)^2 + (n^2-n'^2-2)]^2 - 36n^2n'^2}{F_1^2(n,n')}\right]x^5, \end{aligned} \tag{3.98}$$

is the extinction efficiency to order x^4 in the 'Rayleigh approximation' ($x \ll 1$, $|mx| \ll 1$). The F_1 and F_2 are given by the expressions,

$$F_1(n, n') = (n^2 + n'^2)^2 + 4(n^2 - n'^2) + 4,$$

$$F_2(n, n') = 4(n^2 + n'^2)^2 + 12(n^2 - n'^2) + 9.$$

The parameters P and T are given by the relations:

$$P = A + \mu/x; \quad T = 2 - \exp(-x^{-2/3}).$$

When $x \to 0$, $P \to \infty$ and Q_{ext}^{EFA} becomes equal to Rayleigh formula. As the size parameter increases, Q_R^{ext} becomes very large and Q_{ext}^{EFA} approaches TQ_{ext}^{ADA} (designed to reproduce approximately large particle formula of Nussenzvieg and Wiscombe (1980)). However, if n' is large, Q_R^{ext} outside the Rayleigh region may become negative. In this case one arbitrarily sets the negative coefficient in (3.98) to zero. This ensures a positive growth of Q_R^{ext} as x increases. The behavior of this approximation in the intermediate region between the Rayleigh and ADA limits is controlled by A and μ. By extensive trial and error the following expressions for A and μ have been found:

$$A = \frac{1}{2} + \left[n - 1 - \frac{2}{3}\sqrt{n'} - \frac{n'}{2}\right] + \left[n - 1 + \frac{2}{3}(\sqrt{n'} - 5n')\right]^2;$$

and

$$\mu = \frac{3}{5} - \frac{3}{4}\sqrt{n-1} + 3(n-1)^4 + \frac{25}{6 + [5(n-1)/n']}.$$

Obviously the above expressions are by no means unique.

3.4.5 Bohren and Nevitt approximation

In geometrical optics the absorption efficiency of a sphere with radius a and relative refractive index m is found to be (Bohren and Huffman, 1983):

$$Q_{abs}^{GO} = 2\int_0^{\pi/2} \frac{T[1 - e^{-\alpha\xi}]}{1 - Re^{-\alpha\xi}} \cos\theta_i \sin\theta_i d\theta_i, \tag{3.99}$$

where θ_i is the angle of incidence, T and R are transmittance and reflectance of unpolarized light obtained from Fresnel formulas, $\xi = 2a\sqrt{n^2 - (\sin^2\theta_i/n)}$ and α is the absorption coefficient of the sphere. It is assumed that $n \gg n'$, so that the angle of refraction is approximately real. The superscript GO stands for geometrical optics. Making a change of variable, $u = (n^2 - \sin^2\theta_i)/n^2$, one obtains

$$Q_{abs}^{GO} = n^2 \int_{\frac{n^2-1}{n^2}}^{1} f(u)[1 - exp(-\tau\sqrt{u})]du \tag{3.100}$$

where $\tau = 2a\alpha = 4xn'$ and $f(u) = T(u)/(1 - [1 - T(u)]exp(-\tau\sqrt{u}))$. If $f(u)$ is set equal to 1, the integral in (3.100) is overestimated by at most a few percent

(Bohren and Nevitt, 1983). The advantage is that the integral in (3.100) can then be evaluated analytically. Thus, we have to a good approximation,

$$Q_{abs}^{BNA} = C_1 \left[\frac{1}{n^2} - \frac{2}{n^2} \left[e^{-\tau\sqrt{n^2-1}/n}(1 + \frac{\tau\sqrt{n^2-1}}{n}) - e^{-\tau}(1+\tau) \right] \right], \quad (3.101)$$

where,

$$C_1 = 4n^3/[(n+1)^2 - (n-1)^2 exp(-\tau)].$$

As τ is increased Q_{abs}^{BNA} approaches the limit $4n/(n+1)^2$, which is the transmittance of a plane surface for normally incident light. The Q_{abs}^{BNA} is obviously not correct in this limit. But it is expected to be high by perhaps only a few percent (Bohren and Nevitt, 1983).

For a weakly absorbing sphere ($\tau \ll 1$) the right-hand side of (3.101) can be expanded in powers of τ. The expansion up to the third order leads to

$$Q_{abs}^{BNA} = (2\tau/3)n^2(1 - b^3), \quad (3.102)$$

where $b = (n^2-1)^{1/2}/n$. Equation (3.102) may be compared with weak absorption limit of the Q_{ADA}^{abs}

$$Q_{ADA}^{abs} = 2\tau/3, \quad (3.103)$$

and the weak absorption limit of Q_R^{abs} ,

$$Q_R^{abs} = (2\tau/3)(9n/(n^2+2)^2). \quad (3.104)$$

Note that except for a n-dependent multiplicative factor, (3.102), (3.103) and (3.104) are identical. Bohren and Nevitt (1983) have found that the value of the functions obtained from (3.102) and (3.104) with n in the range 1.0–1.5 do not differ appreciably from unity. The unexpected implication of this is that subject to restrictions on the refractive index of the sphere, the formula (3.102) is valid for geometrical optics as well as in the Rayleigh domain. That is the formula (3.101) will yield good results for small as well as large soft particles. The relationship between (3.102), (3.103) and (3.104) has prompted Flatau (1992) to propose a modified ADA (ADT) in which τ occurring in the usual ADA is replaced by a new τ defined as $\tau_{new} = n^2(1 - b^3)\tau$.

An approximation somewhat similar to the BNA was obtained by Shifrin and Tonna (1992) for weakly refracting small particles. It reads

$$Q_{abs}^{ST} = 1 - \exp(-2\tau n^2(1 - b^3)/3),$$

which coincides with (3.102) for small absorption. Simple formulas for a weakly absorbing sphere ($n' < 0.1$) have been obtained by Kokhanovsky and Zege (1997) through the Mie computation results:

$$\begin{aligned} Q_{abs}^{KZA} \;=\; & T\Bigg(1 - \frac{n^2}{8n'^2x^2}[e^{-4n'xb}(1 + 4n'xb) - e^{-4n'x}(1 + 4n'x)] \\ & -S(n)[1 - e^{-4n'x}]^2\Bigg), \end{aligned} \quad (3.105)$$

where

$$T = 1 + (n-1)(1 - e^{-1/(t\rho)}),$$

$$t = [21.2 - 20.1Z + 11.1Z^2 - Z^3]^{-4}, \quad Z = -\log n',$$

and

$$S(n) = \frac{8n^2(n^4+1)\ln n}{(n^4-1)^2(n^2+1)} - \frac{n^2(n^2-1)^2}{(n^2+1)^3}\ln\frac{n+1}{n-1}$$
$$+\frac{3n^7 - 7n^6 - 13n^5 - 9n^4 + 7n^3 - 3n^2 - n - 1}{3(n^4-1)(n^2+1)(n+1)}.$$

An alternative expression obtained within the complex angular momentum theory for weakly absorbing soft particles ($n \leq 1.2$) is (Kokhanovsky, 1995)

$$Q_{abs}^{K} = Q_{abs}^{BNA} + Q_{abs}^{edge},$$

where

$$Q_{abs}^{edge} = 4nn'x\Big[\cos^{-1}(1/n) - \sqrt{n^2-1}/n^2\Big].$$

3.4.6 Numerical comparisons

Perelman (1978, 1991) has examined the accuracy of Q_{ext}^{MPA} for a large range of m and x values for a homogeneous sphere. The results are reproduced as Table 3.3. The table specifies maximum of ρ values up to which the error is less than 5% for a given m value. For $m \leq 1.06$ errors are less than 5% for all values of x, except possibly at points between $0 < x < 2$. In this region this error can be between 5–25%. Also it has been noted that (3.87) and (3.91), on the whole, are of the same accuracy.

Table 3.3. The values of ρ below which the extinction in the MPA gives errors that are less than 5%

m	1.00–1.06	1.08	1.10	1.12	1.14	1.16	1.18	1.20	1.22
ρ	∞	128	60	31	25	23	18	15	14

Numerical evaluation of the IPA for extinction efficiencies show that for very small size parameters the errors are large in comparison to RGDA. For large phase shifts however, the IPA is seen to reproduce very well both the position and the height of the maxima and minima of the extinction curve. In comparison, the extinction predicted by the ADA is smaller than that given by the exact theory. It is found that the IPA may be used for arbitrarily large values of x. For $m < 1.03$ (errors are $< 1\%$), for $m < 1.10$ (error are $< 5\%$), and for $m < 1.22$ (error are $< 10\%$) (Perelman and Voshchinnikov, 2002).

The extinction efficiency in the MPA is compared with the ADA and the MADA in Table 3.4 for $m = 1.06$. The accuracy of the MSPA is noted to be

nearly same as MPA. The errors in the MADA and the MPA increase with increasing x tending to a constant value. The errors in the ADA decrease with increasing x approaching zero as $\rho \to \infty$. The ρ value above which the ADA is most accurate approximation have been delineated by Perelman (1978). For a given relative error, ϵ, the approximation is preferable in the domain $0 < x < x(m, \epsilon)$. Generally speaking the function $x(m, \epsilon)$ decreases as $|m - 1|$ increases. The rate of decrease of $x(m, \epsilon)$ is not uniform. For example, $x(1.02, 0.002) > 100$, $x(1.10, 0.01) = 55$, $x(1.10, 0.03) = 90, x(1.20, 0.07) = 85$ and so on. Granovskii and Ston (1994a) have compared the extinction efficiency results of their integral representation of the MPA with those of Mie theory, RGDA and the ADA. They considered ρ values up to 10 and $m = 1.1$. Their results are within 2% of the exact Mie theory. A typical comparison for percentage errors in scattered intensities is also shown in Table 3.4. The positions of maxima and minima as well as their amplitudes are reproduced quite well for the first few extrema.

Table 3.4. Percent error in various approximation methods in $1.0 \leq x \leq 10.0$ for Q_{ext} (columns 2–5) and $i(0)$ (columns 6–9) for a homogeneous sphere. Relative refractive index is $m = 1.06$

	extinction efficiency factor				scattered intensity			
x	SPA	MPA	ADA	MADA	SPA	MPA	ADA	MADA
1.0	−60.83	−7.83	−142.21	−155.73	−10.29	−21.03	2.25	−8.96
2.0	−42.30	−3.79	−40.93	−48.79	−6.90	−14.20	5.08	−5.01
3.0	−19.92	−0.35	−16.20	−22.69	−4.18	−8.91	7.24	−3.39
4.0	−12.53	−0.09	−7.83	−13.85	−3.39	−6.81	8.08	−2.96
5.0	−8.54	0.05	−3.21	−8.97	−2.86	−5.50	8.54	−1.95
6.0	−6.03	0.31	−0.64	−6.26	−2.38	−4.46	8.92	−1.53
7.0	−4.66	0.28	0.83	−4.70	−2.19	−3.86	9.13	−1.29
8.0	−3.70	0.26	1.89	−3.58	−2.04	−3.40	9.26	−1.15
9.0	−2.94	0.32	2.65	−2.77	−1.87	−2.97	9.39	−1.00
10.0	−2.46	0.30	3.17	−2.23	−1.78	−2.68	9.49	−0.89

Numerical computations of Q_{ext}^{MPA} show that it overestimates the true extinction. Generally, the same is true for Q_{ext}^{HMA}. But, as $4m/(m+1)^2$ is less than 1, Q_{ext}^{HMA} is expected to be a slightly better approximation. Indeed the error in Q_{ext}^{HMA} for a homogeneous sphere is less than 5% for any x as long as $m \leq 1.10$. This may be contrasted with Q_{ext}^{MPA} where the corresponding upper limit is $m = 1.06$.

Contour plot of maximum percent error in Q_{ext}^{EFA} have been given by Evans and Fournier (1990). The real part of refractive index ranges from 1.0 to 2.0 and the imaginary part of the refractive index ranges from 10^{-6} to 10. For $n \leq 1.62$ the relative error in the EFA does not exceed 20%. For the same domain the errors for typical particle size distribution encountered in many atmospheric problems is less than 3%.

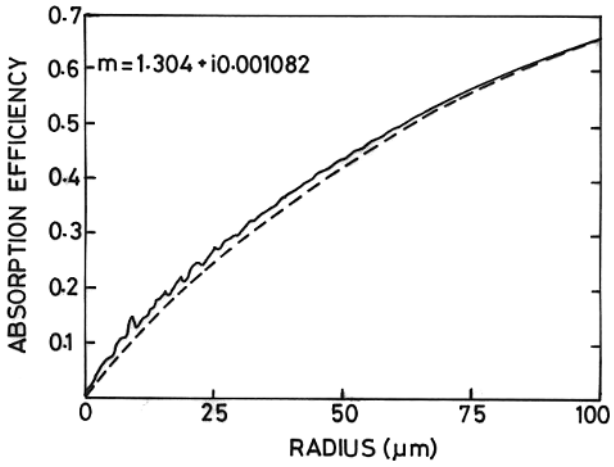

Fig. 3.4. Absorption efficiency factor of a water droplet at $\lambda = 2.0\,\mu\text{m}$, calculated exactly (solid line) and approximately (dashed line). The figure has been reproduced, with permission, from Bohren and Nevitt (1983)

A comparison of absorption efficiency from (3.101) with exact results for a water droplet of $m = 1.304 + i0.001\,082$ has been shown in Fig. 3.4 taken from Bohren and Nevitt (1983). The size range is $a = 0 - 100\,\mu\text{m}$ at $\lambda = 2\,\mu\text{m}$. The BNA can be seen to be adequate over the entire size range. Flatau (1992) has compared Q_{abs}^{BNA}, Q_{abs}^{ADA} and the corrected ADA (τ replaced by τ_{new}). The ADA differs from the BNA in most of the τ region. The corrected ADA, however, gives excellent agreement with the BNA up to $\tau \sim 0.5$.

The error in Q_{abs}^{KZA} given by (3.105) does not exceed 10% for $x \geq 10.0$ for typical aerosol refractive indices $n = 1.2 - 1.55$. Kokhanovsky and Zege (1997) have also compared absorption efficiencies obtained in the KZA, the STA, and the BNA with the exact Mie scattering result. The parameters in these calculations were $n = 1.34$ $x = 20 - 200, n' = 10^{-3}$ for $2n'x < 1$ and $= 10^{-2}$ for $2n'x < 1$. The STA was found to be least in error.

3.5 Nonspherical scatterers

Up to this point we have considered the approximation methods for describing light scattered and absorbed by soft spherical particles to bring out the basic features of implementation of an approximation method and to demonstrate the validity of the approximations in this exactly soluble model. We now briefly consider the approximations employed in the analysis of light scattering by nonspherical soft particles. Some of these approximations require exact solutions for this purpose (e.g., Hart and Montroll approximation, Perelman approximation etc.) and hence are of limited utility. The most useful approximations in this context are the ADA and the EA. General treatment of light scattering

and absorption for non-spherical particles can be found in many books (see, for example, Mishchenko *et al.*, 2000, 2002).

Scattering of electromagnetic waves by an infinitely long cylinder is a two-dimensional scattering problem and exact solutions exist for this problem. Results (angular scattering as well as scattering and absorption efficiency factors) from a number of approximations are examined against the exact results. These include the EA, the ADA, the MPA and the HMA (see, for example, Sharma, 1994; Sharma and Somerford, 1999).

The implementation of the EA and the ADA to scattering by an infinite long cylinder is straightforward. For perpendicular incidence the validity of the EA was examined by Sharma *et al.*, (1981) for the angular scattering function and by Stephens (1984) for the extinction efficiency factor at oblique incidence in the framework of the ADA. For a cylinder of radius a, one obtains:

$$Q_{ext}^{ADA} = \pi Re\big[I_1(\rho') + L_1(\rho')\big], \tag{3.106}$$

$$Q_{abs}^{ADA} = \pi L_1(\tau)/2, \tag{3.107}$$

where I_1 and L_1 are modified Bessel and Struve functions respectively, the phase $\rho' = 2x(m-1)/\sin\Theta$ with Θ as the angle between the cylinder axis and the incident ray direction and as before $x = ka$. Note that for $\Theta = \pi/2$, i.e., for perpendicular incidence, the phase lag suffered by the central ray is $\rho' = 2x(m-1)$. A comparison of the ADA extinction efficiency factors with those obtained from the formal solution of Maxwell's equations shows:

(i) The agreement between the ADA and the exact results is excellent for perpendicular incidence ($\Theta = \pi/2$).
(ii) For oblique incidence the maxima and minima in the extinction curve are not well predicted in the ADA.
(iii) The ADA predicted absorption efficiencies are in good agreement with rigorous results over the entire x domain for weak to moderate absorption. For extinction efficiency factors, Chýlek and Klett (1991a) have shown that except for $\rho < 0.6$, the error in the ADA was within 8% for $n = 1.1$. The error is within 10% for $n = 1.2$. For $\rho < 0.6$, the errors decrease rapidly with increasing absorption. The maximum error decreases from 90% at $m = 1.4 + i0.01$ to approximately 7% at $m = 1.4 + i0.1$.

Fournier and Evans (1996) have suggested that a more appropriate expression for the phase shift could be obtained by taking into account the refraction of a central ray through the cylinder in the way similar to that described in the MGEA. The difference is that instead of assuming that light suffers a deviation $\theta/2$ at each boundary, it is assumed here that the deviation at the first boundary is ϑ. That is $\cos\theta/2$ is replaced by $\cos\vartheta$. Thus, for a homogeneous cylinder one writes

$$\rho' = kL(m - \cos\vartheta), \tag{3.108}$$

where L is the is the distance traveled by the deviated ray through the cylinder. After some straightforward but tedious algebra, it can be shown that ρ' can also

be written as (Fournier and Evans, 1991)

$$\rho' = 2ka\left[(m^2 - \cos^2\Theta)^{1/2} - \sin\Theta\right]. \tag{3.109}$$

The approximation (3.108) has been termed the extended ADA by Fournier and Evans (1991). Note that for $(m^2 - 1) \ll \sin^2\Theta$, ρ' can be approximated as $\rho' = 2ka(m-1)/\sin\Theta$, which is the phase shift for the central ray in the standard ADA. A simple semi-empirical formula for edge contribution which works well for small as well as large particles has been found to be

$$Q_{edge} = \frac{c_0}{(x^{2/3} + x_{crit})\sin^{2/3}\Theta} \tag{3.110}$$

where

$$x_{crit} = \frac{3.6}{4|(m^2 - \cos^2\Theta)^{1/2} - \sin\Theta|} \tag{3.111}$$

The effect of the modification (3.108) is dramatic. Even for highly oblique incidence the ADA prediction for the extinction efficiency factor are found to be in good agreement with exact results.

The basic procedure for obtaining the main form of the Perelman approximation (MPA) is same as that for the scattering by a sphere. The extinction efficiency factor for the scattering of light by an infinitely long cylinder at perpendicular incidence has been found to be (Sharma *et al.* 1997a):

$$Q_{ext}^{MPA} = \frac{\pi(m^2-1)^2 x}{4}\int_0^{2\pi} d\phi \frac{J_1^2(x\omega\cos\phi)}{\omega^2\cos\phi}. \tag{3.112}$$

Numerical calculations show that the maximum error in the extinction efficiency factor for $1 < m \leq 1.05$ and $x = 2.0$ is less than 2.27%.

The errors in scattered intensities have also been examined in the HMA and the HMA1 (Sharma, 1994). These agree with exact results very well for $\theta \leq 60$ deg except at the positions of minima. Table 3.5 shows a typical comparison of the HMA1 with other approximations for $m = 1.05$ for $i(0)$.

Table 3.5. Percent error in various approximations in $1.0 \leq x \leq 25.0$ for $i(0)$ for a homogeneous sphere. Relative refractive index is $m = 1.05$

x	HMA1	EA	ADA	FCEA
1.0	2.10	2.05	6.77	2.05
3.0	0.06	0.10	4.88	0.05
5.0	−0.10	0.11	4.83	0.01
10.0	−0.82	0.22	4.69	−0.17
15.0	−1.74	0.58	4.59	−0.32
20.0	−3.33	1.25	4.59	−0.37
15.0	−5.32	2.12	4.58	−0.46

The model of coated spheres has been often used to study light scattering and absorption from biological and phytoplankton cells. Soft particle approximations have been extensively employed and tested for this model (Morris and Jennings, 1977; Aas, 1984; Chen, 1987; Lopatin and Sid'ko, 1987; Zege and Kokhanovsky, 1989). An interesting result noted by Quirantes and Bernard (2004) is that the ADA compares better to exact results for a coated sphere rather than a homogeneous sphere. Scattering in the ADA or the EA has been studied by Aas (1984) and Huang *et al.*, (1996) for a hollow sphere.

Chen (1995) and Chen and Yang (1996) have studied the scattering of light by a dielectric spheroid and have shown that the scattering function for a dielectric spheroid spheroid, $S_{oid}(a, b, m)$, can be related to the scattering amplitude by a sphere, $S_{ere}(a_{eff}, m_{eff})$, in the following way:

$$S_{oid}(a, \mu_0, m, \theta) = \frac{\alpha_0}{\beta_0^2} S_{ere}(a_{eff}, m_{eff}, \theta). \tag{3.113}$$

In equation (3.113), a and b are semi-major and semi-minor axes of the spheroid, $\mu_0 = a/b$ and n is its refractive index. The radius a_{eff} and refractive index n_{eff} of the equivalent sphere are given by

$$a_{eff} = \frac{\beta_0}{\mu_0} a, \quad \text{and} \quad n_{eff} = 1 + \frac{\mu_0}{\alpha_0 \beta_0}(n-1).$$

If semi-major axis is defined by coordinates (a, θ_0, ϕ_0), α_0 and β_0 are given by the relations

$$\alpha_0 = \sqrt{U^2 + \mu_0^2 V^2}, \quad \beta_0 = \sqrt{\alpha_0^2 R^2 + S^2},$$

where $U^2 + V^2 = R^2 + S^2 = 1$ and $U,\ V,\ R,\ S$ are related to θ_0, ϕ_0 and the scattering angle θ as:

$$R = \frac{\cos(\theta/2)\cos\theta_0 \cos\phi_0 - \sin(\theta/2)\cos\theta_0}{V},$$

$$U = \cos(\theta/2)\cos\theta_0 + \sin(\theta/2)\sin\theta_0 \cos\phi_0.$$

The scattering function for a spheroid can be thus found by calculating S_{ere} employing Mie theory for a sphere of radius a_{eff} and refractive index n_{eff}. Numerical tests for the validity of (3.113) employing T-matrix solutions show that the relationship (3.113) is valid not only within the framework of the ADA but is also valid for the exact scattering function for a spheroid whose size parameter at smallest radius of curvature is at least 4. The approximation is found to work well for scattering angles up to about 30 deg.

A formula similar to that for the extinction efficiency factor for a homogeneous sphere has been obtained for a spheroid (Fournier and Evans, 1991):

$$Q_{ext}^{EFA} = Q_{ext}^{R} \left[1 + \left(\frac{Q_{ext}^{R}}{T Q_{ext}^{ADA}} \right)^{P} \right]^{-1/P}, \tag{3.114}$$

where $P = A + \mu/(kL)$ as before but with

$$\rho' = kL(m - \cos\vartheta)r,$$

which can also be written as

$$\rho' = kb\left\{\frac{2r}{p}\left[\frac{Ap^2 + Bs}{A^2p^2 + B^2q^2 + 2ABs}\right]\right\}(m - \cos\vartheta), \tag{3.115}$$

where

$$A = \frac{s^2 + p^2\Delta}{m(p^4 + s^2)}, \quad B = \frac{s^2(p^2 - \Delta)^2}{m^2(p^4 + s^2)^2},$$

$$\Delta = [m^2(p^4 + s^2) - s^2]^{1/2}, \quad q = [r^2A^2 + B^2]^{1/2}, \quad s = p^2q^2 - r^2,$$

$$p = [A^2 + B^2r^2]^{1/2} \quad \text{and} \quad r = a/b.$$

In the limiting cases of $r \to \infty$ it becomes

$$\rho' = 2kb\big[(m^2 - \cos^2\Theta)^{1/2} - \sin\Theta\big],$$

and for $r \to 0$ for a disk it becomes

$$\rho' = 2ka\big[(m^2 - \sin^2\Theta)^{1/2} - \cos\Theta\big].$$

The angles ϑ and Θ are the deflection angle of the central ray and the spheroid orientation angle respectively. These expressions reproduce accurately the extinction efficiency factor for randomly oriented spheroids, although these need not be good at a particular orientation. Scattering by ellipsoids in the ADA has been studied, among others, by Lind and Greenberg (1966), Latimer (1980), Lopatin and Sid'ko (1988), Paramonov (1994), Paramonov *et al.* (1986), Streekstra *et al.* (1994) and Streekstra (1994).

A general bridging technique has been developed by Zhao and Hu (2003) to calculate the extinction efficiency factors for particles with various shapes and sizes. The proposed expression for extinction efficiency factor is:

$$Q_{ext} = \frac{(Q_{abs}^{small} + Q_{sca}^{small} + c_6(Q_{sca}^{small})^{c_7})Q_{ext}^{large}}{(Q_{sca}^{small} + c_6(Q_{small}^{sca})^{c_7}) + Q_{ext}^{large}} \tag{3.116}$$

where

$$Q_{sca}^{small} = c_3\frac{9kV^2}{16\pi P}, \quad Q_{abs}^{small} = c_1\frac{3kV}{4P} + c_2\frac{3k^3V}{4\pi}\exp\left(-c_4\frac{3k^3V}{4\pi}\right),$$

with

$$c_1 = \mathrm{Im}\left[\frac{4(m^2 - 1)}{m^2 + 2}\right], \quad c_2 = \mathrm{Im}\left[\frac{4}{15}\left(\frac{m^2 - 1}{m^2 + 1}\right)^2\frac{m^4 + 27m^2 + 38}{2m^3 + 3}\right],$$

$$c_3 = \frac{8}{3}\left|\frac{m^2 - 1}{m^2 + 1}\right|^2, \quad c_4 = \left|\frac{\mathrm{Im}(m - 1)}{\mathrm{Re}(m - 1)}\right|, \quad c_5 = c_6 = |m - 1|, \quad c_7 = 2^{c_5}$$

and V is the particle volume. Further,

$$Q_{ext}^{large} = Q_{ADA} \times Z, \tag{3.117}$$

with

$$Z = 1 + \frac{1}{2/Q_{edge} + [|m-1|(Q_{ADA}+1)]}, \tag{3.118}$$

and

$$Q_{edge} = \frac{c_0}{k^{2/3}P} \int_B R^{1/3} ds \tag{3.119}$$

as per the prescription of Jones (1957). In (3.119), c_0 is a function of refractive index in general and is approximately 0.996193 for optically soft particles (Nussenzveig and Wiscombe 1980), R is the radius of curvature of the scattering object profile at the edge which is perpendicular to the incident wave front, ds is the arc length element along the boundary B and P is the projected area of the scattering object. Numerical comparisons for spheres, spheroids, infinite cylinders and finite cylinders with exact results have found the above formula to be valid for a wide range of size parameters in the region $1 < n \leq 2$ and $0 \leq n' \leq 1$. The region of applicability could be as much as $n = 3$ when averaging over size or orientation is performed.

The validity of the ADA for scattering by a cube has been examined by Flatau (1992) and Maslowska *et al.,* (1994). The extinction efficiency factor for side incidence show fairly good agreement with exact results. The error is of the same order as observed for sphere. In contrast, for edge – on incidence the deviation from exact results is much larger.

The model of columnar particles is frequently used for ice particles in clouds. Chylek and Klett (1991a, 1991b) have studied the scattering of light by a column with either triangular, trapezoidal, hexagonal or polygonal base and obtained general expressions for extinction and absorption efficiencies in the framework of the ADA. Sun and Fu (1999) have derived analytic expressions for arbitrarily oriented hexagonal columns. The ADA results for randomly oriented hexagonal ice crystals have been compared with FTDT calculations by Fu *et al.* (1999). The accuracy of the ADA in predicting the extinction efficiency and single scattering albedo for hexagonal column-like ice crystal particles has also been studied be Liu *et al.,* (1998).

For an arbitrarily shaped particle the extinction and absorption efficiency factors in the ADA formulation can be expressed as:

$$Q_{ext}^{ADA} = \frac{2}{P} Re\left\{ \int \int_P [1 - e^{ikl(m-1)}] dP \right\}, \tag{3.120}$$

and

$$Q_{abs}^{ADA} = \frac{1}{P} \int \int_P [1 - e^{-2kln'}] dP \tag{3.121}$$

where P is the projected area of the particle on a plane perpendicular to the incident direction and l is the geometrical length of an individual ray inside the

particle. The integrals in (3.120) and (3.121) can be evaluated analytically for certain shapes such as spheres, spheroids (Bryant and Latimer, 1969; Latimer, 1975) and an infinite cylinder (Cross and Latimer 1970) at an arbitrary orientation. These can also be evaluated analytically at some special orientations for a finite cylinder (Xu 2003), cube (Maslowska *et al.*, 1994) and columns (Chylek and Klett 1991a, 1991b). For more complex geometries a numerical method may be used to evaluate the integrals.

The results from (3.120) and (3.121) are independent of the order in which contributions from the ray path in the integral are accounted. By dividing the projected area into equal-area elements and counting the resultant geometrical paths according to their lengths, a probability function $p(l)dl$ can be found that gives the probability of l between l and $l + dl$. This probabilistic interpretation has led Xu (2003) and Xu *et al.* (2003) to reformulate the conventional ADA extinction efficiency factors (3.120) and (3.121) as:

$$Q_{ext}^{ADA} = 2Re\left\{\int [1 - e^{ikl(m-1)}]p(l)dl\right\}, \tag{3.122}$$

and

$$Q_{abs}^{ADA} = \int [1 - e^{-2kln'}]p(l)dl. \tag{3.123}$$

The normalization is $\int p(l)dl = 1$. The percentage of particle area that corresponds to specific geometric path interval is independent of the particle's physical size if the shape and aspect ratio of the particle remain the same. If we denote by $p_0(l)$ the geometrical path distribution of rays for one particle with unit size, the ray distribution for a particle of same shape and orientation but a different size L is given by $p(l) = (1/L)p_0(l/L)$ from scaling length. This feature of the ADA along with the statistical interpretation of geometrical ray paths makes this approach computationally very efficient for the calculation of efficiency factors for randomly oriented particles and polydispersions of particles. The algorithm for the calculation of efficiency factors has been made computationally more efficient in a recent work by Yang *et al.* (2004).

For a gaussian probability distribution function for l, the integration in the expression for optical efficiencies can be easily performed. This approximation has been termed the gaussian ray approximation (Xu *et al.*, 2003). Numerical comparisons of Mie results for a sphere of $m = 1.05 + i0.0005$ show that the agreement of exact results with (3.120–3.123) in the intermediate size region is excellent. The absorption efficiency factor from gaussian ray approximation differs at most by 2% from the exact Mie calculations.

The ADA assumptions can also be applied to the rigorous relationships in classical electrodynamics. Yang *et al* (2004) have shown that this leads to following expressions for the efficiency factors:

$$Q_{ext}^{ADA} = Re\left\{\frac{m+1}{P}\int\int_P [1 - e^{ikl(m-1)}]dP\right\}, \tag{3.124}$$

and

$$Q_{abs}^{ADA} = \frac{n}{P}\int\int_P [1 - e^{-2kln'}]dP. \tag{3.125}$$

Note that as $m \to 1$ (i.e., $n \to 1$ and $n' \to 0$), the equations (3.124) and (3.125) and the conventional ADA efficiency factors are essentially the same. The asymptotic extinction efficiency factor, however, approaches a value $(m+1)$ when the particle is large and strongly absorptive. This does not agree with the correct value of the extinction efficiency factor which is 2. To ensure that (3.124) and (3.125) lead to their correct asymptotic values, Yang *et al.* (2004) have modified these expressions empirically and obtained the following expressions for efficiency factors:

$$\begin{aligned} Q_{ext}^{ADA} &= Re\Bigg\{\frac{2}{P}\int\int_P [1 - e^{-ikl(m-1)}]dP \\ &\quad + e^{-\epsilon_1 V/\bar{P}}(m-1)\int\int_P [1 - e^{-ikl(m-1)}]dP\Bigg\} \end{aligned} \tag{3.126}$$

and

$$Q_{abs}^{ADA} = \frac{1}{P}\int\int_P [1 - e^{-2kln'}]dP. + \frac{1}{P}e^{-\epsilon_2 V/\bar{P}}\int\int_P [1 - e^{-2kln'}]dP, \tag{3.127}$$

where V and $\bar{P}$ are the particle volume and orientation-averaged projected area respectively. The constants ϵ_1 and ϵ_2 are tuning factors determined from a comparison with corresponding exact solutions. The ϵ_1 and ϵ_2 determined for spherical particles have been used for nonspherical particles too and have been found to work well. The errors in the efficiency factors obtained from these expressions are much less than the errors in their conventional counterparts.

Chen *et al.* (2004) have introduced an approximation for the extinction efficiency of light scattered by a nonspherical dielectric particle. The approximation has been termed as equiphase approximation (EPA) and has been tested for the scattering of light by a spheroid. In this approximation extinction efficiency is expressed as the sum of two terms:

$$Q_{ext}^{EPA} = Q_{ext}(v) + Q(s)$$

where $Q_{ext}(v)$ represents the contribution of an equivalent sphere defined as sphere for which the phase shift suffered by the central ray is equal to the maximum phase shift of light in passing through the nonspherical particle. The term $Q(s)$ represents edge correction.

For an ellipsoid of refractive index n and axes a, b and c, employing ADA, the extinction efficiency factor can be written as (Chen *et al.*, 2004):

$$\begin{aligned} Q_{ext}^{ADA} &= \frac{4}{\pi ab}\left[(\pi ab/2)[1 - 2n\sin\rho_b/\rho_b + 4n\sin^2(\rho_b/2)/\rho_b\right] \\ &\quad + (\pi ab/2)[k(ab^2)^{1/3}/2]^{-2/3}, \end{aligned} \tag{3.128}$$

for TE and TM modes and

$$Q_{ext}^{ADA} = \frac{4}{\pi b^2}\left[(\pi b^2/2)[1-2n\sin\rho_a/\rho_a+4n\sin^2(\rho_a/2)/\rho_a\right] + (\pi ab/2)[k(ab^2)^{1/3}/2]^{-2/3}, \tag{3.129}$$

for TEM mode with $\rho_a = ka(n-1)$ and $\rho_b = kb(n-1)$. The validity of the approximation requires

$$\frac{16b}{\pi^2\lambda}\frac{n^2-1}{n}\left(1-\frac{b}{a}\right)\left(1+\frac{a^2}{b^2}\right)^{-1} < 1 \tag{3.130}$$

for TE and TM modes and

$$\frac{16a}{\pi^2\lambda}\frac{n^2-1}{n}\left(1-\frac{a}{b}\right)\left(1+\frac{b^2}{a^2}\right)^{-1} < 1 \tag{3.131}$$

for TEM mode in addition to the condition $(n-1) < 1$ and $(n-1)kd \gg 1$, d being the characteristic dimension of the scatterer. It is clear from (3.130) and (3.131) that the validity of approximation improves as the spheroid's curvature decreases ($a \to b$) or the relative refractive index approaches unity. It has been found that the periodicity of oscillatory behavior in (3.128) and (3.129) is same as that for extinction efficiency in the ADA for a sphere. This has led Chen *et al.* (2004) to suggest the use of an equiphase sphere. Numerical comparisons show that this approximation gives results that are in good agreement with rigorous numerical computations.

An approximation method for the analysis of light scattered by optically soft scatterers of arbitrary shape and size has been proposed by Rysakov (2004). In this approximation the total field at large distances from the scatterer is expressed as a sum of scattered field and a diffracted field. Calculations of intensities and efficiencies for a sphere, spheroid, parallelepiped and cylinder are given. The calculational error for $m < 1.33$ is shown to be less than 20% which is of similar order as in the ADA.

3.6 Applications

The soft particle approximations have been extensively applied in various branches of science engineering and medicine. Here, however, we very briefly mention some of the applications.

Sharma and Somerford (1983) and Sharma *et al.,* 1984) have applied the EA to particle sizing by a measurement of the ratio of scattered intensities at a pair of convenient angles within the forward lobe. Chen (1994) has deduced relations between the positions of minima in the scattering pattern and the size of a non-absorbing homogeneous dielectric spherical scatterer employing the generalized eikonal approximation. Since the eikonal approximation and its variants are small angle approximations, only the position of the first few minima

will yield accurate results. Sharma *et al.,* (1997b) have obtained similar results employing the EA. Empirical formulas describing the distance between the first and the jth minima $\Delta\theta_j(\phi_d^o)$ that occur after the boundary angle ϕ_d have been obtained by Chernyshev *et al.* (1995) and by Maltsev *et al.* (1996) for certain domains of particle size and refractive indices. For $\Delta\theta_3(20^o)$, in the domain $m = 1.05 - 1.15$, $d = 1 - 12\,\mu\text{m}$, $n_0 = 1.333$ (refractive index of the surrounding medium) and $\lambda_0 = 632.8\,\text{nm}$ is given by

$$d = C_1 + C_2\left[\Delta\theta_3(20^o)\right]^{-2} + C_3\left[\Delta\theta_3(20^o)\right]^{-3} + C_4\left[\Delta\theta_3(20^o)\right]^{-4}, \quad (3.132)$$

where $C_1 = 0.127, C_2 = 52.4, C_3 = 190$ and $C_4 = -660$. As the separation between the adjacent minima is π, the separation between the first and the third minima is

$$z_3 - z_1 = x(\sin\theta_3 - \sin\theta_1) = 2\pi.$$

Taking into account the relation $x = (\pi/\lambda_0)n_0 d$, transforming radians into degrees and approximating $\sin(\theta/2) = \theta/2$, one obtains (Shepelevich *et al.*, 1999)

$$d \cong 54.4/\Delta\theta_3(20^o). \quad (3.133)$$

Equation (3.133) reproduces the principal term of (3.132) with an error less than 4%. The error in approximating $\sin(\theta/2)$ by $\theta/2$ in the angle range 20–40 deg is less than 2%.

The turbidity $\sigma_{ext}(m,k)$ for light scattered by a dilute suspension of polydisperse spherical particles of similar optical properties is given by the relationship

$$\sigma_{ext}(m,k) = \pi N \int Q_{ext}(m,ka)a^2 f(a)da, \quad (3.134)$$

where N is the total number of particles in the suspension and $Q_{ext}(m,ka)$ is the extinction efficiency of a single particle when the light of wavenumber k (in the medium of suspension) is scattered by a particle of radius a and refractive index m (relative to medium). The simplest method is to find an empirical distribution that satisfies (3.134). However, this method does not guarantee the closeness of the $f(a)$ to the actual $f(a)$. An analytic inversion of (3.134) is possible if Q_{ext} appearing as a kernel function is replaced by a suitable approximate form. Shifrin and Perelman (1967) used this idea to invert light scattering data of soft particles using the ADA. Analytic inversion methods based on the ADA have also been derived by (Fymat, 1978; Box and McKeller, 1978) for spheres, by McKellar (1982) for infinitely long cylinders, by Smith (1982) for particles with variable complex refractive index and by Perelman and Punina (1969) and by Klett (1984) for absorbing spheres. An analytic inversion method based on the ADA for non-absorbing spherical particles has been developed by Wang and Hallett (1996). This method eliminates the need for *a priori* knowledge of total number of particles and their total area. Their result has the drawback that it needs the first derivative of the spectral extinction curve. A derivation based on complex analytic extension of the ADA for analytic inversion of spectral extinction data has been presented by Franssens *et al.* (2000). This paper clarifies the

a priori information required to start the inversion and show the equivalence of Fymat, Box and McKellar, Wang and Hallett and smith and Klett results. Roy and Sharma (1997) have developed an approach based on the mean value theorem and the method of Lagrange multipliers. It was shown that the mean value theorem enables one to obtain easily the key parameters associated with the distribution function $f(a)$. Lui *et al.* (1996) have obtained a closed-form approximation for (3.134) based on the ADA by employing the Deirmendjian modified γ function form for the particle size distribution. Borovoi and Krutikov (1976) have calculated, within the framework of the EA, the statistical characteristics of the wave field propagating in the polydispersion of weakly refractive homogeneous spheres and have shown that the measured statistical characteristics can be used to determine the average characteristics of individual particles.

In the context of ocean optics, the ADA has been extensively applied to scatterers in the oceans and it has been found that it can adequately describe the observed attenuation, absorption and total scattering of algal cells (Bricaud and Morel, 1986). However, the homogeneous sphere model is often inadequate to reproduce angular scattering data (Quinby-Hunt *et al.,* 1989; Volten *et al.,* 1998; Vaillancourt *et al.,* 2004). Coated sphere models have also been adopted for some species with chloroplast as core (Quinby-Hunt *et al.*, 1989). Two shapes have been examined by Quirantes and Bernard (2004). (i) a coated spheroid with concentric core and (ii) a coated sphere with non-concentric core. Results have been compared with those obtained from a concentric sphere model. It is noted that scattering and extinction efficiencies are very similar in all the three models. The Q_{abs} is also found to be nearly shape independent. Similar results have been obtained for heterogeneous spherical scatterers by Aas (1984), Zaneveld and Kitchen (1995), Bricaud *et al.* (1992) and Kitchen and Zaneveld (1992).

Most biological scatterers are amenable to soft particle approximations. A number of workers have used RGDA (for example, Koch, 1968; Fiel, 1970; Wyatt, 1973; Shvalov *et al.*, 1999) primarily for smaller cells such as bacteria. For large particles, Fraunhofer diffraction has also been employed (Fiel, 1970). Analytic formulas relating features of scattering pattern to geometrical and physical parameters of biological particles have also been obtained in the framework of the EA and the ADA (Streekstra, 1994; Hammer *et al.*, 1998; Borovoi *et al.*, 1998). In general, biological structures are complex and it is difficult to study individual scatterers. One exception is the red blood cell (RBC), which can be easily isolated and studied experimentally. Experimental measurements have been compared with predictions of Mie theory, the ADA, the RGDA and some empirical phase functions (Hammer *et al.*, 1998). The experimental measurements were in satisfactory agreement with the predictions of Mie theory over the entire measured angular range 0–15 degrees. Better agreement was found with the ADA. Borovoi *et al.* (1998) have developed a computer code that allows one to calculate optical parameters of a RBC such as absorption and scattering efficiencies and the small angle phase function in the framework of the ADA. The difference with Mie theory calculations does not exceed 4%. More recently,

the ADA has been used in early detection of cancer employing light scattering spectroscopy to epithelial tissues (Perelman and Backman, 2002).

Among other applications the ADA has been extensively used in problems related to atmospheric optics. Much of the work mentioned in the subsection on nonspherical particles relates to atmospheric optics applications. The EA has been applied by Sharma (1986) and Sharma and Dasgupta (1987) for plasma density profiling. The effect of surface roughness in the context of astrophysical particles has been studied in the framework of the EA by Chiapetta (1980) and Bourrely *et al.* (1986a, 1986b, 1989). The scattering pattern reveals backward enhancement. This is in qualitative agreement with experimental measurements. This feature of scattering patterns is well suited to exhibiting differences between smooth and rough particles. The EA has also been employed in the context of optical fibres and diffraction by a volume hologram by Calvo and Juncos del Egido, (1979, 1982). The ADA has also been applied to nonlinear medium by Orenstein *et al.* (1984, 1987), to optics of fractal clusters by Khlebtsov (1993) and to colloidal solutions of platelike kaolinite particles by Champion *et al.* (1979). Anomalous diffraction approximation has also been applied to computing scattering patterns of sharp-edged crystals in solution (Heffels *et al.*, 1995) Linear dichroism and complex birefringence has been studied by Meeten (1981a, 1981b) in the framework of the ADA. Kokhanovsky (2004) studied optical rotational dispersion spectra and also circular dichroism spectra of chiral liquids in the framework of the ADA.

References

Aas, E., 1984: *Some aspects of light scattering by marine particles.* Institute of Geophysics, Oslo.

Ackerman, S. A., and Stephens, G. L., 1987: The absorption of solar radiation by clouds droplets: an application of anomalous diffraction theory, *J. Atmos. Sci.*, **44**, 1574–1588.

Bayvel, L. P., and Jones, A, R., 1981: *Electromagnetic scattering and its applications.* Applied Science, London.

Bohren, C. F., and Huffman, D. R., 1983: *Absorption and Scattering of Light by Small Particles.* John Wiley, New York.

Bohren, C. F., and Nevitt, T. J., 1983: Absorption by a sphere, a simple approximation. *Appl. Opt.* **22**, 774–775.

Borovoi, A. G., and Krutikov, V. A., 1976: Statistics of a wave field when propagating in a system of large optically soft scatterers, *Opt. Spectrosc. (USSR)* **40**, 416–419.

Borovoi, A. G., Natts. E. I., and Oppel, U. G., 1998: Scattering of light by a red blood cell. *Journal of Biomedical Optics* **3**, 364–372.

Bourrely, C., Chiappetta, P., and Torrésani, B., 1986a: Light scattering by particles of arbitrary shape: a fractal approach. *J. Opt. Soc. Am. A* **3**, 250–255.

Bourrely, C., Torrésani, B., and Chiappetta, P., 1986b: Scattering of an electromagnetic wave by an irregularly shaped object. *Opt. Commun.* **58**, 365–368.

Bourrely, C., Chiappetta, P., and Lemaire, T., 1989: Electromagnetic scattering by large rotating particles in the eikonal formalism. *Opt. commun.* **70**, 173–176.

Bourrely, C., Lemaire, T., and Chiappetta, P., 1991: A vectorial description of the electromagnetic scattering by large bodies of spherical shape. *J. Mod. Opt.* **38**, 305–315.

Bourrely, C., Chiappetta, P., and Lemaire, T., 1996: Improved version of the eikonal model for absorbing spherical particles, *J. Mod. Opt.* **43**, 409–415.

Box, M. A., and McKellar, B. H. J., 1978: Analytic inversion of multispectral extinction data in the anomalous diffraction approximation. *Opt. Lett.* **3**, 91–93.

Bricaud, A., and Morel, A., 1986: Light attenuation and scattering by phytoplanktonic cells: a theoretical modeling. *Appl. Opt.* **25**, 571–580.

Bricaud, A., Zaneveld, J. R. V., and Kitchen, J. C., 1992: Backscattering efficiency of coccolithophorids: use of three layered sphere model. In Gilbert GD (eds) *Ocean Optics XI.* Proc. SPIE 1750, 27–33.

Bryant, F. D., and Latimer, P., 1969: Optical efficiencies of large particles of arbitrary shape and orientation. *J. Colloid and Interface Sci.* **30**, 291–304.

Burberg, R., 1956: Die Beugung electromagnetischer Wellen am unendlichangen Kreiszylinder. *Z. Naturf.* **A11**, 807.

Byron, F. W., and Joachain, C. J., 1977: Eikonal theory of electron – and positron – atom collisions. *Phys. Rep.* **34**, 233–324.

Calvo, M. L., and Juncos del Egido, P., 1979: Eikonal approximation for electromagnetic wave scattering by a cladded optical fiber, *SPIE Proc.* **213**, 35–37.

Calvo, M. L., and Juncos del Egido, P., 1982: Corrections to Raman-Nath diffraction by volume holograms. *Opt. Acta* **29**, 1061–1072.

Champion, J. V., Meeten, G. H., and Senior, M., 1979: Refraction by spherical colloidal particles. *J. Coll. Interf. Sci.* **72**, 471–482.

Chen, T. W., 1984: Generalized eikonal approximation. *Phys. Rev. C* **30**, 585–592.

Chen, T. W., 1987: Scattering of light by a stratified sphere. *Appl. Opt.* **26**, 4155–4158.

Chen, T. W., 1988: Eikonal approximation method for small-angle light scattering. *J. Mod. Opt.* **35**, 743–752.

Chen, T. W., 1989: High energy light scattering in the generalized eikonal approximation. *Appl. Opt.* **28**, 4096–4102.

Chen, T. W., 1993: Simple formula for light scattering by a large spherical dielectric. *Appl. Opt.* **32**, 7568–7571.

Chen, T. W., 1994: Diffraction by a spherical dielectric at large size parameter. *Opt. Commun.* **107**, 189–192.

Chen, T. W., 1995: Effective sphere for spheroid in light scattering. *Opt. Commun.* **114**, 199–202.

Chen, T. W., and Smith, W. S., 1992: Large-angle light scattering at large size parameters. *Appl. Opt.* **31**, 6558–6560.

Chen, T. W., and Yang, L. M., 1996: Simple formula for small-angle light scattering by a spheroid. *Opt. Commun.* **123**, 437–442.

Chen, Z., Taflove, A., and Backman, V., 2004: Concept of the equiphase sphere for light scattering by non-spherical dielectric particles. *J. Opt. Soc. Am.* **21**, 88–97.

Chernyshev, A. V., Maltsev, V. P., Prots, V. I., and Doroshkin, A. A., 1995: Measurement of scattering properties of individual particles with a scanning flow automate. *Appl. Opt.* **34**, 6301–6305.

Chiappetta, P., 1980: A new model for scattering by irregular absorbing particles. *Astron. Astrophys.* **83**, 348–353.

Chýlek, P., and Klett, J. D., 1991a: Extinction cross-section of nonspherical particles in the anomalous diffraction approximation. *J. Opt. Soc. Am. A* **8**, 274–281.

Chýlek, P., and Klett, J. D., 1991b: Absorption and scattering of electromagnetic radiation by prismatic columns: anomalous diffraction approximation. *J. Opt. Soc. Am. A* **8**, 1713–1720.

Cross, D. A., and Latimer, P., 1970: General solutions for the extinction and absorption efficiencies of arbitrarily oriented cylinder by anomalous-diffraction methods. *J. Opt. Soc. Am.* **60**, 904–907.

Evans, B. T. N., and Fournier, G. R., 1990: Simple approximation to extinction efficiency valid over all size parameters. *Appl. Opt.* **29**, 4666–4670.

Farafonov, V. G., Il'in, V. B., and Prokopjeva, M. S., 2001: Scattering of light by homogeneous and multilayered ellipsoids in quasistatic approximation. *Opt. Spectrosc.* **92**, 608–617.

Farone, W. A., and Robinson, M. J. I., 1968: The range of validity of the anomalous diffraction approximation to electromagnetic scattering by a sphere. *Appl. Opt.* **7**, 643–645.

Fiel, R. J., 1970: Small angle light scattering of bioparticles I. Model systems. *Exp. Cell Res.* **59**, 413.

Flatau, P. J., 1992: Scattering by irregular particles. Colorado State University, Department of Atmospheric Science, paper no. 517 (PhD thesis).

Fournier, G. R., and Evans, B. T. N., 1991: Approximation of extinction efficiency for randomly oriented spheroids. *Appl. Opt.* **30**, 2042–2048.

Fournier, G. R., and Evans, B. T. N., 1996: Approximations to extinction from randomly oriented circular and elliptic cylinders. *Appl. Opt.* **35**, 4271–4282.

Franssens, F., De Maziere, M., and Fonteyn, D., 2000: Determination of aerosol size distribution by analytic inversion of the extinction spectrum in the complex anomalous diffraction approximation. *Appl. Opt.* **39**, 4214–4231.

Fu, Q., Sun, W. B., and Yang, P., 1999: Modeling of scattering and absorption by nonspherical cirrus ice particles at thermal infrared wavelengths. *J. Atmos. Sci.* **56**, 2937–2947.

Fymat, A. L., 1978: Analytical inversions in remote sensing of particle size distributions. 1: Multispectral extinctions in the anomalous diffraction approximation. *Appl. Opt.* **17**, 1675–1676.

Gerjuoy, E., and Thomas, B. K., 1974: Applications of Glauber approximation to atomic collisions. *Rep. Prog. Phys.* **37**, 1345–1431.

Gien, T. T., 1988: The modified Glauber approximation. *Phys. Reports* **160**, 123–187.

Glauber, R. J., 1959: High energy collision theory, in *Theoretical Physics, Vol. I*, Brittin W. E. and Dunham L. G. (eds). Interscience, New York, pp. 315–414.

Gordon, J. E., 1985: Simple method for approximating Mie scattering. *J. Opt. Soc. Am. A* **2**, 156–159.

Granovskii, Ya. I., and Stón, M., 1994a: Light scattering cross-sections – summing of Mie-series. *Physica Scripta* **50**, 140–141.

Granovskii, Ya. I., and Stón, M., 1994b: Attenuation of light scattered by transparent particles. *JETP (USA)* **78**, 645–649.

Hammer, M., Schweitzer, D., Michel, B., Thamm, E., and Kolb, A., 1998: Single scattering by red blood cells. *Appl. Opt.* **37**, 7410–7418.

Hart, R. W., and Montroll, E. W., 1951: On the scattering of plane waves by soft particles: I. Spherical obstacles. *J. Appl. Phys.* **22**, 376–386.

Heffels, C., Heitzmann, D., Hirleman, E. D., and Scarlett, B., 1995: Efficient calculation of scatter patterns of sharp edged crystals in the Fraunhofer and anomalous diffraction approximation. Proc. 4th Int. Congress in Optical Particle Sizing, pp. 439–448.

Huang, Z., Chidichimo, G., Nicoletta, F. P., De Simone, B. C., and Caruso, C., 1996: A model of an aligned nematic droplet for small angle light scattering. *J. Appl. Phys.* **80**, 6155–6159.

Jobst, G., 1925: *Ann. Phys. Lpz.* **78**, 157.

Jones, A. R., Koh, J., and Nassaruddin, A., 1996: Error contour charts for the two-wave WKB approximation. *J. Phys. D(GB)* **29**, 39–42.

Jones, D. S., 1957: High-frequency scattering of electromagnetic waves, *Proc. R. Soc. London Ser. A* **240**, 206–213.

Kerker, M., 1969: *The Scattering of Light and Other Electromagnetic Radiation.* Academic Press, New York.

Khlebtsov, N. G., 1993: Optics of fractal clusters in the anomalous diffraction approximation. *J. Mod. Opt.* **40**, 2221–2235.

Kitchen, J. C., and Zaneveld, J. R. V., 1992: A three-layer sphere model of the optical properties of phytoplankton. *Limnol. Oceanogr.* **37**, 1680–1690.

Klett, J. D., 1984: Anomalous diffraction model for inversion of multispectral extinction data including absorption effects. *Appl. Opt.* **23**, 4499–4508.

Klett, J. D., and Sutherland, R. A., 1992: Approximate methods for modelling the scattering properties of nonspherical particles: evaluation of the Wentzel–Kramers–Brillouin method. *Appl. Opt.* **31**, 373–386.

Koch, A. L., 1968: Theory of the angular dependence of light scattered by bacteria and similar sized biological objects. *J. Theor. Biol.* **18**, 133.

Kokhanovsky, A. A., 1995: About edge effects in light absorption by weak absorbing particles. *Opt. Spectrosc.* **78**, 967–969.

Kokhanovsky, A. A., 1999: *Optics of light scattering media: Problems and solutions.* John Wiley, Chichister.

Kokhanovsky, A. A., 2004: *Polarization optics of random media.* John Wiley, Chichester.

Kokhanovsky, A. A., and Zege, E. P., 1997: Optical properties of aerosol particles: a review of approximate analytic solutions. *J. Aerosol Sci.* **28**, 1–21.

Latimer, P., 1975: Light scattering by ellipsoids. *J. Colloid Interface Sci.* **53**, 102–109.

Latimer, P., 1980: Predicted scattering by spheroids. Comparison of approximate and exact methods. *Appl. Opt.* **19**, 3039–3041.

Lind, A. C., and Greenberg, J. M., 1966: Electromagnetic scattering by obliquely oriented spheroids. *J. Appl. Phys.* **37**, 3195–3203.

Liu, Y., Arnott, W. P., and Hallet, J., 1998: Anomalous diffraction theory for arbitrarily oriented finite circular cylinders and comparison with exact T-matrix results. *Appl. Opt.* **37**, 5019–5029.

Lopatin, V. N., and Sid'ko, Ya. F., 1987: Absorption of electromagnetic radiation by 'soft' structured particles, *Izvestia, Atmospheric and Oceanic Physics* **23**, 396-401.

Lopatin, V. N., and Sid'ko, Ya. F., 1988: *Introduction to Optics of Cell Suspension.* Nauka, Moscow.

Lui, C. W., Clarkson, M., and Nicholls, R. W., 1996: An approximation for spectral extinction of atmospheric aerosols. *J. Quant. Spectrosc. Radiat. Transf.* **55**, 519–531.

Maltsev, V. P., Chernyshev, A. V., Sem'yanov, K. A., and Soini, E., 1996: Absolute real-time measurement of particle size distribution with the flying light-scattering indicatrix method. *Appl. Opt.* **35**, 3275–3280.

Maslowska, A., Flatau, P. J., Stephens, G. L., 1994: On the validity of anomalous diffraction theory to light scattering by cubes. *Optics Commun.* **107**, 35–40.

McKeller, B. H. J., 1982: Light scattering determination of size distribution of cylinders: an analytic approximation. *J. Opt. Soc. Am.* **72**, 671–672.

Meeten, G. H., 1980a: The intrinsic optical anisotropy of colloidal particles in the anomalous diffraction approximation. *J. Coll. Interf. Sci.* **74**, 181–185.

Meeten, G. H., 1980b: Refractive index of colloidal dispersions of spheroidal particles. *J. Coll. Interf. Sci.* **77**, 1–5.

Mishchenko, M. I., Wiscombe, W. J., Hovenier, J. W., and Travis, L. D., 2000: Overview of scattering by nonspherical particles, in Mishchenko, M. I., Hovenier. J. W., and Travis, L. D. (eds), *Light scattering by nonspherical particles.* Academic Press, San Diego, CA, pp. 29–60.

Mishchenko, M. I., Travis, L. D., and Lacis, A. A., 2002: *Scattering, Absorption, and Emission of Light by Small Particles.* Cambridge University Press, Cambridge, UK.

Montroll, E. W., and Hart, R. W., 1951: On the scattering of plane waves by soft particles: II. Scattering by cylinders, spheroids and disks. *J. Appl. Phys.* **22**, 1278–1289.

Morris, V. J., and Jennings, B. R., 1977: Anomalous diffraction approximation to the low-angle light scattering from coated spheres. *Biophys. J.* **17**, 95–101.

Newton, R. G., 1966: *Scattering Theory of Waves and Particles.* McGraw-Hill, New York.

Nussenzveig, H. M., and Wiscombe, W. J., 1980: Efficiency factors in Mie scattering. *Phys. Rev Lett.* **45**, 1490–1494.

Orenstein, M., Speiser, S., and Katriel, J., 1984: An eikonal approximation for non linear resonators exhibiting bistability. *Opt. Commun.* **48**, 367–373.

Orenstein, M., Katriel, J., and Speiser, S., 1987: Optical bistability in molecular systems exhibiting nonlinear absorption. *Phys. Rev. A* **35**, 2175–2183.

Paramonov, L. E., Lopatin, V. N., Sid'ko Ya. F., 1986: Light scattering by soft spheroidal particles. *Opt. Spectrosc.* **61**, 570–576.

Paramonov, L. E., 1994: On optical equivalence of randomly oriented ellipsoidal and polydisperse spherical particles. The extinction, scattering and absorption cross-sections. *Opt. Spectrosc.* **77**, 660–663.

Penndorf, R., 1961: Scattering and extinction coefficients for small spherical aerosols. *J. Atmos. Sci.* **19**, 193.

Perelman, A. Y., 1978: An application of Mie series to soft particles. *Pure and Appl. Geophysics* **116**, 1077–1088.

Perelman, A. Y., 1985: The scattering of light by a translucent sphere described in soft-particle approximation, *Dikl. Akad. Nauk S.S.S.R.* **281**, 51–54.

Perelman, A. Y., 1991: Extinction and scattering by soft particles. *Appl. Opt.* **30**, 475–484.

Perelman, A. Y., and Voshchinnikov, N. V., 2002: Improved S-approximation for dielectric particles. *J. Quant. Spectrosc. Rad. Transf.* **72**, 607–621.

Perelman, A. Y., and Punina, V. A., 1969: Uber die Berechnung der Grossenverteilung von der Absorbierenden Kugelformigen Teilchen. *Pure Appl. Geophys.* **74**, 92–104.

Perelman, L. T., and Backman, V., 2002: Light scattering spectroscopy of epithelial tissues: principles and applications in *Handbook of Optical Biomedical Diagnosis* V. V. Tuchin (ed.). SPIE, Washington, DC, pp. 675–724.

Perrin, J. M., and Chiappetta, P., 1985: Light scattering by large particles I. A new theoretical description of the eikonal picture. *Opt. Acta* **32**, 907–921.

Perrin, J. M., and Lamy, P., 1986: Light scattering by large particles II. A vectorial description in the eikonal picture. *Opt. Acta* **33**, 1001–1022.

Posselt, B., Farfanov, V. G., Il'in, V. B., and Prokopjeva, M. S., 2002: Light scattering by multi-layered ellipsoidal particles in the quasistatic approximation. *Meas. Sci. Technol.* **13**, 256–262.

Quinby-Hunt, M. S., Hunt, A. J., Lofftus, K., and Shapiro, D., 1989: Polarized-light scattering studies of marine *Chlorella*. *Limnol. Oceanogr.* **34**, 1587–1600.

Quirantes, A., and Bernard, S., 2004: Light scattering by marine algae: two-layer spherical and nonspherical models. *J. Quant. Spectrosc. Rad. Transf.* **89**, 311–321.

Roy, A., and Sharma, S. K., 1996: On the validity of soft particle approximations for the light scattering by a homogeneous dielectric sphere. *J. Mod. Opt.* **43**, 2225–2237.

Roy, A., and Sharma, S. K., 1997: A new approach to inverse scattering problem. *Appl. Opt.* **36**, 9487–9495.

Rysakov, V. M., 2004: Light scattering by 'soft' particles of arbitrary shape. *J. Quant. Spectrosc. Rad. Transf.* **87**, 261–287.

Saxon, D. S., and Schiff, L. I., 1957: Theory of high energy potential scattering. *Nuovo Cim.* **6**, 614–627.

Sharma, S. K., 1986: Density profile determination of cylindrically symmetric nonuniform plasma by spatial filtering. *Plasma Phys. Contr. Fusion* **28**, 391–392.

Sharma, S. K., 1992: On the validity of the anomalous diffraction approximation. *J. Mod. Opt.* **39**, 2355–2361.

Sharma, S. K., 1993: A modified anomalous diffraction approximation for intermediate size soft particles. *Opt. Commun.* **100**, 13–18.

Sharma, S. K., 1994: On the validity of soft particle approximations for the scattering of light by infinitely long homogeneous cylinders. *J. Mod. Opt.* **41**, 827–838.

Sharma, S. K., and Dasgupta, B., 1987: Scattering of electromagnetic waves by a nonuniform cylindrical plasma in the eikonal approximation. *Plasma Phys. Contr. Fusion* **29**, 303–311.

Sharma, S. K., and Somerford, D. J., 1983: The eikonal approximation applied to sizing transparent fibres using the forward scattered intensity ratio technique. *J. Phys.(GB)* **D16**, 733–742.

Sharma, S. K., and Somerford, D. J., 1994: An approximation method for backward scattering of light by a soft spherical obstacle. *J. Mod. Opt.* **41**, 1433–1444.

Sharma, S. K., and Somerford, D. J., 1996: On the relationship between the S-approximation and Hart–Montroll approximation. *J. Opt. Soc. Am.* **13A**, 1285–1286.

Sharma, S. K., and Somerford, D. J., 1999: Scattering of light in the eikonal approximation, *Progress in Optics* **39**, 211–290.

Sharma, S. K., Powers, S. R., and Somerford, D. J., 1981: Investigation of domains of validity of approximation methods in light scattering from long cylinders. *Opt. Acta* **28**, 1439–1446.

Sharma, S. K., Somerford, D. J., and Sharma, S., 1982: Investigation of validity domains of corrections to eikonal approximation in forward light scattering from homogeneous spheres. *Opt. Acta* **29**, 1677–1682.

Sharma, S. K., Sharma, S., and Somerford, D. J., 1984: The eikonal approximation applied to sizing transparent homogeneous spheres. *J. Phys. (GB)* **D17**, 2191–2197.

Sharma, S. K., Roy, T. K., and Somerford, D. J., 1988: The eikonal approximation Vs. the high energy approximation in optical scatteringr. *J. Phys. (GB)* **D21**, 1685–1691.

Sharma, S. K., Ghosh, G., and Somerford, D. J., 1997a: The S-approximation for light scattering by an infinitely long cylinder. *Appl. Opt.* **36**, 6109–6114.

Sharma, S. K., Somerford, D. J., and Roy, A. K., 1997b: Simple formulae within the framework of anomalous diffraction approximation for light scattered by an infinitely long cylinder. *Pure and Appl. Opt.* **6A**, 565–575.

Shatilov, A. V., 1960: On the scattering of light by dielectric ellipsoids comparable to the light wavelength. *I. Opt. Spectrosc.* **9**, 86–91.

Shepelevich, N. V., Prostakova, I. V., and Lopatin, V. N., 1999: Extrema in the light scattering indicatrix of a homogeneous spheroid. *J. Quant. Spectrosc. Rad. Transf.* **63**, 353–367.

Shifrin, K. S., and Perelman., A. Y., 1967: Inversion of light scattering data for the determination of spherical particle spectrum, In *Electromagnetic Scattering II*, Powell, R. L. and Stein, R. S. (eds). Gordon & Breach, NY, pp. 131–167.

Shifrin, K. S., and Ston, M., 1976: About using the RGD approximation to calculate light extinction in the ocean and atmosphere optics problems. *Izv. AN SSSR, Fiz. Atm. Okeana* **28**, 107–109.

Shifrin, K. S., and Tonna, G., 1992: Simple formula for absorption coefficient of weakly refracting particles. *Opt. Spectrosc.* **72**, 487–490.

Shimizu, K., 1983: Modification of the Rayleigh–Debye scattering. *J. Opt. Soc. Am.* **73**, 504–507.

Shvalov, A. A., Soini, J. T., Chernyshev, A. V., Tarasov, P. A., Soini, E., and Maltsev, V. P., 1999: Light-scattering properties of individual erythrocytes. *Appl. Opt.* **38**, 230–235.

Smith, C. B., 1982: Inversion of the anomalous diffraction approximation for variable complex refractive index. *Appl. Opt.* **21**, 3363–3366.

Stephens, G. L., 1984: Scattering of plane waves by soft obstacles: Anomalous diffraction theory for circular cylinders. *Appl. Opt.* **23**, 954–959.

Streekstra, G. J., 1994: The deformation of red blood cells in a couette flow. PhD thesis, University of Utrichet.

Streekstra, G. J., Hoekstra, A. G., and Heethaar, R. M., 1994: Anomalous diffraction by arbitrarily oriented ellipsoids: applications in ektacytometry. *Appl. Opt.* **33**, 7288–7296.

Sun, W., and Fu, Q., 1999: Anomalous diffraction theory for arbitrarily oriented hexagonal crystals. *J. Quant. Spectrosc. Rad. Transf.* **63**, 727–737.

Vaillancourt, R. D., Brown, C. W., Guillard, R. R. L., and Blach, W. M., 2004: Light backscattering properties of marine phytoplankton: relationships to cell size, chemical composition and taxonomy. *J. Plankton Res.* **26**, 191–212.

van de Hulst, H. C., 1957: *Light Scattering by Small Particles.* John Wiley, New York.

Volten, H., de Haan, J. F., Hoovenier, J. W., Schreurs Vassen, R. W., Dekker, A. G., Hoogenboom, H. J., Charlton, F., and Warts, R., 1998: Laboratory measurements of angular distributions of light scattered by phytoplankton and silt. *Limnol. Oceanogr.* **43**, 1180–1197.

Voshchinnikov, N. V., and Farafonov, V. G., 2000: Applicability of quasistatic and Rayleigh approximations for spheroidal particles, *Opt. Spectrosc.* **88**, 71–75.

Wallace, S. J., 1971: Eikonal expansion. *Phys. Rev. Lett.* **27**, 622–625.

Walstra, P., 1964: Approximation formulae for light scattering coefficient of dielectric spheres. *Brit. J. Appl. Phys.* **15**, 1545–1551.

Wang, J., and Hallet, F. R., 1996: Spherical particle size determination by analytical inversion of the UV-visible-NIR extinction spectrum. *Appl. Opt.* **35**, 193–197.

Wyatt, P. J., 1973: Differential light scattering technique for microbiology. In *Methods in microbiology.* J. R. Norris and W. B. Ribbons (eds). Academic Press, New York, pp. 183–263.

Xu, M., Lax, M., and Alfano, R. R., 2003: Light anomalous diffraction using geometrical path statistics of rays and Gaussian ray approximation. *Opt. Lett.* **28**, 179–181.

Xu, M., 2003: Light extinction and absorption by arbitrarily oriented finite circular cylinders by use of geometrical path statistics of rays. *Appl. Opt.* **42**, 6710–6723.

Yang, P., Zhang, Z., Baum, B. A., Huang, H-L., and Hu, Y., 2004: A new look at anomalous diffraction theory (ADT): Algorithm in cumulative projected-area distribution *J. Quant. Spectrosc. Radiat. Transf.* **89**, 421–442.

Zaneveld, J. R. V., and Kitchen, J. C., 1995: The variation in inherent optical properties of phytoplankton near an absorption peak as determined by various models of cell structure. *J. Geophys. Res.* **100**, 309–320.

Zege, E. P., and Kokhanovsky, A. A., 1989: Approximation of the anomalous diffraction coated spheres. *Izvestia, Atmospheric and Oceanic Physics* **25**, 1195–1201.

Zhao, J. Q., and Hu, Y. Q., 2003: Bridging technique for calculating the extinction efficiency of arbitrarily shaped particles. *Appl. Opt.* **42**, 4937–4945.

4 Single light scattering: computational methods

Victor G. Farafonov and Vladimir B. Il'in

4.1 Introduction

The problem of light scattering by a nonspherical particle is solved today numerically in many different ways. The computational methods based on single[1] expansions of the electromagnetic fields in terms of certain wave functions form an important group. This group includes the so-called separation of variables method (SVM), the extended boundary condition method (EBCM), and the point matching method (PMM). The methods are characterized by relatively high accuracy and speed, but they can be efficiently applied only to scatterers of rather simplified shapes and structures.

Earlier these methods were mostly studied separately. However, they have much in common so we consider them together in a single context by applying an approach that uses specific scalar potentials to solve the light scattering problem. This provides better understanding of interrelations and differences between the methods and brings to light the main features and properties of the approach itself.

The chapter consists of five sections. Section 4.2 contains a formulation of the light scattering problem, the main ideas of the methods under consideration, some bibliography, and a description of the approach.

The difference between the three methods seems to be in many aspects less important than that caused by the use of different wave functions employed for the field/potential expansions. Therefore, in sections 4.3–4.5 we outline the methods when the spherical, spheroidal or ellipsoidal wave functions are used. In each case the applicability ranges of the methods are discussed.

We hope that our chapter will give a reader an up-to-date outlook on this very important group of the methods widely applied today to study light scattering by nonspherical particles.

[1] 'Single expansions' herein means expansions of the fields at one point.

4.2 Light scattering problem

The behavior of the electromagnetic field in any medium is governed by the macroscopic Maxwell equations.

4.2.1 Maxwell equations

We write these equations in Gaussian units (Jackson, 1975)

$$\begin{aligned} \boldsymbol{\nabla} \times \boldsymbol{E} &= -\tfrac{1}{c}\tfrac{\partial \boldsymbol{B}}{\partial t}, & \boldsymbol{\nabla} \cdot \boldsymbol{D} &= 4\pi\rho, \\ \boldsymbol{\nabla} \times \boldsymbol{H} &= \tfrac{4\pi}{c}\boldsymbol{j} + \tfrac{1}{c}\tfrac{\partial \boldsymbol{D}}{\partial t}, & \boldsymbol{\nabla} \cdot \boldsymbol{B} &= 0, \end{aligned} \tag{4.1}$$

where $\boldsymbol{E}$ and $\boldsymbol{D}$ are the electric field and displacement, $\boldsymbol{H}$ and $\boldsymbol{B}$ the magnetic field and induction, ρ and $\boldsymbol{j}$ the free charge and current densities, c is the speed of light.

The Maxwell equations are supplemented by the constitutive equations that describe the properties of the medium where the electromagnetic field is considered. We assume that the following equations are satisfied for the media which we are going to deal with

$$\boldsymbol{D} = \tilde{\varepsilon}\boldsymbol{E}, \quad \boldsymbol{B} = \mu\boldsymbol{H}, \quad \boldsymbol{E} = \sigma\boldsymbol{j}, \tag{4.2}$$

where $\tilde{\varepsilon}$ and μ are the dielectric permittivity and the magnetic permeability of a medium, σ is its specific conductivity.

Due to linearity of eqs (4.1), (4.2) no generality is lost if we consider further only the harmonic fields, i.e. the fields with the time dependence given by $e^{-i\omega t}$ (Bohren and Huffman, 1983). We also assume that there are no free charges ($\rho = 0$).

4.2.2 Hertz vectors and scalar potentials

For a homogeneous medium, the solution to the Maxwell equations (4.1) and the constitutive equations (4.2) can be expressed through the electric and magnetic Hertz vectors $\boldsymbol{\Pi}_{\mathrm{e}}$ and $\boldsymbol{\Pi}_{\mathrm{m}}$ (Stratton, 1941)

$$\begin{aligned} \boldsymbol{E} &= \boldsymbol{\nabla} \times \boldsymbol{\nabla} \times \boldsymbol{\Pi}_{\mathrm{e}} + ik_0\mu\boldsymbol{\nabla} \times \boldsymbol{\Pi}_{\mathrm{m}}, \\ \boldsymbol{H} &= \boldsymbol{\nabla} \times \boldsymbol{\nabla} \times \boldsymbol{\Pi}_{\mathrm{m}} + ik_0\varepsilon\boldsymbol{\nabla} \times \boldsymbol{\Pi}_{\mathrm{e}}, \end{aligned} \tag{4.3}$$

where $k_0 = \frac{\omega}{c}$ is the wavenumber in vacuum, $\varepsilon = \tilde{\varepsilon} + i\frac{4\pi\sigma}{\omega}$. The Hertz vectors as well as the harmonic fields $\boldsymbol{E}, \boldsymbol{H}$ satisfy the vector Helmholtz (wave) equation

$$\Delta\boldsymbol{E} + k^2\boldsymbol{E} = 0, \tag{4.4}$$

where $k = k_0\sqrt{\varepsilon\mu}$ is the wavenumber in the medium. Equation (4.4) is known to have the following solutions:

$$\boldsymbol{L} = \nabla\psi, \quad \boldsymbol{M}^{\mathbf{a}} = \boldsymbol{\nabla} \times (\psi \cdot \boldsymbol{a}), \quad \boldsymbol{N}^{\mathbf{a}} = \frac{1}{k}\boldsymbol{\nabla} \times \boldsymbol{M}^{\mathbf{a}} = \frac{1}{k}\boldsymbol{\nabla} \times \boldsymbol{\nabla} \times (\psi \cdot \boldsymbol{a}), \tag{4.5}$$

where $\boldsymbol{a}$ can be either a constant vector, e.g. a unit vector of the Cartesian system, or the radius-vector $\boldsymbol{r}$. The function ψ is a solution to the corresponding scalar Helmholtz equation

$$\Delta\psi + k^2\psi = 0. \tag{4.6}$$

Note that for any $\boldsymbol{a}$ the solutions L, M and N satisfy

$$\boldsymbol{\nabla}\cdot\boldsymbol{L} = -k^2\psi, \quad \boldsymbol{\nabla}\cdot\boldsymbol{M}^{\mathbf{a}} = 0, \quad \boldsymbol{\nabla}\cdot\boldsymbol{N}^{\mathbf{a}} = 0. \tag{4.7}$$

These equations and the transversality of the fields expressed by $\boldsymbol{\nabla}\cdot\boldsymbol{E} = 0$, $\boldsymbol{\nabla}\cdot\boldsymbol{H} = 0$ imply that $\boldsymbol{E}$, $\boldsymbol{H}$ can be represented by linear combinations of the vector functions $\boldsymbol{M}^{\mathbf{a}}$ and $\boldsymbol{N}^{\mathbf{a}}$, with the vector function $\boldsymbol{L}$ being excluded.

Only two components of the Hertz vectors (and the fields) are really independent. They are often called the scalar potentials. As such potentials one can use not only the components Π_{x}, Π_{y}, Π_{z} or their linear combinations, but also the Debye potentials related to the radial components of the Hertz vectors. Obviously, all the potentials should satisfy the scalar Helmholtz equation (4.6).

A comparison of eqs (4.3) and (4.5) shows that any choice of the vector wave functions $\boldsymbol{M}^{\mathbf{a}}$ and $\boldsymbol{N}^{\mathbf{a}}$ used for representation of the fields is equivalent to the corresponding choice of the scalar potentials and vice versa.

4.2.3 Light scattering problem for a small particle

To find the field of radiation scattered by a particle, one must supplement the equations presented above with the boundary conditions at the scatterer surface and at infinity.

Let us denote the known field of incident radiation by $\boldsymbol{E}^{\mathrm{in}}$, $\boldsymbol{H}^{\mathrm{in}}$, the unknown fields of scattered radiation by $\boldsymbol{E}^{\mathrm{sca}}$, $\boldsymbol{H}^{\mathrm{sca}}$ and of radiation inside the scatterer by $\boldsymbol{E}^{\mathrm{int}}$, $\boldsymbol{H}^{\mathrm{int}}$.

Then the light scattering problem can be written as follows:

$$\Delta\boldsymbol{E}^{\mathrm{sca}} + k_0^2\boldsymbol{E}^{\mathrm{sca}} = 0, \qquad \boldsymbol{r}\in R^3\setminus\bar{D}, \tag{4.8}$$

$$\Delta\boldsymbol{E}^{\mathrm{int}} + k^2\boldsymbol{E}^{\mathrm{int}} = 0, \qquad \boldsymbol{r}\in D, \tag{4.9}$$

$$\boldsymbol{\nabla}\cdot\boldsymbol{E}^{\mathrm{sca}} = 0, \quad \boldsymbol{\nabla}\cdot\boldsymbol{E}^{\mathrm{int}} = 0, \tag{4.10}$$

$$\left(\boldsymbol{E}^{\mathrm{in}} + \boldsymbol{E}^{\mathrm{sca}}\right)\times\boldsymbol{n} = \boldsymbol{E}^{\mathrm{int}}\times\boldsymbol{n}, \qquad \boldsymbol{r}\in S, \tag{4.11}$$

$$\lim_{r\to\infty} r\left(\frac{\partial\boldsymbol{E}^{\mathrm{sca}}}{\partial r} - ik_0\boldsymbol{E}^{\mathrm{sca}}\right) = 0. \tag{4.12}$$

Here $\boldsymbol{n}$ is the outer normal to the surface S of the particle having the volume D, $\bar{D} = D\cup S$, $r = |\boldsymbol{r}|$. For simplicity we assume that the scatterer is placed in vacuum for which $\varepsilon = \mu = 1$. The magnetic fields $\boldsymbol{H}^{\mathrm{sca}}$, $\boldsymbol{H}^{\mathrm{int}}$ are determined from the known $\boldsymbol{E}^{\mathrm{sca}}$, $\boldsymbol{E}^{\mathrm{int}}$ using the Maxwell equations

$$\boldsymbol{H} = \frac{1}{i\mu k_0}\boldsymbol{\nabla}\times\boldsymbol{E}. \tag{4.13}$$

Sometimes it is more convenient to present the problem in the integral form by using the Stratton–Chu formula. All solutions to the Maxwell equations inside a particle are known to satisfy (Colton and Kress, 1984)

$$\boldsymbol{\nabla} \times \int_S \boldsymbol{n} \times \boldsymbol{E}(\boldsymbol{r}')\, G(\boldsymbol{r}, \boldsymbol{r}')\, \mathrm{d}s' - \frac{1}{ik_0\varepsilon} \boldsymbol{\nabla} \times \boldsymbol{\nabla} \times \int_S \boldsymbol{n} \times \boldsymbol{H}(\boldsymbol{r}')\, G(\boldsymbol{r}, \boldsymbol{r}')\, \mathrm{d}s' = \begin{cases} -\boldsymbol{E}(\boldsymbol{r}), & \boldsymbol{r} \in D, \\ 0, & \boldsymbol{r} \in R^3 \setminus \bar{D}, \end{cases} \tag{4.14}$$

where $G(\boldsymbol{r}, \boldsymbol{r}')$ is the Green function of the scalar Helmholtz equation (4.6) for free space

$$G(\boldsymbol{r}, \boldsymbol{r}') = \frac{e^{ik_0|\boldsymbol{r}-\boldsymbol{r}'|}}{4\pi|\boldsymbol{r}-\boldsymbol{r}'|}. \tag{4.15}$$

For the solutions to the Maxwell equations outside $\bar{D}$ that also satisfy the radiation condition at infinity (4.12), one has integral equations similar to eqs (4.14) with the same left side whereas the right side is equal to 0 for $\boldsymbol{r} \in D$ or $\boldsymbol{E}(\boldsymbol{r})$ for $\boldsymbol{r} \in R^3 \setminus \bar{D}$.

If one applies these integral equations to the incident ($\boldsymbol{E}^{\mathrm{in}}$) and scattered ($\boldsymbol{E}^{\mathrm{sca}}$) fields, adds the equations and takes into account the boundary condition (4.11), the surface integral equation formulation of the light scattering problem can be obtained

$$\boldsymbol{\nabla} \times \int_S \boldsymbol{n} \times \boldsymbol{E}^{\mathrm{int}}(\boldsymbol{r}')\, G(\boldsymbol{r}, \boldsymbol{r}')\, \mathrm{d}s' - \frac{1}{ik_0\varepsilon} \boldsymbol{\nabla} \times \boldsymbol{\nabla} \times \int_S \boldsymbol{n} \times \boldsymbol{H}^{\mathrm{int}}(\boldsymbol{r}')\, G(\boldsymbol{r}, \boldsymbol{r}')\, \mathrm{d}s' = \begin{cases} -\boldsymbol{E}^{\mathrm{in}}(\boldsymbol{r}), & \boldsymbol{r} \in D, \\ \boldsymbol{E}^{\mathrm{sca}}(\boldsymbol{r}), & \boldsymbol{r} \in R^3 \setminus \bar{D}. \end{cases} \tag{4.16}$$

Usually the first step is to solve the integral equation for the domain D and to determine the internal field $\boldsymbol{E}^{\mathrm{int}}$. After that the scattered field $\boldsymbol{E}^{\mathrm{sca}}$ can be easily found from the equation for the domain $R^3 \setminus \bar{D}$.

4.2.4 Methods of solving the problem using field expansions

The available numerical methods to solve the light scattering problem for a nonspherical particle are reviewed, for example, by Khlebtsov (1996), Wriedt (1998), Jones (1999), Mishchenko *et al.* (2000c), and Kahnert (2003b). Here we consider three methods (SVM, EBCM, PMM) in which the fields are expanded in terms of certain vector wave functions. This is equivalent to expansion of the corresponding scalar potentials in terms of orthogonal functions forming a complete set. So far, three sets of the functions – spherical, cylindrical and spheroidal – were employed. The choice of the basis, however, does not affect the main ideas of the methods.

In the *separation of variables method* the field expansions are substituted into the boundary conditions expressed in the 'differential' form given by eqs (4.11)

and (4.12). Equation (4.11) is then multiplied by the angular functions of different indices and integrated over all values of the angular variables. This gives an infinite system of linear algebraic equations relative to unknown field expansion coefficients.

In the *extended boundary condition method* the expansions are substituted into the conditions presented in the surface integral form (see eqs (4.16)). Completeness of the angular functions allows one to get again a system of linear algebraic equations to be solved.

It should be noted that for a long time the SVM and EBCM were developed and considered separately. Only recently they were shown to be equivalent in general (see Schmidt *et al.*, 1998; Farafonov *et al.*, 2003, and references therein). Different forms of the boundary conditions used in the methods naturally lead to different (but very probably equivalent) systems of linear equations relative to unknown coefficients of the same expansions. The EBCM gives two systems – one system relates the coefficients for the internal and incident fields and the other relates the coefficients for the internal and scattered fields. On the other hand, the SVM produces one system of a twice larger dimension[2] that includes the coefficients for all the fields. So, when the scattered field alone is to be found, special efforts are required to reduce the dimension of this system by excluding the internal field. Consequently, in general the EBCM appears to be preferable in the way it provides solution.

However, in the cases of spheres, infinitely long cylinders and spheroids when the boundary of a scatterer coincides with a coordinate hypersurface of the system selected in accordance with the expansion functions used, at least partial separation of variables in the boundary conditions occurs. As a result the integrals in the matrix elements of the systems in both methods are simplified, in particular the radial functions can be removed from the integrals. This simplification changes the properties of the solutions essentially, and this approach may be considered as a separate method.

Traditionally solutions in these cases were obtained by the SVM. That was logical and rather convenient because the boundary conditions easily allowed reduction of the large systems to smaller ones for the scattered field alone. Therefore, in further discussion we consider the SVM *only* for particles whose shapes coincide with coordinate hypersurfaces. Two points should be emphasized: (i) the EBCM can provide very similar solutions in these cases; (ii) the SVM can be applied to scatterers whose shape does not coincide with coordinate hypersurfaces as well.

In the *point matching method* one substitutes the field/potential expansions into the boundary conditions that are considered in a set of points on the particle surface. The number of points is taken so as to obtain the number of equations equal to the number of the expansion coefficients. In the generalized PMM one takes many more points, obtaining thus more equations than necessary, and

[2]Here we mean the dimension of the truncated systems used to calculate the same number of terms in the expansions.

then solves an overdetermined system of linear algebraic equations by the least squares or other technique.

The *names of the methods* are to a certain degree confusing and require a few comments. The separation of variables actually means the following approach to solving the problem. One uses the solution to the scalar Helmholtz equation (4.6) in the form $\phi(\xi_1, \xi_2, \xi_3) = \phi_1(\xi_1)\,\phi_2(\xi_2)\,\phi_3(\xi_3)$, where ξ_i are the coordinates and the functions $\phi_i(\xi_i)$ are determined from ordinary differential equations (see, for example, Kahnert (2003b) for more details). Using eqs (4.5) and selecting the vector $\boldsymbol{a}$, one constructs the solutions to the vector Helmholtz (wave) equation (4.4). Further, the fields (or their scalar potentials) are expanded in terms of the vector (scalar) wave functions, and determination of the expansion coefficients occurs in any described way. Thus, as all three methods use such expansions, they could be called the separation of variable methods. However, traditionally the term SVM is attributed only to the technique where the coefficients are determined from the boundary conditions presented in the form (4.11).

Earlier the EBCM was often called the T-matrix method, where T denoted the matrix relating the coefficients of the expansions of the scattered and incident fields. However, now the matrix T is calculated using different methods, not only EBCM, but also the SVM (Schulz *et al.*, 1998), PMM (Nieminen *et al.*, 2003), generalized multipole technique (Doicu and Wriedt, 1999), discrete dipole moment method (Mackowski, 2002), etc. Therefore, the term T-matrix method should be applied rather to the technique of analytical determining the optical properties of ensembles of (randomly oriented) particles from the elements of the T-matrices of the particles (see, for example, Mishchenko *et al.*, 2002).

Note also that the point matching technique can be applied to the boundary conditions of both forms: the differential one given by eq. (4.11) and the surface integral one represented by eqs (4.16) (see section 4.3.3 for more details). The principal difference between the SVM or EBCM and the PMM is in the fact that the first two techniques try to satisfy the boundary conditions in all points of the scatterer surface, while the last does it only in a finite set of selected points.

One also often relates the PMM with the multiple multipole method and generalized multipole techniques in which the fields are represented by a sum of expansions at different points of a domain with the number of terms in these expansions being usually limited (Wriedt and Doicu, 1997; Mishchenko *et al.*, 2000c). Such multiple expansions change the properties of the PMM (Kahnert, 2003b), and hereafter we deal only with the (generalized) PMM that exploits single expansions.

Thus, the SVM, EBCM and PMM are alike in using the same expansions of the fields, but differ in the way they determine the expansion coefficients. That is why the methods have different theoretical and practical applicability ranges. Both ranges are also essentially affected by the choice of the wave functions utilized in the expansions. Therefore, we consider the solutions using the spherical, spheroidal and ellipsoidal functions in three separate sections. The use of the cylindrical functions is in many aspects similar to that of the spherical functions and is not discussed.

4.2.5 Selected bibliography

The format of our chapter allows us to mention only a few works, while important results were definitely obtained in many others. References to them can be found in the reviews to be mentioned, in the light scattering bibliography database of Babenko (2004) and in special issues of the *J. Quant. Spectr. Rad. Transf.* containing proceedings of the conferences on light scattering by nonspherical particles held practically annually for the last 10 years.

Separation of variables method

The SVM solutions to the light scattering problem for homogeneous spheres were suggested by Lorenz (1890), Mie (1908) and Debye (1909), for cylinders by Rayleigh (1881) and Wait (1955), for spheroids by Möglich (1927), Oguchi (1973), Asano and Yamamoto (1975) and Sinha and McPhie (1977). For ellipsoids, only the scalar diffraction problem has been solved so far (see Abramov *et al.*, 1995, and references therein). The early history of the method development was discussed by Kerker (1969), Khlebtsov (1996) and Ciric and Cooray (2000).

The ansatz of the method for spheres is well described, e.g., by van de Hulst (1957) and Bohren and Huffman (1983) and for spheroids by Asano and Yamamoto (1975), Voshchinnikov and Farafonov (1993), Ciric and Cooray (2000). The latter paper deals with such important questions as application of the SVM to layered spheroids, chiral spheroids, and systems of spheroids.

The recent reviews of works on the method are given by Mishchenko *et al.* (2000c) and Ciric and Cooray (2000). Since publication of these reviews the method has developed in the following main directions:

(i) multilayered scatterers: spheres (Gurwich *et al.*, 2001; Yang, 2003; Babenko *et al.*, 2003), infinite cylinders (Gurwich *et al.*, 1999, 2001), and spheroids (Gurwich *et al.*, 2000, 2003; Barton, 2001);
(ii) extension of the SVM for spheres to particles of other shapes (Rother, 1998; Rother *et al.*, 2001; Kahnert, 2003b; Schmidt *et al.*, 2003);
(iii) applications to complicated cases (Barton, 1999, 2000, 2002; Qingan *et al.*, 1999; Han and Wu, 2001; Han *et al.*, 2003; Borghese *et al.*, 2003 and many others).

It should be added that many new algorithms of calculation for the spheroidal functions used by the SVM for spheroids have been suggested in recent years (e.g., Li *et al.*, 1998, 2002; Eide *et al.*, 1999; Brown and Stringfield, 2000; de Moraes and Guimaraes, 2002, 2003; Kokkorakis and Roumeliotis, 2002; Boyd, 2003; Voshchinnikov and Farafonov, 2003; Barrowes *et al.*, 2004).

The website of Wriedt (2005) is very useful in providing links to a great number of different codes realizing the method for homogeneous spheres (the Mie theory) and to several codes for layered, optically active or magnetic spheres as well as for spheres with inclusions and aggregates of spheres. A few codes for homogeneous and layered cylinders and spheroids are also available.

Extended boundary condition method

The method was introduced by Waterman (1965, 1969) and its useful reformulation was made later by Barber and Yeh (1975). The versions of the method using the spheroidal functions instead of spherical ones in the expansions were developed by Farafonov (2001b), Kahnert (2003a).

The ansatz of the method is well described, for example, by Barber and Hill (1990), Mishchenko *et al.* (2002). It is still worth reading some sections of the book by Varadan and Varadan (1980).

Extended bibliography on development of the method and its applications is presented by Mishchenko *et al.* (2004). The review contains references to about 700 papers presented in two large sections (particles in infinite homogeneous space and near infinite interfaces) that are divided into 52 subsections. All the references include paper titles, which makes the review particularly helpful. This bibliographic paper is expected to appear as an updating site on the internet.

The work of Mishchenko *et al.* (2004) shows that the interest in the method has increased over the last 10 years. This fact seems to be mainly related to a growing number of applications of the EBCM. In particular, the method has been used for the modeling of scattering properties of mineral aerosols and soil particles, cirrus cloud particles, hydrometeors, stratospheric aerosols, noctilucent cloud particles, interstellar, and interplanetary and cometary particles, as well as for analysing laboratory data and for biomedical, industrial and other applications.

Among the recent works developing the method it is worth noting the paper of Kahnert *et al.* (2001b) where the authors show that proper treatment of symmetries of a scatterer within the method can substantially reduce the calculation volume. Another work to be mentioned is Moroz (2005). The applicability of the EBCM was considered analytically by Il'in *et al.* (2004).

Wriedt's (2005) website is useful again in providing links to several EBCM computer codes (see them among the T-matrix codes).

Point matching method

The PMM was suggested by Mullin *et al.* (1965) (see also Morrison *et al.*, 1973; Oguchi, 1973) and the generalized PMM by Ikuno and Yasuura (1973), Davies (1973). The early history of the method development is outlined by Bates *et al.* (1973), Khlebtsov (1980), a recent review of works on the PMM is given by Mishchenko *et al.* (2000c).

If one does not take into account the PMM versions that use multiple expansions, i.e. the multiple multipole method (MMM), generalized multipole techniques (GMT), etc. (see, for example, Wriedt, 1998), the number of recent papers dealing with the PMM will be very small in comparison with that of papers on the SVM and in particular the EBCM. In our opinion it can be explained by two factors: (i) the GMT and similar techniques give more flexible tools for solving the light scattering problem (at least for essentially eccentric particles); (ii) the advantages of the PMM have not been realized yet as compared to other methods using the same single expansions. However, recent papers of Al-Rizzo and

Tranquilla (1995), Petrov and Babenko (1999), Nieminen *et al.* (2003), Kahnert (2003b), Farafonov and Il'in (2005b) and others show that the interest to the PMM can revive.

Note that the MMM, GMT and similar techniques (Hafner and Bomholt, 1993; Doicu *et al.*, 2000) which are not considered in this chapter play an important role since they are shown to have advantages in certain cases (see, for example, Piller and Martin, 1998; Doicu and Wriedt, 2001; Moreno *et al.*, 2002; Eremina and Wriedt, 2003; Eremina *et al.*, 2005).

A few computer codes based on the PMM as well as on the GMT, MMM and similar techniques are linked to Wriedt's (2005) website.

4.2.6 Specific approach for axisymmetric scatterers

The standard SVM solution for spheroids is that of Asano and Yamamoto (1975). A nonstandard solution suggested by Farafonov (1983) was found to be especially efficient for highly eccentric spheroids (see Voshchinnikov and Farafonov, 1993, and references therein). Here we expand the approach of Farafonov (1983) on axisymmetric scatterers and apply it to all the methods under consideration.

For an axisymmetric scatterer, we introduce the Cartesian coordinate system (x, y, z) in such a way that the z-axis coincides with the particle symmetry axis. Then the equation of the particle surface can be written in the related spherical coordinate system (r, θ, φ) as

$$r = r(\theta). \tag{4.17}$$

One feature of the approach is that the incident, scattered and internal fields are represented by the sums

$$\boldsymbol{E} = \boldsymbol{E}_{\mathrm{A}} + \boldsymbol{E}_{\mathrm{N}}, \ \boldsymbol{H} = \boldsymbol{H}_{\mathrm{A}} + \boldsymbol{H}_{\mathrm{N}}, \tag{4.18}$$

where $\boldsymbol{E}_{\mathrm{A}}$, $\boldsymbol{H}_{\mathrm{A}}$ do not depend on the azimuthal angle φ, while averaging of $\boldsymbol{E}_{\mathrm{N}}$, $\boldsymbol{H}_{\mathrm{N}}$ over this angle gives zero.

The axisymmetric and nonaxisymmetric light scattering problems (i.e. determination of $\boldsymbol{E}_{\mathrm{A}}^{\mathrm{sca}}$, $\boldsymbol{H}_{\mathrm{A}}^{\mathrm{sca}}$ and $\boldsymbol{E}_{\mathrm{N}}^{\mathrm{sca}}$, $\boldsymbol{H}_{\mathrm{N}}^{\mathrm{sca}}$, respectively) can be solved separately. It follows from the commutativity of the operator T corresponding to the light scattering problem and the operator $L_{\mathrm{z}} = \partial/\partial\varphi$ (see Farafonov and Slavyanov (1980) for more details).

Another feature of the approach is the use of scalar potentials properly chosen for each of the field parts.

Axisymmetric problem

The axisymmetry of the corresponding parts of the fields allows one to reduce the vector light scattering problem to a scalar one. Then the following specific scalar potentials become useful:

$$p = E_{\mathrm{A},\varphi} \cos\varphi, \quad q = H_{\mathrm{A},\varphi} \cos\varphi, \tag{4.19}$$

where $E_{\mathrm{A},\varphi}$, $H_{\mathrm{A},\varphi}$ are the φ-components of $\boldsymbol{E}_{\mathrm{A}}$, $\boldsymbol{H}_{\mathrm{A}}$. Other components of the fields can be expressed via the potentials using the Maxwell equations (Farafonov, 2001b). Note that the potential p is related with the TE mode, and q with the TM one.

Nonaxisymmetric problem

Two potentials, the z-component of the electric or magnetic Hertz vectors $U = \Pi_{\mathrm{z}}$ and the Debye potential $V = \Pi_{\mathrm{r}}/r$, are utilized to determine the axisymmetric parts of the fields:

(a) for the TE mode

$$\begin{aligned} \boldsymbol{E}_{\mathrm{N}} &= -\tfrac{1}{i\varepsilon k_0}\boldsymbol{\nabla}\times\boldsymbol{\nabla}\times(U\ \boldsymbol{i}_{\mathrm{z}} + V\ \boldsymbol{r})\,, \\ \boldsymbol{H}_{\mathrm{N}} &= \boldsymbol{\nabla}\times(U\ \boldsymbol{i}_{\mathrm{z}} + V\ \boldsymbol{r})\,; \end{aligned} \tag{4.20}$$

(b) for the TM mode

$$\begin{aligned} \boldsymbol{E}_{\mathrm{N}} &= \boldsymbol{\nabla}\times(U\,\boldsymbol{i}_{\mathrm{z}} + V\,\boldsymbol{r})\,, \\ \boldsymbol{H}_{\mathrm{N}} &= \tfrac{1}{i\mu k_0}\boldsymbol{\nabla}\times\boldsymbol{\nabla}\times(U\,\boldsymbol{i}_{\mathrm{z}} + V\,\boldsymbol{r})\,. \end{aligned} \tag{4.21}$$

Note that the potentials U and V are used to solve the light scattering problem for an infinite cylinder and a sphere (the Mie theory), respectively.

Further in the approach one searches either for solutions to the scalar Helmholtz equations corresponding to eqs (4.8) and (4.9) that satisfy the scalar boundary conditions for the potentials produced by eqs (4.11) and (4.12), or for solutions to the surface integral equations (4.16), which depends on the selected method.

The advantages and disadvantages of the approach can be briefly summarized as follows. The approach involves solution of two (axisymmetric and nonaxisymmetric) light scattering problems instead of the initial one. Fortunately, the axisymmetric problem is very simple and its solution is computationally quite fast. Test computations indicate that the solution to the axisymmetric problem can be used to determine the values of such parameters as the number of terms held in the field expansions, the number of knots used to calculate integrals, etc. These parameters are required to solve both axisymmetric and nonaxisymmetric problems, and as our experience shows are practically the same for both problems. The simplicity of the axisymmetric problem also helps in studing analytically the applicability ranges of the methods. Although the approach complicates analytical averaging of scattering matrix elements for randomly oriented particles, this is compensated by its ability to give reliable results for scatterers of a high eccentricity.

4.3 Solutions using the spherical wave functions

In this section we consider solutions to the light scattering problem that use expansions in terms of the spherical wave functions. Sometimes, it is more reasonable to utilize expansions in terms of the spheroidal or even ellipsoidal wave functions, and their use is described in the following sections.

The methods under consideration are applied using the approach presented above. So, further we operate with the potentials p, q, U, V (see section 4.2) rather than with the fields.

4.3.1 Potential expansions

The potentials p and q can be represented by expansions in terms of the spherical wave functions having the index $m = 1$ only, since the dependence of these potentials on the azimuthal angle φ is given explicitly by $\cos\varphi$ (see eq. (4.19) where $\boldsymbol{E}_{\mathrm{A}}$ does not depend on φ by its definition)

$$\begin{matrix} p^{\mathrm{int}} \\ p^{\mathrm{sca}} \end{matrix} = \sum_{l=1}^{\infty} \begin{matrix} a_l^{\mathrm{int}}\, j_l(kr) \\ a_l^{\mathrm{sca}}\, h_l^{(1)}(k_0 r) \end{matrix} P_l^1(\cos\theta)\, \cos\varphi, \tag{4.22}$$

$$\begin{matrix} q^{\mathrm{int}} \\ q^{\mathrm{sca}} \end{matrix} = \sum_{l=1}^{\infty} \begin{matrix} b_l^{\mathrm{int}}\, j_l(kr) \\ b_l^{\mathrm{sca}}\, h_l^{(1)}(k_0 r) \end{matrix} P_l^1(\cos\theta)\, \cos\varphi, \tag{4.23}$$

where $j_l(kr)$, $h_l^{(1)}(k_0 r)$ are the spherical Bessel functions and the first kind Hankel functions, respectively, $P_l^m(\cos\theta)$ the associated Legendre functions. Calculation of the spherical functions is considered in detail, for example, by Babenko *et al.* (2003). One should use $j_l(k_0 r)$ in similar expansions of p^{in},q^{in}, and for a plane wave incident at the angle α to the particle symmetry axis one gets

$$\begin{aligned} a_l^{\mathrm{in}} &= -i^l \frac{2l+1}{l(l+1)} P_l^1(\cos\alpha), \quad b_l^{\mathrm{in}} = 0 \quad \text{for the TM mode,} \\ a_l^{\mathrm{in}} &= 0, \quad b_l^{\mathrm{in}} = i^l \frac{2l+1}{l(l+1)} P_l^1(\cos\alpha) \qquad \text{for the TE mode.} \end{aligned}$$

Taking into account that averaging of the nonaxisymmetric parts of the fields over φ must give zero, the potentials U, V are expanded as follows:

$$\begin{matrix} U^{\mathrm{int}} \\ U^{\mathrm{sca}} \end{matrix} = \sum_{m=1}^{\infty} \sum_{l=m}^{\infty} \begin{matrix} a_{ml}^{\mathrm{int}}\, j_l(kr) \\ a_{ml}^{\mathrm{sca}}\, h_l^{(1)}(k_0 r) \end{matrix} P_l^m(\cos\theta)\, \cos m\varphi, \tag{4.24}$$

$$\begin{matrix} V^{\mathrm{int}} \\ V^{\mathrm{sca}} \end{matrix} = \sum_{m=1}^{\infty} \sum_{l=m}^{\infty} \begin{matrix} b_{ml}^{\mathrm{int}}\, j_l(kr) \\ b_{ml}^{\mathrm{sca}}\, h_l^{(1)}(k_0 r) \end{matrix} P_l^m(\cos\theta)\, \cos m\varphi. \tag{4.25}$$

Again expanding U^{in},V^{in}, one should use $j_l(k_0 r)$ as the radial functions. For a plane wave,

$$a_{ml}^{\mathrm{in}} = i^{l-1} \frac{2(2l+1)}{k_0 \sin\alpha} \frac{(l-m)!}{(l+m)!} P_l^m(\cos\alpha), \quad b_{ml}^{\mathrm{in}} = 0. \tag{4.26}$$

The expansion of the Green function $G(\boldsymbol{r}, \boldsymbol{r}')$ in terms of the spherical wave functions is well known (Morse and Feshbach, 1953)

$$G(\boldsymbol{r},\boldsymbol{r}') = \frac{ik_0}{4\pi}\sum_{m=0}^{\infty}\sum_{l=m}^{\infty}(2-\delta_m^0)(2l+1)\frac{(l-m)!}{(l+m)!}j_l(k_0r_<) \times h_l^{(1)}(k_0r_>)\,P_l^m(\cos\theta)\,P_l^m(\cos\theta')\,\cos(\varphi-\varphi'), \quad (4.27)$$

where $r_< = \min(r,r')$, $r_> = \max(r,r')$, and $\delta_m^0 = 1$ or 0 if $m = 0$ or $m \neq 0$, respectively.

When the unknown expansion coefficients are determined, the characteristics of the scattered radiation can be easily computed. For instance, for the amplitude matrix relating the incident field (a plane wave) and the scattered field in the far-field zone ($r \to \infty$) as follows:

$$\begin{pmatrix} E_\parallel^{\rm sca} \\ E_\perp^{\rm sca} \end{pmatrix} = \frac{1}{-ik_0r}e^{i(k_0r-\boldsymbol{k}_0\boldsymbol{r})}\begin{pmatrix} A_2 & A_3 \\ A_4 & A_1 \end{pmatrix}\begin{pmatrix} E_\parallel^{\rm in} \\ E_\perp^{\rm in} \end{pmatrix}, \quad (4.28)$$

one has

$$A_1 = \sum_{l=1}^{\infty} i^{-l}a_l^{\rm sca}P_l^1(\cos\theta) - \sum_{m=1}^{\infty}\sum_{l=m}^{\infty} i^{-(l-1)}\,(k_0a_{ml}^{\rm sca}P_l^m(\cos\theta) + ib_{ml}^{\rm sca}P_l^{m\,\prime}(\cos\theta))\sin\theta\cos m\varphi, \quad (4.29)$$

$$A_3 = \sum_{m=1}^{\infty}\sum_{l=m}^{\infty} i^{-l}b_{ml}^{\rm sca}\frac{mP_l^m(\cos\theta)}{\sin\theta}\sin m\varphi. \quad (4.30)$$

The expression for A_2 is obtained from that for A_1 by the change of $a_l^{\rm sca}$ for $b_l^{\rm sca}$, the expression for A_4 is identical to that for A_3.

Note that the expansion coefficients that one obtains from solution of the light scattering problem for the TE mode are used in A_1 and A_3, while the coefficients for the TM mode appear in A_2 and A_4.

Other characteristics of the scattered (and internal) radiation such as the elements of the scattering matrix, various cross-sections, etc. (see, for example, Bohren and Huffman, 1983; Mishchenko *et al.*, 2000a) can be presented in the form of eqs (4.29) and (4.30) as well.

Thus, to solve the light scattering problem only the expansion coefficients are to be found. As we expand the fields/potentials in terms of the functions that are solutions to the corresponding wave equations, boundary conditions are required to derive these coefficients.

4.3.2 Boundary conditions

Boundary conditions can be used in two forms: the differential one presented by eqs (4.11) and (4.12) and the integral one given by eq. (4.16). Let us consider the expressions for the conditions in the case of the scalar potentials.

4.3.2.1 Axisymmetric part of the light scattering problem

For the potential q, the boundary conditions (4.11) are written as follows:

$$\left.\begin{array}{l} q^{\rm in}+q^{\rm sca}=q^{\rm int}, \\ \frac{\partial(q^{\rm in}+q^{\rm sca})}{\partial n}=\frac{1}{\varepsilon}\frac{\partial q^{\rm int}}{\partial n}-(1-\frac{1}{\varepsilon})\frac{1}{\sqrt{r^2+r'^2_\theta}}\left(1-\frac{r'_\theta}{r}{\rm ctg}\theta\right)q^{\rm int} \end{array}\right\}_{\boldsymbol{r}\in S}, \tag{4.31}$$

where $r'_\theta=\partial r/\partial\theta$, n is the normal.

The integral form of the boundary conditions for q is obtained if one rewrites eqs (4.16) in the spherical coordinates (it is natural to use such coordinates along with the spherical wave functions) and takes into account the conditions (4.31)

$$\int\limits_S\left\{q^{\rm int}(\boldsymbol{r}')\frac{\partial G(\boldsymbol{r},\boldsymbol{r}')}{\partial n}-\left[\frac{1}{\varepsilon}\frac{\partial q^{\rm int}(\boldsymbol{r}')}{\partial n}+\left(\frac{1}{\varepsilon}-1\right)\frac{1}{\sqrt{(r')^2+\left[(r')'_{\theta'}\right]^2}}\right.\right. \tag{4.32}$$
$$\left.\left.\times\left(1-\frac{(r')'_{\theta'}}{r'}{\rm ctg}\theta'\right)q^{\rm int}(\boldsymbol{r}')\right]G(\boldsymbol{r},\boldsymbol{r}')\right\}{\rm d}s'=\left\{\begin{array}{ll} -q^{\rm in}(\boldsymbol{r}), & \boldsymbol{r}\in D, \\ q^{\rm sca}(\boldsymbol{r}), & \boldsymbol{r}\in R^3\setminus\bar{D}. \end{array}\right.$$

The conditions for the potential p are the same if one replaces q and ε with p and μ, respectively.

4.3.2.2 Nonaxisymmetric part of the light scattering problem

The boundary conditions (4.11) for the potentials U,V can be written as follows:

$$\left.\begin{array}{rcl} U^{\rm in}+U^{\rm sca} &=& U^{\rm int}, \\ V^{\rm in}+V^{\rm sca} &=& V^{\rm int}, \\ \frac{\partial(U^{\rm in}+U^{\rm sca})}{\partial n} &=& \frac{\partial U^{\rm int}}{\partial n}+\left(\frac{1}{\varepsilon}-1\right)\frac{r'_\theta}{r\sin\theta\sqrt{r^2+r'^2_\theta}}\left[r\cos\theta\frac{\partial U^{\rm int}}{\partial r}\right. \\ & & \left.-\sin\theta\frac{\partial U^{\rm int}}{\partial\theta}+r^2\frac{\partial V^{\rm int}}{\partial r}+rV^{\rm int}\right], \\ \frac{\partial(V^{\rm in}+V^{\rm sca})}{\partial n} &=& \frac{\partial V^{\rm int}}{\partial n}-\left(\frac{1}{\varepsilon}-1\right)\frac{\left(r'_\theta\cos\theta-r\sin\theta\right)}{r^2\sin\theta\sqrt{r^2+r'^2_\theta}}\left[r\cos\theta\frac{\partial U^{\rm int}}{\partial r}\right. \\ & & \left.-\sin\theta\frac{\partial U^{\rm int}}{\partial\theta}+r^2\frac{\partial V^{\rm int}}{\partial r}+rV^{\rm int}\right], \end{array}\right\}_{\boldsymbol{r}\in S} \tag{4.33}$$

where we consider the TM mode and take for simplicity $\mu=1$.

In the same way as above one can get the integral equations for the potential U

$$\int_S\left\{U^{\rm int}\frac{\partial G}{\partial n}-\left[\frac{\partial U^{\rm int}}{\partial n}+\left(\frac{1}{\varepsilon}-1\right)\frac{r'_\theta}{r\sin\theta\sqrt{r^2+r'^2_\theta}}\right.\right.$$
$$\left.\left.\times\left(r\cos\theta\frac{\partial U^{\rm int}}{\partial r}-\sin\theta\frac{\partial U^{\rm int}}{\partial\theta}+r^2\frac{\partial V^{\rm int}}{\partial r}+rV^{\rm int}\right)\right]G\right\}{\rm d}s' \tag{4.34}$$
$$=\left\{\begin{array}{ll} -U^{\rm in}(\boldsymbol{r}), & \boldsymbol{r}\in D, \\ U^{\rm sca}(\boldsymbol{r}), & \boldsymbol{r}\in R^3\setminus\bar{D}, \end{array}\right.$$

and a similar equation for the potential V.

Note that these equations are more complicated (each includes both U and V potentials) than eqs (4.32). For the TE mode, the boundary conditions being similar are a bit more complex (see Farafonov and Il'in (2001) for more details).

4.3.3 Methods to determine the expansion coefficients

Now we show in more detail than in section 4.2 how the unknown coefficients of the potential expansions are derived from the boundary conditions within different methods.

4.3.3.1 Separation of variables method for spheres

For a spherical scatterer, the classical and highly efficient solution called the Mie theory is provided by the separation of variables method with the field expansions in terms of the spherical wave functions. This theory uses the vector wave functions $\boldsymbol{M}_\nu^{\mathbf{r}}$ and $\boldsymbol{N}_\nu^{\mathbf{r}}$ or, which is equivalent, the Debye potentials. In this section, we show how the problem for a sphere is solved with the use of the scalar potentials p, q, U, V. This helps us to understand the efficiency of the approach for scatterers being close to spheres.

The surface equation for a sphere of the radius R is $r(\theta) = R$, and the boundary conditions (4.31) in the axisymmetric problem are simplified as $r'_\theta = 0$. Substituting the expansions (4.23) into eqs (4.31) and using orthogonality of the angular spherical functions, one can find the unknown coefficients explicitly. For instance, for the TM mode one gets

$$b_n^{\mathrm{sca}} = -\frac{j_n(x)(j_n(x_0))' - \varepsilon j_n(x_0)(j_n(x))'}{j_n(x)(x_0 h_n^{(1)}(x_0))' - \varepsilon h_n^{(1)}(x_0)(x j_n(x))'}\, b_n^{\mathrm{in}}, \tag{4.35}$$

where $x = kR$, $x_0 = k_0 R$.

Substitution of the expansions (4.24) and (4.25) into the boundary conditions (4.33) allows one to determine other unknown coefficients. The coefficients for U^{sca} and U^{int} are obtained from two equations which coincide with the analogs to eqs (4.31) for the potential p in the case of $\mu = 1$. Those for V^{sca} and V^{int} are determined from two other equations and are expressed through the coefficients of the expansion of U^{int} as follows:

$$\begin{aligned} b_{mn}^{\mathrm{sca}} \;=\; & \frac{\left[\frac{n-m}{2n-1} j_n(x) a_{m,n-1}^{\mathrm{int}} + \frac{n+m+1}{2n+3}\left(j_n(x) + \frac{1}{x} j_{n+1}(x)\right) a_{m,n+1}^{\mathrm{int}}\right]}{\varepsilon j_n(x)(x_0 h_n^{(1)}(x_0))' - h_n^{(1)}(x_0)(x j_n(x))'} \\ & \times \left(\frac{1}{\varepsilon} - 1\right) k j_n(x). \end{aligned} \tag{4.36}$$

As usual, the solution for the TE mode is analogous.

A comparison of eqs (4.35) and (4.36) with the well known equations of the Mie theory (see, for example, van de Hulst, 1957; Bohren and Huffman, 1983)

shows that for spheres the approach presented in section 4.2 is practically as efficient as the Mie theory. Note also that when a plane wave is incident on a sphere, one can always select the coordinate system in such a way that the wave vector will coincide with the z-axis (the particle symmetry axis). As a result the axisymmetric parts of the fields become equal to zero and the nonaxisymmetric parts are not equal to zero only for $m = 1$. This further simplifies eq. (4.36).

4.3.3.2 Extended boundary condition method for axisymmetric particles

The method is based on the integral formulation of the boundary conditions given, for example, by eqs (4.32) and (4.34) and uses the expansions of the fields/potentials similar to eqs (4.22)–(4.25) as well as the expansion of the Green function given by eq. (4.27).

For example, for the *axisymmetric* problem and the TM mode, substituting the expansions (4.22),(4.23),(4.27) into the integral equation (4.32) for the domain D and using completeness and orthogonality of the spherical functions, one can obtain the system

$$B_{\mathrm{S}}\, \boldsymbol{b}^{\mathrm{int}} = \boldsymbol{b}^{\mathrm{in}}, \tag{4.37}$$

where $\boldsymbol{b} = \{b_n\}_{n=1}^{\infty}$ are the vector containing the expansion coefficients and the elements of B_{S} are integrals of the spherical functions and their first derivatives

$$\begin{aligned}\{B_{\mathrm{S}}\}_{ln} \;=\; & -\frac{i(2l+1)}{2l(l+1)} \int\limits_0^{\pi} \left\{ k_0^2 r^2 \left[h_l^{(1)\prime}(k_0 r) j_n(kr) - \frac{k}{k_0} h_l^{(1)}(k_0 r) j_n'(kr) \right] \right. \\ & \times P_l^1(\cos\theta) P_n^1(\cos\theta) \sin\theta + k_0 r_\theta' \sin^2\theta \left[P_l^{1\prime}(\cos\theta) P_n^1(\cos\theta) \right. \\ & \left. - \frac{1}{\varepsilon} P_l^1(\cos\theta) P_n^{1\prime}(\cos\theta) \right] h_l^{(1)}(k_0 r)\, j_n(kr) - h_l^{(1)}(k_0 r)\, j_n(kr) \\ & \left. \times P_l^1(\cos\theta) P_n^1(\cos\theta) \right\} \mathrm{d}\theta, \end{aligned} \tag{4.38}$$

with $r = r(\theta)$ being the particle surface equation.

Substitution of the same expansions into the eq. (4.32) for the domain $R^3 \setminus \bar{D}$ leads to a system for the coefficients of the scattered field expansion

$$B_{\mathrm{R}}\, \boldsymbol{b}^{\mathrm{int}} = \boldsymbol{b}^{\mathrm{sca}}, \tag{4.39}$$

where the elements of B_{R} are equal to those of B_{S} if one replaces the singular at the coordinate origin functions $h_l^{(1)}(k_0 r)$ by the regular ones $j_l(k_0 r)$, i.e. $B_{\mathrm{R}} = \mathrm{Rg}\, B_{\mathrm{S}}$. In the case of the TE mode it is the problem for the potential p that has to be solved. The corresponding equations are easily obtained from those given above after replacing μ and a_l with ε and b_l, respectively.

Thus, for both modes one gets the usual form of the T-matrix

$$T^{\mathrm{A}} = B_{\mathrm{R}} (B_{\mathrm{S}})^{-1}, \tag{4.40}$$

which solves the light scattering problem.

To treat the *nonaxisymmetric* problem, one should substitute the expansions (4.24)–(4.27) into the integral equation (4.34) for U and into a similar equation for V. In the way described above, it gives infinite systems of linear algebraic equations for each index $m \geq 1$

$$\hat{A}_{\mathrm{S},m}\, \hat{\boldsymbol{a}}_m^{\mathrm{int}} = \hat{\boldsymbol{a}}_m^{\mathrm{in}}, \quad \hat{A}_{\mathrm{R},m}\, \hat{\boldsymbol{a}}_m^{\mathrm{int}} = \hat{\boldsymbol{a}}_m^{\mathrm{sca}}, \tag{4.41}$$

where $\hat{\boldsymbol{a}}_m = \{a_{m,m}, a_{m,m+1}, ..., b_{m,m}, b_{m,m+1}, ...\}$ are the vectors containing the expansion coefficients, and the elements of the matrices $\hat{A}_{\mathrm{R},m}$ and $\hat{A}_{\mathrm{S},m}$ are integrals of the scalar spherical wave functions and their derivatives (Farafonov and Il'in, 2001). The dimension of the matrices $\hat{A}$ is twice as large as that of B used in the case of the axisymmetric problem.

In contrast to the described approach, in the standard EBCM (see, for example, Barber and Yeh, 1975; Mishchenko *et al.*, 2002) the matrix elements are integrals of the functions $\boldsymbol{M}_\nu^{\mathrm{r}}$ and $\boldsymbol{N}_\nu^{\mathrm{r}}$, which is equivalent to the use of the Debye potentials. For a sphere, this gives the Mie theory (see, for example, Barber and Hill, 1990), while the introduced version of the EBCM leads to the same eqs (4.35) and (4.36) as the described version of the SVM for spheres with the scalar potentials p, q, U, V.

The case of layered particles

The approach can be easily expanded on n-layered axisymmetric scatterers. Such particles have the following equations of the layer boundaries:

$$r = r^{(j)}(\theta), \quad j = 1, 2, ..., n. \tag{4.42}$$

For a jth layer, one has the dielectric permittivity ε_{j+1}, the magnetic permeability μ_{j+1} and the wavenumber in the media $k_{j+1} = \sqrt{\varepsilon_{j+1}\mu_{j+1}}k_0$, with the values for $j = 1$ corresponding to the medium outside the scatterer (in our case $\varepsilon_1 = \mu_1 = 1$ and $k_1 = k_0$), those for $j = 2$ to the outermost layer (envelope) and so on (see Fig. 4.1).

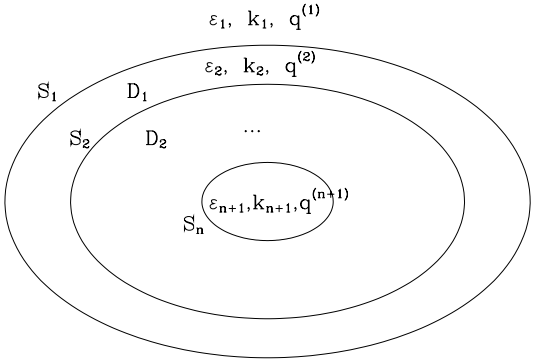

Fig. 4.1. A multilayered axisymmetric particle and the notations used.

The potentials of the jth layer in the axisymmetric problem (the same for the nonaxisymmetric problem) should be represented by the sums

$$q^{(j+1)} = q_{\rm R}^{(j+1)} + q_{\rm S}^{(j+1)}, \quad j = 1, 2, ..., n, \tag{4.43}$$

where the potentials $q_{\rm R}^{(j+1)}$ have no singularities (i.e. are regular) in the domain D_j inside the external boundary of the jth layer, while the potentials $q_{\rm S}^{(j+1)}$ having such singularities satisfy the radiation condition (4.12) where k_0 is replaced by k_{j+1}. Note that the potential of the incident field $q^{\rm in} = q_{\rm R}^{(1)}$, and the potential of the scattered field $q^{\rm sca} = q_{\rm S}^{(1)}$. Since the field in the innermost layer does not have singularities, one has $q_{\rm S}^{(n+1)} = 0$ and $q_{\rm R}^{(n+1)}$ is the potential of the internal field in the particle core.

The potentials $q_{\rm R}^{(j)}$, $q_{\rm S}^{(j)}$ introduced in such a way satisfy eqs (4.32) and hence their sum equal to $q^{(j)}$ also satisfies the same equations (see Farafonov *et al.* (2003), and references therein for more details)

$$\int_{S_j} \left\{ q^{(j+1)} \frac{\partial G_j}{\partial n} - \left[\frac{\varepsilon_j}{\varepsilon_{j+1}} \frac{\partial q^{(j+1)}}{\partial n} + \left(\frac{\varepsilon_j}{\varepsilon_{j+1}} - 1 \right) \frac{1}{\sqrt{(r')^2 + \left[(r')'_{\theta'}\right]^2}} \right.\right.$$
$$\left.\left. \times \left(1 - \frac{(r')'_{\theta'}}{r'} {\rm ctg}\theta' \right) q^{(j+1)} \right] G_j \right\} {\rm d}s' = \begin{cases} -q_{\rm R}^{(j)}(\boldsymbol{r}), & \boldsymbol{r} \in D_j, \\ q_{\rm S}^{(j)}(\boldsymbol{r}), & \boldsymbol{r} \in R^3 \setminus \bar{D}_j. \end{cases} \tag{4.44}$$

Here G_j is the Green function (4.15) with the wavenumber k_j instead of k_0.

The potentials $q_{\rm R}^{(j)}$ and $q_{\rm S}^{(j)}$ can be expanded in terms of the spherical wave functions as follows:

$$\begin{matrix} q_{\rm R}^{(j)} \\ q_{\rm S}^{(j)} \end{matrix} = \sum_{l=1}^{\infty} \begin{matrix} b_{{\rm R},l}^{(j)} \, j_l(k_j r) \\ b_{{\rm S},l}^{(j)} \, h_l^{(1)}(k_j r) \end{matrix} P_l^1(\cos\theta) \, \cos\varphi. \tag{4.45}$$

Substitution of these expansions into the integral equation (4.44) leads to the following system of linear algebraic equations:

$$\begin{aligned} &\boldsymbol{b}_{\rm R}^{(1)} = B_{\rm SR}^{(1)} \boldsymbol{b}_{\rm R}^{(2)} + B_{\rm SS}^{(1)} \boldsymbol{b}_{\rm S}^{(2)}, && \boldsymbol{b}_{\rm S}^{(1)} = B_{\rm RR}^{(1)} \boldsymbol{b}_{\rm R}^{(2)} + B_{\rm RS}^{(1)} \boldsymbol{b}_{\rm S}^{(2)}, \\ &\ldots && \ldots \\ &\boldsymbol{b}_{\rm R}^{(n-1)} = B_{\rm SR}^{(n-1)} \boldsymbol{b}_{\rm R}^{(n)} + B_{\rm SS}^{(n-1)} \boldsymbol{b}_{\rm S}^{(n)}, && \boldsymbol{b}_{\rm S}^{(n-1)} = B_{\rm RR}^{(n-1)} \boldsymbol{b}_{\rm R}^{(n)} + B_{\rm RS}^{(n-1)} \boldsymbol{b}_{\rm S}^{(n)}, \\ &\boldsymbol{b}_{\rm R}^{(n)} = B_{\rm SR}^{(n)} \boldsymbol{b}_{\rm R}^{(n+1)}, && \boldsymbol{b}_{\rm S}^{(n)} = B_{\rm RR}^{(n)} \boldsymbol{b}_{\rm R}^{(n+1)}, \end{aligned} \tag{4.46}$$

where $\boldsymbol{b}_{\rm R}^{(j)} = \{b_{{\rm R},l}^{(j)}\}_{l=1}^{\infty}$, and so on. The lower indices of the matrices $B_{\rm SR}$ indicate the radial functions ($h_n^{(1)}(x)$ for S and $j_n(x)$ for R) to be used in the expressions of the matrix elements that are generally similar to those given by eq. (4.38).

The system (4.46) allows one to obtain the relations

$$\boldsymbol{b}_{\rm R}^{(1)} = B_{\rm S} \, \boldsymbol{b}_{\rm R}^{(n+1)}, \quad \boldsymbol{b}_{\rm S}^{(1)} = B_{\rm R} \, \boldsymbol{b}_{\rm R}^{(n+1)}, \tag{4.47}$$

where

$$\begin{pmatrix} B_{\rm S} \\ B_{\rm R} \end{pmatrix} = \begin{pmatrix} B_{\rm SR}^{(1)} & B_{\rm SS}^{(1)} \\ B_{\rm RR}^{(1)} & B_{\rm RS}^{(1)} \end{pmatrix} \cdot \ \ldots \ \cdot \begin{pmatrix} B_{\rm SR}^{(n-1)} & B_{\rm SS}^{(n-1)} \\ B_{\rm RR}^{(n-1)} & B_{\rm RS}^{(n-1)} \end{pmatrix} \cdot \begin{pmatrix} B_{\rm SR}^{(n)} \\ B_{\rm RR}^{(n)} \end{pmatrix}. \quad (4.48)$$

Taking into account that $\boldsymbol{b}_{\rm R}^{(1)} = \boldsymbol{b}^{\rm in}$ and $\boldsymbol{b}_{\rm S}^{(1)} = \boldsymbol{b}^{\rm sca}$, one can get from eqs (4.47) the solution in the form typical of the EBCM

$$\boldsymbol{b}^{\rm sca} = B_{\rm R}(B_{\rm S})^{-1}\boldsymbol{b}^{\rm in}. \quad (4.49)$$

The nonaxisymmetric problem for layered particles can be solved in the same way as the axisymmetric one. As a result one gets equations similar to eqs (4.47)–(4.49), where the matrices $\hat{A}_{\rm RS}^{(j)}$ and others have a dimension twice as large as $B_{\rm RS}^{(j)}$.

The form of the solution based on eq. (4.48) is *in situ* iterative. Using the T-matrices, it is also possible to represent this solution in the recursive form

$$T^{(n+1)} = \left(B_{\rm RR}^{(0)} + B_{\rm RS}^{(0)}\,T^{(n)}\right)\left(B_{\rm SR}^{(0)} + B_{\rm SS}^{(0)}\,T^{(n)}\right)^{-1}, \quad (4.50)$$

where $T^{(n)}$ and $T^{(n+1)}$ are the matrices for a n-layered particle and a $(n+1)$-layered particle, respectively, $B^{(0)}$ are the matrices for an outer $(n+1)$th layer added as an envelope to the n-layered particle.

Equation (4.50) is analogous to that suggested earlier by Peterson and Ström (1974). It should be noted that the iterative form looks less elegant, nevertheless it may have a computational advantage – there is no need to invert the T-matrices n times, but only once.

The case of randomly oriented particles

For ensembles of such scatterers, the standard EBCM provides a fast way to determine the light scattering characteristics due to the possibility of their analytical averaging (see Mishchenko *et al.* (2000b) and references therein). As the described approach utilizes non-Debye potentials, which is equivalent to the use of nonorthogonal functions, the analytical averaging becomes generally less efficient. However, such an averaging gives an interesting result for cross-sections.

Let us denote the T-matrices for the axisymmetric (A) and nonaxisymmetric (N) problems for an incident plane wave ($\boldsymbol{b}_m^{\rm in} = 0$) as follows:

$$\boldsymbol{b}^{\rm sca} = T^{\rm A}\,\boldsymbol{b}^{\rm in}, \quad \boldsymbol{a}_m^{\rm sca} = T_m^{\rm N,a}\,\boldsymbol{a}_m^{\rm in}, \quad \boldsymbol{b}_m^{\rm sca} = T_m^{\rm N,b}\,\boldsymbol{a}_m^{\rm in}. \quad (4.51)$$

Substituting eqs (4.51) into the expressions for the extinction and scattering cross-sections which are similar to eqs (4.29) and (4.30) and averaging over all particle orientations, one obtains

$$\langle C_{\rm ext}\rangle = \frac{4\pi}{k_0^2}{\rm Re}\left\{\sum_{l=1}^{\infty} T_{ll}^{\rm A} + 2\sum_{m=1}^{\infty}\left[\sum_{l=m}^{\infty} T_{m,ll}^{\rm N,a} + 2\sum_{l,n=m}^{\infty} i^{n-l-1}\,T_{m,ln}^{\rm N,b}\,\zeta_{nl}^{(m)}\right]\right\}, \quad (4.52)$$

$$\langle C_{\rm sca}\rangle = \frac{4\pi}{k_0^2}\left\{\sum_{l,n=1}^{\infty}\frac{2n+1}{2l+1}\frac{l(l+1)}{n(n+1)}\left|T_{ln}^{\rm A}\right|^2 + 2{\rm Re}\sum_{m=1}^{\infty}\sum_{i,j,l,n=m}^{\infty} i^{i-j+n-l}\right.$$
$$\times\left[T_{m,li}^{\rm N,a}\,\omega_{ln}^{(m)}\,T_{m,nj}^{\rm N,a\ *} + iT_{m,li}^{\rm N,b}\,\kappa_{ln}^{(m)}\,T_{m,nj}^{\rm N,a\ *}\right.$$
$$\left.\left. - iT_{m,li}^{\rm N,a}\,\kappa_{nl}^{(m)}\,T_{m,nj}^{\rm N,b\ *} + T_{m,li}^{\rm N,b}\,\tau_{ln}^{(m)}\,T_{m,nj}^{\rm N,b\ *}\right]\Omega_{ij}^{(m)}\right\}, \tag{4.53}$$

where the asterisk means the complex conjugation and $\omega_{ln}^{(m)}$, $\kappa_{ln}^{(m)}$, $\tau_{ln}^{(m)}$, $\zeta_{ln}^{(m)}$ and $\Omega_{ln}^{(m)}$ are integrals of the products of the functions $P_l^m(x)$ and their first derivatives (Farafonov *et al.*, 2004). For the standard EBCM, $\langle C_{\rm ext}\rangle$ is equal to the trace of the T-matrix and $\langle C_{\rm sca}\rangle$ to the sum of squares of all T-matrix elements (Mishchenko *et al.*, 2000b).

It should be mentioned that one must distinguish $\langle C^{\rm TM,TE}\rangle$ actually given by eqs (4.52) and (4.53) and $\langle C\rangle^{\rm TM,TE}$ being the cross-sections for different modes of the polarized incident radiation. For the systems of axisymmetric particles considered, the physical meaning of the quantities leads to $\langle C\rangle^{\rm TM} = \langle C\rangle^{\rm TE}$, while $\langle C^{\rm TM}\rangle = \langle C\rangle^{\rm TM} + \Delta C \neq \langle C^{\rm TE}\rangle = \langle C\rangle^{\rm TE} - \Delta C$. For nonpolarized incident radiation $C = \frac{1}{2}(C^{\rm TM} + C^{\rm TE})$ and hence $\langle C\rangle = \langle\frac{1}{2}(C^{\rm TM} + C^{\rm TE})\rangle = \frac{1}{2}(\langle C^{\rm TM}\rangle + \langle C^{\rm TE}\rangle)$.

It is interesting that for nonpolarized incident radiation the extinction cross-section simplifies further (see Farafonov *et al.*, 2004 for more details)

$$\langle C_{\rm ext}\rangle = \frac{4\pi}{k_0^2}{\rm Re}\left[\sum_{l=1}^{\infty}\tilde{T}_{ll}^{\rm A} + 2\sum_{m=1}^{\infty}\sum_{l=m}^{\infty}\tilde{T}_{m,ll}^{\rm N,a}\right], \tag{4.54}$$

where $\tilde{T} = \frac{1}{2}(T^{\rm TE} + T^{\rm TM})$ and only the traces of the T-matrices are present. Thus the information on the scatterer involved in all the matrices $T_m^{\rm N,b}$ becomes unimportant for the averaged cross-section. Note that $T_m^{\rm N,b}$ relates the expansion coefficients for the Debye potential V of the scattered field with those for the potential U of the incident field.

4.3.3.3 Point matching method

In the framework of this method the boundary conditions (e.g. eqs (4.31) and (4.33)) are considered in a set of points $\{\boldsymbol{r}_s\}_{s=1}^{M}$ at the particle surface ($\boldsymbol{r}_s \in S$). If one treats an axisymmetric scatterer, all the points can be selected in the same plane containing the particle symmetry axis, so the solutions to both the axisymmetric and nonaxisymmetric problems become independent of the azimuthal angle.

In the basic versions of the method, two ways of solution are possible – one either demands the fulfilment of the boundary conditions in M selected points and uses the number of terms in the expansions N equal to M, or minimizes the residual of the boundary conditions. As the former way is to a large extent similar to the EBCM (Kahnert, 2003b), we discuss here only the latter one.

For the axisymmetric problem and the TM mode (the cases of the TE mode and the nonaxisymmetric problem are analogous), the residual is (see also eqs (4.31))

$$\Delta(\boldsymbol{b}^{\rm sca},\boldsymbol{b}^{\rm int}) = \sum_{s=1}^{M}\left\{ \left|q^{\rm in}+q^{\rm sca}-q^{\rm int}\right|^2 + \left|\frac{\partial(q^{\rm in}+q^{\rm sca}-\frac{1}{\varepsilon}q^{\rm int})}{\partial n} + \left(1-\frac{1}{\varepsilon}\right)\frac{1}{\sqrt{r^2+{r'_\theta}^2}}\left(1-\frac{r'_\theta}{r}{\rm ctg}\theta\right)q^{\rm int}\right|^2\right\}_{\boldsymbol{r}=\boldsymbol{r}_s}. \quad (4.55)$$

Minimization of $\Delta(\boldsymbol{b}^{\rm sca},\boldsymbol{b}^{\rm int})$ allows one to derive the unknown coefficients for the scattered ($\boldsymbol{b}^{\rm sca}$) and internal ($\boldsymbol{b}^{\rm int}$) fields from a system of $2N$ equations

$$B\ \boldsymbol{b}^{\rm sca} + D\ \boldsymbol{b}^{\rm int} = F\ \boldsymbol{b}^{\rm in}, \quad (4.56)$$

where the elements of the rectangle matrices B, D, F contain products of spherical functions and their first derivatives (Farafonov and Il'in, 2005b). For example, for $l, n \in [1, N]$ the elements of the matrix B are

$$\{B\}_{ln} = \sum_{s=1}^{M}\left\{ h_l^{(1)^*}(k_0 r_s)\, h_n^{(1)}(k_0 r_s)\, P_l^1(\cos\theta_s)\, P_n^1(\cos\theta_s) + \frac{1}{r_s^2+{r'_s}^2} \times\left[k_0\, r_s\, h_l^{(1)^{*\prime}}(k_0 r_s)\, P_l^1(\cos\theta_s) + \frac{r'_s}{r_s}\sin\theta_s\, h_l^{(1)^*}(k_0 r_s)\, P_l^{1\prime}(\cos\theta_s)\right] \times\left[k_0\, r_s\, h_l^{(1)^{\prime}}(k_0 r_s)\, P_l^1(\cos\theta_s) + \frac{r'_s}{r_s}\sin\theta_s\, h_l^{(1)}(k_0 r_s)\, P_l^{1\prime}(\cos\theta_s)\right]\right\}, \quad (4.57)$$

where $\boldsymbol{r}_s = (r_s, \theta_s, \varphi_s)$. The number of points M is usually taken essensially larger than N, e.g. $M = 2N$.

It should be noted that one can always select the positions of $\{\boldsymbol{r}_s\}_{s=1}^M$ so that the sums in the elements of B, D, F can be replaced by integrals (Farafonov and Il'in, 2005b). This is a convenient way to minimize calculations when one has no better strategy to select the matching points at the scatterer surface.

It is worth mentioning that for axisymmetric scatterers the codes for such different methods as the EBCM and the generalized PMM differ only by a few operators since the GPMM determines the same expansion coefficients using the same expansion functions as the EBCM.

Obviously, one can derive the matrices $T^{\rm A}, T_m^{\rm N,a}$ using the GPMM described above and utilize eqs (4.52)–(4.54) for analytical averaging of the cross-sections for randomly oriented particles.

It is interesting that the (G)PMM can also utilize the extended boundary conditions given by the surface integrals (4.32),(4.34) used in the EBCM. The Huygens principle says that if the field is known at a surface, it can be found everywhere. Taking that into account, one can consider eq. (4.32) in a set of points $\{\boldsymbol{r}_s\}_{s=1}^M$ located at a surface (for example, a sphere) lying completely

inside a scatterer. Then the coefficients of the internal field expansion can be determined by minimizing the residual

$$\Delta(\boldsymbol{b}^{\rm int}) = \sum_{s=1}^{M} \left\{ \left| \int_S \left(q^{\rm int}(\boldsymbol{r}) \frac{\partial G(\boldsymbol{r}, \boldsymbol{r}_s)}{\partial n} - \frac{\partial q^{\rm int}(\boldsymbol{r})}{\partial n} G(\boldsymbol{r}, \boldsymbol{r}_s) \right) {\rm d}s + q^{\rm in}(\boldsymbol{r}_s) \right|^2 \right\}. \tag{4.58}$$

The least-squares method gives a system of linear algebraic equations relative to the unknown coefficients

$$B\,\boldsymbol{b}^{\rm int} = \boldsymbol{f}, \tag{4.59}$$

where

$$\{B\}_{ln} = \sum_{s=1}^{M} \alpha_{ls}^{*}\, \alpha_{ns}, \quad f_l = \sum_{s=1}^{M} \alpha_{ls}\; q^{\rm in}(\boldsymbol{r}_s), \tag{4.60}$$

and

$$\alpha_{ls} \;=\; \int_S \left(j_{ls}(kr)\, P_1^l(\cos\theta)\, \frac{\partial G(\boldsymbol{r}, \boldsymbol{r}_s)}{\partial n} - \frac{\partial (j_{ls}(kr)\, P_1^l(\cos\theta))}{\partial n}\, G(\boldsymbol{r}, \boldsymbol{r}_s) \right) \times \cos\varphi \; {\rm d}s. \tag{4.61}$$

The use of the system (4.59) apparently has some advantages – its dimension is half the size of that of the system (4.56), and the integrals include the Green function $G(\boldsymbol{r}, \boldsymbol{r}_s)$ and should be well calculated. In eqs (4.60) one can replace the sum over s with an integral as has been suggested above.

With the known internal field expansion coefficients one can easily get the coefficient for the scattered field using the second part of eq. (4.32). Obviously, the same can be done for the nonaxisymmetric problem.

4.3.4 Applicability of the methods based on the spherical basis

Owing to the great importance and wide applications of the methods, their ranges of applicability have been studied for a long time (see Millar, 1973; Kahnert, 2003b for reviews). However, there are still many unclear points.

4.3.4.1 Separation of variables method for spheres

This method, giving an explicit solution for any sphere, is known to converge for all values of the parameters which are the radius to wavelength ratio x and the refractive index m. Improvements of the numerical implementations of the solution allow one to reach reliable results for huge values of the parameters (see, for example, Wolf and Voshchinnikov, 2004).

4.3.4.2 Extended boundary conditions method

In contrast to the SVM, the question of theoretical applicability of the EBCM is very complicated and one meets controversial conclusions till now. There have

been generally two opinions in the literature: (i) the method is mathematically correct for any (or only convex) particles; (ii) the method is correctly applicable only if the field expansions converge everywhere up to the scatterer boundary. The second assumption is known as the Rayleigh hypothesis (see Millar (1973) and Kahnert (2003b) for more details). However, both opinions are too simplified, and one should look at this problem from a new angle as has been done in the recent papers of Dallas (2000), Farafonov (2002), Il'in *et al.* (2004).

To start with, it should be noted that convergence of the expansions (4.22)–(4.25) with the coefficients derived within the method is tightly related to the solvability of the systems (4.37), (4.39), etc. that are utilized to find the expansion coefficients. Therefore, one needs to derive the asymptotic expressions for the matrix elements of these systems in the case of very large indices and to consider analytically the properties of the infinite systems (the required mathematical approach is described, for example, by Il'in *et al.*, 2004). One should look for conditions under which the infinite systems have the only solution that could be found by the reduction method or, in other words, when the solutions of the truncated systems one deals with in computations converge to the solution of the infinite systems.

The analysis shows that the ranges of the EBCM applicability in the cases of calculation of the scattered field in the near-field zone (a region close to a particle) and in the far-field zone (a region very far from a particle) differ in principle. Note that such often-used optical characteristics of scatterers as different cross-sections and the scattering matrix are just the characteristics of the scattered field in the far-field zone.

Near-field zone

The mathematically correct application of the EBCM to compute the scattered field at any point in the vicinity of a scatterer obviously needs convergence of the field expansions (with the coefficients derived by the method) everywhere up to the scatterer boundary. This occurs if and only if (see, for example, Apel'tsyn and Kyurkchan, 1990)

$$\max\{d_{\rm sca}\} < \min\{r(\theta)\} \quad \text{and} \quad \max\{r(\theta)\} < \min\{d_{\rm int}\}, \tag{4.62}$$

where $r(\theta)$ is the equation of the scatterer surface, $d_{\rm sca}$ and $d_{\rm int}$ are the distances from the coordinate origin to singularities of the analytic continuations of the scattered and internal fields. There are several methods for localizing these singularities for particles of different shapes (see, for example, Maystre and Cadilhac, 1985). As an example we show in Fig. 4.2 the location of the singularities for a so-called Chebyshev particle. These particles have the surface equation

$$r(\theta) = R\,(1 + \epsilon\, T_n(\theta))\,, \tag{4.63}$$

where R is the radius of an unperturbed sphere, ϵ the deformation parameter, and $T_n(\theta) = \cos(n\theta)$ the Chebyshev polynomial of the degree n.

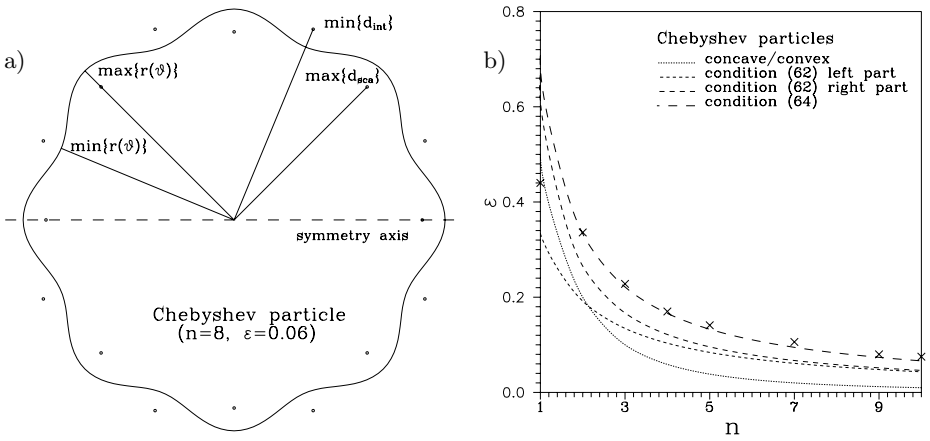

Fig. 4.2. Applicability of the EBCM to Chebyshev particles: (**a**) cross-section of a particle with $n = 8$ and $\epsilon = 0.06$, singularities (points) and all the quantities involved in the conditions (4.62), (4.64) are shown; (**b**) maximum values of ϵ for which these theoretical conditions are satisfied for different n. The dotted curve divides convex (below) and concave (above) particles. Crosses demonstrate the maximum values of ϵ for which convergence was observed in calculations of cross-sections.

Far-field zone

The condition for the applicability of the EBCM only in the far-field zone, i.e. for calculations of the far-field zone characteristics of the scattered field, is found to be weaker (Il'in *et al.*, 2004)

$$\max\{d_{\rm sca}\} < \min\{d_{\rm int}\}, \tag{4.64}$$

where $d_{\rm sca}$ and $d_{\rm int}$ are the same quantities as in eq. (4.62).

Let us consider two popular models of scatterers – spheroids and Chebyshev particles. For *spheroids*, there are no singularities of the analytic continuation of the internal field, i.e. $d_{\rm int} = \infty$, while the singularities of the analytic continuation of the scattered field are located in the foci (so for an oblate spheroid they form a ring in 3D space). Therefore, if the coordinate origin is at the particle center, then $d_{\rm sca} = d/2 = \sqrt{a^2 - b^2}$, where a, b are the particle semiaxis and d is the focal distance. From the conditions (4.62) it follows that the field expansions with the coefficients derived by the EBCM must converge everywhere, provided $d/2 < b$ or $a/b < \sqrt{2}$ (it is not difficult to realize that such an expansion of the internal field converges everywhere, while that of the scattered field should converge at distances larger than $d/2$ (see Colton and Kress, 1984). However, the solution given by the method should always converge when calculations of only far-field characteristics of spheroids are performed – the condition (4.64) is satisfied as $d < \infty$.

For *Chebyshev particles*, all four quantities involved in the conditions (4.62), (4.64) have finite values (their dependence on ϵ, n is considered, for example, by

Il'in *et al.* (2004)). The maximum values of ϵ, for which the first and second parts of the condition (4.62), the condition (4.64) and the condition of convexity of the particles are satisfied, are presented in Fig. 4.2 for different n. The crosses in this figure show the maximum values of ϵ for which the convergence of the EBCM computations of cross-sections was observed by Farafonov and Il'in (2005a). For other values of the particle size and refractive index, the results were similar, which leads to conclusion that the condition (4.64) is really the condition of convergence for such calculations.

It should be noted that the condition (4.64) was obtained for a special version of the EBCM designed for the far-field zone by Farafonov (2002) using ideas of Kyurkchan (1994, 2000). This version included as unknowns not the fields but their patterns as in the far-field zone ($|r| \gg R$) the scattered field being a spherical wave has the standard radial dependence given by $e^{-ik|r|}/ik|r|$ and therefore only the angular dependence of the scattered field is to be searched. Subsequently the systems, both in this special version and the usual version of the method, were demonstrated to be equivalent. It led to conclusion that the condition (4.64) is applicable to any calculations of the far-field characteristics by the EBCM.

The actions described above were completed only for the relatively simple (scalar) axisymmetric problem. For the nonaxisymmetric problem, analogous operations are much more complicated. At the moment it is found only that eq. (4.64) is the necessary condition of convergence. However, two facts allow one to accept it as the sufficient condition as well: (i) the behavior (convergence) of the solutions to the axisymmetric and nonaxisymmetric problems always is very similar; (ii) nontrivial numerical tests for Chebyshev particles of different shape, size and composition confirmed completely this assumption.

At least, two points should be emphasized. First, the results obtained above for our version of the EBCM must be valid for all other versions of the EBCM in which single expansions of the fields are used and their coefficients are determined from the surface integral equations. It is also easy to expand this consideration on the multiple expansions used, for example, by Iskander *et al.* (1983). If one extends the SVM approach to scatterers whose shape does not coincide with a coordinate hypersurface in the way suggested in section 2, the obtained conditions very probably will be the necessary ones for convergence.

Secondly, the EBCM is now applied to such particles as disks, cylinders, prisms, pyramids, etc. (see, for example, Kahnert *et al.*, 2001a). Formally any application of EBCM-like methods to particles with sharp edges would be impossible, if one could calculate the surface integrals exactly. At the edges being nonanalytic points as the first derivative of $r(\theta)$ is not continuous, the scattered and internal fields have singularities. As a result the conditions (4.62) and (4.64) are not fulfilled – instead of inequalities in the conditions one has equality of the involved quantities.

However, in practice the surface integrals are computed numerically. It is generally equivalent to the replacement of a scatterer with sharp edges with a smooth surface body, which makes the convergence of EBCM calculations possible in principle (see Farafonov and Il'in (2005a) for more details).

4.3.4.3 Generalized point matching method

We do not discuss the applicability of the ordinary (not generalized) PMM. It should be close to that of the EBCM which we have considered above, but requires a special investigation.

The situation with applicability of the generalized PMM is very simple. The matrix of the system (4.56) that is solved here to determine the expansion coefficients is obviously positively determined (Ramm, 1982). Therefore, the method must have the only solution for any parameter values. Indeed, calculations show that solution given by the method always converges, but sometimes (in particular for scatterers of large eccentricity) its accuracy can be low (see, for example, Farafonov and Il'in, 2005b).

In Fig. 4.3 we show the convergence of the GPMM and EBCM with a growing number of terms kept in the expansions for several spheroids and Chebyshev particles. The accuracy of the GPMM calculations is well seen to drop rapidly with an increase of the spheroid aspect ratio a/b (the accuracy of the EBCM also decreases but much more slowly). In contrast, for the concave Chebyshev particles the EBCM quickly diverges with growing ϵ, while the GPMM is able to provide a solution of satisfactory accuracy.

It should be noted that for a fixed number N of the terms considered in the expansions, both the GPMM and EBCM determine the same coefficients, for example, for the axisymmetric problem $\{b_n^{\mathrm{sca}}\}_{n=1}^{N}$. If the EBCM solution converges, it gives the coefficients (we denote them by b_n^{EBCM}) that are practically independent of N. The coefficients derived in the GPMM essentially depend on

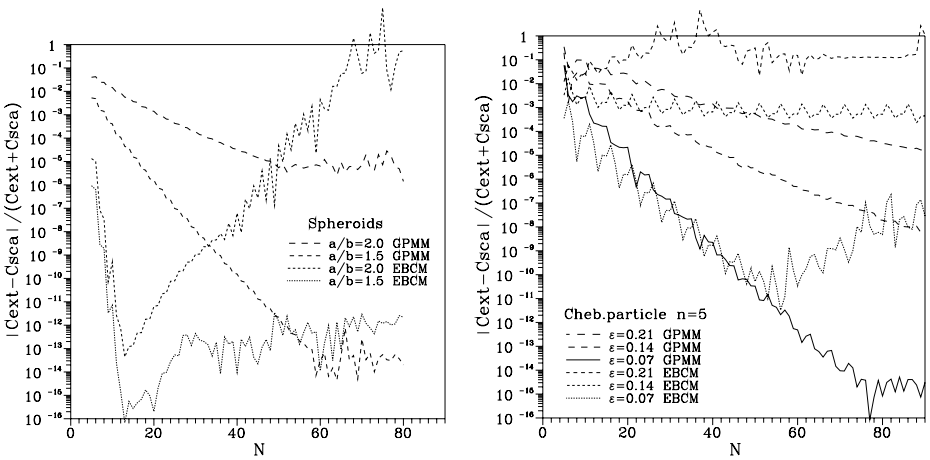

Fig. 4.3. Convergence of the EBCM and GPMM solutions – the relative difference of the cross-sections in dependence on N the number of terms kept in the potential expansions for (left panel) prolate spheroids with $a/b = 1.5$, 2 and (right panel) Chebyshev particles with $n = 5$ and $\epsilon = 0.07$, 0.14, 0.21. The refractive index $m = 1.5$, the size parameter $x_{\mathrm{v}} = 2\pi r_{\mathrm{v}}/\lambda = 1$ (r_{v} is the radius of a sphere of the equal volume), the axial incidence of radiation.

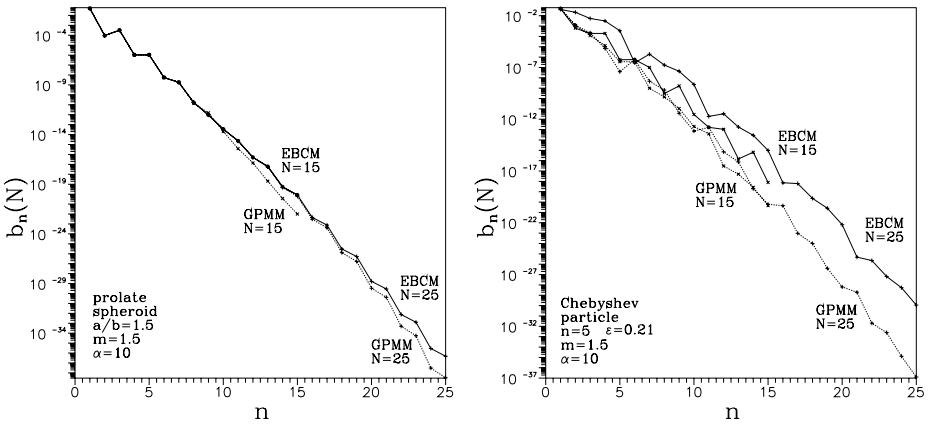

Fig. 4.4. The coefficients $b_n^{\rm sca}$ obtained with the EBCM and GPMM with the number of terms kept in the potential expansions $N = 15$ and 25 for (left panel) prolate spheroid with $a/b = 1.5$, and (right panel) Chebyshev particles with $n = 5$ and $\epsilon = 0.21$. 'The refractive index $m = 1.5$, the size parameter $x_{\rm v} = 1$, the incidence angle $\alpha = 10^\circ$.

N and with $N \to \infty$ one has $b_n^{\rm GPMM}(N) \to b_n^{\rm EBCM}$ (Millar, 1973). From the left panel of Fig. 4.4 we see that for any N only a few last ($n \sim N$) coefficients $b_n^{\rm GPMM}(N)$ differ essentially from $b_n^{\rm EBCM}$.

A natural question arises: what occurs when the EBCM solution diverges? This case is illustrated in the right panel of Fig. 4.4 where we consider the Chebyshev particles for which the condition (4.64) is not satisfied. The divergences of the EBCM solution is well seen by comparison of the coefficients obtained for $N = 15$ and 25. The GPMM solution converges, but the convergence is slow and obviously one needs to take the value of N much larger than 25 to get results with good accuracy. It is just what Fig. 4.3 has demonstrated.

The second scheme of the GPMM presented by eqs (4.58)–(4.61) has the positively determined matrix as well as the first scheme. So the theoretical applicability ranges of both schemes should be the same. Accuracy and the real applicability range of the second scheme is not quite clear, and a special consideration is required.

4.4 Solutions using the spheroidal wave functions

For spheroids and some other (axisymmetric) particles, it can be more efficient to expand the fields/potentials in terms of the spheroidal wave functions rather than the spherical ones. This way of solution to the light scattering problem requires its presentation in a form which in some aspects differs from that used in the previous section.

4.4.1 Features of the problem formulation

To start with, the problem should be formulated by using the spheroidal coordinates.

4.4.1.1 Spheroidal coordinate system

For an axisymmetric scatterer, it is convenient to connect the spheroidal system (ξ, η, φ) with the Cartesian system (x, y, z), whose z-axis coincides with the symmetry axis of the particle, as follows:

$$\begin{aligned} x &= \frac{d}{2}\,(\xi^2 \mp 1)^{1/2}(1-\eta^2)^{1/2}\cos\varphi, \\ y &= \frac{d}{2}\,(\xi^2 \mp 1)^{1/2}(1-\eta^2)^{1/2}\sin\varphi, \\ z &= \frac{d}{2}\,\xi\,\eta, \end{aligned} \tag{4.65}$$

where d is a parameter. For the prolate spheroidal coordinates $\xi \in [1, \infty)$ (see upper sign) and for the oblate ones $\xi \in [0, \infty)$ (see lower sign), $\eta \in [-1, 1]$, $\varphi \in [0, 2\pi)$. Further, we replace $\xi^2 \mp 1$ with $\xi^2 - f$, where for the prolate system $f = 1$ and for oblate one $f = -1$.

Then the surface equation of the particle becomes very simple (cf. eq. (4.17))

$$\xi = \xi(\eta). \tag{4.66}$$

Note that if one considers a spheroid, it is reasonable to make d equal to its focal distance (then the equation comes to $\xi = \text{const}$).

The light scattering problem formulation naturally includes the same equations and boundary conditions as earlier in section 4.2, but in contrast to section 4.3 they should be formulated by using the spheroidal coordinates. The new form of the equations can be found in standard textbooks; the boundary conditions written in these coordinates are considered below.

To solve the problem we use the same scalar potentials p, q, U, V as earlier, but naturally expand them in another way.

4.4.1.2 Expansions of the potentials

The potentials p, q are expanded in terms of the spheroidal wave functions with the index $m = 1$ because the potential dependence on the azimuthal angle φ is given explicitly by $\cos\varphi$. For the prolate spheroidal coordinates, one has

$$\begin{matrix} p^{\text{sca}} \\ q^{\text{sca}} \end{matrix} = \sum_{l=1}^{\infty} \begin{matrix} a_l^{\text{sca}} \\ b_l^{\text{sca}} \end{matrix} R_{1l}^{(3)}(c_1, \xi)\; S_{1l}(c_1, \eta)\; \cos\varphi, \tag{4.67}$$

$$\begin{matrix} p^{\text{int}} \\ q^{\text{int}} \end{matrix} = \sum_{l=1}^{\infty} \begin{matrix} a_l^{\text{int}} \\ b_l^{\text{int}} \end{matrix} R_{1l}^{(1)}(c_2, \xi)\; S_{1l}(c_2, \eta)\; \cos\varphi, \tag{4.68}$$

where $c_1 = k_0 \frac{d}{2}$, $c_2 = k \frac{d}{2}$, $S_{ml}(c,\eta)$ are the prolate angular spheroidal functions with the normalization factors $N_{ml}(c)$ (Komarov *et al.*, 1976), $R_{ml}^{(1),(3)}(c,\xi)$ are the prolate radial spheroidal functions of the first or third kinds. The properties of the spheroidal functions are well known (see, for example, Flammer, 1957), but the methods of their calculations are still being developed (see section 4.2).

The expansions of $p^{\rm in}, q^{\rm in}$ are similar to those of $p^{\rm int}, q^{\rm int}$ and use the coefficients $a_l^{\rm in}$,$b_l^{\rm in}$ and c_1 instead of c_2. For a plane wave,

$$\begin{aligned} a_l^{\rm in} &= 0, \quad b_l^{\rm in} = 2i^l\, N_{1l}^{-2}(c_1)\, S_{1l}(c_1,\cos\alpha), \qquad \text{for the TM mode,} \\ a_l^{\rm in} &= -2i^l\, N_{1l}^{-2}(c_1)\, S_{1l}(c_1,\cos\alpha), \quad b_l^{\rm in} = 0, \qquad \text{for the TE mode.} \end{aligned} \tag{4.69}$$

The expansions of the potentials U and V are

$$\begin{matrix} U^{\rm sca} \\ V^{\rm sca} \end{matrix} = \sum_{m=1}^{\infty} \sum_{l=m}^{\infty} \begin{matrix} a_{ml}^{\rm sca} \\ b_{ml}^{\rm sca} \end{matrix} R_{ml}^{(3)}(c_1,\xi)\; S_{ml}(c_1,\eta)\; \cos m\varphi, \tag{4.70}$$

$$\begin{matrix} U^{\rm int} \\ V^{\rm int} \end{matrix} = \sum_{m=1}^{\infty} \sum_{l=m}^{\infty} \begin{matrix} a_{ml}^{\rm int} \\ b_{ml}^{\rm int} \end{matrix} R_{ml}^{(1)}(c_2,\xi)\; S_{ml}(c_2,\eta)\; \cos m\varphi. \tag{4.71}$$

To expand $U^{\rm in}, V^{\rm in}$, one should use the expressions for $U^{\rm int}, V^{\rm int}$ but with the coefficients $a_{ml}^{\rm in}$,$b_{ml}^{\rm in}$ and c_1 instead of c_2. For a plane wave,

$$a_{ml}^{\rm in} = -\frac{4i^{l-1} N_{ml}^{-2}(c_1)\, S_{ml}(c_1,\cos\alpha)}{k_0 \sin\alpha}, \quad b_{ml}^{\rm in} = 0. \tag{4.72}$$

The Green function is expanded as follows (Komarov *et al.*, 1976):

$$\begin{aligned} G(\boldsymbol{r},\boldsymbol{r}') &= \frac{ik_0}{2\pi} \sum_{m=0}^{\infty} \sum_{l=m}^{\infty} (2-\delta_m^0) N_{ml}^{-2}(c)\, R_{ml}^{(1)}(c,\xi_<)\, R_{ml}^{(3)}(c,\xi_>) \\ &\quad \times S_{ml}(c,\eta)\, S_{ml}(c,\eta')\, \cos m(\varphi-\varphi'), \end{aligned} \tag{4.73}$$

where $\xi_< = \min(\xi,\xi')$ and $\xi_> = \max(\xi,\xi')$.

For the oblate spheroidal coordinates, the expansions are the same after the replacements $c \to -ic$ and $\xi \to i\xi$, and correspondingly the oblate spheroidal functions should be used.

Thus, the potentials are represented by linear combinations of solutions to the scalar Helmholtz (wave) equation, and the unknown expansion coefficients ($a_l^{\rm sca}, a_{ml}^{\rm sca}$, etc.) should be determined from the boundary conditions.

4.4.1.3 Boundary conditions

Axisymmetric problem

The boundary conditions (4.11) for the potential q (the TM mode) are expressed as follows (cf. eq. (4.31)):

$$\left.\begin{aligned} q^{\rm in}+q^{\rm sca} &= q^{\rm int},\\ \tfrac{\partial}{\partial n}(q^{\rm in}+q^{\rm sca}) &= \tfrac{1}{\varepsilon}\tfrac{\partial q^{\rm int}}{\partial n}+\left(\tfrac{1}{\varepsilon}-1\right)\tfrac{(\xi+\eta\xi'_\eta)\frac{d}{2}}{h_\varphi\sqrt{h_\eta^2+{\xi'_\eta}^2h_\xi^2}}q^{\rm int}, \end{aligned}\right\}_{\boldsymbol{r}\in S} \tag{4.74}$$

where S is the surface of a scatterer, h_ξ, h_η, h_φ are the metric coefficients

$$\mathrm{d}s = h_\varphi\sqrt{h_\eta^2+{\xi'_\eta}^2h_\xi^2}\,\mathrm{d}\eta\,\mathrm{d}\varphi.$$

The boundary conditions in the form of surface integrals are (cf. eqs (4.32))

$$\begin{aligned} &\int_0^{2\pi}\int_{-1}^{1}\left\{q^{\rm int}\tfrac{\partial G}{\partial n}-\left[\tfrac{1}{\varepsilon}\tfrac{\partial q^{\rm int}}{\partial n}+\left(\tfrac{1}{\varepsilon}-1\right)\tfrac{(\xi+\eta\xi'_\eta)\frac{d}{2}}{h_\varphi\sqrt{h_\eta^2+{\xi'_\eta}^2h_\xi^2}}q^{\rm int}\right]G\right\}\mathrm{d}s'\\ &\qquad=\begin{cases}-q^{\rm in}(\boldsymbol{r}), & \boldsymbol{r}\in D,\\ q^{\rm sca}(\boldsymbol{r}), & \boldsymbol{r}\in R^3\setminus\bar{D}.\end{cases} \end{aligned} \tag{4.75}$$

The conditions for the potentials p (the TE mode) are similar except for the change of ε for μ.

Nonaxisymmetric problem

For the TM mode, the boundary conditions (4.11) transform to (cf. eq. (4.33))

$$\left.\begin{aligned} U^{\rm in}+U^{\rm sca} &= U^{\rm int},\\ V^{\rm sca} &= V^{\rm int},\\ \tfrac{\partial}{\partial n}(U^{\rm in}+U^{\rm sca}) &= \tfrac{\partial U^{\rm int}}{\partial n}-\left(\tfrac{1}{\varepsilon}-1\right)\tfrac{C_1}{\sqrt{h_\eta^2+{\xi'_\eta}^2h_\xi^2}}\Big[\tfrac{h_\eta}{h_\xi}\tfrac{\partial}{\partial\xi}(\eta U^{\rm int}\\ &\quad+\tfrac{d}{2}\xi V^{\rm int})+\tfrac{h_\xi}{h_\eta}\tfrac{\partial}{\partial\eta}(\xi U^{\rm int}+\tfrac{d}{2}f\eta V^{\rm int})\Big],\\ \tfrac{\partial V^{\rm sca}}{\partial n} &= \tfrac{\partial V^{\rm int}}{\partial n}+\left(\tfrac{1}{\varepsilon}-1\right)\tfrac{C_2}{\sqrt{h_\eta^2+{\xi'_\eta}^2h_\xi^2}}\Big[\tfrac{h_\eta}{h_\xi}\tfrac{\partial}{\partial\xi}(\eta U^{\rm int}\\ &\quad+\tfrac{d}{2}\xi V^{\rm int})+\tfrac{h_\xi}{h_\eta}\tfrac{\partial}{\partial\eta}(\xi U^{\rm int}+\tfrac{d}{2}f\eta V^{\rm int})\Big], \end{aligned}\right\}_{\boldsymbol{r}\in S} \tag{4.76}$$

where $C_1=(\xi\xi'_\eta+f\eta)/(\xi^2-f\eta^2)$, $C_2=(\xi+\eta\xi'_\eta)/(\xi^2-f\eta^2)$, and for simplicity we again assume that $\mu=1$. The case of the TE mode is analogous.

4.4.1.4 Methods of solution

All the methods discussed in section 4.3, i.e. the SVM, EBCM, and PMM, can be applied here as well. The only difference is that equations in the boundary conditions are naturally multiplied by the angular spheroidal functions. Completeness and orthogonality of these functions allows one to get systems of linear algebraic equations relative to the unknown expansion coefficients. When the coefficients are determined, various characteristics of the scattered (and internal) radiation are easily found.

4.4.1.5 Scattering characteristics

In most applications it is necessary to derive characteristics of the scattered radiation in the far-field zone, where $r \to \infty$ and hence $\xi \to \infty$, $\eta \to \cos\theta$, $\boldsymbol{i}_\eta \to -\boldsymbol{i}_\theta$. Using the representation of the fields via the potentials (see section 4.2) and the asymptotics of the radial spheroidal functions for a large argument, one can get for the TM mode

$$\begin{aligned}\boldsymbol{E}^{\rm sca} &= \frac{e^{ik_0 r}}{-ik_0 r}\boldsymbol{A} = \frac{e^{ik_0 r}}{-ik_0 r}\left\{-\sum_{m=1}^{\infty}\sum_{l=m}^{\infty} i^{-l}\, b_{ml}^{\rm sca}\,\frac{mS_{ml}(c_1,\cos\theta)}{\sin\theta}\,\sin m\varphi\;\boldsymbol{i}_\varphi\right.\\ &+\left[-\sum_{l=1}^{\infty} i^{-l}\, b_l^{\rm sca}\, S_{1l}(c_1,\cos\theta)+\sum_{m=1}^{\infty}\sum_{l=m}^{\infty} i^{1-l}\,(k_0\, a_{ml}^{\rm sca}\, S_{ml}(c_1,\cos\theta)\right.\\ &\left.\left.+i\, b_{ml}^{\rm sca}\, S'_{ml}(c_1,\cos\theta))\sin\theta\,\cos m\varphi\right]\,\boldsymbol{i}_\theta\right\} \qquad (4.77)\end{aligned}$$

and for the TE mode

$$\begin{aligned}\boldsymbol{E}^{\rm sca} &= \frac{e^{ik_0 r}}{-ik_0 r}\boldsymbol{A} = \frac{e^{ik_0 r}}{-ik_0 r}\left\{\left[-\sum_{l=1}^{\infty} i^{-l}\, a_l^{\rm sca}\, S_{1l}(c_1,\cos\theta)+\sum_{m=1}^{\infty}\sum_{l=m}^{\infty} i^{1-l}\right.\right.\\ &\left.\times\,(k_0\, a_{ml}^{\rm sca}\, S_{ml}(c_1,\cos\theta)+i\, b_{ml}^{\rm sca}\, S'_{ml}(c_1,\cos\theta))\sin\theta\,\cos m\varphi\right]\,\boldsymbol{i}_\varphi\\ &\left.+\sum_{m=1}^{\infty}\sum_{l=m}^{\infty} i^{-l}\, b_{ml}^{\rm sca}\,\frac{mS_{ml}(c_1,\cos\theta)}{\sin\theta}\sin m\varphi\;\boldsymbol{i}_\theta\right\}. \qquad (4.78)\end{aligned}$$

The elements of the amplitude matrix A_i (see section 4.3.1) are equal to the φ- and θ-components of the vector amplitude $\boldsymbol{A}$ and are well seen in eqs (4.77) and (4.78). The amplitude matrix allows other characteristics of the scattered radiation to be derived (Bohren and Huffman, 1983). For example, the extinction and scattering cross-sections for the TM mode are

$$\begin{aligned}C_{\rm ext} &= \frac{4\pi}{k_0^2}\,{\rm Re}\,\left[\boldsymbol{A},\boldsymbol{i}_{\rm TM}^{\rm in}\right]_{\Theta=0^\circ}\\ &= \frac{4\pi}{k_0^2}\,{\rm Re}\,\left[-\sum_{l=1}^{\infty} i^{-l}\, b_l^{\rm sca}\, S_{1l}\,(c_1,\cos\alpha)+\sum_{m=1}^{\infty}\sum_{l=m}^{\infty} i^{1-l}\right. \qquad (4.79)\\ &\left.\times\left(k_0\, a_{ml}^{\rm sca}\, S_{ml}\,(c_1,\cos\alpha)+\, i\, b_{ml}^{\rm sca}\, S'_{ml}\,(c_1,\cos\alpha)\right)\sin\alpha\right],\end{aligned}$$

$$C_{\rm sca} = \frac{1}{k_0^2}\int\int_{4\pi}|\boldsymbol{A}|^2{\rm d}\Omega$$
$$= \frac{\pi}{k_0^2}\left\{2\sum_{l=1}^{\infty}|b_l^{\rm sca}|^2N_{1l}^2(c_1)+{\rm Re}\sum_{m=1}^{\infty}\sum_{l=m}^{\infty}\sum_{n=m}^{\infty}i^{(n-l)}\left[k_0^2\,a_{ml}^{\rm sca}\,a_{mn}^{\rm sca^*}\,\tilde{\omega}_{ln}^{(m)}+ik_0\right.\right.$$
$$\left.\left.\times\left(b_{ml}^{\rm sca}\,a_{mn}^{\rm sca^*}\,\tilde{\kappa}_{ln}^{(m)}-a_{ml}^{\rm sca}\,b_{mn}^{\rm sca^*}\,\tilde{\kappa}_{nl}^{(m)}\right)+b_{ml}^{\rm sca}\,b_{mn}^{\rm sca^*}\,\tilde{\tau}_{ln}^{(m)}\right]N_{ml}(c_1)N_{mn}(c_1)\right\}, \tag{4.80}$$

where Θ is the scattering angle, i.e. the angle between the directions of propagation of the incident radiation and the scattered one, the vector $\boldsymbol{i}^{\rm in}$ shows the direction of polarization of the incident radiation, Ω is the solid angle, and $S'_{ml}(c,\cos\alpha)$ the derivative of the spheroidal function, $\tilde{\omega}_{ln}^{(m)}$, $\tilde{\kappa}_{ln}^{(m)}$, $\tilde{\tau}_{ln}^{(m)}$ are integrals of products of the angular spheroidal functions (see Voshchinnikov and Farafonov (1993) for more details).

For *randomly oriented particles*, one can easily get the 'spheroidal' T-matrices (the matrices relating the coefficients of expansions in terms of the spheroidal functions) by any method and use analogs to eqs (4.52)–(4.54) for analytical averaging of the cross-sections. Correspondingly, $\tilde{\zeta}_{ln}^{(m)}, \tilde{\Omega}_{ln}^{(m)}$ and other integrals should include the spheroidal functions instead of spherical ones (Farafonov *et al.*, 2004).

Besides, there are other ways of the analytical averaging. Following the idea of Schulz *et al.* (1998), one can transform the spheroidal T-matrices into the corresponding spherical ones and use eqs (4.52)–(4.54) without any change. A more complicated but useful way is to transform the spheroidal T-matrices into the spherical ones utilized in the standard EBCM and then to use all the advantages of the standard analytical averaging procedure (see, for example, Mishchenko *et al.*, 2002).

One should also keep in mind that when high accuracy is not required, a simple numerical averaging of cross-sections may be as fast as the analytical one. For the methods under consideration, the main part of computational time is spent on the calculations of the elements of the matrices $\hat{A}, B, \hat{E}, F$, etc. The particle orientation appears only in the right-hand-side vectors $\hat{\boldsymbol{a}}^{\rm in}, \boldsymbol{b}^{\rm in}$, and so it does not take much time to compute these vectors, to multiply them by the earlier calculated matrix $\hat{E}$ or F and to get the solutions for different scatterer orientations. Our experience with the SVM for spheroids shows that the numerical averaging of cross-section gives results to an accuracy of 3–4 digits and it takes a time nearly equal to that required for one orientation calculation.

In Fig. 4.5 we give a few examples of analytically averaged dimensionless cross-sections of randomly oriented spheroids calculated with the double-precision SVM and EBCM codes. Note that the numerical averaging is inapplicable to computations of the absorption cross-sections for particles of materials having the imaginary part of the refractive index smaller than 10^{-3}, i.e. for most dielectrics in the visual. Results of extensive calculations of different optical characteristics of randomly oriented spheroids, cylinders, etc. are presented in the book of Mishchenko *et al.* (2002) and papers cited there.

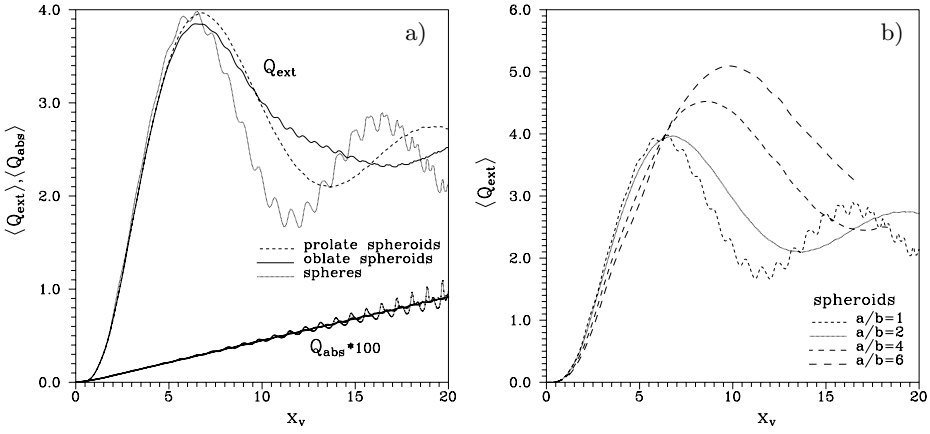

Fig. 4.5. Dimensionless cross-sections $\langle Q\rangle = \langle C\rangle/\pi r_{\rm v}^2$ for randomly oriented spheroids of different aspect ratio a/b and size parameter $x_{\rm v} = 2\pi r_{\rm v}/\lambda$, where r_v is the radius of spheres having the same volume as spheroids: (a) spheres, prolate and oblate spheroids with $a/b = 2$; (b) spheres and prolate spheroids with $a/b = 2, 4, 6$. The refractive index is $m = 1.33 + 0.0001i$.

4.4.2 Some details of the methods

The use of the spheroidal coordinates and functions instead of the spherical ones does not make the methods under consideration much more complex in principle than the standard EBCM (see, for example, Barber and Hill, 1990). Provided the problem of computations of the spheroidal functions is solved, other calculations are not very complicated, though the equations are lengthy.

4.4.2.1 Separation of variables method for spheroids

To find the expansion coefficients for the potential q by this method, one has to substitute the expansions (4.67) and (4.68) into the boundary conditions (4.74). Multiplying the equations by $N_{1n}^{-2}(c_2)\, S_{1n}(c_2,\eta)\, \cos\varphi$ and integrating them over η from -1 to 1 and φ from 0 to 2π, one can get an infinite system of linear algebraic equations relative to the unknown expansion coefficients (Voshchinnikov and Farafonov, 1993). For instance, for a prolate spheroid having the surface equation $\xi = \xi_0$ and the TM mode, one gets

$$B\ \underline{\boldsymbol{b}}^{\rm sca} \ = \ F\ \underline{\boldsymbol{b}}^{\rm in}, \tag{4.81}$$

where the vectors containing the expansion coefficients and the radial spheroidal functions are

$$\underline{\boldsymbol{b}}^{\rm sca} \ = \ \{b_l^{\rm sca}\, R_{1l}^{(3)}(c_1,\xi_0)\, N_{1l}(c_1)\}_{l=1}^{\infty}, \tag{4.82}$$

$$\underline{\boldsymbol{b}}^{\rm in} \ = \ \{b_l^{\rm in}\, R_{1l}^{(1)}(c_1,\xi_0)\, N_{1l}(c_1)\}_{l=1}^{\infty}, \tag{4.83}$$

and

$$B = \xi_0 (\varepsilon - 1) \Delta_1 + \left(\xi_0^2 - f\right) (\varepsilon \Delta_1 R_{1,1} - R_{1,2} \Delta_1), \tag{4.84}$$

$$F = -\xi_0 (\varepsilon - 1) \Delta_1 - \left(\xi_0^2 - f\right) (\varepsilon \Delta_1 R_{1,0} - R_{1,2} \Delta_1). \tag{4.85}$$

Here one has the diagonal matrices including the radial spheroidal functions and their first derivatives

$$\begin{aligned} R_{m,0} &= \left\{ R_{ml}^{(1)\prime}(c_1, \xi_0) / R_{ml}^{(1)}(c_1, \xi_0)\, \delta_l^n \right\}_{l,n=m}^{\infty}, \\ R_{m,1} &= \left\{ R_{ml}^{(3)\prime}(c_1, \xi_0) / R_{ml}^{(3)}(c_1, \xi_0)\, \delta_l^n \right\}_{l,n=m}^{\infty}, \\ R_{m,2} &= \left\{ R_{ml}^{(1)\prime}(c_2, \xi_0) / R_{ml}^{(1)}(c_2, \xi_0)\, \delta_l^n \right\}_{l,n=m}^{\infty}, \end{aligned} \tag{4.86}$$

and the matrix with integrals of the angular spheroidal functions $\Delta_m = \left\{ \tilde{\delta}_{ln}^{(m)}(c_1, c_2) \right\}_{l,n=m}^{\infty}$, where

$$\begin{aligned} \tilde{\delta}_{ln}^{(m)}(c_1, c_2) &= N_{ml}^{-1}(c_1)\, N_{mn}^{-1}(c_2) \int_{-1}^{1} S_{ml}(c_1, \eta)\, S_{mn}(c_2, \eta)\, \mathrm{d}\eta \\ &= N_{ml}^{-1}(c_1)\, N_{mn}^{-1}(c_2) \sum_{r=0,1}^{\infty}{}' d_r^{ml}(c_1)\, d_r^{mn}(c_2) \frac{2}{2r + 2m + 1} \frac{(r + 2m)!}{(r!)}. \end{aligned} \tag{4.87}$$

The integral is expressed using the coefficients of expansion of the angular spheroidal functions in terms of the associated Legendre functions

$$S_{ml}(c, \eta) = \sum_{r=0,1}^{\infty}{}' d_r^{ml}(c)\, P_{m+r}^{m}(\eta), \tag{4.88}$$

where the prime at the sum means summation over either even or odd r in the dependence on the evenness of $(l - m)$.

For the TE mode, ε must be replaced by μ. For an oblate spheroid, one should make the changes $c \to -ic$ and $\xi \to i\xi$, apply $f = -1$ and use the oblate spheroidal wave functions.

The nonaxisymmetric problem is solved similarly. The exclusion of the internal field from the third and fourth equations of eqs (4.76) using the first and second ones gives the following system for the TM mode and each m value

$$\hat{A}_m\, \hat{\underline{\boldsymbol{a}}}_m^{\mathrm{sca}} = \hat{E}_m\, \hat{\underline{\boldsymbol{a}}}_m^{\mathrm{in}}, \tag{4.89}$$

where

$$\hat{A}_m = \begin{pmatrix} A_{11}^{(m)} & A_{12}^{(m)} \\ A_{21}^{(m)} & A_{22}^{(m)} \end{pmatrix}, \ \hat{\underline{\boldsymbol{a}}}_m^{\mathrm{sca}} = \begin{pmatrix} \underline{\boldsymbol{a}}_m^{\mathrm{sca}} \\ \underline{\boldsymbol{b}}_m^{\mathrm{sca}} \end{pmatrix}, \ \hat{E}_m = \begin{pmatrix} E_{11}^{(m)} & E_{12}^{(m)} \\ E_{21}^{(m)} & E_{22}^{(m)} \end{pmatrix}, \ \hat{\underline{\boldsymbol{a}}}_m^{\mathrm{in}} = \begin{pmatrix} \underline{\boldsymbol{a}}_m^{\mathrm{in}} \\ 0 \end{pmatrix}, \tag{4.90}$$

the vectors including the unknown coefficients are (a plane wave is considered, hence $\underline{\boldsymbol{b}}_m^{\rm in} = 0$)

$$\underline{\boldsymbol{a}}_m^{\rm sca} = \{k_0\, a_{ml}^{\rm sca}\, R_{ml}^{(3)}(c_1,\xi_0)\, N_{ml}(c_1)\}_{l=m}^{\infty}, \tag{4.91}$$

$$\underline{\boldsymbol{b}}_m^{\rm sca} = \{c_1\, b_{ml}^{\rm sca}\, R_{ml}^{(3)}(c_1,\xi_0)\, N_{ml}(c_1)\}_{l=m}^{\infty}, \tag{4.92}$$

$$\underline{\boldsymbol{a}}_m^{\rm in} = \{k_0\, a_{ml}^{\rm in}\, R_{ml}^{(1)}(c_1,\xi_0)\, N_{ml}(c_1)\}_{l=m}^{\infty}, \tag{4.93}$$

and the blocks of the matrices $\hat{A}_m, \hat{E}_m$ are

$$\begin{aligned}
A_{11}^{(m)} &= \xi_0 \left(R_{m,2}\Delta_m - \Delta_m R_{m,1}\right), \\
A_{12}^{(m)} &= f\Gamma_m \left(R_{m,2}\Delta_m - \Delta_m R_{m,1}\right), \\
A_{21}^{(m)} &= \Gamma_m \left(\frac{1}{\varepsilon} R_{m,2}\Delta_m\right) - \left(1-\frac{1}{\varepsilon}\right)\frac{\xi_0}{\xi_0^2 - f} K_m, \\
A_{22}^{(m)} &= \frac{1}{\varepsilon}\left(\Delta_m + \xi_0 R_{m,2}\Delta_m\right) - \left(\Delta_m + \xi_0 \Delta_m R_{m,1}\right) - f\left(1-\frac{1}{\varepsilon}\right)\frac{\Sigma_m}{\xi_0^2 - f}, \\
E_{11}^{(m)} &= -\xi_0 \left(R_{m,2}\Delta_m - \Delta_m R_{m,0}\right), \\
E_{21}^{(m)} &= -\Gamma_m \left(\frac{1}{\varepsilon} R_{m,2}\Delta_m - \Delta_m R_{m,0}\right) + \left(1-\frac{1}{\varepsilon}\right)\frac{\xi_0}{\xi_0^2 - f} K_m.
\end{aligned} \tag{4.94}$$

The matrices $R_{m,0}, R_{m,1}, R_{m,2}$ and Δ_m have been defined earlier. The elements of the matrices Γ_m, K_m and Σ_m are integrals of products of the angular spheroidal functions and can be represented by sums of the d_r^{ml} coefficients like the elements of Δ_m (Voshchinnikov and Farafonov, 1993).

4.4.2.2 The case of spheroids of large eccentricity

The asymptotics of the presented SVM solution for $a/b \to \infty$ can be found rather easily (see Voshchinnikov and Farafonov (1993) and references therein). For instance, the asymptotics of the amplitude matrix elements for strongly elongated (prolate) spheroids are

$$\begin{aligned}
A_1 &= \frac{\varepsilon-1}{\varepsilon+1}\left(\frac{b}{a}\right)^2 T_1, \quad A_2 = \left(\frac{b}{a}\right)^2 \left(\frac{\varepsilon-1}{2} T_4 + \frac{\varepsilon-1}{\varepsilon+1} T_5\right), \\
A_3 &= \frac{\varepsilon-1}{\varepsilon+1}\left(\frac{b}{a}\right)^2 T_2, \quad A_4 = \frac{\varepsilon-1}{\varepsilon+1}\left(\frac{b}{a}\right)^2 T_3,
\end{aligned} \tag{4.95}$$

where the functions $T_i(c,\alpha,\theta,\varphi)$ do not depend on ε, and their dependence on φ is explicit: $T_1, T_5 \sim \cos\varphi$, $T_2, T_3 \sim \sin\varphi$, and T_4 is independent of φ. For strongly flattened (oblate) spheroids

$$\begin{aligned}
A_1 &= \frac{\varepsilon-1}{2}\left(\frac{b}{a}\right) T_1, \quad A_2 = \left(\frac{b}{a}\right)\left(\frac{\varepsilon-1}{2\varepsilon} T_4 + \frac{\varepsilon-1}{2} T_5\right), \\
A_3 &= \frac{\varepsilon-1}{2}\left(\frac{b}{a}\right) T_2, \quad A_4 = \frac{\varepsilon-1}{2}\left(\frac{b}{a}\right) T_3,
\end{aligned} \tag{4.96}$$

where as before the functions $T_i(c_1, \alpha, \theta, \varphi)$ do not depend on ε, while T_1, T_2, T_4 are some odd functions of the argument $\cos\alpha$ and T_3, T_5 are some even ones, α is the angle between the wavevector of the incident radiation and the particle symmetry axis.

Quite similar expressions for $A_j, j = 1$–4 are obtained within the Rayleigh–Gans approximation ($|\varepsilon - 1| \ll 1$, $x|\varepsilon - 1| \ll 1$, see, for example, Bohren and Huffman, 1983) for spheroids of large eccentricity. As the asymptotics of the amplitude matrix elements must be the same, one gets the final expressions for the functions

$$T_1 = \frac{2c_1^3}{3} G(u) \cos\varphi, \qquad T_2 = \frac{2c_1^3}{3} G(u) \cos\theta \sin\varphi,$$

$$T_3 = -\frac{2c_1^3}{3} G(u) \cos\alpha \sin\varphi, \quad T_4 = \frac{2c_1^3}{3} G(u) \sin\alpha \sin\theta, \tag{4.97}$$

$$T_5 = \frac{2c_1^3}{3} G(u) \cos\alpha \cos\theta \cos\varphi. \tag{4.98}$$

Here

$$G(u) = \frac{3}{u^3}(\sin u - u\cos u), \tag{4.99}$$

$u = c_1|\cos\theta - \cos\alpha|$ and $u = c_1\sqrt{\sin^2\alpha + \sin^2\theta - 2\sin\alpha \sin\theta \cos\varphi}$ for prolate and oblate highly eccentric spheroids, respectively.

Table 4.1 illustrates the fact that with growing aspect ratio a/b the suggested SVM solution quickly approaches the asymptotic one given by eqs (4.95)–(4.99) and as a result a smaller number of the azimuthal terms and hence less calculations provide the same accuracy. It is possible to show that the accuracy drops with an increasing parameter ka independently of a/b. Note that the standard SVM solution for spheroids suggested by Asano and Yamamoto (1975) has accuracy that decreases with a growing kr_{v} (r_{v} is the radius of a sphere having the same volume as the spheroid) and hence essentially depends on a/b.

Table 4.1. Scattering cross-sections divided by the geometrical cross-section for spheroids having the refractive index $m = 1.33$, the parameter $c_1 = (k_0/2)\sqrt{a^2 - b^2} = 5$, the aspect ratio a/b and $\alpha = 90^\circ$ (M is the number of the azimuthal terms kept in the potential expansions)

	Oblate spheroids		Prolate spheroids	
M	$a/b = 2$	$a/b = 10$	$a/b = 2$	$a/b = 10$
1	1.6149165	0.3384583	1.2145748	0.0605630
2	2.6773439	0.5293369	1.7178704	0.0605630
3	3.5094853	0.6186015	1.7353519	
4	4.3469983	0.6314880	1.7354780	
5	4.5779204	0.6322032	1.7354785	
6	4.5850148	0.6322223	1.7354785	
7	4.5851550	0.6322225		
8	4.5851569	0.6322225		
9	4.5851569			

So, the involvement of two potentials – one used in the classical solution for spheres and another in that for infinitely long cylinders – makes the approach very efficient for highly eccentric particles. In particular, Voshchinnikov and Farafonov (1993) show that the approach when applied to the SVM produces reliable results for spheroids of the aspect ration as high as 100 and more which is practically unreachable by other versions of the SVM. Voshchinnikov and Farafonov (2002) have even used the approach to compare in detail the optical properties of highly elongated prolate spheroids and infinitely long cylinders.

It is interesting to note that eqs (4.95)–(4.99) coincide with the expressions given by the quasistatic approximation. It has been known since the 1950s and has had several names, for example, the modified RDG approximation (see discussion in Khlebtsov, 1996). The approximation is *in situ* generalization of the Rayleigh–Gans and Rayleigh approximations – the field inside a particle is represented by the incident field as in the former approximation, but taking into account the particle polarizability like in the latter one (see, for example, Posselt *et al.*, 2002 for more details and references). Thus, in contrast to the Rayleigh approximation the quasistatic one succeeds in treating the light scattering by particles of a high eccentricity (Posselt *et al.*, 2002).

4.4.2.3 Extended boundary condition method with spheroidal functions

This method can be efficiently applied to axisymmetric homogeneous and layered scatterers. The corresponding equations are rather obvious after the presented discussion of the SVM and EBCM using the spherical functions and the SVM using the spheroidal ones. Therefore, we confine our consideration to the case of layered spheroids. The solution to be suggested to a certain degree is similar to that given for layered axisymmetric particles in section 4.3.2.

The case of spheroids with confocal layers

All layer boundaries of such a spheroid have the same foci. Consequently, a single spheroidal system can be used and the boundary equations can be written as

$$\xi = \xi_j, \tag{4.100}$$

where $j = 1, 2, ..., n$, with $j = 1$ and $j = n$ corresponding to the external boundaries of the particle and its core, respectively.

To solve the axisymmetric problem, two scalar potentials are introduced for the jth layer as was done in section 4.3.3

$$q^{(j+1)} = q_{\mathrm{R}}^{(j+1)} + q_{\mathrm{S}}^{(j+1)}. \tag{4.101}$$

Further we use an expression analogous to eq. (4.44) and written in the spheroidal coordinates

$$\frac{d}{2}\int_0^{2\pi}\int_{-1}^{1}\left(\xi'^2-f\right)\left\{q^{(j+1)}(\boldsymbol{r}')\frac{\partial G_j}{\partial \xi'}-\left[\frac{\varepsilon_j}{\varepsilon_{j+1}}\frac{\partial q^{(j+1)}(\boldsymbol{r}')}{\partial \xi'}+\left(\frac{\varepsilon_j}{\varepsilon_{j+1}}-1\right)\right.\right.$$
$$\left.\left.\times\frac{\xi'}{\xi'^2-f}\,q^{(j+1)}(\boldsymbol{r}')\right]G_j\right\}\mathrm{d}\eta'\mathrm{d}\varphi'=\begin{cases}-q_{\mathrm{R}}^{(j)}(\boldsymbol{r}), & \boldsymbol{r}\in D_j,\\ q_{\mathrm{S}}^{(j)}(\boldsymbol{r}), & \boldsymbol{r}\in R^3\setminus\bar{D}_j,\end{cases}\tag{4.102}$$

where $\boldsymbol{r}'=(\xi',\eta',\varphi')$, $\xi'=\xi_j(\eta')$, ε_{j+1} is the permittivity in the jth layer, D_j the domain inside the boundary S_j defined by $\xi=\xi_j$, $\bar{D}_j=D_j\cup S_j$, $j=1,2,...,n$, and we took into account that $\partial/\partial n=(1/h_\xi)(\partial/\partial\xi)$ as $\xi'_\eta=0$ for any S_j. So, there are $2n$ integral equations to determine $2n$ unknown potentials $q_{\mathrm{S}}^{(1)}$, $q_{\mathrm{R}}^{(2)}$, $q_{\mathrm{S}}^{(2)}$, ..., $q_{\mathrm{R}}^{(n)}$, $q_{\mathrm{S}}^{(n)}$, $q_{\mathrm{R}}^{(n+1)}$.

The scalar potentials are expanded as in eqs (4.45)

$$\begin{matrix}q_{\mathrm{R}}^{(j)}\\ q_{\mathrm{S}}^{(j)}\end{matrix}=\sum_{l=1}^{\infty}\begin{matrix}b_{\mathrm{R},l}^{(j)}\,R_{1l}^{(1)}(c_j,\xi)\\ b_{\mathrm{S},l}^{(j)}\,R_{1l}^{(3)}(c_j,\xi)\end{matrix}S_{1l}(c_j,\eta)\cos\varphi.\tag{4.103}$$

The potential expansions (4.103) and the Green function expansion (4.73) are substituted into the integral equations (4.102). Taking into account the completeness (and orthogonality) of the functions $S_{ml}(c,\eta)\cos\varphi$ for corresponding spheroidal surfaces, one can get an infinite system of linear algebraic equations relative to the unknown expansion coefficients (see Farafonov, 2001a for more details)

$$\begin{aligned}\underline{\boldsymbol{b}}_{\mathrm{R}}^{(j)} &= \left(B_{\mathrm{SR}}^{(j)}\,\underline{\boldsymbol{b}}_{\mathrm{R}}^{(j+1)}+B_{\mathrm{SS}}^{(j)}\,\underline{\boldsymbol{b}}_{\mathrm{S}}^{(j+1)}\right),\\ \underline{\boldsymbol{b}}_{\mathrm{S}}^{(j)} &= \left(B_{\mathrm{RR}}^{(j)}\,\underline{\boldsymbol{b}}_{\mathrm{R}}^{(j+1)}+B_{\mathrm{RS}}^{(j)}\,\underline{\boldsymbol{b}}_{\mathrm{S}}^{(j+1)}\right),\end{aligned}\tag{4.104}$$

where the vectors are

$$\begin{aligned}\underline{\boldsymbol{b}}_{\mathrm{R}}^{(j)} &= \left\{b_{\mathrm{R},l}^{(j)}\,R_{1l}^{(1)}(c_j,\xi_j)\,N_{1l}(c_j)\right\}_{l=1}^{\infty},\\ \underline{\boldsymbol{b}}_{\mathrm{S}}^{(j)} &= \left\{b_{\mathrm{S},l}^{(j)}\,R_{1l}^{(3)}(c_j,\xi_j)\,N_{1l}(c_j)\right\}_{l=1}^{\infty},\end{aligned}\tag{4.105}$$

and the matrices (their lower indices have the same sense as in section 4.3.3) are similar to

$$B_{\mathrm{SR}}^{(j)}=W_j\left\{R_j^{(3)}\,\Delta_{1,j}-\frac{\mu_j}{\mu_{j+1}}\Delta_{1,j}\,\tilde{R}_{j+1}^{(1)}-\left(\frac{\mu_j}{\mu_{j+1}}-1\right)\frac{\xi_j}{\xi_j^2-f}\,\Delta_{1,j}\right\}P_j^{(1)}.\tag{4.106}$$

Here the diagonal matrices are

$$\begin{aligned}P_j^{(i)} &= \left\{R_{1l}^{(i)}(c_{j+1},\xi_j)/R_{1l}^{(i)}(c_{j+1},\xi_{j+1})\delta_l^n\right\}_{n,l=1}^{\infty},\\ R_j^{(i)} &= \left\{R_{1l}^{(i)'}(c_j,\xi_j)/R_{1l}^{(i)}(c_j,\xi_j)\delta_l^n\right\}_{n,l=1}^{\infty},\\ \tilde{R}_{j+1}^{(i)} &= \left\{R_{1l}^{(i)'}(c_{j+1},\xi_j)/R_{1l}^{(i)}(c_{j+1},\xi_j)\delta_l^n\right\}_{n,l=1}^{\infty},\\ W_j &= -\left(R_j^{(3)}-R_j^{(1)}\right)^{-1},\end{aligned}\tag{4.107}$$

and $\Delta_{1,j}$ is obtained from the matrix Δ_1 by the replacements $c_1 \to c_j$ and $c_2 \to c_{j+1}$.

The system (4.104) can be easily brought to the form typical of the EBCM (see section 4.3.3)

$$\underline{\boldsymbol{b}}_{\mathrm{S}}^{(1)} = B_{\mathrm{R}} \left(B_{\mathrm{S}}\right)^{-1} \underline{\boldsymbol{b}}_{\mathrm{R}}^{(1)}, \tag{4.108}$$

where $\underline{\boldsymbol{b}}_{\mathrm{S}}^{(1)} = \underline{\boldsymbol{b}}^{\mathrm{sca}}$, $\underline{\boldsymbol{b}}_{\mathrm{R}}^{(1)} = \underline{\boldsymbol{b}}^{\mathrm{in}}$, and the matrices $B_{\mathrm{R}}, B_{\mathrm{S}}$ can be derived from an equation similar to (4.48) (Farafonov, 2001a).

Determination of the nonaxisymmetric parts of the fields presented by the potentials U and V is analogous (Farafonov, 2001a).

4.4.2.4 Point matching method with spheroidal functions

The construction of the general scheme of the PMM with the use of the spheroidal functions is similar to that of the PMM with the spherical functions discussed in section 4.3.3.

In the generalized PMM for both the axisymmetric and nonaxisymmetric problem, we search for a minimum of the residual. In the first case it is

$$\begin{aligned} \Delta \;=\; \sum_{s=1}^{M} \Bigg\{ & \left| q^{\mathrm{in}} + q^{\mathrm{sca}} - q^{\mathrm{int}} \right|^2 + \left| \frac{\partial}{\partial n} \left(q^{\mathrm{in}} + q^{\mathrm{sca}} - \frac{q^{\mathrm{int}}}{\varepsilon} \right) \right. \\ & \left. - \left(\frac{1}{\varepsilon} - 1 \right) \frac{(\xi + \eta \xi_\eta')\frac{d}{2}}{h_\varphi \sqrt{h_\eta^2 + {\xi_\eta'}^2 h_\xi^2}} q^{\mathrm{int}} \right|^2 \Bigg\}, \end{aligned} \tag{4.109}$$

where $q = q(\boldsymbol{r}_s)$ and $\boldsymbol{r}_s = (\xi_s, \eta_s, \varphi_s)$, $s = 1, 2, ..., M$ are the coordinates of the selected points at the axisymmetric scatterer surface defined by the equation $\xi_s = \xi(\eta_s)$.

The least squares method leads to a system of $2N$ linear algebraic equations relative to $2N$ unknown coefficients. It is generally reasonable to replace the sum over the surface points by integration over η as was suggested for the GPMM with the spherical basis (see section 4.3.3).

4.4.3 Applicability of the methods based on the spheroidal basis

4.4.3.1 Separation of variables method for spheroids

To study the applicability of this method, one should investigate solvability of the infinite systems of linear algebraic equations relative to the unknown field expansion coefficients as well as convergence of these expansions. As far as we know these points were considered so far only by Farafonov (1983). This paper is neither well known nor easily available, so its technique and the main results are briefly described below.

The analysis is based on consideration of the matrix elements of the systems (4.81) and (4.89) for large index values. The necessary asymptotics of the prolate radial spheroidal functions $R_{ml}(c, \xi)$ for $l \gg 1$ ($l \geq m$) are (Farafonov, 1983)

$$R_{ml}^{(1)}(c,\xi) \sim \left(\frac{\xi}{(\xi^2-1)^{\frac{1}{2}}}+1\right)^{\frac{1}{2}} j_l\Big(\frac{c}{2}\left(\xi+(\xi^2-1)^{\frac{1}{2}}\right)\Big)\left[1+O\left(\frac{1}{l}\right)\right], \quad (4.110)$$

$$R_{ml}^{(3)}(c,\xi) \sim \left(\frac{\xi}{(\xi^2-1)^{\frac{1}{2}}}+1\right)^{\frac{1}{2}} h_l^{(1)}\Big(\frac{c}{2}\left(\xi+(\xi^2-1)^{\frac{1}{2}}\right)\Big)\left[1+O\left(\frac{1}{l}\right)\right]. \quad (4.111)$$

For the oblate functions $R_{ml}(-ic, i\xi)$, one should change in the expressions c for $-ic$ and ξ for $i\xi$. The asymptotics allow one to estimate the diagonal elements of the matrices for $l \gg 1$

$$\{R_{m,i}\}_{ll} \sim \frac{(-1)^i l}{(\xi_0^2-f)^{\frac{1}{2}}}\left[1+O\left(\frac{1}{l}\right)\right], \quad i=0,1,2. \quad (4.112)$$

The elements of the matrices Δ_m can be estimated by using the asymptotics of the coefficients $d_r^{ml}(c)$ of the expansions of the angular functions $S_{mn}(c,\nu)$ in terms of the Legendre functions $P_{m+r}^m(\nu)$. For the diagonal elements, one gets

$$|\{\Delta_m\}_{nn}| \sim 1+O\left(\frac{1}{n}\right). \quad (4.113)$$

Other elements quickly decrease with a growing difference $|n-l|$. For instance, for $l > n$

$$|\{\Delta_m\}_{nl}| \le c_2^{l-n}\left(\frac{n!}{l!}\right)^{1/2}\left(1+\frac{2c_2^2}{l}\right)^2. \quad (4.114)$$

For the *axisymmetric problem* in the case of a dielectric spheroid, the matrix B in the system (4.81) has the main diagonal with the elements of the order $O(1)$. Other elements quickly decrease with moving off the diagonal. Therefore, the system can be written as

$$\underline{b}_l^{\rm sca} = \sum_{i=1}^{\infty} c_{li}\,\underline{b}_i^{\rm sca} + d_l, \quad (4.115)$$

where for the coefficients one has

$$\sum_{i=1}^{\infty}|c_{li}| \le \text{const}\ l^{-1}, \quad \sum_{l=1}^{\infty}|d_l|^2 < \infty. \quad (4.116)$$

Such a system is always solvable and has a unique solution (Kantorovich and Krylov, 1964), and hence the potential expansions converge in the region where they are defined.

For the *nonaxisymmetric problem*, we first consider the system arising in a more simple case of *perfectly conducting* spheroids. Taking into account the estimates (4.110)–(4.114), one can get

$$\begin{aligned}\underline{a}_{ml} &= -\frac{1}{2\xi_0}(\underline{b}_{m,l-1}+\underline{b}_{m,l+1}) + \sum_{i=1}^{\infty} c_{li}^{\rm a}(m)\,\underline{b}_{mi} + d_l^{\rm a}(m),\\ \underline{b}_{ml} &= -\frac{1}{2\xi_0}(\underline{a}_{m,l-1}+\underline{a}_{m,l+1}) + \sum_{i=1}^{\infty} c_{li}^{\rm b}(m)\,\underline{a}_{mi} + d_l^{\rm b}(m),\end{aligned} \quad (4.117)$$

where

$$\sum_{i=1}^{\infty} |c_{li}^{\mathrm{a}}(m)| + \sum_{i=1}^{\infty} |c_{li}^{\mathrm{b}}(m)| \le \text{const } l^{-1},$$
$$\sum_{l=1}^{\infty} |d_{l}^{\mathrm{a}}(m)|^2 + \sum_{i=1}^{\infty} |d_{l}^{\mathrm{b}}(m)|^2 < \infty. \tag{4.118}$$

The system (4.117) is quasiregular, i.e. it satisfies the conditions of the regular systems (see Kantorovich and Krylov, 1964) only for large element indices, provided

$$\xi_0 > 1. \tag{4.119}$$

Regular systems are known to be solvable and their solution can be obtained by a reduction method (Kantorovich and Krylov, 1964), the same is obviously true for our quasiregular system.

The condition (4.119) is satisfied for any prolate spheroids, while for oblate ones it means that the minor semiaxis is larger than the focal distance

$$b > d\,. \tag{4.120}$$

This condition is, however, only sufficient. One can make a substitution of variables

$$t_{1,l} = \left[q\left(\xi_0 + (\xi_0^2+1)^{\frac{1}{2}}\right)\right]^l \underline{a}_{ml}, \quad t_{2,l} = \left[q\left(\xi_0 + (\xi_0^2+1)^{\frac{1}{2}}\right)\right]^l \underline{b}_{ml}, \tag{4.121}$$

where $q > 1$, and get the system

$$\begin{aligned} t_{1,l} &= \beta_1^{(1)}\, t_{2,l+1} + \beta_2^{(1)}\, t_{2,l-1} + \sum_{i=1}^{\infty} g_{li}^{(1)}\, t_{2,i} + f_l^{(1)}, \\ t_{2,l} &= \beta_1^{(2)}\, t_{1,l+1} + \beta_2^{(2)}\, t_{1,l-1} + \sum_{i=1}^{\infty} g_{li}^{(2)}\, t_{1,i} + f_l^{(2)} \end{aligned} \tag{4.122}$$

with the coefficients $g_{li}^{(i)}$, $f_l^{(i)}, i = 1, 2$ satisfying the conditions (4.118), and

$$|\beta_1^{(i)}| + |\beta_2^{(i)}| \le \frac{1}{q} < 1. \tag{4.123}$$

Note that the system (4.117) can be transformed into a system similar to eqs (4.122), provided the variables $t_{i,l}$ include either even $\underline{a}_{ml}$ and odd $\underline{b}_{ml}$ or vice versa odd $\underline{a}_{ml}$ and even $\underline{b}_{ml}$. The system (4.122) under the conditions (4.123) is obviously quasiregular. Thus, the system for the nonaxisymmetric problem is solvable for any oblate perfectly conducting spheroids, except for disks having $\xi_0 = 0$.[3]

[3] An algorithm to consider the plane wave diffraction on perfectly conducting very elongated spheroids, including disks, was suggested by Farafonov (1991).

For the nonaxisymmetric problem in the case of a *dielectric* spheroid, the results are analogous (see Farafonov (1983) for more details). However, for strongly oblate dielectric spheroids no problem of their transformation into a disk arises because scattering at the edge becomes negligible and the system gives the null solution.

4.4.3.2 Other methods with spheroidal functions

The theoretical results presented in section 4.3.4 can be easily applied to the versions of the EBCM and (G)PMM which use the spheroidal functions and coordinates instead of the spherical ones.

For *spheroidal* particles, such a version of the EBCM is likely to have the same range of applicability as the SVM with the spheroidal functions discussed above, i.e. the method is applicable to any spheroid and there is no difference whether the near-field or far-field zone is considered.

For *other homogeneous* particles, one should apply the results of Sect. 4.3.4, but replace the distances to the singularities with the corresponding values of the radial spheroidal coordinate ξ. In other words, the solution given by this spheroidal EBCM should converge everywhere in the near-field zone provided the conditions (4.62) written in the spheroidal coordinates is satisfied. The use of the method in the far-field is mathematically correct under the conditions (4.64) expressed again in the spheroidal coordinates.

These conditions are in particular useful provided one considers 'spheroidal' Chebyshev particles having the surface equation (cf. eq. (4.63))

$$\xi = \xi_0 \left[1 + \epsilon \cos\left(n \arccos \eta\right)\right], \tag{4.124}$$

where $\xi = \xi_0$ defines the surface of an unperturbed spheroid, ϵ is the deformation parameter, and n an integer number. A set of such particles (see examples in Fig. 4.6) can be used to study simultaneously the effects of scatterer large-scale and medium- to small-scale nonsphericities characterized by the aspect ration a/b and by the parameters ϵ, n, respectively.

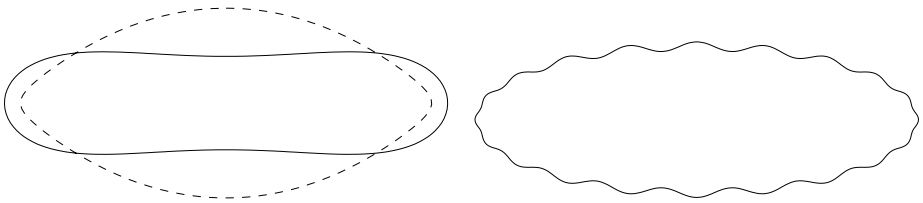

Fig. 4.6. Prolate spheroidal ($a/b = 3$) Chebyshev particles with (a) $n = 2$ and $\epsilon = 0.34$ (the case of $\epsilon = -0.34$ is shown by dashed line) and (b) $n = 20$ and $\epsilon = 0.06$ (the symmetry axis is horizontal). The used values of ϵ for given n correspond to the maximum ones for which the spheroidal EBCM solution should converge in the far-field zone (Farafonov and Il'in, 2005b, in preparation)

It should be noted that because of their general equivalence discussed in section 4.2 the EBCM and SVM with the spheroidal functions when applied to nonspheroidal particles should have the same theoretical ranges of applicability.

In the case of *layered spheroidal* particles, the spheroidal version of EBCM is always mathematically correct only if all the layers have confocal boundaries. Otherwise one should apply the results of section 4.3.4 as has been done by Farafonov *et al.* (2003). For instance, for the far-field zone it can be easily found that the condition (4.64) is to be applied to each layer boundary and besides there arise some additional conditions. It usually makes the applicability range of the EBCM rather narrow and the use of the (G)PMM preferable.

The applicability range of the PMM with the spheroidal functions should be similar to that of the corresponding EBCM. For the GPMM, the matrix of the system used to determine the unknown expansion coefficients is positively determined and hence the method is sure always to give the only solution to the light scattering problem.

The accuracy to be achieved in calculations with the spheroidal EBCM should be similar to that usually obtained with the spheroidal SVM. The latter is typically very close to the curve for the EBCM in the case of spheroids with $a/b = 1.5$ presented on the left panel of Fig. 4.3. In a more complex case of the Chebyshev particles defined by eq. (4.124), the accuracy of the spheroidal EBCM and GPMM is expected to be lower, probably similar to that presented in the right panel of Fig. 4.3.

4.5 Solution using the ellipsoidal wave functions

Practically all light scattering methods known today potentially can be applied to three-dimensional particles. However, the most often used techniques – the standard EBCM, the coupled dipoles and finite difference methods – are found to be nearly equally inefficient for nonaxisymmetric scatterers whose sizes exceed the wavelength of incident radiation (Wriedt and Comberg, 1998). Other methods are not expected to be better. The only exception could be the methods where ellipsoidal coordinates and field expansions in terms of the ellipsoidal wave functions would be used. Below we consider such an ellipsoidal version of the SVM (see also Farafonov *et al.*, 2005). For simplicity, it is applied to the case of an axially incident plane wave.

4.5.1 Ellipsoidal coordinates

The Cartesian coordinate system (x, y, z) connected to the axes of an ellipsoid with the semiaxes $a > b > c > 0$ and the corresponding ellipsoidal coordinate system $(\tilde{\xi}, \tilde{\eta}, \tilde{\zeta})$ are related as follows:

$$\frac{x^2}{a^2+\tilde{\xi}}+\frac{y^2}{b^2+\tilde{\xi}}+\frac{z^2}{c^2+\tilde{\xi}}=1, \quad -c^2<\tilde{\xi}<\infty,$$

$$\frac{x^2}{a^2+\tilde{\eta}}+\frac{y^2}{b^2+\tilde{\eta}}+\frac{z^2}{c^2+\tilde{\eta}}=1, \quad -b^2<\tilde{\eta}<-c^2, \tag{4.125}$$

$$\frac{x^2}{a^2+\tilde{\zeta}}+\frac{y^2}{b^2+\tilde{\zeta}}+\frac{z^2}{c^2+\tilde{\zeta}}=1, \quad -a^2<\tilde{\zeta}<-b^2.$$

One usually applies the dimensionless ellipsoidal coordinates

$$\xi_l=\frac{\nu_l+a^2}{a^2-b^2}, \tag{4.126}$$

where $l=1,2,3$ and $\nu_1=\xi$, $\nu_2=\eta$, $\nu_3=\zeta$. The length element in these coordinates is

$$\mathrm{d}^2 s=h_1^2\,\mathrm{d}^2\xi_1+h_2^2\,\mathrm{d}^2\xi_2+h_3^2\,\mathrm{d}^2\xi_3, \tag{4.127}$$

where $h_1^2=(a^2-b^2)\,(\xi_1-\xi_2)(\xi_1-\xi_3)/4f(\xi_1)$ and other coefficients are obtained by cyclic permutations of the indices, $f(\xi)=\xi(\xi-1)(\xi-\rho^2)$, $\rho^2=(a^2-c^2)/(a^2-b^2)>1$.

4.5.2 Scalar potentials and the separation of variables

For ellipsoids, only the nonaxisymmetric light scattering problem is to be solved. As earlier, we use the scalar potentials U, V that now should be the solutions to the scalar Helmholtz equation written in the ellipsoidal coordinates. The equation is known to allow the separation of variables, i.e. there exists a solution in the form (see, for example, Bateman and Erdelyi, 1955 for more details)

$$U(\boldsymbol{r})=\Lambda_1(\xi_1)\,\Lambda_2(\xi_2)\,\Lambda_3(\xi_3). \tag{4.128}$$

where (ξ_1,ξ_2,ξ_3) are the coordinates of a point defined by $\boldsymbol{r}$, and the functions $\Lambda_l(\xi_l)$ satisfy the Lamé wave equation for different intervals ($0\le\xi_1\le 1$, $1\le\xi_2\le\rho^2$, $\rho^2\le\xi_3<\infty$)

$$\sqrt{f(\xi)}\frac{\mathrm{d}}{\mathrm{d}\xi}\left(\sqrt{f(\xi)}\frac{\mathrm{d}\Lambda(\xi)}{\mathrm{d}\xi}\right)+\frac{1}{4}\left(\lambda_1\rho^2-\lambda_2\rho^2\xi+\omega^2\xi^2\right)\Lambda(\xi)=0, \tag{4.129}$$

where λ_1, λ_2 are the separation parameters, $\omega^2=k^2(a^2-b^2)>0$.

4.5.3 Ellipsoidal wave functions

The angular ellipsoidal wavefunctions are the eigenfunctions of the two-parameter self-conjugate boundary problem presented by eq. (4.129) for $\xi_1\in[0,1]$ and $\xi_2\in[1,\rho^2]$. At the three boundaries defined by $\xi_{1,0}=0$, $\xi_{2,0}=1$ and $\xi_{3,0}=\rho^2$ one of two conditions must be satisfied ($l=1,2,3$)

$$\lim_{\xi\to\xi_{1,0}} \Lambda(\xi) = 0 \tag{4.130}$$

or

$$\lim_{\xi\to\xi_{1,0}} \left(\sqrt{f(\xi)}\frac{\mathrm{d}\Lambda(\xi)}{\mathrm{d}\xi}\right) = 0, \tag{4.131}$$

but the conditions at $\xi_1 \to \xi_{2,0} - 0$ and $\xi_2 \to \xi_{2,0} + 0$ must be the same.

The eigenvalues of this boundary problem are real and form two sequences $\lambda_{1,nm}$, $\lambda_{2,nm}$, where $m \in [0, n], n \geq 0$. The corresponding nontrivial solutions $\Lambda_{nm}(\xi_1)$, $\Lambda_{nm}(\xi_2)$ have m zero values in the interval [0, 1] and $(n - m)$ zero values in the interval [1, ρ^2]. Thus, there are eight different types of the angular ellipsoidal wave functions that can be characterized by the indices (i_1, i_2, i_3), where $i_l = 1$ (or 0) when the first (or second) boundary condition is satisfied at the boundary $\xi_{l,0}$.

The product $\Psi_{nm}(\xi_1, \xi_2) = \Lambda_{nm}(\xi_1)\,\Lambda_{nm}(\xi_2)$ is called the surface ellipsoidal wave function. For each set (i_1, i_2, i_3), the surface ellipsoidal wave functions are orthogonal and form a complete set. Special algorithms of numerical calculations of the eigenvalues and the corresponding angular ellipsoidal functions were presented by Abramov *et al.* (1989).

The radial ellipsoidal functions are solutions to eq. (4.129) in the interval $[\rho^2, \infty)$ with the eigenvalues $\lambda_{1,nm}$, $\lambda_{2,nm}$ and satisfy the boundary condition (4.130) or (4.131) depending on i_3. By analogy to the spherical and spheroidal functions, the radial ellipsoidal functions are of several kinds. The Wronskian of these functions is

$$W = \frac{i}{2\sqrt{f(\xi)}}, \tag{4.132}$$

and an efficient algorithm of their computation was suggested by Abramov *et al.* (1991).

4.5.4 Potential expansions

The scalar potentials are expanded in terms of the ellipsoidal wave functions as follows:

$$\begin{matrix} U^{\mathrm{sca}} \\ V^{\mathrm{sca}} \end{matrix} = \sum_{i=0}^{7}\sum_{n=0}^{\infty}\sum_{m=0}^{n} \begin{matrix} a^{\mathrm{sca}}_{nmi} \\ b^{\mathrm{sca}}_{nmi} \end{matrix} \Psi^{(i)}_{nm}(\xi_1, \xi_2)\,\Lambda^{(3,i)}_{nm}(\xi_3), \tag{4.133}$$

$$\begin{matrix} U^{\mathrm{int}} \\ V^{\mathrm{int}} \end{matrix} = \sum_{i=0}^{7}\sum_{n=0}^{\infty}\sum_{m=0}^{n} \begin{matrix} a^{\mathrm{int}}_{nmi} \\ b^{\mathrm{int}}_{nmi} \end{matrix} \Psi^{(i)}_{nm}(\xi_1, \xi_2)\,\Lambda^{(1,i)}_{nm}(\xi_3), \tag{4.134}$$

and for the incident filed the expansions are similar to eqs (4.134). In the case of propagation of a plane wave along the x-axis one can use only the functions with the indices $(i_1, i_2, i_3) = (0,0,0), (0,0,1)$, i.e. $a^{\mathrm{in}}_{nmi} = -16\pi/(k\sqrt{\omega})\,\exp(-i\,\delta^n_m)$ $\Psi^{(i)}_{nm}(0, 1)$ for $i = 0,1$ and 0 for $i = 2$–7, while $b^{\mathrm{in}}_{nmi} = 0$ for $i = 0$–7.

The boundary conditions for the scalar potentials at $(\xi_1, \xi_2, \xi_3) = (\xi_{1,0}, \xi_{2,0}, \xi_{3,0})$ can be written for the case of the TE mode in the form

$$\begin{aligned}
\frac{\partial P_3}{\partial \xi_2} - \frac{\partial P_2}{\partial \xi_3} &= \frac{\partial \tilde{P}_3}{\partial \xi_2} - \frac{\partial \tilde{P}_2}{\partial \xi_3}, \\
\frac{\partial P_1}{\partial \xi_3} - \frac{\partial P_3}{\partial \xi_1} &= \frac{\partial \tilde{P}_1}{\partial \xi_3} - \frac{\partial \tilde{P}_3}{\partial \xi_1}, \\
\frac{\partial P_1}{\partial \xi_2} - \frac{\partial P_2}{\partial \xi_1} &= \mu \left[\frac{\partial \tilde{P}_1}{\partial \xi_2} - \frac{\partial \tilde{P}_2}{\partial \xi_1} \right], \qquad (4.135) \\
\frac{\partial}{\partial \xi_3} \left[\frac{h_1}{h_2 h_3} \left(\frac{\partial P_3}{\partial \xi_2} - \frac{\partial P_2}{\partial \xi_3} \right) \right] &= \frac{1}{\varepsilon} \left\{ \frac{\partial}{\partial \xi_3} \left[\frac{h_1}{h_2 h_3} \left(\frac{\partial \tilde{P}_3}{\partial \xi_2} - \frac{\partial \tilde{P}_2}{\partial \xi_3} \right) \right] \right. \\
&+ \left. (\mu - 1) \frac{\partial}{\partial \xi_1} \left[\frac{h_3}{h_1 h_2} \left(\frac{\partial \tilde{P}_2}{\partial \xi_1} - \frac{\partial \tilde{P}_1}{\partial \xi_2} \right) \right] \right\},
\end{aligned}$$

where for $l = 1, 2, 3$

$$P_l = \sqrt{\frac{\xi_1 \xi_2 \xi_3}{\xi_l^2}}\, U + \sqrt{\rho^2 (a^2 - b^2)}\, V,$$

$U = U^{\text{in}} + U^{\text{sca}}$, $V = V^{\text{sca}}$, and in $\tilde{P}_l$ one should use the expression for P_l with $U = U^{\text{int}}$ and $V = V^{\text{int}}$, h_1, h_2, h_3 are from eq. (4.127).

4.5.5 Determination of the expansion coefficients

If one substitutes the potential expansions (4.133),(4.134) into the boundary conditions (4.135), integrates them and takes into account orthogonality of the functions, an infinite system of linear algebraic equations relative to the unknown coefficients of the expansions is obtained

$$\hat{A}\, \hat{a}^{\text{sca}} + \hat{C}\, \hat{a}^{\text{int}} = \hat{E}\, \hat{a}^{\text{in}}, \qquad (4.136)$$

where $\hat{a} = \{a_{000}, ..., a_{007},\ a_{010}, ..., a_{0n7},\ a_{100}, ..., a_{nn7},\ b_{000}, ..., b_{nn7}\}_{n=0}^{\infty}$ and the elements of the matrices $\hat{A}, \hat{C}, \hat{E}$ are integrals of the ellipsoidal functions and their derivatives.

The solution to the system allows one to find the scattered field everywhere outside the scatterer and hence any light scattering characteristic. For example, the scattering cross-section is

$$\begin{aligned}
C_{\text{sca}} &= \frac{1}{4k_0^2} \sum_{\nu\nu'} \mathrm{e}^{i(\delta_m^n - \delta_{m'}^{n'})} \left\{ \frac{1}{\rho^2} \omega_{\nu\nu'}\, a_\nu^{\text{sca}}\, a_{\nu'}^{\text{sca}^*} \right. \\
&+ \left. \frac{2i}{\rho} \left[\kappa_{\nu\nu'}\, a_\nu^{\text{sca}}\, b_{\nu'}^{\text{sca}^*} - \kappa_{\nu'\nu}\, a_{\nu'}^{\text{sca}^*}\, b_\nu^{\text{sca}} \right] + 4\tau_{\nu\nu'}\, b_\nu^{\text{sca}}\, b_{\nu'}^{\text{sca}^*} \right\}, \qquad (4.137)
\end{aligned}$$

where ν denotes the group nmi and ν' does $n'm'i'$,

$$\omega_{\nu\nu'} = \int\int \left(\sqrt{\frac{-f(\xi_2)}{f(\xi_1)}} \frac{\xi_1}{\xi_2} + \sqrt{\frac{f(\xi_1)}{-f(\xi_2)}} \frac{\xi_2}{\xi_1} \right) \Psi_\nu(\xi_1, \xi_2)\, \Psi_{\nu'}(\xi_1, \xi_2)\, \mathrm{d}\xi_1 \mathrm{d}\xi_2 \qquad (4.138)$$

and the integrals $\kappa_{\nu\nu'}$, $\tau_{\nu\nu'}$ are similar to $\omega_{\nu\nu'}$. Note that all the integrals can be represented by linear combinations of one-dimensional integrals over ξ_1 and ξ_2.

4.5.6 Comparison with a solution based on the spheroidal basis

Computational time when using the methods under consideration is mainly spent on calculations of the matrix elements in the systems similar to eq. (4.136). Therefore, the main difference between the ellipsoidal and spheroidal versions of the SVM lies in calculations of the corresponding wave functions. The spheroidal functions are computed rather quickly using the available methods. Calculations of the ellipsoidal functions are much longer because there are eight types of the functions and for each of them one must solve Cauchy problems many times, for example, by a Runge–Kutta method (see Abramov *et al.* (1989, 1991) for more details).

So far only preliminary calculations of cross-sections for ellipsoids and for spheroids relatively close to them have been performed using the corresponding SVM codes. The accuracy of the results was kept at the level of 10^{-7}. The size of the particles was characterized by the ratio of the radius of an equivolume sphere to the wavelength $x_{\mathrm{v}} = 2\pi r_{\mathrm{v}}/\lambda$, and two values were utilized $x_{\mathrm{v}} = 1$ and 10. Prolate spheroids with $a/b = 2$ and 30 and ellipsoids with the same a/b and $a/c \approx a/b$ were considered. Calculations of cross-sections for these spheroids took a few seconds, while those for the ellipsoids were about 10^3 times longer. The main part of time in the second case was spent on computations of the eigenvalues and it is unlikely that it can be reduced substantially.

Even though the SVM for ellipsoids is not as fast as the EBCM for axisymmetric particles or the SVM for spheroids, it will have a certain region of applications. For nonaxisymmetric scatterers, the popular methods (EBCM; discrete dipole approximation, DDA; finite different time domain method, FDTD) seem to be slow (Wriedt and Comberg, 1998). Therefore, for ellipsoidal particles, the ellipsoidal SVM can be their successful competitor. Besides, the EBCM is known to meet problems for particles with large eccentricity and the DDA for particles of large sizes. The ellipsoidal SVM should avoid these difficulties and provide reliable, high accuracy results in an essentially larger region of parameter values in both cases.

4.6 Concluding remarks

We have considered the main details of the three highly accurate and fast methods used to treat the light scattering by nonspherical particles – the separation of variables, extended boundary condition and point-matching methods. These methods employ the same single expansions of the fields in terms of spherical, cylindrical, spheroidal or ellipsoidal wave functions. The consideration was done within a single context provided by an approach utilizing specially selected scalar potentials. The approach complicates the analytical averaging of some scattered field characteristics for ensembles of randomly oriented particles but allows one

to treat particles of a high eccentricity (when the spheroidal wave functions are applied). Special attention was paid to theoretical consideration of the applicability ranges of the methods.

The advantages of the methods are essential for scatterers of simplified shapes and structures, in particular for homogeneous and layered axisymmetric particles. The question of how well the optical properties of such particles can represent those of real particles has been considered in a number of recent papers (for example, Kahnert *et al.*, 2002a, 2002b, 2004) and the answer to it seems to depend on the concrete task to be solved.

Acknowledgments

The authors are thankful to V. A. Babenko, L. E. Paramonov, and N. V. Voshchinnikov for helpful comments and suggestions and V. M. Belyakova for improving the style of the manuscript. V. I. acknowledges the support within the grant NSh 1088.2003.2.

References

Abramov, A. A., *et al.* (1989): Evaluation of Lamé angular wave functions by solving of auxiliary differential equations, *Comp. Math. Math. Phys.*, **29**, 119–131.

Abramov, A. A., *et al.* (1991): Computation of radial wave functions for spheroids and triaxial ellipsoids by the modified phase functions method, *Comp. Math. Math. Phys.*, **31**, 25–42.

Abramov, A. A., *et al.* (1995): A numerical-analytic investigation of the diffraction of a plane acoustic wave by ideal prolate spheroids and triaxial ellipsoids, *Comp. Math. Math. Phys.*, **35**, 1103–1123.

Al-Rizzo, H. M., and J. M. Tranquilla (1995): Electromagnetic scattering from dielectrically coated axisymmetric objects using the generalized point-matching technique II. Numerical results and comparison, *J. Comp. Phys.*, **119**, 356–373.

Apel'tsyn, V. F., and A. G. Kyurkchan (1990): *Analytical Properties of Wave Fields*, Moscow University Press, Moscow [in Russian].

Asano, S., and G. Yamamoto (1975): Light scattering by spheroidal particle, *Appl. Opt.*, **14**, 29–49.

Babenko, V. A. (2004): *Bibliography on Light Scattering*, Stepanov Institute of Physics Minsk (the database is available at http://www.astro.spbu.ru/DOP/4-BIBL).

Babenko, V. A., L. G. Astafyeva, and V. N. Kuzmin (2003): *Electromagnetic Scattering by Disperse Media*, Springer-Praxis, London.

Barber, P. W., and S. C. Hill (1990): *Light Scattering by Particles: Computational Methods*, World Scientific, Singapore.

Barber, P. W., and C. Yeh (1975): Scattering of electromagnetic waves by arbitrarily shaped dielectric bodies, *Appl. Opt.*, **14**, 2864–2872.

Barrowes, B. E. *et al.* (2004): On the asymptotic expansion of the spheroidal wave functions and its eigenvalues for complex size parameter, *Studies Appl. Math.*, **113**, 271–301.

Barton, J. P. (1999): Internal and near-surface electromagnetic fields for an infinite cylinder illuminated by an arbitrary focused beam, *J. Opt. Soc. Am. A*, **16**, 160–166.

Barton, J. P. (2000): Electromagnetic fields for a spheroidal particle with an arbitrary embedded sources, *J. Opt. Soc. Am. A*, **17**, 458–464.

Barton, J. P. (2001): Internal, near-surface and scattered electromagnetic fields for a layered spheroid with arbitrary illumination, *Appl. Opt.*, **40**, 3598–3607.

Barton, J. P. (2002): Electromagnetic field calculations for an irregularly shaped, near-spheroidal particle with arbitrary illumination, *J. Opt. Soc. Am. A*, **19**, 2429–2435.

Bateman, H., and A. Erdelyi (1955): *Higher Transcendental Functions*, Vol. 3, McGraw-Hill, New York.

Bates, R. H. T., *et al.* (1973): An overview of point matching, *Radio Electr. Eng.*, **43**, 193–200.

Bohren, C. F., and D. R. Huffman (1983): *Absorption and Scattering of Light by Small Particles*, John Wiley, New York.

Borghese, F., P. Denti, and R. Saija (2003): *Scattering from Model Nonspherical Particles*, Springer, Berlin.

Boyd, J. P. (2003): Large mode number eigenvalues of the prolate spheroidal differential equation, *Appl. Math. Comp.*, **145**, 881–886.

Brown, D. J., and R. M. Stringfield (2000): Iterative methods applied to matrix equations found in calculating spheroidal functions, *J. Comp. Phys.*, **159**, 329–343.

Ciric, I. R., and F. R. Cooray (2000): Separation of variables for electromagnetic scattering by spheroidal particles, *Light Scattering by Nonspherical Particles*, M. I. Mishchenko, J. W. Hovenier, L. D. Travis (eds), Academic Press, San Diego, pp. 89–130.

Colton, D., and R. Kress (1984): *Integral Methods in Scattering Theory*, John Wiley, New York.

Dallas, A. G. (2000): On the convergence and numerical stability of the second Waterman scheme for approximation of the acoustic field scattered by a hard object, Technical Report, University Delaware, pp. 1–35.

Davies, J. B. (1973): A least-squares boundary residual method for the numerical solution of scattering problems, *IEEE Trans. Microw. Theory Techn.*, **MTT-21**, 99–104.

Debye, P. (1909): Der Licht Druck auf Kugeln von beliebigem Material, *Ann. Phys.*, **30**, 57–136.

de Moraes, P. C. G., and L. G. Guimaraes (2002): Uniform asymptotic formulae for the spheroidal angular functions, *J. Quant. Spectr. Rad. Transf.*, **74**, 757–765.

de Moraes, P. C. G., and L. G. Guimaraes (2003): Uniform asymptotic formulae for the spheroidal radial functions, *J. Quant. Spectr. Rad. Transf.*, **79-80**, 973–982.

Doicu, A., and T. Wriedt (1999): Calculation of the T matrix in the null-field method with discrete sources, *J. Opt. Soc. Am. A*, **16**, 2539–2544.

Doicu, A., and T. Wriedt (2001): T-matrix method for electromagnetic scattering from scatterers with complex structure, *J. Quant. Spectr. Rad. Transf.*, **70**, 663–673.

Doicu, A., Y. Eremin, and T. Wriedt (2000): *Acoustic and Electromagnetic Scattering Analysis*, Academic Press, San Diego, CA.

Eide, H. A. *et al.* (1999): New method for computing expansion coefficients for spheroidal functions, *J. Quant. Spectr. Rad. Transf.*, **63**, 191–203.

Eremina, E., and T. Wriedt (2003): Review of light scattering by fiber particles with high aspect ratio, *Rec. Res. Dev. Opt.*, **3**, 297–318.

Eremina, E., Y. Eremin, and T. Wriedt (2005): Analysis of light scattering by erythrocyte based on discrete source method, *Opt. Comm.*, **24**, 15–23.

Farafonov, V. G. (1983): Diffraction of a plane electromagnetic wave by a dielectric spheroid, *(Sov.) Diff. Equat.*, **19**, 1765–1777.

Farafonov, V. G. (1991): Diffraction of a plane electromagnetic wave by strongly elongated perfectly conducting spheroids, *(Sov.) Radiotech. Electron.*, **36**, 1443–1451.
Farafonov, V. G. (2001a): New recursive solution of the problem of scattering of electromagnetic radiation by multilayered spheroidal particles, *Opt. Spectr.*, **90**, 743–752.
Farafonov, V. G. (2001b): Light scattering by axisymmetric multilayered particles, *Opt. Spectr.*, **91**, 92–102.
Farafonov, V. G. (2002): Applicability of the T-matrix method and its modifications, *Opt. Spectr.*, **92**, 748–760.
Farafonov, V. G., and V. B. Il'in (2001): Light scattering by dielectric particles with axial symmetry II, *Opt. Spectr.*, **91**, 960–966.
Farafonov, V. G., and V. B. Il'in (2005a): Light scattering by non-spherical particles: some theoretical aspects. *Proc. SPIE* **5829**, 109–116.
Farafonov, V. G., and V. B. Il'in (2005b): Modification and investigation of the point-matching method, *Opt. Spectr.* **100**, 480–490.
Farafonov, V. G., and S. Y. Slavyanov (1980): Diffraction of a plane wave by a perfectly conducting spheroid, *(Sov.) Radiotech. Electron.*, **25**, 2056–2065.
Farafonov, V. G., V. B. Il'in, and M. S. Prokopjeva (2003): Light scattering by multilayered nonspherical particles: a set of methods, *J. Quant. Spectr. Rad. Transf.*, **79-80**, 599–626.
Farafonov, V. G., M. S. Prokopjeva, and V. B. Il'in (2004): Analytical averaging of cross-sections for randomly oriented layered particles in the modified T-matrix method, *J. Quant. Spectr. Rad. Transf.*, **89**, 111–122.
Farafonov, V. G., V. B. Il'in, and N. V. Voshchinnikov (2005): Separation of variables method for dielectric ellipsoids, *Abstract Book, 8th Conf. Electrom. Light Scatt. Nonsph. Part.*, pp. 84–87.
Flammer, C. (1957): *Sheroidal Wave Functions*, Stanford University Press, Stanford, CA.
Gurwich, I., N. Shiloah, and M. Kleiman (1999): The recursive algorithm for electromagnetic scattering by titled infinite circular multi-layered cylinder, *J. Quant. Spectr. Rad. Transf.*, **63**, 217–229.
Gurwich, I., *et al.* (2000): Scattering of electromagnetic radiation by multilayered spheroidal particles: recursive procedure, *Appl. Opt.*, **39**, 470–477.
Gurwich, I., N. Shiloah, and M. Kleiman (2001): Calculations of the Mie scattering coefficients for multilayered particles with large size parameters, *J. Quant. Spectr. Rad. Transf.*, **70**, 433–440.
Gurwich, I., *et al.* (2003): Scattering by an arbitrary multi-layered spheroid: theory and numerical results, *J. Quant. Spectr. Rad. Transf.*, **79-80**, 649–660.
Hafner Ch., and K. Bomholt (1993): *The 3D Electrodynamic Wave Simulator*, John Wiley, Chichester.
Han, Y., and Z. Wu (2001): Scattering of a spheroidal particle illuminated by a Gaussian beam, *Appl. Opt.*, **40**, 2501–2509.
Han, Y., G. Grahan, and G. Gousbet (2003): Generalized Lorenz–Mie theory for spheroidal particle with off-axis Gaussian-beam illumination, *Appl. Opt.*, **42**, 6621–6629.
Ikuno, H., and K. Yasuura (1973): Improved point-matching method with application to scattering from a periodic surface, *IEEE Trans. Anten. Propag.*, **21**, 657–662.
Il'in, V. B., A. A. Loskutov, and V. G. Farafonov (2004): Modification and investigation of the T-matrix method as applied to scattering of a plane wave from a perfectly conducting axisymmetric body, *Comp. Math. Math. Phys.*, **44**, 329–348.

Iskander, M. F., A. Lakhtakia, and C. H. Durney (1983): A new procedure for improving the solution stability and extending the frequency range of the EBCM, *IEEE Trans. Anten. Propag.*, **31**, 317–324.

Jackson, J. D. (1975): *Classical Electrodynamics*, John Wiley, New York.

Jones, A. R. (1999): Light scattering for particle characterisation, *Prog. Energy Combust. Sci.*, **25**, 1–53.

Kahnert, F. M. (2003a): Surface-integral formulation for electromagnetic scattering in spheroidal coordinates, *J. Quant. Spectr. Rad. Transf.*, **77**, 61–78.

Kahnert, F. M. (2003b): Numerical methods in electromagnetic scattering theory, *J. Quant. Spectr. Rad. Transf.*, **79-80**, 775–824.

Kahnert, F. M. (2004): Reproducing the optical properties of fine desert dust aerosols using ensembles of simple model particles, *J. Quant. Spectr. Rad. Transf.*, **85**, 231–249.

Kahnert, F. M., J. J. Stamnes, and K. Stamnes (2001a): Application of the extended boundary condition method to particles with sharp edges: a comparison of two different surface integration approaches, *Appl. Opt.*, **40**, 3101–3109.

Kahnert, F. M., J. J. Stamnes, and K. Stamnes (2001b): Application of the extended boundary conditions method to homogeneous particles with point group symmetries, *Appl. Opt.*, **40**, 3110–3123.

Kahnert, F. M., J. J. Stamnes, and K. Stamnes (2002a): Can simple particle shapes be used to model scalar optical properties of an ensemble of wavelength-sized particles with complex shapes? *J. Opt. Soc. Am. A*, **19**, 521–531.

Kahnert, F. M., J. J. Stamnes, and K. Stamnes (2002b): Using simple particle shapes to model the Stokes scattering matrix of ensembles of wavelength-sized particles with complex shapes: possibilities and limitations, *J. Quant. Spectr. Rad. Transf.*, **74**, 167–182.

Kantorovich, L. V., and V. I. Krylov (1964): *Approximate Methods of Higher Analysis*, John Wiley, New York.

Kerker, M. (1969): *The Scattering of Light and Other Electromagnetic Radiation*, Academic Press, San Diego, CA.

Khlebtsov, N. G. (1980): Light scattering by nonspherical particles and its applications, Cand. thesis, Saratov State University, Saratov, Russia.

Khlebtsov, N. G. (1996): Extinction and scattering of light in disperse systems: theory and experiments, Doct. Habil. thesis, Saratov State University (English translation of the review is available at http://www.astro.spbu.ru/DOP/3-REVS).

Kokkorakis, G. C., and J. A. Roumeliotis (2002): Power series expansions for spheroidal wave functions with small arguments, *J. Comp. Appl. Math.*, **139**, 95–127.

Komarov, V. I., L. I. Ponamarev, and S. Y. Slavyanov (1976): *Spheroidal and Coulomb Spheroidal Functions*, Nauka, Moscow [in Russian].

Kyurkchan, A. G. (1994): On a method of solving the problem of wave diffraction by a scatterer of finite sizes, *Sov. Phys. Dokl.*, **33**, 728–731.

Kyurkchan, A. G. (2000): Solution of vector scattering problem by the method of diagram equations, *(Sov.) Radiotechn. Electron.*, **45**, 1078–1083.

Li, L.-W., *et al.* (1998): Computations of spheroidal harmonics with complex arguments: a review with an algorithm, *Phys. Rev. E*, **58**, 6792–6806.

Li, L.-W., X.-K. Kang, and M. S. Leong (2002): *Spheroidal Wave Functions in Electromagnetic Theory*, John Wiley, New York.

Lorenz, L. (1890): Über die Refractionconstante, *Ann. Phys. Chem.*, **11**, 70–103.

Mackowski, D. W. (2002): Discrete dipole moment method for calculation of the T matrix for nonspherical particles, *J. Opt. Soc. Am. A*, **19**, 881–893.

Maystre, D., and M. Cadilhac (1985): Singularities of the continuation of fields and validity of Rayleigh's hypothesis, *J. Math. Phys.*, **26**, 2201–2204.

Mie, G. (1908): Beiträge zur Optik Trüber Medien, speziell kolloidaler Metallösungen, *Ann. Phys.*, **25**, 377–445.

Millar, R. F. (1973): The Rayleigh hypothesis and a related least-squares solution to scattering problem for periodic surfaces and other scatterers, *Radio Sci.*, **8**, 785–796.

Mishchenko, M. I., J. W. Hovenier, and L. D. Travis (2000a): Concepts, terms, notations, in *Light Scattering by Nonspherical Particles*, M.I. Mishchenko, J.W. Hovenier, L.D. Travis (eds), Academic Press, San Diego, CA, pp. 3–27.

Mishchenko, M. I., L. D. Travis, and A. Macke (2000b): T-matrix method and its applications, in *Light Scattering by Nonspherical Particles*, M. I. Mishchenko, J. W. Hovenier, L. D. Travis (eds), Academic Press, San Diego, CA, pp. 147–172.

Mishchenko, M. I., *et al.* (2000c): Overview of scattering by nonspherical particles, in *Light Scattering by Nonspherical Particles*, M. I. Mishchenko, J. W. Hovenier, and L. D. Travis (eds), Academic Press, San Diego, CA, pp. 29–60.

Mishchenko, M. I., L. D. Travis, and A. Lacis (2002): *Scattering, Absorption, and Emission of Light by Small Particles*, Cambridge University Press, Cambridge, UK.

Mishchenko, M. I., *et al.* (2004): T-matrix theory of electromagnetic scattering by particles and its applications: a comprehensive reference database, *J. Quant. Spectr. Rad. Transf.*, **88**, 357–406.

Möglich, F. (1927): Beugungserscheinungen an Korpen von ellipsoidischer Gestalt, *Ann. Phys.*, **83**, 609–735.

Moreno, E., *et al.* (2002): Multiple multipole method with automatic multipole setting applied to the simulation of surface plasmons in metallic nanostructures, *J. Opt. Soc. Am. A*, **19**, 101–111.

Moroz, A. (2005): Improvement of Mishchenko's T-matrix code for absorbing particles, *Appl. Opt.*, **44**, 3604-3609.

Morrison, J. A., M.-J. Cross, and T. S. Chu (1973): Rain-induced differential attenuation and differential phase shift at microwave frequencies, *Bell Syst. Tech. J.*, **52**, 599–604.

Morse, P. M., and H. Feshbach (1953): *Methods of Theoretical Physics*, McGraw-Hill, New York.

Mullin, C. R., R. Sandburg, and C. O. Velline (1965): A numerical technique for the determination of scattering cross sections of infinite cylinders of arbitrary geometrical cross section, *IEEE Trans. Anten. Propag.*, **13**, 141–149.

Nieminen, T. A., H. Rubinsztein-Dunlop, and N. R. Heckenberg (2003): Calculation of the T-matrix: general consideration and application of the point-matching method, *J. Quant. Spectr. Rad. Transf.*, **79-80**, 1019–1030.

Oguchi, T. (1973): Attenuation and phase rotation of radio waves due to rain: calculation at 19.3 and 34.8 GHz, *Radio Sci.*, **8**, 31–38.

Peterson, B., and S. Ström (1974): T-matrix formulation of electromagnetic scattering multilayered scatterers, *Phys. Rev. D*, **10**, 2670–2684.

Petrov, P. K., and V. A. Babenko (1999): The variational boundary condition method for solving problems of light scattering by nonspherical particles, *J. Quant. Spectr. Rad. Transf.*, **63**, 237–250.

Piller, N. B., and O. J. F. Martin (1998): Extension of the generalized multipole technique to three-dimensional anisotropic scatterers, *Opt. Lett.*, **23**, 579–581.

Posselt, B., *et al.* (2002): Light scattering by multilayered ellipsoidal particles in the quasistatic approximation, *Measur. Sci. Technol.*, **13**, 256–262.

Qingan, W., C. Kang, and O. Y. Z. Xiang (1999): Discussion of key algorithms for computing scattering cross sections using separate of variables method for spheroids, *J. Quant. Spectr. Rad. Transf.*, **63**, 251–261.

Ramm, A. G. (1982): Convergence of the T-matrix approach to scattering theory, *J. Math. Phys.*, **23**, 1123–1125.

Rayleigh, D. W. (1881): On the electromagnetic theory of light, *Phil. Mag.*, **12**, 81–101.

Rother, T. (1998): Generalization of the separation of variables method for non-spherical scattering of dielectric objects, *J. Quant. Spectr. Rad. Transf.*, **60**, 335–353.

Rother, T., K. Schmidt, and S. Havemann (2001): Light scattering on hexagonal ice columns, *J. Opt. Soc. Am. A*, **18**, 2512–2517.

Schmidt, K., T. Rother, and J. Wauer (1998): The equivalence of applying the extended boundary condition the continuity conditions for solving electromagnetic scattering problems, *Opt. Commun.*, **150**, 1–4.

Schmidt, K., J. Wauer, and T. Rother (2003): Application of the separation of variables method to a plane wave scattering on nonaxisymmetric particles, *Proc. SPIE*, **5059**, 76–86.

Schulz, F. M., K. Stamnes, and J. J. Stamnes (1998): Scattering of electromagnetic waves by spheroidal particles: a novel approach exploiting the T-matrix computed in spheroidal coordinates, *Appl. Opt.*, **37**, 7875–7896.

Sinha, B. P., and R. H. McPhie (1977): Electromagnetic scattering by prolate spheroids for a plane waves with arbitrary polarization and angle of incidence, *Radio Sci.*, **12**, 171–184.

Stratton, J. A. (1941): *Electromagnetic Theory*, McGraw-Hill, New York.

Tsinopoulos, S. V., S. E. Kattis, and D. Polyzos (1998): Three-dimensional boundary element analysis of electromagnetic wave scattering by penetrable bodies, *Comp. Mech.*, **21**, 306–315.

van de Hulst, H. C. (1957): *Light Scattering by Small Particles*, Dover, New York.

Varadan, V. K., and V. V. Varadan (eds) (1980): *Acoustic, Electromagnetic and Elastic Wave Scattering – Focus on the T-Matrix Approach*, Pergamon Press, New York.

Voshchinnikov, N. V., and V. G. Farafonov (1993): Optical properties of spheroidal particles, *Astrophys. Sp. Sci.*, **204**, 19–86.

Voshchinnikov, N. V., and V. G. Farafonov (2002): Light scattering by an elongated particle: spheroid versus infinite cylinder, *Measur. Sci. Technol.*, **13**, 249–255.

Voshchinnikov, N. V., and V. G. Farafonov (2003): Calculation of prolate radial spheroidal functions using Jaffé expansion, *Comp. Math. Math. Phys.*, **43**, 1299–1309.

Wait, J. R. (1955): Electromagnetic scattering from a radially inhomogeneous sphere, *Can. J. Phys.*, **33**, 189–195.

Waterman, P. C. (1965): Matrix formulation of electromagnetic scattering, *Proc. IEEE*, **53**, 805–812.

Waterman, P. C. (1969): Scattering by dielectric obstacles, *Alta. Freq.*, **38**, 348–352.

Wolf, S., and N. V. Voshchinnikov (2004): Mie scattering by ensembles of particles with very large size parameters, *Comp. Phys. Commun.*, **162**, 113–123.

Wriedt, T. (1998): Review of elastic scattering theories, *Part. Part. Syst. Charact.*, **15**, 67–74.

Wriedt, T. (2005): Internet site: http://www.T-matrix.de

Wriedt, T., and A. Doicu (1997): Comparison between various formulations of the extended boundary condition method, *Opt. Commun.*, **142**, 91–98.

Wried, T., and U. Comberg (1998): Comparison of computational scattering methods, *J. Quant. Spectr. Rad. Transf.*, **60**, 411–423.

Yang, W. (2003): Improved recursive algorithm for light scattering by a multilayered sphere, *Appl. Opt.*, **42**, 1710–1720.

Part II

Multiple Light Scattering

5 Multiple scattering of short waves by uncorrelated and correlated scatterers

Anatoli G. Borovoi

There is a large number of books dealing with the problems of either single or multiple scattering of waves. While these waves can be of very different nature: electromagnetic, acoustic, quantum mechanical, etc, the equations used to describe them are quite similar. It is now universally recognized that these problems could be united to form an interdisciplinary theory for both single and multiple scattering of waves.

The books available do not completely solve the unification problem yet. Moreover, they are generally overloaded with mathematics. We know that there are researchers, the author being one of them, who would rather follow a different approach: if mathematics is the skill to avoid numerical calculations, then theoretical physics is the skill to avoid mathematics. One of the purposes of this work is, therefore, to focus on the general equations and physical results of the theory of wave scattering and to describe these findings by mathematics that is as simple as possible.

Until now, the researchers have mainly restricted themselves to the cases where size of scatterers is less than or comparable with wavelengths. Large scatterers as compared with wavelengths have been put aside because of extreme demands on computer resources. Another purpose of this work is to include the case of large scatterers in the general wave scattering approach.

In this way, we show that a number of simple results can be obtained for large scatterers without numerical calculations. To achieve these purposes, the general equations for the quadratic values of the fields and the conservation energy law are widely used, along with the usual way based on the field equations.

This work does not contain a conventional survey. In brief bibliographical comments, several well-known books are referred to where the comprehensive bibliography can be found. As for comments on authors' papers, they are included simply to show that the results presented in this work have been already published (in Russian).

This work has appeared due exclusively to Dr Alexander Kokhanovsky, who suggested the writing of this chapter and encouraged the author in the course of work. He also looked through a part of this work, and his remarks have been very

valuable in improving the presentation. The author is also indebted to INTAS (grant 01-0239) and RFBR (grant 03-05-64745) for current support.

5.1 Waves in free space

Wave motion surrounds us everywhere; it is one of the basic phenomena in the universe. Sound, light, electromagnetic waves of other wavelengths, transverse waves on a water surface, and even elementary particles obeying laws of quantum mechanics are described by the similar wave equations. So, in this chapter, we shall often prefer to pay attention to the universal feature of the wave phenomena discussed instead of restricting ourselves to visible light and to the Maxwell equations, correspondingly. The universal character of wave phenomena becomes evident when the basic equations are written down in the compact form of operator equations.

5.1.1 General equations

Propagation of a wave in a free unbounded space is described by the linear operator equation

$$L\Psi = 0 \tag{5.1}$$

where L is the propagation operator and Ψ is the wave field. Wave sources appear in the right side of eq. (5.1)

$$L\Psi = q \tag{5.2}$$

Then the wave field, i.e. the solution to eq. (5.2), is readily found through the propagator L^{-1}, i.e. the Green function of eq. (5.2)

$$\Psi = L^{-1}q \tag{5.3}$$

Sometimes it is expedient to consider not the unbounded space but a domain D of finite sizes with a boundary S. In this case, an impact from the sources located outside this domain D can be taken into account by the wave field Ψ_S that is created on the boundary by those outside sources. Then the wave field inside the domain D can be found through the surface Green function L_S^{-1} in a similar way to eq. (5.3)

$$\Psi = L_S^{-1}\Psi_S \tag{5.4}$$

If wave sources are present inside the domain D, too, the wave field becomes a superposition

$$\Psi = L^{-1}q + L_S^{-1}\Psi_S \tag{5.5}$$

Equation (5.5) is the general solution to the problem of wave propagation in the free space.

5.1.2 Chain of wave equations

Now, let us write down a number of explicit expressions for the values cited above. We shall use the intuitive coordinate representation for both the fields and the operators of eqs (5.1)–(5.5). The harmonic dependence on time t with the frequency ω is assumed. This harmonic dependence is determined by the factor $\exp(-i\omega t)$ that is always omitted in this study. For a given frequency, the wavelength in the free space λ is the basic parameter of the problems considered. Instead of the wavelength, the wave number $k = 2\pi/\lambda$ will be used, as a rule.

It is known that, in electrodynamics, the Maxwell equations in free space can be used to derive eq. (5.1) for the electric field $\boldsymbol{E}(\boldsymbol{r})$

$$\begin{aligned} \Psi &= \boldsymbol{E}(\boldsymbol{r}) \\ L &= -\mathrm{rot}\,\mathrm{rot} + k^2 \\ L^{-1} &= \left(\frac{\nabla_{\boldsymbol{r}}\nabla_{\boldsymbol{r}'}}{k^2} - \hat{\mathbf{1}}\right)\frac{\mathrm{e}^{ik|\boldsymbol{r}-\boldsymbol{r}'|}}{4\pi|\boldsymbol{r}-\boldsymbol{r}'|} \end{aligned} \tag{5.6}$$

where $\boldsymbol{r} = (x, y, z)$ are Cartesian coordinates, $\hat{\mathbf{1}}$ is the unit matrix of 3×3 dimensions, and $\nabla_{\boldsymbol{r}}\nabla_{\boldsymbol{r}'}$ is the 3×3 matrix formed by the product of two 3×3 matrices where the left column and the upper line are the gradient-vectors $\nabla_{\boldsymbol{r}}$ and $\nabla_{\boldsymbol{r}'}$, respectively, and the other elements are equal to zero.

The propagator L^{-1} of eq. (5.6) has an obvious physical meaning. This is the electric field in the point $\boldsymbol{r}$ that is generated by an electric dipole located in the point $\boldsymbol{r}'$. In general, this vector field has three components. At large distance from the dipole, the longitudinal component becomes negligible and the field turns out into the outgoing transverse wave that is carrying energy out from the source.

For scalar wave fields $\psi(\boldsymbol{r})$, eq. (5.1) is the Helmholtz equation

$$\begin{aligned} \Psi &= \psi(\boldsymbol{r}) \\ L &= \Delta + k^2 \\ L^{-1} &= -\frac{\mathrm{e}^{ik|\boldsymbol{r}-\boldsymbol{r}'|}}{4\pi|\boldsymbol{r}-\boldsymbol{r}'|} \\ L_S^{-1} &= \frac{\partial L^{-1}}{\partial \boldsymbol{n}} - L^{-1}\frac{\partial}{\partial \boldsymbol{n}} \end{aligned} \tag{5.7}$$

Here, the propagator L^{-1} describes the isotropic spherical wave outgoing from a point source located at the point $\boldsymbol{r}'$, and the last expression of eq. (5.7) for the surface Green function corresponds to the well-known Green theorem where $\boldsymbol{n}$ is the external normal to the surface S.

In non-relativistic quantum mechanics, eq. (5.7) corresponds to the fundamental Schrödinger equation where the complex-valued function $\psi(\boldsymbol{r})$ is just the famous wave function of quantum mechanics. Also, the Helmholtz equation is the basic equation for acoustics where $\psi(\boldsymbol{r})$ means either the sound pressure or the acoustic velocity potential. Sometimes, polarization of electromagnetic

waves can be ignored. Then the Maxwell equations of eq. (5.6) are replaced by the Helmholtz equation (5.7), too.

The next important simplification of the wave equations arises if the wave field differs weakly from a plane wave propagating, say, along the x-axis, i.e.

$$\psi(\boldsymbol{r}) = u(\boldsymbol{r})\mathrm{e}^{ikx} \tag{5.8}$$

where the function $u(\boldsymbol{r})$ is assumed to vary smoothly along the x-axis as compared to $\exp(ikx)$. Substituting eq. (5.8) into eq. (5.7) and neglecting certain small quantities, we arrive at the parabolic equation

$$\begin{aligned} \Psi &= u(\boldsymbol{r}) \\ L &= 2ik\frac{\partial}{\partial x} + \Delta_\perp = 2ik\frac{\partial}{\partial x} + \frac{\partial^2}{\partial y^2} + \frac{\partial^2}{\partial z^2} \\ L^{-1} &= -\frac{H(x-x')}{4\pi(x-x')}\exp\left[\frac{ik(\boldsymbol{\rho}-\boldsymbol{\rho}')^2}{2(x-x')}\right] \\ L_S^{-1} &= 2ikL^{-1} \end{aligned} \tag{5.9}$$

Here, H is the Heaviside function

$$\begin{aligned} H(x) &= 1 \quad \text{for} \quad x > 0 \\ H(x) &= 0 \quad \text{for} \quad x < 0 \end{aligned} \tag{5.10}$$

and $\boldsymbol{\rho} = (y, z)$ are the transverse coordinates. The last expression in eq. (5.9) for the surface Green function corresponds to the conventional case, where the initial field is determined in the plane $x' = \text{const}$.

The parabolic equation is widely used in numerous problems of the coherent optics and holography where the term of the paraxial approximation is also used. In radiophysics, the theory based on this equation is sometimes called the quasioptics. The reason for the wide applicability of the parabolic equation is that it accurately describes diffraction phenomena at small angles.

The simplest wave equation is obtained from the parabolic equation if the term $\Delta_\perp$ describing diffraction is ignored. Then it follows

$$\begin{aligned} \Psi &= u(\boldsymbol{r}) \\ L &= 2ik\frac{\partial}{\partial x} \\ L^{-1} &= \frac{1}{2ik}H(x-x') \\ L_S^{-1} &= 2ikL^{-1} = H(x-x')\delta(\boldsymbol{\rho}-\boldsymbol{\rho}') \end{aligned} \tag{5.11}$$

Within the framework of this equation, wave propagation turns out to be a simple motion along the straight rays that are parallel to the x-axis. It is readily seen from the last expression. Equation (5.11) had been widely used in various fields of physics by many authors, as a rule, independently. Therefore, it has a lot of names. The names of eikonal, high-energy, and Molier's approximations are known in quantum mechanics. In optics, the terms of both van de Hulst

and WKB (Wentzel, Kramers, and Brillouin) approximations are used. In the problem of light propagation through the turbulent atmosphere, this approximation is referred to as geometrical optics; and so on. We shall call eq. (5.11) the straight-ray approximation since this term reflects directly the physical entity of this approximation.

5.1.3 Corpuscular treatment of short waves

Because of continuity, wave fields are rather difficult objects for the human imagination since a human brain prefers to deal with discrete quantities. Fortunately, in physics, there are many situations where wave fields can be treated from the discrete, i.e. corpuscular, point of view. If the wavelength of a wave field occurs to be small for a given situation, sometimes certain special efforts are undertaken to reveal the wave nature of the radiation as it takes place, for example, in optics. So, in situations where the wave phenomena are barely detected, the wave field can be treated in the corpuscular manner, i.e. as a lot of corpuscles that are moving according to the laws of classical mechanics. In optics, these corpuscles are called photons. Similarly, for elementary particles in quantum mechanics, particles such as, say, neutrons are roughly considered as corpuscles, and the wave treatment is needed only in situations where their de Broglie wavelengths are revealed.

We pay attention to the following two situations where it is expedient to treat wave fields as corpuscles. The first situation arises when the scales of objects interacting with the wave fields are much larger than the wavelength. In this case, the Maxwell equations can be reduced to the well-known geometric optics equations and quantum mechanics is reduced to classical mechanics, respectively. Geometric optics equations divide the space into a set of ray tubes (Fig. 5.1(a)) that are associated with a curvilinear coordinate system. Here, the longitudinal coordinate corresponds to a path along the tubes and the transverse coordinates form the wavefront surfaces that are constructed perpendicularly to the ray tubes. According to the geometric optics equations, the wave propagation corresponds to motion of the radiation particles along the ray tubes.

The second situation corresponds to randomly distributed objects interacting with the incident wave. For example, solar light entered a room is reflected by rough surfaces of both walls and other obstacles within the room. As a result, the eye detects a lot of photons coming from various directions (Fig. 5.1(b)). In this situation, the ratio between the incident wavelength and sizes of the wall inhomogeneities resulting in light scattering is of no importance. The matter is only that, in a small volume near the observation point $\boldsymbol{r}$, we get a lot of wave packets with different both phases and propagation directions $\boldsymbol{n}$. It is natural to describe this wave field as an ensemble of a great number of corpuscles flying in different directions in the free space (Fig. 5.1(b)).

Let us emphasize that the physical model corresponding to Fig. 5.1(b) is widely used in physics for the description of a lot of physical objects. For example, the dots in Fig. 5.1(b) could be associated with molecules for classical statistical mechanics of gases and liquids, γ-quanta penetrating the protection

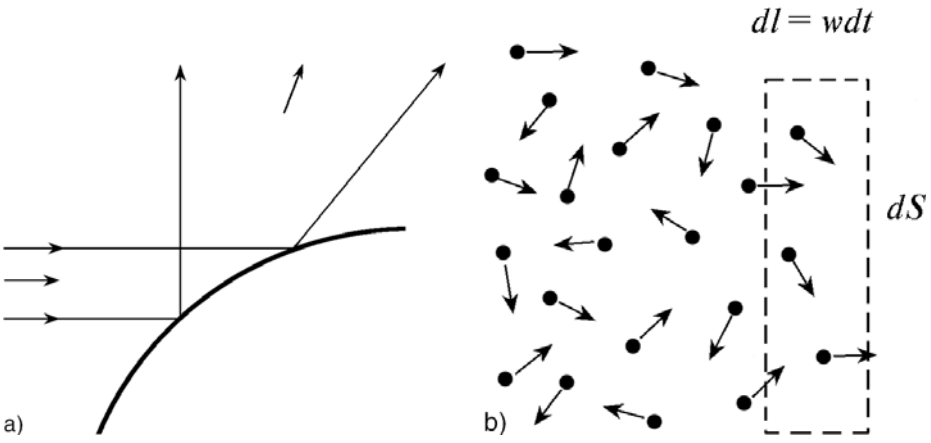

Fig. 5.1. Corpuscular treatment of short-wave fields. (a) Geometric optics approximation; within a wave tube, a corpuscle has one propagation direction at a spatial point. (b) Set of corpuscles with chaotic spatial and propagation direction distributions.

matter around a nuclear reactor, and so on. Even whole physical disciplines such as radiometry and photometry are based on these conceptions.

Ensembles of corpuscles shown in Fig. 5.1(b) are characterized by the number density $N(\boldsymbol{r}, \boldsymbol{w})$ that means the number of corpuscles occurred in the vicinities of the spatial point $\boldsymbol{r}$ and of the velocity $\boldsymbol{w}$, i.e. in the element $d\boldsymbol{r}\, d\boldsymbol{w}$. Instead of the number of corpuscles, their fluxes crossing certain surfaces are often considered. These fluxes are determined by the flux density that is simply connected with the function $N(\boldsymbol{r}, \boldsymbol{w})$. For brevity, we assume that the magnitude w of corpuscle velocities is a constant and consider the number density $N(\boldsymbol{r}, \boldsymbol{n})$, where $\boldsymbol{n} = \boldsymbol{w}/w$ is the propagation direction. Let us mentally separate corpuscles with a given propagation direction $\boldsymbol{n}$ and consider the surface element dS that is perpendicular to the direction $\boldsymbol{n}$. It is obvious that this element dS is crossed per the time of dt by those corpuscles that are located in the volume of wdS (see Fig. 5.1(b)). So, the product

$$I(\boldsymbol{r}, \boldsymbol{n}) = wN(\boldsymbol{r}, \boldsymbol{n}) \tag{5.12}$$

is just the desired flux density of the corpuscles. Every corpuscle is associated with a definite energy; therefore we shall prefer to call this function of five variables the energy flux density. In photometry, the value $I(\boldsymbol{r}, \boldsymbol{n})$ is called the specific intensity or radiance. If the propagation direction $\boldsymbol{n}$ is known and can be omitted, the value $I(\boldsymbol{r})$ is often called the intensity. For our study, we do not need to consider the dimensionality of these quantities since they are usually normalized to the same values of incident fields. So, both the flux density $I(\boldsymbol{r}, \boldsymbol{n})$ and the intensity $I(\boldsymbol{r})$ are assumed in this chapter to be non-dimensional quantities. In particular, the intensity for an incident plane wave is always accepted to be equal to 1. As a result, the energy fluxes through any surface will have the dimension of area.

Of course, both the quantities N and I are applicable to the wave fields shown in Fig. 5.1(a) as well. In such cases, the dependence on the propagation direction $\boldsymbol{n}$ is reduced to the Dirac delta-function $\delta(\boldsymbol{n} - \boldsymbol{n}_0)$ separating the direction of a ray tube.

The corpuscular treatment of wave fields will be often used further for clarification of the results obtained.

5.1.4 Equations for quadratic values

In all fields of physics concerned, it is the wave fields that are usually calculated both analytically and numerically. At the same time, in practice, often only certain quadratic values of the fields are measured but not the fields directly. So, two steps must be taken: first, to calculate the fields and, second, to calculate their quadratic values needed for a comparison with experiments. It is natural to bring up the question: Why not use the respective equations for the quadratic values directly?

An obvious drawback of the equations for the quadratic values is that they double dimensions as compared to the field equations, so they are more tedious. Nevertheless, the quadratic values equations reveal the two following advantages. The first advantage concerns stochastic sources of radiation. Within the wave equation approach, only determinate sources are readily treated while the case of a stochastic source demands certain special efforts. An advantage of the equations for the quadratic values is that these equations readily include both determinate and stochastic sources. The second advantage is that the equations for quadratic values for the cases of stochastic sources and stochastic scattering media can often be treated from the abovementioned corpuscular point of view. Therefore, the quadratic values equations are widely used in this study, and they are considered in detail in this section.

In the language of operators, the quadratic values of the fields are defined as the direct product $\Psi \otimes \Psi^*$, where the asterisk denotes a complex-conjugate value. The direct product means that we go to a space of double dimension. For example, for a scalar function $\psi(\boldsymbol{r})$, the direct product $\Psi \otimes \Psi^*$ is the following function $\psi(\boldsymbol{r}_1)\psi^*(\boldsymbol{r}_2)$ defined in the space of six variables $(\boldsymbol{r}_1, \boldsymbol{r}_2)$. For electromagnetic waves, the direct product of vectors and matrices will be discussed later, in section 5.4.4. One of the main properties of the direct products is determined by the identity: $(AB) \otimes (CD) = (A \otimes C)(B \otimes D)$ where A and C are operators and B and D can be either fields or operators. This identity means that if we need to find a direct product of two values, where every one of the co-factors is an ordinary product of operators, we can construct term by term the operators in the double-dimension space $A \otimes C$ and $B \otimes D$ and then multiply them as operators of the double-dimension space.

Thus, the initial equation (5.2) can be transformed into the following equation for the quadratic values written down in the double-dimension space

$$(L \otimes L^*)\Psi \otimes \Psi^* = q \otimes q^* \tag{5.13}$$

If the wave source is stochastic, often only the average value $\langle q \otimes q^* \rangle$ is of interest, where the angle brackets mean a statistical averaging. In this case, eq. (5.13) is readily generalized

$$(L \otimes L^*)\langle \Psi \otimes \Psi^* \rangle = \langle q \otimes q^* \rangle \tag{5.14}$$

For simplicity, we postpone the case of electromagnetic waves until section 5.4.4 and consider the quadratic values with two spatial points for the case of scalar waves described by the Helmholtz equation (5.7). Here, the quadratic value is as follows

$$\Gamma_{11}(\boldsymbol{r}_1, \boldsymbol{r}_2) = \Gamma(\boldsymbol{R}, \boldsymbol{r}) = \langle \psi(\boldsymbol{r}_1)\psi^*(\boldsymbol{r}_2) \rangle \tag{5.15}$$

where the difference $\boldsymbol{R}$ and mean $\boldsymbol{r}$ arguments, respectively,

$$\boldsymbol{R} = \boldsymbol{r}_1 - \boldsymbol{r}_2; \quad \boldsymbol{r} = (\boldsymbol{r}_1 + \boldsymbol{r}_2)/2 \tag{5.16}$$

are introduced. The quadratic value Γ is called the spatial coherence function.

Consider the equations governing the coherence function (5.15). It obeys the Helmholtz equation

$$(\Delta_1 + k^2)\Gamma_{11} = (\Delta_2 + k^2)\Gamma_{11} = 0 \tag{5.17}$$

where Δ_1 and Δ_2 are the Laplacians relative to the both variables $\boldsymbol{r}_1$ and $\boldsymbol{r}_2$. Hence, it obeys the following equation, too

$$(\Delta_1 - \Delta_2)\Gamma_{11} = 0 \tag{5.18}$$

By means of the identical relation

$$\Delta_1 - \Delta_2 = \nabla_1^2 - \nabla_2^2 = (\nabla_1 - \nabla_2)(\nabla_1 + \nabla_2) = 2\nabla_{\boldsymbol{R}}\nabla_{\boldsymbol{r}} \tag{5.19}$$

equation (5.18) is transformed to the following equation in the variables $\boldsymbol{r}$ and $\boldsymbol{R}$

$$\nabla_{\boldsymbol{R}}\nabla_{\boldsymbol{r}}\Gamma(\boldsymbol{R}, \boldsymbol{r}) = 0 \tag{5.20}$$

Let us define the Fourier transform of the coherence function relative to the difference variable $\boldsymbol{R}$ that is called the Wigner function

$$W(\boldsymbol{r}, \boldsymbol{p}) = \left(\frac{k}{2\pi}\right)^3 \int \Gamma(\boldsymbol{R}, \boldsymbol{r})\mathrm{e}^{-ik\boldsymbol{p}\boldsymbol{R}}\mathrm{d}\boldsymbol{R}; \quad \Gamma(\boldsymbol{R}, \boldsymbol{r}) = \int W(\boldsymbol{r}, \boldsymbol{p}\mathrm{e}^{ik\boldsymbol{p}\boldsymbol{R}}\,\mathrm{d}\boldsymbol{p} \tag{5.21}$$

Substitution of eq. (5.21) in eq. (5.20) gives the following equation for the Wigner function

$$\boldsymbol{p}\nabla_{\boldsymbol{r}}W(\boldsymbol{r}, \boldsymbol{p}) = 0 \tag{5.22}$$

The operator $\boldsymbol{p}\nabla_{\boldsymbol{r}}$ is the directional derivative along the vector $\boldsymbol{p}$. Therefore, we get a solution to eq. (5.22) that is very simple

$$W(\boldsymbol{r}, \boldsymbol{p}) = W(\boldsymbol{r} - l\boldsymbol{p}, \boldsymbol{p}) \tag{5.23}$$

where l ($l > 0$) is an arbitrary number, and $\boldsymbol{r} - l\boldsymbol{p}$ is a running point on the ray until the point reaches a radiation source. If the Wigner function is given on an

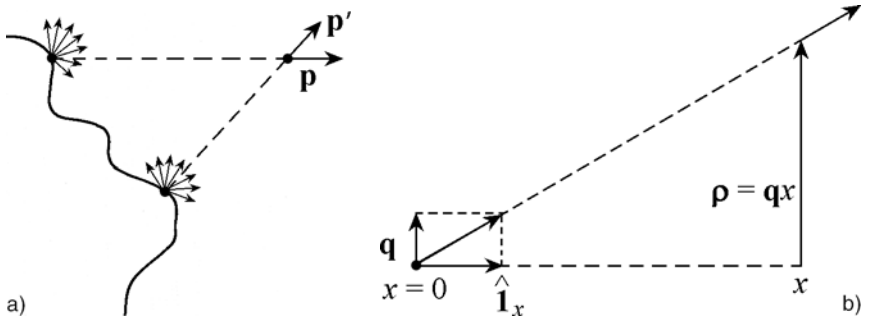

Fig. 5.2. Straight-line propagation of the Wigner function. (a) The Helmholtz equation. (b) The parabolic equation.

arbitrary surface, one can easily find the Wigner function in any point using eq. (5.23) (see Fig. 5.2(a)).

Equation (5.22) reveals a remarkable fact. Indeed, it might seem that a wave motion and a straight-line motion of solid particles in free space are quite different phenomena in the universe. It is eq. (5.22) that proves that the straight-line motion is inherent to any wave motion, too. But this property of wave motion appears explicitly at the level of the quadratic values of the fields. So, propagation of the Wigner function in the free space is just equivalent to propagation of classical particles or corpuscles due to eq. (5.23).

The function $W(\boldsymbol{r}, \boldsymbol{p})$ was proposed by E. Wigner in 1932 to describe the reduction of quantum-mechanical statistical physics to classical statistical physics. In the classical statistical mechanics, a basic quantity is the number density of particles $N(\boldsymbol{r}, \boldsymbol{w})$ in the point $\boldsymbol{r}$ with the velocity $\boldsymbol{w}$ as was described in section 5.1.3. The Wigner function $W(\boldsymbol{r}, \boldsymbol{p})$ is just the wave-motion analog of the function $N(\boldsymbol{r}, \boldsymbol{w})$. So, the vector $k\boldsymbol{p}$ corresponds to the corpuscle velocity. The Wigner function reveals a lot of features inherent to the N-function. For example, $W(\boldsymbol{r}, \boldsymbol{p})$ is the real-valued quantity like the function $N(\boldsymbol{r}, \boldsymbol{w})$. For the plane wave $\exp(ik\boldsymbol{n}_0\boldsymbol{r})$ it results in the Dirac delta function $\delta(\boldsymbol{p} - \boldsymbol{n}_0)$. The main discrepancy between them is that the N function is always positive while the Wigner function can be a negative quantity as well.

Let us consider the quadratic quantities for the parabolic equation. In this case, the quadratic values are usually considered for two points located in the same plane $x = \text{const}$. Then eq. (5.18) is transformed into the equation

$$\left(2ik\frac{\partial}{\partial x} + \Delta_{\perp 1} - \Delta_{\perp 2}\right) \Gamma_{11}(x, \boldsymbol{\rho}_1, \boldsymbol{\rho}_2) = 0 \tag{5.24}$$

where $\boldsymbol{\rho}_1$ and $\boldsymbol{\rho}_2$ are the transverse coordinates, and $\Delta_\perp$ are the Laplacians relative to these variables. The Wigner function should be defined by the 2-D Fourier transform

$$W(x,\boldsymbol{\rho},\boldsymbol{q}) = \left(\frac{k}{2\pi}\right)^2 \int \Gamma(x,\boldsymbol{R},\boldsymbol{\rho})\mathrm{e}^{-ik\boldsymbol{qR}}\,\mathrm{d}\boldsymbol{R};$$
$$\Gamma(x,\boldsymbol{R},\boldsymbol{\rho}) = \int W(x,\boldsymbol{\rho},\boldsymbol{q})\mathrm{e}^{ik\boldsymbol{qR}}\,\mathrm{d}\boldsymbol{q} \tag{5.25}$$

where $\boldsymbol{R}$ and $\boldsymbol{\rho}$ are the difference and mean coordinates, respectively, in the plane $x = \text{const}$

$$\boldsymbol{R} = \boldsymbol{\rho}_1 - \boldsymbol{\rho}_2; \quad \boldsymbol{\rho} = (\boldsymbol{\rho}_1 + \boldsymbol{\rho}_2)/2 \tag{5.26}$$

Since the vector $k\boldsymbol{p}$ of eq. (5.22) was interpreted as the velocity of a corpuscle, the vector $k\boldsymbol{q}$ has the physical meaning of the transverse component of this velocity.

Applying the identity (5.19) to eq. (5.24) and substituting eq. (5.25), we get the following equation for the 2-D Wigner function

$$\left(\frac{\partial}{\partial x} + \boldsymbol{q}\nabla_{\boldsymbol{\rho}}\right) W(x,\boldsymbol{\rho},\boldsymbol{q}) = 0 \tag{5.27}$$

Analogously to the 3-D case, the second term in eq. (5.27) is the directional derivative in the plane $x = \text{const}$. A solution to eq. (5.27) is determined by a given value of the Wigner function in a plane, say, $x = 0$. Then the solution is expressed through the function $W(0,\boldsymbol{\rho},\boldsymbol{q})$ as follows

$$W(x,\boldsymbol{\rho},\boldsymbol{q}) = W(0,\boldsymbol{\rho} - \boldsymbol{q}x,\boldsymbol{q}) \tag{5.28}$$

Equation (5.28) can be also derived from eq. (5.23). The straight-line propagation of the Wigner function described by eq. (5.28) is shown in Fig. 5.2(b). In this case, the velocities of corpuscles $\boldsymbol{p}$ should obey the following restriction

$$\boldsymbol{p} = \hat{\mathbf{1}}_x + \boldsymbol{q} \tag{5.29}$$

where $\hat{\mathbf{1}}_x$ is the unit vector along the x-axis and $\boldsymbol{q}$ is an arbitrary transverse component. It means that projections of corpuscle velocities on the x-axis should be the same. This restriction is justified at small angles $|\boldsymbol{q}| \ll 1$. Let us recall that the parabolic equation is an approximation to the Helmholtz equation, and it is valid only for the case of propagation at small angles relative to the basic direction along the x-axis.

5.1.5 Energy conservation law

Energy conservation law is a basic law for the quadratic values of wave fields. In this section, this law is considered for all wave equations of section 5.1.2.

To make the energy conservation law more obvious, let us start from the corpuscular treatment of wave fields described in section 5.1.3 and shown in Fig. 5.1(b). Assume that corpuscle velocities have equal magnitudes and they differ in propagation directions $\boldsymbol{n}$ only, where $|\boldsymbol{n}| = 1$. According to the definition of eq. (5.12), the energy flux, i.e. the flux of the corpuscles, through an arbitrary surface S of the external normal $\boldsymbol{M}$ is readily written down as the integral over all propagation directions $\boldsymbol{n}$

$$\Phi = \iint (\boldsymbol{n}\boldsymbol{M}) I(\boldsymbol{r}, \boldsymbol{n})\, \mathrm{d}\boldsymbol{n}\, \mathrm{d}S \tag{5.30}$$

We emphasize that $\int \ldots \mathrm{d}\boldsymbol{n}$ means everywhere in this Chapter the integral over the solid angle because of the unit modulus for the vector $\boldsymbol{n}$, i.e. $|\boldsymbol{n}| = 1$.

It is expedient to separate the vector field

$$\boldsymbol{j}(\boldsymbol{r}) = \int \boldsymbol{n} I(\boldsymbol{r}, \boldsymbol{n})\, \mathrm{d}\boldsymbol{n} \tag{5.31}$$

then the energy flux given by eq. (5.30) proves to be the flux of this vector field $\boldsymbol{j}(\boldsymbol{r})$

$$\Phi = \int_S \boldsymbol{j}\boldsymbol{M}\, \mathrm{d}S \tag{5.32}$$

In particular, if S is a closed surface, we get

$$\Phi = P \tag{5.33}$$

where P is a power of the sources that are surrounded by the closed surface S. Equation (5.33) is just the energy conservation law. If there are no sources, we have: $\Phi = 0$.

Now come back to wave fields. In this case, the energy conservation law is described by just the same equation (5.33) but the vector fields $\boldsymbol{j}(\boldsymbol{r})$ are defined by other, not so evident, equations. In particular, for the Helmholtz equation, the energy-flux density $\boldsymbol{j}(\boldsymbol{r})$ is determined by the following quadratic value of the field

$$\boldsymbol{j} = k^{-1} \operatorname{Im} \psi^* \nabla \psi \tag{5.34}$$

where the normalization factor k^{-1} is chosen to provide the conventional normalization. Namely, the intensity of the plane wave of unit amplitude $\exp(ikx)$ is required to be equal to unity ($I = |\boldsymbol{j}| = 1$) as was discussed in connection with eq. (5.12). For the electromagnetic waves (5.6), the energy-flux density is the Poynting vector

$$\boldsymbol{j} = k^{-1} \operatorname{Im} (\boldsymbol{E}^* \times \operatorname{rot} \boldsymbol{E}) \tag{5.35}$$

where the symbol $\times$ means the vector product.

For the cases where the Wigner function $W(\boldsymbol{r}, \boldsymbol{p})$ of eq. (5.21) coincides with the specific intensity $I(\boldsymbol{r}, \boldsymbol{n})$ of eq. (5.12)

$$I(\boldsymbol{r}, \boldsymbol{n}) = W(\boldsymbol{r}, \boldsymbol{p}) \tag{5.36}$$

both the wave and corpuscle approaches are equivalent.

Of course, the language of wave fields is more basic, and certain expressions are impossible to treat from the corpuscular point of view. In particular, if a field is decomposed in, say, two components

$$\Psi = \Psi_1 + \Psi_2 \tag{5.37}$$

any quadratic values including the energy flux Φ are decomposed in three components

$$\Phi = \Phi_1 + \Phi_2 + \Phi_{12} \tag{5.38}$$

where Φ_1 and Φ_2 are the fluxes for every component and Φ_{12} is the interference term. It is the interference term that reveals the wave nature of a radiation.

For any approximations to the wave fields, the energy conservation law is not satisfied automatically. Therefore let us consider the energy conservation law for the cases of the parabolic equation (5.7) and the straight-ray approximation (5.11) where the field $u(x, \boldsymbol{\rho})$ means a weak deviation from the plane wave $\psi = \exp(ikx)$ propagating along the x-axis.

In the straight-ray approximation, the wave is conserved along the ray $\boldsymbol{\rho} = \text{const}$ according to the last expression of eq. (5.11)

$$u(x, \boldsymbol{\rho}) = u(0, \boldsymbol{\rho}) \tag{5.39}$$

Therefore, the energy-flux density $\boldsymbol{j}(\boldsymbol{r})$ given by eq. (5.34) should be conserved along the ray as well. So, we get

$$\boldsymbol{j}(x, \boldsymbol{\rho}) \approx |u(x, \boldsymbol{\rho})|^2 \hat{\mathbf{1}}_x \tag{5.40}$$

where the unit vector $\mathbf{1}_x$ along the x-axis corresponds to the basic plane wave $\psi = \exp(ikx)$. Then the energy fluxes through any plane $x = \text{const}$ are conserved, too

$$\Phi_x = \int |u(x, \boldsymbol{\rho})|^2 \, \mathrm{d}\boldsymbol{\rho} = \Phi_{x=0} \tag{5.41}$$

The straight-ray approximation ignores diffraction phenomena. For example, if an initial field defined in the plane $x = 0$ is a plane-parallel beam with the propagation direction $\mathbf{1}_x$ and the transverse size of a (where $ka \gg 1$), it is well known that, with a good accuracy, this beam conserves its transverse shape in the near zone, i.e. at the distances $x \ll ka^2$. At distances $x \approx ka^2$, the transverse shape is distorted by the Fresnel diffraction. In the wave zone $x \gg ka^2$, the beam is transformed into a divergent spherical wave that is essential only at small scattering angles $|\boldsymbol{q}| \ll 1$. Thus, the straight-ray approximation is just valid in the near zone $x \ll ka^2$ of the initial fields. Then the parabolic equation (5.9) should describe both the Fresnel and Fraunhofer diffractions for initial fields of large transverse dimensions $ka \gg 1$.

Generally speaking, if there are no field sources, the energy flux through any plane $x = \text{const}$ should always be a constant

$$\Phi_x = \Phi_{x'} \tag{5.42}$$

This fact is readily proven if one considers a volume V bounded by the planes $x = \text{const}$ and $x' = \text{const}$ and by an arbitrary lateral surface. Then the limit $V \to \infty$ at $x, x' = \text{const}$ leads to eq. (5.42).

Let us consider how the general equation (5.42) is satisfied within the parabolic equation. The surface Green function L_S^{-1} of the parabolic equation is the unitary operator relative to the 2-D variable $\boldsymbol{\rho}$

$$L_S^{-1}(L_S^{-1})^+ = 1 \tag{5.43}$$

where the superior sign + means the Hermitian-conjugate operator. Equation (5.43) can be checked by a direct substitution of the explicit expression for the propagator L_S^{-1}. As known, a unitary operator A does not change a scalar product

$$(Au, Av) = (u, A^+Av) = (u, v) \tag{5.44}$$

In our case, the scalar product means the integral of a product of two arbitrary functions over a plane $x = \text{const}$

$$(u, v) = \int u(\boldsymbol{\rho})v^*(\boldsymbol{\rho})\,\mathrm{d}\boldsymbol{\rho} \tag{5.45}$$

Substituting $u = v = u(x, \boldsymbol{\rho})$ and $Au = Av = L_S^{-1}u(x, \boldsymbol{\rho}) = u(x', \boldsymbol{\rho}')$ in eq. (5.44), we get

$$\int |u(x, \boldsymbol{\rho})|^2\,\mathrm{d}\boldsymbol{\rho} = \int |u(x', \boldsymbol{\rho}')|^2\,\mathrm{d}\boldsymbol{\rho}' \tag{5.46}$$

Equation (5.46) is just the energy conservation law for the parabolic equation. It is interesting that eq. (5.46) coincides completely with eq. (5.41) obtained for the straight-ray approximation. It means that both eqs (5.40) and (5.41) are valid at any distances from the initial plane $x = 0$ independently whether the observation plane $x = \text{const}$ is located in the near, Fresnel or wave zone of the initial field.

5.2 Wave scattering

5.2.1 Scatterers

In general, any object distorts the initial wave that would exist in free space for certain given sources. Such an object will be called a scatterer. If the scatterer interacts linearly with the incident wave, as will be assumed always in this chapter, the initial equation (5.2) for free space is expanded to the following operator equation for the resulting wave

$$(L - V)\Psi = q \tag{5.47}$$

where the operator V determines the scatterer. This is the general wave scattering equation.

The operator V in the coordinate representation is often reduced to a product of the field Ψ by a scalar function $v(\boldsymbol{r})$, i.e.

$$\langle \boldsymbol{r}|V|\boldsymbol{r}'\rangle = \delta(\boldsymbol{r} - \boldsymbol{r}')\nu(\boldsymbol{r}) \tag{5.48}$$

Thus, the function $v(\boldsymbol{r})$ determines deviation of the space covered by the scatterer from the free space.

Let us go to the specific cases. In particular, eq. (5.6) in appearance of scatterers are turned out into the macroscopic equations

$$[-\mathrm{rot}\,\mathrm{rot}\, + k^2 - v(\boldsymbol{r})]\boldsymbol{E}(\boldsymbol{r}) = \boldsymbol{q}(\boldsymbol{r}) \tag{5.49}$$

where the function $v(\boldsymbol{r})$ is connected with the dielectric permittivity $\varepsilon(\boldsymbol{r})$ by the following expression

$$v(\boldsymbol{r}) = k^2[1 - \varepsilon(\boldsymbol{r})] \tag{5.50}$$

Here, for simplicity, the magnetic permeability is assumed to be equal to 1.

Instead of the dielectric permittivity, scatterers are often characterized by the refractive index $n(\boldsymbol{r})$. The refractive index is usually determined as

$$n^2 = \varepsilon \tag{5.51}$$

Note that eq. (5.51) is valid if absorption of waves is absent. In the case of absorption, both the dielectric permittivity $\varepsilon = \mathrm{Re}\,\varepsilon + i\mathrm{Im}\,\varepsilon$ and the refractive index $m = n + i\kappa$ become the complex values. Generalizing eq. (5.51) for the complex quantities

$$m^2 = \varepsilon \tag{5.52}$$

we get the following relations between their real and imaginary parts

$$\mathrm{Re}\,\varepsilon = n^2 - \kappa^2; \quad \mathrm{Im}\,\varepsilon = 2n\kappa \tag{5.53}$$

Similar equations are also valid for the scalar waves determined by the chain of wave equations (5.7), (5.9), and (5.11) . Thus, the Helmholtz equation (5.7), for example, can be written as

$$[\Delta + k^2 n^2(\boldsymbol{r})]\psi(\boldsymbol{r}) = q(\boldsymbol{r}) \tag{5.54}$$

Equation (5.54) shows obviously that the refractive index has the physical meaning of the local change for the wave velocity that appears as the local change of the wavelength.

In quantum mechanics, eq. (5.47) is the Schrödinger equation where the operators L and V correspond to eqs (5.7) and (5.48), respectively. In particular, the Schrödinger equation is equivalent to eq. (5.54) where the local refractive index is determined by the equation

$$n^2(\boldsymbol{r}) = 1 - U(\boldsymbol{r})/E \tag{5.55}$$

Here, E is the energy of an elementary particle in free space and $U(\boldsymbol{r})$ is the interaction potential.

As for acoustics, there are not one but two local quantities characterizing a scatterer. For instance, they may be the compressibility β and the density ρ of the matter. The refractive index is determined by the following equation

$$n^2(\boldsymbol{r}) = \frac{\beta(\boldsymbol{r})\rho(\boldsymbol{r})}{\beta_0\rho_0} \tag{5.56}$$

where β_0 and ρ_0 are the same quantities as β and ρ except for the free space. If two characterization parameters of the matter are chosen as $n(\boldsymbol{r})$ and $\rho(\boldsymbol{r})$, the equation of scattering for the acoustic waves can be represented by eq. (5.47) as

well. However, eq. (5.50) for the scattering potential must be changed. Namely, we have

$$v(\boldsymbol{r}) = k^2[1 - n^2(\boldsymbol{r})] + \nabla \ln \rho(\boldsymbol{r})\nabla \tag{5.57}$$

Sometimes, the last term of eq. (5.57) is negligible, and we arrive at the full unification of acoustic, quantum mechanics, and electromagnetic waves.

In conclusion of this section, let us emphasize that the scattering wave equation (5.47) is quite general. It embraces numerous problems in various fields of physics which use the terms of scattering, diffraction, or propagation. For example, if a scatterer occupies a rather small volume and an observation point is outside of the scatterer, the problem is conventionally called the scattering problem. As for diffraction, the terms of scattering and diffraction are used sometimes as synonyms in radiophysics while, in optics, the term of diffraction is reserved for small angle scattering by large scatterers as compared to wavelength. Further, if an observation point is located inside a scatterer we arrive at a wave propagation problem, etc.

5.2.2 General wave scattering equation

The general wave scattering equation (5.47) is readily solved at the level of operator equations. Indeed, let us rewrite eq. (5.47) as

$$L\Psi = q + V\Psi \tag{5.58}$$

and act on the equation from the left by the operator L^{-1}. We get

$$\Psi = \Psi_0 + L^{-1}V\Psi \tag{5.59}$$

Here $\Psi_0 = L^{-1}q$ is the incident wave according to eq. (5.3), i.e. it is the field created by a given source in the free space. The total field in eq. (5.59) is represented as the superposition of the incident wave and the additional field Ψ_S created because of appearance of a scatterer. This term is called the scattered field. So, we get

$$\Psi = \Psi_0 + \Psi_S; \quad \Psi_S = L^{-1}V\Psi \tag{5.60}$$

Equation (5.59) is just the general wave equation (5.47) written down as the integral equation. In quantum mechanics, it is called the Lippmann–Schwinger equation. The formal solution of this equation is readily obtained. For this purpose, we rearrange the terms of eq. (5.59) as

$$(1 - L^{-1}V)\Psi = \Psi_0 \tag{5.61}$$

and the solution required is as follows

$$\Psi = \frac{1}{1 - L^{-1}V}\Psi_0 \tag{5.62}$$

If we expand the fraction in eq. (5.62) as the well-known geometric series, the solution is represented by the series

$$\Psi = \Psi_0 + L^{-1}V\Psi_0 + L^{-1}VL^{-1}V\Psi_0 + \dots \tag{5.63}$$

In mathematics, eq. (5.63) is called the iteration expansion or the Neumann series for the integral equation (5.59). In the scattering theory, it is called the Born series, and the first iteration

$$\Psi_B = L^{-1}V\Psi_0 \approx \Psi_S \tag{5.64}$$

is called the Born approximation for the scattered field.

In the solutions (5.62) and (5.63), the incident wave Ψ_0 is included as a factor. It is convenient to separate this factor, and the remaining part will be the general solution not depending on the explicit form of the incident field. For this purpose, the scattering field is represented as

$$\Psi_S = L^{-1}T\Psi_0 \tag{5.65}$$

where all scattering processes are combined in the matrix T. This matrix is called the transition matrix in quantum mechanics. In general, the term of the T-matrix is conventional.

The T-matrix in the series representation is readily obtained from eq. (5.63)

$$T = V + VL^{-1}V + VL^{-1}VL^{-1}V + \dots \tag{5.66}$$

This series corresponds to the following equation

$$T = V + VL^{-1}T \tag{5.67}$$

and to its explicit solution as the fraction as in eq. (5.62)

$$T = V\frac{1}{1 - L^{-1}V} \tag{5.68}$$

Thus, any scattering wave problem is fully solved because of eq. (5.65), if the T-matrix is found. In practice, an explicit form of the T-matrix is obtained either from numerical solution of the integral equation (5.67) or by numerical summation of the series (5.66).

5.2.3 Scattered field in the wave zone

If a scatterer is a 3-D object, the scattered field at large distances from the scatterer transforms into a divergent spherical wave as shown in Fig. 5.3. This fact follows directly from eq. (5.65) taking into account the explicit expressions for the propagators L^{-1}. The domain where the scattered fields are the divergent spherical waves is called the wave zone.

Let us consider scattering of scalar waves. In the wave zone, the total field as given in eq. (5.60) is the superposition of the incident plane wave and the divergent spherical wave

$$\psi(\boldsymbol{r}) = \psi_0(\boldsymbol{r}) + \psi_s(\boldsymbol{r}) = \mathrm{e}^{ik\boldsymbol{n}_0\boldsymbol{r}} + f(\boldsymbol{n}, \boldsymbol{n}_0)\frac{\mathrm{e}^{ikr}}{r} \tag{5.69}$$

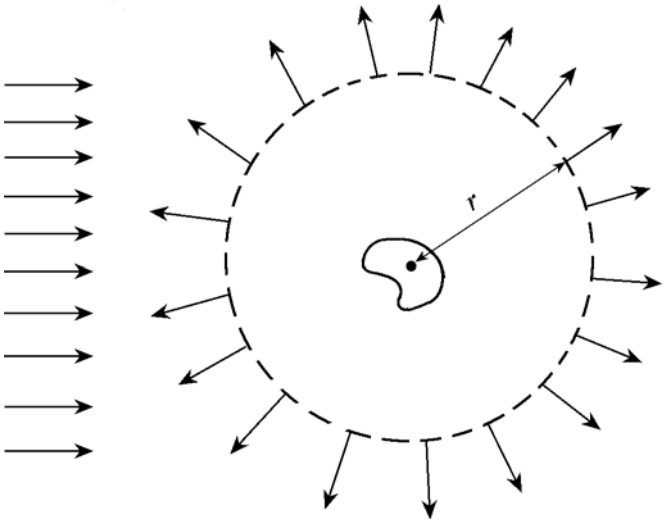

Fig. 5.3. Wave scattering to the wave zone.

Here $\boldsymbol{n}_0$ is an incident direction, r is a distance from the scatterer, and the complex-valued function $f(\boldsymbol{n}, \boldsymbol{n}_0)$ of both the incident $\boldsymbol{n}_0$ and scattering $\boldsymbol{n} = \boldsymbol{r}/r$ directions is called the scattering amplitude. Thus, the solution to any scattering problem is reduced to finding the scattering amplitude only. The generality of the scattering amplitude can be also confirmed by the fact that the scattering amplitude is just the T-matrix of eqs (5.65)–(5.68) written down in the momentum representation $T(k\boldsymbol{n}, k\boldsymbol{n}_0)$.

For the electromagnetic waves, the similar superposition of plane and spherical waves takes place

$$\boldsymbol{E}(\boldsymbol{r}) = \boldsymbol{E}^0 \mathrm{e}^{ik\boldsymbol{n}_0\boldsymbol{r}} + \boldsymbol{E}_s(\boldsymbol{n}, \boldsymbol{n}_0)\frac{\mathrm{e}^{ikr}}{r} = \boldsymbol{E}^0 \mathrm{e}^{ik\boldsymbol{n}_0\boldsymbol{r}} + S(\boldsymbol{n}, \boldsymbol{n}_0)\boldsymbol{E}^0\frac{\mathrm{e}^{ikr}}{r} \qquad (5.70)$$

where the complex-valued 2-D vector $\boldsymbol{E}^0$ with unit amplitude ($|\boldsymbol{E}^0| = 1$) determines the polarization state of the incident wave. The scattered field is also a transversal wave, and its vector scattering amplitude $\boldsymbol{E}_s$ is convenient to determine by means of the 2×2 scattering matrix S.

5.2.4 Optical theorem

The energy conservation law applied to a wave scattering action is reduced to the so-called optical theorem. This term was introduced in quantum mechanics when it was understood that the obtained theorem was already known in optics. In this section, we consider this theorem by use of the wave-zone scattered field.

Let us consider the energy flux through a closed surface surrounding a scatterer. The flux for the superposition of the incident Ψ_0 and scattered Ψ_s waves is decomposed into three terms according to eq. (5.38)

$$\Phi = \Phi_0 + \Phi_s + \Phi_{0s} \tag{5.71}$$

where the last term corresponds to interference between the incident and scattered waves. The flux of the incident wave through a closed surface is always equal to zero: $\Phi_0 = 0$. The flux of the scattered field Φ_s is a conserved value, i.e. its magnitude does not depend on either the shape of the surrounding surface or the distance from the scatterer. Consequently, the interference flux Φ_{0s}, as well as the flux of the total field Φ, prove to be the similar conservative values.

It is important to emphasize that the conservation of the interference fluxes is a quite general conclusion that is valid for any superposition of wave fields. This fact will be often used in our further study.

Now go to the spherical surface surrounding a scatterer at $r \to \infty$ that is shown in Fig. 5.3. For the scalar scattered field ψ_s, the energy-flux density defined by eq. (5.34) is directed normally to the spherical surface at $r \to \infty$

$$\boldsymbol{j}(\boldsymbol{r}) = \frac{|f(\boldsymbol{n}, \boldsymbol{n}_0)|^2}{r^2}\boldsymbol{n} \tag{5.72}$$

So, the flux Φ_s is equal to

$$\Phi_s = \int |f(\boldsymbol{n}, \boldsymbol{n}_0)|^2 \, \mathrm{d}\boldsymbol{n} = \sigma_s(\boldsymbol{n}_0) \tag{5.73}$$

where $\mathrm{d}\boldsymbol{n}$ is an element of the solid angle of scattering directions ($\mathrm{d}S = r^2 \, \mathrm{d}\boldsymbol{n}$). This flux is called the scattering cross-section since it has dimensionality of area. For nonspherical scatterers, the cross-section depends on the incident direction.

If there is no absorption of energy inside the scatterer, i.e. the refractive index is real-valued, the flux of the total field is equal to zero, too, and the interference flux proves to be the negative value $\Phi_{0s} = -\sigma_s$. Thus, we get the obvious physical conclusion that the energy of the outgoing spherical wave is extracted from the energy of the incident wave as a result of interference between these waves.

If there is absorption inside a scatterer, an energy sink appears, and the flux of the total field becomes non-vanishing and negative. Its modulus is called the absorption cross-section σ_a

$$\Phi = -\sigma_a(\boldsymbol{n}_0) \tag{5.74}$$

The sum of these cross-sections is called the extinction cross-section σ_e, and eq. (5.71) is reduced to the following

$$\Phi_{0s} = -[\sigma_s(\boldsymbol{n}_0) + \sigma_a(\boldsymbol{n}_0)] = -\sigma_e(\boldsymbol{n}_0) \tag{5.75}$$

i.e. the interference flux should include absorption as well. As a consequence, we conclude that even an absolutely absorbing scatterer creates a scattered wave otherwise the energy conservation law would be violated.

The essence of the optical theorem is the fact that the interference flux Φ_{0s} is determined by the value of the scattering amplitude $f(\boldsymbol{n}, \boldsymbol{n}_0)$ that is taken in the single scattering direction only, namely, in the forward scattering direction $f(\boldsymbol{n}_0, \boldsymbol{n}_0)$. This fact is easily understood. Indeed, the energy-flux density corresponding to interference between the plane and spherical waves given in eq.

(5.69) is a quickly oscillating function at any point $\boldsymbol{n}$ on the sphere shown in Fig. 5.3 at $r \to \infty$. So, in average, it results in zero. Only in the forward scattering direction $\boldsymbol{n}_0$ the phase difference between these waves does not depend on the sphere radius r, and the interference results in a nonvanishing contribution that is simply calculated. The analytical derivation of the flux Φ_{0s} results in the desired optical theorem

$$\sigma_e(\boldsymbol{n}_0) = \frac{4\pi}{k}\mathrm{Im}\, f(\boldsymbol{n}_0, \boldsymbol{n}_0) \tag{5.76}$$

We do not represent the calculation of eq. (5.76) here since similar integrals are calculated later (see eq. (5.134)).

The optical theorem is directly generalized for electromagnetic waves as well. Here, the scattered wave is the transversal spherical wave determined by the vector scattering amplitude $\boldsymbol{E}_s(\boldsymbol{n}, \boldsymbol{n}_0)$. In this case, the interference between the scattered wave in the forward direction and the incident wave of the vector amplitude $\boldsymbol{E}^0$ (where $|\boldsymbol{E}^0| = 1$) takes place only for a projection of the scattered wave onto the vector of the incident wave that is described by the scalar product $(\boldsymbol{E}^0\boldsymbol{E}_s(\boldsymbol{n}_0, \boldsymbol{n}_0))$. Therefore, the optical theorem (5.76) for electromagnetic waves is generalized as the following

$$\sigma_e(\boldsymbol{n}_0) = \frac{4\pi}{k}\mathrm{Im}\, \left(\boldsymbol{E}^0\boldsymbol{E}_s(\boldsymbol{n}_0, \boldsymbol{n}_0)\right) \tag{5.77}$$

So, the scattering cross-section of eq. (5.77) depends not only on the incident direction but on the polarization of the incident wave as well.

5.2.5 Scattering of waves by small scatterers

If a 3-D scatterer is small as compared to the incident wavelength ($ka \ll 1$, where a is a characteristic size of a scatterer), its scattered field outside the scatterer is similar to the wave emitted by a point source that is described by the propagator or Green function L^{-1}. Indeed, if the scattered field $L^{-1}V\Psi$ given by eq. (5.60) is considered in the coordinate representation, it is seen that the Green function does not practically oscillate during the integration over the scatterer volume because of the condition $ka \ll 1$. Hence it can be replaced by the Green function originated from the scatterer center.

So, in quantum mechanics, the small scatterers are monopoles producing the isotropic scattering. It means that the scattered wave is described by eq. (5.69) at any distance from the scatterer ($r > a$), and the scattering amplitude does not vary with the scattering directions. In electrodynamics, monopoles are impossible. Therefore, small scatterers in electrodynamics are similar to the electric dipoles. In acoustics, if the compressibility of a scatterer differs from that of the surrounding medium but its density is the same, such a scatterer is a monopole, too. But if an acoustic scatterer differs from the surrounding medium by its density only, such a scatterer is the scalar dipole. For instance, the scattered field of a scalar dipole is given by

$$\psi_s(\boldsymbol{r}) = d(\boldsymbol{n}\boldsymbol{n}_0)\left(ik - \frac{1}{r}\right)\frac{\mathrm{e}^{ikr}}{r} \tag{5.78}$$

where d is a constant depending on scatterer shape. For the dipole, at the distance

$$r \gg \lambda \tag{5.79}$$

the second term in eq. (5.78) becomes negligible as compared with the first term. So, the inequality (5.79) determines the area of the wave zone where the field is described by eq. (5.69). Note that the scattering amplitude $f(\boldsymbol{n}, \boldsymbol{n}_0)$ for the dipole is not isotropic as for monopoles but it is described by the rather smooth angular function $(\boldsymbol{n}\boldsymbol{n}_0)$.

In the near zone

$$a < r < \lambda \tag{5.80}$$

conversely, the second term of Eq, (5.78) decreasing with distance as r^{-2} becomes predominant. It is interesting that this near-zone term describes only a redistribution of energy near the scatterer not contributing to the total energy flux of the scattered field carried out from the scatterer. Indeed, owing to the energy conservation law, the flux over any closed surface surrounding a scatterer must be the same. This flux calculated through the wave-zone term in eq. (5.73) results in the scattering cross-section. Therefore, if the energy flux over a closed surface located near the scatterer is calculated, the predominant near-zone term will give zero contribution but the weak first component of eq. (5.78) will result, as in the wave zone, in the scattering cross-section. All these peculiarities are valid for the electromagnetic waves, too.

Similarly, when the parameter ka is increasing, new components resembling the fields emitted by quadrupoles, octopoles, and higher-order sources are appearing in the scattered field. In the near zone, the components of the higher-order K contain terms with various powers of $(1/r)$ up to r^{-K}. Analogously to the dipoles, these terms are predominant in the near zone but they do not contribute to the energy carried out by the scattered wave. In the wave zone, these terms are presented in the scattering amplitude $f(\boldsymbol{n}, \boldsymbol{n}_0)$ by more complicated and quickly oscillating functions of the scattering directions $\boldsymbol{n}$ as compared with the dipoles. Roughly, the necessary number of these multipole components is estimated as $K \approx ka$. Therefore the scattered fields for the scatterers of moderate sizes $a \sim (5 - 10)\lambda$ can be calculated only numerically for both near and wave zones.

5.2.6 Large scatterers

5.2.6.1 Geometric optics approach

For large scatterers ($ka \gg 1$), the conventional series that are widely used for scatterers of moderate sizes are scarcely applied since they demand much computer time. Fortunately, this limit case is well described by the intuitive equations and conceptions of geometric optics. The geometric optics can be derived from

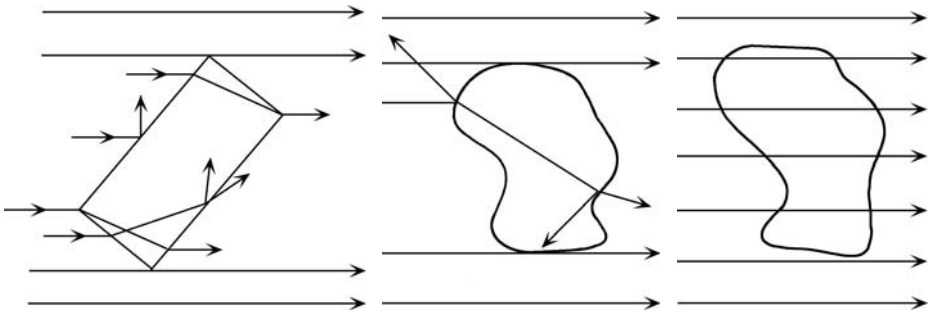

Fig. 5.4. Wave scattering by large scatterers to the near zone. (a) Optically hard crystal. (b) Optically hard scatterer of irregular shape. (c) Optically soft scatterer.

the Maxwell equations, for example, as the asymptotic limit $k \to \infty$. Of course, the term geometric optics is used here for brevity. Classical mechanics is the same asymptotic limit of quantum mechanics at $k \to \infty$, etc.

In Fig. 5.4, wave scattering by certain typical scatterers within the geometric optics approach is shown. Let us emphasize that the geometric optics approach is valid only inside the scatterer and in its near zone. A qualitative justification of the geometric optics approach can be tentatively explained as follows.

Consider, for specificity, light scattering by an ice crystal particle in cirrus clouds (Fig. 5.4(a)). Here the condition $ka \gg 1$ is usually valid, where a is the typical size of a crystal facet It is obvious that the scattering action consists of successive reflections and refractions of plane-parallel beams by crystal facets. In the first step, every illuminated facet creates a plane-parallel beam reflected by the facet and a refracted beam transmitted into the crystal. Then any transmitted plane-parallel beam crosses one or several other facets and these facets divide the beam into reflected and refracted plane-parallel beams again, and so on. As a result, the outgoing scattered field at the crystal surface consists of a set of plane-parallel beams of various sizes and shapes propagating in various directions.

As known, any plane-parallel beam with the transverse size of $a(ka \gg 1)$ propagating in free space reveals three propagation regimes:

$$\begin{aligned} r &\ll ka^2; \quad \text{near zone, straight-ray approximation} \\ r &\approx ka^2; \quad \text{Fresnel zone, parabolic equation} \\ r &\gg ka^2; \quad \text{wave (Fraunhofer) zone, parabolic equation} \end{aligned} \tag{5.81}$$

In the near zone, the beam conserves its transverse shape. Then, in the Fresnel zone, its shape is distorted by the Fresnel diffraction. Finally, the beam is transformed into a divergent spherical wave in the wave zone.

Therefore, if a rather narrow beam of the size b obeying the condition $kb^2 < a$ appears inside a crystal particle, geometric optics is not valid to describe its propagation inside the crystal, and we should take into account diffraction. For-

tunately, this case is quite exotic and it can be usually ignored. Indeed, such narrow beams can occur if very small facets exist in crystal shape. As a rule, the pristine crystals have rather simple shapes without these small facets. As the second possibility, these narrow beams should appear after a great number of reflection actions inside the crystal because of multiple transverse divisions of an initial transverse size. But the energy of such narrow beams is usually negligible because of essential energy loss in the early reflection/refraction actions. Also, there is the third possible objection to geometric optics that should be considered. Namely, from the wave point of view, the sharp vertexes and edges of a crystal are sources of certain additional waves that are not described by geometric optics. But these fields are weak on the background of the plane-parallel beams and they can be ignored in a majority of practical problems, too.

The same arguments in favor of the geometric optics approach can be expanded for scatterers with smooth surfaces like the scatterer in Fig. 5.4(b). Indeed, any essential inhomogeneity of the smooth surface plays the same role as a crystal facet and all the abovementioned arguments are valid. Moreover, diffraction for beams with curved phase surfaces distorts the beam shapes to a lesser degree than for plane-parallel beams.

Figs 5.4(a) and 5.4(b) correspond to the case where the refractive index of scatterers differs essentially from that of the free space. Conversely, Fig. 5.4(c) corresponds to the case of so-called optically soft scatterers having the refractive index n close to that of the surrounding space

$$|n-1| \ll 1 \tag{5.82}$$

The case of optically soft scatterers is important in various fields of physics. For example, the turbulent inhomogeneities of refractive index in the atmosphere are just the optically soft scatterers, and they result in both the stellar scintillations and the wandering of laser beams propagating in the atmosphere. As for particulate media, biological liquids such as blood and biological tissues are also typical examples of optically soft scatterers for visible light. In quantum mechanics, the case of optically soft scatterers corresponds to high-energy particles, and so on. Thus, the term 'optically' is used by convention only and it does not refer to visible light. The opposite case, shown in Figs 5.4(a) and 5.4(b) where eq. (5.82) is not valid, will be called optically hard scatterers.

5.2.6.2 Scattered fields in the near and wave zones

A remarkable feature of wave scattering by large scatterers is that the scattered field Φ_s can be effectively decomposed into two parts. One part is determined by the shape of a scatterer only, while the second part depends on both the shape and the magnitude of the refractive index. These components will be called the shadow-forming Ψ_h and refracted Ψ_r fields, respectively

$$\Psi_s = \Psi_h + \Psi_r \tag{5.83}$$

The appearance of the shadow-forming field is evident in the case of an absolutely absorbing scatterer. In this case, the total field in the near zone disappears behind

the scatterer. Remembering that the total field, due to the general equation (5.60), is the superposition of the incident and scattered fields, we conclude that the scattered field behind the scatterer is equal to the incident wave field with the opposite sign. In particular, for the incident electromagnetic plane wave $\boldsymbol{E}_0$, we have

$$\boldsymbol{E}_h(x,\boldsymbol{\rho}) = \begin{cases} -\boldsymbol{E}_0 & \text{if } \boldsymbol{\rho} \text{ is inside the shadow} \\ 0 & \text{otherwise} \end{cases} \tag{5.84}$$

Thus, the shadow-forming field Ψ_h in the near zone is a plane-parallel beam with the transverse shape of scatterer's shadow, and it propagates in the same direction as the incident wave. Note that eq. (5.84) is valid for the near zone only but the superposition given in eq. (5.83) is quite general and it is valid everywhere. Therefore, at arbitrary distance from the scatterer, the shadow-forming field evolves as shown in eq. (5.81).

This shadow-forming field is expedient to consider as a component of the scattered fields for arbitrary large scatterers. The physical reason for the appearance of this field is the break in amplitude of the incident wave along the scatterer contour as shown in Fig. 5.4. For example, it is obviously seen in Fig. 5.4(a) that the plane-parallel beam of the shadow-forming field is one of the superpositions of the plane-parallel beams of the scattered field.

The remaining part of the scattered field, i.e. the refracted field Ψ_r, is defined in the near zone by the conventional laws of geometric optics that are illustrated in Fig. 5.4. Then its propagation from the near zone to larger distances is governed by the wave propagation equations.

It is interesting to distinguish the shadow-forming field in the case of optically soft scatterers shown in Fig. 5.4(c). Here, the refraction of the geometric optics rays can be ignored. As a result, the straight-ray approximation of eq. (5.11) is applicable both inside the scatterer and in its near zone. In this approximation, the total field in the near zone behind a scatterer $u(x,\boldsymbol{\rho})$ is readily found. This field corresponds to shadowing the incident field $u_0 = 1$ by the equivalent amplitude-phase screen $A(\boldsymbol{\rho})$

$$u(x,\boldsymbol{\rho}) \;=\; \mathrm{e}^{iA(\boldsymbol{\rho})} = \mathrm{e}^{i\varphi(\boldsymbol{\rho})-\chi(\boldsymbol{\rho})} \tag{5.85}$$

$$A(\boldsymbol{\rho}) \;=\; ik\int_{-\infty}^{\infty}[m(x',\boldsymbol{\rho})-1]\,\mathrm{d}x' \tag{5.86}$$

Here m is the complex-valued refractive index of eq. (5.52), φ is the additional phase shift in the wave caused by appearance of the scatterer, and $\exp(-\chi)$ is amplitude of the transmitted wave if absorption takes place inside the scatterer. Here the condition (5.82) of optical softness is used to approximate the expression of eq. (5.50) as follows: $v = k^2(1-m^2) \approx 2k^2(1-m)$.

Now the scattered field is found by subtraction of the incident field $u_0 = 1$ from the total field

$$u_s(\boldsymbol{\rho}) = [\mathrm{e}^{iA(\boldsymbol{\rho})} - 1]\eta(\boldsymbol{\rho}) \tag{5.87}$$

This scattered field equals to zero outside the scatterer shadow. Therefore we have set in eq. (5.87) the additional factor $\eta(\boldsymbol{\rho})$ that does not distort the equation. This factor is the shadow function defined as follows

$$\eta(\boldsymbol{\rho}) = \begin{cases} 1 & \text{inside the scatterer shadow} \\ 0 & \text{otherwise} \end{cases} \tag{5.88}$$

Equation (5.87) proves to be a particular case of the general equation (5.83). Here, the shadow-forming field for the case of optically soft scatterers

$$u_h(\boldsymbol{\rho}) = -\eta(\boldsymbol{\rho}) \tag{5.89}$$

appears analytically as a component of the scattered field. The remaining part of the scattered field is the refracted field

$$u_r(\boldsymbol{\rho}) = \mathrm{e}^{iA(\boldsymbol{\rho})}\eta(\boldsymbol{\rho}) \tag{5.90}$$

Now the scattered field can be found at arbitrary distances from the optically soft scatterer. In particular, in the wave zone, the scattering amplitude of eq. (5.69) can be determined by the classical Fraunhofer diffraction equation for the amplitude–phase screen of eq. (5.87)

$$f(\boldsymbol{n}, \boldsymbol{n}_0) = \frac{k}{2\pi i} \int u_s(\boldsymbol{\rho}) \mathrm{e}^{ik\boldsymbol{n}\boldsymbol{\rho}} \, \mathrm{d}\boldsymbol{\rho} \tag{5.91}$$

where $(\boldsymbol{\rho}\boldsymbol{n}_0) = 0$. In the forward scattering direction, it results in the simple integral

$$f(\boldsymbol{n}_0, \boldsymbol{n}_0) = \frac{k}{2\pi i} \int u_s(\boldsymbol{\rho}) \, \mathrm{d}\boldsymbol{\rho} \tag{5.92}$$

The superposition given by eq. (5.87) splits the scattering amplitude into the refracted f_r and shadow-forming f_h parts

$$f(\boldsymbol{n}, \boldsymbol{n}_0) = f_r(\boldsymbol{n}, \boldsymbol{n}_0) + f_h(\boldsymbol{n}, \boldsymbol{n}_0) \tag{5.93}$$

$$f_r(\boldsymbol{n}, \boldsymbol{n}_0) = \frac{k}{2\pi i} \int \mathrm{e}^{iA(\boldsymbol{\rho})} \eta(\boldsymbol{\rho}) \mathrm{e}^{ik\boldsymbol{n}\boldsymbol{\rho}} \, \mathrm{d}\boldsymbol{\rho} \tag{5.94}$$

$$f_h(\boldsymbol{n}, \boldsymbol{n}_0) = -\frac{k}{2\pi i} \int \eta(\boldsymbol{\rho}) \mathrm{e}^{ik\boldsymbol{n}\boldsymbol{\rho}} \, \mathrm{d}\boldsymbol{\rho} \tag{5.95}$$

Let us consider the optically hard scatterers shown in Figs 5.4(a) and 5.4(b). In the near zone, the scattered fields should be found by means of the ray patterns shown in Figs 5.4(a) and 5.4(b), where the transverse polarization of electromagnetic waves along the rays can be included as well. It is interesting that there is also an intermediate regime of scattering appearing at the distance r_g, where $a \ll r_g \ll ka^2$. Here, all geometric optics rays coming to a point $\boldsymbol{n}r_g$ on the sphere of the radius r_g are concentrated within a narrow cone with the angles $\theta \leq a/r_g$. We can replace this narrow cone by the normal $\boldsymbol{n}$ to the sphere (Fig. 5.5(a)) resulting approximately in a divergent spherical wave. The angular dependence of this field on the sphere of scattering directions $\boldsymbol{n}$ will be called the geometric optics scattering amplitude $f_g(\boldsymbol{n}, \boldsymbol{n}_0)$. It is obvious that the geometric optics scattering amplitude is similar to the exact one

$$f_g(\boldsymbol{n}, \boldsymbol{n}_0) \approx f(\boldsymbol{n}, \boldsymbol{n}_0) \tag{5.96}$$

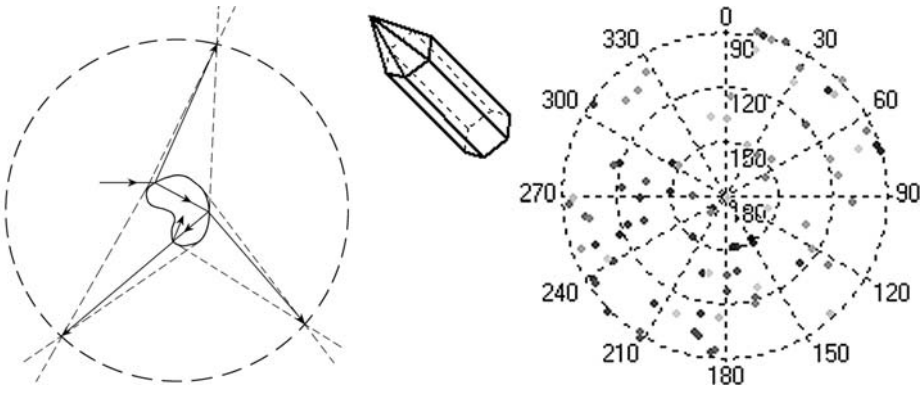

Fig. 5.5. Geometric optics scattering. (a) Geometric optics rays, at large distances, approach a divergent spherical wave. (b) Scattering of light by an ice crystal of cirrus clouds; the dots are the Dirac delta functions for scattering directions, and the dot brightness shows the energy scattered in this direction.

but f_g depends on the scattering directions $\boldsymbol{n}$ more sharply. After propagation of the scattered wave from the distance r_g to the wave zone, diffraction smooths out the sharp angular structure resulting in the exact scattering amplitude. For example, the shadow-forming plane-parallel beam of the near zone should be included in the geometric optics scattering amplitude by the means of the Dirac delta function $\delta(\boldsymbol{n} - \boldsymbol{n}_0)$. In the wave zone $r \gg ka^2 \gg r_g$, this singularity is transformed into the regular function given by eq. (5.95). Analogously, every plane-parallel beam of the near zone created by a crystal scatterer is represented in the geometric optics scattering amplitude by the Dirac delta function factors at other directions as illustrated in Fig. 5.5(b). For the optically hard scatterers with smooth surfaces as in Fig. 5.4(b), the function $f_g(\boldsymbol{n}, \boldsymbol{n}_0)$ is mainly a regular function of the scattering directions. Note that to avoid certain mathematical difficulties, it is preferable to use the Dirac delta function not for the field but for its quadratic values such as $|f_g|^2$.

Thus, the refracted field for the optically hard scatterers is characterized by either geometric optics f_{rg} or exact f_r scattering amplitudes that are originated by the ray patterns of the near zone. This is in contrast to the simple analytical equations (5.90) and (5.94) in the case of optically soft scatterers. But the shadow-forming field is the same for both optically hard and optically soft scatterers, and it is described analytically by eqs (5.84), (5.89) and (5.95).

5.2.6.3 Scattering and extinction cross-sections

A great advantage of these simple expressions obtained for scattered fields in the near zone is that they can be effectively used for the calculation of the scattering cross-sections. Let us begin from the case of optically soft scatterers where the scattered field is described analytically by eq. (5.87). Propagation of the field given by eq. (5.87) obeys the parabolic equation outside the near zone.

Therefore its energy flux Φ_s through any plane $x = \text{const}$ is conserved due to eq. (5.46). This flux is just equal to the scattering cross-section presented by eq. (5.73) since the scattered field does not exist in the backward hemisphere of scattering directions for optically soft scatterers. So, we get

$$\sigma_s = \Phi_s = \int |u_s(\boldsymbol{\rho})|^2 \, \mathrm{d}\boldsymbol{\rho} \tag{5.97}$$

If there is absorption inside a scatterer, a difference between the energy flux for the incident wave $u_0 = 1$ and for the total field u behind the scatterer defined by eq. (5.85) results in the absorption cross-section

$$\sigma_a = \Phi_0 - \Phi = \int (1 - |u(\boldsymbol{\rho})|^2) \, \mathrm{d}\boldsymbol{\rho} \tag{5.98}$$

The sum of these values is the extinction cross-section

$$\begin{aligned} \sigma_e &= \sigma_s + \sigma_a = \int \left(|u(\boldsymbol{\rho}) - 1|^2 + (1 - (|u(\boldsymbol{\rho})|^2 \right) \, \mathrm{d}\boldsymbol{\rho} \\ &= -\int [u_s(\boldsymbol{\rho}) + u_s^*(\boldsymbol{\rho})] \, \mathrm{d}\boldsymbol{\rho} \end{aligned} \tag{5.99}$$

Note that, according to the energy conservation law (see eq. (5.75)), the same expression for the extinction cross-section can be obtained as the interference flux Φ_{0s} between the incident and scattered fields

$$-\sigma_e = \Phi_{0s} = \int (u_0 u_s^* + u_0^* u_s) \, \mathrm{d}\boldsymbol{\rho} = 2\mathrm{Re} \int u_s(\boldsymbol{\rho}) \, \mathrm{d}\boldsymbol{\rho} \tag{5.100}$$

The integrands of eqs (5.97)–(5.100) are nonzero only inside the scatterer shadow, and every ray $\boldsymbol{\rho} = \text{const}$ crossing the scatterer contributes to all cross-sections independently of each other. Therefore the corresponding scattering, absorption and extinction coefficients for the rays $\boldsymbol{\rho} = \text{const}$ can be defined as

$$Q_s(\boldsymbol{\rho}) = |u_s(\boldsymbol{\rho})|^2; \quad Q_a(\boldsymbol{\rho}) = 1 - |u(\boldsymbol{\rho})|^2; \quad Q_e(\boldsymbol{\rho}) = -[u_s(\boldsymbol{\rho}) + u_s^*(\boldsymbol{\rho})] \tag{5.101}$$

Then any cross-section of eqs (5.97)–(5.99) can be represented as the product of the shadow area

$$s = \int \eta(\boldsymbol{\rho}) \, \mathrm{d}\boldsymbol{\rho} \tag{5.102}$$

by the corresponding coefficients Q

$$\sigma = s\langle Q \rangle \tag{5.103}$$

where the angle brackets mean an average over the shadow area.

These coefficients defined by eq. (5.101) have an elegant geometric interpretation shown in Fig. 5.6. For this interpretation, the conventional 2-D plane of the complex-valued numbers is considered where the axes correspond to the real and imaginary parts of the numbers. The incident wave $u_0 = 1$ is represented

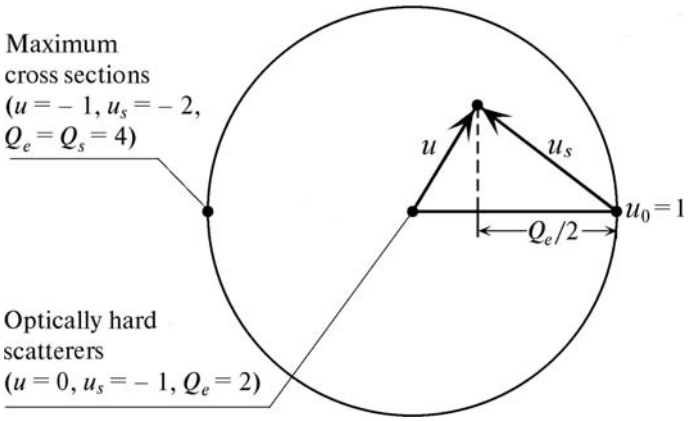

Fig. 5.6. Extinction and scattering coefficients for large scatterers.

by the point $(1, 0)$ in this plane. The total field u given by eq. (5.85) for the ray with $\boldsymbol{\rho} = \text{const}$ is represented by a point situated on a circular curve of the unit radius if there is no absorption, and it is situated inside the unit circle otherwise. The scattered field as given by eq. (5.87) is represented in this circle as a difference of two vectors u and u_0 shown in Fig. 5.6. Namely, the scattered wave u_s is represented by the vector with the origin in the point $(1, 0)$ and with the end in any point within the unit circle. In general, this unit circle and the vector representation of the scattered field demonstrate quite general geometric restriction for all possible values of the scattered fields. The quadratic values of the vectors u and u_s correspond to the absorption and scattering coefficients due to eq. (5.101). But the most useful quantity is the linear characteristic of the vector u_s since the length of the projection of the vector u_s on the horizontal axis demonstrates all possible values for the extinction coefficient.

So, it is readily seen geometrically in Fig. 5.6, that the extinction coefficient is restricted by the number 4, and, as a result, the extinction cross-section for any large scatterer cannot exceed the shadow area by more than four times

$$Q_e \leq 4; \quad \sigma_e \leq 4s \tag{5.104}$$

The sign of equality takes place for a ray with $\boldsymbol{\rho} = \text{const}$ when absorption is absent and the total field has the phase of π, i.e. $u = \exp(i\pi) = -1$; $u_s = -2$; $Q_e = 4$. In other words, the maximum extinction (and scattering) cross-section $\sigma_e = 4s$ is reached only by a transparent plane-parallel plate producing the phase shift of $(2N + 1)\pi$, where N is an integer.

Let us prove that this diversity of the extinction cross-sections from zero to the quadruplicate shadow area is caused by interference between the shadow-forming and refracted fields. For this purpose, the decomposition of the scattered wave into the shadow-forming and refracted fields given by eq. (5.83) should be inserted in the initial decomposition of the fluxes given by eq. (5.71). This insertion results in the following equations

$$\sigma_s = \Phi_s = \Phi_h + \Phi_r + \Phi_{hr} \tag{5.105}$$

$$-\sigma_e = \Phi_{0s} = \Phi_{0h} + \Phi_{0r} \tag{5.106}$$

We recall that for any superposition of waves, both the fluxes of the wave constituents and their interference fluxes are the conservative values that do not depend on distance from a scatterer. So, calculation of the fluxes by use of the simple analytical equations obtained for the near zone proves to be an effective method for an analytical study.

The first terms in eqs (5.105) and (5.106) concerning the shadow-forming field are immediately obtained. They equal to the single and double shadow area due to eqs (5.97) and (5.100), respectively, where the scattered field is replaced by the shadow-forming field

$$\sigma_h = \Phi_h = \int \eta(\boldsymbol{\rho})\,\mathrm{d}\boldsymbol{\rho} = s \tag{5.107}$$

$$\Phi_{0h} = \int (u_0 u_h^* + u_0^* u_h)\,\mathrm{d}\boldsymbol{\rho} = -2\int \eta(\boldsymbol{\rho})\,\mathrm{d}\boldsymbol{\rho} = -2s \tag{5.108}$$

Note that the result of eq. (5.108) can be also simply obtained from the wave-zone field if the forward-scattering amplitude resulting from eq. (5.95)

$$f_h(\boldsymbol{n}_0, \boldsymbol{n}_0) = is/\lambda \tag{5.109}$$

is substituted in the optical theorem given by eq. (5.76).

Calculation of the interference fluxes Φ_{hr} and Φ_{0r} is reduced to integration of the refracted field over either the shadow domain or the whole plane, respectively. Since the refracted field in eq. (5.90) is nonzero only in the shadow domain, we have the same integrands but with the opposite signs. So, we obtain

$$\Phi_{hr} = -\Phi_{0r} \tag{5.110}$$

and only one new quantity should be considered

$$\Phi_{hr} = -2\mathrm{Re}\int u_r(\boldsymbol{\rho})\,\mathrm{d}\boldsymbol{\rho} = -2\int \mathrm{e}^{-\chi(\boldsymbol{\rho})}\cos\varphi(\boldsymbol{\rho})\eta(\boldsymbol{\rho})\,\mathrm{d}\boldsymbol{\rho} \tag{5.111}$$

Magnitudes of this interference flux Φ_{hr} falls in the following interval

$$-2s \le \Phi_{hr} \le 2s \tag{5.112}$$

Let us go to the flux of the refracted field Φ_r that can also be called the scattering cross-section for the refracted field σ_r. According to eqs (5.90) and (5.97), it is equal to the shadow area s if there is no absorption. Absorption decreases the flux by the absorption cross-section σ_a, and we get

$$\Phi_r + \sigma_a = \sigma_r + \sigma_a = s \tag{5.113}$$

where these quantities are restricted by the inequalities

$$0 \le \sigma_r \le s; \quad 0 \le \sigma_a \le s \tag{5.114}$$

Substitution of eqs (5.112)–(5.114) in eq. (5.105) gives the desired intervals for the diversities of the scattering σ_s and extinction $\sigma_e = \sigma_s + \sigma_a$ cross-sections

$$0 \le \sigma_s \le \sigma_e \le 4s \tag{5.115}$$

Thus, this is only the alternating-sign interference flux between the refracted and shadow-forming fields Φ_{hr} that can either decrease the scattering cross-section to zero or, on the other hand, increase it up to $4s$. The case where the interference flux Φ_h is equal to zero will be called the basic situation. Here we have

$$\Phi_{hr} = \Phi_{0r} = 0; \quad \sigma_e = \sigma_h + \sigma_r + \sigma_a = 2s \tag{5.116}$$

In the basic situation, only the shadow-forming field interferes with the incident wave providing the double shadow area for the extinction cross-section. Half of this energy is carried out with the shadow-forming field, and the other half is shared between the refracted field and absorption.

If the interference flux Φ_{hr} is not zero, it changes both the scattering cross-section due to eq. (5.105) and, correspondingly, the extinction cross-section due to eqs (5.106) and (5.110). Two extreme cases occur. If the scatterer is a plane-parallel plate shifting the phase of the refracted field to $(2N + 1)\pi$, where N is an integer, this phase coincides with the phase of the shadow-forming field. As a result, these two waves are coherently added, the amplitude of the scattered field is doubled, the intensity is quadrupled, and the scattering cross-section reaches its maximum of $4s$. In the opposite extreme case, the phase shift is $2N\pi$. Here the shadow-forming and refracted fields are in the antiphase states, and the scattered field and, correspondingly, the scattering cross-section become equal to zero. This is a case of an absolutely transparent scatterer that does not disturb the initial wave and, consequently, does not create scattering. Note that the cases of $\Phi_{hr} = 0$ and $\Phi_{hr} \neq 0$ were called by van de Hulst the normal and anomalous diffraction, respectively. Therefore, the straight-ray approximation is often referred to as the anomalous diffraction approximation.

Though we have considered above only optically soft scatterers, all these qualitative results are valid for optically hard scatterers as well. An optically hard scatterer of irregular shape shown in Fig. 5.4(b) creates the refracted field that is not described by eq. (5.90). Nevertheless, it is obvious that the interference of such a field with the shadow-forming field in the near zone must be a quickly oscillating function within a plane $x = \text{const}$ giving $\Phi_{hr} = 0$ and $\Phi_{0r} = 0$. It just corresponds to the basic situation described by eq. (5.116). Moreover, the scattering cross-section for the refracted field is also equal to s without absorption and obeys eq. (5.113) with absorption, as follows from the energy conservation law. So, only the shadow-forming field provides the extinction cross-section for such scatterers.

On the other hand, the crystal particles shown in Fig. 5.4(a) can create plane-parallel beams of the refracted field that propagate in the forward direction. These beams interfere with the shadow-forming field resulting in certain deviations from the basic situation given by eq. (5.116) as was discussed for optically soft scatterers. These deviations obey eq. (5.115) as well.

5.3 Multiple scattering of waves

5.3.1 General equations

Let us decompose a scatterer of the general wave scattering equation (5.47) into an arbitrary sum

$$V = \sum V_j \tag{5.117}$$

and assume that the solution to the wave scattering equation for every scatterer V_j

$$(L - V_j)\Psi_j = 0 \tag{5.118}$$

is known either as a certain analytical expression for the field Ψ_j or as the T-matrix of eq. (5.65) that determines the field by the equation

$$\Psi_j = \Psi_0 + L^{-1}T_j\Psi_0 \tag{5.119}$$

Within this assumption, the equation

$$\left(L - \sum V_j\right)\Psi = 0 \tag{5.120}$$

is considered as the general equation for multiple scattering of waves.

We emphasize that the decomposition into the scatterers in eq. (5.117) can be arbitrary. For example, a scatterer of a complicated shape can be cut into a set of its parts that do not overlap each other in space. On the other hand, a certain inclusion within a scatterer can be considered as a disturbance overlapping the basic scatterer, and so on. However, the main applications for the multiple scattering equations appear for the particulate media that consist of a great number of discrete scatterers not overlapping in space. For example, they are the numerous problems of light scattering in astrophysics, atmospheric optics, and biomedical optics. In quantum mechanics, they are the problems of particle propagation in the matter, and so on.

As the wave scattering equation (5.47) for one scatterer was represented in the form of an integral equation (5.59) called the Lippmann–Schwinger equation, eq. (5.120) for multiple scattering can be easily represented as integral equations, too. Certain algebraic transforms result in the following system of the operator or integral equations

$$\begin{cases} \Psi &= \Psi_0 + \sum_j L^{-1}T_j\tilde{\Psi}_j \\ \tilde{\Psi}_j &= \Psi_0 + \sum_{l\neq j} L^{-1}T_l\tilde{\Psi}_l \end{cases} \tag{5.121}$$

If the number of scatterers in the decomposition of eq. (5.117) is equal to N, the number of equations (5.121) is $N + 1$. In quantum mechanics, eqs (5.121) are called the theory of multiple scattering by K. Watson.

At first glance, the system of the integral equations looks complicated. But factually, it has a very simple physical meaning, and it is quite convenient for

both physical interpretation and calculations. Indeed, a substitution of the second line equations of (5.121) to the first line leads to the series

$$\begin{aligned}\Psi &= \Psi_0 + \sum_j L^{-1}T_j\Psi_0 + \sum_{l\neq j}\sum_j L^{-1}T_lL^{-1}T_j\Psi_0 \\ &+ \sum_{n\neq l}\sum_{l\neq j}\sum_j L^{-1}T_nL^{-1}T_lL^{-1}T_j\Psi_0 + \dots \end{aligned} \tag{5.122}$$

This is the series of multiple scattering of waves that represents the field as a superposition of waves with all possible 'histories'. The second term of eq. (5.122) is the single scattering field that is created by scattering of the incident field on every scatterer. The next term is the double scattering field that is created by the scattering of every component of the single scattering field on other scatterers, and so on. It is obvious that the neighbor indexes m of the matrices T_m in any term of the series (5.122) should be different. But the same scatterer can appear again after, for example, the nearest neighbor scatterer. Such terms describe the repeated scattering of waves by the same scatterers. These terms appear in the triple and higher-order scattering terms.

In physics, it is conventional to represent series such as eq. (5.122) by certain diagrams. For example, in quantum mechanics, the famous Feynman diagrams are used. A lot of different kinds of diagrams are used in both classical and quantum-mechanical statistical physics. In this chapter, we prefer to use in parallel both the Feynman diagrams and the other, more intuitive, diagrams that can sometimes be more illustrative for our purposes. So, the series of eq. (5.122) is represented by the following diagrams

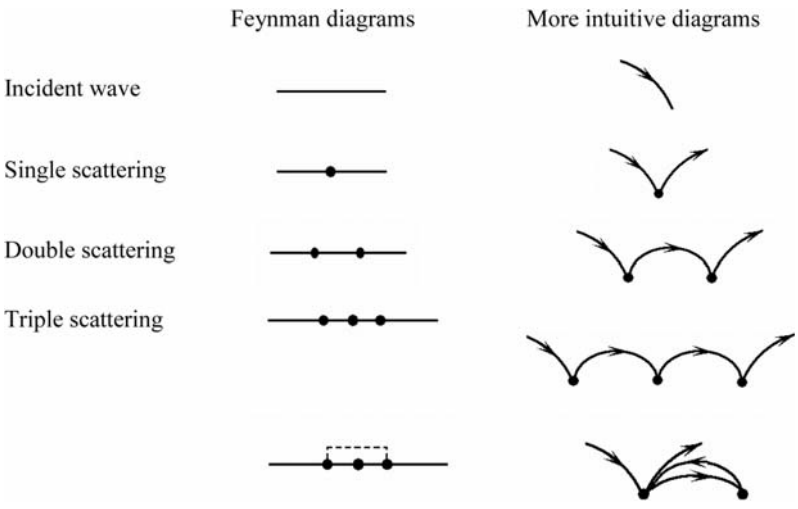

(5.123)

Here, the dots mean the scatterers, i.e. the T_j-matrices, and the lines mean propagation between the scatterers described by the operator L^{-1}. The coincidence of scatterers, i.e. of indexes of the T_j-matrices, should be shown in the Feynman diagrams by additional dotted lines, while the problem of distinguishing the same scatterers does not appear for the second kind of diagrams at all.

We emphasize that, in this chapter, every diagram will reflect only the structure of the terms. Any numerical coefficients and symbols depending on a context will be omitted. For example, a given diagram can be treated either as a field scattered by a fixed set of scatterers or as a sum of all similar fields averaged over their spatial configuration, where the signs of sum and averaging are omitted, etc.

The series representations of the multiple scattering field by eqs (5.122) or (5.123) also clarify the physical meaning of eqs (5.121). Indeed, the first line of eqs (5.121) means that the wave coming to an observation point consists of the incident wave and a superposition of the waves leaving all scatterers. Every wave leaving a scatterer is created by the waves coming to the scatterer. Their superposition is called the exciting wave, and this value is denoted in eq. (5.121) with the tilde symbol. In their turn, the exciting waves are formed by the waves leaving other scatterers that is just written by the second line of eqs (5.121). To clarify the conception of the exciting field in more detail, one could write down a series for these values like the series of eq. (5.122).

By the way we note that the Born series of eq. (5.63) can be applied directly to the original equation (5.117). Then, after gathering the terms combined by the T-matrix of eq. (5.66) for every scatterer, we arrive at the same multiple scattering equations of eqs (5.121) or (5.122).

The quadratic values for the multiply scattered fields defined by eqs (5.13) and (5.14) are readily obtained by termwise multiplication of the series of (5.122)

$$\Psi \otimes \Psi^* = \Psi_0 \otimes \Psi_0^* + \Psi_0 \otimes \sum_j (L^{-1} T_j \Psi_0)^* + \Psi_0^* \otimes \sum_j L^{-1} T_j \Psi_0 + \dots \quad (5.124)$$

This series is convenient to represent by diagrams as well, denoting the complex-conjugate factor by the lower part. Such typical diagrams of both kinds are shown below

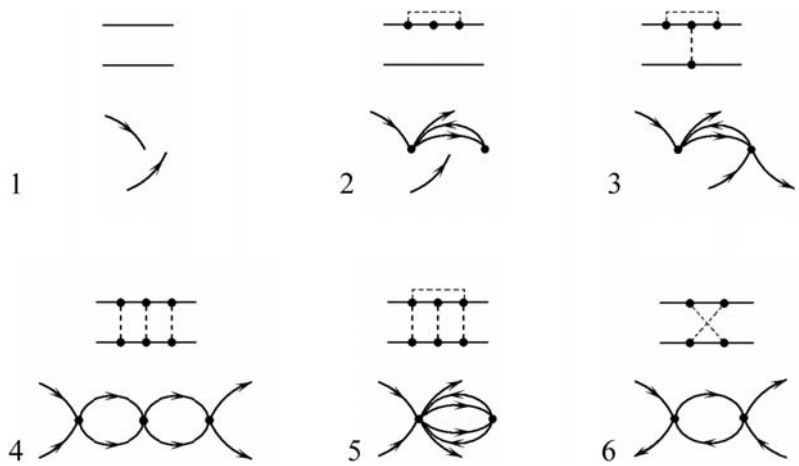

(5.125)

Here, there is a simplest class of the diagrams where the complex-conjugate co-factors do not contain common scatterers like diagrams 1 and 2. The other

diagrams 3–6 include common scatterers that are connected in the Feynman diagrams by the dotted lines as well.

If the complex-conjugate co-factors in eq. (5.125) are certain different fields, the diagrams correspond factually to interference between the fields. There are also the terms that are created by multiplication of any field by the same but complex-conjugate field as in the diagrams 4 and 5. These diagrams correspond to the quadratic value of the given fields. So, they describe multiple scattering as successive scattering acts within only quadratic field values. Interference is not accounted for in these diagrams at all. For short waves, where the interference phenomena are often negligible, these terms become predominant. Thus, diagrams such as number 4 will play a main role hereinafter. Because of their specific Feynman diagram views, terms such as diagram 4 are called ladder diagrams.

5.3.2 Two limiting cases for multiple scattering of waves

In this chapter, scattering media consisting of a great number of scatterers non-overlapping in space will be of main interest. We consider two limiting cases that are most intuitive.

In the first limiting case shown in Fig. 5.7(a), the re-scattering among the scatterers is carried out by means of the divergent spherical waves. This situation arises for both small ($ka \ll 1$) and large ($ka \gg 1$) scatterers. In particular, if the scatterers are small, the scattered waves are transformed into the spherical wave of eq. (5.69) at rather short distances from the scatterers $r \gg \lambda \gg a$. So, the distance between the scatterers, d, should obey the inequality $kd \gg 1$. For large scatterers, the distance between the scatterers, d, should satisfy the more severe condition: $d \gg ka^2$.

The second limiting case corresponds to large scatterers situated in the near zones of each other. This case is subdivided by Figs 5.7(b) and 5.7(c) for optically soft and optically hard scatterers, respectively. It is instructive to consider the

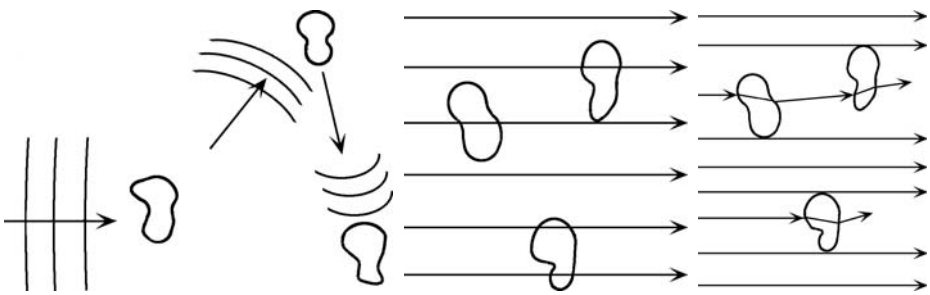

Fig. 5.7. Limiting cases of multiple scattering of waves. (a) Scatterers are positioned in each others' wave zones. (b) Large optically soft scatterers are positioned in each others' near zones. (c) The same for large optically hard scatterers.

case of optically soft scatterers, where the problem of multiple scattering is solved analytically in the straight-ray approximation. Within this approximation, a set of optically soft scatterers is equivalent to a set of the amplitude–phase screens overlapping each other in a projection onto an observation plane $x = \text{const}$

$$u(x, \boldsymbol{\rho}) = \mathrm{e}^{i \sum A_j(\boldsymbol{\rho})} \tag{5.126}$$

according to eqs (5.85) and (5.86). Following the ideology of multiple scattering of waves, we have to introduce the field scattered by the single jth scatterer

$$u_{sj}(\boldsymbol{\rho}) \equiv \omega_j(\boldsymbol{\rho}) = \mathrm{e}^{iA_j(\boldsymbol{\rho})} - 1 \tag{5.127}$$

where the new notation ω_j for the scattered field is used to avoid double indexes. A substitution of eq. (5.127) into eq. (5.126) results in the following sum

$$\begin{aligned} u(x, \boldsymbol{\rho}) &= \prod (1 + \omega_j(\boldsymbol{\rho})) \\ &= 1 + \sum_j \omega_j(\boldsymbol{\rho}) + \sum_{l>j} \sum_j \omega_l(\boldsymbol{\rho}) \omega_j(\boldsymbol{\rho}) \\ &\quad + \sum_{m>l} \sum_{l>j} \sum_j \omega_m(\boldsymbol{\rho}) \omega_l(\boldsymbol{\rho}) \omega_j(\boldsymbol{\rho}) + \dots \end{aligned} \tag{5.128}$$

This sum is just the series of multiple scattering given by eq. (5.122) for this specific case. Indeed, every term is easily interpreted if the longitudinal positions of the scatterers x_j are taken into account. Thus, the scattered field ω_j is nonzero only in the shadow domain behind the jth scatterer, i.e. only for $x > x_j$. Then this field is incident on the next scatterers, producing the double scattered field $\omega_l \omega_j$. This double-scattered field appears and propagates behind the lth scatterer for $x > x_l > x_j$, and so on.

Of course, all diagrams of eq. (5.123) represent these multiple scattering waves of eq. (5.128) as well, but the specificity of this case leads to certain peculiarities. In particular, the waves with repeated scattering by the same scatterer become impossible, so the last diagram of eq. (5.123) vanishes. Also, the number of addends in eq. (5.128) is limited by the number of scatterers. For example, two scatterers produce here only single- and double-scattered waves, while in the case shown in Fig. 5.7(a), two scatterers create waves of arbitrary scattering multiplicities because of repeated scattering by them.

For optically hard scatterers shown in Fig. 5.7(c), eq. (5.128) is valid only for the shadow-forming fields determined by eq. (5.89). In this case, the total field $u(x, \boldsymbol{\rho})$ is equal to zero if a ray $\boldsymbol{\rho} = \text{const}$ is crossed by one or by several scatterers, and equals 1 otherwise. Formally, the substitution of $u_j = -\eta_j$ into eq. (5.128) turns out every constituent of the sum into ± 1 that leads to the final total value of zero or one.

Thus, we have obtained an important physical conclusion: in the language of wave scattering theory, a shadowing by a large scatterer is just a scattering action. Consequently, a shadowing by N large scatterers corresponds to multiple scattering of waves, N being the maximum multiplicity of the scattering.

5.4 Multiple scattering by uncorrelated scatterers

5.4.1 Uncorrelated scatterers

One of the most important objects considered in physics is an ensemble of a great number of particles. In particular, matter consisting of molecules is an obvious example of such ensembles. Various particulate media consisting of macroscopic particles surround us as well. They are the interstellar dust in astrophysics, droplets of clouds in the atmosphere, powders used in technologies, and so on. These particles play the role of scatterers for a wave incident on the ensemble.

The main characteristics of such scatterer ensembles is their number density c

$$c = N/Q = d^{-3} \tag{5.129}$$

where N is a number of scatterers in a volume Q. Instead of the number density, the average distance between the scatterers, d, defined by eq. (5.129) will be often used. Usually centers of scatterers are not situated in space closer than a certain distance a because of certain repulsive forces. This distance will be treated as a scatterer size. In addition, other long-distance forces can exist, resulting in long-distance correlations of scatterer centers. If the long-distance correlations are negligible and the scatterer sizes obey the condition $a \ll d$, i.e.

$$ca^3 \ll 1 \tag{5.130}$$

the scatterers can be considered as spatially independent or uncorrelated objects. For example, a rarefied gas in physics corresponds to the uncorrelated objects. On the contrary, the theory of dense gases demands taking the short-distance correlation into consideration, and the theory deals with the values of the order of ca^3.

Turning to the problem of multiple scattering of waves, we note that the multiple scattering of waves for a fixed configuration of a large number of scatterers is of no interest. On the one hand, such a numerical solution for a large number of scatterers is hardly feasible, even for modern computers. On the other hand, the solution obtained would be overloaded with the details that are of interest for this given configuration only, and it would be scarcely useful for both theoretical consideration and practical applications. Therefore, the usual procedure in statistical physics is to consider the values that are averaged over all configurations.

In statistical physics, an ensemble of N scatterers is determined by the probability density $P(\boldsymbol{r}^N)$ for its configurations $\boldsymbol{r}^N = (\boldsymbol{r}_1, \boldsymbol{r}_2, \ldots, \boldsymbol{r}_N)$, where $\boldsymbol{r}_j$ are the scatterer centers. The term of uncorrelated scatterers means their statistical independence, i.e.

$$P(\boldsymbol{r}^N) = p(\boldsymbol{r}_1)p(\boldsymbol{r}_2)\ldots p(\boldsymbol{r}_N) \tag{5.131}$$

where $p(\boldsymbol{r}_j) = 1/Q$ for the homogeneous distribution within the volume Q. It is worth noting that in an averaging over scatterer positions according to eq. (5.131), it is formally assumed that the scatterers can freely penetrate each other. Sometimes, calculations accounting for such fictitious penetration can result in certain artifacts.

5.4.2 Average or coherent field

Now, the averaged multiple scattering field $\langle\Psi\rangle$ for the ensemble of uncorrelated scatterers can be calculated by averaging the series (5.122) term by term. The averaging of the single-scattering field is reduced to the following integral

$$\langle\Psi\rangle_1 = \left\langle \sum_j L^{-1} T_j \Psi_0 \right\rangle = \frac{N}{Q} \int L^{-1} T(\boldsymbol{r}_j) \Psi_0 \, \mathrm{d}\boldsymbol{r}_j \tag{5.132}$$

Here, the integrand is the field scattered by the jth scatterer with the center position $\boldsymbol{r}_j$, and the averaging is written down relative to all its positions in the volume Q. Then, if the scatterers reveal a distribution over their sizes, shapes and internal structure, this averaging can be readily taken into account after the integral of eq. (5.132) is calculated.

To begin with, a scalar plane wave $\psi_0 = \exp(ikx)$ is assumed to be incident on a scattering medium occupying the half-space $x > 0$. We consider the first limiting case shown in Fig. 5.7(a) where the scattered wave is the divergent spherical wave of eq. (5.69)

$$\langle\psi(\boldsymbol{r})\rangle_1 = c \int \mathrm{e}^{ikx_j + ik|\boldsymbol{r}-\boldsymbol{r}_j|} \frac{f(\boldsymbol{n}, \boldsymbol{n}_0)}{|\boldsymbol{r}-\boldsymbol{r}_j|} \, \mathrm{d}\boldsymbol{r}_j \tag{5.133}$$

Similar integrals over a surface are often considered in the diffraction theory both in optics and radiophysics, when one calculates diffracted fields according to the Huyghens principle. For our purpose, consider the plane $x_j = \text{const}$ and use the new variables: $|\boldsymbol{r}-\boldsymbol{r}_j|^2 = (x-x_j)^2 + (\boldsymbol{\rho}-\boldsymbol{\rho}_j)^2 = p^2$ and ϕ is the polar angle in the plane, so that $\mathrm{d}\boldsymbol{\rho}_j = p \, \mathrm{d}p \, \mathrm{d}\phi$. Then the integral of eq. (5.133) over the plane $x_j = \text{const}$ is taken analytically

$$\begin{aligned} \int \mathrm{e}^{ik|\boldsymbol{r}-\boldsymbol{r}_j|} \frac{f(\boldsymbol{n}, \boldsymbol{n}_0)}{|\boldsymbol{r}-\boldsymbol{r}_j|} \, \mathrm{d}\boldsymbol{\rho}_j &= \int_0^{2\pi} \mathrm{d}\phi \int_{|x-x_j|}^{\infty} \mathrm{e}^{ikp} f(\boldsymbol{n}, \boldsymbol{n}_0) \, \mathrm{d}p \\ &= -\frac{2\pi}{ik} \mathrm{e}^{ik|x-x_j|} f(\pm\boldsymbol{n}_0, \boldsymbol{n}_0) \end{aligned} \tag{5.134}$$

A justification of the final expression is as follows. The internal integral of the second part of eq. (5.134) is well interpreted in the classical diffraction theory by contributions from the Fresnel zones of various orders. As known, these zones compensate each other, and only a contribution from the central zone is of importance. Mathematically, it corresponds to the procedure where the antiderivative from the function $\exp(ikp)$ should be taken only at the lower limit of integration $p = |x - xj|$. In our case, the scattering amplitude f can be considered as a constant within the central Fresnel zone. So, the function f does not prevent us from this procedure, and the final result of eq. (5.134) is justified.

It is worth noting that the same procedure can also be used for any curved surface. As a rule, such integrals are calculated both in optics and radiophysics by the method of stationary phase. But the stationary phase method is rather cumbersome for the 2-D case, unlike our procedure resulting in eq. (5.134). Also,

it is interesting to note that it is just eq. (5.134) that proves the optical theorem of eq. (5.76).

Substitution of the expression (5.134) into eq. (5.133) yields

$$\langle\psi(\boldsymbol{r})\rangle_1 = c\mu x \mathrm{e}^{ikx} + O(c\lambda^2 f(-\boldsymbol{n}_0, \boldsymbol{n}_0)) \tag{5.135}$$

where

$$\mu = i\lambda f(\boldsymbol{n}_0, \boldsymbol{n}_0) \tag{5.136}$$

and the scattering amplitude f in the forward direction is averaged over any scatterer distribution of their internal parameters: sizes, shapes, orientation, etc.

The first term of eq. (5.135) takes into account contributions from the forward part of the scattering medium $x_j < x$. Here, the exponential factor in the integral of eq. (5.133) disappears and all layers $x_j = \text{const}$ yield the same contributions. For the backward part of the scattering medium $x < x_j$, on the contrary, the exponential factor is not compensated. The quickly oscillating exponential function sharply decreases the magnitude of the integral resulting in the factor of order of the wavelength λ instead of the macroscopic factor x for the previous case. So, the contribution from the backward part of the scattering medium is very small and it is denoted in eq. (5.135) only by its order.

Remembering that statistical physics of sparse particulate ensembles is based on the small parameter ca^3, we see that another dimensionless parameter appears for the scattered waves. Since the scattering amplitude in the backward direction appearing in eq. (5.135) is of the order of either the wavelength λ for small scatterers or the scatterer size a for large scatterers, it is expedient to introduce a new small parameter

$$c\lambda^3 \ll 1 \tag{5.137}$$

The inequality (5.137) is equivalent to the condition $\lambda \ll d$. It will be called the condition of short waves in contrast to the case of the long waves $\lambda \gg d$. Thus, the conditions both of uncorrelated scatterers (5.130) and of short waves (5.137) allow us to throw away the last addend in eq. (5.135).

Then an application of these procedures to higher multiplicities of scattering is reduced to the integration over the longitudinal coordinate within the forward part of the scattering medium

$$\langle\psi(\boldsymbol{r})\rangle_2 = \mathrm{e}^{ikx} c\mu \int_0^x (c\mu x')\,\mathrm{d}x' = e^{ikx}(c\mu x)^2/2! \tag{5.138}$$

and so on, where the condition $N \gg 1$ is also used. The series of these terms forms the exponential function

$$\langle\psi(\boldsymbol{r})\rangle = \sum \langle\psi(\boldsymbol{r})\rangle_n = e^{ikx} \sum (c\mu x)^n/n! = \mathrm{e}^{ikx + c\mu x} \tag{5.139}$$

In this series, the terms with the repeated scattering by the same scatterer like the last diagram of eq. (5.123) are not included. But it is easily seen from these diagrams that the integrands of such terms contain additionally the exponential functions quickly oscillating with the distance between the scatterers. So, such

terms prove to be negligible under the conditions of eqs (5.130) and (5.137) like the last term of eq. (5.135).

These results are directly generalized for the incident electromagnetic wave $\boldsymbol{E}_0(\boldsymbol{r}) = \boldsymbol{E}^0 \exp(ikx)$. Indeed, the scattered electromagnetic field of eq. (5.70) is included in the previous calculations by its vector scattering amplitude in the forward direction $\boldsymbol{E}_s(\boldsymbol{n}_0, \boldsymbol{n}_0)$. A transformation of polarization of the incident wave $\boldsymbol{E}^0$ into polarization of the scattered field $\boldsymbol{E}_s$ is defined by the 2×2 scattering matrix $\boldsymbol{S}$

$$\boldsymbol{E}_s(\boldsymbol{n}, \boldsymbol{n}_0) = \boldsymbol{S}(\boldsymbol{n}, \boldsymbol{n}_0)\boldsymbol{E}^0 \tag{5.140}$$

In eqs (5.133)–(5.135), the scalar scattering amplitude in the forward direction $f(\boldsymbol{n}_0, \boldsymbol{n}_0)$ is replaced by the vector scattering amplitude $\boldsymbol{S}(\boldsymbol{n}_0, \boldsymbol{n}_0)\boldsymbol{E}^0$ that does not change the calculations. For the nth order of scattering, the matrix factor $\boldsymbol{S}^n(\boldsymbol{n}_0, \boldsymbol{n}_0)$ appears in the terms of the sum (5.139) instead of the factor f^n. As a result, the sum of eq. (5.139) is replaced by the similar matrix equation

$$\langle \boldsymbol{E}(\boldsymbol{r}) \rangle = \mathrm{e}^{ikx + ic\lambda \boldsymbol{S}(\boldsymbol{n}_0, \boldsymbol{n}_0)x} \boldsymbol{E}^0 \tag{5.141}$$

Thus, the averaged electromagnetic field changes during its propagation not only its phase and amplitude as the scalar field of eq. (5.139) but also its polarization state.

Now we go to the second limiting case where large scatterers are situated in the near zones of each other as shown in Fig. 5.7(b). Here, an averaging termwise of the series of eq. (5.128) is much simpler. Indeed, the single scattered field is equal to

$$\langle u(x, \boldsymbol{\rho}) \rangle_1 = cx \left\langle \int \omega_j(\boldsymbol{\rho} - \boldsymbol{\rho}_j)\, \mathrm{d}\boldsymbol{\rho}_j \right\rangle = cx \int \omega_j(\boldsymbol{\rho})\, \mathrm{d}\boldsymbol{\rho} = ci\lambda f(\boldsymbol{n}_0, \boldsymbol{n}_0)x \tag{5.142}$$

where eq. (5.92) is used to get the final expression. It is remarkable that the analytical expression for the single scattered field proves to be the same for both eqs (5.135) and (5.142). Analogously, the higher-order terms completely coincide for the both limiting cases, including the average field of eq. (5.139).

For evidence, let us distinguish the important case of the shadow-forming fields $\omega_j = -\eta_j$. In accordance wiht the straight-ray approximation, the averaged field is obtained as a result of shadowing a ray by statistically independent and absolutely absorbing screens corresponding to scatterer projections. As a result, the series (5.128) yields

$$\langle u(x, \boldsymbol{\rho}) \rangle = \mathrm{e}^{-csx} \tag{5.143}$$

Here, s is the shadow area averaged over the statistical ensemble. Equation (5.143) is valid both for optically soft scatterers with chaotic phase shift in the interval $[0, 2\pi]$ and for optically hard scatterers. If such scatterers are situated in the near zone of each other as shown in Figs 5.7(b) and 5.7(c), the refractive fields are quickly oscillating functions in the transverse direction as compared to the shadow-forming fields. Consequently, the contribution of the refracted fields to the averaged field is negligible according to the integrals such as (5.142). On the other hand, if these scatterers are situated in the wave zones of each other,

as shown in Fig. 5.7(a), the scattering amplitudes of the refracted fields in the forward direction are also negligible as compared to that of the shadow-forming fields as seen from eqs (5.91)–(5.95). Then eq. (5.143) can be obtained as a particular case of eq. (5.139) by substitution of eq. (5.109) for the scattering amplitude of the shadow-forming field. We recall that the same possibility for neglecting the refracted fields was discussed also in section 5.2.6.3 in detail.

The complete coincidence of the results obtained for two opposite limiting cases shown in Figs 5.7(a), 5.7(b) and 5.7(c) allows us to state that the analytical solution for the averaged field given by eq. (5.139) is quite general and it does not depend on either scatterer sizes or distances between the scatterers.

5.4.3 Multiple scattering of short and long waves

The independence of the analytical equations for the averaged field on sizes, refractive indexes and distance among scatterers can be explained by means of more general physical concepts. We can state that any scattering medium proves to be a continuous medium relative to the averaged field. This averaged-field-continuous medium is described by an effective refractive index that can be derived from the individual properties of scatterers. This value will be called the bulk refractive index.

In particular, we see that the averaged field of eq. (5.139) corresponds to the following bulk refractive index

$$m = n + i\kappa = 1 + c\mu/ik = 1 + c2\pi k^{-2}\mathrm{Re}\, f(\boldsymbol{n}_0, \boldsymbol{n}_0) + ic2\pi k^{-2}\mathrm{Im}\, f(\boldsymbol{n}_0, \boldsymbol{n}_0) \quad (5.144)$$

It is important that this continuous medium proves to be optically soft and absorbing. The optical softness ($|c2\pi k^{-2}\,\mathrm{Re}\, f(\boldsymbol{n}_0, \boldsymbol{n}_0)| \ll 1$) is provided mainly by the condition of short waves $\lambda \ll d$. In addition, the condition of uncorrelated scatterers $a \ll d$ is accounted for since the inequality $|\mathrm{Re}\, f(\boldsymbol{n}_0, \boldsymbol{n}_0)| \leq a$ is valid for both small and large scatterers. The imaginary part of the bulk refractive index describing absorption of incident waves in the scattering medium is, however, essential. We emphasize that this absorption is presented for both absorbing and non-absorbing scatterers since it corresponds to an extraction of energy from the averaged or coherent wave for creation of divergent scattered waves.

It is important that eq. (5.144) allows us to generalize all the results obtained for a particular case of the incident plane wave and of the half-space scattering medium to any kind of incident waves and any shape and internal structure of scattering media. Indeed, because of the optical softness of such effective media, the straight-ray approximation (5.11) or its generalization for other kinds of incident waves can be applied to calculate the averaged field inside a scattering medium of any shape and internal structure. In particular, the averaged field for a point source of radiation will be described by the same divergent spherical wave where the additional complex-valued phase appears along a ray due to eq. (5.144). This result could be obtained by the previous procedures of eq. (5.134) applied to the incident spherical wave, but the conception of the effective

scattering medium allows us to avoid these calculations. So, the averaged field can be readily written inside the scattering medium for any radiation source. As for the observation points outside the scattering medium, the standard laws of wave propagation in free space can be applied, as we used this approach to describe scattering by large optically soft scatterers in section 5.2.

The averaged field is also called the coherent field. In general, if the scattered waves of the series of eq. (5.122) do not change the phase shifts among them when a configuration of the statistical ensemble is changed, they are added coherently. Otherwise, when the phases among them are chaotically shifted in the interval $[0, 2\pi]$, we get incoherent adding. In the case shown in Fig. 5.7(a), the phases of the scattered waves would only not shifted at scattering in the forward direction. This fact was discussed in detail in section 5.2 when the optical theorem was derived. So, we conclude that, for the incident plane wave, the coherent field at a spatial point $\boldsymbol{r} = (x, \boldsymbol{\rho})$ is formed only by a superposition of those waves that are coming from the scatterers positioned along a ray $\boldsymbol{\rho} = \text{const}$ at $x_j < x$. Factually, eqs (5.135), (5.138), and (5.139) prove this fact mathematically.

In the case of large scatterers shown in Figs 5.7(b) and 5.7(c), the forward scattering appears because of the shadowing of the incident wave that is demonstrated by eqs (5.142) and (5.143). It is curious to discuss the following paradox: if, say, large scatterers of the refractive index of n are closely packed in space resulting in a large volume density of the scatterers, one can suppose that the bulk refractive index should approach the same magnitude of n. On the other hand, eq. (5.144) states that this continuous medium should be optically soft. To overcome this discrepancy, consider the case shown in Fig. 5.7(b). Here, if the phase shifts along the rays $\boldsymbol{\rho} = \text{const}$ crossing one or more scatterers are chaotically distributed within the interval $[0, 2\pi]$, these scattered waves do not contribute to the coherent field independently of the volume density of the scatterers. Only the rays $\boldsymbol{\rho} = \text{const}$ that are not crossed by scatterers contribute to the coherent wave resulting in eq. (5.143) for the shadow-forming fields. The velocity of these waves coincides with the velocity in free space, so the real part of the bulk refractive index of eq. (5.144) is equal to 1. Thus, these effective media prove to be optically soft in full accordance to eq. (5.144).

It is interesting to compare multiple scattering of short ($c\lambda^3 \ll 1$) and long ($c\lambda^3 \gg 1$) waves. For the long waves, the terms of the series of eq. (5.122) corresponding to repeated scatterings by the same scatterer become, on the contrary, essential. Indeed, the phase shifts between the waves rescattered by any neighbor scatterers are small, and these waves are added coherently. The repeated scattering by the same scatterers results in a considerable delay of the initial incident wave inside the medium. Thus, this continuous medium is not already optically soft and its real part of the refractive index can essentially deviate from the magnitude of 1. The repeated scattering by the same scatterers is determined by the scattering amplitude in the backward direction $f(-\boldsymbol{n}_0, \boldsymbol{n}_0)$. This is the reason that the both values $f(\boldsymbol{n}_0, \boldsymbol{n}_0)$ and $f(-\boldsymbol{n}_0, \boldsymbol{n}_0)$ appear in the known equations for the bulk refractive index that are not considered here.

In any averaged quadratic value of fields, one can separate a part formed by only the averaged or coherent field

$$\langle \Psi \otimes \Psi^* \rangle_c = \langle \Psi \rangle \otimes \langle \Psi^* \rangle \tag{5.145}$$

called the coherent part. Then the quadratic value is divided into its coherent and incoherent parts

$$\langle \Psi \otimes \Psi^* \rangle = \langle \Psi \otimes \Psi^* \rangle_c + \langle \Psi \otimes \Psi^* \rangle_{ic} \tag{5.146}$$

For example, compare an interaction of visible light with either a pane of glass or a cloud in the sky. Here, the scatterers are either atoms in the glass or water drops in the cloud, and they correspond to the conditions of long and short waves, respectively. For the glass, we watch only well-ordered light reflected from or transmitted through the glass. It is just the coherent part; here incoherent scattering is too small to be detected. On the contrary, we watch a quite different chaotic pattern for the light reflected from the cloud that is formed by incoherent scattering. It is easy to find a lot of similar examples distinguishing multiple scattering of long and short waves in acoustics, quantum mechanics, etc.

5.4.4 Exponential extinction law

In this section, we consider the coherent part for the energy flux density defined by eqs (5.34) and (5.35). For the averaged scalar field of eq. (5.139), its Wigner function can be replaced by the specific intensity (see Eq. 1.36). The specific intensity is directed only along the x-axis, and it is conventionally called the intensity $I_c(x)$. Thus, eq. (5.139) yields the exponential decrease of the intensity with distance

$$I_c(x) = \langle |\boldsymbol{j}(\boldsymbol{r})| \rangle_c = |\langle \psi(\boldsymbol{r}) \rangle|^2 = \mathrm{e}^{c(\mu+\mu^*)x} = \mathrm{e}^{-c\sigma_e x} = \mathrm{e}^{-\tau(0,x)} \tag{5.147}$$

where the optical theorem given by eq. (5.76) is used. The exponent τ is called the optical depth. In general, the optical depth is defined as the integral over the straight segment between two points $\boldsymbol{r}$ and $\boldsymbol{r}'$

$$\tau(\boldsymbol{r}, \boldsymbol{r}') = \int_{\boldsymbol{r}}^{\boldsymbol{r}'} c\sigma_e \, \mathrm{d}l \tag{5.148}$$

where the both values $c(\boldsymbol{r})$ and $\sigma_e(\boldsymbol{r})$ can be certain spatial functions if a scattering medium is inhomogeneous.

Equation (5.147) is the fundamental exponential law for extinction of any short-wave radiation in scattering media. For example, it is true for penetration of high-energy elementary particles such as electrons, neutrons, etc. in matter. In optics, it is connected with the names of Bouguer, Lambert, and Beer.

The exponential extinction law obeys the following differential equation

$$\left(\frac{\mathrm{d}}{\mathrm{d}x} + \alpha \right) I(x) = 0 \tag{5.149}$$

where $\alpha = c\sigma_e$. In this equation, the value α can be treated as a probability to cross the ray in any point of the observation path x by a scatterer with the

transversal area of σ_e. So, the intensity I has a physical meaning of the probability for a corpuscle to reach the point x without a collision with scatterers. In other words, the value I describes the flux of the corpuscles that did not undergo any collisions. So, the value $1/\alpha$ is called the averaged free path. From the point of view of the wave scattering theory, on the other hand, the exponential law is the result of interference of the incident wave with a lot of waves scattered in the forward direction along the ray.

We would like to emphasize that the differential equation (5.149) implies that scatterers cover the ray independently of each other. This independence is provided, on the one hand, by the condition of uncorrelated scatterers $ca^3 \ll 1$ of eq. (5.130). On the other hand, the additional condition $a \ll x$ is necessary, otherwise scatterers with sizes larger then the observation path x will not result in the extinction cross-section. Thus, the exponential extinction law is true if the scatterers covering a propagation ray are not only statistically independent but they are also small as compared to the observation path.

For the transverse electromagnetic plane waves, the quadratic values describe not only energy–flux density called intensity but also three additional parameters accounting for polarization. To begin with, we indicate the definition of the direct products for 2-D vectors and matrices. We remind that the direct product results in 4-D vectors and matrices because of the doubling dimensionality that was discussed in section 5.1.4

$$\begin{aligned}
\boldsymbol{a}\otimes\boldsymbol{b}^* &= \begin{pmatrix} a_1 \\ a_2 \end{pmatrix} \otimes \begin{pmatrix} b_1^* \\ b_2^* \end{pmatrix} = \begin{pmatrix} a_1\boldsymbol{b}^* \\ a_2\boldsymbol{b}^* \end{pmatrix} = \begin{pmatrix} a_1 b_1^* \\ a_1 b_2^* \\ a_2 b_1^* \\ a_2 b_2^* \end{pmatrix} \\
\boldsymbol{A}\otimes\boldsymbol{B}^* &= \begin{pmatrix} A_{11} & A_{12} \\ A_{21} & A_{22} \end{pmatrix} \otimes \begin{pmatrix} B_{11}^* & B_{12}^* \\ B_{21}^* & B_{22}^* \end{pmatrix} = \begin{pmatrix} A_{11}\boldsymbol{B}^* & A_{12}\boldsymbol{B}^* \\ A_{21}\boldsymbol{B}^* & A_{22}\boldsymbol{B}^* \end{pmatrix} = \\
&= \begin{pmatrix} A_{11}B_{11}^* & A_{11}B_{12}^* & A_{12}B_{11}^* & A_{12}B_{12}^* \\ A_{11}B_{21}^* & A_{11}B_{22}^* & A_{12}B_{21}^* & A_{12}B_{22}^* \\ A_{21}B_{11}^* & A_{21}B_{12}^* & A_{22}B_{11}^* & A_{22}B_{12}^* \\ A_{21}B_{21}^* & A_{21}B_{22}^* & A_{21}B_{21}^* & A_{22}B_{22}^* \end{pmatrix}
\end{aligned} \tag{5.150}$$

For the transverse electromagnetic waves determined by the complex-valued 2-D vectors $\boldsymbol{E} = (E_1, E_2)$, the 4-D vectors defined by eq. (5.150) will be denoted as $\boldsymbol{J} = \boldsymbol{E}\otimes\boldsymbol{E}^*$. Now the coherent part of this quadratic value $\boldsymbol{J}_c$ can be obtained from the 2-D matrix equation (5.141) for the averaged field. In this way, the general property of the direct products $(AB)\otimes(CD) = (A\otimes C)(B\otimes D)$ discussed in section 5.1.4 is used. Besides, we use the equation

$$(\exp\boldsymbol{A})\otimes(\exp\boldsymbol{B}) = \exp[(\boldsymbol{A}\otimes\mathbf{1}) + (\mathbf{1}\otimes\boldsymbol{B})] \tag{5.151}$$

where $\mathbf{1}$ is the 2-D unit matrix ($1_{jl} = 1$ for $j = l$ and $1_{jl} = 0$ for $j \neq l$). Equation (5.151) can be checked, for example, by the Taylor series. So, we get

$$\begin{aligned}
\boldsymbol{J}_c(x) &= \left(\mathrm{e}^{i\lambda cx\boldsymbol{S}_0}\boldsymbol{E}^0\right)\otimes\left(\mathrm{e}^{-i\lambda cx\boldsymbol{S}_0^*}\boldsymbol{E}^{0^*}\right) = \left(\mathrm{e}^{i\lambda cx\boldsymbol{S}_0}\otimes\mathrm{e}^{-i\lambda cx\boldsymbol{S}_0^*}\right)\left(\boldsymbol{E}^0\otimes\boldsymbol{E}^{0^*}\right) \\
&= \mathrm{e}^{i\lambda cx(\boldsymbol{S}_0\otimes\mathbf{1}-\mathbf{1}\otimes\boldsymbol{S}_0^*)}\left(\boldsymbol{E}^0\otimes\boldsymbol{E}^{0^*}\right) = \mathrm{e}^{i\lambda cx(\boldsymbol{S}_0\otimes\mathbf{1}-\mathbf{1}\otimes\boldsymbol{S}_0^*)}\boldsymbol{J}^0
\end{aligned} \tag{5.152}$$

Here $\boldsymbol{S}_0 = \boldsymbol{S}(\boldsymbol{n}_0, \boldsymbol{n}_0)$ is the 2-D scattering matrix given by eq. (5.140) that is taken in the forward scattering direction.

Instead of the complex-valued 4-D vectors $\boldsymbol{J}$, the real-valued 4-D vectors are more convenient. In particular, the well-known Stokes vector-parameters $\boldsymbol{I} = (I_1, I_2, I_3, I_4)$ are conventional that are determined by the following equations

$$\boldsymbol{I} = \boldsymbol{D}\boldsymbol{J}$$

where

$$\boldsymbol{D} = \begin{pmatrix} 1 & 0 & 0 & 1 \\ 1 & 0 & 0 & -1 \\ 0 & -1 & -1 & 0 \\ 0 & -i & i & 0 \end{pmatrix} \qquad \boldsymbol{D}^{-1} = \frac{1}{2}\begin{pmatrix} 1 & 1 & 0 & 0 \\ 0 & 0 & -1 & i \\ 0 & 0 & -1 & -i \\ 1 & -1 & 0 & 0 \end{pmatrix}$$

$$\begin{aligned} I_1 &= \langle |E_1|^2 + |E_2|^2 \rangle \\ I_2 &= \langle |E_1|^2 - |E_2|^2 \rangle \\ I_3 &= -\langle E_1 E_2^* + E_1^* E_2 \rangle \\ I_4 &= -i\langle E_1 E_2^* - E_1^* E_2 \rangle \end{aligned} \tag{5.153}$$

For the Stokes vectors, any matrix $\boldsymbol{A}$ transforming the vectors $\boldsymbol{J}$ should be replaced by the matrix: $\boldsymbol{A}' = \boldsymbol{D}\boldsymbol{A}\boldsymbol{D}^{-1}$. So, the coherent part of the Stokes vector is found from eq. (5.152) as the following 4-D matrix equation

$$\boldsymbol{I}_c(x) = \mathrm{e}^{-cx\boldsymbol{N}}\boldsymbol{I}^0 \tag{5.154}$$

where the 4-D matrix $\boldsymbol{N}$ called the extinction matrix, describes both extinction and transformation of polarization by one scatterer. The extinction matrix is determined by the elements $S^0 j_l$ of the 2-D scattering matrix $\boldsymbol{S}_0$ as follows

$$\begin{aligned} \boldsymbol{N} &= -\boldsymbol{D}[i\lambda(\boldsymbol{S}_0 \otimes \mathbf{1} - \mathbf{1} \otimes \boldsymbol{S}_0^*)]\boldsymbol{D}^{-1} = \\ &= \lambda \begin{pmatrix} \mathrm{Im}\,(S_{11}^0 + S_{22}^0) & \mathrm{Im}\,(S_{11}^0 - S_{22}^0) & -\mathrm{Im}\,(S_{12}^0 + S_{21}^0) & \mathrm{Re}\,(S_{21}^0 - S_{12}^0) \\ \mathrm{Im}\,(S_{11}^0 + S_{22}^0) & \mathrm{Im}\,(S_{11}^0 + S_{22}^0) & \mathrm{Im}\,(S_{21}^0 - S_{12}^0) & -\mathrm{Re}\,(S_{12}^0 + S_{21}^0) \\ -\mathrm{Im}\,(S_{12}^0 + S_{21}^0) & -\mathrm{Im}\,(S_{21}^0 - S_{12}^0) & \mathrm{Im}\,(S_{11}^0 + S_{22}^0) & \mathrm{Re}\,(S_{22}^0 - S_{11}^0) \\ \mathrm{Re}\,(S_{21}^0 - S_{12}^0) & \mathrm{Re}\,(S_{12}^0 + S_{21}^0) & -\mathrm{Re}\,(S_{22}^0 - S_{11}^0) & \mathrm{Im}\,(S_{11}^0 + S_{22}^0) \end{pmatrix} \end{aligned} \tag{5.155}$$

Generally speaking, the scalar exponential extinction of eq. (5.147) for the intensity is not already true for the intensity I_1 of the electromagnetic waves. The reason for this is that the extinction cross-section depends on the polarization state according to eq. (5.77), but the polarization state is changed during propagation. Nevertheless, the matrix equation (5.154) written in the differential equation form

$$\left(\frac{\mathrm{d}}{\mathrm{d}x} + c\boldsymbol{N}\right)\boldsymbol{I}_c(x) = 0 \tag{5.156}$$

is similar to the scalar differential equation (5.149).

5.4.5 Radiative transfer equation

As was shown in section 5.2, every scattering action of a wave consists of two phenomena. First, the energy is extracted from the incident wave by means of interference between the incident wave and the wave scattered in the forward direction. In the case of an ensemble of scatterers, a lot of the multiply scattered waves take part in the interference. This phenomenon, called coherent scattering, was studied above. Second, the extracted energy is redistributed over all possible scattering directions. This is the incoherent scattering. In quantum mechanics, the terms of the elastic and inelastic scattering are used, respectively. Equation (5.146) just represents the decomposition of the quadratic values of the fields on the coherent and incoherent parts.

The incoherent quadratic values of the multiple scattered waves are expedient to study in the language of the diagrams of eq. (5.125). In eq. (5.125), those Feynman diagrams that have no links between the upper and lower lines, such as the diagrams 1 and 2, belong to the coherent part. They have been considered above. Other diagrams concerning the incoherent part are studied below.

For the beginning, we consider the case shown in Fig. 5.7(a) where at least a majority of scatterers are positioned in the wave zone of each other. It is important that in this case any scattered wave-zone fields coming to a next scatterer can be assumed in the vicinity of the scatterer as plane waves. Then two ways for calculation of the diagrams are possible. In the first way, any diagram of eq. (5.125) can be readily written down analytically in the coordinate representation due to the following approximation

$$(L^{-1}T_j)_{\boldsymbol{r}\boldsymbol{r}'} \approx \frac{\mathrm{e}^{ik|\boldsymbol{r}-\boldsymbol{r}_j|}}{|\boldsymbol{r}-\boldsymbol{r}_j|} f_j \left(\frac{\boldsymbol{r}-\boldsymbol{r}_j}{|\boldsymbol{r}-\boldsymbol{r}_j|}, \boldsymbol{n}_0 \right) \delta(\boldsymbol{r}'-\boldsymbol{r}_j) \tag{5.157}$$

where $\boldsymbol{r}_j$ is the center of the jth scatterer, f_j is its scattering amplitude, $\boldsymbol{n}_0$ is a propagation direction of an incoming wave, and δ is the Dirac δ-function. Then the analytical expression for any diagram containing n scatterers should be averaged over their configurations $\boldsymbol{r}^n = (\boldsymbol{r}_1, \boldsymbol{r}_2, \ldots, \boldsymbol{r}_n)$. A number of the waves described by the same diagram is equal to $N!/(N-n)!$. In the limit $N \to \infty$, $Q \to \infty$ at $c = \text{const}$, this factor is reduced to c^n. Thus, every scatterer of a diagram is associated after the averaging with the dimensional factor c.

There is another way to calculate the diagrams of eq. (5.125). Any piece of a diagram cut out by two vertical lines can be treated as a certain operator in the six-dimensional space. This space is either two spatial coordinates $\boldsymbol{r}_1$ and $\boldsymbol{r}_2$ for the coherence function or spatial $\boldsymbol{r}$ and velocity $\boldsymbol{p}$ variables for the Wigner function $W(\boldsymbol{r}, \boldsymbol{p})$ as was discussed in section 5.1.4. Since multiple scattering in this case is reduced to re-scattering of plane waves only, the Wigner function is reduced to the Wigner function $W(\boldsymbol{r}, \boldsymbol{n})$ depending on five variables, i.e. one variable can be excluded, and the variable $\boldsymbol{n}$ is treated as a velocity direction. This Wigner function is similar to the specific intensity $I(\boldsymbol{r}, \boldsymbol{n})$ defined by eq. (5.12). Both the specific intensity and Wigner function mean the flux density of the corpuscles at the point $\boldsymbol{r}$ with the propagation direction $\boldsymbol{n}$, except the Wigner function can possess negative values. In such an interpretation, it is obvious that

a vertical dotted bar of the Feynman diagrams of eq. (5.125) corresponding to scattering by one scatterer is equal to

$$\langle \boldsymbol{r}, \boldsymbol{n}|T_j \otimes T_j^*|\boldsymbol{r}', \boldsymbol{n}'\rangle = \delta(\boldsymbol{r} - \boldsymbol{r}_j)|f_j(\boldsymbol{n}, \boldsymbol{n}')|^2\delta(\boldsymbol{r}' - \boldsymbol{r}_j) \tag{5.158}$$

and the horizontal segments of the Feynman diagrams describe the straight-line propagation of the quadratic values for a divergent spherical wave given by eq. (5.69)

$$\langle \boldsymbol{r}, \boldsymbol{n}|L^{-1} \otimes L^{-1*}|\boldsymbol{r}', \boldsymbol{n}'\rangle = \delta(\boldsymbol{n} - \boldsymbol{n}')/|\boldsymbol{r} - \boldsymbol{r}'|^2 \tag{5.159}$$

So, eqs (5.158) and (5.159) give us another way to write down the analytical expressions for any diagram.

Now let us consider only the sum of the ladder diagrams like diagram 4 of eq. (5.125). As a first step, we introduce the auxiliary series

$\langle \Psi \otimes \Psi^* \rangle =$ 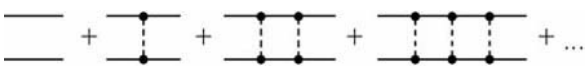 (5.160)

According to eqs (5.158) and (5.159), this series, except for the first term, can be interpreted as multiple collisions of corpuscles. In other words, these diagrams represent the series of multiple incoherent scatterings. To satisfy the energy conservation law, the coherent scattering must be included in this series, too. For this purpose, every diagram of eq. (5.160) is expanded by adding an arbitrary number of independent scatterers along all horizontal segments of these Feynman diagrams. A statistical averaging of such 'loaded' horizontal segments corresponds to the calculation of the coherent field worked out in section 5.4.2. These calculations summarize the terms with various multiplicities of scattering that can be also represented by the following diagrams

 (5.161)

Thus, the thick horizontal segment means either the coherent field given by eq. (5.139) or the similar coherent field obtained for a spherical incident wave that is originated by the jth scatterer with the fixed location $\boldsymbol{r}_j$ of its center

$$\langle \psi(\boldsymbol{r}|\boldsymbol{r}_j)\rangle = \mathrm{e}^{(ik+c\mu)|\boldsymbol{r}-\boldsymbol{r}_j|}/|\boldsymbol{r} - \boldsymbol{r}_j| \tag{5.162}$$

Finally, the series (5.161) expanded for inclusion of the coherent scattering is represented by the following operator equation

$\langle \Psi \otimes \Psi^* \rangle =$ 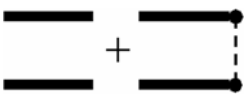 $\langle \Psi \otimes \Psi^* \rangle$ (5.163)

In this equation, the vertical dotted bar corresponds to the operator of eq. (5.159) as before. The first thick horizontal segments describe the coherent part that is equal to

$$\langle \psi \otimes \psi^* \rangle_c = \langle \psi \rangle \otimes \langle \psi^* \rangle = \mathrm{e}^{-\tau(0,x)}\delta(\boldsymbol{n} - \boldsymbol{n}_0) = I_0(\boldsymbol{r}, \boldsymbol{n}) \tag{5.164}$$

The second pair of thick segments corresponds to the coherent part obtained from the spherical wave of eq. (5.162)

$$\langle L^{-1}\rangle \otimes \langle L^{-1}\rangle^* = \delta(\boldsymbol{n}-\boldsymbol{n}')\mathrm{e}^{-\tau(\boldsymbol{r},\boldsymbol{r}')}/|\boldsymbol{r}-\boldsymbol{r}'|^2 \tag{5.165}$$

Here, eq. (5.165) differs from the previous eq. (5.159) only by the additional exponential extinction where the optical depth $\tau(\boldsymbol{r},\boldsymbol{r}')$ is defined by eq. (5.148).

In an analytical form, eq. (5.163) is written as the integral equation

$$I(\boldsymbol{r},\boldsymbol{n}) = I_0(\boldsymbol{r},\boldsymbol{n}) + c\int K(\boldsymbol{r},\boldsymbol{n}|\boldsymbol{r}',\boldsymbol{n}')I(\boldsymbol{r}',\boldsymbol{n}')\,\mathrm{d}\boldsymbol{r}'\,\mathrm{d}\boldsymbol{n}' \tag{5.166}$$

where the kernel K is readily obtained by multiplication of the operators given by eqs (5.165) and (5.158)

$$K(\boldsymbol{r},\boldsymbol{n}|\boldsymbol{r}',\boldsymbol{n}') = \delta\left(\boldsymbol{n}-\frac{\boldsymbol{r}-\boldsymbol{r}'}{|\boldsymbol{r}-\boldsymbol{r}'|}\right)\frac{\mathrm{e}^{-\tau(\boldsymbol{r},\boldsymbol{r}')}}{|\boldsymbol{r}-\boldsymbol{r}'|^2}|f(\boldsymbol{n},\boldsymbol{n}')|^2 \tag{5.167}$$

This is the fundamental radiative transfer equation in the form of the integral equation in the space of five variables. Here we have substituted the conventional specific intensity $I(\boldsymbol{r},\boldsymbol{n})$ though the general Wigner function $W(\boldsymbol{r},\boldsymbol{n})$ can be used in this equation as well. Also, the sign of statistical averaging $\langle\dots\rangle$ is conventionally omitted for the averaged specific intensity.

The kernel K describing the incoherent scattering has a transparent physical meaning on the level of the corpuscular treatment of radiation. The kernel means that a corpuscle undergoing a collision with a scatterer changes its propagation direction with the probability determined by the function $|f|^2$. Then it propagates along a straight ray from the scatterer where the exponential determines a probability of the next collision, and the factor $|\boldsymbol{r}-\boldsymbol{r}'|^{-2}$ describes the decrease of the flux density for a point source.

In practice, the radiative transfer equation is used in other forms that can be obtained by exclusion of the Dirac delta function from the kernel. For this purpose, the spherical coordinates originated in the observation point r are introduced. In these coordinates, the current point r' is determined by the direction $n = (\boldsymbol{r}-\boldsymbol{r}')/|\boldsymbol{r}-\boldsymbol{r}'|$ from the current to observation points and by the distance between the points $l = |\boldsymbol{r}-\boldsymbol{r}'|$ (see Fig. 5.8). The substitution $\mathrm{d}\boldsymbol{r}' = l^2\,\mathrm{d}l\,\mathrm{d}\boldsymbol{n}$ transforms eq. (5.166) into the integral equation along the straight ray $\boldsymbol{r}-l\boldsymbol{n}$ where $l \geq 0$

$$I(0,\boldsymbol{n}) = \int_0^\infty dl\mathrm{e}^{-\tau(0,l)}q(l,\boldsymbol{n}) + c\int_0^\infty dl\mathrm{e}^{-\tau(0,l)}\int d\boldsymbol{n}'|f(\boldsymbol{n},\boldsymbol{n}')|^2 I(l,\boldsymbol{n}') \tag{5.168}$$

The first term of the right side of eq. (5.168) is the coherent part where $q(l,\boldsymbol{n})$ means the density of radiation sources in the point $\boldsymbol{r}' = (l,\boldsymbol{n})$ emitting corpuscles in the direction $\boldsymbol{n}$. So, in eq. (5.168), two spatial variables have been excluded, and only the integrals along a ray account for a spatial coordinate.

In practice, both radiation sources and scattering media are bounded by certain surfaces, and, moreover, they are inhomogeneous. Our calculations did not

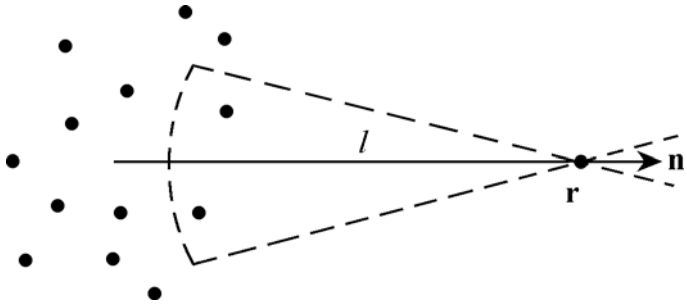

Fig. 5.8. Conservation of specific intensity along a ray.

forbid us to include these inhomogeneities in both the coherent and incoherent parts. It was only for the sake of brevity that we did not include them. For the further study, we shall imply that the scattering medium and radiation sources are inhomogeneous. In particular, both the scatterer number density and scattering amplitude will be certain spatial functions $c(\boldsymbol{r})$ and $f(\boldsymbol{n}, \boldsymbol{n}', \boldsymbol{r})$. So, the number density $c(\boldsymbol{r})$ or $c(l)$ should be inserted under the integral signs in eqs (5.166) and (5.168), respectively.

We note that the length of the ray $\boldsymbol{r} - l\boldsymbol{n}$ where $l \geq 0$ is unrestricted. Therefore, every piece of the ray crossing a source contributes to the coherent part. Similarly, the second term of the right side of eq. (5.168) is the incoherent part that is formed by the corpuscles incoming to the point $\boldsymbol{r}' = (l, \boldsymbol{n})$ with various propagation directions $\boldsymbol{n}'$ and then scattered from a vicinity of this point to the direction $\boldsymbol{n}$ along the same ray.

The standard form of the radiative transfer equation is obtained if the integrals along a ray in eq. (5.168) are replaced by the differential extinction law along the ray given by eq. (5.149)

$$\frac{\mathrm{d}I}{\mathrm{d}l} + \alpha I = \beta \int \mathrm{d}\boldsymbol{n}' p(\boldsymbol{n}, \boldsymbol{n}') I(l, \boldsymbol{n}') + q \tag{5.169}$$

Here the coefficients $\alpha = c\sigma_e$ and $\beta = c\sigma_s$ are called the extinction and scattering coefficients, respectively, and the normalized angular function

$$p(\boldsymbol{n}, \boldsymbol{n}') = |f(\boldsymbol{n}, \boldsymbol{n}')|^2 / \sigma_s \tag{5.170}$$

is conventionally called the phase function, though this name could be criticized.

For the transverse electromagnetic waves, eq. (5.169) is directly generalized into a matrix equation. Here the specific intensity is replaced by the Stokes vector, the extinction law given by the left side of eq. (5.169) is replaced by eq. (5.156) and the value $|f|^2$ is replaced by the 4×4 phase matrix $\boldsymbol{P} = \boldsymbol{S} \otimes \boldsymbol{S}^*$ that is derived from the 2×2 scattering matrix $\boldsymbol{S}$ of eq. (5.140) by means of the direct product defined by eqs (5.150). So, we get

$$\frac{\mathrm{d}\boldsymbol{I}}{\mathrm{d}l} + c\boldsymbol{N}\boldsymbol{I} = c \int \mathrm{d}\boldsymbol{n}' \boldsymbol{P}(\boldsymbol{n}, \boldsymbol{n}') \boldsymbol{I}(l, \boldsymbol{n}') + \boldsymbol{Q} \tag{5.171}$$

The radiative transfer equation was originally obtained about a century ago in the form of eq. (5.169) as an equation for a local balance of corpuscles incoming and leaving an elementary volume. At the same time, the physical nature of the elementary volume was not clearly understood and that led to a lot of confusion. We emphasize that the approach of multiple scattering of waves does not need such a terminology. We see that for the uncorrelated scatterer, it is an individual scatterer that produces scattering actions, and the conception of a mysterious elementary volume is not needed at all.

At present, the radiative transfer equation is widely used in various fields of physics. In particular, it describes the propagation of light in astrophysics and Earth's atmosphere optics, in the neutron multiplication in nuclear reactors, and so on. Even in nuclear physics, the scattering of high-energy elementary particles in heavy atomic nuclei is described by the radiative transfer equation.

By the way, let us discuss also two imaginary discrepancies that could appear under a consideration of the radiative transfer equation. First, on the one hand, eqs (5.168) and (5.169) look to be obvious if one considers a corpuscle emitted by a source or scattered in this direction that is flying along the ray. Due to these equations, this corpuscle is conserved along the ray except for the possible extinction described by the exponential. On the other hand, the flux density for a corpuscle emitted or scattered by a point source should decrease with distance as $|\boldsymbol{r}-\boldsymbol{r}'|^{-2}$ due to eqs (5.159) and (5.165). The question is how to join these conceptions. To answer this question, let us go to Fig. 5.8. We note that the specific intensity $I(\boldsymbol{r},\boldsymbol{n})$ has the physical meaning of density relative to the solid angles $\boldsymbol{n}$, i.e. it is always included in the measured quantities as the product $I(\boldsymbol{r},\boldsymbol{n})\,\mathrm{d}\boldsymbol{n}$. In other words, the narrow cone $\Delta\boldsymbol{n}$ should be considered. We see that the number of the point sources contributing to the cone $\Delta\boldsymbol{n}$ is increased as l^2 when the distance l is increased. This factor l^2 compensates the factor $|\boldsymbol{r}-\boldsymbol{r}'|^{-2}$ resulting in the desired conservation of the specific intensity along a ray given by eqs (5.168) and (5.169). So, we conclude that the conservation law along a ray is true only for spatially distributed scattering media (or radiation sources) that are described by regular spatial functions. If we have, for example, a singular source positioned at the distance l_0, its contribution to the observation point is proportional to the factor $1/l_0^2$. Indeed, such a singular source is described by not a regular spatial function but the Dirac delta function. This function in the spherical coordinates has the form

$$\delta(\boldsymbol{r}-\boldsymbol{r}_0)=\delta(l-l_0)\delta(\boldsymbol{n}-\boldsymbol{n}_0)/l^2 \tag{5.172}$$

Substitution of eq. (5.172) in eq. (5.168) results in the desired decrease of the specific intensity along the ray.

The second imaginary discrepancy is as follows. Let us consider the specific intensity at large distances $R \gg L$ from a scattering medium (or a radiation source) of the finite size of L as shown in Fig. 5.8. On the one hand, for every ray crossing this volume, the specific intensity does not decrease due to eq. (5.168) when an observation point is running far from the volume. Indeed, new sources of radiation do not appear in this action. On the other hand, all this volume can be considered from large distances as a point source where its specific

intensity should decrease as R^{-2} due to eq. (5.159). This imaginary discrepancy is overcome as follows. Though a specific intensity does not decrease along a ray crossing the volume, all the rays in an observation point are gathered in a narrow cones $\Delta \boldsymbol{n}$ of the solid angle of about L^2/R^2. If we want to replace this narrow cone by the Dirac delta function in the radial direction, this delta function should be accompanied by the integral of the specific intensity over this cone. This integral can be replaced by a product of the averaged intensity by the solid angle of the cone that gives the desired factor of R^{-2}.

5.4.6 Assessment of remaining diagrams

In section 5.4.5, only the ladder diagrams loaded by the coherent fields were calculated. Let us show that all other diagrams of eq. (5.125) can be asymptotically neglected. We recall that even in the calculation of the single-scattered coherent field in eq. (5.135), there was a negligible term. This term corresponded to a contribution from the backscattering part of the scattering media, and a quickly oscillating exponential containing in the integrand caused its smallness. Just the same quickly oscillating exponential appears in the integrands for the diagrams with repeated scattering by the same scatterer such as the last diagram of eq. (5.123). These oscillating exponentials are seen more obviously if the intuitive kind of diagram is considered and eq. (5.157) is used for their analytical representation. In these diagrams, the repeated scattering is drawn as a loop. If the first scatterer in the loop of, say, the diagram 2 of eq. (5.125) is fixed, an averaging over position of the second scatterer will result in a small nondimensional factor of the following order

$$cv_1v_2v_3 \ll 1 \tag{5.173}$$

instead of the factor τ of the ladder diagrams. Here v_i means either the wavelength λ or scatterer size a remembering that the scattering amplitude in the backward direction does not exceed these quantities. The inequality (5.173) combines the both conditions of independent scatterers and short waves defined by eqs (5.129) and (5.137), respectively. It is also seen that the loops in the diagrams for incoherent scattering, as in the diagram 3 of eq. (5.125), also contain the quickly oscillating exponential and, consequently, they contain one or more factors given by eq. (5.173).

If the exact sum of the diagrams of eq. (5.125) was known explicitly, this solution could be expanded into a power series relative to the small parameter given by eq. (5.173). Therefore, a neglect of all diagrams containing the factor given by eq. (5.173) can be treated as a separation of the zero-order term in an asymptotic expansion of the exact solution relative to this small parameter. This is a conventional approach used in various fields of physics.

We note that there are also other diagrams, such as diagram 5 of eq. (5.125), that have a loop on the level of the quadratic values of the field. They correspond to repeated scattering of the specific intensity by the same scatterers, and their integrands are not the oscillating functions. But these integrands are a quickly decreasing function at large distances. Application of eq. (5.157) to these diagrams shows that the magnitude of these integrals over space depends on only

the lower integration limit. If the lower limit is formally taken as zero, it leads to divergent integrals. This is just an artifact. Factually, we have to restrict the distance between two scatterers by their sizes. In this case, these integrals are again small values of the order of the parameter (5.173).

Finally, there is a class of diagrams, such as diagram 6 of eq. (5.125), that are called the cyclical diagrams. In these diagrams, the complex-conjugate partner shown by lower lines corresponds to the same scatterers as for the direct partner, but the complex-conjugate wave passes these scatterers strictly in the inverse order. For the backward scattering direction, these diagrams are not negligible. They describe the so-called coherent backscattering that has been studied both theoretically and experimentally for the last 20–30 years. However, it is a rather difficult to measure phenomenon, and we omit this problem.

In this section, the limiting case corresponding to Fig. 5.7(a) has been considered. In the next sections 5.4.7 and 5.4.8, we shall expand the operator equation (5.163) to other limiting cases shown in Figs 5.7(b) and 5.7c.

5.4.7 Spatial coherence function for random media with large scatterers

For any ensembles of large scatterers, there is a strong small-angle scattered field that is described by the parabolic wave equation (5.9). Within this equation, there is no scattering in the backward hemisphere of scattering directions. So, this is the operator equation (5.163) that describes the case of large scatterers except for the refracted fields appearing for optically hard scatterers. Thus, the operator equation (5.163) proves to be the radiative transfer equation that is applicable to both small and large scatterers independently of distances between scatterers. Only the conditions of short waves ($\lambda \ll d$) and uncorrelated scatterers ($a \ll d$) should be kept.

Within the framework of the parabolic equation, certain analytical solutions to the radiative transfer equation (5.163) can be obtained. These analytical expressions are obtained not for the specific intensity but for the spatial coherence function that is the Fourier counterpart of the specific intensity. Therefore, in this section, the spatial coherence function is discussed.

Let us consider a very simple scattering geometry where a plane wave is incident normally on a layer consisting of large scatterers. This layer is assumed to be unbounded and homogeneous in the transversal direction but its parameters can vary along the longitudinal axis x. For the beginning, it is expedient to consider propagation of the wave in free space behind the layer after the wave has been multiple-scattered inside the layer. The equations describing propagation of the average field $\langle u \rangle$ and of the averaged coherence function $\langle \Gamma(x, \boldsymbol{R}, \boldsymbol{\rho}) \rangle$ (defined by eq. (5.25)) behind the layer are as follows

$$\left(2ik \frac{\partial}{\partial x} + \Delta_\perp \right) \langle u(x, \boldsymbol{\rho} \rangle \;=\; 0 \tag{5.174}$$

$$\left(2ik \frac{\partial}{\partial x} + 2\nabla_{\boldsymbol{R}} \nabla_{\boldsymbol{p}} \right) \langle \Gamma(x, \boldsymbol{R}, \boldsymbol{\rho}) \rangle \;=\; 0 \tag{5.175}$$

Since the average field of eq. (5.174) for a statistically homogeneous layer does not depend on the transverse coordinates $\boldsymbol{\rho}$, the Laplacian gives zero, and it can be thrown out. So, the averaged field proves to be the same, as it would be calculated in the straight-ray approximation (5.9). Analogously, the coherence function $< \Gamma(x, \boldsymbol{R}, \boldsymbol{\rho})\rangle = \langle \Gamma(x, \boldsymbol{R})\rangle$ does not depend on the mean coordinate $\boldsymbol{\rho} = (\boldsymbol{\rho}_1 + \boldsymbol{\rho}_2)/2$ of eq. (5.26). Therefore, the gradient relative to $\boldsymbol{\rho}$ also results in zero, and eq. (5.175) can also be replaced by the equation of the straight-ray approximation. We see that either the Fresnel or Fraunhofer diffractions described by the parabolic equations are compensated because of the averaging in the transversal direction. This compensation takes place for any thin layer inside the scattering medium. Therefore, we conclude that both the averaged field and the coherence function can be calculated both inside and behind the scattering medium in the straight-ray approximation. These solutions are true independently of whether the scatterers are in each other's near or wave zones.

The averaged field for ensembles of large scatterers was calculated in section 5.4.2. The coherence function is also readily found by use of the explicit expression (5.126) for the multiple scattered field in the straight-ray approximation. We get

$$\begin{aligned}
\Gamma_{11}(x, \boldsymbol{\rho}_1, \boldsymbol{\rho}_2) &= \langle u(x, \boldsymbol{\rho}_1) u^*(x, \boldsymbol{\rho}_2)\rangle = \left\langle \mathrm{e}^{\sum [A_j(\boldsymbol{\rho}_1) - A_j(\boldsymbol{\rho}_2)]} \right\rangle = \\
&= \left\langle \prod_{j=1}^{n} \left([1 + \omega_j(\boldsymbol{\rho}_1)][1 + \omega_j^*(\boldsymbol{\rho}_2)) \right) \right\rangle \\
&= \sum_{n=0}^{\infty} p_n \left\langle 1 + \omega_j(\boldsymbol{\rho}_1) + \omega_j^*(\boldsymbol{\rho}_2) + \omega_j(\boldsymbol{\rho}) \omega_j^*(\boldsymbol{\rho}_2) \right\rangle^n \\
&= \mathrm{e}^{\langle n \rangle \langle \omega_j(\boldsymbol{\rho}_1) + \omega_j^*(\boldsymbol{\rho}_2) + \omega_j(\boldsymbol{\rho}_1) \omega_j^*(\boldsymbol{\rho}_2) \rangle} \qquad (5.176)
\end{aligned}$$

where the sign of statistical averaging $\langle \dots \rangle$ is omitted for the coherence function. In the straight-ray approximation, multiple scattering of waves is reduced to shadowing two rays $\boldsymbol{\rho}_{1,2} = \text{const}$ by the scatterers described by the functions $\omega_j(\boldsymbol{\rho})$ of eq. (5.127). Let us comment the procedure used in eq. (5.176). The number of scatterers crossing a given ray is a random value that should be accounted for in the averaging over the statistical ensemble. For this purpose, an auxiliary volume of the longitudinal length x and of arbitrary large transverse domain of the area P can be considered. The number of scatterers in this volume n obeys the Poisson law

$$p_n = \langle n \rangle^n \mathrm{e}^{-\langle n \rangle} / n! \quad \text{where } \langle n \rangle = cxP \qquad (5.177)$$

that is used in eq. (5.176), $\langle n \rangle$ is the average number of scatterers in this volume. So, the first term in the exponent of eq. (5.176) proves to be equal to

$$\langle n \rangle \langle \omega_j(\boldsymbol{\rho}_1) \rangle = \langle n \rangle \left\langle \int \omega_j(\boldsymbol{\rho}_1 - \boldsymbol{\rho}_j)\, \mathrm{d}\boldsymbol{\rho}_j \right\rangle / P = cx\mu \qquad (5.178)$$

where the constant quantity μ was defined by eqs (5.136) and (5.142). Here the diversity of scatterers relative to their sizes, shape, orientations, etc. is accounted

for by the angle brackets in addition to the integral producing the averaging over the center positions. So, the quantity μ has a simple geometrical meaning. In particular, for the shadow-forming field we get $\mu = -s$ where s is he average area for projections onto the plane $x = \text{const}$.

The last term in the exponent of eq. (5.176) differs from zero if the jth scatterer crosses simultaneously the both rays $\boldsymbol{\rho}_1$ and $\boldsymbol{\rho}_2$. So, the averaging over positions of the jth scatterer creates the function $D_j(\boldsymbol{R})$ depending on the difference variable $\boldsymbol{R} = \boldsymbol{\rho}_1 - \boldsymbol{\rho}_2$

$$D_j(\boldsymbol{R}) = \int \omega_j(\boldsymbol{\rho}_j)\omega_j^*(\boldsymbol{\rho}_j - \boldsymbol{R})\,\mathrm{d}\boldsymbol{\rho}_j \tag{5.179}$$

The main features of this function are as follows. This function differs from zero only at the distances that are less than the diameter: $|\boldsymbol{R}| < 2a$, where a is a transverse size of the scatterer. In the center $\boldsymbol{R} = 0$, it is equal to the scattering cross-section owing to eq. (5.97)

$$D_j(0) = \sigma_{js} \tag{5.180}$$

and its Fourier transform (5.25) gives a distribution of this energy flux σ_s over the 2-D scattering directions $\boldsymbol{q}$

$$\left(\frac{k}{2\pi}\right)^2 \int D_j(\boldsymbol{R})\mathrm{e}^{-ik\boldsymbol{q}\boldsymbol{R}}\,\mathrm{d}\boldsymbol{R} = \sigma_{js}p_j(\boldsymbol{q}), \qquad \int p_j(\boldsymbol{q})\,\mathrm{d}\boldsymbol{q} = 1 \tag{5.181}$$

The indexes j in all these values will be omitted after their averaging over the internal parameters of the scatterers such as sizes, etc.

Substitution of eqs (5.178) and (5.179) into eq. (5.176) yields the remarkably simple closed expression for the coherence function

$$\Gamma(x, \boldsymbol{R}) = \mathrm{e}^{-cx|\sigma_e - D(\boldsymbol{R})|} \tag{5.182}$$

where σ_e is the extinction cross-section. We recall that this solution is valid independently of whether the scatterers are positioned in each other's near or wave zones.

This solution has the following features

$$\Gamma(x, 0) = I(x) = \langle |u(x, \boldsymbol{\rho}_1)|^2 \rangle = \mathrm{e}^{-c\sigma_a x} \tag{5.183}$$

$$\begin{aligned} \Gamma(x, \boldsymbol{R}) &= \Gamma_c(x, \boldsymbol{R}) = \langle u(x, \boldsymbol{\rho}_1)\rangle\langle u^*(x, \boldsymbol{\rho}_2)\rangle \\ &= \Gamma(x, 0)\mathrm{e}^{-c\sigma_s x} = \mathrm{e}^{-c\sigma_e x}, \quad \text{for } |\boldsymbol{R}| > 2a \end{aligned} \tag{5.184}$$

that are obvious from the point of shadowing these two rays by the amplitude–phase screens The coherence function is maximal at $\boldsymbol{R} = 0$ where it corresponds to the averaged intensity of the field along any ray $\boldsymbol{\rho}_1$. Then, for $|\boldsymbol{R}| > 0$, the coherence function decreases reaching its limit at $|\boldsymbol{R}| > 2a$ where a is the transverse size of scatterers. This limit is just the coherent part of this quadratic value of the field since the rays $\boldsymbol{\rho}_1$ and $\boldsymbol{\rho}_2$ are crossed by the scatterers independently of each other. At the distances $|\boldsymbol{R}| > 2a$, the coherence function is decreased, as

compared to its magnitude at $|\boldsymbol{R}| = 0$, by the factor $\exp(-c\sigma_s s)$ where σ_s is the scattering cross-section.

In particular, for optically soft non-absorbing scatterers, the coherence function decreases from 1 to $\exp(-c\sigma_s x)$. Absorption, if exists, multiplies these values by the factor $\exp(-c\sigma_a x)$. We remind that for optically hard scatterers, we have to substitute $\sigma_a = s$, where s is the averaged area of their projections.

The coherence function obtained in eq. (5.182) obeys the differential equation

$$\left(\frac{\mathrm{d}}{\mathrm{d}x} + c\sigma_e - cD(\boldsymbol{R})\right) \Gamma(x, \boldsymbol{R}) = 0 \tag{5.185}$$

This equation means that the propagation of the coherence function can be treated as a transmittance through a lot of statistically independent infinitesimally thin screens described by the correlation function

$$C = c(\sigma_e - D(\boldsymbol{R})) \tag{5.186}$$

Thus, the mathematical procedure presented by eq. (5.176) has allowed us to get the analytical solution (5.182) quickly. Of course, this expression could be also obtained by summation of the diagrams of the operator equation (5.163).

5.4.8 Small-angle radiative transfer equation

It is instructive to consider in parallel the Fourier counterpart of the coherence function, i.e. the Wigner function $W(x, \boldsymbol{\rho}, \boldsymbol{q})$ defined by eq. (5.25). Remembering that all equations are valid for the more general value $W(x, \boldsymbol{\rho}, \boldsymbol{q})$, we shall use the conventional specific intensity $I(x, \boldsymbol{\rho}, \boldsymbol{q})$ for clarity.

We decompose the analytical expression of eq. (5.182) into the Taylor series

$$\Gamma(x, \boldsymbol{R}) = \mathrm{e}^{-c\sigma_e x}\left[1 + cxD(\boldsymbol{R}) + \frac{(cxD(\boldsymbol{R}))^2}{2!} + \dots\right] \tag{5.187}$$

where the exponential is the coherent part due to eq. (5.184) and the series is just the sum of incoherent scatterings of various multiplicities given by the diagrams of eq. (5.160) since the multiplicity m is determined by the exponents of the factors c^m. In the language of the specific intensity I, it looks as follows

$$\begin{aligned} I(x, \boldsymbol{q}) &= \left(\frac{k}{2\pi}\right)^2 \mathrm{e}^{-c\sigma_e x} \int \mathrm{e}^{cxD(\boldsymbol{R}) - ik\boldsymbol{q}\boldsymbol{R}}\, \mathrm{d}\boldsymbol{R} \\ &= \mathrm{e}^{-\alpha x}\left[1 + \beta p(\boldsymbol{q}) + \frac{\beta^2}{2!}\int p(\boldsymbol{q}')p(\boldsymbol{q} - \boldsymbol{q}')\,\mathrm{d}\boldsymbol{q}' + \dots\right] \end{aligned} \tag{5.188}$$

Here α and β are the extinction and scattering coefficients, respectively, defined in eq. (5.169), and $p(\boldsymbol{q})$ is the transversal phase function determined by eqs (5.170) and (5.181). So, the series of eq. (5.188) is the specific case for the general radiative transfer equation given by eqs (5.163) and (5.166).

Equation (5.188) emphasizes the equivalence of multiple shadowing and multiple scattering for the averaged values. This equivalence has already been noted

for a fixed scatterer configuration in section 5.3.2. Here, the mth order of the incoherent scattering is described by either the term $(cxD)^m$ for the coherence function or the convolution of the mth order from the phase function of eq. (5.181) that correspond to the natural, from the corpuscular treatment, spreading of angular distribution because of multiple scattering.

So, we can state that both eqs (5.182) and the integral in eq. (5.188) are just the closed analytical solution to the radiative transfer equation for this specific case. Moreover, we state that the both expressions (5.182) and (5.188) are valid independently of whether scatterers are positioned in each other's near or wave zones.

If the incident wave or scattering media are not homogeneous in the transversal directions, the diffraction is not compensated and the parabolic wave equation should be used instead of the straight-ray approximation. The large $ka \gg 1$ scatterers can be treated as the infinitesimal thin screens of eq. (5.186) as before, but the operator $\mathrm{d}/\mathrm{d}x$ describing propagation in the free space should be supplemented with the operator $\Delta_{\perp 1} - \Delta_{\perp 2} = 2\nabla_{\boldsymbol{\rho}}\nabla_{\boldsymbol{R}}$ like eq. (5.175). Taking into account the spatial inhomogeneities of the scattering media by the dependence of the number density on the spatial coordinates $c(x, \boldsymbol{\rho})$, we arrive at the following equation for the coherence function

$$\left(\frac{\partial}{\partial x} - \frac{1}{ik}\nabla_{\boldsymbol{\rho}}\nabla_{\boldsymbol{R}} + c(x,\boldsymbol{\rho})(\sigma_e - D(\boldsymbol{R}))\right)\Gamma(x,\boldsymbol{\rho},\boldsymbol{R}) = 0 \tag{5.189}$$

This equation also admits a simple analytical solution if the scattering medium is inhomogeneous only along the x-axis. To get this solution, let us go to the specific intensity $I(x, \boldsymbol{\rho}, \boldsymbol{q})$ by means of eq. (5.25). It yields the following equation

$$\left(\frac{\partial}{\partial x} + \boldsymbol{q}\nabla_{\boldsymbol{\rho}} + c(x)\sigma_e\right) I(x,\boldsymbol{\rho},\boldsymbol{q}) = c(x)\sigma_s \int \mathrm{d}\boldsymbol{q}' p(\boldsymbol{q}-\boldsymbol{q}') I(x,\boldsymbol{\rho},\boldsymbol{q}') \tag{5.190}$$

Equation (5.190) is the well-known small-angle radiation transfer equation. Let us indicate the differences between the exact and small-angle equations defined by eqs (5.169) and (5.190), respectively. First, the derivative along an arbitrary ray $\mathrm{d}/\mathrm{d}l$ in eq. (5.169) is replaced in eq. (5.190) by the derivative along the vector $\mathbf{1}_x + \boldsymbol{q}$ defined by eq. (5.29) that is a bit different procedure. Second, extinction for a corpuscle that has undergone, say, m collisions depends on the whole length of its trajectory in the exact equation (5.169), while in eq. (5.190) it depends only on the projection of this trajectory onto the x-axis. Third, for the corpuscles coming to a scatterer, the phase function in the right side of eq. (5.190) ignores a deviation of propagation directions from the forward direction All these differences are acceptable, of course, only at small angles $|\boldsymbol{q}| \ll 1$.

To obtain the analytical solution to eq. (5.190), the Fourier transform from the coherence function of eq. (5.189) over the variable $\boldsymbol{\rho}$ is taken

$$\begin{aligned} B(x,\boldsymbol{Q},\boldsymbol{R}) &= \left(\frac{k}{2\pi}\right)^2 \int \mathrm{e}^{-ik\boldsymbol{Q}\boldsymbol{\rho}}\Gamma(x,\boldsymbol{\rho},\boldsymbol{R})\,\mathrm{d}\boldsymbol{\rho} \\ &= \left(\frac{k}{2\pi}\right)^2 \int \mathrm{e}^{-ik\boldsymbol{Q}\boldsymbol{\rho}+ik\boldsymbol{q}\boldsymbol{R}} I(x,\boldsymbol{\rho},\boldsymbol{q})\,\mathrm{d}\boldsymbol{\rho}\,\mathrm{d}\boldsymbol{q} \end{aligned} \tag{5.191}$$

This function obeys the equation

$$\left(\frac{\partial}{\partial x} + \boldsymbol{Q}\nabla_{\boldsymbol{R}} + c(x)\sigma_e\right) B(x, \boldsymbol{Q}, \boldsymbol{R}) = c(x)\sigma_s D(\boldsymbol{R}) B(x, \boldsymbol{Q}, \boldsymbol{R}) \tag{5.192}$$

that has the solution in the form of the product

$$B(x, \boldsymbol{Q}, \boldsymbol{R}) = B_0(x, \boldsymbol{Q}, \boldsymbol{R}) B_s(x, \boldsymbol{Q}, \boldsymbol{R}) \tag{5.193}$$

Here the first factor is formed by the left side of eq. (5.192), and it describes propagation of the quantity B_0 in the absorbing medium along the straight rays

$$B_0(x, \boldsymbol{Q}, \boldsymbol{R}) = B_0(0, \boldsymbol{Q}, \boldsymbol{R} - \boldsymbol{Q}x)\mathrm{e}^{-\tau(0,x)} \tag{5.194}$$

The quantity B_s describes a spreading of one ray over the transversal variables $\boldsymbol{Q}$ and $\boldsymbol{R}$ because of scattering by means of the function $D(\boldsymbol{R})$. It is equal to

$$B_s(x, \boldsymbol{Q}, \boldsymbol{R}) = \exp \int_0^x c(\xi) D[\boldsymbol{R} - \boldsymbol{Q}(x - \xi)]\, \mathrm{d}\xi \tag{5.195}$$

The validity of the solution (5.193) can be checked by its direct substitution into eq. (5.192). Turning back to the specific intensity in eq. (5.191), we obtain the desired closed solution to the small-angle radiative transfer equation as the convolution of the proper specific intensities I_0 and I_s over the both variables $\boldsymbol{\rho}$ and $\boldsymbol{q}$

$$\begin{aligned} I(x, \boldsymbol{\rho}, \boldsymbol{q}) &= I_0(x, \boldsymbol{\rho}, \boldsymbol{q}) *_{\boldsymbol{\rho q}} I_s(x, \boldsymbol{\rho}, \boldsymbol{q}) \\ &= \left(\frac{k}{2\pi}\right)^2 \int I_0(x, \boldsymbol{\rho}', \boldsymbol{q}') I_s(x, \boldsymbol{\rho} - \boldsymbol{\rho}', \boldsymbol{q} - \boldsymbol{q}')\, \mathrm{d}\boldsymbol{\rho}'\, \mathrm{d}\boldsymbol{q}' \end{aligned} \tag{5.196}$$

where the asterisk denotes the convolution.

Equation (5.196) has a transparent physical meaning. Here I_0 is the coherent part of the specific intensity, i.e. it describes the corpuscles coming to an observation point $\boldsymbol{\rho}'$ with the propagation direction $\mathbf{1}_x + \boldsymbol{q}'$. These corpuscles were emitted from the point $(0, \boldsymbol{\rho}' - \boldsymbol{q}'x)$ on the initial plane $x = 0$. On the way to the observation point, a part of the corpuscles are extracted because of scattering that is accounted for by the exponential $\exp(-\tau)$. The scattered corpuscles are situated near this ray considered. The second factor I_s of eq. (5.196) just describes a distribution of the scattered corpuscles around this ray. Indeed, we have

$$I_s(x, \boldsymbol{\rho}, \boldsymbol{q}) = \left(\frac{k}{2\pi}\right)^2 \int \mathrm{e}^{ik\boldsymbol{Q\rho} - ik\boldsymbol{qR}} \mathrm{e}^{\int_0^x c(\xi) D[\boldsymbol{R} - \boldsymbol{Q}(x-\xi)]\, \mathrm{d}\xi}\, \mathrm{d}\boldsymbol{Q}\, \mathrm{d}\boldsymbol{R} \tag{5.197}$$

An expansion of the last exponential into the Taylor series results in the incoherent multiple scattering series such as eq. (5.188). In the case of eq. (5.197), the corpuscles scattered at the distance ξ from the initial plane $x = 0$ are distributed over the scattering directions by the same phase function as in eq. (5.188). But

we have to account for their spatial distribution over an observation plane. This distribution depends on the distance $x - \xi$ that is just reflected by the shifted argument for the D-function.

So, we conclude that eq. (5.197) gives a closed expression for the solution to the small-angle radiative transfer equation (5.190). This expression describes the Green function of this equation, i.e. the angular-spatial distribution arising around any ray of the coherent part I_0. In its turn, the coherent part I_0 is originated by radiation sources.

5.5 Multiple scattering by correlated scatterers

5.5.1 Correlated scatterers

For ensembles of a great number of scatterers, the case of uncorrelated spatial positions of scatterers considered above is an idealized model. Usually, the scatterers interact with each other forming certain regularities in their positions. The limiting case is a crystal structure. Here we consider only the cases where correlations among scatterer positions are rather weak. So, their positions are chaotic in space but the correlations create certain spatial statistical inhomogeneities. In classical statistical physics, it corresponds to dense gases and liquids.

Such a statistical ensemble occupying a volume Q and consisting of N particles is fully characterized by the probability density $P(\boldsymbol{r}^N)$ for its configurations $\boldsymbol{r}^N = (\boldsymbol{r}_1, \boldsymbol{r}_2, \ldots, \boldsymbol{r}_N)$, where $\boldsymbol{r}_j$ are the particle centers. The conventional normalization is as follows: $\int P(\boldsymbol{r}^N)\,\mathrm{d}\boldsymbol{r}^N = 1$. The probability densities to find one particle in the point $\boldsymbol{r}$, two particles in the points $\boldsymbol{r}$ and $\boldsymbol{r}'$, and so on, are determined by the s-particle probability densities $p_s(\boldsymbol{r}^s)$. In particular, we have

$$p_1(\boldsymbol{r}) = \frac{Q}{N}\int \sum_{j=1}^{N} \delta(\boldsymbol{r} - \boldsymbol{r}_j) P(\boldsymbol{r}^N)\,\mathrm{d}\boldsymbol{r}^N \tag{5.198}$$

$$p_2(\boldsymbol{r}, \boldsymbol{r}') = \frac{Q^2}{N(N-1)}\int \sum_{l\neq j}\sum_{j} \delta(\boldsymbol{r} - \boldsymbol{r}_j)\delta(\boldsymbol{r}' - \boldsymbol{r}_l) P(\boldsymbol{r}^N)\,\mathrm{d}\boldsymbol{r}^N \tag{5.199}$$

These s-particle probability densities are normalized as $\int p(\boldsymbol{r}^s)\,\mathrm{d}\boldsymbol{r}^s = Q^s$. In this study, we consider only cases where interaction among the particles reveals at a finite distance b that is much less than sizes of the volume $Q (b^3 \ll Q)$. This value b is called the correlation length. In this case, the s-particle probability densities $p_s(\boldsymbol{r}^s)$ approach constants when the distance between the observation points exceeds the distance b. Therefore, it is more convenient to use such functions that are zero beyond the domains of the size b. Such functions are called the correlation functions, and the following chain of equations defines them

$$\begin{aligned} p_1(1) &= g_1(1) \\ p_2(1,2) &= g_1(1)g_1(2) + g_2(1,2) \\ p_3(1,2,3) &= g_1(1)g_1(2)g_1(3) + g_1(1)g_2(2,3) + g_1(2)g_2(1,3) \\ &\quad + g_1(3)g_2(1,2) + g_3(1,2,3) \end{aligned} \tag{5.200}$$

and so on. Here the spatial coordinates are replaced by their indexes for brevity. This chain of equations is visualized by the diagrams

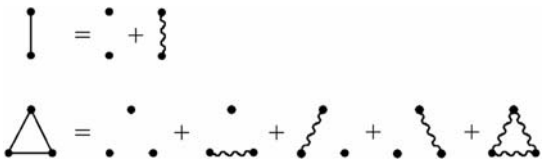

(5.201)

and so on.

Here the wavy lines denote the correlation functions of various orders. These diagrams are easily drawn by separation of all groups with a different number of particles. Therefore, a correlation function of the s-order turns into zero if only one of these particles becomes spatially independent, i.e. it is farther on b from other particles of this group. We note that these correlation functions are normalized to zero

$$\int g_s(\boldsymbol{r}^s)\,\mathrm{d}\boldsymbol{r}^s = 0 \tag{5.202}$$

These ensembles with a fixed number of particles called the canonical ensembles are not applicable to practice. A subsystem of the particles occupying a small part q of the volume Q is usually considered. In this case, a number of the particles n in the volume q is a random quantity. Usually the limit $N \to \infty$ and $Q \to \infty$ at $c = N/Q = \text{const}$ called the thermodynamics limit is introduced. In the thermodynamics limit, the normalization of eq. (5.202) is not already valid. Moreover, the integral of the pair correlation function g_2 becomes a basic thermodynamic quantity characterizing the variance of the particle number n by means of the equation

$$\frac{\langle n^2\rangle - \langle n\rangle^2}{\langle n\rangle} = 1 + c\int g_2(\boldsymbol{R})\,\mathrm{d}\boldsymbol{R} \equiv F \tag{5.203}$$

where $\boldsymbol{R} = \boldsymbol{r} - \boldsymbol{r}'$ is the difference coordinates. For isotropic systems, the function g_2 depends on only the module $|\boldsymbol{R}|$, and g_2 is called the radial function. In statistical physics, eq. (5.203) is called the Ornstein–Zernike theorem. We see that the factor F in eq. (5.203) is equal to 1 for the statistically independent particles, and its deviation from unity characterizes particle correlations.

Theoretical calculation of the radial function is a difficult problem of statistical physics that is not strictly solved yet even for the simplest case of rigid spheres with equal radii. However, Wertheim and Thiele in 1963 obtained an approximate expression of the radial function for the rigid spheres. In particular, their solution determines the factor F as follows

$$F(\eta) = \frac{(1-\eta)^4}{(1+2\eta)^2} \tag{5.204}$$

where $\eta = 4\pi c r^3/3$ is the volume fraction for the spheres of the radius r.

5.5.2 General equations

Let us average the general series of multiple scattering of waves (5.122) for both the field and its quadratic values in the case of correlated scatterers. Here every term of the series containing s scatterers should be averaged by means of the s-particle probability density discussed in section 5.5.1. Since correlations among the scatterer positions are assumed to be restricted by the finite correlation length b, the s-particle correlation functions given by eqs (5.200) and (5.201) become more convenient to use instead of the probability densities. As a result, every term is decomposed into a sum of the terms that are averaged by means of the correlation functions. For visualization of these terms, the Feynman diagrams are used in this section.

In particular, the coherent field is represented by the following series

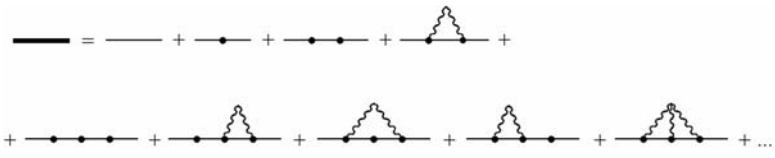

(5.205)

In this series, every part of a diagram connected by wavy lines, i.e. by the correlation functions, can be interpreted as an additional scatterer with the size of b. All these scatterers can be combined into one effective scatterer by means of the series

(5.206)

In quantum electrodynamics, such a value is called the mass operator. By means of the mass operator, the initial series (5.205) is represented as iterations of the following integral equation

(5.207)

that is written down analytically as follows

$$\langle\Psi\rangle = \Psi_0 + L^{-1}M\langle\Psi\rangle \tag{5.208}$$

Substituting $\Psi_0 = L^{-1}q$ and rearranging the terms of eq. (5.208), we get the equivalent equation

$$(L - M)\langle\Psi\rangle = q \tag{5.209}$$

Equations (5.207)–(5.209) are various forms of the so-called Dyson equation.

All diagrams of the series (5.206) are called the irreducible diagrams since it is impossible to divide them into a product of the similar diagrams connected only by the straight-line segment, i.e. by the propagator L^{-1}. So, the mass operator determines an effective scatterer and the Dyson equation describes multiple scattering among these effective scatterers by means of the propagator L^{-1}.

As seen from eq. (5.209), if the mass operator can be reduced to the local operator like the operator of eq. (5.48), the problem of calculation of the mass operator is equivalent to the problem of finding the bulk refractive index for the scattering medium as it was discussed in section 5.4.3 for the case of uncorrelated scatterers.

Just the same procedure used to get the Dyson equation is applicable for the quadratic values of the field drawn by the diagrams of eq. (5.125). Like eq. (5.163), the sum of these averaged diagrams is represented by the operator equation

$$\langle \Psi \otimes \Psi^* \rangle = \quad + \quad \langle \Psi \otimes \Psi^* \rangle \tag{5.210}$$

where the kernel called the intensity operator is the sum of all irreducible diagrams

$$= + + + + \ldots \tag{5.211}$$

Equation (5.210) is the Bethe–Salpeter equation. So, the intensity operator describes an effective scatterer for incoherent scattering while the mass operator determines the scatterer relative to coherent scattering. The conventional method for solutions to either the Dyson or Bethe–Salpeter equations is to account for a few first terms in the series (5.206) and (5.211) for the kernel of these integral equations. If these terms are checked to provide the energy conservation law for one scattering event, a solution to the Bethe–Salpeter equation will satisfy the energy conservation law, too.

5.5.3 Transparency for ensembles of correlated scatterers

The effective scatterers appeared for the ensembles of correlated scatterers are determined relative to coherent and incoherent scattering, respectively, by the series (5.206) and (5.211) where the first terms correspond to uncorrelated scatterers. We recall that only ensembles with weak correlations among scatterers are considered in this study. It means that the correlations produce only the spatial inhomogeneities of finite sizes of b. In this case, the next terms of both the series (5.206) and (5.211) can be treated as the desired corrections accounting for the scatterer correlations.

One can put a question: What is influence of the spatial correlation of scatterers on both the coherent and incoherent parts of radiation as compared to the same but uncorrelated scatterers? If we restrict ourselves to the coherent radiation only, the question is: Do the correlations increase or decrease the transparency of the scattering media as compared to the same but uncorrelated scatterers?

To answer the questions, we have to introduce certain new parameters since the new parameter b characterizing the correlation length appeared. For uncorrelated scatterers, we distinguish the cases of short and long waves by the

inequalities $\lambda \ll d$ and $\lambda \gg d$, respectively, where λ is the wavelength and d is the average distance between the scatterers. For the correlated scatterers, we refer to the case of short waves if the additional condition $\lambda \ll b$ is satisfied. The case $\lambda \gg b$ is referred to long waves and this case is beyond the present study.

It is worth noting that, for the last 20–30 years, a considerable number of researchers have considered both theoretically and experimentally the problem of transparency for a particular case of ensembles of rigid, i.e. non-penetrable, spheres. Usually this transparency has been investigated as a function of the volume fraction η defined after Eq. (5.204). At present, the majority of the researchers have agreed that, for the case of long waves, these short-distance correlations appearing because of the repulsive forces among the rigid spheres result in an increase of the transparency. As for the case of short waves, a number of conflicting opinions are known.

For the case of short waves, basing on the conclusion that coherent scattering is equivalent to shadowing by scatterers, we propose the following rules:

Rule 1: Any change in scatterer configuration resulting in additional shadowing of the incident field will decrease the transparency of the scattering medium, and vice versa.

In particular, for the correlated scatterers, we get

Rule 2: The correlations that increase shadowing of scatterers by each other should increase the transparency of the ensembles, and vice versa.

For instance, let us consider two scatterers interacting by isotropic forces. Their projection onto a plane perpendicular to the incident wave gives two shadows on the plane. For the spatially independent scatterers, these projections are independent, and they freely penetrate each other. If the forces are repulsive, the probability for these projections overlapping decreases, resulting, correspondingly, in a decrease of the transparency, and vice versa.

A plausibility of rule 2 follows, for example, from the series (5.206) for the mass operator. We note that, for the short waves, a part of the terms in the mass operator like the third diagram of eq. (5.206) describing the repeated scattering by the same scatterer can be neglected, as was done for uncorrelated scatterers. So, the mass operator is represented for the short waves by the more simple diagrams

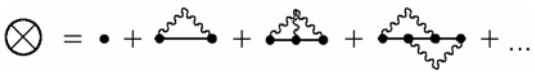

(5.212)

The first term of the series corresponds to the bulk refractive index for uncorrelated scatterers given by eq. (5.144). So, the next diagrams give the desired corrections accounting for correlation of scatterers as the series relative to powers of the number density c. In particular, the extinction coefficient α can be represented as the series

$$\alpha = \alpha_0(1 + Ac + Bc^2 + \dots) \tag{5.213}$$

where $\alpha_0 = c\sigma_e$ corresponds to uncorrelated scatterers, the coefficient A is determined by the two-particle correlation function g_2, B by the function g_3, and so on. Our knowledge of the higher-order correlation functions is poor, since only the radial function $g_2(\boldsymbol{R})$ is of importance for thermodynamics, and practically all papers in statistical physics are devoted to this function. Therefore, a calculation of the higher-order diagrams of eq. (5.212) is a difficult problem. But for weak correlations, a restriction to the second term of the series (5.213) is acceptable where the coefficient A can be calculated analytically.

For the calculation of the coefficient A, we consider two cases. The first case occurs when certain long-distance forces among the scatterers exist. It means that the correlation length b is much larger than the scatterer sizes a. Also we assume $b \gg ka^2$ that allows us to use the wave-zone scattered field like eq. (5.133). In this case, the second term of eq. (5.212) is calculated analogously to the double-scattered field considered in section 5.4.2. Taking a position for the second scatterer to be fixed and averaging over positions of the first one, we get, like eqs (5.135) and (5.138),

$$A = 2\mathrm{Re}\,\mu \int_{-\infty}^{0} g_2(R)\,\mathrm{d}R = -\sigma_e \int_{0}^{\infty} g_2(R)\,\mathrm{d}R \tag{5.214}$$

The radial function g_2 at a given distance R is either negative or positive if repulsive or attractive forces, respectively, are dominant in this point. So, due to eq. (5.214), the repulsive forces increase the extinction coefficient and the attractive forces decrease it in full accordance with rule 2.

The second case corresponds to the second limiting case of multiple scattering shown in Fig. 5.7(c) where large $ka \gg 1$ scatterers are situated in the near zone of each other. If the large scatterers are rigid, i.e. non-penetrable, the conditions of short waves $\lambda \ll d$ and $\lambda \ll b$ are satisfied automatically.

We consider the correction coefficient A from eq. (5.213) for the large ($ka \gg 1$) rigid spheres of the radius a. The spheres are assumed to be optically hard, so only the shadow-forming fields are taken into consideration. For the weak correlations, the radial function can be taken in the simplest approximation corresponding to pair collisions

$$g_2(R) = \begin{cases} -1 & \text{for } R \le 2a \\ 0 & \text{for } R > 2a \end{cases} \tag{5.215}$$

The second diagram in eq. (5.212) is calculated in the straight-ray approximation as it was applied in eq. (5.142). As a result, we get

$$A = -\int_{-\infty}^{0} \mathrm{d}x \int \omega(\boldsymbol{\rho}_1)\omega(\boldsymbol{\rho}_2) g_2(x, \boldsymbol{\rho}_2 - \boldsymbol{\rho}_1)\,\mathrm{d}\boldsymbol{\rho}_1\,\mathrm{d}\boldsymbol{\rho}_2/s = -\int S(\boldsymbol{\rho}) w(\boldsymbol{\rho})\,\mathrm{d}\boldsymbol{\rho}/s \tag{5.216}$$

where $s = \pi a^2$ is the area of a circle, S is the area of intersection of two circles shifted at the vector $\boldsymbol{\rho}$

$$S(\rho) = \begin{cases} 2a^2 \left[\arccos \dfrac{\rho}{2a} - \dfrac{\rho}{2a} \sqrt{1 - \left(\dfrac{\rho}{2a} \right)^2} \right] & \text{for } \rho \le 2a \\ 0 & \text{for } \rho > 2a \end{cases} \tag{5.217}$$

and w is the integral of the radial function over the longitudinal coordinate

$$w(\rho) = \int_{-\infty}^{0} g_2(x, \boldsymbol{\rho})\, \mathrm{d}x = \begin{cases} -2a\sqrt{1 - (\rho/2a)^2} & \text{for } \rho \le 2a \\ 0 & \text{for } \rho > 2a \end{cases} \tag{5.218}$$

Substitution of eqs (5.217) and (5.218) in eq. (5.216) gives the desired correction

$$\begin{aligned} A &= -2 \int_0^\infty S(\rho) w(\rho) \rho \, \mathrm{d}\rho / a^2 = 32a^3 \int_0^1 \left(\arccos \xi - \xi \sqrt{1 - \xi^2} \right) \sqrt{1 - \xi^2} \xi \, \mathrm{d}\xi \\ &= 32a^3 \left(\frac{\pi}{6} - \frac{16}{45} \right) \approx 5.38 a^3 \end{aligned} \tag{5.219}$$

Thus, this correction decreases transparency in accordance to rule 2.

We have considered the transparency corrections that are factually caused by double-scattered waves for two correlated scatterers in the mass operator. Let us turn to the kernel of the general Bethe–Salpeter equation (5.211). There is the second term in the series (5.211) that is caused by not double- but single-scattered fields created by a pair of the correlated scatterers. Because of the single scattering, there is no shadowing in this term. Therefore, it might seem that this term violates the proposed rule 2. Let us show that it is not true. A magnitude of this term in arbitrary scattering direction is proportional to the Fourier transform of the radial function. We recall that scattering in only the forward direction forms transparency. In the forward direction, the Fourier transform becomes the integral of the radial function. For the ensembles with a fixed number of scatterers, this integral is equal to zero owing to the normalization of eq. (5.202). For the ensembles with variable number of scatterers, this integral is also small as compared to other scattering directions since not interaction but only the variable number of scatterers determines this nonzero value. Thus, this diagram does not impact on the transparency.

Since this diagram is essential in other scattering directions but its integral over scattering directions is negligible, we conclude that this term is alternating-sign. Thus we see that the certain effective scatterers listed in the series (5.211) have the zero scattering cross-section, and their role is only to redistribute the scattered energy over scattering directions.

5.5.4 Transparency of monolayers

Let us imagine an ensemble of rigid, i.e. non-penetrable, scatterers that are initially uncorrelated. For example, these scatterers create a 3-D low-density scattering medium. Then the scatterers are pressed in one direction forming a closely packed layer. Such a situation is easily modeled experimentally if, for example, a suspension of polystyrene particles creates a bottom sediment in a

vessel. One can put a question: Is transparency of the layer smaller or larger than that of the initial uncorrelated ensemble?

If the scatterers are large ($ka \gg 1$), we have the case of short waves, and the answer follows from our rules 1 and 2. Namely, the layer should be less transparent as compared to the initial ensemble.

If the number of scatterers is rather small, the layer is turned into a monolayer where the scatterer projections on a plane substrate do not overlap each other. The problem of wave scattering by a monolayer of large ($ka \gg 1$) scatterers can be solved exactly. So, this monolayer proves to be a useful theoretical object to verify the rules formulated in the previous section. Besides, certain physical objects in nature and technologies, for example, the cornea in the eye, correspond to the monolayers. This is a reason to consider the problem of wave scattering by monolayers in this section.

The field transmitted through a monolayer of large rigid scatterers is described by the single-scattering term of the general series (5.128) since multiple scattering can appear only because of overlapping projections. So, we have strictly

$$u(\boldsymbol{\rho}) = 1 + \sum \omega_j(\boldsymbol{\rho}) \tag{5.220}$$

The monolayer is assumed to be unbounded in the transversal direction and statistically homogeneous. For the unbounded layer, the statistical averaging over an ensemble can be replaced by the averaging over the plane for the fixed scatterer positions according to the ergodicity. Though both methods of averaging are almost equivalent, we prefer to use the averaging over the plane that is simpler for interpretation.

We recall that though the field of eq. (5.220) is written down for the near zone of scatterers the averaged field and the averaged quadratic values calculated by means of eq. (5.220) are quite universal quantities that are conserved at any distance from the scattering medium, as was proven in section 5.4.7 (see eqs (5.174) and (5.175)). Besides, eq. (5.220) is applicable to both optically soft and optically hard scatterers. If the scatterers are optically hard, only the shadow-forming component defined in section 5.2.6.2

$$\omega_j(\boldsymbol{\rho}) = -\eta_j(\boldsymbol{\rho}) \tag{5.221}$$

should be used in eq. (5.220). As was shown, it is a strict replacement. Indeed, a creation of the refracted scattered field should be considered as an effective absorption within the framework of the parabolic equation. So, eq. (5.221) allows us to calculate correctly all averaged values of interest since interference between the refracted and incident fields is negligible.

Now it is expedient to define two quantities characterizing the scatterer ensemble. The first is the fraction of the plane covered by the scatterers called the shadow fraction

$$\nu = \frac{\text{Area of the shadowed part}}{\text{Total area}} \tag{5.222}$$

The second quantity is the scattered field of eq. (5.220) that is averaged only over the shadowed part of the plane. This quantity will be denoted by the tilde, $\tilde{\omega}$.

The quantity $\tilde{\omega}$ is complex-valued, so it determines two real-valued parameters, say $\mathrm{Re}\,\tilde{\omega}$ and $\mathrm{Im}\,\tilde{\omega}$.

An averaging of the field of eq. (5.220) over the plane with fixed positions of scatterers readily yields

$$\langle u\rangle = 1 + \nu\tilde{\omega} \tag{5.223}$$

We emphasize that these three parameters ν, $\mathrm{Re}\,\tilde{\omega}$ and $\mathrm{Im}\,\tilde{\omega}$ completely describe the coherent field and, consequently, the transparency of the monolayer. It is interesting to emphasize that neither the shapes of the scatterer projections nor any spatial correlations of the projection within the plane x = 0 impact the monolayer transparency.

In the language of the individual scatterers, these three parameters can also be chosen as 2-D number density denoted as c_2 and two parameters characterizing a scatterer, say, the complex-valued scattering amplitude in the forward direction f_0. Indeed, the averaging of eq. (5.220) gives

$$\langle u\rangle = 1 + N\langle\omega_j\rangle = 1 + c_2\int\langle\omega_j(\boldsymbol{\rho})\rangle\,\mathrm{d}\boldsymbol{\rho} = 1 + c_2 i\lambda f_0 \tag{5.224}$$

where the scattering amplitude in the forward direction f_0 appears due to eq. (5.92). The quantity f_0 also includes the averaging over all kinds of scatterers presented in the monolayer.

Thus, the density of a monolayer is determined by either the shadow fraction ν or the 2-D number density c_2 that are connected by the simple equation: $\nu = c_2 s$, where s is the area of one scatterer projection averaged over all scatterers in the ensemble. In addition to the density, two parameters characterize the internal properties of scatterers. These parameters are either $\tilde{\omega}$ introduced in eq. (5.223) or the scattering amplitude in the forward direction f_0 that are connected by the equation: $\tilde{\omega} = i\lambda f_0/s$.

So, the transparency of the monolayer is determined by two equivalent equations

$$t = |1 + \nu\tilde{\omega}|^2 = 1 + \nu 2\mathrm{Re}\,\tilde{\omega} + \nu^2|\tilde{\omega}|^2 \tag{5.225}$$

$$t = |1 + c_2 i\lambda f_0|^2 = 1 - c_2\sigma_e + c_2^2\lambda^2|f_0|^2 \tag{5.226}$$

In eq. (5.226), the optical theorem given by eq. (5.76) is used, where σ_e is the extinction cross-section for one scatterer. In particular, these equation are simplified for optically hard scatterers

$$\langle u\rangle = 1 - \nu = 1 - c_2 s \tag{5.227}$$

$$t = (1-\nu)^2 \tag{5.228}$$

Though eqs (5.223) and (5.224) are equivalent, the presentation of eq. (5.223) is much more preferable for the geometric interpretation that is presented below.

The dependence of the monolayer transparency on the three characterizing parameters is readily visualized in Fig. 5.9(a) that is similar to Fig. 5.6. Here two parameters characterizing shapes, internal structure, etc. of scatterers are

denoted by the complex-valued number $\tilde{\omega}$. Instead of this number $\tilde{\omega}$, another complex number $\tilde{u}$ can be used

$$\tilde{u} = 1 + \tilde{\omega} \tag{5.229}$$

All possible complex numbers $\tilde{u}$ are represented by the points within a circle of unit radius as was used in Fig. 5.6, where the real and imaginary parts correspond to the horizontal and vertical axes, respectively. The numbers $\tilde{u}$ and $\tilde{\omega}$ are also represented by the vectors $\tilde{u}$ and $\tilde{\omega}$ in Fig. 5.9(a) originated from the circle center and the point $(1, 0)$, respectively. Then, whereas the density of a monolayer is increasing, the averaged field is represented due to eq. (5.223) by a point sliding along the vector $\tilde{\omega}$. At any shadow fraction ν, this sliding point separates that part of the vector length that is just equal to the fraction ν. When fully covering the plane with this kind of scatterers, the averaged field would arrive at the point $\tilde{\omega}$. Of course, the limiting situation $\nu = 1$ is reachable only, for example, for aligned rectangular scatterers. For other shapes, this upper limit is variable. For example, ensembles of circles with the same radii have the maximum fraction of $\pi/2\sqrt{3} \approx 0.9$.

Now the dependence of the transparency on the shadow fraction ν is obtained geometrically in Fig. 5.9a as the modulus squared for the vector $\langle u \rangle$. The vector $\tilde{\omega}$ determines the point $\tilde{\omega}_0$ marked by the dotted line in Fig. 5.9(a) where the vectors $\langle u \rangle$ and $\tilde{\omega}$ are perpendicular. For this point, the transparency possesses its minimum value along the vector $\tilde{\omega}$ that is equal to

$$t_0 = (\mathrm{Im}\,\tilde{\omega}/|\tilde{\omega}|)^2 \tag{5.230}$$

In Fig. 5.9(a) we see that in the beginning, at small shadow fraction $\nu \ll 1$, the transparency $t(\nu)$ decreases for any kind of scatterers. Then, if the point $\tilde{\omega}$ is

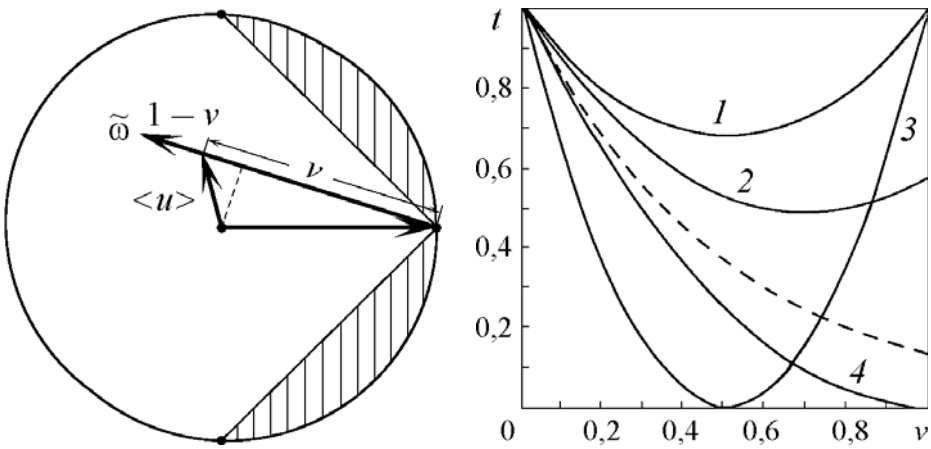

Fig. 5.9. Transparency of monolayers. (a) Geometric interpretation of the monolayer transparency; the hatched domains are the anomalous scatterers. (b) transparencies for various scatterer parameters $\tilde{\omega} =:$ (1) $\exp(i3\pi/8) - 1$; (2) $0.76\exp(i3\pi/8) - 1$; (3) $\exp(i\pi) - 1 = -2$; (4) -1; the dotted curve – uncorrelated scatterers with $\tilde{\omega} = -1$.

located to the left from its point $\tilde{\omega}_0$, the transparency passes its minimum value t_0 and steadily increases on the remaining part of the interval of the variable ν. If the point $\tilde{\omega}$ is located to the right from its point $\tilde{\omega}_0$, the transparency is a steadily decreasing function that does not reach the value t_0. In particular, if the point $\tilde{\omega}$ is situated on the circle border that corresponds to non-absorbing scatterers, the minimum transparency t_0 defined by eq. (5.230) is observed at $\nu = 0.5$. Absorption shifts the point $\tilde{\omega}$ inside the circle, and the same transparency minimum t_0 takes place at $\nu > 0.5$. The position of this minimum ν_0 is readily found by putting the derivative of the expression (5.225) to zero, and we get

$$\nu_0 = -\mathrm{Re}\,\tilde{\omega}/|\tilde{\omega}|^2 \tag{5.231}$$

These regularities obtained geometrically are easily explained. Indeed, the averaged field (5.223) is equivalent to the field when a part of ν of the total plane is covered by a homogeneous plane-parallel plate with the constant transmission $\tilde{u} = \exp(i\varphi)$. Let us denote the fields transmitted through uncovered and covered parts as u_1 and u_2, respectively

$$\langle u \rangle = u_1 + u_2 \tag{5.232}$$

As an example, assume that the scatterers are transparent plane-parallel plates with the phase φ that is equal to π (or to multiple π), i.e. $\tilde{\omega} = -2$. Then these two waves u_1 and u_2 occur in the antiphase states. At $\nu = 0.5$, these waves cancel each other, resulting in zero transparency. Thus, the monolayer becomes an absolutely opaque screen relatively to the coherent scattering. Then, at $\nu > 0.5$, the second field u_2 corresponding to the wave transmitted through scatterers becomes dominant. It leads to an increase of the monolayer transparency with an increase of the shadow fraction. At $\nu = 1$, the field u_1 disappears, and the field u_2 covers the total plane resulting in the transparency of 1 (see curve 3 in Fig. 5.9(b)). The same regularities take place for another values of $\tilde{\omega}$. In all cases, an increase of transparency with ν demonstrated by curves 1 and 3 in Fig. 5.9(b) is also explained by prevalence of the field u_2 over the field u_1. Of course, this is a rather exotic situation. It takes place, for example, if the scatterers are plane-parallel plates. Besides, the phase shifts for the plane-parallel plates should be the same.

By the way we note that, as seen from either Fig. 5.9(a) or eq. (5.230), the absolutely opaque monolayers can be obtained only under the condition: $-2 \le \tilde{\omega} < -1$. This condition is satisfied by only the same plane-parallel plates with the phase shift of π but absorption inside the scatterers or reflection from them are acceptable. Then the full darkness of the monolayers is reached at the area fraction $\nu_0 = 1/|\tilde{\omega}| \ge 0.5$. Of course, the incoherent part is nonzero behind such screens.

Now we can switch on the initial question: If a system of initially uncorrelated scatterers precipitates into a monolayer, will the transparency be greater or less? To answer the question, now we can compare their transparencies. In the notation of this section, the transparency for uncorrelated scatterers determined by eq. (5.147) is represented as follows

$$t_{un} = \mathrm{e}^{-c\sigma_e x} = \mathrm{e}^{c_2 s(\tilde{\omega}+\tilde{\omega}^*)} = 1 - c_2\sigma_e + \left[c_2 s(\tilde{\omega}+\tilde{\omega}^*)\right]^2/2! + \ldots \qquad (5.233)$$

where x is the initial depth of the 3-D scattering medium and the 2-D and 3-D number densities are connected as $c_2 = cx$. Comparing eqs (5.225), (5.226), and (5.233), we see that the linear terms relative to the number density c_2 coincide completely. We recall that this term describes interference of the single scattered field with the incident wave. As for the quadratic term relative to the number density, it corresponds to interference of the single-scattered fields among each other in the case of the monolayer. For the uncorrelated scatterers, an additional term corresponding to interference of double-scattered fields with the incident wave appears. So, expressions (5.225) and (5.233) are different in the quadratic term not saying that the higher-order terms appear only in the case of uncorrelated scatterers. This difference between the quadratic terms is equal to

$$\Delta t = t_{un} - t = \mathrm{Re}\,(\tilde{\omega}^2) + O(c^3) = |\tilde{\omega}|^2 \cos 2\phi + O(c^3) \qquad (5.234)$$

where $\tilde{\omega} = |\tilde{\omega}| \exp(i\phi)$ and the phase ϕ is determined in the interval $(\pi/2, 3\pi/2)$ giving, for example, $\phi = \pi$ for $\tilde{\omega} = -1$.

According to the rules 1 and 2 formulated in section 5.5.3, the difference Δt should be positive. Let us show that these rules are valid only in a majority of situations, but certain exclusions can take place.

Indeed, the alternative-sign cosine in eq. (5.234) divides the scatterers into two parts that will be called the normal and anomalous scatterers for brevity. The normal and anomalous scatterers possess the parameters $\tilde{\omega}$ that are situated in the non-hatched and hatched parts of the circle in Fig. 5.9(a), respectively. At small density $\nu \ll 1$, a monolayer consisting of the normal scatterers is less transparent than the ensemble of the same but uncorrelated scatterers that is in accordance with rules 1 and 2 of section 5.5.3. On the other hand, a monolayer consisting of the anomalous scatterers proves to be more transparent. We see in Fig. 5.9(a) that the normal scatterers have an overwhelming majority. Moreover, the normal scatterers include the prevailing class of optically hard scatterers $\tilde{\omega} = -1$ as well.

The conclusions based on eq. (5.234) are valid only for small 2-D density for monolayers $\nu \ll 1$. As for monolayers with arbitrary shadow fraction ν, we can use the fact that the exponential of eq. (5.233) and the parabola of eq. (5.225) either do not intersect each other on the interval $\nu = [0, 1]$ or they are intersected once. For the anomalous scatterers, the parabola goes higher at $\nu \ll 1$ than the exponential; therefore these curves do not intersect each other at all. So, the monolayer of anomalous scatterers proves to be always more transparent than the medium of uncorrelated scatterers. As for the normal scatterers, the parabola goes lower than the exponential that corresponds to the rules of section 5.5.3. However, if the parabola has the minimum determined in eqs (5.230) and (5.231), it increases at $\nu > \nu_0$. Sometimes, it leads to an intersection of these curves producing an anomalous situation. However, such situations are rare. In particular for the optically hard scatterers, the transparency of the monolayer $(1-\nu)^2$ is always less than the transparency of these uncorrelated scatterers

$\exp(-2\nu)$ that are represented by curve 4 and the dotted curves in Fig. 5.9(b), respectively.

In this section, we have discussed only the coherent field or the transparency. By the way, let us indicate certain properties of the incoherent part of the intensity in the case of monolayers. Only two diagrams of eq. (5.210) determine the incoherent part where two horizontal lines are connected by both the dotted and wavy lines corresponding to the first terms in the series (5.211). The first term describes the incoherent scattering corresponding to uncorrelated scatterers, and the second term accounts for spatial correlations among them. Unlike the coherent part, the incoherent part depends explicitly on shapes of scatterers. For the large uncorrelated scatterers, the scattered intensity is concentrated within the cone of the angle $\theta \leq \lambda/a$ where λ is the wavelength and a is the transverse size of scatterers. The second term accounting for spatial correlation only redistributes the scattered energy over scattering directions without changing the amount of the energy. In the forward direction, its contribution should be negligible, as was discussed in section 5.5.3.

Thus, the case of the large scatterer monolayers solved exactly has shown that rules 1 and 2 formulated in section 5.5.3 are satisfied in a majority of situations, but certain exotic exclusions are possible.

5.5.5 Transparency of random media in the framework of the stochastic radiative transfer theory

In previous sections, we considered statistically homogeneous scattering media where spatial inhomogeneities were caused by interaction among the scatterers. In practice, scattering media are always spatially inhomogeneous because of certain external forces, surface bounds, etc. In this section, such macro-inhomogeneous scattering media will be taken into consideration.

For simplicity, we assume that scatterers do not interact with each other, i.e. they are statistically independent. But their positions will be determined by not the constant single-particle probability function but by the certain spatial function $p_1(\boldsymbol{r})$. So, the number density of scatterers becomes a spatial function $c(\boldsymbol{r})$ that has been used already in section 5.4.5 when the radiative transfer equation was discussed. Generally speaking, if the mathematical procedure used before for deriving the radiative transfer equation is applied to such media, these spatial inhomogeneities turn out to be new effective scatterers. But they are too weak under the conditions of multiple scattering of short waves given by eqs (5.130) and (5.137). So, the quadratic values of the multiple scattered waves can be described by the conventional radiative transfer equation (5.169) where the coefficients of extinction α and scattering β become certain spatial functions $\alpha(\boldsymbol{r})$ and $\beta(\boldsymbol{r})$.

Sometimes the scattering medium described by its coefficients $\alpha(\boldsymbol{r})$ and $\beta(\boldsymbol{r})$ can be treated as a random medium. For example, it arises when the functions $\alpha(\boldsymbol{r})$ and $\beta(\boldsymbol{r})$ are rather chaotic. Then a solution for a given medium realization is of no interest, and only averaged quantities are needed. In these cases, we arrive at the stochastic radiative transfer equation where the coefficients $\alpha(\boldsymbol{r})$ and $\beta(\boldsymbol{r})$ are treated as random functions. In such an approach, no additional

wave phenomena are included, so the corpuscular treatment of radiation is quite reasonable.

Putting aside the incoherent scattering, we consider only the coherent part, i.e. the transparency of the inhomogeneous scattering media. Let us imagine a layer of a scattering medium where the scatterers fill up this volume homogeneously. Then external forces redistribute the scatterers into certain spatial inhomogeneities. The traditional question is: Is the layer with spatial inhomogeneities more or less transparent as compared with that of the homogeneous scatterer distribution?

To answer the question, we have to average the exponential extinction law of eq. (5.147) over realizations of the random extinction coefficient $\alpha(\boldsymbol{r})$. For generality, consider the transparency between two arbitrary spatial points $\boldsymbol{r}$ and $\boldsymbol{r}'$, determined by the optical depth $\tau(\boldsymbol{r}, \boldsymbol{r}')$ of eq. (5.148)

$$t(\boldsymbol{r}, \boldsymbol{r}') = \mathrm{e}^{-\tau(\boldsymbol{r}, \boldsymbol{r}')} = \mathrm{e}^{-\int_{\boldsymbol{r}}^{\boldsymbol{r}'} \alpha(l)\,\mathrm{d}l} \tag{5.235}$$

For the random function $\alpha(\boldsymbol{r})$, the optical depth τ is a random number with its average magnitude

$$\langle \tau(\boldsymbol{r}, \boldsymbol{r}') \rangle = \int_{\boldsymbol{r}}^{\boldsymbol{r}'} \langle \alpha(l) \rangle \,\mathrm{d}l \tag{5.236}$$

In mathematics, there is the general Jensen inequality. The inequality states that an average of a concave function is always larger than the magnitude of this function taken for the averaged argument. Thus, we get immediately the following inequality

$$\langle \mathrm{e}^{-\tau} \rangle \geq \mathrm{e}^{-\langle \tau \rangle} \tag{5.237}$$

In spite of mathematical triviality, eq. (5.237) gives two physically important conclusions:

A: Any scattering medium with a fluctuating number density $c(\boldsymbol{r})$ is, on average, more transparent along any ray than is the same medium with the averaged number density $\langle c(\boldsymbol{r}) \rangle$.

B: A layer having a finite longitudinal size but infinite transversality exhibits lowest longitudinal transmittance in the case of uniform distribution of scatterers inside the layer. Any redistribution of the scatterers in space forming transversal inhomogeneities will result in an increase in the longitudinal transmittance of the layer.

Thus, the statement B gives the answer to the initial question: an appearance of spatial inhomogeneities in scattering media always increases transparency of the media. This increase of transparency can also be calculated analytically. For this purpose, let us use the well-known equation from probability theory that expresses an average from an exponential through cumulants or correlation functions

$$\begin{aligned}\langle t\rangle &= \langle \mathrm{e}^{-\tau}\rangle = \exp\sum_{n=1}^{\infty}(-1)^n\kappa_n/n! \\ &= \exp\sum_{n=1}^{\infty}(-\sigma_e)^n\int_{\boldsymbol{r}}^{\boldsymbol{r}'} g_n(\boldsymbol{r}_1,\boldsymbol{r}_2,\ldots,\boldsymbol{r}_n)\,\mathrm{d}l_1\,\mathrm{d}l_2\ldots\mathrm{d}l_n \qquad (5.238)\end{aligned}$$

Here the numbers κ_n are the cumulants or semi-invariants of the random optical depth τ that are connected with the moments of the optical depth $m_n = \langle\tau^n\rangle$ by the same chain of equations as the correlation functions g_n are connected with the moment functions $\langle\alpha(\boldsymbol{r}_1)\alpha(\boldsymbol{r}_2)\ldots\alpha(\boldsymbol{r}_n)\rangle$. This chain of equations is completely equivalent to eq. (5.200) connecting the correlation functions with the n-particle probability densities. In the integral of eq. (5.238), the extinction cross-sections σ_e are assumed to be constant, for simplicity, and the correlation functions g_n of the number density $c(\boldsymbol{r})$ are present.

The spatial inhomogeneities described by the correlation functions g_n have a certain characteristic size that is called the correlation length b. In the case of small inhomogeneities $b \ll L$ as compared to the observation path $L = |\boldsymbol{r} - \boldsymbol{r}'|$, the integrals in eq. (5.238) taken over the difference spatial coordinates $l_2 - l_1$, $l_3 - l_1$, etc. result in certain constants c_n owing to the vanishing of the correlation functions beyond the distance b

$$(-\sigma_e)^{n-1}\int_0^L g_n\,\mathrm{d}(l_2-l_1)\,\mathrm{d}(l_3-l_1)\ldots\mathrm{d}(l_n-l_1) = c_n(l_1) \qquad (5.239)$$

These constants can be treated as corrections to the averaged number density $\langle c(l_1)\rangle$ forming the effective number density

$$\tilde{c} = \langle c\rangle + \sum_{n=2}^{\infty} c_n/n! \qquad (5.240)$$

In this case, the transparency has the conventional form of the exponential extinction law

$$\langle t\rangle = \mathrm{e}^{-\sigma_e\int_0^L \tilde{c}(l)\,\mathrm{d}l} \qquad (5.241)$$

where the inequality (5.237) leads to the inequality $\tilde{c}(l) \le \langle c(l)\rangle$. This result is easily explained. Indeed, these small inhomogeneities can be treated as certain effective and uncorrelated scatterers. An intersection of the observation ray by these small spatially independent scatterers results in the exponential law. As known in mathematics, the exponential law just describes a probability for a corpuscle to collide with statistically independent objects.

In the opposite case of large inhomogeneities $b \gg L$, we can consider the number density c as a random constant along the observation path L that is distributed with the probability density $p(c)$. Here the averaged transparency corresponds to the Laplace transform Λ of the function $p(c)$

$$\langle t\rangle = \int_0^{\infty} p(c)\mathrm{e}^{-c\sigma_e L}\,\mathrm{d}c = \Lambda_{p(c)}(\sigma_e L) \qquad (5.242)$$

As we see, this function of the distance L is not exponential.

Bibliographic Comments

Numerous problems of wave scattering are considered in various fields of physics: acoustics, optics, radiophysics, quantum mechanics, etc. These problems can be divided into three branches: scattering by one scatterer, multiple scattering of waves, and radiative transfer. Any book on wave scattering has to touch, more or less, upon all these branches.

Thus, the problem of scattering by one scatterer is discussed at great length for both electrodynamics and quantum mechanics by Newton (1966). In optics, the book by van de Hulst (1981) is classical. Recent results in optics of light scattering media are presented by Mishchenko *et al.* (2000, 2002) and Kokhanovsky (2001, 2002). In quantum mechanics, scattering by one scatterer is discussed, for example, by Goldberger and Watson (1964) in detail and by Landau and Lifshitz (1963) in brief.

The problem of derivation of the radiative transfer equation from the equations of multiple wave scattering was initiated by Foldy (1945). Then this problem was attacked by many authors, as a rule, independently of each other. In particular, K.Watson (see Goldberger and Watson, 1964) formulated the operator equations for multiple scattering of waves and obtained a number of valuable results. In Russia, Barabanenkov studied the problem extensively. This problem is, factually, the central problem of the books by Ishimaru (1997) and Tsang *et al.* (1985) where comprehensive references can be also found. The recent results concerning the radiative transfer are presented in the abovementioned books by Mishchenko *et al.* (2002) and Kokhanovsky (2001, 2002).

The problem of multiple scattering of waves is overlapped in great degree with the problem of wave propagation in random media that is widely investigated in radiophysics, optics, acoustics, etc. Here, the small-angle radiative transfer equation is derived, in the same manner as in scattering, from the parabolic wave equation (see, for example, Rytov *et al.* (1978)). The small-angle radiative transfer equation is discussed by Zege *et al.* (1985).

Newton, R.G. (1966) *Scattering Theory of Waves and Particles.* McGraw-Hill, New York.

Van de Hulst, H.C. (1981) *Light Scattering by Small Particles.* John Wiley, New York.

Mishchenko, M.I., Hovenier, J.W., and Travis, L.D. (eds) (2000) *Light Scattering by Nonspherical Particles: Theory, Measurements, and Applications.* Academic Press, San Diego, CA.

Mishchenko, M.I., Travis, L.D., and Lacis, A.A. (2002) *Scattering, Absorption, and Emission of Light by Small Particles.* Cambridge University Press, Cambridge, UK.

Kokhanovsky, A.A. (2001) *Light Scattering Media Optics: Problems and Solutions.* Springer-Praxis, Chichester, UK.

Kokhanovsky, A.A. (2002) *Polarization Optics of Random Media.* Springer-Praxis, Chichester, UK.

Goldberger, M.L., and Watson K.M. (1964) *Collision Theory.* John Wiley, New York.

Landau, L.D., and Lifshitz, E.M. (1963) *Quantum Mechanics: Nonrelativistic Theory.* Fizmat, Moscow (in Russian).

Foldy, L.L. (1945) The multiple scattering of waves. *Phys. Rev.* **67**, 107–119.
Barabanenkov, Yu.N. (1975) Multiple scattering of waves by ensembles of particles and the theory of radiative transfer, *Usp. Fiz. Nauk*, **117**, 49–78 (in Russian).
Ishimaru, A. (1997) *Wave Propagation and Scattering in Random Media.* IEEE Press, New York.
Tsang, L., Kong, J.A., and Shin, R.T. (1985) *Theory of Microwave Remote Sensing.* John Wiley, New York.
Rytov, S.M., Kravtsov Yu.A., and Tatarskii, V.I. (1978) *Introduction to Statistical Radiophysics: Random Fields.* Fizmat, Moscow (in Russian).
Zege, E.P., Ivanov, A.P., and Katsev, I.L. (1985). *Image Transfer in Scattering Media*, Nauka I Technika, Minsk (in Russian).

The results and conclusions of this work are based on the author's papers published in Russian. In particular, the radiative transfer equation was derived from the Maxwell equations (1966, 1967) basing it on an approach like eq. (5.157) of this work. Large scatterers, as compared with wavelengths, were considered in connection with the problem of light propagation in precipitation (1982). Here the conceptions of the straight-ray approximation and shadow-forming fields were worked out. Then these conceptions were applied to other problems of multiple scattering by both uncorrelated (1984b, 1985, 1988a) and correlated scatterers (1983, 1988b). Also, the solution to the stochastic radiative transfer equation was discussed (1984a).

Borovoi, A.G. (1966a) Iteration method in multiple scattering *Izv. Vuzov, Fizika*, No. 2, 175–177.
Borovoi, A.G. (1966b) Iteration method in multiple scattering: radiative transfer equation *Izv. Vuzov, Fizika*, No. 6, 50–54.
Borovoi, A.G. (1967a) Multiple scattering of short waves by a system of correlated particles: I. Averaged field *Izv. Vuzov, Fizika*, No. 4, 97–101.
Borovoi, A.G. (1967b) Multiple scattering of short waves by a system of correlated particles: II. Kinetic equation *Izv. Vuzov, Fizika*, No. 5, 7–11.
Borovoi, A.G. (1982) Light propagation in precipitations. *Izv. Vuzov, Radiofizika*, **25**, 391–400.
Borovoi, A.G. (1983) Light propagation in media with closely packed particles. *Opt. i Spectrosc.*, **54**, 757–759.
Borovoi, A.G. (1984a) Radiative transfer in inhomogeneous media. *Dokl. Akad. Nauk*, **276**, 1374–1378.
Belov, V.F., Borovoi, A.G., Vagin, N.I., and Volkov, S.M. (1984b) Small-angular method in single and multiple scattering. *Izv. Akad. Nauk, Fiz. Atmos. i Okeana*, **20**, 323–327.
Borovoi, A.G., and Vagin, N.I. (1985) Propagation of laser radiation in precipitations. *Izv. Akad. Nauk, Fiz. Atmos. i Okeana*, **21**, 93–95.
Borovoi, A.G. (1988a) Straight-ray approximation in problems of wave scattering and propagation in random media. *Opt. Atmos.* **1**, No. 7, 17–21.
Borovoi, A.G. and Reutova, O.A. (1988b) Light propagation in media consisting of large correlated scatterers. *Opt. Atmos.* **1**, No. 8, 13–18.

6 Asymptotic radiative transfer

A.A. Kokhanovsky

6.1 Introduction

Light propagation in turbid media such as the atmosphere and the ocean is usually studied in the framework of radiative transfer theory. In particular, solutions of the integro-differential radiative transfer equation (RTE) are analysed for media having different shapes and internal microstructure. A number of numerical and analytical techniques have been developed to date (Chandrasekhar, 1950; Sobolev, 1975; van de Hulst, 1980; Nakajima and Tanaka, 1988; Thomas and Stamnes, 1999; Siewert, 2000; Liou, 2002).

A popular technique for a numerical algorithm is based on the iteration approach (Liou, 2002). Then the single scattering solution is used to obtain the result for the first iteration. The obtained solution is substituted in the integral term of RTE to find the next iteration and the procedure is repeated until the convergence is reached. This technique is of a special importance for studies of radiative transfer in turbid media with complex shapes (Nikolaeva *et al.*, 2005). However, the iteration technique requires quite large computational time for optically thick media.

Therefore, yet another approach has been developed to treat a special case of optically thick turbid media. In particular, this technique allows us to represent the turbid layer reflectance as a combination of the reflectance for the case of a semi-infinite turbid medium minus the correction term, which accounts for the finite thickness of a layer under consideration. The correspondening asymptotic radiative transfer theory (ARTT) has been developed by Germogenova (1961), Rozenberg (1962), Sobolev (1968, 1975), van de Hulst (1968a, 1968b), Minin (1988), Zege *et al.* (1991), and Yanovitskij (1997).

The task of this chapter is to make a review of recent results obtained in the framework of ARTT. We hope that this work will stimulate the application of the theory to the solution of various applied problems related to light propagation in turbid media.

6.2 Radiative transfer equation

Light scattering by a single macroscopic particle can be studied in the framework of electrodynamics of continuous media. The same applies to clusters of particles or scattering volumes, where multiple light scattering does not play an important role. This is not the case for optically thick light scattering media. Here multiple scattering dominates the registered signal. Therefore, generally speaking, techniques of multiple wave scattering should be used in this case. However, they are quite complex and do not always lead to results, which can be used as a base for the numerical algorithm.

Moreover, electromagnetic fields $\boldsymbol{E}$ cannot be measured in the optical range. This is mostly due to their high oscillations ($\approx 10^{15}$ oscillations per second). Clearly, a measuring device makes temporal and spatial averaging of the registered signal. Also optical instruments measure quantities quadratic with respect to the field. This is similar to quantum mechanics, where the amplitude ψ is the main notion of the theory, but it is $|\psi|^2$, which is measured.

Therefore, it is of importance to formulate multiple light scattering theory, not in terms of field vectors but in terms of quadratic values, which can be easily measured. The Stokes-vector parameter $\boldsymbol{I}$ with components $\mathrm{I}, \mathrm{Q}, \mathrm{U}, \mathrm{V}$ (Stokes, 1852) is usually used in this case. Of course, this leads to the omission of a number of theoretical details (e.g., related to the phase effects). However, such an approach allows an interpretation of most optical measurements. Also light beams having the same values of $\mathrm{I}, \mathrm{Q}, \mathrm{U}, \mathrm{V}$ (but in principle different values of $\boldsymbol{E}$) cannot be distinguished by optical instruments, which measure quadratic values. Therefore, the main point is to force multiple light scattering theory to deal with intensities rather than fields from the very beginning. Then we do not need to make corresponding averaging procedures at the end of calculations to bring calculated values into correspondence to the measured ones. The main aim of this section is to introduce an equation, which governs the transformation of the light intensity due to multiple scattering processes in turbid media.

For the sake of simplicity, we consider the transformation of light intensity and ignore other components of the Stokes vector. Clearly, if the process of scattering is ignored we can write in the linear approximation for the change of the light intensity I:

$$\mathrm{dI} = -K_{\mathrm{ext}} \mathrm{I}\, \mathrm{d}l\,.$$

This underlines the experimental fact that the reduction of light intensity on the length $\mathrm{d}l$ is proportional to this length and the value of I itself. The coefficient of proportionality K_{ext} is called the extinction coefficient. Actually K_{ext} coincides with the absorption coefficient K_{abs} in this simple case. It follows that

$$\mathrm{I} = \mathrm{I}_0 \exp(-K_{\mathrm{ext}} l)$$

for a homogeneous ($K_{\mathrm{ext}} = \mathrm{const}$) layer, which is the well-known extinction law. Here I_0 is the incident light intensity at $l = 0$. This formula should be modified for light scattering media to account for light scattering from all other directions $\boldsymbol{\Omega}'$ to a given direction $\boldsymbol{\Omega}$. Then we have:

$$\mathrm{dI}(\mathbf{\Omega}) = -K_{\mathrm{ext}}\mathrm{I}(\mathbf{\Omega})\mathrm{d}l + \int_{4\pi} K_{\mathrm{sca}}(\mathbf{\Omega}, \mathbf{\Omega}')\mathrm{I}(\mathbf{\Omega})\,\mathrm{d}\mathbf{\Omega}'\,\mathrm{d}l\,,$$

where the differential scattering coefficient $K_{\mathrm{sca}}(\mathbf{\Omega}, \mathbf{\Omega}')$ describes the local scattering law. This formula can be written in the following form:

$$\frac{\mathrm{dI}(\mathbf{\Omega})}{\mathrm{d}l} = -K_{\mathrm{ext}}\mathrm{I}(\mathbf{\Omega}) + \int_{4\pi} K_{\mathrm{sca}}(\mathbf{\Omega}, \mathbf{\Omega}')\mathrm{I}(\mathbf{\Omega}')\,\mathrm{d}\mathbf{\Omega}'\,,$$

which is called the radiative transfer equation. The radiative transfer theory is concerned with the solution of this equation for scattering volumes (e.g., clouds), having different shapes, types of illuminations, and microstructure.

We will consider with solutions of RTE for a plane-parallel homogeneous turbid layer illuminated by a wide light beam. The interaction of solar radiation with extended cloud fields is well-approximated by the solution of this idealized problem. The geometry of the problem is given in Fig. 6.1. The wide light beam uniformly illuminates a plane-parallel scattering layer from above. We will assume that properties of the layer do not change in the horizontal direction. Then the light field changes only along the vertical coordinate Z (see Fig. 6.1). The intensity of light field also depends on the direction $\mathbf{\Omega}$, specified by the zenith angle ϑ and the azimuth φ. The main task of the radiative transfer theory is to calculate distributions $\mathrm{I}(\vartheta, \varphi, z)$. Usually only measurements of $\mathrm{I}(\vartheta, \varphi, 0)$ at the top of the turbid layer (reflected light) and $\mathrm{I}(\vartheta, \varphi, z_0)$ at the base of the turbid layer (transmitted light) are performed (see Fig. 6.1). Therefore, we will be concerned mostly with these two angular distributions.

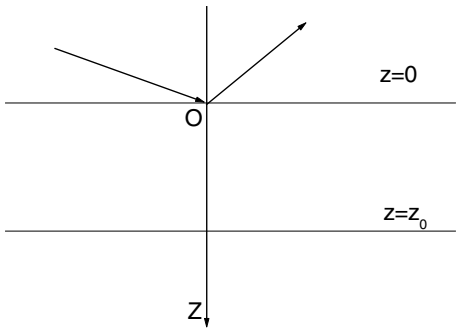

Fig. 6.1. The geometry of the problem

RTE for a plane-parallel light scattering vertically and horizontally homogeneous layer is reduced to the following simpler form:

$$\cos\vartheta\frac{\mathrm{dI}(\vartheta, \varphi)}{\mathrm{d}\tau} = -\mathrm{I}(\vartheta, \varphi) + \frac{\omega_0}{4\pi}\int_0^{2\pi}\mathrm{d}\varphi'\int_0^{\pi}\mathrm{d}\vartheta' p(\vartheta', \varphi' \to \vartheta, \varphi)\mathrm{I}(\vartheta', \varphi')\,,$$

if the polarization effects are ignored. Here we introduced the optical depth

$$\tau = \sigma_{\rm ext} z\,,$$

the phase function

$$p(\vartheta', \varphi' \to \vartheta, \varphi) = \frac{4\pi K_{\rm sca}(\vartheta', \varphi' \to \vartheta, \varphi)}{K_{\rm sca}}\,,$$

the scattering coefficient $K_{\rm sca} = K_{\rm ext} - K_{\rm abs}$, and the single scattering albedo

$$\omega_0 = \frac{K_{\rm sca}}{K_{\rm ext}}\,.$$

It is useful to make a separation of diffuse I and direct (or coherent) $I_c = A\delta(\cos\vartheta - \cos\vartheta_0)\delta(\varphi - \varphi_0)$ light in the general solution $\mathrm{I}(\vartheta, \varphi)$. The value of A is determined below and $\delta(x)$ is the delta function.

It is assumed that the layer is illuminated in the direction defined by the incidence zenith angle $\vartheta_0 = \arccos(\mu_0)$ and the azimuth φ_0. The density of the incident light flux on the area perpendicular to the beam is equal to F at the top of a scattering layer. The multiply scattered light is observed in the direction specified by the zenith observation angle $\vartheta = \arccos(\mu)$ and the azimuth φ. Namely, we write: $\mathrm{I}(\vartheta, \varphi) = I(\vartheta, \varphi) + I_c(\vartheta, \varphi)$. The substitution of this formula in RTE gives

$$\begin{aligned}\cos\vartheta \frac{{\rm d}I(\vartheta,\varphi)}{{\rm d}\tau} &= -I(\vartheta,\varphi) + \frac{\omega_0}{4\pi}\int_0^{2\pi}{\rm d}\varphi' \int_0^{\pi} {\rm d}\vartheta' p(\vartheta', \varphi' \to \vartheta, \varphi) I(\vartheta', \varphi') \\ &\quad + \frac{\omega_0}{4\pi} p(\vartheta_0, \varphi_0 \to \vartheta, \varphi) F \exp\left(-\frac{\tau}{\cos\vartheta_0}\right).\end{aligned}$$

The solution of this equation under boundary conditions stating that there is no diffuse light entering the turbid layer from above and below allows us to find $I(\vartheta, \varphi)$. $I_c(\vartheta, \varphi)$ is given simply by

$$I_c(\vartheta, \varphi) = F\delta(\cos\vartheta - \cos\vartheta_0)\delta(\varphi - \varphi_0)\exp\left(-\frac{\tau}{\cos\vartheta_0}\right).$$

The solution of RTE for the diffuse intensity I is simpler than that for the total intensity I because we avoid the necessity to deal with the divergence in the direction of incident light.

6.3 Reflection and transmission functions

Reflectance and transmittance of light by turbid layers is usually defined in terms of reflection R and transmission T functions. They relate incident light intensity $I_0(\vartheta_0, \varphi_0)$ with reflected $I_R(\mu, \varphi)$ and transmitted $I_T(\mu, \varphi)$ light intensity. Namely, it follows by definition:

$$I_R(\mu,\varphi) = \frac{1}{\pi}\int_0^{2\pi} \mathrm{d}\varphi' \int_0^1 R(\mu,\varphi,\mu',\varphi') I_0(\mu',\varphi')\mu' \,\mathrm{d}\mu' ,$$
$$I_T(\mu,\varphi) = \frac{1}{\pi}\int_0^{2\pi} \mathrm{d}\varphi' \int_0^1 T(\mu,\varphi,\mu',\varphi') I_0(\mu',\varphi')\mu' \,\mathrm{d}\mu' .$$

Reflection and transmission functions allow to find the intensity of reflected and transmitted light for arbitrary angular distributions of incident light with the intensity $I_0(\mu',\varphi')$.

If incident light is azimuthally independent, these formulas simplify:

$$I_R(\mu,\varphi) = 2\int_0^1 \overline{R}(\mu,\varphi,\mu') I_0(\mu')\mu' \,\mathrm{d}\mu' ,$$
$$I_T(\mu,\varphi) = 2\int_0^1 \overline{T}(\mu,\varphi,\mu') I_0(\mu')\mu' \,\mathrm{d}\mu' ,$$

where

$$\overline{R}(\mu,\varphi,\mu') = \frac{1}{2\pi}\int_0^{2\pi} R(\mu,\varphi,\mu',\varphi') \,\mathrm{d}\varphi' ,$$
$$\overline{T}(\mu,\varphi,\mu') = \frac{1}{2\pi}\int_0^{2\pi} T(\mu,\varphi,\mu',\varphi') \,\mathrm{d}\varphi' .$$

The general equations given above can also be simplified for unidirectional illumination of a turbid layer by a wide beam (e.g., solar light). Then we can assume that

$$I_0(\mu',\varphi') = F\delta(\mu'-\mu_0)\delta(\varphi'-\varphi_0) ,$$

where F is the incident light flux density at the top of a layer as introduced above and $\delta(x)$ is the delta function, having the following property:

$$f(x_0) = \int_0^\infty \delta(x-x_0) f(x) \,\mathrm{d}x$$

for arbitrary $f(x)$. Using this relation and equations for reflection and transmission functions given above, we arrive at the following results:

$$I_R(\mu,\varphi) = \frac{F\mu_0 R(\mu,\varphi,\mu_0,\varphi_0)}{\pi} ,$$
$$I_T(\mu,\varphi) = \frac{F\mu_0 T(\mu,\varphi,\mu_0,\varphi_0)}{\pi} ,$$

and, therefore,

$$R(\mu,\varphi,\mu_0,\varphi_0) = \frac{\pi I_R(\mu,\varphi)}{F\mu_0} ,$$
$$T(\mu,\varphi,\mu_0,\varphi_0) = \frac{\pi I_T(\mu,\varphi)}{F\mu_0} .$$

These equations allow us to make the physical interpretation of reflection and transmission functions. Indeed, we have for an absolutely white Lambertian surface by definition:

$$\begin{aligned} P_R^L(\mu,\varphi) &= \int_{2\pi} I_R^L(\mu,\mu',\varphi,\varphi')\mu'\,\mathrm{d}\Omega' = \int_0^{2\pi}\mathrm{d}\varphi'\int_0^1 I_R^L(\mu,\mu',\varphi,\varphi')\mu'\,\mathrm{d}\mu' \\ &= \int_0^{2\pi}\mathrm{d}\varphi'\int_0^1 C\mu_0\mu'\,\mathrm{d}\mu' = \pi C\mu_0\,, \end{aligned}$$

where $P_R^L(\vartheta,\varphi)$ is the total power scattered by a unit area of a Lambertian surface into the upper hemisphere and we have used the fact that intensity of light reflected from a Lambertian surface is proportional to the cosine of the incidence angle $\mu_0 (I_R^L = C\mu_0)$. The constant C can be found from the condition that the scattered $(P_R^L(\vartheta,\varphi))$ and incident (P_0) powers are equal in the case of the absolute white Lambertian surface by definition. We have for the incident power:

$$\begin{aligned} P_0 &= \int_{2\pi} I_0(\mu',\mu_0,\varphi',\varphi_0)\mu'\,\mathrm{d}\Omega' \\ &= F\int_0^{2\pi}\mathrm{d}\varphi'\int_0^1 \delta(\mu'-\mu_0)\delta(\varphi'-\varphi_0)\mu'\,\mathrm{d}\mu' = F\mu_0 \end{aligned}$$

and, therefore: $C = F/\pi$. It means that intensity of light reflected from an absolutely Lambertian surface is given by:

$$I_R^L(\vartheta_0,\vartheta,\varphi) = \frac{F}{\pi}\mu_0\,.$$

We conclude that $R(\mu,\vartheta,\mu_0,\vartheta_0)$ is equal to the ratio of light reflected from a given surface I_R to the value of I_R^L:

$$R = I_R/I_R^L\,.$$

It means that $R \equiv 1$ for a Lambertian ideally white surface.

Accordingly, it follows that

$$T = I_T/I_R^L\,.$$

The results of calculations will be mostly presented in terms of functions R and T in this work. These functions do not depend on the intensity of incident light, and characterize inherent properties of a turbid layer. The integration of reflection and transmission functions with respect to angles allows us to find the cloud plane r_d and spherical r albedos, the diffuse t_d and global t transmittances, the absorptance a_d and the global absorptance a as specified in Table 6.1.

Table 6.1. Radiative transfer characteristics ($\overline{R}$ and $\overline{T}$ are azimuthally averaged reflection and transmission functions, respectively)

Radiative characteristic	Symbol	Definition
Plane albedo	$r_d(\mu_0)$	$2\int_0^1 \overline{R}(\mu_0,\mu)\mu\,\mathrm{d}\mu$
Spherical albedo	r	$2\int_0^1 r_d(\mu_0)\mu_0\,\mathrm{d}\mu_0$
Diffuse transmittance	$t_d(\mu_0)$	$2\int_0^1 \overline{T}(\mu_0,\mu)\mu\,\mathrm{d}\mu$
Global transmittance	t	$2\int_0^1 t_d(\mu_0)\mu_0\,\mathrm{d}\mu_0$
Absorptance	$a_d(\mu_0)$	$1-r_d(\mu_0)-t_d(\mu_0)$
Global absorptance	a	$1-r-t$

6.4 Asymptotic theory

6.4.1 Auxiliary functions and relationships

Let us find the solution of RTE valid for optically thick turbid media ($z_0 \gg K_{\mathrm{ext}}^{-1}$, see Fig. 6.1). It is known that light intensity in deep layers of optically thick light scattering media is azimuthally independent. Then the radiative transfer equation can be written in the following form:

$$\eta\frac{\mathrm{d}I(\tau,\eta)}{\mathrm{d}\tau} = -I(\tau,\eta) + B(\tau,\eta) + B_0(\tau,\eta)\,,$$

where

$$\begin{aligned} B(\tau,\eta) &= \frac{\omega_0}{2}\int_{-1}^{1} p(\eta,\eta')I(\tau,\eta')\,\mathrm{d}\eta'\,,\\ B_0(\tau,\eta) &= \frac{\omega_0 F}{4\pi}p(\eta,\xi)e^{-\tau/\xi}\,, \end{aligned}$$

$\xi = \cos\vartheta_0$, $\eta = \cos\vartheta$, and

$$p(\eta,\xi) = \frac{1}{2\pi}\int_0^{2\pi} p(\eta,\xi,\varphi)\,\mathrm{d}\varphi$$

is the azimuthally averaged phase function. This result can be obtained from RTE (see section 6.2) performing integration with respect to the azimuth.

Let us assume that $\tau \to \infty$. Then it follows that $B_0(\tau,\eta) \to 0$ and (Sobolev, 1975)

$$I(\tau,\eta) = i(\eta)e^{-k\tau}\,.$$

The last equation corresponds to the so-called deep-layer regime, when parameters η and τ are decoupled. Then the light field intensity decreases with the distance from the illuminated boundary preserving the scattered light angular pattern given by the function $i(\eta)$. The value of I decreases in e times at the optical depth $\tau_e = 1/k$. Both the function $i(\eta)$ and the diffusion exponent k play an important role in the theory considered here. It is interesting that these characteristics of the deep-layer regime also define the intensity of transmitted and reflected light of optically thick layers as will be shown below.

It is easy to derive, using equations given above, that

$$(1 - k\eta)i(\eta) = \frac{\omega_0}{2}\int_{-1}^{1} p(\eta, \eta')i(\eta')\,\mathrm{d}\eta'\,,$$

which is called the deep regime radiative transfer equation (DRTE). This integral equation is usually solved numerically. Let us assume that $p = 1$. Then we have:

$$i(\eta) = \frac{\omega_0}{2(1 - k\eta)}\int_{-1}^{1} i(\eta')\,\mathrm{d}\eta'$$

or

$$i(\eta) = \frac{D}{1 - k\eta}\,,$$

where

$$D = \frac{\omega_0}{2}\int_{-1}^{1} i(\eta')\,\mathrm{d}\eta'$$

does not depend on the angle. Note that $i(\eta)$ satisfies DRTE for any constants D and, therefore,

$$i(\eta) = \frac{1}{1 - k\eta}\,,$$

where we used the normalization condition: $D = 1$. The diffusion constant k can be found substituting the last equation in DRTE. Then we have:

$$\frac{\omega_0}{2k}\ln\left(\frac{1+k}{1-k}\right) = 1$$

at $p = 1$. This equation allows to find k at arbitrary ω_0 and $p = 1$.

We can also write:

$$(1 + k\eta)i(-\eta) = \frac{\omega_0}{2}\int_{-1}^{1} p(-\eta, \eta')i(\eta')\,\mathrm{d}\eta'$$

or

$$(1 + k\eta)i(-\eta) = \frac{\omega_0}{2}\int_{-1}^{1} p(\eta, \eta')i(-\eta')\,\mathrm{d}\eta'\,,$$

where we used the property: $p(-\eta, -\eta') = p(\eta, \eta')$.

Let us establish now the relationship between the intensity $i^{\downarrow}(\eta)$ for light propagated downwards and the intensity $i^{\uparrow}(-\eta)$ for light propagated upwards.

Arrows and signs before η indicate the direction of light propagation. For this we consider a cut parallel to the upper boundary but at a large optical depth. The correspondent plane at $\tau \gg 1$ is illuminated not only by light coming from above and having the intensity i_a but also by light coming from below and reflected from the layer above the plane of cut. We denote this contribution to the total intensity as i_b. Then we have:

$$i^{\downarrow}(\eta) = i_a(\eta) + i_b(\eta)\,.$$

So the function $i^{\downarrow}(\eta)$ can be presented as a sum of two terms. Clearly, $i_a(\eta)$ is proportional to the angular distribution $u(\eta)$ of light transmitted by the upper layer:

$$i_a(\eta) = Mu(\eta)\,,$$

where M is the unknown proportionality constant. We will find this constant at later stages of our derivations. Also it follows for the intensity $i_b(\eta)$ by definition (see section 6.3) that

$$i_b(\eta) = 2\int_0^1 R(\eta,\eta')i(-\eta')\eta'\,\mathrm{d}\eta'\,,$$

where $R(\eta,\eta')$ is the azimuthally averaged reflection function of the upper layer under illumination from below ($\eta > 0, \eta' > 0$). This layer can be chosen to be arbitrarily thick. So we will assume that $R(\eta,\eta')$ coincides with the azimuthally averaged reflection function of a semi-infinite layer $R_\infty(\eta,\eta')$.

Summing up, it follows that

$$i^{\downarrow}(\eta) = Mu(\eta) + 2\int_0^1 R_\infty(\eta,\eta')i(-\eta')\eta'\,\mathrm{d}\eta'\,.$$

Let us find M. We multiply the last equation by $\eta i^{\downarrow}(\eta)$ and integrate it from 0 to 1 with respect to η. Then we have:

$$\int_0^1 {i^{\downarrow}}^2(\eta)\eta\,\mathrm{d}\eta = M\int_0^1 u(\eta)i^{\downarrow}(\eta)\eta\,\mathrm{d}\eta + \mathfrak{I}$$

where the two-dimensional integral

$$\mathfrak{I} = 2\int_0^1 i^{\downarrow}(\eta)\eta\,\mathrm{d}\eta\int_0^1 i^{\uparrow}(-\eta')R_\infty(\eta,\eta')\eta'\,\mathrm{d}\eta'$$

can be simplified. For this we note that it follows by definition (see section 6.3) that

$$i^{\uparrow}(-\eta') = 2\int_0^1 i_{\downarrow}(\eta)R_\infty(\eta,\eta')\eta\,\mathrm{d}\eta$$

and, therefore,

$$\mathfrak{I} = \int_0^1 {i^{\uparrow}}^2(-\eta')\eta'\,\mathrm{d}\eta'$$

or

$$\mathfrak{I} = -\int_{-1}^{0} i^{\uparrow^2}(\eta')\eta' \,\mathrm{d}\eta' \,.$$

Therefore, it follows, omitting arrows, that

$$M = \mathbb{C}\int_{-1}^{1} i^2(\eta)\eta \,\mathrm{d}\eta \,,$$

where

$$\mathbb{C} = \left[\int_{0}^{1} u(\eta) i(\eta)\eta \,\mathrm{d}\eta\right]^{-1} \,.$$

We will use the normalization condition: $\mathbb{C} = 2$. Then it follows:

$$M = 2\int_{-1}^{1} i^2(\eta)\eta \,\mathrm{d}\eta \,.$$

We present the equation for M together with other important relations in Table 6.2. The constant N defined in the property 6.8 (see Table 6.2) will be used in further derivations devoted to studies of relationships between auxiliary functions

$$P(\tau) = \int_{-1}^{1} \eta i(\eta) I(\tau, \eta) \,\mathrm{d}\eta$$

Table 6.2. Main equations and constants

No.	Property
6.1	$(1 - k\eta)i(\eta) = \dfrac{\omega_0}{2}\displaystyle\int_{-1}^{1} p(\eta, \eta')i(\eta') \,\mathrm{d}\eta'$
6.2	$(1 + k\eta)i(-\eta) = \dfrac{\omega_0}{2}\displaystyle\int_{-1}^{1} p(\eta, \eta')i(-\eta') \,\mathrm{d}\eta'$
6.3	$\dfrac{\omega_0}{2}\displaystyle\int_{-1}^{1} i(\eta) \,\mathrm{d}\eta = 1$
6.4	$i(-\eta) = 2\displaystyle\int_{0}^{1} i(\xi) R_\infty(\xi, \eta)\xi \,\mathrm{d}\xi$
6.5	$i(\eta) = 2\displaystyle\int_{0}^{1} i(-\xi) R_\infty(\xi, \eta)\xi \,\mathrm{d}\xi + Mu(\eta)$
6.6	$2\displaystyle\int_{0}^{1} u(\eta) i(\eta)\eta \,\mathrm{d}\eta = 1$
6.7	$M = 2\displaystyle\int_{-1}^{1} i^2(\eta)\eta \,\mathrm{d}\eta$
6.8	$N = 2\displaystyle\int_{0}^{1} i(-\eta) u(\eta)\eta \,\mathrm{d}\eta$
6.9	$\eta\dfrac{\mathrm{d}I}{\mathrm{d}\tau} = -I + B + B_0$

and

$$Q(\tau) = \int_{-1}^{1} \eta i(-\eta) I(\tau, \eta)\, \mathrm{d}\eta\,.$$

The relationships between functions $P(\tau)$ and $Q(\tau)$ are of importance for the derivation of asymptotical equations for reflection and transmission functions valid as the optical thickness $\tau_0 = K_{\mathrm{ext}} z_0 \to \infty$. Let us show this.

First of all, we note that it follows after multiplication of eq. (6.9) in Table 6.2 by $i(\eta)$ and integration from -1 to 1:

$$\frac{\mathrm{d}P(\tau)}{\mathrm{d}\tau} = -kP(\tau) + P_0(\tau)\,,$$

where

$$P_0(\tau) = \int_{-1}^{1} i(\eta) B_0(\tau, \eta)\, \mathrm{d}\eta$$

and we used the equality

$$-kP(\tau) = \int_{-1}^{1} B(\tau, \eta) i(\eta)\, \mathrm{d}\eta - \int_{-1}^{1} i(\eta) I(\tau, \eta)\, \mathrm{d}\eta\,.$$

This equality can be obtained from eq. (6.1) in Table 6.2. Let us show it. We have after multiplying eq. (6.1) in Table 6.2 by $I(\tau, \eta)$ and integrating this equation from -1 to 1 with respect to η:

$$\int_{-1}^{1} I(\tau, \eta) i(\eta)\, \mathrm{d}\eta - kP(\tau) = \frac{\omega_0}{2} \int_{-1}^{1} \mathrm{d}\eta \int_{-1}^{1} I(\tau, \eta) p(\eta, \eta') i(\eta')\, \mathrm{d}\eta'$$

or

$$\int_{-1}^{1} I(\tau, \eta) i(\eta)\, \mathrm{d}\eta - kP(\tau) = \int_{-1}^{1} B(\tau, \eta) i(\eta)\, \mathrm{d}\eta\,,$$

where we used the property: $p(\eta, \eta') = p(\eta', \eta)$. This completes the proof.

The next step is to find $P(\tau)$ from the differential equation given above. For this we use the following substitution:

$$P(\tau) = f(\tau) e^{-k\tau}\,.$$

Then it follows that

$$\frac{\mathrm{d}f(\tau)}{\mathrm{d}\tau} = P_0(\tau) e^{k\tau}$$

or

$$f_{\tau_1}^{\tau} = \int_{\tau_1}^{\tau} P_0(t) e^{kt}\, \mathrm{d}t\,.$$

It means that

$$f(\tau) = f(\tau_1) + \int_{\tau_1}^{\tau} P_0(t) e^{kt}\, \mathrm{d}t\,.$$

So we have:

$$P(\tau) = f(\tau_1)e^{-k\tau} + e^{-k\tau}\int_{\tau_1}^{\tau} P_0(t)e^{kt}\,\mathrm{d}t\,.$$

The value of τ_1 can be found from boundary conditions. In particular, we interested in the diffuse light. Diffused light does not enter the medium from above or below of a turbid slab ($I(0,\eta) = 0$ for $\eta > 0$ and $I(\tau_0,\eta) = 0$ for $\eta < 0$). Therefore, we have: $\tau_1 = 0$. Then the boundary condition at the upper boundary is satisfied. Finally, it follows that

$$P(\tau) = P(0)e^{-k\tau} + \int_0^{\tau} P_0(t)e^{k(t-\tau)}\,\mathrm{d}t\,.$$

A similar relationship can be obtained for $Q(\tau,\eta)$. Namely, we have after multiplication of eq. (6.9) in Table 6.2 by $i(-\eta)$ and performing the integration from -1 to 1:

$$\frac{\mathrm{d}Q(\tau)}{\mathrm{d}\tau} = kQ(\tau) + Q_0(\tau)\,,$$

where

$$Q_0(\tau) = \int_{-1}^{1} i(-\eta)B_0(\tau,\eta)\,\mathrm{d}\eta\,.$$

This equation differs from the corresponding equation for $P(\tau)$ only in the sign before k. So it follows that

$$Q(\tau) = \psi(\tau_1^*)e^{k\tau} + e^{k\tau}\int_{\tau_1^*}^{\tau} Q_0(t)e^{-kt}\,\mathrm{d}t\,,$$

where it was assumed that

$$Q(\tau) = \psi(\tau)e^{k\tau}\,.$$

The value of τ_1^* can be found from the boundary condition at the lower boundary of a medium. Namely, we have: $\tau_1^* = \tau_0$. Therefore, it follows that

$$Q(\tau) = Q(\tau_0)e^{k(\tau-\tau_0)} + \int_{\tau_0}^{\tau} Q_0(t)e^{-k(t-\tau)}\,\mathrm{d}t\,.$$

This equation gives an identity at $\tau = \tau_0$ due to the accurate account for the boundary conditions.

Summing up, we have the following important relationships:

$$\begin{aligned} P(\tau) &= P(0)e^{-k\tau} + V(\tau)\,,\\ Q(\tau) &= Q(\tau_0)e^{-k(\tau-\tau_0)} + W(\tau)\,, \end{aligned}$$

where

$$\begin{aligned} V(\tau) &= \int_0^{\tau} P_0(t)e^{k(t-\tau)}\,\mathrm{d}t\,,\\ W(\tau) &= \int_{\tau_0}^{\tau} Q_0(t)e^{-k(t-\tau)}\,\mathrm{d}t\,. \end{aligned}$$

These fundamental relationships are valid for any τ and for any light sources represented by B_0. They can be used for the derivation of a number of important results of light scattering media optics.

We will use a particular case at $\tau = \tau_0$ in the first equation and a case $\tau = 0$ in the second equation. Then it follows that

$$\begin{aligned} P(\tau_0) &= P(0)\exp(-k\tau_0) + V(\tau_0)\,, \\ Q(0) &= Q(\tau_0)\exp(-k\tau_0) + W(0)\,, \end{aligned}$$

where

$$\begin{aligned} V(\tau_0) &= e^{-k\tau_0}\int_0^{\tau_0}\mathrm{d}t\int_{-1}^{1} i(\eta)\frac{\omega_0 F}{4\pi}p(\eta,\xi)e^{-t\left(\frac{1}{\xi}-k\right)}\,\mathrm{d}\eta \\ &= \frac{1}{2\pi}\left(e^{-k\tau_0} - e^{-\frac{\tau_0}{\xi}}\right)\xi i(\xi)F\,, \\ W(0) &= \int_{\tau_0}^{0} e^{-kt}\,\mathrm{d}t\int_{-1}^{1} i(-\eta)\frac{\omega_0 F}{4\pi}p(\eta,\xi)e^{-t/\xi}\,\mathrm{d}\eta \\ &= \frac{1}{2\pi}\left(e^{-\left(k+\frac{1}{\xi}\right)\tau_0} - 1\right)\xi i(-\xi)F\,, \end{aligned}$$

where we used properties 1 and 2 in Table 6.2. Therefore, neglecting small numbers proportional to $e^{-\tau_0/\xi}$, it follows that

$$\begin{aligned} P(0) &= P(\tau_0)e^{k\tau_0} - \frac{\xi i(\xi)F}{2\pi}\,, \\ Q(0) &= Q(\tau_0)e^{-k\tau_0} - \frac{\xi i(-\xi)F}{2\pi}\,. \end{aligned}$$

These are auxiliary relations we were bound to establish from the very start. They can be also written in the following form:

$$\begin{aligned} i(\xi) &= \frac{2\pi e^{k\tau_0}}{\xi F}\int_{-1}^{1} I(\eta,\tau_0)i(\eta)\eta\,\mathrm{d}\eta - \frac{2\pi}{\xi F}\int_{-1}^{1} I(\eta,0)i(-\eta)\eta\,\mathrm{d}\eta\,, \\ i(-\xi) &= \frac{2\pi e^{-k\tau_0}}{\xi F}\int_{-1}^{1} I(\eta,\tau_0)i(-\eta)\eta\,\mathrm{d}\eta - \frac{2\pi}{\xi F}\int_{-1}^{1} I(\eta,0)i(-\eta)\eta\,\mathrm{d}\eta\,. \end{aligned}$$

Now we take into account that

$$I(-\eta,0) = \frac{\xi F}{\pi}\overline{R}(\xi,\eta)$$

at $\eta > 0$ and $I(-\eta,0) = 0$, otherwise. Also it follows that

$$I(\eta,\tau_0) = \frac{\xi F}{\pi}\overline{T}(\xi,\eta)$$

at $\eta > 0$ and $I(\eta,\tau_0) = 0$, otherwise. This means that we can write:

$$-\int_{-1}^{1} I(\eta,0)i(\eta)\eta\,\mathrm{d}\eta = -\int_{1}^{-1} I(-\eta,0)i(-\eta)\eta\,\mathrm{d}\eta = -\int_{1}^{0} I(-\eta,0)i(-\eta)\eta\,\mathrm{d}\eta$$

and

$$-\int_{-1}^{1} I(\eta,0)i(-\eta)\eta\,\mathrm{d}\eta = -\int_{1}^{-1} I(-\eta,0)i(\eta)\eta\,\mathrm{d}\eta = -\int_{1}^{0} I(-\eta,0)i(\eta)\eta\,\mathrm{d}\eta\,.$$

Similar relationships can be written for integrals containing $I(\eta,\tau_0)$. Then one obtains:

$$\begin{aligned} i(\xi) &= 2e^{k\tau_0}\int_0^1 \overline{T}(\eta,\xi,\tau_0)i(\eta)\eta\,\mathrm{d}\eta + 2\int_0^1 \overline{R}(\eta,\xi,\tau_0)i(-\eta)\,\mathrm{d}\eta\,,\\ i(-\xi) &= 2e^{-k\tau_0}\int_0^1 \overline{T}(\eta,\xi,\tau_0)i(-\eta)\eta\,\mathrm{d}\eta + 2\int_0^1 \overline{R}(\eta,\xi,\tau_0)i(\eta)\eta\,\mathrm{d}\eta\,. \end{aligned}$$

6.4.2 Asymptotic equations

The general form of functions $\overline{R}(\eta,\xi,\tau_0)$ and $\overline{T}(\eta,\xi,\tau_0)$ can be obtained using physical arguments. In particular, $\overline{T}$ should be proportional to $u(\eta)$ (and, actually, due to the reciprocity principle also to $u(\xi)$). Therefore, we have:

$$T(\eta,\xi,\tau_0) = \alpha(\tau_0)u(\eta)u(\xi)\,,$$

where $\alpha(\tau_0)$ is the unknown function.

Let us consider now a semi-infinite layer and take a cut at a large optical thickness τ_0. Then we can represent $R_\infty(\eta,\xi)$ as a sum of reflection from upper layer $\overline{R}(\eta,\xi,\tau_0)$ and light transmitted by the upper layer and reflected back. The angular distribution of the transmitted light should be proportional to $u(\eta)u(\xi)$ as was specified above. So we have:

$$R_\infty(\eta,\xi) = \overline{R}(\tau,\eta,\xi) + \beta(\tau_0)u(\eta)u(\xi)\,.$$

Let us find unknown functions $\alpha(\tau_0)$ and $\beta(\tau_0)$ using expressions for $i(\pm\xi)$ derived above and also properties specified in Table 6.2. Then it follows that

$$\begin{aligned} i(\xi) &= 2e^{k\tau_0}\int_0^1 \alpha(\tau_0)u(\eta)u(\xi)i(\eta)\eta\,\mathrm{d}\eta\\ &\quad +2\int_0^1 \left(R_\infty(\eta,\xi) - \beta(\tau_0)u(\eta)u(\xi)\right) i(-\eta)\eta\,\mathrm{d}\eta\,,\\ i(-\xi) &= 2e^{-k\tau_0}\int_0^1 \alpha(\tau_0)u(\eta)u(\xi)i(-\eta)\eta\,\mathrm{d}\eta\\ &\quad +2\int_0^1 \left(R_\infty(\eta,\xi) - \beta(\tau_0)u(\eta)u(\xi)\right) i(\eta)\,\mathrm{d}\eta\,. \end{aligned}$$

One obtains, using properties given in Table 6.2:

$$
\begin{aligned}
i(\xi) &= e^{k\tau_0}\alpha(\tau_0)u(\xi) + i(\xi) - Mu(\xi) - \beta(\tau_0)u(\xi)N\,, \\
i(-\xi) &= i(-\xi) - \beta(\tau_0)u(\xi) + \alpha(\tau_0)Ne^{-k\tau_0}u(\xi)\,,
\end{aligned}
$$

where we introduced the integral

$$
N = 2\int_0^1 u(\eta)i(-\eta)\eta\,\mathrm{d}\eta\,.
$$

Therefore, it follows that

$$
\begin{gathered}
\alpha(\tau_0) - Me^{-k\tau_0} - \beta Ne^{-k\tau_0} = 0\,, \\
\beta(\tau_0) = \alpha(\tau_0)Ne^{-k\tau_0}\,.
\end{gathered}
$$

So one obtains:

$$
\alpha(\tau_0) = \frac{Me^{-k\tau_0}}{1 - N^2e^{-2k\tau_0}}\,, \quad \beta(\tau_0) = \frac{MNe^{-2k\tau_0}}{1 - N^2e^{-2k\tau_0}}
$$

Finally, we have, as $\tau_0 \to \infty$ at arbitrary ω_0 and $p(\theta)$:

$$
\begin{aligned}
\overline{R}(\xi,\eta) &= R_\infty(\xi,\eta) - \overline{T}(\xi,\eta)Ne^{-k\tau_0}\,, \\
\overline{T}(\xi,\eta) &= \frac{Me^{-k\tau_0}}{1 - N^2e^{-2k\tau_0}}u(\eta)u(\xi)\,.
\end{aligned}
$$

These formulas are central equations of the light scattering media optics. The importance of these equations is due to the fact that the dependence of radiative characteristics on τ_0 is given explicitly. Our next task is to derive approximate equations for constants k, M, N and functions $u(\eta)$, $R_\infty(\xi,\eta)$ in a number of particular cases.

The dependence of the transmitted light on the azimuth is weak. So we may write:

$$
\begin{aligned}
R(\xi,\eta,\varphi) &= R_\infty(\xi,\eta,\varphi) - T(\xi,\eta)Ne^{-k\tau_0}\,, \\
T(\xi,\eta) &= \frac{Me^{-k\tau_0}}{1 - N^2e^{-2k\tau_0}}u(\eta)u(\xi)\,,
\end{aligned}
$$

where we have accounted for the fact that the reflection function of a semi-infinite turbid medium does depend on the azimuth.

The choice of the normalization condition for the function $i(\eta)$ and also for the function $u(\eta)$ is arbitrary. We have followed the notation of Sobolev (1975). It differs from that in the corresponding equations used by van de Hulst (1980). For instance, van de Hulst's diffusion pattern $P(\eta)$ must be divided by ω_0 to yield $i(\eta)$. His escape function $K(\eta)$ must be multiplied by ω_0 to yield $u(\eta)$, and his M equals that used by Sobolev multiplied by ω_0^2. These differences do not lead to extra factors in main equations given in this section. They are also of no importance at $\omega_0 = 1$.

6.4.3 Weak absorption

Equations given above can be simplified considerably for the case of values of ω_0 close to unity. Therefore, we need to find approximate expressions for functions $R_\infty(\xi,\eta)$, $u(\eta)$ and also for parameters k, M, N as $\omega_0 \to 1$. Let us concentrate on this problem now.

6.4.3.1 The constants *k*, *M* and the diffuse light field in deep layers

The parameter M depends on the diffuse light intensity $i(\eta)$ in deep layers of a turbid medium:

$$M = 2\int_{-1}^{1} i^2(\eta)\eta\,\mathrm{d}\eta\,.$$

So we need to study functions $i(\eta)$ as $\omega_0 \to 1$. The radiative transfer equation for the normalized light intensity $i(\eta)$ deep inside of a turbid medium has the following form:

$$(1-k\eta)i(\eta) = \frac{\omega_0}{2}\int_{-1}^{1} p(\eta,\eta')i(\eta')\,\mathrm{d}\eta'\,,$$

where $p(\eta,\eta')$ is the azimuthally averaged phase function, ω_0 is the single scattering albedo and k is the diffusion exponent. The normalization condition for $i(\eta)$ has the following form:

$$\frac{\omega_0}{2}\int_{-1}^{1} i(\eta')\,\mathrm{d}\eta' = 1\,.$$

We use the following expansions:

$$p(\eta,\eta') = \sum_{n=0}^{\infty} x_n P_n(\eta)P_n(\eta')$$

and

$$i(\eta) = \sum_{n=0}^{\infty} \sigma_n P_n(\eta)\,.$$

The task is to find σ_n from the set of x_n. Substituting these expressions in DRTE, we have:

$$B = \sum_{n=0}^{\infty} \sigma_n P_n(\eta) - k\eta\sum_{n=0}^{\infty} \sigma_n P_n(\eta)\,,$$

where

$$B = \frac{\omega_0}{2}\sum_{l=0}^{\infty}\sum_{n=0}^{\infty}\int_{-1}^{1} x_l\sigma_n P_l(\eta)P_l(\eta')P_n(\eta')\,\mathrm{d}\eta'$$

or

$$B = \omega_0\sum_{l=0}^{\infty}\sum_{n=0}^{\infty}\sigma_n x_l\delta_{nl}[2n+1]^{-1}P_n(\eta)$$

and after simplifications:

$$B = \omega_0\sum_{n=0}^{\infty} x_n\sigma_n[2n+1]^{-1}P_n(\eta)\,,$$

where we used the fact that Legendre polynomials are orthogonal. This means that

$$\int_{-1}^{1} P_n(\eta)P_l(\eta)\,\mathrm{d}\eta = 2\delta_{nl}[2n+1]^{-1}\,,$$

where δ_{nl} is the Kronecker symbol.

Therefore, it follows that

$$\frac{1}{k}\sum_{n=0}^{\infty}\sigma_n\left\{1-\frac{x_n\omega_0}{2n+1}\right\}P_n(\eta) = \sum_{n=0}^{\infty}\sigma_n\left\{\frac{n+1}{2n+1}P_{n+1}(\eta)+\frac{n}{2n+1}P_{n-1}(\eta)\right\}\,,$$

where we have used the property:

$$\eta P_n(\eta) = \frac{n+1}{2n+1}P_{n+1}(\eta)+\frac{n}{2n+1}P_{n-1}(\eta)\,.$$

The expressions for

$$\zeta(\eta) = \sum_{n=0}^{\infty}\sigma_n\frac{n+1}{2n+1}P_{n+1}(\eta)$$

and

$$\upsilon(\eta) = \sum_{n=0}^{\infty}\sigma_n\frac{n}{2n+1}P_{n-1}(\eta)$$

can be written as:

$$\zeta(\eta) = \sum_{l=0}^{\infty}\sigma_{l-1}\frac{l}{2l-1}P_l(\eta)$$

and

$$\upsilon(\eta) = \sum_{s=0}^{\infty}\sigma_{s+1}\frac{s+1}{2s+3}P_l(\eta)\,,$$

where $l = n+1$, $s = n-1$.

Therefore, we have:

$$\sum_{m=0}^{\infty}\left[\frac{1}{k}\sigma_m - \frac{x_m\omega_0}{(2m+1)k}\sigma_m - \frac{m}{2m-1}\sigma_{m-1} - \frac{m+1}{2m+3}\sigma_{m+1}\right]P_m(\eta) = 0$$

at arbitrary η. This means that

$$\frac{1}{k}\sigma_m - \frac{x_m\omega_0}{(2m+1)k}\sigma_m - \frac{m}{2m-1}\sigma_{m-1} - \frac{m+1}{2m+3}\sigma_{m+1} = 0$$

or

$$\sigma_{m+1} = \frac{(2m+3)(2m-\omega_0 x_m+1)}{(2m+1)(m+1)k}\sigma_m - \frac{(2m+3)m}{(2m-1)(m+1)}\sigma_{m-1}\,.$$

We have at $m = 0$:

$$\sigma_1 = \frac{3\sigma_0(1-\omega_0)}{k}\,.$$

Let us derive the expression for the value of σ_0 now. It follows that

$$\sigma_m = \frac{2m+1}{2}\int_{-1}^{1} i(\eta) P_m(\eta)\,\mathrm{d}\eta$$

and, therefore,

$$\sigma_0 = \frac{1}{2}\int_{-1}^{1} i(\eta)\,\mathrm{d}\eta\,.$$

Comparing this result with property 6.3 in Table 6.2, we derive: $\sigma_0 = \omega_0^{-1}$, and, therefore,

$$\sigma_1 = \frac{3(1-\omega_0)}{k\omega_0}\,.$$

This allows us to obtain the following expansion for $i(\eta)$ as $\omega_0 \to 1$:

$$i(\eta) = \omega_0^{-1}\left\{1 + 3k^{-1}(1-\omega_0)\eta\right\}\,,$$

where we neglected higher-order terms with respect to the probability of photon absorption $\beta \equiv 1-\omega_0$. So it follows, as $\omega_0 \to 1$, that

$$i(\eta) = 1 + 3k^{-1}(1-\omega_0)\eta\,.$$

Recurrence relations allow us to find σ_m and $i(\eta)$ at any k. We will not consider this problem here, however, but rather concentrate on the derivation of the approximate equation for k valid as $\omega_0 \to 1$.

For this we introduce:

$$\Upsilon_m = \frac{\sigma_m}{\sigma_{m-1}}\,.$$

Then it follows that

$$\Upsilon_{m+1} = \frac{(2m+3)(2m-\omega_0 x_m+1)}{(2m+1)(m+1)k} - \frac{(2m+3)m}{(2m-1)(m+1)\Upsilon_m}$$

and

$$\Upsilon_m = \frac{(2m+3)m}{(2m-1)(m+1)\left[\dfrac{(2m+3)(2m-\omega_0 x_m+1)}{(2m+1)(m+1)k} - \Upsilon_{m+1}\right]}$$

or

$$\Upsilon_m = \frac{(2m+3)(2m+1)mk}{(2m+3)(2m-1)(2m+1-\omega_0 x_m) - \varepsilon_m}\,,$$

where

$$\varepsilon_m = (4m^2-1)(1+m)k\Upsilon_{m+1}\,.$$

We are interested in the asymptotic solution valid as $k \to 0$. So we can ignore ε_m and derive at $m = 1$:

$$\Upsilon_1 = \frac{3k}{(3-\omega_0 x_1)}\,.$$

Therefore, it follows that

$$\sigma_1 = \frac{3k}{(3-\omega_0 x_1)}\sigma_0$$

or

$$\sigma_1 = \frac{3k}{(3-\omega_0 x_1)\omega_0}\,.$$

This formula must produce the same result as the expression for σ_1 derived above. It means that

$$k = \sqrt{3(1-\omega_0 g)(1-\omega_0)}\,,$$

where $g = x_1/3$ is the asymmetry parameter. This important equation shows that the intensity in the deep layers of optically thick weakly absorbing media clouds decreases more quickly for smaller values of the asymmetry parameter g (less extended in the forward direction phase functions). Our derivations are valid as $\omega_0 \to 1$ only. So we can also write: $k = \sqrt{3(1-\omega_0)(1-g)}$. The approximate expression for $i(\eta)$ given above can be written using the similarity parameter

$$s = \sqrt{\frac{1-\omega_0}{1-\omega_0 g}}\,.$$

Namely, we have:

$$i(\eta) = 1 + \frac{s\eta}{\sqrt{3}}\,.$$

Note that it follows as $\omega_0 \to 1$: $s \approx \sqrt{\dfrac{1-\omega_0}{1-g}}$.

The angular pattern $i(\eta)$ does not depend on the choice of a particular light scattering medium if s kept constant. The function $i(\eta)$ is completely determined by the similarity parameter s as $\omega_0 \to 1$. Therefore, light scattering media having different values of ω_0 and g but the same s have very similar light angular distributions in the deep-layer regime.

The parameters k and s are of a crucial importance for the theory considered here. We must expect that constants and functions in asymptotic equations must depend on these values. In particular, taking into account property 6.7 in Table 6.2, we obtain:

$$M = \frac{8s}{\sqrt{3}}$$

as $k \to 0$.

6.4.3.2 The constant N and the escape function

The expansion of $u(\eta)$ with respect to the diffusion coefficient k can be presented as

$$u(\eta) = \sum_{n=0}^{\infty} k^n u_n(\eta)\,.$$

We are interested only in the case of weak absorption. Then it follows that

$$u(\eta) = u_0(\eta) + k u_1(\eta)\,.$$

The task is to calculate the function $u_1(\eta)$. This will be performed in two steps. First of all we note that the weak absorption of light does not alter the single scattering law considerably. The angular distribution of emerging light $u(\eta)$ is determined largely by the scattering processes. So it is safe to assume that $u(\eta) \approx u_0(\eta)$ as $k \to 0$ or $u_1(\eta) = bu_0(\eta)$, where the constant b should be determined. Clearly, due to physical reasons we should have: $u(\eta) < u_0(\eta)$ and $b < 0$. Therefore, absorption plays the role of a veil in this case. It reduces the contrast but it does not change details of the scattering pattern. We start from the expression:

$$2\int_0^1 u(\eta)i(\eta)\eta\,\mathrm{d}\eta = 1\,.$$

Let us substitute the following expansions in this formula:

$$u(\eta) = u_0(\eta)(1 + bk)$$

and

$$i(\eta) = 1 + ak\eta\,,$$

where we assume that $\omega_0 \to 1$ and, therefore,

$$k = \sqrt{3(1-g)(1-\omega_0)}\,, \quad s = \sqrt{\frac{1-\omega_0}{1-g}}\,, \quad \text{and} \quad a = (1-g)^{-1}\,.$$

Then it follows that

$$2\int_0^1 u_0(\eta)\eta\,\mathrm{d}\eta + 2bk\int_0^1 u_0(\eta)\eta\,\mathrm{d}\eta + 2ak\int_0^1 u_0(\eta)\eta^2\,\mathrm{d}\eta = 1\,,$$

where we neglected high-order terms. So we have:

$$b = -2a\int_0^1 u_0(\eta)\eta^2\,\mathrm{d}\eta\,,$$

where we have accounted for the fact that (see property 6.6 in Table 6.2 at $\omega_0 = 1$, $i \equiv 1$)

$$2\int_0^1 u_0(\eta)\eta\,\mathrm{d}\eta = 1\,.$$

Finally, it follows that

$$b = -\frac{2\nu}{1-g}\,,$$

where we have accounted for the fact that $a = (1-g)^{-1}$ and

$$\nu = \int_0^1 u_0(\eta)\eta^2\,\mathrm{d}\eta$$

is the second moment of the escape function. Therefore, one finally derives:

$$u(\eta) = \left(1 - \frac{2\nu k}{1-g}\right) u_0(\eta)\,.$$

This equation together with expression for $i(\eta)$ allows to find the constant N (see Table 6.2). Namely, we arrive at the following result:

$$N = 2\int_0^1 \mathrm{d}\eta u_0(\eta)\eta \left\{1 - \frac{2\nu k}{1-g}\right\}\left\{1 - \frac{k\eta}{1-g}\right\}$$

or

$$N = 1 - \frac{4\nu k}{1-g}\,,$$

where we have neglected terms of the second order with respect to k. We can also write:

$$N = 1 - 4\sqrt{3}\nu s\,.$$

Note that functions $u(\eta)$ enter asymptotic formulas in the combination: $\Psi(\eta,\xi) = Mu(\eta)u(\xi)$. This means that one can use the following approximation, valid as $k \to 0$:

$$\Psi(\eta,\xi) = \frac{8s}{\sqrt{3}}u_0(\eta)u_0(\xi)\,.$$

6.4.3.3 The reflection function of a semi-infinite layer

The last point in our derivations of asymptotics as $\omega_0 \to 1$ is to derive the weak absorption approximation for the reflection function of a semi-infinite medium R_∞. This will be done in two steps.

Step 1

The expression for a plane albedo of a semi-infinite medium is written by a definition as

$$r_p(\xi) = 2\int_0^1 R_\infty(\xi,\eta)\eta\,\mathrm{d}\eta\,.$$

We will use the following expansion of $R_\infty(\xi,\eta)$ with respect to k:

$$R_\infty(\xi,\eta) = R_{0\infty}(\xi,\eta) - kR_{1\infty}(\xi,\eta)\,,$$

where $R_{1\infty}(\xi,\eta)$ is the function we need to find. The minus sign signifies the fact that $R_\infty(\xi,\eta) \le R_{0\infty}(\xi,\eta)$ by definition. One can see that

$$r_p(\xi) = 1 - kJ(\xi)\,,$$

where

$$J(\xi) = 2\int_0^1 R_{1\infty}(\xi,\eta)\eta\,\mathrm{d}\eta\,,$$

and we used the property:

$$2\int_0^1 R_{0\infty}(\xi,\eta)\eta\,\mathrm{d}\eta = 1\,.$$

Step 2

We now derive the asymptotic equation for $r_p(\xi)$ as $k \to 0$ using another set of equations. This will allow us to give a relationship between $J(\xi)$ and $u_0(\xi)$. We start from the following equation (see Table 6.2):

$$i(-\xi) = 2\int_0^1 i(\eta) R_\infty(\xi,\eta)\eta \,\mathrm{d}\eta\,.$$

Substituting expansions with respect to k in this expression and ignore high-order terms, we obtain:

$$1 - \frac{k\xi}{1-g} = 2\int_0^1 \left(1 + \frac{k\eta}{1-g}\right)\left(R_{0\infty}(\xi,\eta) - kR_{1\infty}(\xi,\eta)\right)\eta \,\mathrm{d}\eta\,.$$

This means that (see Table 6.2)

$$1 - \frac{k\xi}{1-g} = 1 - kJ(\xi) + \frac{2k}{1-g}\int_0^1 R_{0\infty}(\xi,\eta)\eta^2 \,\mathrm{d}\eta$$

or

$$J(\xi) = (1-g)^{-1}\left\{\xi + 2\int_0^1 R_{0\infty}(\xi,\eta)\eta^2 \,\mathrm{d}\eta\right\}\,,$$

where

$$J(\xi) = \frac{1 - r_p(\xi)}{k}$$

as was shown above. Therefore, it holds that

$$(1-g)(1-r_p(\xi))k^{-1} = 2\int_0^1 R_{0\infty}(\xi,\eta)\eta^2 \,\mathrm{d}\eta + \xi$$

or

$$r_p(\xi) = 1 - \frac{k}{1-g}\left\{\xi + 2\int_0^1 R_{0\infty}(\xi,\eta)\eta^2 \,\mathrm{d}\eta\right\}\,.$$

On the other hand, we have:

$$i(\xi) = Mu(\xi) + 2\int_0^1 i(-\eta) R_\infty(\xi,\eta)\eta \,\mathrm{d}\eta\,.$$

Therefore, it follows, as $k \to 0$, that

$$1 + \frac{k\xi}{1-g} = \frac{8ku_0(\xi)}{3(1-g)} + 2\int_0^1 \left(1 - \frac{k\eta}{1-g}\right)\left(R_{0\infty}(\xi,\eta) - kR_{1\infty}(\xi,\eta)\right)\eta \,\mathrm{d}\eta\,.$$

This means that

$$1 + \frac{k\xi}{1-g} = \frac{8ku_0(\xi)}{3(1-g)} + 1 - \frac{2k}{1-g}\int_0^1 R_{0\infty}(\xi,\eta)\eta^2 \,\mathrm{d}\eta - kJ(\xi)$$

or

$$\xi = \frac{8}{3}u_0(\xi) - 2\int_0^1 R_{0\infty}(\xi,\eta)\eta^2\,\mathrm{d}\eta - (1-g)J(\xi)$$

and

$$J(\xi) = (1-g)^{-1}\left\{\frac{8}{3}u_0(\xi) - 2\int_0^1 R_{0\infty}(\xi,\eta)\eta^2\,\mathrm{d}\eta - \xi\right\}.$$

Comparing this expression with the formula for $J(\xi)$ given above, we derive that

$$\frac{8u_0(\xi)}{3} = 2\xi + 4\int_0^1 R_{0\infty}(\xi,\eta)\eta^2\,\mathrm{d}\eta\,.$$

This allows us to establish the following important relationship:

$$u_0(\xi) = \frac{3}{4}\left[\xi + 2\int_0^1 R_{0\infty}(\xi,\eta)\eta^2\,\mathrm{d}\eta\right].$$

The expression in brackets is equal to $(1-g)J(\xi)$. So we have:

$$J(\xi) = \frac{4u_0(\xi)}{3(1-g)}$$

and, therefore,

$$r_p(\xi) = 1 - \frac{4ku_0(\xi)}{3(1-g)}\,.$$

The function $R_{1\infty}(\xi,\eta)$ must be symmetric with respect to the pair (ξ,η). Therefore, it follows, using the expression

$$J(\xi) = 2\int_0^1 R_{1\infty}(\xi,\eta)\eta\,\mathrm{d}\eta = \frac{4u_0(\xi)}{3(1-g)}\,,$$

that

$$R_{1\infty}(\xi,\eta) = cu_0(\xi)u_0(\eta)\,.$$

Substituting this formula in the equation given above, we derive the analytical expression for the constant c:

$$c = \frac{4}{3(1-g)}\,,$$

where we used the property

$$2\int_0^1 u_0(\xi,\eta)\eta\,\mathrm{d}\eta = 1\,.$$

Finally, we have:

$$R(\xi,\eta) = R_{0\infty}(\xi,\eta) - \frac{4k}{3(1-g)}u_0(\xi)u_0(\eta)$$

or

$$R(\xi,\eta) = R_{0\infty}(\xi,\eta) - \frac{4}{\sqrt{3}} s u_0(\xi) u_0(\eta)\,.$$

All asymptotic equations derived as $k \to 0$ are given in Table 6.3. It follows that the case of weak absorption can be studied analytically if the function $R_{0\infty}(\xi,\eta)$ is known. The escape function $u_0(\xi)$ is calculated by the integration of $R_{0\infty}(\xi,\eta)$ with respect to η as was shown above. Let us study the functions $R_{0\infty}(\xi,\eta)$ and $u_0(\xi)$ in more detail now.

Table 6.3. Asymptotic equations valid as $k \to 0$ $\left(\nu = \int_0^1 u_0(\xi)\xi^2\,\mathrm{d}\xi,\ g = \frac{1}{4}\int_0^\pi p(\theta)\sin 2\theta\,\mathrm{d}\theta\right)$

$R_\infty(\xi,\eta,\varphi)$	$R_{0\infty}(\xi,\eta,\varphi) - \frac{4k}{3(1-g)} u_0(\xi)u_0(\eta)$
$u(\xi)$	$\left(1 - \frac{k\nu}{2}\right) u_0(\xi)$
M	$\frac{8k}{3(1-g)}$
N	$1 - \frac{4k\nu}{1-g}$
$Mu(\xi)u(\eta)$	$\frac{8k}{3(1-g)} u_0(\xi)u_0(\eta)$
k	$\sqrt{3(1-\omega_0)(1-\omega_0 g)}$
$r_d(\xi)$	$1 - \frac{4k u_0(\xi)}{3(1-g)}$
r	$1 - \frac{4k}{3(1-g)}$

6.4.4 Nonabsorbing media

6.4.4.1 General equations

We assume that there is no absorption in a scattering medium (e.g., clouds in the visible). Then it follows, using general asymptotic equations and results presented in Table 6.3 at $\omega_0 = 1$:

$$R(\xi,\eta,\varphi) = R_{0\infty}(\xi,\eta,\varphi) - t u_0(\xi) u_0(\xi)$$

and

$$T(\xi,\eta) = t u_0(\xi) u_0(\xi)\,,$$

where

$$t = \frac{1}{0.75(1-g)\tau_0 + b}$$

and $b = 3\nu$. The plane albedo $r_p(\xi)$, the spherical albedo r, the diffuse transmittance $t_d(\xi)$ and the global transmittance t are defined in Table 6.1. We have, using results presented in Table 6.1:

$$r_p(\xi) = 1 - tu_0(\xi), \quad r = 1 - t, \quad t_d(\xi) = tu_0(\xi)$$

at $\omega_0 = 1$ and also we confirm that t coincides with the global transmittance.

It follows that the calculation of reflection and transmission functions of optically thick light scattering layers is reduced to the calculation of the reflection function of a semi-infinite layer. The function $R_{0\infty}(\xi, \eta, \varphi)$ can be used to calculate $u_0(\xi)$ and the parameter

$$\nu = \int_0^1 u_0(\xi)\xi^2 \, \mathrm{d}\xi \, .$$

Generally speaking, the functions $u_0(\xi)$ and $R_{0\infty}(\xi, \eta, \varphi)$ can be derived from the numerical solution of the corresponding integral equations (Dlugach and Yanovitskij, 1974; Sobolev, 1975; Mishchenko *et al.*, 1999). Now we introduce useful approximations for the calculation of $u_0(\xi)$, $R_{0\infty}(\xi, \eta, \varphi)$. The important property of these functions that they do not depend on the pair (ω_0, τ_0) by definition. They are completely determined by the phase function. Moreover, the dependence on the phase functions is rather weak because functions $u_0(\xi)$, $R_{0\infty}(\xi, \eta, \varphi)$ are related to the problems involving semi-infinite non-absorbing media. So multiple light scattering is quite important in this case. It leads to the averaging of the scattering features chracteristic for a single scattering event. This also means that a good starting point for the derivation of approximate solutions valid at arbitrary g is the case of $g = 0$ (e.g., isotropic scattering, $p \equiv 1$).

6.4.4.2 Auxiliary functions

We start the consideration of auxiliary functions from the well studied case of isotropic scattering. Then the nonlinear integral equation for the reflection function of a non-absorbing semi-infinite medium (de Rooij, 1985) can be presented in the following form:

$$R_{0\infty}(\xi, \eta) = \frac{1 + 2\xi \int_0^1 R_{0\infty}(\eta, \eta') \, \mathrm{d}\eta' + 2\eta \int_0^1 R_{0\infty}(\xi, \eta') \, \mathrm{d}\eta' + G(\xi, \eta)}{4(\xi + \eta)} \, ,$$

where

$$G(\xi, \eta) = 4\xi\eta \int_0^1 \int_0^1 R_{0\infty}(\xi, \eta') R_{0\infty}(\eta, \eta'') \, \mathrm{d}\eta'' \, .$$

The inspection of this equation shows that it can be reduced to the following more simple form:

$$R_{0\infty}(\xi,\eta) = \frac{H(\xi)H(\eta)}{4(\xi+\eta)}$$

with

$$H(\xi) = 1 + 2\xi \int_0^1 R_{0\infty}(\xi,\eta)\,\mathrm{d}\eta\,.$$

The last two equations allow us to formulate the integral equation for the function $H(\xi)$:

$$H(\xi) = 1 + 0.5\xi H(\xi) \int_0^1 \frac{H(\eta)}{\xi+\eta}\,\mathrm{d}\eta\,.$$

It follows immediately that $H(0) = 1.0$. Numerical calculations show that the function $H(\eta)$ can be approximated by the linear function $H(\eta) = 1 + 2\eta$. This approximation can be used as a first-guess value under the integral in the equation given above to solve the integral equation for the function $H(\xi)$ by the iteration technique. The substitution of this linear equation into the expression for $R_{0\infty}(\xi,\eta)$ presented above gives:

$$R_{0\infty}(\xi,\eta) = \frac{1 + 2(\xi+\eta) + 4\xi\eta}{4(\xi+\eta)}\,.$$

This is a rather good approximation for the isotropic scattering case. Further, we note that the value of $R_{0\infty}(\xi,\eta)$ can be separated into two parts:

$$R_{0\infty}(\xi,\eta) = R^s_{0\infty}(\xi,\eta) + R^m_{0\infty}(\xi,\eta)\,,$$

where the first term is due to single scattering ($R^s_{0\infty}(\xi,\eta) = 0.25(\xi+\eta)^{-1}$ (Chandrasekhar, 1950)) and the second term $\left(R^m_{0\infty}(\xi,\eta) = [0.5 + \xi\eta(\xi+\eta)^{-1}]\right)$ is due to multiple scattering at $p = 1$.

We make the same separation for the nonisotropic scattering case. Then, however, we have (Chandrasekhar, 1950; Kokhanovsky, 2004a):

$$R^s_{0\infty}(\xi,\eta) = 0.25p(\theta)(\xi+\eta)^{-1}$$

and we assume that it holds for multiple nonisotropic light scattering:

$$R_{0\infty}(\xi,\eta) = \frac{A + B(\xi+\eta) + C\xi\eta}{4(\xi+\eta)}\,,$$

where A, B, and C are constants to be determined. There are different ways to get these constants. In particular, integral relationships involving the function $R_{0\infty}(\xi,\eta)$ can be used (Sobolev, 1975).

Constants can be also found using the following fitting technique. The function $R_{0\infty}(\xi,\eta,\varphi)$ is calculated using the exact radiative transfer equation (see, for example, Mishchenko *et al.*, 1999) and then functions $\Xi(\xi,\eta,\varphi) = 4(\xi+\eta)\tilde{R}_{0\infty}(\xi,\eta,\varphi)$, where $\tilde{R}_{0\infty}(\xi,\eta,\varphi) = R_{0\infty}(\xi,\eta,\varphi) - R^s_{0\infty}(\xi,\eta,\varphi)$, are fitted by linear functions of the argument assuming, for example, $\eta = 1$. This technique gives: A = 3.944, B = −2.5, C = 10.664 for water clouds (Kokhanovsky, 2004b) and $A = 1.247$, $B = 1.186$, $C = 5.157$ for ice clouds (Kokhanovsky, 2006).

The next point is to derive the corresponding equation for the function $u_0(\xi)$. This can be done in the following way.

It was shown above that the following relationship holds:

$$u_0(\xi) = \frac{3}{4}\left[\xi + 2\int_0^1 R_{0\infty}(\xi,\eta)\eta^2\,\mathrm{d}\eta\right].$$

Let us substitute $R_{0\infty}(\xi,\eta)$ for the isotropic scattering case derived above in this equation. Then it follows that

$$u_0(\xi) = \frac{3}{4}\left[\xi + \frac{1}{2}\int_0^1 \frac{H(\xi)H(\eta)}{\xi+\eta}\eta^2\,\mathrm{d}\eta\right].$$

We substitute $H(\eta)(1-\xi(\xi+\eta)^{-1})$ for $H(\eta)\eta(\xi+\eta)^{-1}$. Then one derive:

$$u_0(\xi) = \frac{3}{4}\left[\xi + \frac{1}{2}H(\xi)\int_0^1 H(\eta)\eta\,\mathrm{d}\eta - \frac{\xi H(\xi)}{2}\int_0^1 \frac{H(\eta)}{\xi+\eta}\eta\,\mathrm{d}\eta\right].$$

This can be written as

$$u_0(\xi) = \frac{3}{4}\left[\xi + \frac{1}{2}\mathbb{C}H(\xi) - \Lambda\xi\right],$$

where

$$\mathbb{C} = \int_0^1 H(\eta)\eta\,\mathrm{d}\eta$$

and

$$\Lambda = 2\int_0^1 R_{0\infty}(\xi,\eta)\eta\,\mathrm{d}\eta\,.$$

Due to the conservation of energy law we have: $\Lambda \equiv 1$ (see Table 6.2) and, therefore,

$$u_0(\xi) = \frac{3\mathbb{C}}{8}H(\xi)\,.$$

This means that the function $u_0(\xi)$ is proportional to $H(\xi)$ at $\omega_0 = 1$. The constant $\mathbb{C}$ can easily be derived for the isotropic scattering. For this we multiply the last equation by 2ξ and integrate with respect to ξ. Then it follows that

$$\mathbb{C} = \frac{2}{\sqrt{3}}$$

where we have used the property 6.6 in Table 6.2 ($i \equiv 1$ at $\omega_0 = 1$). Therefore, we establish an important relationship:

$$u_0(\xi) = \frac{\sqrt{3}}{4}H(\xi)\,.$$

Surprisingly, two completely separate radiative transfer problems (for the determination of $H(\xi)$ and $u_0(\xi)$) have shown themselves to be interrelated. This

important theoretical result, valid for isotropic scattering, allows us to derive approximate equations for $u_0(\xi)$ using the corresponding equations for $H(\xi)$ at $\omega_0 = 1$. A number of parameterizations and approximations can be derived in such a way.

We will use the fact that $H(\xi)$ is well approximated by the function $1 + 2\xi$. Then it follows that

$$u_0(\xi) = \mathbb{Q}(1 + 2\xi)\,,$$

where $\mathbb{Q} = \sqrt{3}/4 \approx 3/7$. We use the approximate equality (the error is under 1%) here to satisfy the normalization condition (property 6.6 at $i \equiv 1$ in Table 6.2). So finally, we have:

$$u_0(\xi) = \frac{3}{7}(1 + 2\xi)\,.$$

Although this result is strictly valid only for isotropic scattering, we find that the error of this approximation is below 2% as $\xi \geq 0.2$ for arbitrary phase functions. We also obtain that $\nu = 5/14$ and $b = 15/14 \approx 1.072$. This completes our derivations for the case $\omega_0 = 1$.

6.5 Exponential approximation

6.5.1 Semi-infinite light scattering media

Asymptotic solutions for weak absorption derived above allow us to study the influence of light absorption on radiative characteristics of turbid layers for small values of the probability of photon absorption $\beta = 1 - \omega_0$ if corresponding characteristics are known for the non-absorbing case. The results are limited to a very narrow range of β (typically, $\beta < 0.0001$). There are two possibilities for avoiding this problem. One is related to the derivation of higher-order corrections to the results given above (generally, following the same path (Minin, 1988; Yanovitskij, 1997; Melnikova and Vasyliev, 2005)).

Yet another approach is based on the exponential approximation often used in diffusion theory (Rozenberg, 1962). To demonstrate this technique, we consider the case of a semi-infinite medium. Then the spherical albedo depends on the phase function $p(\theta)$ and the single scattering albedo ω_0 only. We represent the spherical albedo as a series with respect to ω_0:

$$r(\omega_0) = \sum_{n=1}^{\infty} a_n \omega_0^n$$

with

$$r(1) = \sum_{n=1}^{\infty} a_n\,.$$

However, it also follows by the definition: $r(1) = 1$, which is due to the energy conservation law. Thus, one obtains that

$$\sum_{n=1}^{\infty} a_n = 1$$

and numbers a_n can be interpreted in terms of probability theory. In particular, the value of a_1 gives us the probability that a photon will be singly scattered before escaping a turbid medium. Let us substitute the following exact expansion in the expression for $r(\omega_0)$:

$$\omega_0^n \equiv (1-\beta)^n = \sum_{j=0}^{n} (-1)^j \binom{n}{j} \beta^j ,$$

where

$$\binom{n}{j} \equiv \frac{n!}{j!(n-j)!} .$$

Then it follows that

$$r = \sum_{n=1}^{\infty} a_n \sum_{j=0}^{n} (-1)^j \binom{n}{j} \beta^j$$

or in the explicit form:

$$r = \sum_{n=1}^{\infty} a_n \left[1 - \beta n + \frac{\beta^2 n(n-1)}{2} - \frac{\beta^3 n(n-1)(n-2)}{6} + \dots \right] ,$$

where we accounted for equalities:

$$\binom{n}{0} = 1, \ \binom{n}{1} = n, \ \binom{n}{2} = \frac{n(n-1}{2}, \ \binom{n}{3} = \frac{n(n-1)(n-2)}{6} .$$

So we have:

$$r_s = 1 - \beta\overline{n} + \frac{\beta^2 \overline{nn(n-1)}}{2} - \frac{\beta^3 \overline{n(n-1)(n-2)}}{6} + \dots ,$$

where we used the normalization condition and defined the following averages:

$$\overline{n} = \sum_{n=1}^{\infty} n a_n, \ \overline{n(n-1)} = \sum_{n=1}^{\infty} n(n-1) a_n, \ \overline{n(n-1)(n-2)} = \sum_{n=1}^{\infty} n(n-1)(n-2) a_n$$

and so on. Here $\overline{n}$ is the average number of scattering events in the medium.

The derived expression for r is an exact formula. We have not made any approximations so far. Now we should make some assumptions so that we have the possibility of summing up the series. First of all, we assume that the value of $\overline{n}$ is large and, consequently, $\overline{n(n-1)} \approx \overline{n^2}$, $\overline{n(n-1)(n-2)} = \overline{n^3}$ and so on. Clearly, such an approximation is valid as $\beta \to 0$. This gives us:

$$r = 1 - \beta\overline{n} + \frac{\beta^2}{2}\overline{n^2} - \frac{\beta^3}{6}\overline{n^3} + \dots$$

or

$$r = \overline{\exp(-\beta n)}\,,$$

where we have used the expansion

$$\exp(-\beta n) = \sum_{k=0}^{\infty} \frac{(-1)^k (\beta n)^k}{k!}\,.$$

Thus, the value of r is given by

$$r = \sum_{n=1}^{\infty} \exp(-\beta n) a_n\,.$$

Applying the sum formula, we have:

$$\sum_{n=1}^{\infty} f(n) = \int_0^{\infty} f(x)\,\mathrm{d}x\,,$$

and

$$r = \int_0^{\infty} \exp(-\beta x) a(x)\,\mathrm{d}x\,.$$

One obtains, using the mean value theorem:

$$r = \exp(-\beta \overline{x})\,,$$

which is called the exponential approximation. We have also used the integral form of the normalization condition:

$$\int_0^{\infty} a(x)\,\mathrm{d}x = 1\,.$$

The problem we face now is the determination of the parameter $\overline{x}$. For this we will use the well-known asymptotic result of the radiative transfer theory derived above (see Table 6.3):

$$r = 1 - \frac{4s}{\sqrt{3}}\,,$$

which is valid as $\beta \to 0$.

The exponential approximation takes the following form as $\beta \to 0$:

$$r = 1 - \beta \overline{x}\,.$$

So, comparing these equations, we have:

$$\overline{x} = \frac{4}{k}\,,$$

where

$$k = \sqrt{3(1 - g\omega_0)\beta}$$

is the diffusion exponent of the radiative transfer theory.

Therefore, we have:

$$r = \exp\left(-\frac{4s}{\sqrt{3}}\right).$$

We notice that the combination of local optical characteristics, given by

$$y = 4\sqrt{\frac{1-\omega_0}{3(1-g\omega_0)}}$$

completely determines the spherical albedo. The value of $y = 4s/\sqrt{3}$ can be also easily measured experimentally ($y = \ln(1/r)$).

By analogy, relationships similar to the derived expression for r must be valid also for other asymptotic parameters and functions (Zege *et al.*, 1991; Kokhanovsky, 2004a). This allows us to obtain equations for the reflection function $R_\infty(\xi,\eta,\varphi)$, the plane albedo $r_{d\infty}(\xi)$, and the spherical albedo r_∞ of a semi-infinite weakly absorbing plane-parallel light scattering layer. They are shown in Table 6.4 together with correspondent equations for auxiliary constants.

Table 6.4. Asymptotic equations valid as $k \to 0$ in the framework of the exponential approximation $\left(\nu = \int_0^1 u_0(\xi)\xi^2\,\mathrm{d}\xi,\ s = \sqrt{\frac{1-\omega_0}{1-g\omega_0}}\right)$

$R_\infty(\xi,\eta,\varphi)$	$R_{0\infty}(\xi,\eta,\varphi)\exp\left\{-\frac{4su_0(\xi)u_0(\eta)}{\sqrt{3}R_{0\infty}(\xi,\eta,\varphi)}\right\}$
M	$1-\exp\left\{-\frac{8s}{\sqrt{3}}\right\}$
N	$\exp\left\{-4\sqrt{3}\nu s\right\}$
$Mu(\xi)u(\eta)$	$\left[1-\exp\left\{-\frac{8s}{\sqrt{3}}\right\}\right]u_0(\xi)u_0(\eta)$
$r_{d\infty}(\xi)$	$\exp\left\{-\frac{4su_0(\xi)}{\sqrt{3}}\right\}$
r_∞	$\exp\left\{-\frac{4s}{\sqrt{3}}\right\}$

6.5.2 Optically thick light scattering layers

The substitution of results given in Table 6.4 in general asymptotic equations presented in section 6.4.2 allows us to obtain the following analytical formula for the reflection function of an optically thick finite turbid layer valid as $\omega_0 \to 1$:

$$R(\xi,\eta,\varphi,\tau_0) = R_{0\infty}\exp(-yB(\xi,\eta,\varphi)) - te^{-x-y}u_0(\xi)u_0(\eta)\,,$$

where we introduced a new parameter $x = k\tau$ and

$$B(\xi, \eta, \varphi) = \frac{u_0(\xi)u_0(\eta)}{R_{0\infty}(\xi, \eta, \varphi)} .$$

Also we have:

$$T(\xi, \eta) = tu_0(\xi)u_0(\eta) ,$$

where the global transmittance t is given by:

$$t = \frac{\sinh y}{\sinh(x + by)} .$$

Other radiative transfer characteristics calculated in the framework of this approximation are given in Table 6.5 (Kokhanovsky, 2004a).

Table 6.5. Radiative transfer characteristics in the framework of the exponential approximation

$$(r_{d\infty}(\xi) = \exp\left[-yu_0(\xi)\right],\ u_0(\xi) = \frac{3}{7}(1 + 2\xi),$$
$$r_\infty = e^{-y},\ x = k\tau,\ y = k\tau,\ k = \sqrt{3(1 - \omega_0)(1 - g)},\ b = 15/14 \approx 1.072).$$

Radiative characteristic	Symbol	Equation
Plane albedo	$r_d(\xi)$	$r_{d\infty}(\xi) - (r_\infty - r)u_0(\xi)$
Spherical albedor	r	$r_\infty - t\exp(-x - y)$
Diffuse transmittance	$t_d(\xi)$	$tu_0(\xi)$
Global transmittance t	$\frac{\sinh(y)}{\sinh(x + by)}$	

The exponential approximation can be used for the rapid estimations of light reflection from cloudy media and also for speeding up cloud retrieval algorithms (Kokhanovsky *et al.*, 2003). The range of the applicability of the exponential approximation with respect to smaller values of τ_0 and ω_0 can be extended using correction terms derived from the numerical solution of the radiative transfer equation. In particular, Kokhanovsky and Rozanov (2003) found that the accuracy of the exponential approximation for cloudy media can be increased using following substitutions: $B \to (1 - 0.05y)B$, $t \to t - \Delta$, where

$$\Delta = \frac{a_1 + a_2\xi\eta + a_3\xi^2\eta^2}{\tau^3} \exp(x)$$

and $a_1 = 4.86$, $a_2 = -13.08$, $a_3 = 12.76$. Therefore, the final equation for the reflection function can be written as

$$R(\xi, \eta, \varphi, \tau_0) = R_{0\infty}(\xi, \eta, \varphi) \exp(-y(1-0.05y)B(\xi, \eta, \varphi)) - (t-\Delta)e^{-x-y}u_0(\xi)u_0(\eta) .$$

This formula gives the so-called modified exponential approximation (MEA) for the reflection function of weakly absorbing optically thick turbid layers. MEA can be used at much larger values of β as compared to the linear approximation presented in section 6.4.3. We show the accuracy of MEA in Figs. 6.2 and 6.3 for the nadir observation conditions, the solar zenith angle 60° and wavelengths 550 nm and 1550 nm. It was assumed that the light scattering medium is composed of water droplets with the effective radius 4, 6, and 16 μm (Kokhanovsky and Rozanov, 2003). The gamma particle size distribution with the effective variance 38% (Kokhanovsky, 2004a) was used to model the polydispersity of droplets in clouds.

One concludes from Figs. 6.2 and 6.3 that the top-of-atmosphere reflectance over cloudy scenes can be accurately modeled in the framework of the MEA in the visible and also in the near-infrared for optically thick clouds having different microstructure. The accuracy of MEA decreases with $\beta = 1 - \omega_0$. Then general asymptotic formulas valid at arbitrary β (see section 6.4.2) must be used. However, calculations become much more involved as compared to the case of weak absorption considered in this section (King and Harshvardhan, 1986; Nakajima and King, 1992; Wauben, 1992).

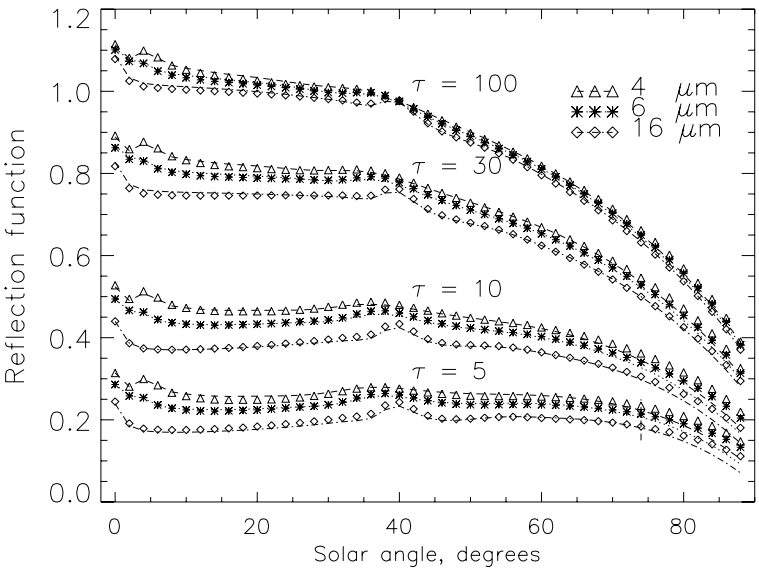

Fig. 6.2. Dependence of the reflection function of a cloud on the solar zenith angle for several values of cloud optical thickness τ and effective radius of droplets $a_{ef} = 4$, 6, and 16 μm for the nadir observation and wavelength $\lambda = 0.65$ μm (Kokhanovsky and Rozanov, 2003)

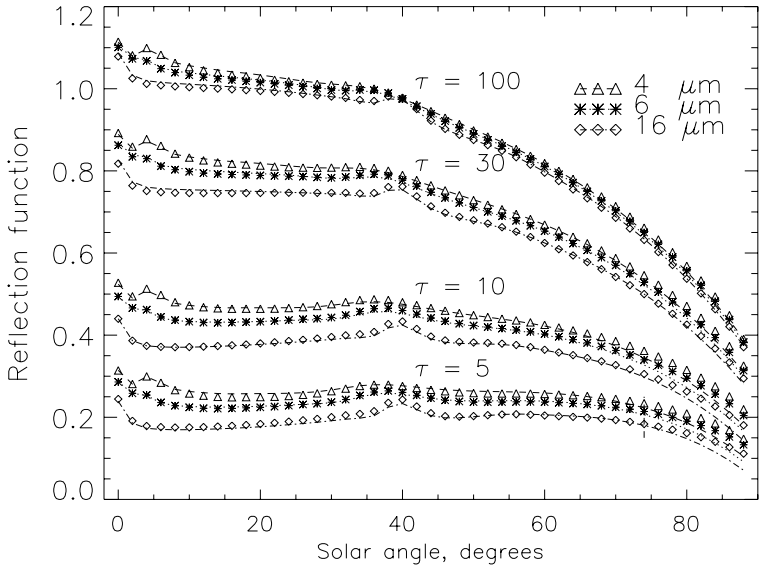

Fig. 6.3. The same as in Fig. 6.2 except at $\lambda = 1.55\,\mu\text{m}$ (Kokhanovsky and Rozanov, 2003)

6.6 Conclusion

We have reviewed here the asymptotic radiative transfer theory as applied to the calculation of light reflectance and transmittance by optically thick turbid media. Derivations as presented by Sobolev (1984) are closely followed. This theory has a number of important applications in atmospheric remote sensing as described by Danielson *et al.* (1969), Zege and Katsev (1974), Melnikova and Minin (1977), Zege (1982), King (1987), Zege *et al.* (1991), Kokhanovsky *et al.* (2003), and Kokhanovsky (2004a). We hope that this review will lead to a much wider spread of this theory for the solution of direct and inverse problems of modern light scattering media optics and spectroscopy.

A historical comment must be added. Asymptotic equations for reflection and transmission functions of optically thick layers were derived for the first time by T. A. Germogenova (1961) using a different set of arguments compared to those given here. Later main equations were re-derived by van de Hulst (1968a, 1980) and also independently by Sobolev (1968, 1975, 1984). The vertical inhomogeneity of a scattering layer in the framework of ARTT was considered by Germogenova and Konovalov (1974), Ivanov (1976), Minin (1988), and Yanovitskij (1971, 1997).

The exponential approximation was initially developed by Rozenberg (1962) and improved by Bushmakova *et al.* (1971) and Zege *et al.* (1991). Kokhanovsky and Rozanov (2004a, 2004b) extended the theory to the case of radiative transfer in the gaseous absorption band. Kokhanovsky (2003) used ARTT to study light reflection and transmission by horizontally inhomogeneous turbid media.

The account for the vector properties of light has been performed by Domke (1978a, 1978b) (see also Hovenier *et al.* (2005)).

Numerical aspects of the problem were thoroughly treated by van de Hulst (1968b), Dlugach and Yanovitskij (1974), Konovalov (1974, 1975), Nakajima and King (1992), and Wauben (1992).

Acknowledgements

The author is grateful to T. A. Germogenova, I. L. Katsev, V. V. Rozanov, and E. P. Zege for important discussions of the asymptotic radiative transfer theory.

References

Bushmakova, O. V., E. P. Zege, I. L. Katsev, 1971: On asymptotical equations for brightness coefficients of thick layers of a scattering medium, *Doklady, Acad. Sci. Belarussian SSR*, **4**, 309–311.

Bushmakova, O. V., E. P. Zege, I. L. Katsev, and N. V. Konovalov, 1979: Reflection and transmission of light by an optically thick layer, *Zurnal Appl. Spectr.*, **30**, 900–907.

Chandrasekhar, S., 1950: *Radiative Transfer*, Oxford University Press, Oxford.

Danielson, R. E., *et al.*, 1969: The transfer of visible radiation through clouds, *J. Atmos. Sci.*, **26**, 1078–1087.

de Rooij, W.A., 1985: Reflection and transmission of polarized light by planetary atmospheres. PhD thesis, Free University of Amsterdam, Amsterdam.

Dlugach, I. M., and E. G. Yanovitskij, 1974: The optical properties of Venus and the Jovian planets, II. Methods and results of calculations of the intensity of radiation diffusely reflected from semi-infinite homogeneous atmospheres, *Icarus*, **22**, 66–81.

Domke, H., 1978a: Linear Fredholm integral equations for radiative transfer problems in finite plane-parallel media. I. Imbedding in an infinite medium, *Astron. Nachr.*, **299**, 87–93.

Domke, H., 1978b: Linear Fredholm integral equations for radiative transfer problems in finite plane-parallel media. II. Imbedding in a semi-infinite medium, *Astron. Nachr.*, **299**, 95–102.

Germogenova, T. A., 1961: On the properties of the transport equation for a plane-parallel layer, *J. Appl. Math. Comp. Phys.*, **1**, 928–946.

Germogenova, T. A., and N. V. Konovalov, 1974: Asymptotic characteristic solutions of transport equation for the inhomogeneous slab problem, *J. Appl. Math. Comp. Phys.*, **14**, 928–946.

Hovenier, J. W., C. Van der Mee, H. Domke, 2005: *Transfer of Polarized Light in Planetary Atmospheres: Basic Concepts and Practical Methods*, Elsevier, Amsterdam.

Ivanov, V. V., 1976: Radiative transfer in a multilayered optically thick atmosphere, II, *Tr. Astron. Observ. LGU*, **32**, 23–39.

King, M. D. and Harshvardhan, 1986: Comparative accuracy of selected multiple scattering approximations, *J. Atmos. Sci.*, **43**, 784–801.

King, M.D., 1987: Determination of the scaled optical thickness of clouds from reflected soar radiation measurements, *J. Atmos. Sci.*, **44**, 1734–1751.

Kokhanovsky, A. A., 2003: The influence of the horizontal inhomogeneity on radiative characteristics of clouds: an asymptotic case study, *IEEE Transactions, Geosciences and Remote Sensing*, **41**, 817–825.

Kokhanovsky, A. A., 2004a: *Light Scattering Media Optics*, Springer-Verlag, Berlin.

Kokhanovsky, A. A., 2004b: Reflection of light from nonabsorbing semi-infinite cloudy media: a simple approximation, *J. Quant. Spectr. Rad. Transfer*, **85**, 25–33.

Kokhanovsky, A. A., 2006: *Cloud Optics*, Springer-Verlag Berlin.

Kokhanovsky, A. A., and V. V. Rozanov, 2003: The reflection function of optically thick weakly absorbing turbid layers: a simple approximation, *J. Quant. Spectr. Rad. Transfer*, **77**, 165–175.

Kokhanovsky, A. A., and V. V. Rozanov, 2004a: The physical parameterization of the top-of-atmosphere reflection function for a cloudy atmosphere-underlying surface system: the oxygen A-band study, *J. Quant. Spectr. Rad. Transfer*, **85**, 35–55.

Kokhanovsky, A. A., and V. V. Rozanov, 2004b: Simple approximate solutions of the radiative transfer equation for a cloudy atmosphere, in *Remote Sensing of Clouds and the Atmosphere, IX*, K. P. Schafer *et al.* (eds), (Proc. of SPIE, v. 5571), SPIE, Bellingham, WA, 86–93.

Kokhanovsky, A. A., V. V. Rozanov, E. P. Zege, H. Bovensmann, and J. P. Burrows, 2003: A semi-analytical cloud retrieval algorithm using backscattering radiation in 04.–2.4 μm spectral range, *J. Geophys. Res., D*, **108**, 10.1029/2001JD001543.

Konovalov, N. V., 1974: Asymptotical properties of the solution of one-speed transport equation in a uniform plane-parallel layer. The problem with the azimuthal dependence, Reprint no. 65, Institute of Applied Mathematics, Moscow.

Konovalov, N. V., 1975: On the range of applicability of asymptotical formulae for calculations of monochromatic radiation in a nonuniform optically thick plane-parallel layer, *Izv. AN SSSR, FAO*, **11**, 1263–1271.

Liou, K. N., 2002: *An Introduction to Atmospheric Radiation*, Academic Press, New York.

Melnikova, I. N., and Minin, I. N., 1977: On the monochromatic radiative transfer in cloud layers, *Izvestiya, Atmospheric and Oceanic Physics*, **13**, 3, 254–263.

Melnikova, I. N., and A. V. Vasilyev, 2005: *Short-Wave Solar Radiation in the Earth's Atmosphere*, Berlin, Springer.

Minin, I. N., 1988: *Radiative Transfer Theory in Planetary Atmospheres*, Nauka, Moscow.

Mishchenko, M. I., J. M. Dlugach, E. G. Yanovitskij, and N. T. Zakharova, 1999: Bidirectional reflectance of flat, optically thick particulate layers: An efficient radiative transfer solution and applications to snow and soil surfaces. *J. Quant. Spectrosc. Radiat. Transfer*, **63**, 409–432.

Nakajima, T., and M. Tanaka, 1988: Algorithms for radiative intensity calculations in moderately thick atmospheres using a truncation approximation, *J. Quant. Spectr. Rad. Transfer*, **40**, 51–69.

Nakajima, T., and M. D. King, 1992: Asymptotic theory for optically thick layers: application to the discrete ordinates method, *Appl. Opt.*, **31**, 7669–7683.

Nikolaeva, O. V., L. P. Bass, T. A. Germogenova, A. A. Kokhanovsky, V. S. Kuznetsov, B. Mayer, 2005: The influence of neighbouring clouds on the clear sky reflectance studied with the 3–D transport code RADUGA, *J. Quant. Spectr. Rad. Transfer*, **94**, 405–424.

Rozenberg, G. V., 1962: Light characteristics of thick layers of a weakly absorbing scattering medium, *Doklady, Acad. Sci. USSR*, **145**, 775–777.

Siewert, C. E., 2000: A discrete-ordinates solution for radiative-transfer models that include polarization effects, *J. Quant. Spectr. Rad. Transfer*, **64**, 227–254.

Sobolev, V. V., 1968: The diffusion of radiation in an optically thick medium under anisotropic scattering conditions, *Doklady, Academy of Sciences of USSR*, **1**, 41–44.

Sobolev, V.V., 1975: *Light Scattering in Planetary Atmospheres*, Pergamon Press, New York.

Sobolev, V. V., 1984: Integral relations and asymptotic expressions in the theory of radiative transfer, *Astrofizika*, **20**, 123–132.

Stokes, G. G., 1852: On the composition and resolution of streams of polarized light from different sources, *Trans. Camb. Phil. Soc.*, **9**, 399–416.

Thomas, G., and K. Stamnes, 1999: *Radiative Transfer in the Atmosphere and Ocean*, Cambridge University Press, Cambridge.

van de Hulst, H. C., 1968a: Radiative transfer in thick atmospheres with an arbitrary scattering function, *Bull. Astr. Netherlands*, **20**, 77–90.

van de Hulst, H. C., 1968b: Asymptotic fitting, a method for solving anisotropic transfer problems in thick layers, *J. Comput. Physics*, **3**, 291–306.

van de Hulst, H. C., 1980: *Multiple Light Scattering: Tables, Formulas and Applications*, Academic Press, New York.

Wauben, W. M. F., 1992: *Multiple scattering of polarized radiation in planetary atmospheres*, PhD thesis, Free University of Amsterdam, Amsterdam.

Yanovitskij, E. G., 1971: Anisotropic light scattering in inhomogeneous atmosphere, I, *Astronom. Zurnal*, **48**, 323–332.

Yanovitskij, E. G., 1997: *Light Scattering in Inhomogeneous Atmospheres*, Springer-Verlag, New York.

Zege, E. P., 1982: Engineering techniques to calculate light fields in multiple light scattering conditions, in *Light Propagation in a Disperse Medium*, A. P. Ivanov (ed.), Nauka and Tekhnika, Minsk, 84–105.

Zege, E. P., and I. L. Katsev, 1974: On the relationship between nonstationary radiation fields in absorbing and nonabsorbing media, *Astrofizika*, **2**, 219–225.

Zege, E. P., A. P. Ivanov, and I. L. Katsev, 1991: *Image Transfer through a Scattering Medium*, Springer-Verlag, New York.

7 Multiple scattering of polarized light in turbid media with large particles

Evgenii E. Gorodnichev, Alexander I. Kuzovlev, and Dmitrii B. Rogozkin

7.1 Introduction

In the recent years, the polarization effects in multiply scattering media with large-scale (size a is larger than wavelength λ) inhomogeneities has been of special interest in connection with many applications. A large number of experimental and theoretical studies have been devoted to this problem [1]–[31]. New effects were revealed, in particular, the difference in the depolarization rates between linearly and circularly polarized beams of light [7]–[10],[13, 31].

In most theoretical studies dealing with multiple scattering of polarized light in turbid media [14]-[31], methods of numerical calculations are generally discussed. A Monte Carlo approach is the main tool in computational investigations of light polarization in multiply scattering media [14, 22–24, 28, 30, 31]. Simple analytical results that could explain basic experimentally observed effects were not available until recently. Within the framework of simplifying assumptions, the first results along this line were obtained in Refs [18, 25],[32]–[39].

In this study, we consider the depolarization of light in optically isotropic turbid media with large inhomogeneities. Single scattering of light by large-scale inhomogeneities occurs predominantly through small angles. In this case, two different mechanisms of depolarization, viz-, the 'geometrical' mechanism and the 'dynamical' one [33, 34, 36], can be distingnished. The 'geometrical' mechanism is due to the Rytov rotation [40–42]. The plane of polarization turns simultaneously with the ray of light. The wave remains linearly polarized along the overall path of propagation. The depolarization observed in multiple scattering of linearly polarized light results from superposition of randomly oriented polarizations of the different rays. The 'dynamical' mechanism [43] is due to the difference between the amplitudes $A_{\|}$ and $A_{\perp}$ of the cross-polarized scattered waves ($A_{\|}$ and $A_{\perp}$ are the scattering amplitudes of waves polarized, respectively, parallel and perpendicularly to the scattering plane). For small angles, the amplitudes $A_{\|}$ and $A_{\perp}$ differ weakly [44]. This permits us to develop a procedure for decoupling the vector radiative transfer equation. This procedure is based on selecting the basic and additional modes. In the case of single scattering through small angles the interaction between the basic polarization modes appears to be

weak. To a first approximation we can neglect this interaction. In the succeeding approximation, the interaction between the basic modes results in the excitation of the additional modes (or overtones). Allowance for the overtones makes it possible to describe in detail the polarization state of multiply scattered light deep in the medium. With the method proposed, the polarization state of multiply scattered light is calculated for two limiting cases (namely, diffusive propagation and small-angle multiple scattering). Most attenuation is concentrated on the presentation of explicit analytical results that describe the polarization state of scattered light.

7.2 General relations

Let a wide polarized beam of light be incident on a medium normally to its surface. The medium is assumed to be a statistically isotropic disordered ensemble of large-scale scatterers. The polarization state of scattered light is generally described by the four Stokes parameters

$$\hat{S} = \begin{pmatrix} I \\ Q \\ U \\ V \end{pmatrix} \tag{7.1}$$

which obey the vector radiative transfer equation [45–47],

$$\left\{ \mu \frac{\partial}{\partial z} + \sigma_{tot} \right\} \hat{S}(z, \mathbf{n}) = \sigma \int d\mathbf{n}' \hat{d}(\mathbf{n}, \mathbf{n}') \hat{S}(z, \mathbf{n}') \tag{7.2}$$

Here, σ_{tot} is the coefficient of total attenuation, σ is the scattering coefficient, and $\sigma_a = \sigma_{tot} - \sigma$ is the absorption coefficient.

The Stokes parameters in eq. (7.2) are defined in the system of unit vectors $\{\mathbf{e}_\parallel = \partial\mathbf{n}/\partial\theta,\ \mathbf{e}_\perp = [\mathbf{e}_\parallel, \mathbf{n}],\ \mathbf{n}\}$, $\mathbf{n} = (\sin\theta\cos\varphi,\ \sin\theta\sin\varphi,\ \cos\theta)$ [47]. The vector $\mathbf{e}_\parallel$ lies in the plane formed by the vectors $\mathbf{n}_0$ and $\mathbf{n}$ ($\mathbf{n}_0$ is the internal normal to the surface); the vector $\mathbf{e}_\perp$ is perpendicular to this plane (Fig. 7.1). The plane $\{\mathbf{n}, \mathbf{n_0}\}$ is usually used as the reference plane for the description of the polarization state of light.

The matrix $\hat{d}(\mathbf{n}, \mathbf{n}')$ in (7.2) is related to the scattering matrix $\hat{d}(\mathbf{nn}')$ in the scattering plane (i.e., in the plane formed by the vectors $\mathbf{n}$ and $\mathbf{n}'$) as follows:

$$\hat{d}(\mathbf{n}, \mathbf{n}') = \hat{L}(\pi - \beta)\hat{d}(\mathbf{nn}')\hat{L}(-\beta') \tag{7.3}$$

The matrix

$$\hat{L}(-\beta') = \begin{pmatrix} 1 & 0 & 0 & 0 \\ 0 & \cos 2\beta' & -\sin 2\beta' & 0 \\ 0 & \sin 2\beta' & \cos 2\beta' & 0 \\ 0 & 0 & 0 & 1 \end{pmatrix} \tag{7.4}$$

describes the transformation of the Stokes parameters of the incident light in going from the system of unit vectors ($\mathbf{e'}_\parallel$, $\mathbf{e'}_\perp$, $\mathbf{n}'$) to the scattering plane (see

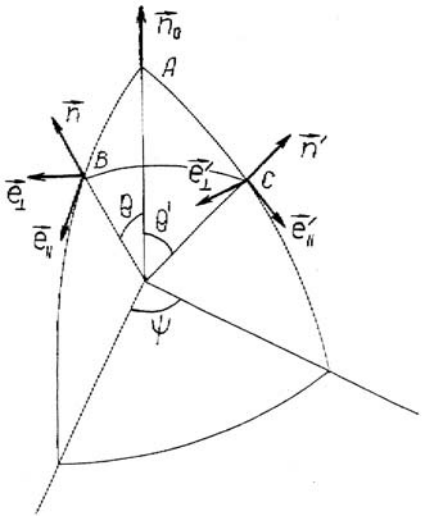

Fig. 7.1.

Fig. 7.1). The matrix $\hat{L}(\pi - \beta)$, corresponding to the inverse transformation from the scattering plane to the system of unit vectors $(\mathbf{e}_\parallel, \mathbf{e}_\perp, \mathbf{n})$ related to the direction of propagation of the scattered light, is defined similarly to (7.4). The angles entering into eq. (7.3) are defined by the formulas

$$\cos 2\beta = 1 - \frac{2(1-\mu'^2)(1-\cos^2\psi)}{1-(\mathbf{n}\mathbf{n}')^2}$$

$$\sin 2\beta = \frac{2\sqrt{1-\mu'^2}(\mu'\sqrt{1-\mu^2} - \mu\sqrt{1-\mu'^2}\cos\psi)\sin\psi}{1-(\mathbf{n}\mathbf{n}')^2}$$

$$\mathbf{n}\mathbf{n}' = \mu\mu' + \sqrt{(1-\mu^2)(1-\mu'^2)}\cos\psi, \quad \mu = \cos\theta, \quad \mu' = \cos\theta', \quad \psi = \varphi - \varphi'.$$

Functions $\cos 2\beta$ and $\sin 2\beta$ differ from functions $\cos 2\beta$ and $\sin 2\beta$ by the substitution of μ for μ'.

For an optically isotropic medium, the scattering matrix $\hat{d}(\mathbf{n}\mathbf{n}')$ appearing in eq. (7.3) has the form (see, for example, [1]):

$$\hat{d}(\mathbf{n}\mathbf{n}') = \begin{pmatrix} a_1 & b_1 & 0 & 0 \\ b_1 & a_2 & 0 & 0 \\ 0 & 0 & a_3 & b_2 \\ 0 & 0 & -b_2 & a_4 \end{pmatrix} \tag{7.5}$$

For the forward scattering ($\mathbf{n} = \mathbf{n}'$), the matrix $\hat{d}$ is diagonal: $\hat{d}(\mathbf{n}\mathbf{n}' = 1) = \mathrm{diag}(a_1, a_2, a_2, a_4)$; for spherical particles, $\hat{d}(1) = a_1\mathrm{diag}(1,1,1,1)$ [1]. Quantity $a_1(\mathbf{n}\mathbf{n}')$ is the phase function of single scattering; it is normalized by condition

$$\int d\mathbf{n}' a_1(\mathbf{n}\mathbf{n}') = 1 \tag{7.6}$$

The vector radiative transfer equation for the other Stokes parameters (I, Q, U) can be transformed as follows.

The intensity $I(\mathbf{r},\mathbf{n})$ and the fourth Stokes parameter $V(\mathbf{r},\mathbf{n})$ are a scalar and a pseudoscalar, respectively [48]. Under rotations, they are transformed via themselves. In contrast, the second and third Stokes parameters (Q and U, respectively) are expressed in terms of each other under spatial rotations. This fact is essential for description of the scattering process, because matrix (7.3) includes two rotations (these rotations are described by the $\hat{L}$ matrices entering into eq. (7.3)). These rotations transform the system of unit vectors $(\mathbf{e}'_{\parallel}, \mathbf{e}'_{\perp}, \mathbf{n}')$, in which the Stokes vector $\hat{S}(\mathbf{r},\mathbf{n}')$ is defined, to the system $(\mathbf{e}_{\parallel}, \mathbf{e}_{\perp}, \mathbf{n})$, to which the $\hat{S}(\mathbf{r},\mathbf{n})$ vector is related. Therefore, even if we assume the scattering matrix (7.5) to be diagonal and neglect the difference between the diagonal elements a_2 and a_3, the Stokes parameters Q and U are transformed via each other.

In order to avoid coupling between the Stokes parameters Q and U we introduce new quantities [49, 50]:

$$I_{\pm 2} = \frac{1}{\sqrt{2}}(Q \mp iU) \tag{7.7}$$

Unlike the Stokes parameters Q and U, either quantity defined by equality (7.7) is transformed via itself under rotations.

With regard to the preceding, in order to describe the polarization state of light, we will use the vector

$$\hat{I} = \begin{pmatrix} \frac{1}{\sqrt{2}}(Q - iU) \\ I \\ V \\ \frac{1}{\sqrt{2}}(Q + iU) \end{pmatrix} = \begin{pmatrix} I_2 \\ I_0 \\ I_{-0} \\ I_{-2} \end{pmatrix} \tag{7.8}$$

The radiative transfer equation for $\hat{I}$ has the form

$$\left\{\mu\frac{\partial}{\partial z} + \sigma_{tot}\right\}\hat{I}(z,\mathbf{n}) = \sigma\int d\mathbf{n}'\hat{\hat{d}}(\mathbf{n},\mathbf{n}')\hat{I}(z,\mathbf{n}') \tag{7.9}$$

where the scattering matrix $\hat{\hat{d}}(\mathbf{n},\mathbf{n}')$ is given by ($a_{\pm} = (a_2 \pm a_3)/2$)

$$\hat{\hat{d}}(\mathbf{n},\mathbf{n}') = \begin{pmatrix} a_+\exp(2i\chi_+) & \frac{b_1}{\sqrt{2}}\exp(-2i\beta) & \frac{ib_2}{\sqrt{2}}\exp(-2i\beta) & a_-\exp(2i\chi_-) \\ \frac{b_1}{\sqrt{2}}\exp(-2i\beta') & a_1 & 0 & \frac{b_1}{\sqrt{2}}\exp(2i\beta') \\ \frac{ib_2}{\sqrt{2}}\exp(-2i\beta') & 0 & a_4 & -\frac{ib_2}{\sqrt{2}}\exp(-2i\beta') \\ a_-\exp(-2i\chi_-) & \frac{b_1}{\sqrt{2}}\exp(2i\beta) & -\frac{ib_2}{\sqrt{2}}\exp(-2i\beta) & a_+\exp(-2i\chi_+) \end{pmatrix} \tag{7.10}$$

Angles $\chi_{\pm}$ appearing in matrix (7.10) are defined by formula

$$\chi_{\pm} = \pi - (\beta \pm \beta'),$$

Let us clarify the transformations from eq. (7.1) to eq. (7.8). The transformation from eq. (7.1) to $\hat{I}$

$$\begin{pmatrix} \frac{1}{\sqrt{2}}(Q - iU) \\ I \\ V \\ \frac{1}{\sqrt{2}}(Q + iU) \end{pmatrix} = \hat{M} \begin{pmatrix} I \\ Q \\ U \\ V \end{pmatrix}$$

is performed with the unitary matrix

$$\hat{M} = \frac{1}{\sqrt{2}} \begin{pmatrix} 0 & 1 & -i & 0 \\ \sqrt{2} & 0 & 0 & 0 \\ 0 & 0 & 0 & \sqrt{2} \\ 0 & 1 & i & 0 \end{pmatrix} \tag{7.11}$$

Therefore the matrix $\hat{\tilde{d}}(\mathbf{n}, \mathbf{n}')$ is related to the matrix $\hat{d}(\mathbf{n}, \mathbf{n}')$ (7.3) as follows:

$$\hat{\tilde{d}} = \hat{M} \hat{d} \hat{M}^{-1} \tag{7.12}$$

Instead of formula (7.3), we have

$$\hat{\tilde{d}}(\mathbf{n}, \mathbf{n}') = \hat{\tilde{L}}(\pi - \beta) \hat{\tilde{d}}(\mathbf{n}\mathbf{n}') \hat{\tilde{L}}(-\beta') \tag{7.13}$$

where

$$\hat{\tilde{d}}(\mathbf{n}\mathbf{n}') = \begin{pmatrix} a_+ & \frac{b_1}{\sqrt{2}} & \frac{ib_1}{\sqrt{2}} & a_- \\ \frac{b_1}{\sqrt{2}} & a_1 & 0 & \frac{b_1}{\sqrt{2}} \\ \frac{ib_2}{\sqrt{2}} & 0 & a_4 & -\frac{ib_2}{\sqrt{2}} \\ a_- & \frac{b_1}{\sqrt{2}} & -\frac{ib_2}{\sqrt{2}} & a_+ \end{pmatrix} \tag{7.14}$$

and

$$\hat{\tilde{L}}(-\beta') = \begin{pmatrix} \exp(-2i\beta') & 0 & 0 & 0 \\ 0 & 1 & 0 & 0 \\ 0 & 0 & 1 & 0 \\ 0 & 0 & 0 & \exp(2i\beta') \end{pmatrix} \tag{7.15}$$

Note, that eq. (7.13) coincides with eq. (7.10).

Expression (7.10) shows clearly the advantage of representation (7.8). Single scattering from large-scale inhomogeneities occurs mainly through small angles. In this case, the off-diagonal elements of matrix (7.10) are much smaller than the diagonal elements of this matrix (see, for example, [18, 34]). In the first approximation, we can neglect the off-diagonal elements. In this approximation, vector equation (7.9) decomposes into the independent equations for each component of the $\hat{I}$ vector (7.8). The mutual coupling of Q and U under rotations in space is already excluded because we use representation (7.7). Coupling between the equations for the quantities I_n ($n = \pm 0, \pm 2$) arises only in the succeeding approximation, where the off-diagonal elements of matrix (7.10) are taken into account.

7.3 Polarization mode approximation

The further approximations in eq. (7.9) are based on the properties of the scattering matrix of large-scale inhomogeneities.

The properties of the scattering matrix of large inhomogeneities (spherical and nonspherical) have been discussed in many publications in the last few years (see, for example, [1, 25, 51]). The interest in this problem is caused by wide applications of optical methods for studying natural scattering media (aerosols, seawater, biological tissues, etc.). On the basis of measurements and numerical calculations, the most properties of the elements a_i and b_i were determined [1].

For spherical scatterers of a given size, the matrix elements a_i and b_i are expressed in terms of the amplitudes $A_\parallel$ and $A_\perp$ of single scattered cross-polarized waves [44]

$$a_1(\cos\gamma) = a_2(\cos\gamma) = \frac{n_0}{2\sigma}(|A_\parallel(\cos\gamma)|^2 + |A_\perp(\cos\gamma)|^2) \tag{7.16}$$

$$a_3(\cos\gamma) = a_4(\cos\gamma) = \frac{n_0}{\sigma}\mathrm{Re}A_\parallel(\cos\gamma)A_\perp^*(\cos\gamma) \tag{7.17}$$

$$b_1(\cos\gamma) = \frac{n_0}{2\sigma}(|A_\parallel(\cos\gamma)|^2 - |A_\perp(\cos\gamma)|^2) \tag{7.18}$$

$$b_2(\cos\gamma) = \frac{n_0}{\sigma}\mathrm{Im}A_\parallel^*(\cos\gamma)A_\perp(\cos\gamma) \tag{7.19}$$

where n_0 is the number of scattering particles per unit volume. According to eqs (7.16)–(7.19), the off-diagonal elements of matrix (7.14) are determined by eq. (7.18) and by

$$\frac{1}{2}(a_2(\cos\gamma) - a_3(\cos\gamma)) = \frac{n_0}{2\sigma}|A_\parallel(\cos\gamma) - A_\perp(\cos\gamma)|^2 \tag{7.20}$$

As single scattering by large inhomogeneities occurs predominantly through small angles ($1 - \cos\gamma \ll 1$), the difference between amplitudes $A_\parallel$ and $A_\perp$ is much less than each of them [44]. Therefore the off-diagonal elements b_1 and a_- in eq. (7.10) (or in eq. (7.14)) appears to be small as compared to the diagonal elements of the corresponding scattering matrix. In many practical cases, the off-diagonal matrix element b_2 that is responsible for interaction between the linear and circular polarizations can be neglected [1].

The order of ratio between the off-diagonal elements and the diagonal ones can be estimated as follows.

In the case of weak scatterers (it is the case of the Born or Rayleigh–Gans approximation [44] $ka|n-1| \ll 1$, where $k = 2\pi/\lambda$, n is the relative refractive index of the scattering particles, a is their radius), the amplitudes $A_\parallel$ and $A_\perp$ are related by the following equation [44]

$$A_\parallel(\cos\gamma) = A_\perp(\cos\gamma)\cos\gamma \tag{7.21}$$

In accordance with eq. (7.21), the off-diagonal element b_2 is equal to zero, $b_2 = 0$. The elements b_1 and a_- are of the following order of magnitude [1, 44]

$$b_1/a_1 \sim \gamma^2, \quad (a_2 - a_3)/a_1 \sim \gamma^4 \tag{7.22}$$

The estimations (7.22) hold also true in the general case of a statistically isotropic ensemble of strong ('non-Born') inhomogeneities. This can be easily verified by expanding the scattering matrix elements in generalized spherical functions [1, 49]. In the 'non-Born' case, as follows from the abovementioned expansions,

$$b_2/a_4 \sim \gamma^2 \tag{7.23}$$

The angular dependence of the scattering matrix elements for various media is the subject of a large body of experimental and theoretical works [1,24,44–46, 51,52]. The effects associated with sizes and shapes of scattering particles, their refractive index and the spread in these parameters are studied with a number of numerical methods [1,24,51]. For spherical particles, the matrix elements can be calculated with the use of eqs (7.16)–(7.19) and the Mie formulas for the scattering amplitudes $A_\parallel$ and $A_\perp$ [44].

The results of numerical calculations of the matrix elements for several scattering systems are presented in Figs 7.2–7.4. These results confirm the validity of eq. (7.22). In the region of small angles the off-diagonal elements of the scattering matrix eq. (7.14) are small as compared with the phase function $a_1(\cos\gamma)$; the value of the diagonal elements are close to $a_1(\cos\gamma)$ (for spherical particles, $a_1 - a_+ = (a_1 - a_4)/2 = a_-$). The results derived from eq. (7.21) are shown in Figs 7.2–7.4 as well.

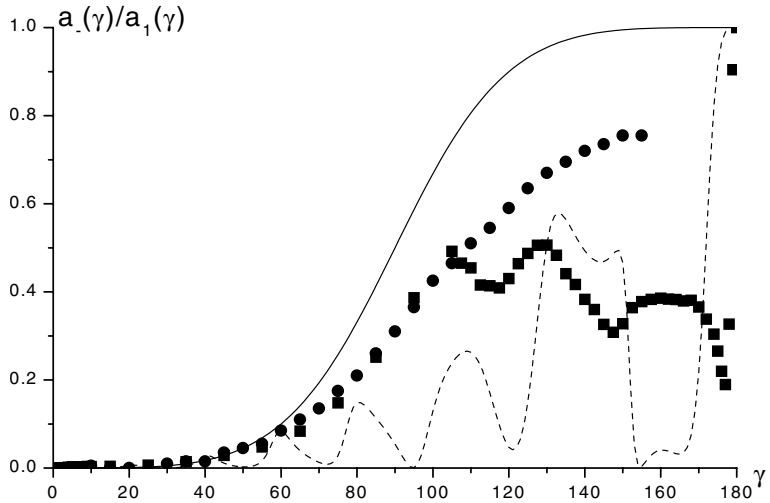

Fig. 7.2. Ratio $a_-(\cos\gamma)/a_1(\cos\gamma)$) as a function of scattering angle γ. Latex spheres in water ($n = 1.19$, $ka = 10$ (dashed line)); *cloud 1* [52] (■); *sea water* [2] (•). Solid line corresponds to the case of weak scattering (see eq. (7.21))

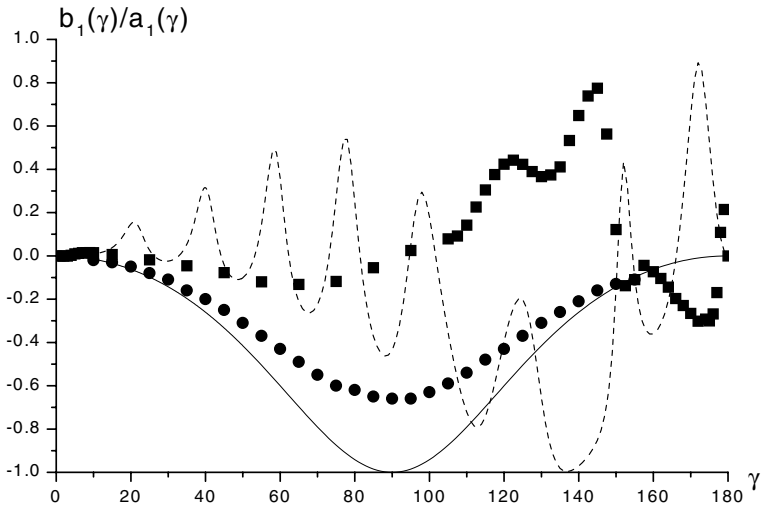

Fig. 7.3. Ratio $(b_1(\cos\gamma)/a_1(\cos\gamma))$ as a function of scattering angle γ. Latex spheres in water ($n = 1.19$, $ka = 10$ (dashed line)); *cloud 1* [52] (■); *sea water* [2] (•). Solid line corresponds to the case of weak scattering (see eq. (7.21))

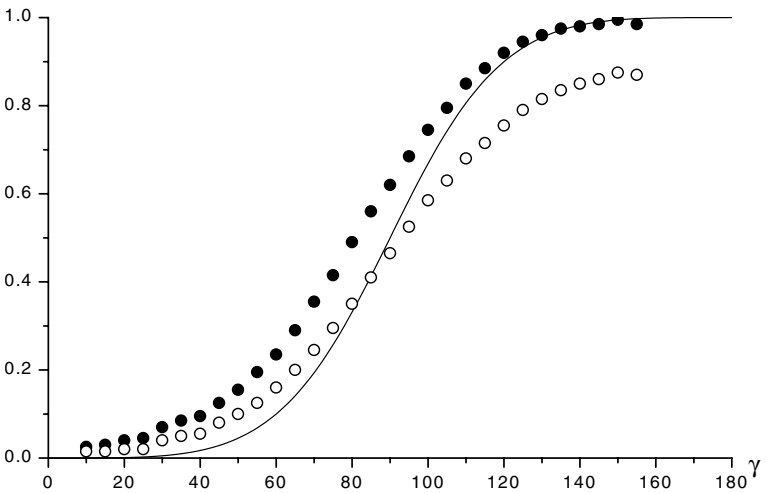

Fig. 7.4. Ratios $(a_1(\cos\gamma) - a_+(\cos\gamma))/a_1(\cos\gamma))$ (•) and $(a_1(\cos\gamma) - a_4(\cos\gamma))/(2a_1(\cos\gamma))$ (○) as functions of scattering angle γ. *Sea water* [2]. Solid line corresponds to the case of weak scattering (see eq. (7.21))

There are a great deal of numerical and experimental data concerning the phase function of large-scale inhomogeneities [1, 2, 45, 51, 52]. In particular, the phase function of particles of a given radius and a given refractive index may be approximated by [35, 44, 53]

$$a_1(\cos\gamma) = \frac{\alpha}{(\gamma_0^2 + 2(1-\cos\gamma))^2} \tag{7.24}$$

where γ_0 is a characteristic angle of single scattering; for weak scatterers ($ka|n-1| \ll 1$), $\gamma_0 \approx 1/(ka)$, otherwise $\gamma_0 \approx 2|n-1|$. Under the assumption that $\gamma_0 \ll 1$, the coefficient α entering into eq. (7.24) is equal to

$$\alpha \approx \frac{\gamma_0^2}{\pi}$$

The results of numerical calculations of $a_1(\cos\gamma)$ with the Mie formulas and the approximate dependence (7.24) are shown in Fig. 7.5.

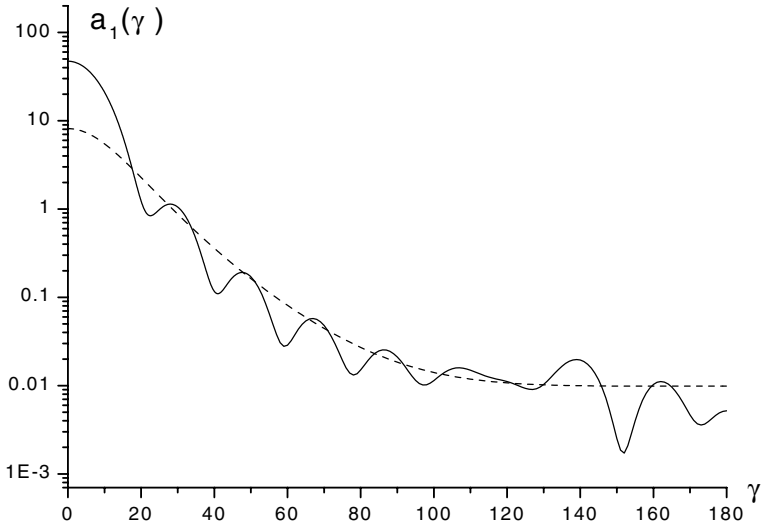

Fig. 7.5. Phase function of latex spheres in water (solid line, $ka = 10$). The dashed line is the result of calculations with eq. (7.24)

The relationship between the elements of matrix (7.10) allows us to develop an iterative procedure for solving the vector radiative transfer equation (see eq. (7.9)). As a first approximation, we neglect the off-diagonal elements of scattering matrix (7.10). Then eq. (7.9) falls into four independent equations,

$$\left\{\mu\frac{\partial}{\partial z} + \sigma_{tot}\right\}\hat{I}(z,\mathbf{n}) =$$
$$\sigma\int d\mathbf{n}'\begin{pmatrix} a_+\exp(2i\chi_+) & 0 & 0 & 0 \\ 0 & a_1 & 0 & 0 \\ 0 & 0 & a_4 & 0 \\ 0 & 0 & 0 & a_+\exp(-2i\chi_+) \end{pmatrix}\hat{I}(z,\mathbf{n}') \tag{7.25}$$

The first and fourth equations in eq. (7.25) are different from each other only by the sign of their complex conjugation.

The scalar mode, the intensity I_{scal}, obeys the conventional radiative transfer equation

$$\left\{\mu\frac{\partial}{\partial z}+\sigma_{tot}\right\}I_{scal}(z,\mu)=\sigma\int d\mathbf{n}'a_1(\mathbf{nn}')I_{scal}(z,\mu') \tag{7.26}$$

The transfer equation for the circularly polarized mode V has the form

$$\left\{\mu\frac{\partial}{\partial z}+\sigma_{tot}\right\}V(z,\mu)=\sigma\int d\mathbf{n}'a_4(\mathbf{nn}')V(z,\mu') \tag{7.27}$$

The third equation following from eq. (7.25) describes the basic mode of linear polarization. Separating out the phase factors in the angular dependence of $I_{\pm 2}$ (these factors are responsible for the transformation of $I_{\pm 2}$ under rotations),

$$I_{\pm 2}=\frac{1}{\sqrt{2}}W(z,\mu)\exp(\pm 2i\varphi)$$

we arrive at the following equation for W [34]

$$\left\{\mu\frac{\partial}{\partial z}+\sigma_{tot}\right\}W(z,\mu)=\sigma\int d\mathbf{n}'\frac{a_2(\mathbf{nn}')+a_3(\mathbf{nn}')}{2}\exp(2i(\chi_+-\psi))W(z,\mu') \tag{7.28}$$

The equations for V and W (see eqs (7.27) and (7.28)) differ from the scalar transfer equation (eq. (7.26)) by the form of the phase functions. The phase functions appearing in eqs (7.27) and (7.28) are a_4 and $(a_2+a_3)\exp(2i(\chi_+-\psi))/2$, respectively. The difference between these phase functions and phase function a_1 entering into eq. (7.26) gives rise to nonzero effective 'absorption' in eqs (7.27) and (7.28) (even in the absence of true absorption). The effective 'absorption' in eqs (7.27) and (7.28) is responsible for the additional attenuation of V and W as compared to the intensity I_{scal} and describes the effect of depolarization of circularly and linearly polarized light.

There are two different mechanisms of wave depolarization in a random medium. These mechanisms were first pointed out by Kravtsov [41] within the framework of the study of wave propagation through a turbulent atmosphere.

The 'geometrical' mechanism of depolarization is due to Rytov's rotation of the polarization plane [40]. According to [40], the plane of polarization turns, as the ray of light propagates along a nonplanar curve. The depolarization observed in multiple scattering of linearly polarized light results from superposition of the polarizations of the waves propagating along different random paths. Therefore, depolarization by the 'geometrical' mechanism occurs simultaneously with isotropization of the beam of light over directions [8, 33]. Note that a characteristic length of isotropization coincides with the transport length l_{tr} ($l_{tr}=\sigma_{tr}^{-1}$, where $\sigma_{tr}=\sigma(1-\langle\cos\gamma\rangle)$ is the transport scattering coefficient, $\langle\cos\gamma\rangle$ is the mean cosine of single scattering angle γ).

The pure geometrical depolarization can be obtained in the limit $A_{\|} = A_{\perp}$. In this case, the single scattering matrix entering into eq. (7.9) (or eq. (7.25)) can be written as

$$\hat{\tilde{d}} = a_1 \hat{\tilde{L}}(\pi - \beta - \beta') = a_1 \begin{pmatrix} \exp(2i\chi_+) & 0 & 0 & 0 \\ 0 & 1 & 0 & 0 \\ 0 & 0 & 1 & 0 \\ 0 & 0 & 0 & \exp(-2i\chi_+) \end{pmatrix} \tag{7.29}$$

Matrix (7.29) gives rise to depolarization due to multiple turns of the polarization plane as the direction of wave propagation changes randomly. The 'geometrical' mechanism contributes to depolarization of linearly polarized light, but has no effect on circular polarization.

The difference between the scattering amplitudes $A_{\perp}$ and $A_{\|}$ (or, in the general case, nonzero elements b_1, b_2 and the differences between diagonal elements a_i, $i = 1 \div 4$) is responsible for the 'dynamical' depolarization. Physically the depolarization of this kind occurs as the difference between amplitudes of cross-polarized fields increases [43]. The 'dynamical' depolarization occurs independently of the initial polarization of light. In particular, circularly polarized light depolarizes only due to the 'dynamical' mechanism (the difference between a_1 and a_4 is a single reason for depolarization of circularly polarized waves). Depolarization of circularly polarized light is described by the additional 'absorption' appearing in the equation for the Stokes parameter V (see eq. (7.27)). The additional 'absorption' coefficient is equal to [33, 37, 38].

$$\sigma_{dep}^{(4)} = \sigma \int d\mathbf{n}'(a_1(\mathbf{n}\mathbf{n}') - a_4(\mathbf{n}\mathbf{n}')) \tag{7.30}$$

In the case of the linearly polarized incident beam, the role of one or the other mechanism depends on the optical properties of the scattering particles, their size and shape. As shown below the geometrical mechanism can be either dominant [33,34] or as important as the dynamical mechanism of depolarization.

In the range of small angles the scattering-matrix elements $a_{1\div3}$ differ little from each other (see, for example, [44]), and it is instructive to represent the phase function appearing in eq. (7.28) in the form

$$\frac{a_2 + a_3}{2} \exp(2i(\chi_+ - \psi)) = a_1 + a_1[\exp(2i(\chi_+ - \psi)) - 1] + \left(\frac{a_2 + a_3}{2} - a_1\right) + \left(\frac{a_2 + a_3}{2} - a_1\right)[\exp(2i(\chi_+ - \psi)) - 1] \tag{7.31}$$

Each term in equality (7.31) has its own physical meaning.

If we neglect the difference between the diagonal elements of the scattering matrix $a_{1\div3}$ and disregard the deviation of the spherical triangle ABC shown in Fig. 7.1 from a planar one (i.e., we assume $\chi_+ = \psi$), equality (7.31) contains only the first term. In this approximation, the equation for W does not differ from the scalar transfer equation (eq. (7.26)) and W coincides with I_{scal}. There is no depolarization of light in this approximation.

Depolarization is described by the second, third, and fourth terms in eq. (7.31). The second term in eq. (7.31) is responsible for the geometrical depolarization. This term is due to the deviation of the spherical triangle ABC (Fig. 7.1) from a planar triangle. The difference between the angles

$$\chi_+ - \psi = \pi - \beta - \beta' - (\varphi - \varphi') \tag{7.32}$$

is the difference between the sum of angles in the spherical triangle and the sum of angles in the corresponding planar triangle [54].

The third term in eq. (7.31) is due to the difference between the diagonal elements $a_{1\div 3}$. This term decribes the dynamical depolarization.

The mutual influence of the geometrical and dynamical mechanisms is described by the fourth term in eq. (7.31).

In scattering by large inhomogeneities, the second, third, and fourth terms in eq. (7.31) are small as compared with the first term. Therefore, the depolarization process occurs slowly, as a result of many acts of scattering. For large inhomogeneities, the fourth term in eq. (7.31) is of minor importance. The relationship between the contributions from the geometrical and depolarization mechanisms depends on the specific angular dependence of the matrix elements $a_{1\div 3}(\cos\gamma)$.

Independent propagation of the basic polarization modes I, W, and V represents the first approximation. In the succeeding approximation, one must account for off-diagonal elements of the scattering matrix.

In what follows, we assume that $b_2 = 0$. This approximation corresponds to the most of practical situations [1]. Under this assumption there is no interaction between the circular and linear polarizations, and the equation for V appears to be separated from the other equations for the Stokes parameters.

The calculations of the linear polarization state can be represented in the compact form by introducing the polarization Green matrix of the third rank,

$$\hat{G} = \begin{pmatrix} G_{22} & G_{20} & G_{2-2} \\ G_{02} & G_{00} & G_{0-2} \\ G_{-22} & G_{-20} & G_{-2-2} \end{pmatrix} \tag{7.33}$$

This matrix allows one to express the scattered light through parameters $\hat{I}^{(0)}$ of the incident beam,

$$\hat{I} = \hat{G}\hat{I}^{(0)}$$

Similarly to the vector $\hat{I}$, the matrix $\hat{G}$ obeys the vector radiative transfer equation (7.9). The matrix $\hat{G}$ has the same symmetry as the scattering matrix $\hat{\hat{d}}$ (see eq. (7.10)). The complex conjugation of elements G_{mn} is equivalent to changing the sign of the index:

$$G_{0\pm 2} = G^*_{0\mp 2}, \quad G_{\pm 20} = G^*_{\mp 20}, \quad G_{\pm 2\pm 2} = G^*_{\mp 2\mp 2} \tag{7.34}$$

In the first approximation, the matrix $\hat{G}$ describes independent propagation of the basic modes and has the diagonal form

$$\hat{G} \approx \begin{pmatrix} W\exp(2i\varphi) & 0 & 0 \\ 0 & I_{scal} & 0 \\ 0 & 0 & W^*\exp(-2i\varphi) \end{pmatrix} \tag{7.35}$$

In the succeeding approximation, allowance for nonzero off-diagonal elements of the scattering matrix (see eq. (7.10)), generates the off-diagonal elements of the matrix $\hat{G}$. These quantities can be termed additional modes (or overtones).

In the explicit form the equation for the elements G_{km} can be written as

$$\left\{\mu\frac{\partial}{\partial z} + \sigma_{tot}\right\} G_{km}(z,\mathbf{n}) = \sigma\int d\mathbf{n}'\tilde{d}_{kk}(\mathbf{n},\mathbf{n}')G_{km}(z,\mathbf{n}') + Q_{km}(z,\mathbf{n}) \tag{7.36}$$

where the sources Q_{km} have the form

$$Q_{km}(z,\mathbf{n}) = \sum_{l\neq k}\sigma\int d\mathbf{n}'\tilde{d}_{kl}(\mathbf{n},\mathbf{n}')G_{lm}(z,\mathbf{n}') \tag{7.37}$$

The terms involving the basic modes make the main contribution to the sources (7.37),

$$Q_{km}(z,\mathbf{n}) \approx \sigma\int d\mathbf{n}'\tilde{d}_{km}(\mathbf{n},\mathbf{n}')G_{mm}(z,\mathbf{n}') \tag{7.38}$$

In the case of normal incidence, the non-zero off-diagonal elements G_{02}, G_{20} and G_{2-2} have the following azimuth dependence:

$$\begin{aligned} &G_{02}(z,\mathbf{n}) = \frac{1}{\sqrt{2}}Q_W(z,\mu)\exp(2i\varphi), \quad G_{20}(z,\mathbf{n}) = \frac{1}{\sqrt{2}}Q_{un}(z,\mu), \\ &G_{2-2}(z,\mathbf{n}) = w(z,\mu)\exp(-2i\varphi) \end{aligned} \tag{7.39}$$

where the functions Q_W, Q_{un} and w obey the following equations:

$$\begin{aligned} &\left\{\mu\frac{\partial}{\partial z} + \sigma_{tot}\right\} Q_W(z,\mu) \\ &= \sigma\int d\mathbf{n}'a_1(\mathbf{n}\mathbf{n}')\exp(-2i\psi)Q_W(z,\mu') \\ &\quad +\sigma\int d\mathbf{n}'b_1(\mathbf{n}\mathbf{n}')\exp(-2i(\beta'+\psi))W(z,\mu') \end{aligned} \tag{7.40}$$

$$\begin{aligned} &\left\{\mu\frac{\partial}{\partial z} + \sigma_{tot}\right\} Q_{un}(z,\mu) \\ &= \sigma\int d\mathbf{n}'\left[\frac{a_2(\mathbf{n}\mathbf{n}') + a_3(\mathbf{n}\mathbf{n}')}{2}\right]\exp(2i\chi_+)Q_{un}(z,\mu') \\ &\quad +\sigma\int d\mathbf{n}'b_1(\mathbf{n}\mathbf{n}')\exp(-2i\beta)I_{scal}(z,\mu') \end{aligned} \tag{7.41}$$

$$\left\{\mu\frac{\partial}{\partial z}+\sigma_{tot}\right\}w(z,\mu)$$
$$=\ \sigma\int d\mathbf{n}'\left[\frac{a_2(\mathbf{nn}')+a_3(\mathbf{nn}')}{2}\right]\exp(2i(\chi_+ +\psi))w(z,\mu')$$
$$+\sigma\int d\mathbf{n}'\left[\frac{a_2(\mathbf{nn}')-a_3(\mathbf{nn}')}{2}\right]\exp(2i(\chi_- +\psi))W(z,\mu') \qquad (7.42)$$

At relatively small depths of penetration, where the scattered waves do not forget the initial polarization of the incident beam, the contribution of the overtones to the polarization state of light has a small effect. With increasing depths, the depolarization of the incident beam continues to escalate and the contribution of the overtones becomes significant.

Note the special role of the overtone $G_{20}=Q_{un}/\sqrt{2}$. For unpolarized incident beam the basic polarization modes W and V are nil and the polarization state of scattered light is governed only by the the second Stokes parameter $Q=Q_{un}$ [45, 47].

7.4 Diffusive propagation

In the case of diffusive propagation of light, the solutions of the transfer equations for the basic modes (see eqs (7.27), (7.26), and (7.28)) can be presented in the form of the expansions in the corresponding spherical functions. In the scalar transfer theory this approach is well-known as the $P_l(\mu)$ approximation [55].

In the case of normal incidence of a wide beam, the intensity of light and the basic mode of circular polarization can be presented as expansions in the Legendre polynomials:

$$I_{scal}(z,\mu)=\sum_{l=0}\frac{2l+1}{4\pi}I_{scal}(z,l)P_l(\mu),\quad V(z,\mu)=\sum_{l=0}\frac{2l+1}{4\pi}V(z,l)P_l(\mu) \qquad (7.43)$$

The coefficients $I_{scal}(z,l)$ and $V(z,l)$ obey the following equations

$$\frac{l}{(2l+1)}\frac{\partial I_{scal}(z,l-1)}{\partial z}+$$
$$\frac{l+1}{2l+1}\frac{\partial I_{scal}(z,l+1)}{\partial z}+[\sigma(1-a_1(l))+\sigma_a]I_{scal}(z,l)=0 \qquad (7.44)$$

$$\frac{l}{(2l+1)}\frac{\partial V(z,l-1)}{\partial z}+$$
$$\frac{l+1}{2l+1}\frac{\partial V(z,l+1)}{\partial z}+[\sigma(1-a_4(l))+\sigma_a]V(z,l)=0 \qquad (7.45)$$

where

$$a_{1,4}(l) = 2\pi \int_{-1}^{1} d\mu a_{1,4}(\mu) P_l(\mu)$$

The basic mode of linear polarization is expanded in terms of the generalized spherical functions [56]

$$W(z,\mu) = \sum_{l=2} \frac{2l+1}{4\pi} W(z,l) P_{22}^l(\mu) \tag{7.46}$$

Substitution of eq. (7.46) into eq. (7.28) gives

$$\frac{l^2-4}{l(2l+1)} \frac{\partial W(z,l-1)}{\partial z} + \frac{4}{l(l+1)} \frac{\partial W(z,l)}{\partial z} + \frac{(l+1)^2-4}{(l+1)(2l+1)} \frac{\partial W(z,l+1)}{\partial z} + [\sigma(1-a_+(l)) + \sigma_a] W(z,l) = 0 \tag{7.47}$$

where the coefficient $a_+(l)$ appearing in eq. (7.47) is defined by equality

$$a_+(l) = 2\pi \int_{-1}^{1} d\mu \left[\frac{a_2(\mu) + a_3(\mu)}{2} \right] P_{22}^l(\mu) \tag{7.48}$$

The explicit expressions for several first generalized spherical functions have the form

$$P_{22}^2(\mu) = \frac{1}{4}(1+\mu)^2, P_{22}^3(\mu) = \frac{1}{4}(1+\mu)^2(3\mu-2), P_{22}^4(\mu) = \frac{1}{4}(1+\mu)^2(1-7\mu+7\mu^2) \tag{7.49}$$

The coefficients $I_{scal}(z,l)$, $V(z,l)$ and $W(z,l)$ can be easily calculated in the case of the asymptotical state of propagation. This limiting case is of practical importance for many applications (see, for example, [8, 9, 11]).

Substituting $I_{scal}(z,l)$, $V(z,l)$ and $W(z,l)$ in the exponential form (e.g. $I_{scal}(z,l) \approx I_{scal}(l) \exp(-\epsilon_I z)$) into eqs (7.44), (7.45), and (7.47), we arrive at an eigenvalue problem. A minimal eigenvalue gives the attenuation coefficient of the corresponding mode in the asymptotical state. For the scalar transfer equation this case has been discussed in detail [55].

For diffusive propagation of light the contribution from the higher terms to expansions (7.43), (7.46) appears to be small. Several first terms in these expansions have a dominant role.

The asymptotic state of the basic polarization modes is determined by the following expressions:

$$\begin{aligned} I_{scal}(z,\mu) &\approx C_I \Phi_I(\mu) \exp(-\epsilon_I z) \\ &\approx \frac{C_I}{4\pi} \left(P_0(\mu) + \alpha_I P_1(\mu) + \beta_I P_2(\mu) + \ldots\right) \exp\left(-\epsilon_I z\right) \end{aligned} \tag{7.50}$$

$$V(z,\mu) \approx C_V\Phi_V(\mu)\exp(-\epsilon_V z) \approx \frac{C_V}{4\pi}\left(P_0(\mu)+\alpha_V P_1(\mu)+\beta_V P_2(\mu)+\ldots\right)\exp\left(-\epsilon_V z\right) \quad (7.51)$$

$$W(z,\mu) \approx C_W\Phi_W(\mu)\exp(-\epsilon_W z) \approx \frac{5C_W}{4\pi}\left(P_{22}^2(\mu)+\alpha_W P_{22}^3(\mu)+\beta_W P_{22}^4(\mu)+\ldots\right)\exp\left(-\epsilon_W z\right) \quad (7.52)$$

where $\epsilon_{I,V,W}$ and $\Phi_{I,V,W}$ are the corresponding eigenvalues and angular eigenfunctions. The eigenvalues $\epsilon_{I,V}$ and the coefficients $\alpha_{I,V}$, $\beta_{I,V}$ entering into eqs (7.50)–(7.52) can be approximated by formulas

$$\epsilon_I \approx \sqrt{3(\sigma_{tr}+\sigma_a)\sigma_a}, \quad \alpha_I \approx \sqrt{\frac{3\sigma_a}{\sigma_{tr}+\sigma_a}}, \quad \beta_I \approx \frac{2\sigma_a}{\sigma(1-a_1(2))+\sigma_a} \quad (7.53)$$

$$\epsilon_V \approx \sqrt{3(\sigma_{tr}^{(4)}+\sigma_{dep}^{(4)}+\sigma_a)(\sigma_a+\sigma_{dep}^{(4)})}, \quad \alpha_V \approx \sqrt{\frac{3(\sigma_a+\sigma_{dep}^{(4)})}{\sigma_{tr}^{(4)}+\sigma_{dep}^{(4)}+\sigma_a}}$$

$$\beta_V = \frac{2\left(\sigma_a+\sigma_{dep}^{(4)}\right)}{\sigma(1-a_4(2))+\sigma_a} \quad (7.54)$$

where

$$a_1(0)=1, \ \sigma_{tr}=\sigma(1-a_1(1)), \quad \sigma_{tr}^{(4)}=\sigma(a_4(0)-a_4(1)), \quad \sigma_{dep}^{(4)}=\sigma(1-a_4(0)) \quad (7.55)$$

Equations (7.53), (7.54) are valid in the limit $\sigma_a \ll \sigma_{tr}$ and $\sigma_a, \sigma_{dep}^{(4)} \ll \sigma_{tr}^{(4)}$, respectively.

Within the leading approximation the corresponding parameters entering into eq. (7.52) are determined by more complicated expressions:

$$\epsilon_W \approx \frac{7}{6}\Big(\sigma(3-2a_+(3)-a_+(2)\big)+3\sigma_a - \sqrt{(\sigma(3-2a_+(3)-a_+(2))+3\sigma_a)^2-\frac{36}{7}(\sigma(1-a_+(3))+\sigma_a)(\sigma(1-a_+(2))+\sigma_a)}\Big)$$

$$\alpha_W \approx \frac{21}{5}\left(\frac{\sigma(1-a_+(2))+\sigma_a}{\epsilon_W}-\frac{2}{3}\right)$$

$$\beta_W \approx \frac{63}{5}\left(\frac{\sigma(1-a_+(2))+\sigma_a}{\epsilon_W}-\frac{1}{3}\right)\left(\frac{\sigma(1-a_+(2))+\sigma_a}{\epsilon_W}-\frac{2}{3}\right)-1 \quad (7.56)$$

where the coefficients $a_+(l)$ are calculated with eq. (7.48).

Equation (7.56) permits us also to calculate the values ϵ_W, α_W, β_W within the framework of the 'geometrical' approximation in the scattering matrix. This approximation is in substitution of the approximate scattering matrix (7.29) for the exact matrix (7.10). The values ϵ_W^{geom}, α_W^{geom}, β_W^{geom} can be obtained

from eq. (7.56), if we replace $(a_2(\mu) + a_3(\mu))/2$ by $a_1(\mu)$ in definition (7.48). The difference between ϵ_W and ϵ_W^{geom} is a measure of the contribution from the 'dynamical' mechanism to depolarization of a linearly polarized beam.

As follows from eqs (7.54), (7.56), depolarization of light manifests itself as additional effective 'absorption' of the basic modes V and W. The coefficient of the additional 'absorption' equals $\sigma_{dep}^{(4)}$ for V. For W the corresponding coefficient should be estimated as $\epsilon_W^2/(\sigma(a_+(2) - a_+(3)) - \sigma_a$ (or, roughly, as $(\epsilon_W^2/3(\sigma_{tr}) - \sigma_a) \sim \sigma_{tr}$).

In the case of normal incidence the coefficients $C_{I,V,W}$ can be calculated by the following approximate formula [39]

$$C_{I,V,W} = \frac{\Phi_{I,V,W}(\mu = 1)}{2\pi \int\limits_0^1 \mu d\mu \Phi_{I,V,W}^2(\mu)} \tag{7.57}$$

For an absorbing medium eq. (7.57) gives a good agreement with numerical calculations (see, for example, [45]). As applied to C_I the difference between eq. (7.57) and the numerical results of [45] is less than 10% for $\sigma_a > 0.1\sigma_{tr}$ and falls off with increasing ratio σ_a/σ_{tr}.

Within the considered approximation, where only the basic modes I_{scal}, V and W are taken into account, the degree of polarization of circularly (P_C) and linearly (P_L) polarized beams are determined by

$$P_C = \frac{\sqrt{Q^2 + V^2}}{I} \approx \frac{V}{I_{scal}} \approx \frac{C_V}{C_I} \left[1 - \mu\left(\alpha_I - \alpha_V\right)\right] \exp\left(-z\left(\epsilon_V - \epsilon_I\right)\right) \tag{7.58}$$

$$P_L = \frac{\sqrt{Q^2 + U^2}}{I} \approx \frac{W}{I_{scal}} \approx$$
$$\frac{5C_W}{4C_I}(1+\mu)^2 \left[1 - 2\alpha_W - \mu(\alpha_I - 3\alpha_W)\right] \exp\left(-z\left(\epsilon_W - \epsilon_I\right)\right) \tag{7.59}$$

According to eqs (7.58) and (7.59) the degree of polarization depends primarily on the difference in the attenuation coefficients of the basic modes I_{scal}, V and W.

The numerical values of the scattering matrix parameters entering into eqs (7.50)–(7.59) are presented in Table 7.1. For latex particles in water and water droplets in air the numerical results were obtained with the Mie formulas [44]. The scattering matrix elements for clouds and sea water were taken from Refs [2, 52].

The numerical values of the attenuation coefficients and the other parameters appearing in the expressions for the basic modes V and W can be found in Tables 7.2 and 7.3. For comparison, the values ϵ_W^{geom} that correspond to the 'geometrical' approximation (see eq. (7.29)) are also presented in Table 7.2. In our calculations, the scattering medium is assumed to be virtually nonabsorbing ($\sigma_a \ll \sigma_{dep}, \sigma_{tr}$). Therefore our result obtained with the seawater scattering

Table 7.1. Integral parameters of the diagonal matrix elements for large scattering inhomogeneities ($x = 2\pi a/\lambda$)

	σ_{tr}/σ	$1 - a_+(2)$	$1 - a_+(3)$	$\sigma_{dep}^{(4)}/\sigma$	$\sigma_{tr}^{(4)}/\sigma$
Latex spheres ($x = 5, n = 1.19$)	$1.1{\cdot}10^{-1}$	$9.4{\cdot}10^{-2}$	$2.9{\cdot}10^{-1}$	$1.7{\cdot}10^{-2}$	$8.4{\cdot}10^{-2}$
Latex spheres ($x = 10, n = 1.19$)	$6.7{\cdot}10^{-2}$	$5.8{\cdot}10^{-2}$	$1.7{\cdot}10^{-1}$	$9.8{\cdot}10^{-3}$	$5.6{\cdot}10^{-2}$
water droplets ($x = 5, n = 1.33$)	$1.5{\cdot}10^{-1}$	$1.3{\cdot}10^{-2}$	$3.5{\cdot}10^{-1}$	$3.4{\cdot}10^{-2}$	$1.1{\cdot}10^{-1}$
water droplets ($x = 10, n = 1.33$)	$2.9{\cdot}10^{-1}$	$2.3{\cdot}10^{-1}$	$5.1{\cdot}10^{-1}$	$8.4{\cdot}10^{-2}$	$1.9{\cdot}10^{-1}$
Cloud 1	$1.5{\cdot}10^{-1}$	$1.1{\cdot}10^{-1}$	$2.7{\cdot}10^{-1}$	$4.9{\cdot}10^{-2}$	$8.5{\cdot}10^{-2}$
sea water	$7.0{\cdot}10^{-2}$	$8.1{\cdot}10^{-2}$	$1.7{\cdot}10^{-1}$	$5.8{\cdot}10^{-2}$	$2.6{\cdot}10^{-2}$

Table 7.2. Attenuation coefficients of the basic polarization modes

	ϵ_V/σ	ϵ_W/σ	ϵ_W^{geom}/σ	ϵ_V/ϵ_W
Latex spheres ($x = 5, n = 1.19$)	$7.1{\cdot}10^{-2}$	$1.32{\cdot}10^{-1}$	$1.29{\cdot}10^{-1}$	$5.4{\cdot}10^{-1}$
Latex spheres ($x = 10, n = 1.19$)	$4.3{\cdot}10^{-2}$	$8.13{\cdot}10^{-2}$	$7.95{\cdot}10^{-2}$	$5.3{\cdot}10^{-1}$
water droplets ($x = 5, n = 1.33$)	$1.2{\cdot}10^{-1}$	$1.81{\cdot}10^{-1}$	$1.75{\cdot}10^{-1}$	$6.6{\cdot}10^{-1}$
water droplets ($x = 10, n = 1.33$)	$2.1{\cdot}10^{-1}$	$3.09{\cdot}10^{-1}$	$2.93{\cdot}10^{-1}$	$6.8{\cdot}10^{-1}$
Cloud 1	$1.3{\cdot}10^{-1}$	$1.59{\cdot}10^{-1}$	$1.52{\cdot}10^{-1}$	$8.2{\cdot}10^{-1}$
sea water	$1.0{\cdot}10^{-1}$	$1.10{\cdot}10^{-1}$	$0.80{\cdot}10^{-1}$	$9.1{\cdot}10^{-1}$

Table 7.3. Parameters of the basic polarization modes in the asymptotic state

	C_V	C_W	α_V	α_W
Latex spheres ($x = 5, n = 1.19$)	3.08	1.55	0.74	0.18
Latex spheres ($x = 10, n = 1.19$)	3.13	1.55	0.69	0.19
water droplets ($x = 5, n = 1.33$)	2.95	1.56	0.87	0.22
water droplets ($x = 10, n = 1.33$)	2.51	1.56	1.38	0.27
Cloud 1	2.70	1.56	1.14	0.25
sea water	2.30	1.56	1.68	0.30

matrix should be considered as a modeling example, because natural seawater possesses rather great absorption ($\sigma_a > \sigma_{tr}$) [2].

The additional modes Q_W, Q_{un} and w are governed by the basic modes I_{scal} and W (see eqs (7.40)–(7.42)). In the asymptotic state the additional modes can be easily expressed in terms of the coefficients of the basic mode expansions (see eqs (7.50) and (7.52)) [39]

$$Q_W(z,\mu) \approx \frac{5C_W}{4\pi} \frac{\sigma b_1(2)}{\sigma(1 - a_1(2)) + \sigma_a} P_{20}^2(\mu) \exp\left(-\epsilon_W z\right) \tag{7.60}$$

$$Q_{un}(z,\mu) \approx \frac{5C_I\beta_I}{4\pi} \frac{\sigma b_1(2)}{\sigma(1 - a_+(2)) + \sigma_a} P_{20}^2(\mu) \exp\left(-\epsilon_I z\right) \tag{7.61}$$

$$w(z,\mu) \approx \frac{5C_W}{4\pi} \frac{\sigma a_-(2)}{\sigma(1 - a_+(2)) + \sigma_a + \frac{2}{3}\epsilon_W} P_{2-2}^2(\mu) \exp\left(-\epsilon_W z\right) \tag{7.62}$$

where

$$b_1(2) = 2\pi \int_{-1}^{1} d\mu b_1(\mu) P_{20}^2(\mu),$$

$$a_-(2) = 2\pi \int_{-1}^{1} d\mu \frac{a_2(\mu) - a_3(\mu)}{2} P_{2-2}^2(\mu) \tag{7.63}$$

$$P_{20}^2(\mu) = -\sqrt{\frac{3}{8}}(1-\mu^2), \quad P_{2-2}^2(\mu) = \frac{1}{4}(1-\mu)^2$$

With the overtones Q_W, Q_{un} and w taken into account, the Stokes vector has the form

$$\begin{pmatrix} I \\ Q \\ U \end{pmatrix} = \begin{pmatrix} I_{scal} + Q_W \cos 2\varphi \\ (W+w)\cos 2\varphi + Q_{un} \\ (-W+w)\sin 2\varphi \end{pmatrix} \tag{7.64}$$

As follows from eqs (7.60)–(7.62), the contributions of the overtones to the polarization state involve the small factors, $b_1(2)/(\sigma(1-a_1(2))+\sigma_a)$, $b_1(2)/(\sigma(1-a_+(2))+\sigma_a)$ and $a_-(2)/(\sigma(1-a_+(2))+\sigma_a+2\epsilon_W/3)$ (see Table 7.4 and Fig. 7.6). Hence, the overtone contributions to the transmitted intensity I and the Stokes parameter U are always small quantities. The contribution to the Stokes parameter Q becomes evident only at large depths, where the incident beam completely depolarizes.

Table 7.4. Integral parameters of the off-diagonal elements of the scattering matrix

	$b_1(2)$	$a_-(2)$
Latex spheres ($x=5, n=1.19$)	$1.0\cdot10^{-2}$	$4.0\cdot10^{-3}$
Latex spheres ($x=10, n=1.19$)	$2.0\cdot10^{-3}$	$2.0\cdot10^{-3}$
water droplets ($x=5, n=1.33$)	$-2.0\cdot10^{-3}$	$8.0\cdot10^{-3}$
water droplets ($x=10, n=1.33$)	$-2.3\cdot10^{-2}$	$1.8\cdot10^{-2}$
Cloud 1	$1.4\cdot10^{-2}$	$4.8\cdot10^{-2}$
sea water	$1.6\cdot10^{-2}$	$4.0\cdot10^{-2}$

With allowance for the overtones, the degree of polarization can be written as

$$P_L \approx \frac{\sqrt{W^2 + 2Ww\cos 4\varphi + 2WQ_{un}\cos 2\varphi + Q_{un}^2}}{I_{scal}} \left(1 - \frac{Q_W}{I_{scal}}\cos 2\varphi\right) \tag{7.65}$$

As depth z increases, the incident light depolarizes ($Q_{un} \gg W$) and P_L tends to the degree of polarization of unpolarized light, $P_L \approx P_{un} = Q_{un}/I_{scal}$.

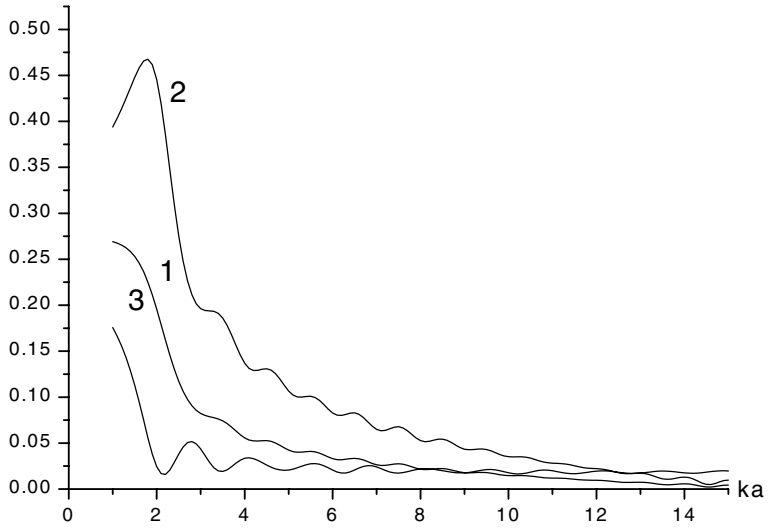

Fig. 7.6. Ratios $b_1(2)/(\sigma(1-a_1(2)))$ (curve 1), $b_1(2)/(\sigma(1-a_+(2))$ (curve 2) and $a_-(2)/(\sigma(1-a_+(2))+2\epsilon_W/3)$ (curve 3) as functions of radius a of the scattering particles. Latex spheres in water, no absorption

7.5 Small-angle multiple scattering

The spread of multiply scattered waves over the directions of propagation depends on the absorption properties of the medium. Propagation of light is diffusive provided that the absorption coefficient is much less than the transport scattering coefficient ($\sigma_a \ll \sigma_{tr}$). In the case of strong absorption ($\sigma_a > \sigma_{tr}$) the situation reverses. The prevailing attenuation of the waves scattered through relatively large angles prevents the propagation regime from being diffusive and results in retaining the small-angle distribution of radiation at any depth z. The average cosine of multiple scattering angle is close to unity ($1-\langle\cos\theta\rangle_\infty \ll 1$) in the asymptotic state (see, for example, [32,45,55,58,59]. Below the condition of strong absorption is assumed to be fulfilled.

In what follows we present analytical results for the Stokes parameters of multiply scattered light. Various types of initial polarization are considered. We restrict our calculations to the case of weak single scattering that is described within the Born (or Rayleigh–Gans) approximation (see eq. (7.21)). The effects of strong single scattering that are beyond the Born approximation are discussed in [32,35,57].

7.5.1 Unpolarized light

Let a wide beam of unpolarized light be incident normally on a surface. In this case quantities W and V are equal to zero and the polarization state of light is

determined only by the contribution of the overtone Q_{un} (see eqs (7.39)–(7.42), (7.64)). To derive a small-angle version of eqs (7.26) and (7.41) we take advantage a number of approximations. In the first place, eqs (7.16)–(7.19) and eq. (7.21) are assumed to be valid. Second, we neglect the difference between the spherical triangle shown in Fig. 7.1 and a planar one and put $\chi_+ = \psi$. Then, expanding the terms appearing in eqs (7.26) and (7.41) in small angles θ, θ', we find the small-angle equations for I_{scal} and Q_{un} [32]

$$\left\{\frac{\partial}{\partial z} + \sigma + \frac{\sigma_a}{2}\theta^2\right\}\tilde{I}_{scal}(z,\theta) = \sigma\int d\boldsymbol{\theta}' a_1(|\boldsymbol{\theta}-\boldsymbol{\theta}'|)\tilde{I}_{scal}(z,\theta') \tag{7.66}$$

$$\left\{\frac{\partial}{\partial z} + \sigma + \frac{\sigma_a}{2}\theta^2\right\}\tilde{Q}_{un}(z,\theta) = \sigma\int\limits_0^\infty d\theta'\left[\int\limits_0^{2\pi} d\psi a_1(|\boldsymbol{\theta}-\boldsymbol{\theta}'|)\cos 2\psi\right]\tilde{Q}_{un}(z,\theta')$$
$$+\frac{\sigma}{2}\int d\boldsymbol{\theta}' a_1(|\boldsymbol{\theta}-\boldsymbol{\theta}'|)[\theta'^2(1-\cos 2\psi) - (\boldsymbol{\theta}-\boldsymbol{\theta}')^2]\tilde{I}_{scal}(z,\theta') \tag{7.67}$$

where $\tilde{I}_{scal} = I_{scal}\,\exp(\sigma_a z)$, $\tilde{Q}_{un} = Q_{un}\,\exp(\sigma_a z)$; $\boldsymbol{\theta} = (\theta\cos\varphi,\ \theta\sin\varphi)$ is a two dimensional vector. We assume that the main contribution to the integrals appearing in eqs (7.66) and (7.67) is determined by the range of small angles and the upper limit of integration over θ can be extended to infinity. The boundary conditions for eqs (7.66) and (7.67) have the form

$$\tilde{I}_{scal}(z=0,\theta) = \frac{\delta(\theta)}{2\pi\theta} \tag{7.68}$$

$$\tilde{Q}_{un}(z=0,\theta) = 0 \tag{7.69}$$

Equation (7.68) corresponds to the incident radiation of unit flux density.

Equations (7.66) and (7.67) can be reduced to the differential form. Using the Bessel transform

$$\tilde{I}_{scal}(z,\omega) = 2\pi\int\limits_0^\infty \theta d\theta J_0(\omega\theta)\tilde{I}_{scal}(z,\theta) \tag{7.70}$$

$$\tilde{Q}_{un}(z,\omega) = 2\pi\int\limits_0^\infty \theta d\theta J_2(\omega\theta)\tilde{Q}_{un}(z,\theta) \tag{7.71}$$

we obtain the following differential equations [32]:

$$\left\{\frac{\partial}{\partial z} + \sigma(1-a_1(\omega)) - \frac{\sigma_a}{2}\Delta_\omega\right\}\tilde{I}_{scal}(z,\omega) = 0 \tag{7.72}$$

$$\left\{\frac{\partial}{\partial z} + \sigma(1-a_1(\omega)) - \frac{1}{2}\sigma_a\left(\Delta_\omega - \frac{4}{\omega^2}\right)\right\}\tilde{Q}_{un}(z,\omega) = \Xi(\omega)\tilde{I}_{scal}(z,\omega) \tag{7.73}$$

where

$$a_1(\omega) = 2\pi \int_0^\infty \gamma d\gamma J_0(\omega\gamma) a_1(\gamma), \quad \Delta_\omega = \frac{1}{\omega}\frac{\partial}{\omega}\left[\omega\frac{\partial}{\omega}\right] \tag{7.74}$$

$$\Xi(\omega) = -\frac{\sigma\omega}{2}\frac{\partial}{\partial\omega}\frac{1}{\omega}\frac{\partial a_1(\omega)}{\partial\omega} \tag{7.75}$$

The boundary conditions for eqs (7.72) and (7.73) take the form

$$\tilde{I}_{scal}(z=0,\omega) = 1, \quad \tilde{Q}_{un}(z=0,\omega) = 0 \tag{7.76}$$

In the case of multiple scattering, two inequalities are assumed to be fulfilled

$$z \gg l, \quad \theta \gg \gamma_0 \tag{7.77}$$

where l is the mean free path, $l = \sigma^{-1}$, and γ_0 is the characteristic angle of the phase function (see eq. (7.24)). As applied to the ω-representation, the second inequality implies

$$\omega \ll 1/\gamma_0 \tag{7.78}$$

Therefore, to calculate $\tilde{I}_{scal}(z,\omega)$ and $\tilde{Q}_{un}(z,\omega)$ we should know the ω-dependence of the function $a_1(\omega)$ for relatively small values of ω.

As the phase function $a_1(\gamma)$ falls off rapidly with increasing γ, the function $a_1(\omega)$ can be written as

$$a_1(\omega) = 1 - \frac{\langle\gamma^2\rangle\omega^2}{4} + \frac{\langle\gamma^4\rangle\omega^4}{64} - \ldots \tag{7.79}$$

where

$$\langle\gamma^{2n}\rangle = 2\pi\int_0^\infty \gamma d\gamma\gamma^{2n} a_1(\gamma)$$

is the even angular moment of the scattering phase function. Within the framework of this model for the function $a_1(\omega)$, eqs (7.72) and (7.73) are simplified [32, 37, 58, 59]. Performing the inverse Bessel transform of the equations for $I_{scal}(z,\omega)$ and $\tilde{Q}_{un}(z,\omega)$, we obtain the following results:

$$\left\{\frac{\partial}{\partial z} + \frac{\sigma_a}{2}\theta^2 - D\frac{1}{\theta}\frac{\partial}{\partial\theta}\theta\frac{\partial}{\partial\theta}\right\}\tilde{I}_{scal}(z,\theta) = 0 \tag{7.80}$$

$$\left\{\frac{\partial}{\partial z} + \frac{\sigma_a}{2}\theta^2 - D\left[\frac{1}{\theta}\frac{\partial}{\partial\theta}\theta\frac{\partial}{\partial\theta} - \frac{4}{\theta^2}\right]\right\}\tilde{Q}_{un}(z,\theta) = b_1^{tr}\left[\theta\frac{\partial}{\partial\theta}\frac{1}{\theta}\frac{\partial}{\partial\theta}\right]\tilde{I}_{scal}(z,\theta) \tag{7.81}$$

where

$$D = \frac{1}{4}\sigma\langle\gamma^2\rangle, \quad b_1^{tr} = -\frac{1}{4}\sigma\langle\gamma^4\rangle \tag{7.82}$$

Equation (7.80) is the radiative transfer equation within the small-angle diffusion (or Fokker-Planck) approximation [58, 59].

Quantity D is the coefficient of photon diffusion in the angular domain. Within the small-angle approximation $\sigma_{tr} \approx \sigma\langle\gamma^2\rangle/2$, and the coefficient of angular diffusion can be expressed in terms of the transport scattering coefficient,

$$D = \frac{\sigma_{tr}}{2} = \frac{1}{2}\sigma\pi \int\limits_0^\infty \gamma^3 d\gamma a_1(\gamma). \tag{7.83}$$

The solutions of eqs (7.80) and (7.81) are given by [32, 37, 58, 59]

$$\tilde{I}_{scal}(z,\theta) = \frac{1}{\pi A_0^{(I)}(z) A_1^{(I)}(z)} \exp\left(-\frac{\theta^2}{A_1^{(I)}(z)}\right) \tag{7.84}$$

$$\tilde{Q}_{un}(z,\theta) = \frac{\theta^2 b_1^{tr}}{\sigma_a \langle\theta^2\rangle_\infty^3}\ f(z)\tilde{I}_{scal}(z,\theta) \tag{7.85}$$

where

$$A_0^{(I)}(z) = \cosh\left(z\sqrt{2D\sigma_a}\right), \quad A_1^{(I)}(z) = 2\sqrt{\frac{2D}{\sigma_a}}\tanh\left(z\sqrt{2D\sigma_a}\right)$$
$$f(z) = \frac{1}{\sinh^2\left(z\sqrt{2D\sigma_a}\right)}\left(z\sqrt{2D\sigma_a} + \frac{1}{2}\sinh 2\left(z\sqrt{2D\sigma_a}\right)\right) \tag{7.86}$$

In accordance with eq. (7.84), the mean square of scattering angle θ at depth z coincides with the function $A_1^{(I)}(z)$

$$\langle\theta^2\rangle_z = A_1^{(I)}(z) \tag{7.87}$$

The z-dependence of $\tilde{I}_{scal}(z,\theta)$ and $\tilde{Q}_{un}(z,\theta)$ is characterized by the scale

$$l_d = \left(\sqrt{2D\sigma_a}\right)^{-1} \tag{7.88}$$

At large depths ($z > l_d$) $\tilde{I}_{scal}(z,\theta)$ tends to its asymptotic state:

$$\tilde{I}_{scal}^{(as)}(z,\theta) = \frac{2}{\pi\langle\theta^2\rangle_\infty} \exp\left(-\frac{z}{l_d} - \frac{\theta^2}{\langle\theta^2\rangle_\infty}\right) \tag{7.89}$$

where

$$\langle\theta^2\rangle_\infty = 2\sqrt{\frac{2D}{\sigma_a}} \tag{7.90}$$

is the asymptotic value of the mean square of scattering angle [58, 59]. For strong absorption ($\sigma_a \gg \sigma_{tr}$), we have: $\langle\theta^2\rangle_\infty < 1$. From eq. (7.89), it follows that the asymptotic angular distribution of radiation is invariable with z.

According to eqs (7.84) and (7.85), the degree of polarization P_{un} is equal to

$$P_{un}(z,\theta) = \frac{\tilde{Q}_{un}}{\tilde{I}_{scal}} = \frac{\theta^2 b_1^{tr}}{\sigma_a\langle\theta^2\rangle_\infty^3}\ f(z) \tag{7.91}$$

At relatively small depths ($z \ll l_d$), eq. (7.91) gives

$$P_{un}(z \ll l_d, \theta) = \frac{1}{4}\ \frac{b_1^{tr}}{\sigma_{tr}}\ \frac{\theta^2}{\sigma_{tr} z} \tag{7.92}$$

As z increases the degree of polarization falls off monotonically. In the asymptotic state ($z \gg l_d$) P_{un} tends to its limiting value

$$P_{un}(z \to \infty, \theta) = \frac{b_1^{tr}}{\sigma_{tr}} \frac{\theta^2}{\langle \theta^2 \rangle_\infty} \tag{7.93}$$

As analysis shows [32,38,60], the small angle diffusion model (see eqs (7.79)–(7.81))) is too rough to provide qualitative results in actual experimental conditions.

Let us consider a more realistic model of scattering. The phase function of small-angle scattering by large spherical inhomogeneities of a given size can be approximated by [35, 44]

$$a_1(\gamma) = \frac{\gamma_0^2}{\pi(\gamma_0^2 + \gamma^2)^2} \tag{7.94}$$

where γ_0 denotes a characteristic angle of single scattering, $\gamma_0 \ll 1$ (see eq. (7.24)). For relatively small values of ω ($\omega \ll 1/\gamma_0$), the function $a_1(\omega)$ that corresponds to eq. (7.94) can be written as

$$a_1(\omega) = 1 - \frac{1}{4}\gamma_0^2\omega^2 \ln \frac{4}{\gamma_0^2\omega^2} + \ldots \tag{7.95}$$

For the function $a_1(\omega)$ of the type (7.95) eqs (7.72) and (7.73) can not be solved analytically at any depth z. $\tilde{I}_{scal}$ and $\tilde{Q}_{un}$ can be calculated only in two limiting cases, namely, at small depths and in the asymptotic state.

At relatively small depths ($z < l_a = \sigma_a^{-1}$) we can neglect the effect of absorption on the angular divergence of the radiation and put $\sigma_a = 0$ in eqs (7.72) and (7.73). With this constraint, the solutions of eqs (7.72) and (7.73) take the form [32, 61]

$$\tilde{I}_{scal}(z, \theta) = \int_0^\infty \frac{\omega d\omega}{2\pi} J_0(\omega\theta) \exp(-\sigma z(1 - a_1(\omega)) \tag{7.96}$$

$$\tilde{Q}_{un}(z, \theta) = z \int_0^\infty \frac{\omega d\omega}{2\pi} \Xi(\omega) J_2(\omega\theta) \exp(-\sigma z(1 - a_1(\omega)) \tag{7.97}$$

We can distinguish a 'dome' ($\theta < \theta_z$) and 'wings' ($\theta > \theta_z$) in the angular dependence of intensity [32]. The value of θ_z can be estimated as $\theta_z \approx \sqrt{\sigma_{tr} z}$ (for the phase function (7.94), $\sigma_{tr} = \sigma\gamma_0^2 \ln(2/\gamma_0)$). Within the 'dome' region the angular distribution of radiation results from photon diffusion over small ($\theta < \theta_z$) angles. The 'wings' are formed by photons which undergo multiple deflections through small angles ($\theta < \theta_z$) and a single scattering through a relatively large angle ($\theta > \theta_z$).

The results of calculations of $\tilde{I}_{scal}(z, \theta)$ and $\tilde{Q}_{un}(z, \theta)$ with eqs (7.96) and (7.97) are given by

$$\tilde{I}_{scal}(z, \theta) = \frac{\ln(2/\gamma_0)}{\pi\sigma_{tr} z \ln(\sigma_{tr} z/\gamma_0^2)} \exp\left(-\frac{\theta^2 \ln(2/\gamma_0)}{\sigma_{tr} z \ln(\sigma_{tr} z/\gamma_0^2)}\right), \theta < \theta_z$$

$$\tilde{I}_{scal}(z,\theta) = \frac{\sigma_{tr} z}{\pi\theta^4 \ln(2/\gamma_0)} \left(1 + \frac{8\sigma_{tr} z}{\theta^2 \ln(2/\gamma_0)} \ln\frac{\theta}{\gamma_0} - \ldots\right), \theta > \theta_z \qquad (7.98)$$

$$P_{un} = \frac{\tilde{Q}_{un}}{\tilde{I}_{scal}} = -\frac{\theta^2}{4\ln(\sigma z)} \quad , \theta < \theta_z$$

$$P_{un} = -\frac{\theta^2}{2} \cdot \left(1 - \frac{8\sigma_{tr} z}{\theta^2 \ln(2/\gamma_0)} \cdot \ln\frac{\theta}{\gamma_0} + \ldots\right), \quad \theta > \theta_z \qquad (7.99)$$

As follows from eq. (7.99), the degree of polarization P_{un} for relatively large angles is close to the degree of polarization of singly scattered light [44].

In the asymptotic state, the intensity $\tilde{I}_{scal}(z,\theta)$ can be calculated in the following way. We can represent $\tilde{I}_{scal}(z,\theta)$ as a product of two functions, one of which describes the exponential z-dependence, the other depends on θ (see eq. (7.50)). Substituting $\tilde{I}_{scal}(z,\theta)$ into eq. (7.72) we arrive at an eigenvalue problem. A minimal eigenvalue gives the attenuation coefficient in the asymptotic state. The corresponding eigenfunction describes the angular dependence. The specific calculations can be perfomed, for example, with the use of the direct variational procedure [62].

Here we consider an alternative method of calculations. This method can be interpreted as the extension of the small-angle diffusion approximation to the phase function of the type (7.94). We assume that a layer of the medium of a given thickness z is characterized by a certain value of the diffusion coefficient D_z. Then, the intensity $\tilde{I}_{scal}(z,\theta)$ can be described by eq. (7.84) with corresponding coefficient D_z. The value of D_z can be determined as follows. For the phase function (7.94), the integral (7.82) diverges at the upper limit. Assuming that the main contribution to the intensity of transmitted radiation is given by photons that deflects through angles $\theta < \sqrt{\langle\theta^2\rangle_z}$, we put the upper limit of integral (7.82) equal to the characteristic angle of multiple scattering in the layer, i.e. $\sqrt{\langle\theta^2\rangle_z}$. For eq. (7.94), we obtain the following equations [32]:

$$D_z = \frac{\sigma\gamma_0^2}{4} \ln\frac{\langle\theta^2\rangle_z}{\gamma_0^2}, \quad \langle\theta^2\rangle_z = 2\sqrt{\frac{2D_z}{\sigma_a}} \tanh(z\sqrt{2D_z\sigma_a}) \qquad (7.100)$$

Two equations (7.100) present the self-consistent method for calculating $\tilde{I}_{scal}(z,\theta)$ within the 'dome' region ($\theta < \sqrt{\langle\theta^2\rangle_z}$).

At relatively small depths ($z \ll l_d$) we obtain

$$D_z = \frac{\sigma_{tr}}{2} \frac{\ln(\sigma_{tr} z/\gamma_0^2)}{\ln(4/\gamma_0^2)}$$

and come back to eq. (7.98). In the asymptotic state ($z > l_d$), the diffusion coefficient is equal to

$$D_\infty = \frac{\sigma_{tr}}{2} \cdot \frac{\ln(\langle\theta^2\rangle_\infty/\gamma_0^2)}{\ln(4/\gamma_0^2)}$$

and the mean square of scattering angle θ can be approximated by

$$\langle\theta^2\rangle_\infty = 2\sqrt{\frac{\sigma_{tr}}{\sigma_a}\frac{\ln((\sqrt{4\sigma_{tr}/\sigma_a})/\gamma_0^2)}{\ln(4/\gamma_0^2)}} \tag{7.101}$$

The 'wings' of the intensity $\tilde{I}_{scal}(z,\theta)$ ($\theta > \sqrt{\langle\theta^2\rangle_z}$) are governed by the expansion of $\tilde{I}_{scal}(z,\omega)$ in small ω. Substituting the expansion of $\tilde{I}_{scal}(z,\omega)$ in ω into eq. (7.72) and equating the coefficients before equal powers of ω, we find the expansion of $\tilde{I}_{scal}(z,\theta)$ in inverse powers of θ [32, 63, 64]. With the use of a similar procedure, we can also calculate the second Stokes parameter $\tilde{Q}_{un}(z,\theta)$.

Combining the results outlined above, we obtain the following analytical results [32, 35]

$$\tilde{I}_{scal}(z,\theta) \approx \frac{2}{\pi\langle\theta^2\rangle_\infty}\cdot\exp\left(-\frac{z}{l_d}-\frac{\theta^2}{\langle\theta^2\rangle_\infty}\right), \quad \theta < \sqrt{\langle\theta^2\rangle_\infty}$$

$$\tilde{I}_{scal}(z,\theta) \approx \frac{4\sigma_{tr}\exp(-z/l_d)}{\pi\sigma_a\theta^6\ln(2/\gamma_0)}\cdot\left(1+5\frac{\langle\theta^2\rangle_\infty}{\theta^2}-\ldots\right), \quad \theta > \sqrt{\langle\theta^2\rangle_\infty} \tag{7.102}$$

$$P_{un} = -\frac{\theta^2}{2}\cdot\ln 2\cdot\frac{\sigma\gamma_0^2}{\sigma_a\langle\theta^2\rangle_\infty^2}, \quad \theta < \sqrt{\langle\theta^2\rangle_\infty}$$

$$P_{un} = -\frac{\theta^2}{2}\cdot\left(1-\frac{4\langle\theta^2\rangle_\infty}{\theta^2}\right), \quad \theta > \sqrt{\langle\theta^2\rangle_\infty} \tag{7.103}$$

where

$$l_d = \left(\frac{1}{2}\sigma_a\langle\theta^2\rangle_\infty\right)^{-1} \tag{7.104}$$

Note that the relationship between the asymptotic length l_d and $\langle\theta^2\rangle_\infty$ is a consequence of the small-angle transfer equation and does not depend on the specific values of $a_1(\gamma)$ and $\langle\theta^2\rangle_\infty$.

7.5.2 Circularly polarized light

Let us consider depolarization of right-hand circularly polarized light. The difference between eq. (7.26) for the intensity and eq. (7.27) for the circularly polarized mode is due to the difference between the scattering functions $a_1(\mathbf{nn}')$ and $a_4(\mathbf{nn}')$ appearing in the right-hand side of eqs (7.26), (7.27).

Assuming that the Born condition (eq. (7.21)) and the small-angle approximation are fulfilled, we can write

$$\sigma\int d\mathbf{n}'\,(a_4(\mathbf{nn}')-a_1(\mathbf{nn}'))\,V(z,\mu') \approx -\frac{\sigma}{8}\int d\boldsymbol{\theta}' a_1(|\boldsymbol{\theta}-\boldsymbol{\theta}'|)(\boldsymbol{\theta}-\boldsymbol{\theta}')^4 V(z,\theta') \tag{7.105}$$

The effect of this term depends on the form of the phase function $a_1(\gamma)$.

Within the small-angle diffusion approximation, eq. (7.105) gives

$$-\frac{\sigma}{8}\int d\boldsymbol{\theta}' a_1(|\boldsymbol{\theta}-\boldsymbol{\theta}'|)(\boldsymbol{\theta}-\boldsymbol{\theta}')^4 V(z,\theta') = \left(-\frac{\sigma\langle\gamma^4\rangle}{8} - \frac{\sigma\langle\gamma^6\rangle}{16}\frac{1}{\theta}\frac{\partial}{\partial\theta}\theta\frac{\partial}{\partial\theta} + \cdots\right) V(z,\theta) \tag{7.106}$$

With allowance for eq. (7.106), the small-angle diffusion equation for the circularly polarized mode can be written as [34]

$$\left\{\frac{\partial}{\partial z} + \frac{\sigma_a^{(V)}}{2}\theta^2 - D\frac{1}{\theta}\frac{\partial}{\partial\theta}\theta\frac{\partial}{\partial\theta}\right\}\tilde{V}(z,\theta) = 0 \tag{7.107}$$

where $\tilde{V}(z,\theta) = \exp\left(\sigma_a^{(V)} z\right) V(z,\theta)$ and

$$\sigma_a^{(V)} = \sigma_a + \frac{\sigma\langle\gamma^4\rangle}{8} \tag{7.108}$$

Equation (7.108) defines the effective 'absorption' coefficient for the fourth Stokes parameter. The additional term in eq. (7.108) is responsible for depolarization of circularly polarized light (see eq. (7.30)). We neglect the contribution of $\sigma\langle\gamma^6\rangle/16$ to the angular diffusion coefficient D.

The boundary condition for eq. (7.107) has the form

$$\tilde{V}(z=0,\theta) = \frac{\delta(\theta)}{2\pi\theta} \tag{7.109}$$

From eqs (7.107) and (7.109) we obtain the expression for $\tilde{V}$ that differs from eq. (7.84) only by substitution of $\sigma_a^{(V)}$ for σ_a.

The degree of polarization

$$P_C = \sqrt{\left(\frac{V}{I_{scal}}\right)^2 + P_{un}^2} \tag{7.110}$$

is determined by the following expression:

$$P_C \approx \left(\frac{\sigma_a^{(V)}}{\sigma_a}\exp\left(-2\theta^2\left(\frac{1}{\langle\theta^2\rangle_z^{(V)}} - \frac{1}{\langle\theta^2\rangle_z}\right)\right)\times \frac{\sinh^2\left(z\sqrt{\sigma_{tr}\sigma_a}\right)}{\sinh^2\left(z\sqrt{\sigma_{tr}\sigma_a^{(V)}}\right)}\exp\left(-\frac{\sigma z\langle\gamma^4\rangle}{4}\right) + P_{un}^2\right)^{1/2} \tag{7.111}$$

Equation (7.111) permits us to find the attenuation length for circularly polarized light

$$l_{circ} = \left(\frac{\sigma\langle\gamma^4\rangle}{8} + \sqrt{\sigma_{tr}}(\sqrt{\sigma_a^{(V)}} - \sqrt{\sigma_a})\right)^{-1}$$
$$\approx \left(\frac{\sigma\langle\gamma^4\rangle}{8}\left(1 + \frac{1}{2}\sqrt{\frac{\sigma_{tr}}{\sigma_a}} + \ldots\right)\right)^{-1} \tag{7.112}$$

The length l_{circ} is much larger than the asymptotic length l_d (see eq. (7.88)):

$$\frac{l_{circ}}{l_d} \approx 8\frac{\langle\gamma^2\rangle}{\langle\gamma^4\rangle\langle\theta^4\rangle_\infty} \gg 1 \tag{7.113}$$

Next, let us consider depolarization of light in the medium with the phase function (7.94). In this case eq. (7.105) gives [35]

$$-\frac{\sigma}{8}\int d\boldsymbol{\theta}' a_1(|\boldsymbol{\theta} - \boldsymbol{\theta}'|)(\boldsymbol{\theta} - \boldsymbol{\theta}')^4 V(z,\theta') \approx -\frac{\sigma\gamma_0^2}{8\pi}\int d\boldsymbol{\theta}' V(z,\theta') \tag{7.114}$$

As follows from eq. (7.114), the depolarization term appears to be angular independent. Treating the term (7.114) as a pertubartion, we develop an iterative procedure for solving the transfer equation for $V(z,\theta)$. As $l_{circ} \gg l_d$, we restrict our consideration to the asymptotic case.

The 'wings' of $V(z,\theta)$ $\left(\theta > \sqrt{\langle\theta^2\rangle_\infty}\right)$ can be described as follows. The contribution from the term (7.114) to $V(z,\theta)$ can be estimated as [35]

$$\delta\tilde{V}(z,\theta) = -\frac{\sigma\gamma_0^2}{8\pi}\int\limits_0^z dz' \exp\left(-\frac{\sigma_a(z-z')\theta^2}{2}\right)\tilde{E}^{(V)}(z') \tag{7.115}$$

where

$$\tilde{E}^{(V)}(z) = \int d\boldsymbol{\theta}\tilde{V}(z,\theta) \tag{7.116}$$

For large angles

$$\delta\tilde{V}(z,\theta) = -\frac{\sigma\gamma_0^2}{4\pi\sigma_a\theta^2}\tilde{E}^{(V)}(z) \tag{7.117}$$

The contribution (7.115) is the component of $\tilde{V}(z,\theta)$ that falls off most slowly as θ increases. Separating out the contribution (7.115) from $\tilde{V}(z,\theta)$,

$$\tilde{V}(z,\theta) = \tilde{v}(z,\theta) + \delta V(z,\theta) \tag{7.118}$$

we obtain the following equation for $\tilde{v}(z,\theta)$ [35]:

$$\left\{\frac{\partial}{\partial z} + \sigma_a\frac{\theta^2}{2}\right\}\tilde{v}(z,\theta) = \sigma\int d\boldsymbol{\theta}' a_1(|\boldsymbol{\theta} - \boldsymbol{\theta}'|)(\tilde{v}(z,\theta') - \tilde{v}(z,\theta)) -$$
$$-\sigma\int d\boldsymbol{\theta}' a_1(|\boldsymbol{\theta} - \boldsymbol{\theta}'|)\frac{\sigma\gamma_0^2}{8\pi}\int\limits_0^z dz'\tilde{E}^{(V)}(z')\left(\exp\left(-\frac{\sigma_a(z-z')\theta'^2}{2}\right) -\right.$$
$$\left. - \exp\left(-\frac{\sigma_a(z-z')\theta^2}{2}\right)\right) \tag{7.119}$$

Using the expansion of $\tilde{v}(z,\theta)$ in inverse powers of θ [32, 63, 64]) (see also section 7.5.1) we can find the θ-dependence of $\tilde{v}(z,\theta)$ at the 'wings' [35].

As a result, the 'wings' of the fourth Stokes parameter in the asymptotic state are given by [35]

$$\tilde{V}(z,\theta) \approx \tilde{E}^{(V)}(z) \left[\frac{2\sigma\gamma_0^2}{\pi\sigma_a\theta^6} \cdot \left(1 + 5\frac{\langle\theta^2\rangle_z}{\theta^2} + \dots\right) - \frac{\sigma\gamma_0^2}{4\pi\sigma_a\theta^2} \cdot \left(1 + \frac{\langle\theta^2\rangle_z}{\theta^2} + \dots\right)\right], \tag{7.120}$$

The angular distributions $\tilde{V}(z,\theta)$ and $\tilde{I}_{scal}(z,\theta)$ are close to each other. The difference between them is of the order of θ^4 (see eq. (7.102) and eq. (7.120)). In the asymptotic state the difference between $\tilde{V}(z,\theta)$ and $\tilde{I}_{scal}(z,\theta)$ is mainly due to the z-dependence of these quantities.

To calculate $\tilde{E}^{(V)}(z)$, we consider the asymptotic equation (7.51). The angular function entering into eq. (7.51) and the eigenvalue ϵ_V can be calculated with a perturbation theory on the basis of the results for the intensity at large depths (see section 7.5.1) [32]. Within the first approximation in small quantity $\sigma\gamma_0^2/\sigma_a \ll 1$, the eigenvalue ϵ_V is given by [35]

$$\epsilon_V = \epsilon_I + \frac{1}{4}\sigma\gamma_0^2\langle\theta^2\rangle_\infty \tag{7.121}$$

where $\langle\theta^2\rangle_\infty$ is determined by eq. (7.101).

Within the 'dome' region ($\theta < \sqrt{\langle\theta^2\rangle_\infty}$) the contribution from the term (7.114) to the angular dependence $\tilde{V}(z,\theta)$ is of the order of $\langle\theta^2\rangle_\infty^2$.

As follows from eq. (7.121), the degree of polarization decreases as

$$P_C = \sqrt{\left(\frac{V}{I_{scal}}\right)^2 + P_{un}^2} \approx \frac{V}{I_{scal}} \approx \exp\left(-\frac{1}{4}\sigma\gamma_0^2\langle\theta^2\rangle_\infty z\right) \tag{7.122}$$

and the attenuation length for circularly polarizaed light is equal to

$$l_{circ} \approx \left(\frac{1}{4}\sigma\gamma_0^2\langle\theta^2\rangle_\infty\right)^{-1} \tag{7.123}$$

Ratio between l_{circ} and the asymptotical length l_d is proportional to $\sigma_a/(\sigma\gamma_0^2) \gg 1$.

7.5.3 Linearly polarized light

In order to derive the small-angle equation for W we expand the phase factor entering into eq. (7.28) in the small spherical excess $\chi_+ - \psi = \pi - \beta - \beta' - \psi$ [54] and keep the first three terms. As a result, we have

$$\exp(2i(\chi_+ - \psi) \approx 1 - \frac{1}{2}\theta_\alpha\theta'_\beta(\theta_\alpha\theta'_\beta - \theta_\beta\theta'_\alpha) + ie_{\alpha\beta}\theta_\alpha\theta'_\beta \tag{7.124}$$

where $e_{\alpha\beta}$ is two-dimensional antisymmetric tensor

$$e_{\alpha\beta} = \begin{pmatrix} 0 & 1 \\ -1 & 0 \end{pmatrix}$$

With allowance for eq. (7.124) and the Born relation (7.21), the small-angle equation for $\tilde{W} = W\exp(\sigma_a z)$ takes the form [38]

$$\left\{\frac{\partial}{\partial z} + \sigma + \frac{\sigma_a}{2}\theta^2\right\}\tilde{W}(z,\theta) =$$
$$\sigma\int d\boldsymbol{\theta}' a_1(|\boldsymbol{\theta}-\boldsymbol{\theta}'|)\tilde{W}(z,\theta') - \frac{\sigma}{2}\int d\boldsymbol{\theta}' a_1(|\boldsymbol{\theta}-\boldsymbol{\theta}'|)[\theta_\alpha\theta'_\beta(\theta_\alpha\theta'_\beta - \theta_\beta\theta'_\alpha)$$
$$+ 2ie_{\alpha\beta}\theta_\alpha\theta'_\beta]\tilde{W}(z,\theta') - \frac{\sigma}{16}\int d\boldsymbol{\theta}' a_1(|\boldsymbol{\theta}-\boldsymbol{\theta}'|)|\boldsymbol{\theta}-\boldsymbol{\theta}'|)|^4 W(z,\theta') \qquad (7.125)$$

When deriving eq. (7.125), we expand the terms appearing in the right-hand side of eq. (7.28) to terms of order θ^4 and θ'^4.

The boundary condition for eq. (7.125) has the form

$$\tilde{W}(z=0,\theta) = \frac{\delta(\theta)}{2\pi\theta} \qquad (7.126)$$

The second and third terms in the right-hand side of eq. (7.125) are responsible for the geometrical depolarization and the dynamical one, respectively.

Equation (7.125) as well as the scalar radiative transfer equation (eq. (7.66)) can be transformed into a differential equation of the same type as eq. (7.72). For this purpose, we perform the Bessel transfom of $\tilde{W}(z,\theta)$,

$$\tilde{W}(z,\omega) = 2\pi\int_0^\infty \theta d\theta J_0(\omega\theta)\tilde{W}(z,\theta) \qquad (7.127)$$

As a result, we obtain the following equation for $\tilde{W}(z,\omega)$ [38]

$$\left\{\frac{\partial}{\partial z} + \sigma(1-a_1(\omega)) - \frac{1}{2}\sigma_a\Delta_\omega + \hat{\Xi}_g + \frac{\sigma}{16}(\Delta^2_\omega a_1(\omega))\right\}\tilde{W}(z,\omega) = 0 \qquad (7.128)$$

where $\hat{\Xi}_g(\omega)$ is given by

$$\hat{\Xi}_g(\omega) = \frac{\sigma}{2\omega}\frac{\partial}{\partial\omega}\left[\frac{\partial a_1(\omega)}{\partial\omega}\frac{\partial}{\partial\omega}\right] \qquad (7.129)$$

The boundary condition for eq. (7.128) has the form

$$\tilde{W}(z=0,\omega) = 1 \qquad (7.130)$$

The small-angle version of the transfer equations for the overtones Q_W, Q_{un} and w (see eqs (7.40)–(7.42)) can be obtained as follows. As a first approximation,

we neglect the difference between the spherical triangle shown in Fig. 7.1 and a planar one. Then we can write

$$\chi_+ - \psi = \pi - \beta - \beta' - (\varphi - \varphi') = 0$$

and

$$\exp(-2\mathrm{i}(\beta + \psi)) = \exp(-2\mathrm{i}(\beta - \varphi'))$$

Assuming also the Born approximation for single scattering, we perform the small-angle expansion of the terms appearing in eqs (7.40)–(7.42). For $\tilde{Q}_{un}$, we arrive at eq. (7.67). The small-angle equation for overtone $\tilde{Q}_W = Q_W \exp(\sigma_a z)$ differs from eq. (7.67) only by the substitution of $\tilde{W}$ for $\tilde{I}_{scal}$. The small-angle equation for the overtone $\tilde{w} = w \exp(\sigma_a z)$ has the following form [34]:

$$\left\{\frac{\partial}{\partial z} + \sigma + \frac{\sigma_a}{2}\theta^2\right\}\tilde{w}(z,\theta) =$$
$$\sigma \int\limits_0^\infty d\theta' \left[\int\limits_0^{2\pi} d\psi a_1(|\boldsymbol{\theta} - \boldsymbol{\theta}'|)\cos 4\psi\right]\tilde{w}(z,\theta') + \frac{\sigma}{16}\int d\boldsymbol{\theta}' a_1(|\boldsymbol{\theta} - \boldsymbol{\theta}'|)[|\boldsymbol{\theta} - \boldsymbol{\theta}'|^4 -$$
$$\theta'^2(\theta'^2(1 - \cos 4\psi) + 4\theta^2(1 - \cos 2\psi) - 4\theta\theta'(\cos\psi - \cos 3\psi))]\tilde{W}(z,\theta') \quad (7.131)$$

Using the Bessel transform

$$\tilde{Q}_W(z,\omega) = 2\pi \int\limits_0^\infty \theta d\theta J_2(\omega\theta)\tilde{Q}_W(z,\theta), \quad \tilde{w}(z,\omega) = 2\pi \int\limits_0^\infty \theta d\theta J_4(\omega\theta)\tilde{w}(z,\theta) \quad (7.132)$$

we present the small-angle equations for $\tilde{Q}_W$ and $\tilde{w}$ in the differential form [34, 38]

$$\left\{\frac{\partial}{\partial z} + \sigma(1 - a_1(\omega)) - \frac{1}{2}\sigma_a\left(\Delta_\omega - \frac{4}{\omega^2}\right)\right\}\tilde{Q}_W(z,\omega) = \Xi(\omega)\tilde{W}(z,\omega) \quad (7.133)$$

$$\left\{\frac{\partial}{\partial z} + \sigma(1 - a_1(\omega)) - \frac{1}{2}\sigma_a\left(\Delta_\omega - \frac{16}{\omega^2}\right)\right\}\tilde{w}(z,\omega) = \Xi_w(\omega)\tilde{W}(z,\omega) \quad (7.134)$$

where

$$\Xi_{\tilde{w}}(\omega) = \frac{\sigma}{16}\left[\omega^4\left(\frac{\partial}{\omega\partial\omega}\right)^4 a_1(\omega)\right] \quad (7.135)$$

The quantity $\Xi(\omega)$ has already been defined by eq. (7.75).

Let us consider now the depolarization of linearly polarized light for various models of the phase function $a_1(\gamma)$ (or its Bessel image $a_1(\omega)$).

Starting from eq. (7.79), we arrive at the small-angle diffusion model. Within the framework of eq. (7.79), we have

$$\hat{\Xi}_g(\omega) = \frac{1}{2}\sigma\langle\gamma^2\rangle\Delta_\omega, \quad \frac{1}{16}\sigma(\Delta_\omega^2 a_1(\omega)) = \frac{1}{16}\sigma\langle\gamma^4\rangle \quad (7.136)$$

As follows from eq. (7.136), the last term in the left-hand side of eq. (7.128) is a negligibly small quantity as compared with other terms appearing in eq. (7.128). Hence, the geometrical mechanism is mainly responsible for the depolarization of linearly polarized light. Perfoming the inverse Bessel transform, we obtain the small-angle diffusion equation for $\tilde{W}(z,\theta)$ [34, 37]

$$\left\{\frac{\partial}{\partial z}+\frac{\sigma_a^{(W)}}{2}\theta^2-D\frac{1}{\theta}\frac{\partial}{\partial\theta}\theta\frac{\partial}{\partial\theta}\right\}\tilde{W}(z,\theta)=0 \tag{7.137}$$

where

$$\sigma_a^{(W)}=\sigma_a+\sigma_{tr} \tag{7.138}$$

is the effective 'absorption' coefficient for $\tilde{W}$. The difference between $\sigma_a^{(W)}$ and σ_a is responsible for additional attenuation of W due to depolarization.

The solution of eq. (7.137) is expressed in terms of eq. (7.84). In accordance with eq. (7.84), the function $\tilde{W}$ can be written as [34, 37]

$$\tilde{W}(z,\theta)=\frac{1}{\pi A_0^{(W)}(z)A_1^{(W)}(z)}\exp\left(-\frac{\theta^2}{A_1^{(W)}(z)}\right) \tag{7.139}$$

where

$$A_0^{(W)}(z)=\cosh\left(z\sqrt{2D\sigma_a^{(W)}}\right),\quad A_1^{(W)}(z)=2\sqrt{\frac{2D}{\sigma_a^{(W)}}}\tanh\left(z\sqrt{2D\sigma_a^{(W)}}\right)$$

Taking into account only the basic modes $\tilde{I}_{scal}$ and $\tilde{W}$, we can describe the depolarization of linearly polarized light (see eq. (7.59)). The degree of polarization of multiply scattered light is governed by the difference in attenuation of the basic modes $\tilde{I}_{scal}$ and $\tilde{W}$ [34, 37]

$$P_L=\frac{\sqrt{Q^2+U^2}}{I}\approx\frac{\tilde{W}}{\tilde{I}_{scal}}=$$
$$\sqrt{\frac{\sigma_a^{(W)}}{\sigma_a}}\left(\frac{\sinh\left(z\sqrt{2D\sigma_a}\right)}{\sinh\left(z\sqrt{2D\sigma_a^{(W)}}\right)}\right)\exp\left(-\theta^2\left(\frac{1}{A_1^{(W)}(z)}-\frac{1}{A_1^{(I)}(z)}\right)\right) \tag{7.140}$$

At relatively small z ($z<l_d$), the degree of polarization is close to unity

$$P_L\approx 1-\frac{\langle\theta^2\rangle_z^2}{24}\left(1+\frac{2\theta^2}{\langle\theta^2\rangle_z}+\ldots\right),\quad \theta<\sqrt{\langle\theta^2\rangle_z} \tag{7.141}$$

In the asymptotic state ($z>l_d$), we have

$$P_L\approx\left(1+\frac{\langle\theta^2\rangle_\infty^2}{8}\left(1-\frac{\theta^2}{\langle\theta^2\rangle_\infty}\right)\right)\exp\left(-\frac{1}{4}\sigma_{tr}z\langle\theta^2\rangle_\infty\right),\quad \theta<\sqrt{\langle\theta^2\rangle_\infty} \tag{7.142}$$

As follows from eq. (7.142), the polarization degree P_L decays over distance of order

$$l_{lin} = \left(\frac{1}{4}\sigma_{tr}\langle\theta^2\rangle_\infty\right)^{-1}$$

The length l_{lin} is much larger than the length l_d, that describes the asymptotic state of propagation,

$$l_{lin} = 2\frac{\sigma_a}{\sigma_{tr}}l_d \gg l_d$$

For intermediate depths, $l_d < z < l_{lin}$, eq. (7.142) results in the following expression for the polarization degree:

$$P_L \approx 1 - \frac{\langle\theta^2\rangle_\infty^2}{8}\left(\frac{z}{l_d} - 1 + \frac{\theta^2}{\langle\theta^2\rangle_\infty}\right) \tag{7.143}$$

As the degree of polarization decreases to small values, the contribution of the overtones should be taken into account. Within the framework of eq. (7.79), equations (7.133), (7.134) can be transformed into the following form [34, 37]

$$\left\{\frac{\partial}{\partial z} + \frac{\sigma_a}{2}\theta^2 - D\left[\frac{1}{\theta}\frac{\partial}{\partial\theta}\theta\frac{\partial}{\partial\theta} - \frac{4}{\theta^2}\right]\right\}\tilde{Q}_W(z,\theta) = -\frac{\sigma\langle\gamma^4\rangle}{4}\left[\theta^2\left(\frac{1}{\theta}\frac{\partial}{\partial\theta}\right)^2\right]\tilde{W}(z,\theta) \tag{7.144}$$

$$\left\{\frac{\partial}{\partial z} + \frac{\sigma_a}{2}\theta^2 - D\left[\frac{1}{\theta}\frac{\partial}{\partial\theta}\theta\frac{\partial}{\partial\theta} - \frac{16}{\theta^2}\right]\right\}\tilde{w}(z,\theta) = \frac{\sigma\langle\gamma^8\rangle}{3\cdot 2^{11}}\left[\theta^4\left(\frac{\partial}{\theta\partial\theta}\right)^4\right]\tilde{W}(z,\theta) \tag{7.145}$$

The corresponding equation for the overtone $\tilde{Q}_{un}$ has already been derived above (see eq. (7.81)).

As follows from eqs (7.81), (7.144), and (7.145), the source in the right-hand side of eq. (7.145) is many times smaller than the sources in eqs (7.81) and (7.144). Therefore the quantity $\tilde{w}$ can be neglected as compared with $\tilde{Q}_{un}$ and $\tilde{Q}_W$.

The overtone $\tilde{Q}_{un}$ is given by eq. (7.85). The overtone $\tilde{Q}_W$ can be described by a similar expression [34, 37]

$$\tilde{Q}_W(z,\theta) \approx \frac{b_1^{tr}\theta^2}{\sigma_a\langle\theta^2\rangle_\infty^3}f(z)\tilde{W}(z,\theta) \tag{7.146}$$

With allowance for the overtones Q_W and Q_{un}, the Stokes parameters can be written as

$$\tilde{I} \approx \tilde{I}_{scal} + \tilde{Q}_W\cos 2\varphi, \quad \tilde{Q} - \mathrm{i}\tilde{U} \approx \tilde{W}\exp(-2\mathrm{i}\varphi) + \tilde{Q}_{un} \tag{7.147}$$

Equation (7.147) permits us to derive a more accurate expression for the degree of polarization as compared with eq. (7.140). With allowance for inequality $\tilde{Q}_W \ll \tilde{I}_{scal}$ the degree of polarization takes the form

$$P_L \approx \frac{\sqrt{\tilde{W}^2 + 2\tilde{W}\tilde{Q}_{un}\cos 2\varphi + \tilde{Q}_{un}^2}}{\tilde{I}_{scal}}\left(1 - \frac{\tilde{Q}_W}{\tilde{I}_{scal}}\cos 2\varphi\right) \tag{7.148}$$

At depths $z < l_{lin}$, the contribution from overtones is responsible for the azimuth dependence of the degree of polarization,

$$P_L \approx \frac{\tilde{W}(z,\theta)}{\tilde{I}_{scal}(z,\theta)} \left(1 + \left(\frac{\tilde{Q}_{un}(z,\theta)}{\tilde{W}(z,\theta)} - \frac{\tilde{Q}_W(z,\theta)}{\tilde{I}_{scal}(z,\theta)}\right) \cos 2\varphi\right) \tag{7.149}$$

As depth z increases, the incident radiation depolarizes ($Q_{un} \gg W$) and P_L tends to the polarization degree P_{un} of unpolarized light (see eq. (7.93)).

Now consider depolarization of light in the medium with the phase function (7.94).

As noted above, depolarization of light is a relatively slow process. Depolarization becomes observable at large depths ($z \gg l_d$), i.e. in the asymptotical state. The last two terms entering into eqs (7.125) and (7.128), that are responsible for the depolarization, are assumed to be small as compared with the other terms. This allows us to use a pertubation theory to solve eq. (7.128), taking as an initial approximation the solution of the scalar transfer equation (7.72) (see also [35]).

As a result, the polarization mode $\tilde{W}$ in the asymptotic state can be written as

$$\begin{aligned} \tilde{W}(z,\theta) \;\approx\; & \tilde{I}_{scal}(z,\theta) \left(1 + \frac{\langle\theta^2\rangle_\infty^2}{8} \left(1 - \frac{\theta^2}{\langle\theta^2\rangle_\infty}\right)\right) \times \\ & \exp\left(-\frac{\sigma z \gamma_0^2 \langle\theta^2\rangle_\infty}{8} \left(\ln \frac{\langle\theta^2\rangle_\infty}{2\gamma_0^2} + 1\right)\right) \end{aligned} \tag{7.150}$$

In accordance with eq. (7.150) the polarization degree of forward propagating waves is given by

$$P_L \approx \exp\left(-\frac{\sigma z \gamma_0^2 \langle\theta^2\rangle_\infty}{8} \left[\ln \frac{\langle\theta^2\rangle_\infty}{2\gamma_0^2} + 1\right]\right) \tag{7.151}$$

From eq. (7.151) it follows that the depolarization length for linearly polarized light can be estimated as

$$\left(-\frac{\sigma z \gamma_0^2 \langle\theta^2\rangle_\infty}{8} \left[\ln \frac{\langle\theta^2\rangle_\infty}{2\gamma_0^2} + 1\right]\right)^{-1}$$

The geometrical mechanism and the dynamical one contribute additively to the attenuation of $\tilde{W}$ and P_L. The contribution of the geometrical mechanism to the attenuation coefficient is equal to

$$\frac{1}{8}\sigma\gamma_0^2 \langle\theta^2\rangle_\infty \ln \frac{\langle\theta^2\rangle_\infty}{2\gamma_0^2}$$

and exceeds the dynamical contribution by the logarithmic factor.

The overtones $\tilde{Q}_W$ and $\tilde{w}$ can be calculated in the close analogy with $\tilde{Q}_{un}$ (see eq. (7.103)) [32]. In the 'dome' region ($\theta < \sqrt{\langle\theta^2\rangle_\infty}$), the overtones $\tilde{Q}_W$ and $\tilde{w}$ can be written as

$$\tilde{Q}_W(z,\theta) \approx -\frac{\sigma\gamma_0^2\theta^2}{\sigma_a\langle\theta^2\rangle_\infty^2}\frac{\ln 2}{2}\tilde{W}(z,\theta)$$

$$\tilde{Q}_{un}(z,\theta) \approx -\frac{\sigma\gamma_0^2\theta^2}{\sigma_a\langle\theta^2\rangle_\infty^2}\frac{\ln 2}{2}\tilde{I}_{scal}(z,\theta)$$

$$\tilde{w}(z,\theta) \approx \frac{\sigma\gamma_0^2\theta^4}{144\sigma_a\langle\theta^2\rangle_\infty^2}\tilde{W}(z,\theta) \tag{7.152}$$

As follows from eq. (7.152), the overtone $\tilde{w}$ is relatively small as compared with $\tilde{Q}_W$ and $\tilde{Q}_{un}$, and the contribution of $\tilde{w}$ to the polarization state can be neglected. Equations (7.148) and (7.149) remain valid.

Expressions (7.152) allow us to determine the degree of polarization of scattered light and the angle of rotation of the polarization plane. Orientation of the polarization plane was investigated in [34, 37, 38].

7.6 A narrow beam of linearly polarized light

As shown above (see also [33]–[38]), the depolarization of linearly polarized light in random media with large-scale inhomogeneities is mainly due to the geometrical mechanism. This circumstance makes it possible to observe directly the Rytov rotation of the polarization plane along the three-dimensional (nonplanar) path of propagation.

A beam propagating in a scattering medium can be considered as the superposition of random rays. A wave propagating along a separate ray remains linearly polarized. However, the polarization planes related to the different rays appear to be tilted with respect to each other. As the spread in orientation of the polarization planes increases, the beam depolarizes.

For a wide beam of linearly polarized light, the average ray trajectory for any direction of propagation is a planar curve. As a result, the average orientation of the polarization plane coincides with the initial polarization of the incident light.

A different situation arises in the case of a narrow beam. For a given transverse displacement from the beam axis, the average trajectory of the ray propagation may differ from a planar curve. Therefore, the propagation of light along this trajectory is accompanied by deflection of the polarization plane from its initial orientation. The tilt of the average polarization plane for an off-axis trajectory is the direct manifestation of the Rytov rotation.

In this section we discuss multiple scattering of a narrow beam. The incident light is assumed to be linearly polarized. We take advantage of the scattering matrix within the geometrical approximation (see eq. (7.29)) and restrict our consideration to the case of small-angle scattering [65].

Let us consider a narrow linearly polarized beam propagating along the direction of inner normal $\mathbf{n}_0 = \{0, 0, 1\}$. In this case the equation for the polarization Green matrix (see eq. (7.33)) can be written as

$$\left\{\mathbf{n}\frac{\partial}{\partial \mathbf{r}} + \sigma_{tot}\right\}\hat{G}(\mathbf{r}, \mathbf{n}|\mathbf{r}_0, \mathbf{n}_0) = \sigma \int d\mathbf{n}'\hat{L}(\{\mathbf{n}_0, \mathbf{n}\} \leftarrow \{\mathbf{n}, \mathbf{n}'\}|\mathbf{n}) \times$$
$$\times\, \hat{d}(\mathbf{n}\mathbf{n}')\hat{L}(\{\mathbf{n}, \mathbf{n}'\} \leftarrow \{\mathbf{n}', \mathbf{n}_0\}|\mathbf{n}')\hat{G}(\mathbf{r}, \mathbf{n}'|\mathbf{r}_0, \mathbf{n}_0) \tag{7.153}$$

where

$$\hat{L}(\{\mathbf{n}, \mathbf{n}'\} \leftarrow \{\mathbf{n}', \mathbf{n}_0\}|\mathbf{n}') \equiv \hat{L}(-\beta'), \quad \hat{L}(\{\mathbf{n}_0, \mathbf{n}\} \leftarrow \{\mathbf{n}, \mathbf{n}'\}|\mathbf{n}) \equiv \hat{L}(\pi - \beta) \tag{7.154}$$

The angular dependence of the matrix $\hat{G}$ is due to both scattering of light and transformations of the $\hat{G}$ matrix elements under rotations of the reference plane (these rotations are described by $\hat{L}$ matrices). To exclude the geometrical factors due to rotation of the reference plane, we represent the matrix $\hat{G}$ in the form that is similar to the single scattering matrix $\hat{L}(...|\mathbf{n})\hat{d}(\mathbf{n}\mathbf{n}')\hat{L}(...|\mathbf{n}')$ (see eq. (7.13))

$$\hat{G}(\mathbf{r}, \mathbf{n}|\mathbf{r}_0, \mathbf{n}_0) = \hat{L}(\{\mathbf{n}_0, \mathbf{n}\} \leftarrow \{\mathbf{n}, \mathbf{n}'\}|\mathbf{n})\hat{G}^{scat}(\mathbf{r}, \mathbf{n}|\mathbf{r}_0, \mathbf{n}') \times$$
$$\times\, \hat{L}(\{\mathbf{n}, \mathbf{n}'\} \leftarrow \{\mathbf{n}', \mathbf{n}_0\}|\mathbf{n}')\Big|_{\mathbf{n}'=\mathbf{n}_0} = \hat{G}^{scat}(\mathbf{r}, \mathbf{n}|\mathbf{r}_0, \mathbf{n}_0)\hat{L}(\varphi) \tag{7.155}$$

The matrix $\hat{G}^{scat}$ relates polarization parameters of the scattered light to those of the incident light, which are defined with respect to the scattering plane $\{\mathbf{n}, \mathbf{n}_0\}$.

Substituting eq. (7.155) into eq. (7.153), we derive the following equation for the matrix $\hat{G}^{scat}$:

$$\left\{\mathbf{n}\frac{\partial}{\partial \mathbf{r}} + \sigma_{tot}\right\}\hat{G}^{scat}(\mathbf{r}, \mathbf{n}|\mathbf{r}_0, \mathbf{n}_0) = \sigma \int d\mathbf{n}'\hat{L}(\{\mathbf{n}_0, \mathbf{n}\} \leftarrow \{\mathbf{n}, \mathbf{n}'\}|\mathbf{n})\hat{d}(\mathbf{n}\mathbf{n}') \times$$
$$\times\, \hat{L}(\{\mathbf{n}, \mathbf{n}'\} \leftarrow \{\mathbf{n}', \mathbf{n}_0\}|\mathbf{n}')\hat{G}^{scat}(\mathbf{r}, \mathbf{n}'|\mathbf{r}_0, \mathbf{n}_0)\hat{L}(\{\mathbf{n}', \mathbf{n}_0\} \leftarrow \{\mathbf{n}, \mathbf{n}_0\}|\mathbf{n}_0) \tag{7.156}$$

Within the geometrical approximation (see eq. (7.29)) multiple scattering of polarized light can be considered as propagation of the scalar mode I_{scal} and the linearly polarized mode W (see eq. (7.35)) [34, 37, 38].

The intensity obeys the well-known scalar transfer equation

$$\left\{\mathbf{n}\frac{\partial}{\partial \mathbf{r}} + \sigma_{tot}\right\} I_{scal}(\mathbf{r}, \mathbf{n}|\mathbf{r}_0, \mathbf{n}_0) = \sigma \int d\mathbf{n}' a_1(\mathbf{n}\mathbf{n}') I_{scal}(\mathbf{r}, \mathbf{n}'|\mathbf{r}_0, \mathbf{n}_0) \tag{7.157}$$

The equation for the linearly polarized mode W can be written as

$$\left\{\mathbf{n}\frac{\partial}{\partial \mathbf{r}} + \sigma_{tot}\right\} W(\mathbf{r}, \mathbf{n}|\mathbf{r}_0, \mathbf{n}_0) = \sigma \int d\mathbf{n}' L_{22}(\{\mathbf{n}_0, \mathbf{n}\} \leftarrow \{\mathbf{n}, \mathbf{n}'\}|\mathbf{n})a_1(\mathbf{n}\mathbf{n}') \times$$
$$\times\, L_{22}(\{\mathbf{n}, \mathbf{n}'\} \leftarrow \{\mathbf{n}', \mathbf{n}_0\}|\mathbf{n}')L_{22}(\{\mathbf{n}', \mathbf{n}_0\} \leftarrow \{\mathbf{n}, \mathbf{n}_0\}|\mathbf{n}_0)W(\mathbf{r}, \mathbf{n}'|\mathbf{r}_0, \mathbf{n}_0) \tag{7.158}$$

The product of the matrix elements L_{22} in the right-hand side of eq. (7.158) yields the phase factor (see eq. (7.28))

$$\exp(2i(\pi - \beta - \beta' - \varphi + \varphi'))$$

The boundary conditions to eqs (7.157) and (7.158) for a unit incident flux have the form

$$I_{scal}(z = 0, (\mathbf{n}) = W(z = 0, (\mathbf{n}) = \delta(\mathbf{r} - \mathbf{r}_0)\delta(\mathbf{n} - \mathbf{n}_0) \tag{7.159}$$

Within the small-angle approximation, eqs (7.157) and (7.159) can be written as [60]

$$\left\{\frac{\partial}{\partial z} + \boldsymbol{\theta}\frac{\partial}{\partial \boldsymbol{\rho}} + \sigma + \frac{\sigma_a}{2}\theta^2\right\}\tilde{I}_{scal}(z, \boldsymbol{\rho}, \boldsymbol{\theta}|\boldsymbol{\theta}_0) = \sigma\int d\boldsymbol{\theta}' a_1(|\boldsymbol{\theta} - \boldsymbol{\theta}'|)\tilde{I}_{scal}(z, \boldsymbol{\rho}, \boldsymbol{\theta}'|\boldsymbol{\theta}_0) \tag{7.160}$$

$$\tilde{I}_{scal}(z = 0, \boldsymbol{\rho}, \boldsymbol{\theta}) = \delta(\boldsymbol{\rho})\delta(\boldsymbol{\theta}) \tag{7.161}$$

where $\tilde{I}_{scal} = I_{scal}\exp(\sigma_a z)$ and $\boldsymbol{\rho} = \mathbf{r}_\perp - \mathbf{r}_{0\perp}$ is the vector of transverse displacement from the beam axis.

Perfoming the Fourier transform over variables $\boldsymbol{\theta}$ and $\boldsymbol{\rho}$, we find that

$$\tilde{I}_{scal}(z, \mathbf{q}, \boldsymbol{\omega}) = \int\int d\boldsymbol{\rho} d\boldsymbol{\theta}\exp(-i\mathbf{q}\boldsymbol{\rho} - i\boldsymbol{\omega}\boldsymbol{\theta})\tilde{I}_{scal}(z, \boldsymbol{\rho}, \boldsymbol{\theta}) \tag{7.162}$$

obeys by the differential equation

$$\left\{\frac{\partial}{\partial z} - \mathbf{q}\frac{\partial}{\partial \boldsymbol{\omega}} + \sigma(1 - a_1(\omega)) - \frac{\sigma_a}{2}\Delta_{\boldsymbol{\omega}}\right\}\tilde{I}_{scal}(z, \mathbf{q}, \boldsymbol{\omega}) = 0 \tag{7.163}$$

The small-angle equation for $\tilde{W} = W\exp(\sigma_a z)$ takes the following form (see eq. (7.125)) [65]

$$\left\{\frac{\partial}{\partial z} + \boldsymbol{\theta}\frac{\partial}{\partial \boldsymbol{\rho}} + \sigma + \frac{\sigma_a}{2}\theta^2\right\}\tilde{W}(z, \boldsymbol{\rho}, \boldsymbol{\theta}) = \sigma\int d\boldsymbol{\theta}' a_1(|\boldsymbol{\theta} - \boldsymbol{\theta}'|)\tilde{W}(z, \boldsymbol{\rho}, \boldsymbol{\theta}') - \frac{\sigma}{2}\int d\boldsymbol{\theta}' a_1(|\boldsymbol{\theta} - \boldsymbol{\theta}'|)[\theta_\alpha\theta'_\beta(\theta_\alpha\theta'_\beta - \theta_\beta\theta'_\alpha) - 2ie_{\alpha\beta}\theta_\alpha\theta'_\beta]\tilde{W}(z, \boldsymbol{\rho}, \boldsymbol{\theta}') \tag{7.164}$$

$$\tilde{W}(z = 0, \boldsymbol{\rho}, \boldsymbol{\theta}) = \delta(\boldsymbol{\rho})\delta(\boldsymbol{\theta}) \tag{7.165}$$

In the case of normal incidence of a wide beam, $\tilde{W}$ does not depend on the azimuthal angle φ. As a result, the contribution of the imaginary term in the right-hand side of eq. (7.164) is equal to zero, and we obtain eq. (7.125).

The Fourier transform of $\tilde{W}(z,\boldsymbol{\rho},\boldsymbol{\theta})$ over variables $\boldsymbol{\rho}$ and $\boldsymbol{\theta}$ results in the differential equation [65]

$$\left\{\frac{\partial}{\partial z}-\mathbf{q}\frac{\partial}{\partial\boldsymbol{\omega}}+\sigma(1-a_1(\omega))-\frac{\sigma_a}{2}\Delta_{\boldsymbol{\omega}}\right\}\tilde{W}(z,\mathbf{q},\boldsymbol{\omega})=-\frac{\sigma}{2}\left\{\Big[\Delta_\omega a_1(\omega)\Delta_{\boldsymbol{\omega}}-\right.$$

$$\left.-\frac{\partial^2 a_1(\omega)}{\partial\omega_\alpha\partial\omega_\beta}\frac{\partial^2}{\partial\omega_\alpha\partial\omega_\beta}\Big]+ie_{\alpha\beta}\frac{\partial a_1(\omega)}{\partial\omega_\alpha}\frac{\partial}{\partial\omega_\beta}\right\}\tilde{W}(z,\mathbf{q},\boldsymbol{\omega}) \tag{7.166}$$

The quantities $\tilde{I}_{scal}(z=0,\mathbf{q},\boldsymbol{\omega})$ and $\tilde{W}(z=0,\mathbf{q},\boldsymbol{\omega})$ are subject to the boundary condition

$$\tilde{I}_{scal}(z=0,\mathbf{q},\boldsymbol{\omega})=\tilde{W}(z=0,\mathbf{q},\boldsymbol{\omega})=1 \tag{7.167}$$

Equations (7.164) and (7.167) describe the polarization state of scattered light within the geometrical approximation. Within the framework of this approximation, the angle $\delta\chi$, that determines the deflecion of the polarization plane of multiply scattered light from its initial orientation, is equal to

$$\delta\chi=-\frac{1}{2}\arg W \tag{7.168}$$

This formula describes the Rytov rotation of the polarization plane for a wave propagating along some average trajectory.

To understand special features of the beam depolarization it is convenient to consider the multiple scattering process within an exactly solvable model, namely, within the small-angle diffusion approximation. In this approximation the function $a_1(\omega)$ is assumed to be equal to $a_1=1-(\langle\gamma^2\rangle\omega^2/4)$.

The small-angle diffusion equation for the intensity has the form [59]

$$\left\{\frac{\partial}{\partial z}+\boldsymbol{\theta}\frac{\partial}{\partial\boldsymbol{\rho}}+\frac{\sigma_a}{2}\theta^2\right\}\tilde{I}_{scal}(z,\boldsymbol{\rho},\boldsymbol{\theta})=D\Delta_{\boldsymbol{\theta}}\tilde{I}_{scal}(z,\boldsymbol{\rho},\boldsymbol{\theta}) \tag{7.169}$$

The solution of eq. (7.169) with the boundary condition (7.161) is given by [59]

$$\tilde{I}_{scal}(z,\boldsymbol{\rho},\boldsymbol{\theta})=\frac{1}{\pi^2 A_0^{(I)}(z)\Delta^{(I)}(z)}\times$$

$$\exp\left\{-\frac{1}{\Delta^{(I)}(z)}(A_1^{(I)}(z)\rho^2-2A_2^{(I)}(z)\boldsymbol{\rho}\boldsymbol{\theta}+A_3^{(I)}(z)\theta^2)\right\} \tag{7.170}$$

The functions $A_{0,1}^{(I)}$ are defined by eq. (7.86). The functions $A_{2,3}^{(I)}$ and $\Delta^{(I)}$ have the form

$$\begin{aligned}A_2^{(I)}(z) &= \frac{2}{\sigma_a}\left(1-\frac{1}{\cosh(z\sqrt{2D\sigma_a})}\right),\\ A_3^{(I)}(z) &= \frac{2z}{\sigma_a}\left(1-\frac{\tanh(z\sqrt{2D\sigma_a})}{z\sqrt{2D\sigma_a}}\right)\end{aligned} \tag{7.171}$$

$$\Delta^{(I)}(z)=A_1^{(I)}(z)A_3^{(I)}(z)-(A_2^{(I)}(z))^2 \tag{7.172}$$

The small-angle diffusion equation for the linearly polarized mode $\tilde{W}(z,\boldsymbol{\rho},\boldsymbol{\theta})$ can be written as [65]

$$\left\{\frac{\partial}{\partial z}+\boldsymbol{\theta}\frac{\partial}{\partial\boldsymbol{\rho}}+\frac{\sigma_a^{(W)}}{2}\theta^2\right\}\tilde{W}(z,\boldsymbol{\rho},\boldsymbol{\theta})= \left\{D\Delta_{\boldsymbol{\theta}}+i\sigma_{tr}e_{\alpha\beta}\theta_\alpha\frac{\partial}{\partial\theta_\beta}\right\}\tilde{W}(z,\boldsymbol{\rho},\boldsymbol{\theta}) \tag{7.173}$$

where $\sigma_a^{(W)}$ is defined by eq. (7.138).

As compared with eq. (7.169), eq. (7.173) includes two new terms. The first term, $\sigma_{tr}\theta^2\tilde{W}/2$, describes additional attenuation of $\tilde{W}$. This term is responsible for the depolarization of linearly polarized light. The imaginary term in the right-hand side of eq. (7.173) describes a qualitatively new effect, which cannot be observed in the case of a wide beam. This effect manifests itself as the rotation of the polarization plane at nonzero transverse displacements from the beam axis.

The solution of eq. (7.173) has the form [65]

$$\tilde{W}(z,\boldsymbol{\rho},\boldsymbol{\theta})=\frac{1}{\pi^2A_0^{(W)}(z)\Delta^{(W)}(z)}\exp\left\{-\frac{1}{\Delta^{(W)}(z)}\times \left(A_1^{(W)}(z)\rho^2-A_+^{(W)}(z)\rho_+\theta_--A_-^{(W)}(z)\rho_-\theta_++A_3^{(W)}(z)\theta^2\right)\right\} \tag{7.174}$$

where $\rho_\pm=x\pm iy$, $\theta_\pm=\theta_x\pm i\theta_y$, the functions $A_0^{(W)}$ and $A_1^{(W)}$ differ from the functions (7.86) only by the substitution of $\sigma_a^{(W)}$ for σ_a. The remaining functions involved in eq. (7.174) are given by

$$\Delta^{(W)}(z)=A_1^{(W)}(z)A_3^{(W)}(z)-A_+^{(W)}(z)A_-^{(W)}(z) \tag{7.175}$$

$$A_\pm^{(W)}(z)=2l_a\left[1-\frac{\cosh(2Dz)\pm\sinh(2Dz)}{\cosh(\sqrt{2D\sigma_a^{(W)}}z)}\pm\sqrt{\frac{\sigma_{tr}}{\sigma_a^{(W)}}}\tanh(\sqrt{2D\sigma_a^{(W)}}z)\right] \tag{7.176}$$

$$A_3^{(W)}(z)=-\int_0^z dz'\left[\frac{\sigma_a^{(W)}}{2}A_+^{(W)}(z')A_-^{(W)}(z')-A_+^{(W)}(z')-A_-^{(W)}(z')\right] \tag{7.177}$$

Substituting eq. (7.174) into eq. (7.168), we find the rotation angle of the polarization plane

$$\delta\chi=\frac{A_+^{(W)}(z)-A_-^{(W)}(z)}{4\Delta^{(W)}(z)}\mathrm{Im}(\theta_+\rho_--\theta_-\rho_+) \tag{7.178}$$

This expression can also be written as

$$\delta\chi=\frac{A_+^{(W)}(z)-A_-^{(W)}(z)}{2\Delta^{(W)}(z)}\mathbf{n}_0[\mathbf{r}\times\mathbf{n}] \tag{7.179}$$

For relatively small depths

$$z < l_d^{(W)} = (2D\sigma_a^{(W)})^{-1/2}$$

Equation (7.179) yields

$$\delta\chi \approx \frac{1}{2z}\mathrm{Im}(\theta_+\rho_- - \theta_-\rho_+) = -\frac{\rho\theta}{z}\sin(\varphi - \phi) \tag{7.180}$$

where ϕ is the azimuth of the vector $\boldsymbol{\rho}$ ($\tan\phi = y/x$). In the asymptotic state ($z > l_d^{(W)}$), the angle $\delta\chi$ is halved,

$$\delta\chi \approx \frac{1}{4z}\mathrm{Im}(\theta_+\rho_- - \theta_-\rho_+) \tag{7.181}$$

If the azimuth angles φ and ϕ coincide with each other or differ from each other by π, then the polarization plane does not deflect from its initial orientation. The reason is that the corresponding average ray trajectories appear to be planar curves. As the vectors $\boldsymbol{\rho}$ and $\boldsymbol{\theta}$ are orthogonal to each other, the angle $\delta\chi$ reaches its maximum and the corresponding average trajectory is characterized by the maximum degree of twisting. The orientation of the polarization plane as a function of the difference between angles $\varphi - \phi$ is shown in Fig. 7.7.

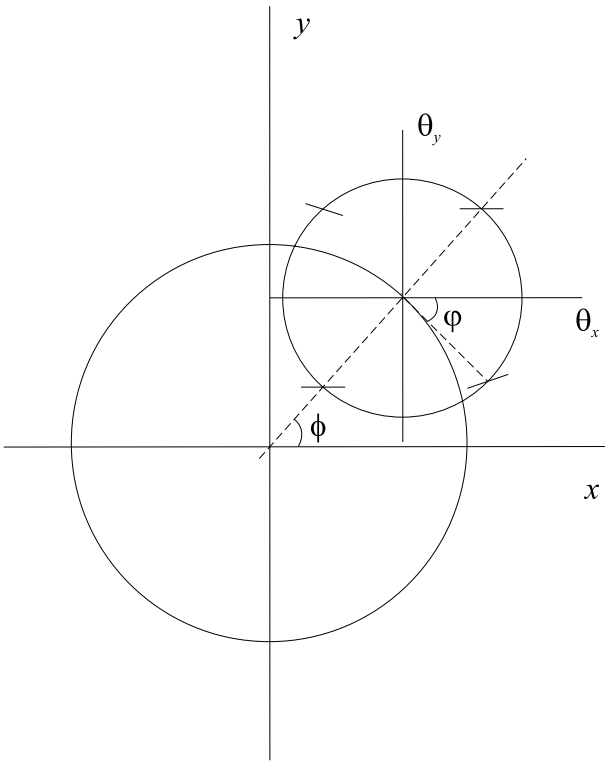

Fig. 7.7.

7.7 Discussion

The results obtained above allow us to understand how the parameters of inhomogeneities and absorption in the medium influence on the depolarization of light.

The integral parameters of the scattering matrix for various media with large inhomogeneities are presented in Tables 7.1 and 7.4 ($x = 2\pi a/\lambda$). For spherical scatterers, the numerical calculations were perfomed with the Mie formulas [1, 44]. For natural media, we used the numerical [52] and experimental [2] data.

As follows from Tables 7.1 and 7.4 the integral parameters of the off-diagonal elements of the scattering matrix appear to be small as compared with the corresponding parameters of the diagonal elements. Therefore, the contribution of the additional modes to the Stokes parameters is relatively small in all considered cases.

The relationship between the 'geometrical' and 'dynamical' mechanisms of depolarization depends on the radius of scatterers, their refractive index and the spread of inhomogeneities in sizes and shapes (see Table 7.2). As the size of particles increases and the relative refractive index approaches unity, the role of the 'geometrical' mechanism increases. The spread of inhomogeneities in sizes and their deviation from the spherical shape (Table 7.2, *sea water*) enhance the role of the 'dynamical' mechanism. This law can best be appreciated from comparison of the depolarization coefficients ϵ_W and ϵ_W^{geom}. As follows from Table 7.2, the effect of slow decay of circular polarization is typical only for large spherical scatterers. For media with inhomogeneities distributed in sizes and shapes the depolarization coefficients for circularly (ϵ_V) and linearly (ϵ_W) polarized beams are of the same order of magnitude (Table 7.2, *cloud 1* and *sea water*).

The effect of absorption on the depolarization of multiply scattered light in the medium is illustrated in Fig. 7.8. As follows from Fig. 7.8, the ratio of the depolarization lengths depends nonmonotonically on single scattering albedo σ/σ_{tot}. For strong absorbing ($\sigma_a > \sigma_{tr}$), ratio l_{circ}/l_{lin} increases logarithmically with increasing σ/σ_{tot}:

$$\frac{l_{circ}}{l_{lin}} \approx \frac{1}{2} + \frac{1}{2} \ln \frac{\langle \theta^2 \rangle_\infty}{2\gamma_0^2}$$

where $\langle \theta^2 \rangle_\infty$ is determined by eq. (7.101). Ratio l_{circ}/l_{lin} has a maximum at

$$\frac{\sigma}{\sigma_{tot}} \approx 1 - \frac{\sigma_{tr}}{\sigma}$$

i.e. at $\sigma_a \approx \sigma_{tr}$. In the vicinity of $\sigma/\sigma_{tot} = 1$, ratio l_{circ}/l_{lin} tends to its value for a non-absorbing medium.

It is of interest to compare the results obtained above with the experimental data [8, 9] and the results of numerical simulations [8].

In the case $\sigma_{dep} \ll \sigma_{tr}$, as follows from our calculations, the circular polarization falls off more slowly as compared with linear polarization. This effect is well pronounced in a medium with no absorption, in particular, in a suspension of

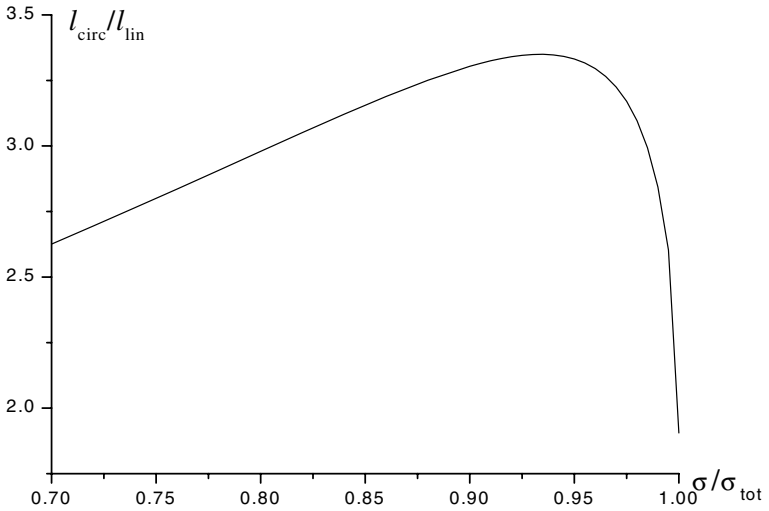

Fig. 7.8. Ratio of the depolarization lengths as a function of single scattering albedo σ/σ_{tot} for latex particles in water ($ka = 10$)

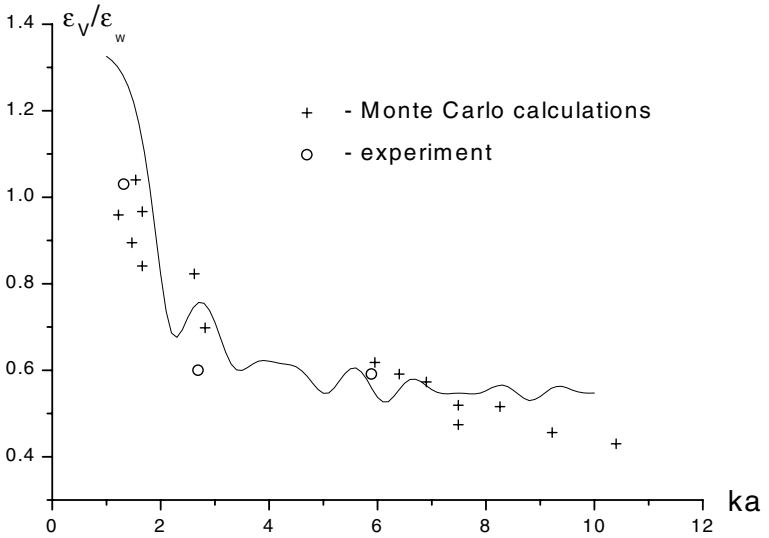

Fig. 7.9. Ratio ϵ_V/ϵ_W for a water suspension of latex particles as a function of their radius

latex particles in water [8,9]. As shown in Fig. 7.9, the ratio between the attenuation coefficients calculated from ϵ_V/ϵ_W with eqs (7.54) and (7.56) (solid curve) is in good agreement with data of experiments and Monte Carlo calculations [8].

Our results for the degree of polarization also correlate well with experimental data [9]. The degree of polarization for the circularly and linearly polarized beams as a function of the slab thickness L is shown in Fig. 7.10. In this case,

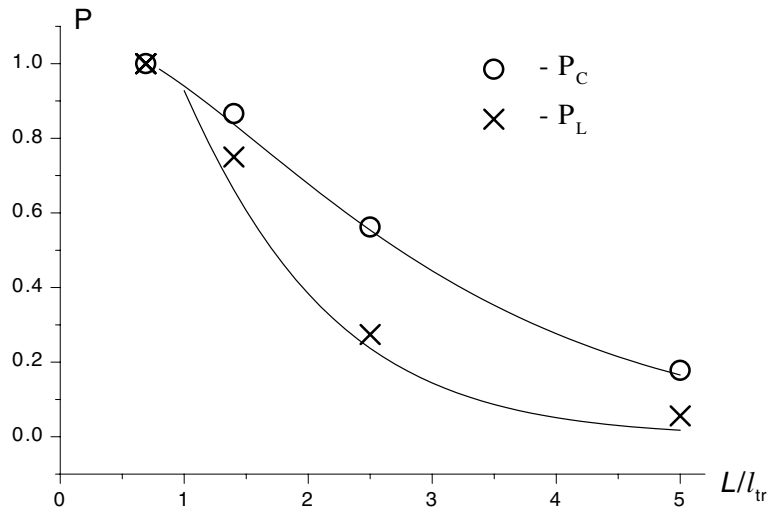

Fig. 7.10. Degree of polarization as a function of the normalized thickness of the scattering slab L/l_{tr} for a water suspension of latex particles ($ka = 7$)

instead of eq. (7.50) we used the formula for the intensity of light transmitted through a non-absorbing slab [45].

In summary, we present the analytical method for solving the vector radiation transfer equation. The representation for the Stokes vector that was first proposed by Kuscer and Ribaric [49] is used. Our approach is based on the assumption that single scattering of light by large-scale inhomogeneities occurs through small angles and the off-diagonal elements of the scattering matrix are small as compared with the diagonal ones. This approximation allows us to decouple the vector radiative transfer equation. In the first approximation, we derive three independent equations for the basic modes, namely, for the intensity and for the basic modes of linear and circular polarizations. In the succeeding approximation, allowance for the interaction between the basic modes results in the exitation of the additional modes (overtones). Within the framework of this approach, the Stokes parameters of multiply scattered light are calculated. Two limiting cases, diffusive propagation of light and small-angle multiple scattering, are disscussed in detail. The validity of our results is illustrated by comparison with data of experiments [8, 9] and Monte Carlo simulation [8].

Acknowledgments

We thank A.Borovoi, A.Kokhanovsky, V.Marinyuk and V.S.Remizovich for interest in this work and helpful discussions. This work was supported in part by the Ministry of Education of the Russian Federation, project N E02-3.2-203 and by President program “Support of leading scientific schools” 5898.2003.02.

References

1. *Light Scattering by Nonspherical Particles. Theory, Measurements and Applications.* Ed. by Mishchenko M.I., Hovenier J.W. and Travis L.D., Academic Press, New York (2000).
2. K.J. Voss, E.S. Fry, Measurement of the Mueller matrix for ocean water, *Appl. Opt.* **23**, pp. 4427–4439, 1984.
3. C.E. Mandt, L. Tsang, and A. Ishimaru, Copolarized and depolarized backscattering enhancement of random discrete scatterers of large size based on second-order ladder and cyclical theory, *JOSA* **A7**, pp. 585–592, 1990.
4. S.G. Demos, and R.R. Alfano, Optical polarization imaging, *Appl. Opt.* **36**, pp. 150–155, 1997.
5. G.W. Kattawar, M.J. Rakovic, and B.D. Cameron, Laser backscattering polarization patterns from turbid media, in *Advances in Optical Imaging and Photon Migration* **21**, pp. 105–110, 1998.
6. V.V. Tuchin, Coherence-domain methods in tissue and cell optics, *Laser Phys.* **8**, pp. 807–849, 1998.
7. F.C. MacKintosh, J.X. Zhu, D.J. Pine, and D.A. Weitz, Polarization memory of multiple scattering light, *Phys. Rev.* **B40**, pp. 9342-9345, 1989.
8. D. Bicout, C. Brosseau, A.S. Martinez, and J.M. Schmitt, Depolarization of multiply scattered waves by spherical diffusers: influence of the size parameter, *Phys. Rev.* **E49**, pp. 1767–1770, 1994.
9. V. Sankaran, M.J. Everett, D.J. Maitland, and J.T. Walsh, Comparison of polarized-light propagation in biological tissue and phantoms, *Opt. Lett.* **24**, pp. 1044–1046, 1999.
10. N. Ghosh, P.K. Gupta, H.S. Patel, B. Jain, and B.N. Singh, Depolarization of light in tissue phantoms – effect of collection geometry, *Opt. Comm.* **222**, pp. 93–100, 2003.
11. J.M. Schmitt, A.H. Gandjbakhche, and R.F. Bonner, Use of polarized light to discriminate short-path photons in a multiply scattering medium, *Appl. Opt.* **31**, pp. 6535–6546, 1992.
12. S. Mujumdar, H. Ramachandran, Imaging through turbid media using polarization modulation: dependence on scattering anisotropy, *Opt. Commun.* **241**, pp. 1–9, 2004.
13. N. Glosh, A. Pradhan, P.K. Gupta, S. Gupta, V. Jaiswal, R.P. Singh, Depolarization of light in a multiply scattering medium: Effect of the refractive index of a scatterer, *Phys. Rev.* **E70**, pp. 066607-1-066607-7, 2004.
14. M. Moscoso, J.B. Keller, and G. Papanicolaou, Depolarization and blurring of optical images by biological tissue, *JOSA* **A18**, pp. 948–960, 2001.
15. A.D. Kim, and M. Moscoso, Influence of the relative refractive index on the depolarization of multiply scattered waves, *Phys. Rev.* **E64**, pp. 026612-1-026612-5, 2001.
16. A.D. Kim, and M. Moscoso, Backscattering of circularly polarized pulses *Opt. Lett.* **27**, pp. 1589–1591, 2002.
17. E.P. Zege, and L.I. Chaikovskaya, Approximate transfer equations for polarized radiation in media with strongly anisotropic scattering, *Izv. Akad. Nauk SSSR, Fiz. Atmos. Okeana* **21**, pp. 1043–1049, 1986.
18. E.P. Zege, and L.I. Chaikovskaya, Features of the propagation of polarized radiation in media with strongly anisotropic scattering, *Zh. Prikl. Spektrosk.*, **44**, pp. 996–1004, 1986.

19. E.P. Zege, and L.I. Chaikovskaya, An approximate theory of polarized radiation transfer in scattering media. Splitting of sets of simultaneous equations, *Izv. Akad. Nauk SSSR, Fiz.Atmos.Okeana* **30**, pp. 644–654, 1994.
20. E.P. Zege, and L.I. Chaikovskaya, New approach theory to the polarized radiative transfer problem, *JQSRT* **55**, pp. 19–31, 1996.
21. M.I. Mishchenko, Multiple scattering of polarized light in anisotropic plane-parallel media, *Transp. Theory and Stat. Phys.* **19**, pp. 293–316, 1990.
22. P. Bruscaglioni, G. Zaccanti, and A. Wei, Transmission of a pulsed polarized light beam through thick turbid media: numerical results, *Appl. Opt.* **32**, pp. 6142–6150, 1993.
23. A. Ambirajan, D.C. Look, A backward Monte Carlo study of the multiple scattering of a polarized laser beam, *JQSRT* **58**, pp. 171–192, 1997.
24. A. Kouzoubov, M.J. Brennan, J.C. Thomas, R.H. Ablot, Monte-Carlo simulations of the influence of particle nonsphericity on remote sensing of ocean water, *Journ. Geophys. Res.* **104**, pp. 31,731–31,737, 1999.
25. E.P. Zege, and L.I. Chaikovskaya, Approximate theory of linearly polarized light propagation through a scattering medium, *JQSRT* **66**, pp. 413–435, 2000.
26. A.A. Kokhanovsky, Reflection and transmission of polarized light by thick weakly absorbing random media, *JOSA* **A18**, pp. 883–887, 2001.
27. W. Cai, M. Lax, and R.R. Alfano, Analitycal solution of the polarized photon transport equation in an infinite uniform medium using cumulant expansion, *Phys. Rev.* **E63**, pp. 016606-1-016606-10, 2000.
28. B.D. Cameron, M.J. Rakovic, M. Mehrubeoglu *et al.* Measurement and calculation of the two-dimensional backscattering Mueller matrix of a turbid medium, *Opt. Lett.* **23**, pp. 485–487, 1998.
29. A. Ishimaru, S. Jaruwatanadilok, Y. Kuga, Polarized pulse waves in random duscrete scatterers, *Appl. Opt.* **40**, pp. 5495–5502, 2001.
30. H. Ishimoto, K. Masuda, A Monte Carlo approach for the calculation of polarized light: application to an incident narrow beam, *JQSRT* **72**, pp. 467–483, 2002.
31. G. Yao, Differential optical polarization imaging in turbid media with different embedded objects, *Opt. Commun.* **241**, pp. 255–261, 2004.
32. E.E. Gorodnichev, and D.B. Rogozkin, Small-angle multiple scattering of light in random media, *JETP* **80**, pp. 112–127, 1995.
33. E.E. Gorodnichev, A.I. Kuzovlev, and D.B. Rogozkin, Diffusion of circularly polarized light in a disordered medium with large-scale inhomogeneities, *JETP Lett.* **68**, pp. 22-28, 1998.
34. E.E. Gorodnichev, A.I. Kuzovlev, and D.B. Rogozkin, Depolarization of light in small-angle multiple scattering in random media, *Laser Phys.* **9**, pp. 1210–1227, 1999.
35. E.E. Gorodnichev, A.I. Kuzovlev, and D.B. Rogozkin, Propagation of circularly polarized light in media with large-scale inhomogeneities, *JETP* **88**, pp. 421–432, 1999.
36. E.E. Gorodnichev, A.I. Kuzovlev, D.B. Rogozkin, Depolarization of light in scattering media with large-scale inhomogeneities, *IRS 2000: Current Problems in Atmospheric Radiation*, W.L. Smith and Yu.M. Timofeev (eds.), A. Deepak Publishing. Hampton, VA, 2001, pp. 287–290.
37. E.E. Gorodnichev, A.I. Kuzovlev, and D.B. Rogozkin, Small-angle multiple scattering of polarized light in turbid media, *Izvestiya, Atmospheric and Oceanic Physics* **39**, pp. 333–345, 2003.

38. E.E. Gorodnichev, A.I. Kuzovlev, and D.B. Rogozkin, Propagation of polarized light in media with large discrete inhomogeneities, *Opt.Spectrosc.* **94**, pp. 273–285, 2003.
39. E.E. Gorodnichev, A.I. Kuzovlev, and D.B. Rogozkin, Influence of the inhomogeneity properties on the depolarization of multiply scattered light in a turbid medium, *Spie Proceedings* **5829**, pp. 74–87, 2005.
40. S.M. Rytov, On the transition from wave to geometrical optics, *Dokl. Acad. Nauk USSR* **18**, pp. 263-266,1938 (in Russia). Reprinted in *Topological Phases in Quantum Theory*, edited by B. Markovski and S.I. Vinitsky, World Scientific, Singapore, 1989.
41. Yu.A. Kravtsov, Geometrical depolarization of light in a turbulent atmosphere, *Izv. Vyssh. Uchebn. Zaved., Radiofiz.* **13**, pp. 281–284, 1970.
42. L.D. Landau, E.M. Lifshits, *Electrodynamics of Continuous Media*, Pergamon, New York, 1984.
43. V.I. Tatarskii, Estimation of light depolarization by turbulent inhomogeneities of the atmosphere, *Izv. Vyssh. Uchebn. Zaved., Radiofiz.* **10**, pp. 1762–1765, 1967.
44. R.G. Newton, *Scattering Theory of Waves and Particles*, McGraw-Hill, New York, 1966.
45. H.C. van de Hulst *Multiple Light Scattering*, Academic Press, New York, 1980.
46. H.C. van de Hulst *Light Scattering by Small Particles*, Wiley, New York, 1957.
47. A.I shimaru, *Wave Propagation and Scattering in Random Media*, Academic Press, New York, 1978, vols 1,2.
48. L.D. Landau, E.M. Lifshits, *The Classical Theory of Fields*, Pergamon, Oxford, 1975.
49. I. Kuscer, M. Ribaric, Matrix formalism in the theory of diffusion of light, *Optica Acta* **6**, pp. 42–57, 1959.
50. H. Domke, Depth regime of polarized light in a semi-infinite atmosphere, *Astrofizika* **15**, pp. 205–217, 1975.
51. A.A. Kokhanovsky, *Polarization Optics of Random Media*, Praxis Publishing, 2003.
52. D. Deirmendjian, *Electromagnetic Scattering of Spherical Polydispersions*, Elsevier, New York, 1969.
53. E. Amic, J.M. Luck, Th.M. Nieuwenhuizen, Anisotropic multiple scattering in diffusive media, *J. Phys. A: Math. Gen.* **29**, pp. 4915–4955, 1996.
54. G.A. Korn, T.M. Korn, *Mathematical Handbook for Scientists and Engineers: Definitions, Theorems, and Formulas for Reference and Review*, Dover, New York, 2000.
55. V.V. Sobolev, *Light Scattering in Planetary Atmospheres*, Pergamon, Oxford, 1975.
56. I.M. Gel'fand, R.A. Minlos, and Z.Ya. Shapiro, *Representations of the Rotation and Lorentz Groups and their Applications*, Oxford, 1963.
57. E.E. Gorodnichev, A.I. Kuzovlev, D.B. Rogozkin, Rotation of the polarization ellipse under multiple light scattering in disordered media, *Optics and Spectrocopy* **89**, pp. 914–922, 2000.
58. L.S. Dolin, Self-similar approximation in the theory of multiple strongly anisotropic scattering of light, *Dokl. Akad. Nauk SSSR* **260**, pp. 1344–1347, 1981.
59. V.S. Remizovich, D.B. Rogozkin, M.I. Ryazanov, Propagation of a modulated narrow light beam in a scattering medium with allowance for photon-path fluctuations during multiple scattering, *Izv. Vyssh. Uchebn. Zaved., Radiofiz.* **24**, pp. 891–898, 1982.

60. D.B. Rogozkin, Light pulse beam propagation in anisotropically scattering medium, *Izv. Akad. Nauk SSSR, Fiz. Atmos. Okeana* (Atmospheric and Oceanic Physics) **23**, pp. 366–374, 1987.
61. G. Moliere, Therie der Streuung Schneller geladener Teilchen II: Mehrfach – und Vielfachstreuung, *Z. Naturforsch*,**3a**, pp. 78–97, 1948.
62. L.D. Landau, E.M. Lifshits, *Quantum Mechanics (Nonrelativistic Theory)*, 3rd edn, Pergamon, New York, 1976.
63. E.E. Gorodnichev, A.I. Kuzovlev, D.B. Rogozkin, Propagation of electromagnetic radiation through random media with long-range fluctuation correlations of the dielectric constant, *Laser Physics* **6**, pp. 1188–1197, 1996.
64. E.E. Gorodnichev, A.I. Kuzovlev, D.B. Rogozkin, Small-angle multiple light scattering in a substance near a critical point, *Optics and Spectrocopy* **82**, pp. 451–458, 1997.
65. E.E. Gorodnichev, A.I. Kuzovlev, D.B. Rogozkin, Propagation of a narrow beam of polarized light in a random medium with large-scale inhomogeneities, *Laser Physics* **10**, pp. 1236–1243, 2000.

8 Adjoint radiative transfer equation and inverse problems

Vladimir V. Rozanov

8.1 Introduction

The interaction of radiation with a medium can be described in the framework of the radiative transfer theory, which is based on the solution of the integro-differential vector radiative transfer equation (VRTE). The solution of the VRTE provides the radiation field inside and outside of a medium and can be fully described by the intensity vector $\boldsymbol{I}(\tau, \mu, \phi)$ which has the Stokes parameters as its components. The vector $\boldsymbol{I}$ is also called the Stokes vector [12]. The intensity vector is function of the optical coordinate τ, the direction of the propagation which is characterized by the cosine of the polar angle, μ, measured with respect to a fixed axis in space (such as the τ-axis or z-axis) and a corresponding azimuthal angle, ϕ. The determination of $\boldsymbol{I}(\tau, \mu, \phi)$ under assumption that optical parameters of the medium such as phase matrix, extinction coefficient and single-scattering albedo are known is called usually a direct (or forward) problem.

Another situation takes place if the scattered radiation can be measured inside or at the boundaries of a medium and the optical parameters are unknown. There usually exists a linear relationship between the measured value, Φ, for example the first component of the intensity vector at a given position and direction, and the intensity vector describing the radiation field. This relationship can be written for a measurement at a single wavelength and a given position and direction as a scalar product (also referred to as an inner product) of the instrument response function, $\boldsymbol{\mathcal{R}}$, and the intensity vector, $\boldsymbol{I}$, as follows:

$$\Phi = (\boldsymbol{\mathcal{R}}, \boldsymbol{I}) \ , \tag{8.1}$$

where the notation (,) is used to define the scalar product in an appropriate functional space. The linear functional Φ is also called the radiative effect [3], or the observable radiative quantity [28]. The specific form of the response function is of minor importance for our mathematical consideration. Therefore, in section 8.2 we formulate a model of the ideal measurement and the ideal response function which will be used throughout the chapter.

The measured value contains information about various parameters describing the interaction of radiation with a medium. The procedure of the retrieval of these parameters is called an inverse problem. The theory of the inverse problem is well developed only in the case of a linear relationship between the measured value and the parameter to be retrieved. It is the so-called linear inverse problem. In section 8.3 we demonstrate that such a linear relationship can be found expanding the intensity vector in the functional Taylor series as follows:

$$\delta\Phi = (\mathfrak{R}, \boldsymbol{\delta I}) = \int_0^{\tau_0} \mathcal{W}(\tau)\delta p(\tau)\mathrm{d}\tau \ , \tag{8.2}$$

where the variation of the intensity vector, $\boldsymbol{\delta I}$, and, therefore, the variation of the measured value, $\delta\Phi$, is caused by the variation of a certain optical parameter $p(\tau)$. The weighting function (WF), $\mathcal{W}(\tau)$, describes a contribution of a variation of a certain optical parameter in an infinitesimal layer having optical thickness $\mathrm{d}\tau$ located at the optical depth τ into a variation of the measured value, $\delta\Phi$.

From the mathematical point of view, the most efficient and elegant way to derive the weighting function is to employ the linearized direct radiative transfer equation and adjoint radiative transfer equation written in the generalized form. Following this way, we formulate in section 8.4 the generalized form of the direct VRTE as follows [17]:

$$\mathbf{L}\boldsymbol{I} = \boldsymbol{S} \ , \tag{8.3}$$

where $\boldsymbol{S}$ is a source function and $\mathbf{L}$ is the generalized radiative transfer operator. The main feature of (8.3) is that the operator $\mathbf{L}$ comprises all operations with the intensity vector $\boldsymbol{I}$ including boundary conditions. Therefore, the radiative transfer equation written in the generalized form consists of a single operator equation.

In section 8.5, we demonstrate that the operator $\mathbf{L}$ has an adjoint operator $\mathbf{L}^*$ satisfying the Lagrange identity, i.e.,

$$(\boldsymbol{I}^*, \mathbf{L}\boldsymbol{I}) = (\mathbf{L}^*\boldsymbol{I}^*, \boldsymbol{I}) \ , \tag{8.4}$$

where $\boldsymbol{I}^* \equiv \boldsymbol{I}^*(\tau, \mu, \phi)$ we will refer to as an adjoint intensity vector.

Having defined the adjoint radiative transfer operator, we formulate in section 8.6 the adjoint radiative transfer equation in the generalized form as follows:

$$\mathbf{L}^*\boldsymbol{I}^* = \boldsymbol{W} \ , \tag{8.5}$$

where $\boldsymbol{W}$ is an adjoint source function and operator $\mathbf{L}^*$ in analogy to the operator $\mathbf{L}$ comprises all operations with the adjoint intensity vector, $\boldsymbol{I}^*$, including boundary conditions.

Employing the linear perturbation theory to the direct VRTE as given by (8.3), we find in section 8.7 the following form of the linearized direct radiative transfer equation:

$$\mathbf{L}\delta\boldsymbol{I} = \delta\boldsymbol{S} - \delta\mathbf{L}\boldsymbol{I} \ , \tag{8.6}$$

where variations of the intensity vector, source function and radiative transfer operator are caused by the variation of a certain optical parameter. For a given optical parameter, $p(\tau)$, the right-hand side of this equation can always be expressed (in the linear approximation) as a product of $\delta p(\tau)$ and the known function, $\boldsymbol{\Psi}_p(\tau, \mu, \phi)$:

$$\delta \boldsymbol{S} - \delta \mathbf{L} \boldsymbol{I} = \delta p(\tau) \boldsymbol{\Psi}_{\boldsymbol{p}} \, . \tag{8.7}$$

The analytical expressions for functions $\boldsymbol{\Psi}_{\boldsymbol{p}}$ are given in section 8.7 for main optical and surface parameters. Further we demonstrate that, using the adjoint approach, the variation of the measured value $\delta\Phi$ given by (8.2) can be written in the following form:

$$\delta\Phi = (\boldsymbol{\mathcal{R}}, \boldsymbol{\delta I}) = (\boldsymbol{I}^*, \delta p(\tau) \boldsymbol{\Psi}_{\boldsymbol{p}}) = \int_0^{\tau_0} \mathcal{W}_p(\tau) \delta p(\tau) \mathrm{d}\tau \, , \tag{8.8}$$

where $\boldsymbol{I}^*$ is the solution of the adjoint radiative transfer equation (8.5) with the adjoint source function $\boldsymbol{W} = \boldsymbol{\mathcal{R}}$. The general expression for the weighting function can be formulated now as follows:

$$\mathcal{W}_p(\tau) = \int_0^{2\pi} \int_{-1}^{1} \boldsymbol{I}^{*T}(\tau, \mu, \phi) \boldsymbol{\Psi}_p(\tau, \mu, \phi) \mathrm{d}\mu \mathrm{d}\phi \, , \tag{8.9}$$

where superscript T denotes an transposed vector. Therefore, WF can be found solving the adjoint VRTE for $\boldsymbol{I}^*$ and finding auxiliary functions $\boldsymbol{\Psi}_p$.

In section 8.8, we derive, using (8.9), the weighting functions for such optical parameters as extinction, absorption, scattering coefficients, single-scattering albedo, phase matrix, surface albedo and surface emissivity.

In section 8.9, we present other expressions for the weighting functions. In particular, we derive weighting functions which can be calculated using diffuse forward and/or diffuse adjoint intensity instead of total ones. We demonstrate as well that the employing the formal solution of the direct radiative transfer equation (the source function integration) to the derivation of the weighting function is equivalent to the general expression (8.9) written for the diffuse adjoint intensity.

In section 8.10, we compare the obtained expressions for the weighting functions with the derivations given by other authors.

8.2 Instrument response function and the mathematical model of the ideal measurement

Let us assume that an instrument allows us to measure certain component of the intensity vector in the spectral range characterized by the wavelength λ_v. The instrument can be placed inside or at the boundaries of a medium. We will characterize the position of the instrument using as a vertical coordinate the

optical depth, τ_v, changing from 0 at the top of the plane-parallel medium to the value $\tau_v = \tau_0$ at the bottom and a function $h(\tau_v, \tau)$ describing the possible uncertainty in the instrument position. The viewing direction of the instrument is given by the variable $\Omega_v = (\mu_v, \phi_v)$ where μ_v and ϕ_v are the cosine of the zenith angle and azimuthal angle, respectively. The spatial resolution of the instrument can be described using the spatial slit function $s(\Omega_v, \Omega)$, where we will use the variable $\Omega := \{\mu, \phi\}$ to describe the set of variables $\mu \in [-1, 1]$ and $\phi \in [0, 2\pi]$. The propagation of the radiation through the instrument can be characterized by 4×4 matrix, $\mathbf{A}(\lambda)$, which is very specific for each particular instrument and can be obtained using an instrument simulator model. The spectral properties of the instrument are usually described by the spectral slit function $f(\lambda_v, \lambda)$.

Thus, a spectroscopic measurement, denoted by Φ, e.g., a radiance measurement at a certain position, viewing direction and wavelength, can be considered as a linear integral transformation of the radiation field $\boldsymbol{I}(\tau, \Omega, \lambda)$. To simplify further consideration we introduce the function $r(\tau_v, \Omega_v; \tau, \Omega)$ comprising functions $h(\tau_v, \tau)$ and $s(\Omega_v, \Omega)$ as

$$r(\tau_v, \Omega_v; \tau, \Omega) \equiv h(\tau_v, \tau) s(\Omega_v, \Omega) \, . \tag{8.10}$$

In the most common case the linear relationship between Φ and $\boldsymbol{I}(\tau, \Omega, \lambda)$ can be written as follows:

$$\Phi(\varpi_v) = \int\limits_{V(\varpi)} f(\lambda_v, \lambda) \boldsymbol{E}_i^T \mathbf{A}(\lambda) \boldsymbol{I}(\varpi) r(\tau_v, \Omega_v; \tau, \Omega) \mathrm{d}\varpi \, . \tag{8.11}$$

Here, the variable ϖ represents the set of variables $\{\tau, \Omega, \lambda\}$ where $\tau \in [0, \tau_0]$ and $\lambda \in [0, \infty]$; $\boldsymbol{E}_i$ is the four-component unity vector in the direction of the ith component of the intensity vector, i.e., if, for example, $i = 1$ we have $\boldsymbol{E}_1 = [1, 0, 0, 0]^T$; $\boldsymbol{I}(\varpi)$ is the intensity vector of the radiation field in the direction Ω at the optical depth τ and the spectral point λ; the integration over the volume $V(\varpi)$ is given by

$$\int\limits_{V(\varpi)} \mathrm{d}\varpi = \int\limits_0^\infty \mathrm{d}\lambda \int\limits_0^{\tau_0} \mathrm{d}\tau \int\limits_{4\pi} \mathrm{d}\Omega = \int\limits_0^\infty \mathrm{d}\lambda \int\limits_0^{\tau_0} \mathrm{d}\tau \int\limits_0^{2\pi} \mathrm{d}\phi \int\limits_{-1}^{1} \mathrm{d}\mu \, , \tag{8.12}$$

where τ_0 is the optical thickness of a medium. Introducing the instrument response function as follows:

$$\boldsymbol{\mathcal{R}}(\varpi_v; \varpi) = f(\lambda_v, \lambda) r(\tau_v, \Omega_v; \tau, \Omega) \mathbf{A}^T(\lambda) \boldsymbol{E}_i \, , \tag{8.13}$$

we obtain

$$\Phi(\varpi_v) = \int\limits_{V(\varpi)} \boldsymbol{\mathcal{R}}^{\boldsymbol{T}}(\varpi_v; \varpi) \boldsymbol{I}(\varpi) \mathrm{d}\varpi \, . \tag{8.14}$$

For our mathematical consideration the specific form of the matrix $\mathbf{A}(\lambda)$ and the spectral slit function $f(\lambda_v, \lambda)$ which can be very different for the particu-

lar instrument is of a minor importance. Thereby, we introduce here an ideal instrument with properties defined as follows:

— the instrument response matrix is the unity matrix

$$\mathbf{A}(\lambda) = \mathrm{diag}\{1, 1, 1, 1\} \; ; \tag{8.15}$$

— the spectral slit function is the Dirac δ function

$$f(\lambda_v, \lambda) = \delta(\lambda_v - \lambda) \; ; \tag{8.16}$$

— the instrument position is at the optical depth τ_v and the spatial slit function is written in terms of the Dirac δ functions

$$r(\tau_v, \Omega_v; \tau, \Omega) \; = \; \delta(\tau - \tau_v)\delta(\mu - \mu_v)\delta(\phi - \phi_v) \; . \tag{8.17}$$

Under the above assumptions, we can introduce the ideal instrument response function as follows:

$$\boldsymbol{R}(\varpi_v; \varpi) = \delta(\lambda_v - \lambda)\delta(\tau - \tau_v)\delta(\mu - \mu_v)\delta(\phi - \phi_v)\boldsymbol{E}_i \tag{8.18}$$

and the measured value Φ can be written now in the following form

$$\Phi(\varpi_v) = \int\limits_{V(\varpi)} \boldsymbol{R}^T(\varpi_v; \varpi)\boldsymbol{I}(\varpi)\mathrm{d}\varpi \; . \tag{8.19}$$

According to (8.19), Φ can be considered as a convolution of the scattered radiation field described by the intensity vector, $\boldsymbol{I}(\varpi)$, and the instrument response function, $\boldsymbol{R}(\varpi_v; \varpi)$, which projects only the part of $\boldsymbol{I}$ seen by the instrument. In the case of the measurement in a single viewing direction and at a single wavelength Φ is a functional of $\boldsymbol{I}$. For the multispectral and multi-angle measurements, Φ is also a function of the viewing direction of the instrument (denoted by variables with the subscript 'v') and of the spectral point λ_v. In both cases Φ will be referred to as a measured functional.

It can be seen that the measured functional Φ for our ideal instrument is simply the appropriate component of the intensity vector in the direction (Ω_v) at the optical depth τ_v and the wavelength λ_v.

8.3 Linearization and the variational derivative

We will assume throughout the chapter that optical parameters are functions of the vertical coordinate (optical depth) in contrast to the surface parameters such as, for example, surface albedo or surface emissivity which will be considered as scalar parameters. The intensity vector $\boldsymbol{I}(\varpi)$ and, therefore, $\Phi(\varpi_v)$ are nonlinear functionals of optical parameters describing the radiation propagation in a

medium. One is confronted with the so-called nonlinear inverse problem in this case. However, the theory of the inverse problem is well developed for the linear inverse problem only. The inverse problem is usually called linear if one has a linear relationship between measured values and parameters to be retrieved. Such a linear relationship provides, for example, the expansion of the intensity vector in a functional Taylor series around mean values of these parameters. Namely, restricting ourselves to the linear term with respect to the variation of a certain optical parameter, we have

$$\boldsymbol{I}(\varpi, p(\tau)) = \boldsymbol{I}(\varpi, \bar{p}(\tau)) + \int_0^{\tau_0} \boldsymbol{V}(\varpi, \tau')\delta p(\tau')\mathrm{d}\tau' \,, \tag{8.20}$$

where $\delta p(\tau) = p(\tau) - \bar{p}(\tau)$ denotes the deviation of a corresponding parameter from its mean value, $\bar{p}(\tau)$, $\boldsymbol{I}(\varpi, \bar{p}(\tau))$ is the intensity vector corresponding to $\bar{p}(\tau)$ and

$$\boldsymbol{V}(\varpi, \tau') = \frac{\delta \boldsymbol{I}(\varpi, p(\tau))}{\delta p(\tau')} = \lim_{\Delta\tau \to 0} \frac{\boldsymbol{I}(\varpi, p(\tau) + \delta p(\tau)) - \boldsymbol{I}(\varpi, p(\tau))}{\int_{(\Delta\tau)} \delta p(\tau') d\tau'} \tag{8.21}$$

is the variational derivative of $\boldsymbol{I}$ with respect to the parameter $p(\tau)$. A complete discussion of functionals and variational derivatives are given, for example, by Volterra [31].

Further, the variation of the radiation field caused by the variation of the certain parameter, $p(\tau)$, will be denoted as

$$\delta \boldsymbol{I}(\varpi) = \boldsymbol{I}(\varpi, p(\tau)) - \boldsymbol{I}(\varpi, \bar{p}(\tau)) \,, \tag{8.22}$$

and the variation of the measured functional as

$$\delta\Phi(\varpi_v) = \Phi(\varpi_v) - \bar{\Phi}(\varpi_v) \,. \tag{8.23}$$

We note that, in contrast to the measured functional, $\Phi(\varpi_v)$, corresponding to the unknown parameter $p(\tau)$, the value of the functional $\bar{\Phi}(\varpi_v)$ can be calculated according to the following expression:

$$\bar{\Phi}(\varpi_v) = \int_{V(\varpi)} \boldsymbol{\mathcal{R}}^{\boldsymbol{T}}(\varpi_v; \varpi)\boldsymbol{I}(\varpi, \bar{p}(\tau))\mathrm{d}\varpi \,. \tag{8.24}$$

Thus, the variation of the measured functional is the difference between the measured value and the calculated value corresponding to the known parameter $\bar{p}(\tau)$.

It follows from (8.14) and (8.24) that

$$\delta\Phi(\varpi_v) = \int_{V(\varpi)} \boldsymbol{\mathcal{R}}^{\boldsymbol{T}}(\varpi_v; \varpi)\delta \boldsymbol{I}(\varpi)\mathrm{d}\varpi \tag{8.25}$$

and from (8.20)

$$\boldsymbol{\delta I}(\varpi) = \int_0^{\tau_0} \boldsymbol{V}(\varpi, \tau')\delta p(\tau')\mathrm{d}\tau' \,. \tag{8.26}$$

The substitution $\delta \boldsymbol{I}(\varpi)$ given by (8.26) into (8.25) leads to a linear integral equation, which relates $\delta\Phi(\varpi_v)$ to the variation $\delta p(\tau)$ of the corresponding parameter:

$$\delta\Phi(\varpi_v) = \int_0^{\tau_0} \int_{V(\varpi)} \boldsymbol{\mathcal{R}^T}(\varpi_v; \varpi)\boldsymbol{V}(\varpi, \tau')\delta p(\tau')\mathrm{d}\varpi\mathrm{d}\tau' \,. \tag{8.27}$$

We define the convolution of the variational derivative as given by (8.21) with the response function as follows:

$$\mathcal{W}_i(\varpi_v, \tau) = \int_{V(\varpi)} \boldsymbol{\mathcal{R}}^T(\varpi_v; \varpi)\boldsymbol{V}(\varpi, \tau)\mathrm{d}\varpi \,. \tag{8.28}$$

The introduced function, $\mathcal{W}_i(\varpi_v, \tau)$, is called a weighting function. Substituting it into (8.27), we obtain

$$\delta\Phi(\varpi_v) = \int_0^{\tau_0} \mathcal{W}_i(\varpi_v, \tau)\delta p(\tau)\mathrm{d}\tau \,. \tag{8.29}$$

Equation (8.29) is the desired linear relationship between measured value $\Phi(\varpi_v)$ and the variation of the parameter $\delta p(\tau)$. The weighting function, $\mathcal{W}_i(\varpi_v, \tau)$, is the convolution of the instrument response function and the variational derivative. The expression for the weighting function can be considerably simplified if we use the ideal instrument response function as given by (8.18). Indeed, substituting $\boldsymbol{R}$ instead of $\boldsymbol{\mathcal{R}}$ into (8.28) and using properties of the Dirac δ function, we obtain

$$\mathcal{W}_i(\varpi_v, \tau) = \boldsymbol{E}_i^T\boldsymbol{V}(\varpi_v, \tau) = \mathcal{V}_i(\tau, \varpi_v) \,, \tag{8.30}$$

where $\mathcal{V}_i(\tau, \varpi_v)$ is the variational derivative of the corresponding component of the intensity vector with respect to the parameter $p(\tau)$. Considering the intensity vector as a function of a scalar parameter, the expression for the weighting function can be derived in a way analogous to (8.30). Namely, we obtain

$$\mathcal{W}_i(\varpi_v) = \boldsymbol{E}_i^T\boldsymbol{V}(\varpi_v) = \mathcal{V}_i(\varpi_v) \,, \tag{8.31}$$

where $\mathcal{V}_i(\varpi_v)$ is the partial derivative of the corresponding component of the intensity vector with respect to the certain scalar parameter.

Thus, in the case of the ideal response function the weighting function for the given optical parameter coincides with the variational derivative and for the scalar parameter with the partial derivative of the intensity vector with respect to the corresponding parameter.

The linear integral relationship given by (8.29) is widely used in the linear inverse theory to analyze the information content of the experimental data, to investigate theoretical precision of the retrieval and to estimate parameters (see [24] for further details).

The solution of inverse problems requires knowledge of the mean value of the measured functional $\bar{\Phi}(\varpi_v)$, as well as the weighting functions for all relevant parameters. The calculation of $\bar{\Phi}(\varpi_v)$ and the $\mathcal{V}_i(\tau, \varpi_v)$ can be carried out using the radiative transfer model.

The variational derivative is calculated, for example, employing the numerical perturbation technique. In this case, the following approximation is used instead of (8.21):

$$\frac{\delta \boldsymbol{I}(\varpi, p(\tau))}{\delta p(\tau_k)} = \frac{\boldsymbol{I}(\varpi, p(\tau) + \Delta p(\tau_k)) - \boldsymbol{I}(\varpi, p(\tau) - \Delta p(\tau_k))}{2\Delta p(\tau_k)} \,, \tag{8.32}$$

where $\Delta p(\tau_k)$ is the variation of the parameter, $p(\tau)$ at the level having optical depth τ_k, and the radiation fields $\boldsymbol{I}(\varpi, p(\tau) \pm \Delta p(\tau_k))$ are solutions of the radiative transfer equation for two perturbed values of this parameter, $p(\tau) \pm \Delta p(\tau_k)$. Equation (8.32) provides an approximation for the variational derivative of the intensity with respect to the parameter $p(\tau)$ at the level τ_k. The derivative is constructed applying (8.32) at each discrete level.

Although the application of (8.32) to the calculation of variational derivatives is straightforward, it requires multiple solutions of the radiative transfer equation for the intensity vector. It is very time-consuming in many practical situations. Therefore, our main task is to find simple analytical expressions to calculate the variational derivatives and, also, weighting functions. The most effective and elegant way to derive such expressions is to employ the linearized direct and adjoint radiative transfer equations written in the generalized form. Therefore, in the following section we formulate the basic radiative transfer equation and rewrite it in the generalized form.

8.4 Standard and generalized forms of the vector RTE

Taking into account that the weighting functions are often used for the retrieval of parameters from the measurements carried out on the satellite, airborne and ground-based platforms, we formulate here our basic radiative transfer model which can be employed to model radiation field in the atmosphere including polarization, thermal emission and bidirectional surface reflection.

Our main restrictions are as follows:

— independent scattering by molecules and small particles such as aerosol and cloud particles;
— scattering without changing the wavelength, i.e., an elastic scattering;
— the medium is locally plane-parallel;
— the medium is macroscopically isotropic and symmetric;

— the medium is illuminated by a monodirectional beam of light incident at each point of the top of the medium;
— both medium and light source are assumed to be time-independent and possible nonlinear and close-packed effects are neglected;
— thermal emission is the single internal source in the medium;
— the medium is in the local thermodynamic equilibrium.

8.4.1 Standard form of the vector RTE

Under the above assumptions the plane-parallel vector RTE for a scattering, absorbing, and emitting medium is written as follows (see [9, 22] for details of derivation):

$$\mu \frac{\mathrm{d}\boldsymbol{I}(\tau,\Omega)}{\mathrm{d}\tau} = -\boldsymbol{I}(\tau,\Omega) + \boldsymbol{J}(\tau,\Omega) + \boldsymbol{Q}(\tau,\Omega)\ . \tag{8.33}$$

Here, $\tau \in [0,\tau_0]$ is the optical depth changing from 0 at the top of the plane-parallel medium to the value $\tau = \tau_0$ at the bottom, the variable $\Omega := \{\mu,\phi\}$ describes the set of variables $\mu \in [-1,1]$ and $\phi \in [0,2\pi]$, μ is the cosine of the polar angle θ as measured from the positive τ-axis and ϕ is the azimuthal angle, $\boldsymbol{Q}(\tau,\Omega)$ is an internal emission source, $\boldsymbol{J}(\tau,\Omega)$ is the multiple scattering source function:

$$\boldsymbol{J}(\tau,\Omega) = \frac{\omega(\tau)}{4\pi} \int\limits_{4\pi} \mathbf{Z}(\tau,\Omega,\Omega')\boldsymbol{I}(\tau,\Omega')\mathrm{d}\Omega'\ , \tag{8.34}$$

where $\omega(\tau)$ is the single-scattering albedo, $\mathbf{Z}(\tau,\boldsymbol{\Omega},\boldsymbol{\Omega}')$ is the phase matrix. We assume here that the internal emission is due to the thermal emission only. In this case the source function $\boldsymbol{Q}(\tau,\Omega)$ can be represented as

$$\boldsymbol{Q}(\tau,\Omega) = (1-\omega(\tau))B(T(\tau))\boldsymbol{E}_1\ , \tag{8.35}$$

where $B(T(\tau))$ is the Planck function, $T(\tau)$ is the kinetic temperature of the medium, and the vector $\boldsymbol{E}_1 = [1,0,0,0]^T$ shows that thermal emission is not polarized. Taking into account that the internal emission source as defined by (8.35) is isotropic, the argument Ω will be omitted in the remainder of this chapter. The explicit notation of the wavelength dependence will be omitted as well.

The components of the intensity vector $\boldsymbol{I}$ are defined as follows [10]: $I = I_l + I_r$, $Q = I_l - I_r$, $U = E_l E_r^* + E_r E_l^*$, $V = \mathrm{i}(E_l E_r^* - E_r E_l^*)$, where we neglected a common multiplier and $I_l = E_l E_l^*$ is the scattered light intensity in the meridional plane. This plane contains the normal to a light scattering medium and the direction of observation. The value of $I_r = E_r E_r^*$ gives the scattered light intensity in the plane perpendicular to the meridional plane. E_l and E_r are components of the electric vector of the scattered wave defined relatively to the meridional plane in the same way as I_l, I_r.

As discussed by Chandrasekhar [6], the phase matrix is related to the scattering matrix $\mathbf{P}(\tau, \cos\beta)$ as follows:

$$\mathbf{Z}(\tau, \mathbf{\Omega}, \mathbf{\Omega}') = \mathbf{L}(\pi - \chi_{\mathbf{1}})\mathbf{P}(\tau, \cos\beta)\mathbf{L}(-\chi_{\mathbf{2}}) \,, \tag{8.36}$$

where β is the scattering angle, and $\mathbf{L}(\chi)$ is the matrix which is required to rotate a meridional plane through angles $\pi - \chi_1$ and $-\chi_2$ before and after scattering onto a local scattering plane. The first element of the scattering matrix, $P_{11}(\tau, \cos\beta)$, is normalized so that

$$\frac{1}{2}\int\limits_0^\pi P_{11}(\tau, \cos\beta)\sin(\beta)\mathrm{d}\beta = 1 \,. \tag{8.37}$$

We will assume that there is a surface with a spherical albedo A below the plane-parallel medium under consideration. The medium is illuminated by a wide unidirectional light beam at the top ($\tau = 0$) having the flux $\pi F_0 \mu_0$.

Under these assumptions the boundary conditions for the intensity vector, $\boldsymbol{I}(\tau, \Omega)$, can be formulated as follows:

$$\boldsymbol{I}(0, \Omega) = \pi\delta(\mu - \mu_0)\delta(\phi - \phi_0)F_0\boldsymbol{E}_1 \,, \mu > 0 \,, \tag{8.38}$$

$$\boldsymbol{I}(\tau_0, \Omega) = \frac{A}{\pi}\int\limits_{\Omega_+} \mathbf{M}(\Omega, \Omega')\boldsymbol{I}(\tau_0, \Omega')\mu'\mathrm{d}\Omega' + \epsilon B(T_s)\boldsymbol{E}_1 \,, \mu < 0 \,, \tag{8.39}$$

where F_0 is an arbitrary constant (we assume further that $F_0 = 1$), Ω_+ is defined by the set of variables $\{\mu, \phi\}$ in the range of $\mu \in [0, 1]$, $\phi \in [0, 2\pi]$, the integration over Ω_+ is given by

$$\int\limits_{\Omega_+} \mathrm{d}\Omega \equiv \int\limits_0^{2\pi} \mathrm{d}\phi \int\limits_0^1 \mathrm{d}\mu \,, \tag{8.40}$$

$\mathbf{M}(\Omega, \Omega')$ is the matrix determining the angular reflection properties of the boundary surface, ϵ is the surface emissivity, $B(T_s)$ is the Planck function for the surface temperature T_s. In the simplest case of Lambertian reflection, the matrix $\mathbf{M}$ has the following form:

$$\mathbf{M}(\Omega, \Omega') = \mathrm{diag}\{1, 0, 0, 0\} \,. \tag{8.41}$$

The radiative transfer equation (8.33) along with the boundary conditions given by (8.38) and (8.39) will be referred to as the standard form of the direct VRTE. The formulated VRTE can be used to simulate the radiation field in the planetary atmosphere in the spectral regions from the ultraviolet (UV) to the thermal infrared.

8.4.2 Operator form of the direct VRTE

It is convenient to rewrite the standard form of the direct VRTE using an operator representation. Let us define a linear differential-integral operator, $\mathbf{L}_e$, which comprises all operations with the intensity vector, $\boldsymbol{I}(\tau,\Omega)$, in (8.33) as follows:

$$\mathbf{L}_e = \mu\frac{\mathrm{d}}{\mathrm{d}\tau} + \mathbf{1} - \frac{\omega(\tau)}{4\pi}\int\limits_{4\pi}\mathrm{d}\Omega'\mathbf{Z}(\tau,\Omega,\Omega')\otimes\,, \tag{8.42}$$

where the symbol $\otimes$ is used to denote an integral operator, not a finite integral. The radiative transfer equation is now written in the following operator form:

$$\mathbf{L}_e\,\boldsymbol{I} = \boldsymbol{Q}\,, \tag{8.43}$$

where $\boldsymbol{Q} \equiv \boldsymbol{Q}(\tau)$.

The operator $\mathbf{L}_e$ is referred to as the direct radiative transfer operator. To rewrite boundary conditions (8.38) and (8.39) in the operator form as well, we define two linear integral operators $\mathbf{L}_t$ and $\mathbf{L}_b$ as follows:

$$\mathbf{L}_t \;=\; \int\limits_0^{\tau_0}\mathrm{d}\tau\delta(\tau)\otimes\,, \tag{8.44}$$

$$\mathbf{L}_b \;=\; \int\limits_0^{\tau_0}\mathrm{d}\tau\delta(\tau-\tau_0)\left(\otimes - \frac{A}{\pi}\int\limits_{4\pi}\mathrm{d}\Omega'\lambda(\mu')\mathbf{M}(\Omega,\Omega')\otimes\right)\,, \tag{8.45}$$

where $\delta(\tau)$ and $\delta(\tau-\tau_0)$ are the Dirac δ functions, $\lambda(\mu) = \mu\Theta(\mu)$ is an auxiliary function introduced in [28] and $\Theta(\mu)$ is the Heaviside step-function over $\mu \in [-1,1]$ given by

$$\Theta(\mu) = \begin{cases} 1, & \mu > 0 \\ 0, & \mu < 0 \end{cases}\,. \tag{8.46}$$

The function $\Theta(\mu)$ is used here to expand the integration range over μ in the lower boundary condition given by (8.39) to the whole range of the variable μ.

Operators $\mathbf{L}_t$ and $\mathbf{L}_b$ operate in a way analogous to the operator $\mathbf{L}_e$ on the intensity vector $\boldsymbol{I}(\tau,\Omega)$ and have the same domain. These operators allow us to rewrite boundary conditions given by (8.38) and (8.39) in the operator form. Thus, the operator form of the direct VRTE alone with boundary conditions is written as follows:

$$\mathbf{L}_e\,\boldsymbol{I} \;=\; \boldsymbol{Q}\,, \tag{8.47}$$

$$\mathbf{L}_t\boldsymbol{I} \;=\; \boldsymbol{S}_t(\Omega),\;\; \mu > 0\,, \tag{8.48}$$

$$\mathbf{L}_b\boldsymbol{I} \;=\; \boldsymbol{S}_b(\Omega),\;\; \mu < 0\,, \tag{8.49}$$

where $\boldsymbol{S}_t(\Omega)$ and $\boldsymbol{S}_b(\Omega)$ can be an arbitrary vector functions in the general case. In the case considered here we have according to (8.38) and (8.39):

$$\boldsymbol{S}_t(\Omega) \;=\; \pi\delta(\mu-\mu_0)\delta(\phi-\phi_0)\boldsymbol{E}_1\,, \tag{8.50}$$

$$\boldsymbol{S}_b(\Omega) \;=\; \epsilon B(T_s)\boldsymbol{E}_1\,. \tag{8.51}$$

8.4.3 Generalized form of the direct VRTE

The operator representation of the direct VRTE and corresponding boundary conditions formulated above describe a specific boundary value problem consisting of three independent operator equations. In this section it will be demonstrated that the boundary value problem can be rewritten in the form of a single operator equation. Such representation will be called the generalized form of the direct VRTE.

To derive the generalized from of the direct VRTE let us sum (8.47)–(8.49). Multiplying (8.48) by an function $t(\tau,\Omega)\Theta(\mu)$ and (8.49) by $b(\tau,\Omega)\Theta(-\mu)$, we obtain

$$\begin{aligned}\mathbf{L}_e\boldsymbol{I} \;+\; & t(\tau,\Omega)\Theta(\mu)\mathbf{L}_t\boldsymbol{I} + b(\tau,\Omega)\Theta(-\mu)\mathbf{L}_b\boldsymbol{I} = \\ = \; & \boldsymbol{Q}(\tau) + t(\tau,\Omega)\Theta(\mu)\boldsymbol{S}_t(\Omega) + b(\tau,\Omega)\Theta(-\mu)\boldsymbol{S}_b(\Omega)\,. \end{aligned} \tag{8.52}$$

Here we have used functions $\Theta(\mu)$ and $\Theta(-\mu)$ to expand (8.48) and (8.49), respectively, to the whole range of the variable μ. Functions $t(\tau,\Omega)$ and $b(\tau,\Omega)$ are arbitrary at this point. The only requirement is that they are nonzero everywhere where the right-hand side of the corresponding equation is nonzero.

Functions $t(\tau,\Omega)$ and $b(\tau,\Omega)$ can be found requiring (8.52) to result in the same solution for the transmitted and reflected intensity, respectively, as the direct VRTE given by (8.47)–(8.49). The derivation is given in Appendix A. The result is as follows:

$$t(\tau,\Omega) \;=\; \mu\delta(\tau)\,, \tag{8.53}$$

$$b(\tau,\Omega) \;=\; -\mu\delta(\tau-\tau_0)\,. \tag{8.54}$$

We see that both functions are independent of the variable ϕ. Thereby, argument μ will be used henceforth instead of Ω .

Substituting now $t(\tau,\mu)$ and $b(\tau,\mu)$ into (8.52) and introducing for the simplification the auxiliary functions $\psi_t(\tau,\mu)$ and $\psi_b(\tau,-\mu)$ as

$$\psi_t(\tau,\mu) \quad = t(\tau,\mu)\Theta(\mu) \quad = \mu\delta(\tau)\Theta(\mu)\,, \tag{8.55}$$

$$\psi_b(\tau,-\mu) = b(\tau,\mu)\Theta(-\mu) = -\mu\delta(\tau-\tau_0)\Theta(-\mu)\,, \tag{8.56}$$

we obtain

$$\begin{aligned}\mathbf{L}_e\boldsymbol{I} + \psi_t(\tau,\mu)\mathbf{L}_t\boldsymbol{I} + \psi_b(\tau,-\mu)\mathbf{L}_b\boldsymbol{I} = \\ = \boldsymbol{Q}(\tau) + \psi_t(\tau,\mu)\boldsymbol{S}_t(\Omega) + \psi_b(\tau,-\mu)\boldsymbol{S}_b(\Omega)\,. \end{aligned} \tag{8.57}$$

The derived radiative transfer equation is equivalent to (8.47)–(8.49) but incorporate all operations with the radiance field on the boundaries, i.e., at this point, the boundary conditions are already included in the radiative transfer equation and do not need to be supplied separately.

The generalized form of the direct radiative transfer operator is determined by the left-hand side of (8.57) as

$$\mathbf{L} = \mathbf{L}_e + \psi_t(\tau, \mu)\mathbf{L}_t + \psi_b(\tau, -\mu)\mathbf{L}_b \tag{8.58}$$

and the source function, $\boldsymbol{S}(\tau, \Omega)$, is determined by the right-hand side of (8.57) as

$$\boldsymbol{S}(\tau, \Omega) = \boldsymbol{Q}(\tau) + \psi_t(\tau, \mu)\boldsymbol{S}_t(\Omega) + \psi_b(\tau, -\mu)\boldsymbol{S}_b(\Omega)\,. \tag{8.59}$$

Using the operator $\mathbf{L}$ and the source function $\boldsymbol{S}$, equation (8.57) can be rewritten as follows:

$$\mathbf{L}\boldsymbol{I} = \boldsymbol{S}\,. \tag{8.60}$$

Equation (8.60) is the desired generalized form of the direct radiative transfer equation containing all operations with the intensity field including boundary conditions. It is worth to notice that the described technique of the inclusion of boundary conditions in the direct radiative transfer operator is a standard approach in the framework of the finite differences technique (see [16] for details). In this case the operator L is approximated by an appropriate matrix which contains the boundary conditions.

8.5 Generalized form of the adjoint radiative transfer operator

To derive the adjoint radiative transfer operator, we start from the generalized form of the direct radiative transfer operator given by (8.58). Taking into account that the operator $\mathbf{L}_e$ as given by (8.42) consists of three parts: the first-order differential operator $\mu d/d\tau$, the identity operator, $\mathbf{1}$, and the integral operator with the kernel $(\omega(\tau)/4\pi)\ \mathbf{Z}(\tau, \Omega, \Omega')$, we have

$$\mathbf{L} = \mu\frac{d}{d\tau} + \psi_t(\tau, \mu)\mathbf{L}_t + \psi_b(\tau, -\mu)\mathbf{L}_b + \mathbf{1} - \frac{\omega(\tau)}{4\pi}\int\limits_{4\pi} d\Omega'\mathbf{Z}(\tau, \Omega, \Omega') \otimes\ . \tag{8.61}$$

Let $\mathbf{A}$ be a linear operator operating on the vector function $\boldsymbol{I}(\tau, \Omega)$. Then, according to the definition, the adjoint operator $\mathbf{A}^*$ has to satisfy the Lagrange identity [13]

$$(\boldsymbol{I}^*, \mathbf{A}\boldsymbol{I}) = (\mathbf{A}^*\boldsymbol{I}^*, \boldsymbol{I})\,, \tag{8.62}$$

where $(\ ,\ )$ is used to define the scalar product in the appropriate functional space and $\boldsymbol{I}^*(\tau, \Omega)$ is an arbitrary vector function which belongs to the domain of the operator $\mathbf{A}^*$. Throughout this chapter we will assume that a scalar product of two arbitrary vector functions $\boldsymbol{f}(\tau, \Omega)$ and $\boldsymbol{g}(\tau, \Omega)$ is defined as follows:

$$(\boldsymbol{f}, \boldsymbol{g}) = \int\limits_0^{\tau_0}\int\limits_{4\pi} \boldsymbol{f}^T(\tau, \Omega)\boldsymbol{g}(\tau, \Omega)\mathrm{d}\tau\mathrm{d}\Omega\,. \tag{8.63}$$

Let us take the scalar product given by (8.63) of the functions $\boldsymbol{f} = \boldsymbol{I}^*$ and $\boldsymbol{g} = \mu d\boldsymbol{I}/d\tau$. Then, using the integration by parts in the integral over τ, we obtain

$$\left(\boldsymbol{I}^*, \mu\frac{\mathrm{d}\boldsymbol{I}}{\mathrm{d}\tau}\right) = -\left(\mu\frac{\mathrm{d}\boldsymbol{I}^*}{\mathrm{d}\tau}, \boldsymbol{I}\right) + R\,, \tag{8.64}$$

where R includes values of functions $\boldsymbol{I}(\tau,\Omega)$ and $\boldsymbol{I}^*(\tau,\Omega)$ on the boundaries, $\tau = 0$ at the top and $\tau = \tau_0$ at the bottom of a medium, namely

$$R = \left(\int\limits_{4\pi} \mu\boldsymbol{I}^T(\tau,\Omega)\boldsymbol{I}^*(\tau,\Omega)\mathrm{d}\Omega\right)\Bigg|_0^{\tau_0}\,. \tag{8.65}$$

Comparing (8.64) with the Lagrange identity given by (8.62), we see that the operator $A = \mu d/d\tau$ has the adjoint operator, namely $A^* = -\mu d/d\tau$, in the case of $R = 0$ only. This is the case, for example, for the vacuum boundary conditions (see [10]) for the function $\boldsymbol{I}(\tau,\Omega)$. Indeed, inserting vacuum boundary conditions (no incoming radiance): $\boldsymbol{I}(0,\Omega) = 0$ for $\mu > 0$, and $\boldsymbol{I}(\tau_0,\Omega) = 0$ for $\mu < 0$ into (8.65), we have

$$R = \int\limits_{\Omega_+} \mu\boldsymbol{I}^T(\tau_0,\Omega)\boldsymbol{I}^*(\tau_0,\Omega)\mathrm{d}\Omega - \int\limits_{\Omega_-} \mu\boldsymbol{I}^T(0,\Omega)\boldsymbol{I}^*(0,\Omega)\mathrm{d}\Omega\,, \tag{8.66}$$

where Ω_- is defined the set of variables $\{\mu,\phi\}$ in the range $\mu \in [-1,0]$, $\phi \in [0,2\pi]$, and integration over Ω_- is as follows:

$$\int\limits_{\Omega_-} \mathrm{d}\Omega \equiv \int\limits_0^{2\pi} \mathrm{d}\phi \int\limits_{-1}^{0} \mathrm{d}\mu\,. \tag{8.67}$$

Taking into account that $\boldsymbol{I}(\tau,\Omega)$ and $\boldsymbol{I}^*(\tau,\Omega)$ are arbitrary and independent functions, requirement $R = 0$ can be satisfied assuming that $\boldsymbol{I}^*(0,\Omega) = 0$ for $\mu < 0$, and $I^*(\tau_0,\Omega) = 0$ for $\mu > 0$. Thus, we require no outgoing adjoint radiance as the boundary conditions for the adjoint intensity.

Thereby, the adjoint operator can be immediately defined for the direct radiative transfer operator in the case of vacuum boundary conditions. However, the reflection from the surface is important in most atmospheric radiative transfer calculations introducing a nonzero boundary condition at the bottom of a medium.

There are different ways to overcome this obstacle. For example, Marchuk [17] has derived the adjoint RTE for the vacuum boundary conditions. In the case of the reflecting boundary he has found appropriate lower boundary condition for the function $I^*(\tau_0,\mu)$ to ensure $R = 0$ in (8.64). Min and Harrison [19] have suggested that the solution of the radiative transfer equation with a Lambertian surface can be constructed from the solutions of two standard problems. Namely, the standard problem with no ground reflection (vacuum conditions) and the

solution of the problem with collimated illumination from the bottom can be used. Box and co-authors [3] following Bell and Glasstone [1] have postulated the adjoint operator and then determined an appropriate set of boundary conditions on $I^*(\tau,\mu)$. The generalized form of the direct radiative transfer operator has been formulated by Ustinov [28] to derive the adjoint operator in the case of arbitrary boundary conditions.

Here we show that the modified differential operator, namely

$$\mathbf{D} = \mu d/d\tau + \psi_t(\tau,\mu)\mathbf{L}_t + \psi_b(\tau,-\mu)\mathbf{L}_b\,, \tag{8.68}$$

which includes boundary conditions operators, has an adjoint operator, D^*, satisfying the Lagrange identity as given by (8.62) independently of the specific form of the boundary conditions for the intensity $\boldsymbol{I}(\tau,\Omega)$. To demonstrate this and find the adjoint operator $\mathbf{D}^*$, let us consider the following scalar product:

$$P = (\boldsymbol{I}^*, \mathbf{D}\boldsymbol{I}) = \left(\boldsymbol{I}^*, \left[\mu\frac{\mathrm{d}}{\mathrm{d}\tau} + \psi_t(\tau,\mu)\mathbf{L}_t + \psi_b(\tau,-\mu)\mathbf{L}_b\right]\boldsymbol{I}\right)\,. \tag{8.69}$$

Our task is to rewrite this scalar product in the form of: $P = (\mathbf{D}^*\boldsymbol{I}^*, \boldsymbol{I})$. Details of the derivation are given in Appendix B. The final expression for the adjoint modified differential operator, $\mathbf{D}^*$, is:

$$D^* = -\mu\frac{\mathrm{d}}{\mathrm{d}\tau} + \psi_t(\tau,-\mu)\mathbf{L}_t^* + \psi_b(\tau,\mu)\mathbf{L}_b^*\,, \tag{8.70}$$

where the upper and lower boundary conditions operators are:

$$\mathbf{L}_t^* = \int_0^{\tau_0} \mathrm{d}\tau\delta(\tau)\otimes\,, \tag{8.71}$$

$$\mathbf{L}_b^* = \int_0^{\tau_0} \mathrm{d}\tau\delta(\tau-\tau_0)\left[\otimes - \frac{A}{\pi}\int_{4\pi}\mathrm{d}\Omega'\lambda(-\mu')\mathbf{M}^T(\Omega',\Omega)\otimes\right]\,. \tag{8.72}$$

Although the superscript $*$ is used for the integral operators $\mathbf{L}_t^*$ and $\mathbf{L}_b^*$, we note that it does not mean that they are adjoint operators to $\mathbf{L}_t$ and $\mathbf{L}_b$. We emphasize only that these operators operate on the adjoint intensity in contrast to $\mathbf{L}_t$ and $\mathbf{L}_b$ operating on the direct intensity.

Concluding, we consider remaining operators in (8.61). The identity operator is the self-adjoint operator. Thereby, the adjoint operator to the identity operator is the identity operator again. The adjoint operator to the integral operator in (8.61) can be found using the following equation:

$$\left(\boldsymbol{I}^*, \frac{\omega(\tau)}{4\pi}\int_{4\pi}\mathbf{Z}(\tau,\Omega,\Omega')\boldsymbol{I}(\tau,\Omega')\mathrm{d}\Omega'\right)$$
$$= \left(\boldsymbol{I}, \frac{\omega(\tau)}{4\pi}\int_{4\pi}\mathbf{Z}^T(\tau,\Omega',\Omega)\boldsymbol{I}^*(\tau,\Omega')\mathrm{d}\Omega'\right)\,, \tag{8.73}$$

which can be derived changing the integration order over Ω and Ω' and after that replacing $\Omega \leftrightarrow \Omega'$. From this equation we can see that adjoint operator to the integral operator is the integral operator with the kernel $(\omega(\tau)/4\pi)\ \mathbf{Z}^T(\tau, \Omega', \Omega)$.

Summing up all obtained results, we can write the desired expression for the adjoint radiative transfer operator in the following form:

$$\mathbf{L}^* = \mathbf{L}_e^* + \psi_t(\tau, -\mu)\mathbf{L}_t^* + \psi_b(\tau, \mu)\mathbf{L}_b^* \,, \tag{8.74}$$

where $\mathbf{L}_e^*$ is

$$\mathbf{L}_e^* = -\mu \frac{\mathrm{d}}{\mathrm{d}\tau} + \mathbf{1} - \frac{\omega(\tau)}{4\pi} \int\limits_{4\pi} \mathrm{d}\Omega' \mathbf{Z}^T(\tau, \Omega', \Omega) \otimes \ . \tag{8.75}$$

Equation (8.74) is the desired generalized form of the adjoint radiative transfer operator. The adjoint operator, $\mathbf{L}^*$, contains, as in the case with the direct operator, $\mathbf{L}$, all operations with the adjoint intensity field including boundary conditions.

8.6 Adjoint radiative transfer equation

The generalized form of the adjoint radiative transfer operator has been derived in the previous section. Here we will demonstrate how the adjoint radiative transfer equation can be formulated. We start from the generalized form of the direct VRTE according to (8.60):

$$\mathbf{L}\boldsymbol{I} = \boldsymbol{S} \,, \tag{8.76}$$

where

$$\boldsymbol{S} = \boldsymbol{Q} + \psi_t(\tau, \mu)\boldsymbol{S}_t + \psi_b(\tau, -\mu)\boldsymbol{S_b} \tag{8.77}$$

is the right-hand side of the direct VRTE written in the generalized form.

Let us assume that we need to calculate a functional, say G, of the intensity vector $\boldsymbol{I}$

$$G = (\boldsymbol{W}, \boldsymbol{I}) \,, \tag{8.78}$$

where $\boldsymbol{W}$ is at this point an arbitrary vector function of variables τ and Ω.

There are two ways to solve this problem [3]. One way (the forward approach) is to find the solution $\boldsymbol{I}$ of the direct VRTE and apply (8.78) to calculate G. Another way (the adjoint approach) is to take the scalar product of (8.76) and the arbitrary function $\boldsymbol{I}^*$:

$$(\boldsymbol{I}^*, \mathbf{L}\boldsymbol{I}) = (\boldsymbol{I}^*, \boldsymbol{S}) \,, \tag{8.79}$$

then employing the definition of the adjoint operator (8.62) on the left-hand side of this equation, we obtain

$$(\mathbf{L}^*\boldsymbol{I}^*, \boldsymbol{I}) = (\boldsymbol{I}^*, \boldsymbol{S}) \,. \tag{8.80}$$

If we require now that $\boldsymbol{I}^*$ is the solution of the following adjoint equation:

$$\mathbf{L}^* \boldsymbol{I}^* = \boldsymbol{W} \,, \tag{8.81}$$

it follows from (8.80) that

$$(\boldsymbol{W}, \boldsymbol{I}) = (\boldsymbol{I}^*, \boldsymbol{S}) = G \,. \tag{8.82}$$

Thus, the functional G can be found not only using (8.78) but also as the scalar product of the solution of the adjoint VRTE, $\boldsymbol{I}^*$, and the right-hand side of the direct VRTE written in the generalized form, i.e., $\boldsymbol{S}$.

Equation (8.81) describes a certain boundary value problem for the adjoint intensity written in the generalized form. The operator $\mathbf{L}^*$ given by (8.74) includes the boundary conditions operators simular to the operator $\mathbf{L}$ in (8.76). Thereby, the right-hand side of (8.81) must include the boundary conditions as well. Thus, it must be possible to rewrite $\boldsymbol{W}(\tau, \Omega)$ in the following form:

$$\boldsymbol{W}(\tau, \Omega) = \boldsymbol{W}_e(\tau, \Omega) + \psi_t(\tau, -\mu)\boldsymbol{W}_t(\Omega) + \psi_b(\tau, \mu)\boldsymbol{W}_b(\Omega) \,, \tag{8.83}$$

where subscripts 'e', 't' and 'b' stand for 'equation', upper ('top') and lower ('bottom') boundary conditions for the adjoint intensity, respectively.

Substituting (8.83) into (8.81), we obtain the generalized form of the adjoint radiative transfer equation as follows:

$$\mathbf{L}^* \boldsymbol{I}^* = \boldsymbol{W}_e + \psi_t(\tau, -\mu)\boldsymbol{W}_t(\Omega) + \psi_b(\tau, \mu)\boldsymbol{W}_b(\Omega) \,. \tag{8.84}$$

This equation can be treated in analogy to the generalized form of the direct VRTE as a sum of three independent operator equations, namely, the operator form of the adjoint VRTE and premultiplying by the appropriate functions the boundary condition equations written in the operator form as well. Thereby, (8.84) can be separated into the three independent equations as follows:

$$\mathbf{L}_e^* \boldsymbol{I}^* = \boldsymbol{W}_e(\tau, \Omega) \,, \tag{8.85}$$

$$\mathbf{L}_t^* \boldsymbol{I}^* = \boldsymbol{W}_t(\Omega) \,, \mu < 0 \,, \tag{8.86}$$

$$\mathbf{L}_b^* \boldsymbol{I}^* = \boldsymbol{W}_b(\Omega) \,, \mu > 0 \,. \tag{8.87}$$

Equations (8.85)–(8.87) are referred to as the operator representation of the adjoint VRTE.

Employing in these equations operators $\mathbf{L}_t^*$, $\mathbf{L}_b^*$ and $\mathbf{L}_e^*$ as given by (8.71), (8.72) and (8.75), respectively, the standard form of the adjoint VRTE can be formulated as follows:

$$-\mu \frac{\mathrm{d}\boldsymbol{I}^*(\tau, \Omega)}{\mathrm{d}\tau} = -\boldsymbol{I}^*(\tau, \Omega) + \boldsymbol{J}^*(\tau, \Omega) + \boldsymbol{W}_e(\tau, \Omega) \,, \tag{8.88}$$

$$\boldsymbol{I}^*(0, \Omega) = \boldsymbol{W}_t(\Omega), \;\; \mu < 0 \,, \tag{8.89}$$

$$\boldsymbol{I}^*(\tau_0, \Omega) = \boldsymbol{W}_b(\Omega) - \frac{A}{\pi} \int\limits_{\Omega_-} \mathbf{M}^T(\Omega', \Omega)\boldsymbol{I}^*(\tau_0, \Omega')\mu' \mathrm{d}\Omega', \;\; \mu > 0 \,, \tag{8.90}$$

where the multiple scattering adjoint source function, $\boldsymbol{J}^*(\tau, \Omega)$, is defined as

$$\boldsymbol{J}^*(\tau,\Omega) = \frac{\omega(\tau)}{4\pi}\int\limits_{4\pi} \mathbf{Z}^T(\tau,\Omega',\Omega)\boldsymbol{I}^*(\tau,\Omega')\,\mathrm{d}\Omega' \,. \tag{8.91}$$

Thus, we have formulated three equivalent representations of the adjoint VRTE starting from the generalized form of the adjoint operator. We note that there are other ways to formulate the adjoint RTE. Thus, for example, it can be found by developing a variational principle for the integro-differential transport equation (see [22] for details).

The adjoint and direct VRTEs are closely related. Moreover, as is demonstrated in [1, 3, 19–21] a solution of the adjoint VRTE given by (8.88) can be found as a solution of the direct VRTE with the appropriate right-hand side and boundary conditions. Therefore, we do not need in fact to develop special methods for the solution of the adjoint VRTE.

To illustrate the application of the adjoint approach we consider some simple examples of the functional G providing the different right-hand side of the adjoint VRTE written in the generalized form:

— functional G is the transmitted radiance in the direction μ_v, ϕ_v at the optical depth τ_v, then

$$\begin{aligned} &G = \int\limits_0^{\tau_0}\int\limits_{4\pi} \delta(\tau-\tau_v)\delta(\Omega-\Omega_v)\boldsymbol{E}_1^T\boldsymbol{I}(\tau,\Omega)\mathrm{d}\tau\mathrm{d}\Omega \equiv I(\tau_v,\Omega_v)\,,\\ &\boldsymbol{W}(\tau,\Omega) = \delta(\tau-\tau_v)\delta(\Omega-\Omega_v)\boldsymbol{E}_1 \equiv \boldsymbol{W}_e(\tau,\Omega)\,,\\ &\boldsymbol{W}_t(\Omega) = \mathbf{0}\,,\ \boldsymbol{W}_b(\Omega) = \mathbf{0}\,; \end{aligned} \tag{8.92}$$

— functional G is the downward flux at the bottom of the medium, then

$$\begin{aligned} &G = \int\limits_0^{\tau_0}\int\limits_{4\pi} \delta(\tau-\tau_0)\Theta(\mu)\boldsymbol{E}_1^T\boldsymbol{I}(\tau,\Omega)\mu\mathrm{d}\tau\mathrm{d}\Omega \equiv F_d\,,\\ &\boldsymbol{W}(\tau,\Omega) = \delta(\tau-\tau_0)\Theta(\mu)\mu\boldsymbol{E}_1 = \psi_b(\tau,\mu)\boldsymbol{W}_b(\Omega)\,,\\ &\boldsymbol{W}_e(\tau,\Omega) = \mathbf{0}\,,\ \boldsymbol{W}_t(\mu) = \mathbf{0}\,, \end{aligned} \tag{8.93}$$

where $\boldsymbol{W}_b(\Omega) = \boldsymbol{E}_1$;

— functional G is the upward flux at the top of the medium, then

$$\begin{aligned} &G = \int\limits_0^{\tau_0}\int\limits_{4\pi} \delta(\tau)\Theta(-\mu)\boldsymbol{E}_1^T\boldsymbol{I}(\tau,\Omega)\mu\mathrm{d}\tau\mathrm{d}\Omega \equiv F_u\,,\\ &\boldsymbol{W}(\tau,\Omega) = \delta(\tau)\Theta(-\mu)\mu\boldsymbol{E}_1 = \psi_t(\tau,-\mu)\boldsymbol{W}_t(\Omega)\,,\\ &\boldsymbol{W}_e(\tau,\Omega) = \mathbf{0}\,,\ \boldsymbol{W}_b(\Omega) = \mathbf{0}\,, \end{aligned} \tag{8.94}$$

where $\boldsymbol{W}_t(\Omega) = -\boldsymbol{E}_1$.

In the next section the application of the adjoint approach to the derivation of the weighting function will be considered. Other numerous applications of the adjoint radiative transfer equation and the adjoint approach have recently been reviewed by Marchuk [18] and Box [5].

8.7 General expression for the weighting function

In this section we apply the generalized form of the direct and adjoint VRTEs as given by (8.60) and (8.84), respectively, to the derivation of the variational and partial derivative (or weighting function) of the intensity vector with respect to the main optical and surface parameters of a scattering medium. The obtained expressions contain the total forward and total adjoint intensity vectors and related functions only. Thereby, these expressions are referred to as total-total (TT) representation of the weighting functions. In section 8.9 the appropriate expressions containing the diffuse forward and diffuse adjoint intensity will be formulated.

8.7.1 Linearization of the direct VRTE with respect to the variation of optical and surface parameters

We start from the direct VRTE written in the generalized form for the total forward intensity as given by (8.60). Varying both sides of this equation, the resulting operator equation for the variation of the intensity vector can be written in the framework of the linear perturbation theory as follows [17]:

$$\mathbf{L}\delta\boldsymbol{I} = \delta\boldsymbol{S} - \delta\mathbf{L}\boldsymbol{I} \,, \tag{8.95}$$

where the variation of the source function, $\boldsymbol{S}$, and the radiative transfer operator, $\mathbf{L}$, as given by (8.59) and (8.58), respectively, are caused by the variation of optical and surface parameters. The terms in the right-hand side of this equation can be rewritten to contain variations of the various optical and surface parameters. In the most common case an atmospheric perturbation can result from variations of the extinction coefficient, single-scattering albedo, phase matrix, surface emissivity and surface albedo.

Let us assume at first that the variation of the radiation field is caused by the variation of the extinction coefficient only. We note that the optical depth and the single-scattering albedo are considered here as two independent variables. Therefore, we assume that the variation of the extinction coefficient leads to the variation of the optical depth only. Substituting $\boldsymbol{S}(\tau, \Omega)$ as given by (8.59) into the right-hand side of (8.95), we obtain

$$\mathbf{L}\delta_e\boldsymbol{I} = \delta_e[\boldsymbol{Q}(\tau) + \psi_t(\tau, \mu)\boldsymbol{S}_t(\Omega) + \psi_b(\tau, -\mu)\boldsymbol{S}_b(\Omega)] - \delta_e\mathbf{L}\boldsymbol{I} \,, \tag{8.96}$$

where δ_e denotes that the variation of the appropriate function caused by the variation of the extinction coefficient. Taking into account that according to the definition of functions $\boldsymbol{Q}$, $\boldsymbol{S}_t$ and $\boldsymbol{S}_b$ as given by (8.35), (8.50) and (8.51), respectively, they are independent of the extinction coefficient, we have

$$\delta_e \boldsymbol{Q} = \delta_e \boldsymbol{S}_t = \delta_e \boldsymbol{S}_b = 0 \; . \tag{8.97}$$

The variation of the direct radiative transfer operator $\mathbf{L}$ written in the generalized form can be expressed using (8.58) as follows:

$$\delta_e \mathbf{L} \boldsymbol{I} = \delta_e [\mathbf{L}_e + \psi_t(\tau, \mu)\mathbf{L}_t + \psi_b(\tau, -\mu)\mathbf{L}_b]\boldsymbol{I} = \delta_e \mathbf{L}_e \boldsymbol{I} \; , \tag{8.98}$$

where we have taken into account that the boundary condition operators $\mathbf{L}_t$ and $\mathbf{L}_b$ given by (8.44) and (8.45), respectively, are independent of the extinction coefficient. The variation of the direct radiative transfer operator L_e as given by (8.42) can be now easily found. Indeed, taking into account that only τ depends on the extinction coefficient, namely $\mathrm{d}\tau = -\sigma_e(z)\mathrm{d}z$, we obtain

$$\delta_e \mathbf{L}_e \boldsymbol{I} \; = \; \delta_e \left[-\frac{\mu}{\sigma_e(z)} \frac{\mathrm{d}}{\mathrm{d}z} \right] \boldsymbol{I} \; = \; \frac{\delta\sigma_e(z)}{\sigma_e^2(z)} \mu \frac{\mathrm{d}\boldsymbol{I}}{\mathrm{d}z} \; = \; - \frac{\delta\sigma_e(\tau)}{\sigma_e(\tau)} \mu \frac{\mathrm{d}\boldsymbol{I}}{\mathrm{d}\tau} \; . \tag{8.99}$$

Introducing the relative variation of the extinction coefficient as $v_e(\tau) = \delta\sigma_e(\tau)/\sigma_e(\tau)$ and substituting the right-hand side of (8.33) instead of $\mu \mathrm{d}\boldsymbol{I}/\mathrm{d}\tau$, equation (8.99) can be rewritten as follows:

$$\delta_e \mathbf{L}_e \boldsymbol{I} = v_e(\tau)[\boldsymbol{I}(\tau, \Omega) - \boldsymbol{J}(\tau, \Omega) - \boldsymbol{Q}(\tau)] \; . \tag{8.100}$$

Substituting (8.100) into right-hand side of (8.96) and taking into account (8.97), we obtain the final expression for the linear radiative transfer equation describing the variation of the intensity vector caused by the variation of the extinction coefficient

$$\mathbf{L}\delta_e \boldsymbol{I} = v_e(\tau)[-\boldsymbol{I}(\tau, \Omega) + \boldsymbol{J}(\tau, \Omega) + \boldsymbol{Q}(\tau)] \; . \tag{8.101}$$

Employing the considered approach in the case of the variation of the single-scattering albedo, we obtain

$$\mathbf{L}\delta_\omega \boldsymbol{I} = \delta_\omega \boldsymbol{Q} - \delta_\omega \mathbf{L}_e \boldsymbol{I} \; , \tag{8.102}$$

where we have taken into account that functions $\boldsymbol{S}_t$ and $\boldsymbol{S}_b$ and the boundary condition operators $\mathbf{L}_t$ and $\mathbf{L}_b$ are independent of the single-scattering albedo. Taking further into account that $\boldsymbol{Q}$ and $\mathbf{L}_e$ given by (8.35) and (8.42), respectively, are linear functions of the single-scattering albedo, equation (8.102) can be rewritten as follows:

$$\mathbf{L}\delta_\omega \boldsymbol{I} = v_\omega(\tau)[-\omega(\tau)B(\tau)\boldsymbol{E}_1 + \boldsymbol{J}(\tau, \Omega)] \; , \tag{8.103}$$

where $v_\omega(\tau)$ is the relative variation of the single-scattering albedo.

The variation of the surface emissivity, ϵ, causes only the variation of the function $\boldsymbol{S}_b$ describing the lower boundary condition. Thereby, using (8.51), we obtain

$$\mathbf{L}\delta_\epsilon \boldsymbol{I} = v_\epsilon \epsilon \psi_b(\tau, -\mu) B(T_s) \boldsymbol{E}_1 \ , \tag{8.104}$$

where v_ϵ is the relative variation of the surface emissivity.

The variation of the surface albedo, A, causes only the variation of the lower boundary condition operator, $\mathbf{L}_b$, as given by (8.45). Thereby, the equation describing the variation of the intensity vector can be written as follows:

$$\mathbf{L}\delta_A \boldsymbol{I} = -\psi_b(\tau, -\mu)\delta_A \mathbf{L}_b \boldsymbol{I} \ . \tag{8.105}$$

Varying (8.45) with respect to the surface albedo and substituting the result into (8.105), we obtain

$$\mathbf{L}\delta_A \boldsymbol{I} = v_A \psi_b(\tau, -\mu) \frac{A}{\pi} \int\limits_{\Omega_+} \mathbf{M}(\Omega, \Omega') \boldsymbol{I}(\tau_0, \Omega') \mu' \mathrm{d}\Omega' \ , \tag{8.106}$$

where v_A is the relative variation of the surface albedo.

The phase matrix, $\mathbf{Z}(\tau, \Omega, \Omega')$, depends on the number of parameters such as size, shape, internal structure, and refractive index of particles [12]. Even in the simplest case of spherical isotropic homogeneous particles the dependence on the size parameter and refractive index remains. However, for our consideration it is only important that a linear relationship between the variation of the phase matrix and the variation of the desired parameter can be defined. Let us assume that such a linear relationship can be written as follows:

$$\delta \mathbf{Z}(\tau, \Omega, \Omega') = \frac{\partial}{\partial m} \mathbf{Z}(\tau, \Omega, \Omega') \delta m(\tau) \ , \tag{8.107}$$

where $\partial \mathbf{Z}/\partial m$ is the partial derivative of the phase matrix with respect to a certain parameter $m(\tau)$. Taking into account that the variation of the phase matrix is cased only the variation of the direct radiative transfer operator $\mathbf{L}_e$ as given by (8.42), we obtain

$$\mathbf{L}\delta_m \boldsymbol{I} = v_m(\tau) m(\tau) \frac{\omega(\tau)}{4\pi} \int\limits_{4\pi} \frac{\partial}{\partial m} \mathbf{Z}(\tau, \Omega, \Omega') \boldsymbol{I}(\tau, \Omega') \mathrm{d}\Omega' \ , \tag{8.108}$$

where $v_m(\tau)$ is the relative variation of the parameter $m(\tau)$.

Introducing the auxiliary vector functions $\boldsymbol{\Psi}_e, \boldsymbol{\Psi}_{\boldsymbol{\omega}}, \boldsymbol{\Psi}_{\boldsymbol{\epsilon}}, \boldsymbol{\Psi}_{\boldsymbol{A}}$ and $\boldsymbol{\Psi}_{\boldsymbol{m}}$ as follows:

$$\boldsymbol{\Psi}_e(\tau, \Omega) = \boldsymbol{J}(\tau, \Omega) + \boldsymbol{Q}(\tau) - \boldsymbol{I}(\tau, \Omega) \ , \tag{8.109}$$

$$\boldsymbol{\Psi}_\omega(\tau, \Omega) = \boldsymbol{J}(\tau, \Omega) - \omega(\tau) B(\tau) \boldsymbol{E}_1 \ , \tag{8.110}$$

$$\boldsymbol{\Psi}_\epsilon(\tau, \Omega) = \epsilon \psi_b(\tau, -\mu) B(T_s) \boldsymbol{E}_1 \ , \tag{8.111}$$

$$\boldsymbol{\Psi}_A(\tau, \Omega) = \psi_b(\tau, -\mu) \frac{A}{\pi} \int\limits_{\Omega_+} \mathbf{M}(\Omega, \Omega') \boldsymbol{I}(\tau_0, \Omega') \mu' \mathrm{d}\Omega' \ , \tag{8.112}$$

$$\boldsymbol{\Psi}_m(\tau, \Omega) = m(\tau) \frac{\omega(\tau)}{4\pi} \int\limits_{4\pi} \frac{\partial}{\partial m} \mathbf{Z}(\tau, \Omega, \Omega') \boldsymbol{I}(\tau, \Omega') \mathrm{d}\Omega' \ , \tag{8.113}$$

we can rewrite (8.95) in the case of simultaneous variations of all relevant optical and surface parameters in the following form:

$$\begin{aligned}\mathbf{L}\boldsymbol{\delta I} &= v_e(\tau)\boldsymbol{\Psi}_e(\tau,\Omega) + v_\omega(\tau)\boldsymbol{\Psi}_\omega(\tau,\Omega) + v_\epsilon\boldsymbol{\Psi}_\epsilon(\tau,\Omega) \\ &+ v_A\boldsymbol{\Psi}_A(\tau,\Omega) + v_m(\tau)\boldsymbol{\Psi}_m(\tau,\Omega)\,. \end{aligned} \tag{8.114}$$

In fact the variation of the radiation field can be caused by variations of other parameters which are not yet included in (8.114). Thus, for example, the variation of the kinetic temperature, $T(\tau)$, causes the variation of the Planck function, $B(T(\tau))$, and, therefore, the variation of the internal emission source, the variation of the phase matrix can be caused by the simultaneous variations of various parameters, etc. Therefore, we can rewrite (8.114) in the most general case in the following form:

$$\mathbf{L}\boldsymbol{\delta I} = \sum_{p=1}^{P} v_p(\tau)\boldsymbol{\Psi}_p(\tau,\Omega)\,, \tag{8.115}$$

where P is full number of parameters which cause the variation of the radiation field.

Equation (8.115) provides the linear relationship between the variations of the intensity field and variations of the desired optical and surface parameters. Thereby, this equation can be treated as the generalized form of the linearized direct VRTE with respect to the variations of a given parameter. In the following subsection we apply this linearized VRTE to the derivation of the weighting function.

8.7.2 Adjoint approach and the weighting function

As pointed out in section 8.3, the variation of the measured functional $\delta\Phi$ can be expressed in the form

$$\delta\Phi(\varpi_v) = (\boldsymbol{R}, \delta\boldsymbol{I})\,, \tag{8.116}$$

where $\boldsymbol{R}(\varpi_v;\varpi)$ is the ideal instrument response function. Equation (8.116) provides the linear relationship between the variation of the measured functional and the variation of the intensity vector. Taking into account that we have already established the linear relationship between $\delta\boldsymbol{I}$ and the variation of the certain parameter, $v_p(\tau)$, as given by (8.115), it must exist the direct linear connection between $\delta\Phi$ and $v_p(\tau)$ as well. To find this relationship, we employ the adjoint approach to the functional (8.116) as discussed in section 8.6.

Let us assume that the function $\boldsymbol{I}^*(\tau,\Omega)$ is the solution of the following adjoint VRTE:

$$\mathbf{L}^*\boldsymbol{I}^* = \boldsymbol{R}\,, \tag{8.117}$$

where $\mathbf{L}^*$ is the adjoint radiative transfer operator and $\boldsymbol{R}$ is the ideal instrument response function as given by (8.74) and (8.18), respectively. Applying the adjoint approach, we obtain in a way analogous to (8.82):

$$\delta\Phi(\varpi_v) = (\boldsymbol{R}, \delta\boldsymbol{I}) = \left(\boldsymbol{I}^*, \sum_{p=1}^{P} v_p(\tau)\boldsymbol{\Psi}_p(\tau,\Omega) \right) . \tag{8.118}$$

Thus, we have expressed the functional $(\boldsymbol{R}, \delta\boldsymbol{I})$ as a scalar product of the adjoint intensity, $\boldsymbol{I}^*$, and the right-hand side of the linearized VRTE as given by (8.115).

Introducing the short notation for the integral of two vector functions $\boldsymbol{f}(\tau,\Omega)$ and $\boldsymbol{g}(\tau,\Omega)$ over Ω as follows:

$$\int\limits_{4\pi} \boldsymbol{f}^T(\tau,\Omega)\boldsymbol{g}(\tau,\Omega)\mathrm{d}\Omega \equiv \langle \boldsymbol{f}^T\boldsymbol{g} \rangle , \tag{8.119}$$

the variation of the measured functional $\delta\Phi$ caused by the variation of a certain parameter $p(\tau)$ can be written as:

$$\delta\Phi(\varpi_v) = \int\limits_0^{\tau_0} \left\langle \boldsymbol{\Psi}_p^T \boldsymbol{I}^* \right\rangle v_p(\tau)\mathrm{d}\tau , \tag{8.120}$$

Comparing (8.120) and (8.29) we see that the weighting function for a given optical parameter which is a function of the optical depth can be expressed as

$$\mathcal{V}_p(\tau,\varpi_v) = \left\langle \boldsymbol{\Psi}_p^T \boldsymbol{I}^* \right\rangle \equiv \int\limits_{4\pi} \boldsymbol{\Psi}_p^T(\tau,\Omega)\boldsymbol{I}^*(\tau,\Omega)\mathrm{d}\Omega , \tag{8.121}$$

and as

$$\mathcal{V}_p(\varpi_v) = \int\limits_0^{\tau_0} \left\langle \boldsymbol{\Psi}_p^T \boldsymbol{I}^* \right\rangle \mathrm{d}\tau \equiv \int\limits_0^{\tau_0} \int\limits_{4\pi} \boldsymbol{\Psi}_p^T(\tau,\Omega)\boldsymbol{I}^*(\tau,\Omega)\mathrm{d}\Omega\mathrm{d}\tau , \tag{8.122}$$

in the case of scalar parameters such as the surface emissivity and the surface albedo.

The dependence of the right-hand side of these equations on the variable ϖ_v is due to $\boldsymbol{I}^*$ which is the solution of the adjoint VRTE (8.117) with the right-hand side as $\boldsymbol{R}(\varpi_v;\varpi) = \delta(\tau-\tau_v)\delta(\mu-\mu_v)\delta(\phi-\phi_v)\boldsymbol{E}_i$. Thus, the adjoint intensity vector, $\boldsymbol{I}^*$, is a function of the variables $\varpi = \{\tau,\mu,\phi\}$ and $\varpi_v = \{\tau_v,\mu_v,\phi_v\}$, i.e., $\boldsymbol{I}^*(\varpi,\varpi_v)$. However, for the simplicity reason we will drop the argument ϖ_v in the adjoint intensity vector in the following discussion.

8.8 Weighting functions for main optical and surface parameters

Equation (8.121) represents the general expression for the weighting function for a given optical parameter $p(\tau)$. In this section we derive expressions for the weighting functions of extinction, absorption and scattering coefficients, single-scattering albedo, phase matrix, surface albedo and surface emissivity. We note

that for the derivation of the weighting function we have used the ideal instrument response function. Thereby, as pointed out in section 8.3 the weighting function coincides with the variational derivative for optical parameters and with the partial derivative for the surface parameters.

Extinction coefficient weighting function

To find the weighting function for the extinction coefficient ($p(\tau) \equiv \sigma_e(\tau)$) we only need to replace function $\mathbf{\Psi}_p(\tau, \Omega)$ in (8.121) by $\mathbf{\Psi}_e(\tau, \Omega)$ as given by (8.109). The extinction coefficient weighting function can be written then as follows:

$$\mathcal{V}_e(\tau, \varpi_v) = \left\langle [\boldsymbol{J} + \boldsymbol{Q} - \boldsymbol{I}]^T \boldsymbol{I}^* \right\rangle \ . \tag{8.123}$$

Single scattering albedo weighting function

Substituting now $\mathbf{\Psi}_\omega(\tau, \Omega)$ given by (8.110) into general equation (8.121) we obtain the expression for the single-scattering albedo weighting function as follows:

$$\mathcal{V}_\omega(\tau, \varpi_v) = \left\langle [\boldsymbol{J} - \omega(\tau) B(\tau) \boldsymbol{E}_1]^T \boldsymbol{I}^* \right\rangle \ . \tag{8.124}$$

Absorption and scattering coefficients weighting functions

The above expressions derived for the extinction coefficient and single-scattering albedo weighting functions allow us to find weighting functions for the scattering and absorption coefficients as well. Indeed, assuming that both extinction coefficient and single-scattering albedo are changed simultaneously we can write

$$\delta\phi(\varpi_v, \tau) = \mathcal{V}_e(\tau, \varpi_v) v_e(\tau) + \mathcal{V}_\omega(\tau, \varpi_v) v_\omega(\tau) \ , \tag{8.125}$$

where $\delta\phi(\varpi_v, \tau)\mathrm{d}\tau$ can be treated as the differential contribution of the extinction coefficient and single-scattering albedo variations in an infinitesimal layer positioned at the optical depth τ, into the variation of the measured functional, $\delta\Phi(\varpi_v)$, i.e.,

$$\delta\Phi(\varpi_v) = \int_0^{\tau_0} \delta\phi(\varpi_v, \tau)\mathrm{d}\tau \ . \tag{8.126}$$

The relative variation $v_e(\tau)$ and $v_\omega(\tau)$ can be caused by variations of the absorption and/or scattering coefficients, namely

$$v_e(\tau) \ = \ v_s(\tau)\omega(\tau) + v_a(\tau)[1 - \omega(\tau)] \ , \tag{8.127}$$

$$v_\omega(\tau) \ = \ [v_s(\tau) - v_a(\tau)][1 - \omega(\tau)] \ , \tag{8.128}$$

where the relative variations of the scattering, $\sigma_s(\tau)$, and absorption, $\sigma_a(\tau)$, coefficients are given by $v_s(\tau) = \delta\sigma_s(\tau)/\sigma_s(\tau)$ and $v_a(\tau) = \delta\sigma_a(\tau)/\sigma_a(\tau)$, respectively. Substituting $v_e(\tau)$ and $v_\omega(\tau)$ according to (8.127) and (8.128) into (8.125) and introducing functions $\mathcal{V}_a$ and $\mathcal{V}_s$ as follows:

$$\mathcal{V}_a(\tau,\varpi_v) = \big[\mathcal{V}_e(\tau,\varpi_v) - \mathcal{V}_\omega(\tau,\varpi_v)\big]\big[1-\omega(\tau)\big] , \tag{8.129}$$

$$\mathcal{V}_s(\tau,\varpi_v) = \mathcal{V}_e(\tau,\varpi_v)\omega(\tau) + \mathcal{V}_\omega(\tau,\varpi_v)[1-\omega(\tau)] , \tag{8.130}$$

we have

$$\delta\phi(\varpi_v,\tau) = \mathcal{V}_a(\tau,\varpi_v)v_a(\tau) + \mathcal{V}_s(\tau,\varpi_v)v_s(\tau) . \tag{8.131}$$

Thus, functions $\mathcal{V}_a(\tau,\varpi_v)$ and $\mathcal{V}_s(\tau,\varpi_v)$ defined by (8.129) and (8.130) are the weighting functions for the absorption and scattering coefficients, respectively. Substituting now $\mathcal{V}_e$ and $\mathcal{V}_\omega$ given by (8.123) and (8.124), into (8.129) and (8.130), we obtain the final expressions for the absorption and scattering coefficients weighting functions as follows:

$$\mathcal{V}_a(\tau,\varpi_v) = \big\langle [B(\tau)\boldsymbol{E}_1 - \boldsymbol{I}]^T \boldsymbol{I}^* \big\rangle \big(1-\omega(\tau)\big) , \tag{8.132}$$

$$\mathcal{V}_s(\tau,\varpi_v) = \big\langle [\boldsymbol{J} - \omega(\tau)\boldsymbol{I}]^T \boldsymbol{I}^* \big\rangle . \tag{8.133}$$

The derived expression for the absorption coefficient weighting function, $\mathcal{V}_a(\tau,\varpi_v)$, can be further used to find, for example, the weighting function with respect to the variation of the number density, $n(\tau)$, of an arbitrary atmospheric trace gas which has the absorption band in the selected spectral range. Assuming that the variation of the absorption coefficient is caused by the variation of the absorbing gas number density we have

$$v_a(\tau) = \frac{\delta\sigma_a(\tau)}{\sigma_a(\tau)} = \frac{\sigma(\tau)\delta n(\tau)}{\sigma_a(\tau)} = v_n(\tau) , \tag{8.134}$$

where $\sigma(\tau)$ is the absorption cross-section of the trace gas, $v_n(\tau)$ is the relative variation of the number density, $\delta n(\tau)/n(\tau)$, and we have used that $\sigma_a(\tau) = \sigma(\tau)n(\tau)$. Thus, the weighting function for the relative variation of the number density of the absorbing gas is the same as that for the relative variation of the absorption coefficient.

Surface albedo weighting function

To derive the surface albedo weighting function we start from the variation of the measured functional $\delta\Phi$ caused by the variation of the surface albedo. Equation (8.120) can be written in the following form:

$$\delta\Phi(\varpi_v) = v_A \int_0^{\tau_0} \big\langle \boldsymbol{\Psi}_A^T \boldsymbol{I}^* \big\rangle \mathrm{d}\tau , \tag{8.135}$$

where we have used $v_p(\tau) = v_A = \delta A/A$. Introducing vector function $\boldsymbol{F}(\Omega)$ as follows:

$$\boldsymbol{F}(\Omega) = \int_{\Omega_+} \mathbf{M}(\Omega,\Omega')\boldsymbol{I}(\tau_0,\Omega')\mu'\mathrm{d}\Omega' \tag{8.136}$$

and substituting it into (8.112), we rewrite the function $\boldsymbol{\Psi}_A$ in the following form:

$$\boldsymbol{\Psi}_A(\tau,\Omega) = \psi_b(\tau,-\mu)\frac{A}{\pi}\boldsymbol{F}(\Omega)\ . \tag{8.137}$$

Substituting $\boldsymbol{\Psi}_A$ given by (8.137) into (8.135) and taking into account that the function $\psi_b(\tau,-\mu) = -\delta(\tau-\tau_0)\mu\Theta(-\mu)$ as given by (8.56), we have

$$\delta\Phi(\varpi_v) = -v_A\frac{A}{\pi}\int\limits_{4\pi}\mu\Theta(-\mu)\boldsymbol{F}^T(\Omega)\boldsymbol{I}^*(\tau_0,\Omega)\mathrm{d}\Omega\ . \tag{8.138}$$

Using (8.138), we can state that the surface albedo weighting function is

$$\mathcal{V}_A(\varpi_v) = -\frac{A}{\pi}\int\limits_{\Omega_-}\boldsymbol{F}^T(\Omega)\boldsymbol{I}^*(\tau_0,\Omega)\mu\mathrm{d}\Omega\ . \tag{8.139}$$

We note that $\mathcal{V}_A(\varpi_v)$ is written for the relative variation of the albedo, i.e., $\delta A/A$. Therefore, it is proportional to the surface albedo, A.

Surface emissivity weighting function

We obtain surface emissivity weighting function writing (8.120) for the variation of the surface emissivity, namely

$$\delta\Phi(\varpi_v) = v_\epsilon\int\limits_0^{\tau_0}\left\langle\boldsymbol{\Psi}_\epsilon^T,\boldsymbol{I}^*\right\rangle\mathrm{d}\tau\ , \tag{8.140}$$

where v_ϵ is the relative variation of the surface emissivity, i.e., $v_\epsilon = \delta\epsilon/\epsilon$. Substituting $\boldsymbol{\Psi}_{\boldsymbol{\epsilon}}$ as given by (8.111) in this equation, we have an expression for the variation of the measured functional $\delta\Phi$ caused by the variation of the surface emissivity as follows:

$$\delta\Phi(\varpi_v) = -v_\epsilon\epsilon B(T_s)\int\limits_{4\pi}\mu\Theta(-\mu)\mathbf{E}_1^T\boldsymbol{I}^*(\tau_0,\Omega)\mathrm{d}\Omega\ , \tag{8.141}$$

where the function $\psi_b(\tau,-\mu)$ is used as given by (8.56). Equation (8.141) allows us to formulate the emissivity weighting function in the form of

$$\mathcal{V}_\epsilon(\varpi_v) = -\epsilon B(T_s)\int\limits_{\Omega_-}\boldsymbol{E}_1^T\boldsymbol{I}^*(\tau_0,\Omega)\mu\mathrm{d}\Omega\ . \tag{8.142}$$

Taking into account the fact that the thermal radiance is not polarized and, hence, only the first component of the vector $\boldsymbol{E}_1$ is nonzero, we define the upward adjoint flux, F^*, at the bottom of the medium under consideration analogically to the flux of the forward intensity, namely

$$F^* = -\int\limits_{\Omega_-}I^*(\tau_0,\Omega)\mu\mathrm{d}\Omega\ , \tag{8.143}$$

where $I^*(\tau_0, \Omega)$ is the first component of the vector $\boldsymbol{I}^*(\tau_0, \Omega)$. Using the definition (8.143), we obtain the emissivity weighting function as follows:

$$\mathcal{V}_\epsilon(\varpi_v) = \epsilon B(T_s) F^* \, . \tag{8.144}$$

Expression (8.144) is valid for the emissivity weighting function under the assumption that $\delta\epsilon$ and δA are independent. Following [30], let us assume that $A = 1 - \epsilon$. We have in this case $\delta A = -\delta\epsilon$ and the emissivity weighting function is

$$\mathcal{V}_\epsilon(\varpi_v) = \epsilon B(T_s) F^* + \frac{\epsilon}{\pi} \int\limits_{\Omega_-} \boldsymbol{F}^T(\Omega) \boldsymbol{I}^*(\tau_0, \Omega) \mu \mathrm{d}\Omega \, . \tag{8.145}$$

Simularly to the albedo weighting function $\mathcal{V}_\epsilon(\varpi_v)$ is written for the relative variation of the surface emissivity and, therefore, is proportional to ϵ.

Phase matrix weighting function

The general expression for the phase matrix weighting function can be derived substituting $\boldsymbol{\Psi}_m(\tau, \Omega)$ given by (8.113) into (8.121):

$$\begin{aligned} \mathcal{V}_m(\tau, \varpi_v) \; &= \; \left\langle \boldsymbol{\Psi}_m^T \boldsymbol{I}^* \right\rangle = m(\tau) \frac{\omega(\tau)}{4\pi} \times \\ &\times \int\limits_{4\pi} \int\limits_{4\pi} \boldsymbol{I}^{*T}(\tau, \Omega) \frac{\partial}{\partial m} \mathbf{Z}(\tau, \Omega, \Omega') \boldsymbol{I}(\tau, \Omega') \mathrm{d}\Omega' \mathrm{d}\Omega \, . \end{aligned} \tag{8.146}$$

Thus, for example, in the case of the spherical polydisperse particles either the effective radius and effective variance of the corresponding size distribution function or a real and imaginary part of the refractive index can be used as parameter $m(\tau)$. If a certain parameter is chosen we need to calculate the matrix of derivatives, $\partial \mathbf{Z}(\tau, \Omega, \Omega')/\partial m$, with respect to a given parameter to use derived expression for the weighting function calculation.

8.9 Other representations for weighting functions

Expressions for the weighting functions derived in section 8.7 can be used for the numerical calculations if solutions of the forward and the adjoint VRTEs are found. However, the appropriate radiative transfer equations should be solved in this case for the total forward and total adjoint intensity vector, respectively. Both the forward and the adjoint VRTEs written for the total intensity include Dirac δ functions as follows from (8.33) and (8.117). In the first case, it is the upper boundary condition (8.38) and, in the second case, it is the right-hand side of (8.117), i.e., the adjoint source function. As is well known, solutions of such equations contain the generalized functions as well. The standard approach to eliminating the generalized function in the solution of the radiative transfer

equation is to separate the total intensity in the direct and the diffuse component and to formulate the radiative transfer equation for the diffuse component only [6]. Such a separation is a standard procedure in radiative transfer theory. However, as we show in this section, the expression for the weighting function should be rewritten appropriately if we intend to use the diffuse intensity instead of total one.

Clearly, the radiative transfer equation can be solved for the total component of the intensity as well and then directly used for the WF calculation. Such an approach has been employed, for example, in [20, 25]. However, in this case the special technique should be used to handle the singularity contained in the direct component of the forward and adjoint intensities. Thus, in [25] the solution for the total adjoint intensity has been derived in the framework of the finite difference method employing the dummy nod technique (see [7] for details). In [20] the solution for the total forward and adjoint intensities has been derived in the framework of the spherical harmonic method employing the formal solution (or source function integration) technique to avoid singularity.

In the following subsections it will be demonstrated that desired expressions for the weighting functions containing the diffuse forward and diffuse adjoint intensities can be easily found substituting the total intensities as a sum of the diffuse and direct components. Taking into account that the expression for the direct component of the forward intensity is well known, we derive at first the analytical expression for the direct component of the adjoint intensity.

8.9.1 Separation of the total adjoint intensity in the diffuse and direct components

In this subsection the analytical expressions for the direct component of the adjoint intensity vector will be found and the VRTE for the diffuse component of the adjoint intensity will be formulated. To do this we rewrite the generalized form of the adjoint VRTE given by (8.117) in the operator representation (see section 8.6) as follows:

$$\mathbf{L}_e^* \boldsymbol{I}_-^* = \delta(\tau - \tau_v)\delta(\mu + \mu_v)\delta(\phi - \phi_v)\boldsymbol{E}_i \,, \tag{8.147}$$

$$\mathbf{L}_t^* \boldsymbol{I}_-^* = \mathbf{0} \,, \mu < 0 \,, \tag{8.148}$$

$$\mathbf{L}_b^* \boldsymbol{I}_-^* = \mathbf{0} \,, \mu > 0 \,, \tag{8.149}$$

where $\mathbf{L}_t^*$, $\mathbf{L}_b^*$ and $\mathbf{L}_e^*$ are defined according to (8.71), (8.72) and (8.75), respectively, and the measured functional, Φ, is the ith component of intensity vector in the viewing direction $\Omega_-^v = (-\mu_v, \phi_v)$. The inhomogeneous adjoint source function like the right-hand side of (8.147) will be called following Qin *et al.* [23] as a parallel surface source (PSS). It means that the source illuminates at a given vertical position in a given direction and extends infinitely in horizontal directions. For reasons of simplicity we define the adjoint intensity by $\boldsymbol{I}_-^* \equiv \boldsymbol{I}^*(\tau, \Omega; \tau_v, \Omega_-^v)$ in the case of an upward PSS (source illuminates towards the upper boundary) and by $\boldsymbol{I}_+^* \equiv \boldsymbol{I}^*(\tau, \Omega; \tau_v, \Omega_+^v)$ in the case of a downward PSS (source illuminates towards the lower boundary).

Applying the same approach as is usually used for the separation of the total forward intensity, the total adjoint intensity vector, $\boldsymbol{I}^*_-$, is represented by the following sum:

$$\boldsymbol{I}^*_-(\tau,\Omega) = \boldsymbol{I}^*_{d-}(\tau,\Omega) + \boldsymbol{D}^*_-(\tau,\Omega)\ , \tag{8.150}$$

where $\boldsymbol{I}^*_{d-}(\tau,\Omega)$ and $\boldsymbol{D}^*_-(\tau,\Omega)$ are the diffuse and the direct component of the adjoint intensity, respectively, and $\boldsymbol{D}^*_-(\tau,\Omega)$ we define as follows:

$$\boldsymbol{D}^*_-(\tau,\Omega) = d^*(\tau,\mu)\delta(\mu+\mu_v)\delta(\phi-\phi_v)\boldsymbol{E}_i\ , \tag{8.151}$$

where $d^*(\tau,\mu)$ is an arbitrary nonnegative function at this point. Substituting $\boldsymbol{I}^*_-(\tau,\Omega)$ given by (8.150) into (8.147), we obtain

$$\begin{aligned}\mathbf{L}^*_e\boldsymbol{I}^*_{d-} - \mu\frac{\mathrm{d}}{\mathrm{d}\tau}\boldsymbol{D}^*_-(\tau,\Omega) \ &+\ \boldsymbol{D}^*_-(\tau,\Omega) - d^*(\tau,-\mu_v)\frac{\omega(\tau)}{4\pi}\mathbf{Z}^T(\Omega^v_-,\Omega)\boldsymbol{E}_i \\ &=\ \delta(\tau-\tau_v)\delta(\mu+\mu_v)\delta(\phi-\phi_v)\boldsymbol{E}_i\ .\end{aligned} \tag{8.152}$$

This equation can be considered as the sum of two following equations:

$$\mathbf{L}^*_e\boldsymbol{I}^*_{d-} = d^*(\tau,-\mu_v)\frac{\omega(\tau)}{4\pi}\mathbf{Z}^T(\Omega^v_-,\Omega)\boldsymbol{E}_i\ , \tag{8.153}$$

$$-\mu\frac{\mathrm{d}\boldsymbol{D}^*_-(\tau,\Omega)}{\mathrm{d}\tau} = -\boldsymbol{D}^*_-(\tau,\Omega) + \delta(\tau-\tau_v)\delta(\mu+\mu_v)\delta(\phi-\phi_v)\boldsymbol{E}_i\ . \tag{8.154}$$

The upper boundary conditions for the diffuse and direct adjoint components follow from the upper boundary condition for the total adjoint intensity as given by (8.148). Substituting $\boldsymbol{I}^*_-$ according to (8.150) into (8.148) and using $\mathbf{L}^*_t$ as given by (8.71) we obtain

$$\boldsymbol{I}^*_-(0,\Omega) = \boldsymbol{I}^*_{d-}(0,\Omega) + \boldsymbol{D}^*_-(0,\Omega) = 0\ ,\mu<0\ . \tag{8.155}$$

Taking into account that both function $\boldsymbol{I}^*_{d-}(0,\Omega)$ and $\boldsymbol{D}^*_-(0,\Omega)$ are nonnegative, equation (8.155) results in

$$\boldsymbol{I}^*_{d-}(0,\Omega) = 0\ ,\mu<0\ , \tag{8.156}$$

$$\boldsymbol{D}^*_-(0,\Omega) = 0\ ,\mu<0\ . \tag{8.157}$$

We note that in contrast to the forward intensity the boundary condition at the top of the medium for the adjoint intensity is given for the outgoing radiation.

In the considered case of the upward PSS the downward direct adjoint component does not exist. Thereby, the lower boundary condition should be formulated for the diffuse adjoint component only. Substituting the total adjoint intensity $\boldsymbol{I}^*_-$ as given (8.150) into (8.149) and taking into account that the operator $\mathbf{L}^*_b$ is given by (8.72), we obtain the lower boundary condition for the diffuse adjoint component as follows:

$$\mathbf{L}^*_b I^*_{d-} = \frac{A}{\pi}\mu_v d(\tau_0,-\mu_v)\mathbf{M}^T(\Omega^v_-,\Omega)\boldsymbol{E}_i\ . \tag{8.158}$$

Equation (8.154) contains only $\boldsymbol{D}^*_-(\tau,\Omega)$ as unknown function and can be solved analytically. Indeed, substituting in this equation $\boldsymbol{D}^*_-(\tau,\Omega)$ as given by (8.151), we obtain the first-order ordinary inhomogeneous differential equation for the function $d^*(\tau,-\mu_v)$:

$$\mu_v \frac{\mathrm{d}}{\mathrm{d}\tau} d^*(\tau,-\mu_v) = -d^*(\tau,-\mu_v) + \delta(\tau-\tau_v)\ , \tag{8.159}$$

$$d^*(0,-\mu_v) = 0\ , \tag{8.160}$$

where we have used the following property of the Dirac δ function [13]:

$$\delta(\mu+\mu_v)f(\mu) = \delta(\mu+\mu_v)f(-\mu_v)\ . \tag{8.161}$$

It is easily proved that the function $d^*(\tau,-\mu_v)$ defined as

$$d^*(\tau,-\mu_v) = \frac{1}{\mu_v}\Theta(\tau-\tau_v)\mathrm{e}^{-(\tau-\tau_v)/\mu_v} \tag{8.162}$$

is the solution of (8.159). Indeed, substituting (8.162) into (8.159) and using the two following properties of the Dirac δ function [13], namely,

$$\delta(\tau-\tau_v) = \frac{\mathrm{d}}{\mathrm{d}\tau}\Theta(\tau-\tau_v)\ , \tag{8.163}$$

$$\delta(\tau-\tau_v)f(\tau) = \delta(\tau-\tau_v)f(\tau_v)\ , \tag{8.164}$$

we state that the function $d^*(\tau,-\mu_v)$ given by (8.162) satisfies (8.159) and the boundary condition given by (8.160).

Having defined $d^*(\tau,-\mu_v)$, we obtain the following expression for the direct component of the adjoint intensity in the case of an upward PSS:

$$\boldsymbol{D}^*_-(\tau,\Omega) = \frac{1}{\mu_v}\Theta(\tau-\tau_v)\delta(\mu+\mu_v)\delta(\phi-\phi_v)\mathrm{e}^{-(\tau-\tau_v)/\mu_v}\boldsymbol{E}_i\ . \tag{8.165}$$

Substituting now $d^*(\tau,-\mu_v)$ as given by (8.162) into (8.153) and (8.158), introducing the inhomogeneous adjoint source function $\boldsymbol{W}_{e-}$ as

$$\boldsymbol{W}_{e-}(\tau,\Omega) = \frac{\omega(\tau)}{4\pi\mu_v}\Theta(\tau-\tau_v)e^{-(\tau-\tau_v)/\mu_v}\mathbf{Z}^T(\Omega^v_-,\Omega)\boldsymbol{E}_i \tag{8.166}$$

and defining the right-hand side of the lower boundary condition for the diffuse adjoint component given by (8.158) as

$$\boldsymbol{W}_{b-}(\Omega) = \frac{A}{\pi}e^{-(\tau_0-\tau_v)/\mu_v}\mathbf{M}^T(\Omega^v_-,\Omega)\boldsymbol{E}_i\ , \tag{8.167}$$

we obtain the following radiative transfer equation for the diffuse adjoint component in the operator form:

$$\mathbf{L}^*_e\boldsymbol{I}^*_{d-} = \boldsymbol{W}_{e-}(\tau,\Omega)\ , \tag{8.168}$$

$$\mathbf{L}^*_t I^*_{d-} = \mathbf{0}\ ,\mu<0\ , \tag{8.169}$$

$$\mathbf{L}^*_b I^*_{d-} = \boldsymbol{W}_{b-}(\Omega)\ ,\mu>0\ \ , \tag{8.170}$$

and in the generalized form:

$$\mathbf{L}^* \boldsymbol{I}^*_{d-} = \boldsymbol{W}_{e-}(\tau, \Omega) + \psi_b(\tau, \mu)\boldsymbol{W}_{b-}(\Omega) \,, \tag{8.171}$$

where $\psi_b(\tau, \mu)$ is given by (8.56).

Equations (8.168)–(8.170) describe the VRTE for the diffuse adjoint intensity vector in the case of an upward PSS. Using the approach described above, the expression for the direct adjoint component in the case of measurements in the viewing direction $\Omega^v_+ \equiv (\mu_v, \phi_v)$ (downward PSS) can be easily found as well. Indeed, substituting $\delta(\mu - \mu_v)$ in (8.147) instead of $\delta(\mu + \mu_v)$, we obtain the following expression for the direct adjoint intensity in the case of the downward PSS:

$$\boldsymbol{D}^*_+(\tau, \Omega) = d^*(\tau, \mu_v)\delta(\mu - \mu_v)\delta(\phi - \phi_v)\boldsymbol{E}_i \,, \tag{8.172}$$

where

$$d^*(\tau, \mu_v) = \frac{1}{\mu_v}\Theta(\tau_v - \tau)\mathrm{e}^{-(\tau_v - \tau)/\mu_v} \,, \tag{8.173}$$

and the diffuse adjoint component, I^*_{d+}, is the solution of the following boundary value problem:

$$\mathbf{L}^*_e \boldsymbol{I}^*_{d+} = \boldsymbol{W}_{e+}(\tau, \Omega) \,, \tag{8.174}$$

$$\mathbf{L}^*_t I^*_{d+} = \mathbf{0} \,, \mu < 0 \,, \tag{8.175}$$

$$\mathbf{L}^*_b I^*_{d+} = \mathbf{0} \,, \mu > 0 \,, \tag{8.176}$$

with the adjoint source function defined as

$$\boldsymbol{W}_{e+}(\tau, \Omega) = \frac{\omega(\tau)}{4\pi\mu_v}\Theta(\tau_v - \tau)e^{-(\tau_v - \tau)/\mu_v}\mathbf{Z}^T(\Omega^v_+, \Omega)\boldsymbol{E}_i \,. \tag{8.177}$$

8.9.2 Representation of weighting functions for the total forward and diffuse adjoint intensity (TD representation)

Let us assume that for the calculation of the weighting functions we use now the diffuse adjoint intensity, $\boldsymbol{I}^*_d$, instead of total, $\boldsymbol{I}^*$, one. We will refer further to this representation as the total-diffuse (TD) one.

To obtain the expression for the weighting function in the TD representation we need only to substitute the total adjoint intensity, $I^*_\pm(\tau, \Omega)$, as a sum of the direct and diffuse components into the expression for the WF in TT representation as given by (8.121). It follows then that

$$\mathcal{V}_p(\tau, \varpi_v) = \int\limits_{4\pi} \boldsymbol{\Psi}^T_p(\tau, \Omega)\left[\boldsymbol{I}^*_{d\pm}(\tau, \Omega) + D^*_\pm(\tau, \Omega)\right] \mathrm{d}\Omega \,, \tag{8.178}$$

where $\boldsymbol{I}^*_{d-}$ and $\boldsymbol{I}^*_{d+}$ are solutions of the adjoint VRTE as given by (8.168)–(8.170) and (8.174)–(8.176), respectively. Substituting the direct adjoint compo-

nent given by (8.165) or by (8.172) into this equation, we obtain

$$\mathcal{V}_p(\tau,\varpi_v) = \int\limits_{4\pi} \boldsymbol{\Psi}_p^T(\tau,\Omega)\boldsymbol{I}_{d\pm}^*(\tau,\Omega)\mathrm{d}\Omega + d^*(\tau,\pm\mu_v)\boldsymbol{\Psi}_p^T(\tau,\Omega_\pm^v)\boldsymbol{E}_i \ . \tag{8.179}$$

The final general expression for the weighting function in the TD representation is obtained using the short notation for the integral over Ω as given by (8.119):

$$\mathcal{V}_p(\tau,\varpi_v) = \left\langle \boldsymbol{\Psi}_p^T\boldsymbol{I}_{d\pm}^*\right\rangle + d^*(\tau,\pm\mu_v)\boldsymbol{\Psi}_p^T(\tau,\Omega_\pm^v)\boldsymbol{E}_i \ . \tag{8.180}$$

We note that variables with the subscript '$\pm$' should be used for the weighting function calculations in the case of the transmitted and the reflected radiation, respectively.

Thus, applying (8.180), for example, to the extinction coefficient and the single-scattering albedo WF we obtain following expressions:

$$\begin{aligned}
\mathcal{V}_e(\tau,\varpi_v) &= \left\langle [\boldsymbol{J}+\boldsymbol{Q}-\boldsymbol{I}]^T\boldsymbol{I}_{d\pm}^*\right\rangle \\
&+ d^*(\tau,\pm\mu_v)[\boldsymbol{J}(\tau,\Omega_\pm^v)+\boldsymbol{Q}(\tau)-\boldsymbol{I}(\tau,\Omega_\pm^v)]^T\boldsymbol{E}_i \ , \qquad (8.181)\\
\mathcal{V}_\omega(\tau,\varpi_v) &= \left\langle [\boldsymbol{J}-\omega(\tau)B(\tau)\boldsymbol{E}_1]^T\boldsymbol{I}_{d\pm}^*\right\rangle \\
&+ d^*(\tau,\pm\mu_v)[\boldsymbol{J}(\tau,\Omega_\pm^v)-\omega(\tau)B(\tau)\boldsymbol{E}_1]^T\boldsymbol{E}_i \ . \qquad (8.182)
\end{aligned}$$

As can be seen, if for the calculation of the weighting function the diffuse adjoint intensity is used, the coresponding expressions such as (8.181) and (8.182) include additional terms which should be calculated for the viewing directions $\Omega_\pm^v$ only.

8.9.3 Representation of weighting functions for the diffuse forward and diffuse adjoint intensity (DT and DD representation)

In the spectral region where direct solar radiance cannot be neglected and the direct VRTE contains a δ function in the upper boundary condition, it is reasonable to use for the WF calculation the diffuse forward intensity instead of the total one. It is well known that in this case the total forward intensity can be represented as follows [6]:

$$\boldsymbol{I}(\tau,\Omega) = \boldsymbol{I}_d(\tau,\Omega) + \boldsymbol{D}(\tau,\Omega) \ , \tag{8.183}$$

where $\boldsymbol{I}_d(\tau,\Omega)$ and $\boldsymbol{D}(\tau,\Omega)$ are the diffuse and direct components of the total forward intensity. For the direct component we have

$$\boldsymbol{D}(\tau,\Omega) = \pi\delta(\mu-\mu_0)\delta(\phi-\phi_0)\boldsymbol{E}_1\mathrm{e}^{-\tau/\mu} \ . \tag{8.184}$$

Substituting (8.183) into direct VRTE for the total forward intensity vector as given by (8.33), we obtain the following VRTE for the diffuse component:

$$\mu\frac{\mathrm{d}\boldsymbol{I}_d(\tau,\Omega)}{\mathrm{d}\tau} = -\boldsymbol{I}_d(\tau,\Omega) + \boldsymbol{J}_m(\tau,\Omega) + \boldsymbol{Q}(\tau) + \boldsymbol{J}_s(\tau,\Omega) \ , \tag{8.185}$$

where the multiple scattering, $\boldsymbol{J}_m$, and single-scattering, $\boldsymbol{J}_s$, source functions are defined as follows:

$$\boldsymbol{J}_m(\tau,\Omega) = \frac{\omega(\tau)}{4\pi}\int\limits_{4\pi}\mathbf{Z}(\tau,\Omega,\Omega')\boldsymbol{I}_d(\tau,\Omega')\mathrm{d}\Omega' , \tag{8.186}$$

$$\boldsymbol{J}_s(\tau,\Omega) = \frac{\omega(\tau)}{4}\mathrm{e}^{-\tau/\mu_0}\mathbf{Z}(\tau,\Omega,\Omega_0)\boldsymbol{E}_1 , \tag{8.187}$$

and $\Omega_0 \equiv (\mu_0,\phi_0)$. The boundary conditions for the diffuse component of the forward intensity are:

$$\boldsymbol{I}_d(0,\Omega) = \mathbf{0}\,,\mu>0\,, \tag{8.188}$$

$$\begin{aligned}\boldsymbol{I}_d(\tau_0,\Omega) &= \frac{A}{\pi}\int\limits_{\Omega_+}\mathbf{M}(\Omega,\Omega')\boldsymbol{I}_d(\tau_0,\Omega')\mu'\mathrm{d}\Omega' \\ &+ \epsilon B(T_s)\boldsymbol{E}_1 + A\mathrm{e}^{-\tau_0/\mu_0}\mu_0\mathbf{M}(\Omega,\Omega_0)\boldsymbol{E}_1\,,\mu<0\,.\end{aligned} \tag{8.189}$$

The direct VRTE for the diffuse intensity as given by (8.185) does not contain generalized functions and is usually used in numerical calculations [16].

Let us rewrite now the expression for the WF given by (8.180), substituting the total forward intensity as a sum of the diffuse and direct component. This representation we will refer to as the diffuse-diffuse (DD) representation. To obtain the appropriate expression for the weighting functions in the DD representation, we substitute at first (8.183) instead of the total intensity $\boldsymbol{I}$ into auxiliary functions given by (8.109)–(8.113). We obtain

$$\boldsymbol{\Psi}_e(\tau,\Omega) = \boldsymbol{\Psi}_e^d(\tau,\Omega) + \boldsymbol{J}_s(\tau,\Omega) - \pi\delta(\Omega-\Omega_0)\boldsymbol{E}_1\mathrm{e}^{-\tau/\mu} , \tag{8.190}$$

$$\boldsymbol{\Psi}_\omega(\tau,\Omega) = \boldsymbol{\Psi}_\omega^d(\tau,\Omega) + \boldsymbol{J}_s(\tau,\Omega) , \tag{8.191}$$

$$\boldsymbol{\Psi}_A(\tau,\Omega) = \boldsymbol{\Psi}_A^d(\tau,\Omega) + \psi_b(\tau,-\mu)A\mu_0\mathrm{e}^{-\tau/\mu_0}\mathbf{M}(\Omega,\Omega_0)\boldsymbol{E}_1 , \tag{8.192}$$

$$\boldsymbol{\Psi}_m(\tau,\Omega) = \boldsymbol{\Psi}_m^d(\tau,\Omega) + \frac{\omega(\tau)}{4}m(\tau)\mathrm{e}^{-\tau/\mu_0}\frac{\partial}{\partial m}\mathbf{Z}_m(\tau,\Omega,\Omega_0)\boldsymbol{E}_1 , \tag{8.193}$$

where superscript 'd' denotes that functions $\boldsymbol{\Psi}_p$ have to be calculated as given by (8.109)–(8.113) using the diffuse component of the forward intensity.

Substituting these representations for the auxiliary functions into (8.121) and (8.178), we obtain the general expression for the WF in the DT representation:

$$\mathcal{V}_p(\tau,\varpi_v) = \left\langle \boldsymbol{I}^{*T}(\boldsymbol{\Psi}_p^d + \boldsymbol{\Delta}_p)\right\rangle \tag{8.194}$$

and in the DD representation:

$$\begin{aligned}\mathcal{V}_p(\tau,\varpi_v) &= \left\langle \boldsymbol{I}_{d\pm}^{*T}(\boldsymbol{\Psi}_p^d + \boldsymbol{\Delta}_p)\right\rangle + \left\langle \boldsymbol{\Delta}_p\boldsymbol{D}_\pm^*\right\rangle \\ &+ d^*(\tau,\pm\mu_v)\boldsymbol{E}_i^T[\boldsymbol{\Psi}_p^d(\tau,\Omega_\pm^v) + \boldsymbol{\Delta}_p(\tau,\Omega_\pm^v,\Omega_0)] ,\end{aligned} \tag{8.195}$$

where $d^*(\tau,\pm\mu_v)$ are given by (8.162) and (8.173), respectively, and functions $\boldsymbol{\Delta}_p(\tau,\Omega,\Omega_0)$ are defined according to (8.190)–(8.193) as follows:

$$\boldsymbol{\Delta}_e(\tau,\Omega) = \boldsymbol{J}_s(\tau,\Omega) - \pi\delta(\Omega-\Omega_0)\boldsymbol{E}_1 \mathrm{e}^{-\tau/\mu} , \quad (8.196)$$

$$\boldsymbol{\Delta}_\omega(\tau,\Omega) = \boldsymbol{J}_s(\tau,\Omega) , \quad (8.197)$$

$$\boldsymbol{\Delta}_A(\tau,\Omega) = \psi_b(\tau,-\mu)A\mu_0\mathrm{e}^{-\tau/\mu_0}\mathbf{M}(\Omega,\Omega_0)\boldsymbol{E}_1 , \quad (8.198)$$

$$\boldsymbol{\Delta}_m(\tau,\Omega) = \frac{\omega(\tau)}{4}m(\tau)\mathrm{e}^{-\tau/\mu_0}\frac{\partial}{\partial m}\mathbf{Z}_m(\tau,\Omega,\Omega_0)\boldsymbol{E}_1 . \quad (8.199)$$

Thus, substituting $\boldsymbol{\Psi}_e(\tau,\Omega)$ given by (8.190) into (8.181), we obtain for the extinction coefficient WF the following expression:

$$\begin{aligned}\mathcal{V}_e(\tau,\varpi_v) &= \left\langle[\boldsymbol{Q}+\boldsymbol{J}_{ms}-\boldsymbol{I}_d]^T\boldsymbol{I}^*_{d\pm}\right\rangle - \pi\mathrm{e}^{-\tau/\mu_0}\boldsymbol{E}_1^T\boldsymbol{I}^*_{d\pm}(\tau,\Omega_0)\\ &+ d^*(\tau,\pm\mu_v)[\boldsymbol{Q}(\tau)+\boldsymbol{J}_{ms}(\tau,\Omega^v_\pm)-\boldsymbol{I}_d(\tau,\Omega^v_\pm)]^T\boldsymbol{E}_i\\ &- \pi\mathrm{e}^{-\tau/\mu_0}d^*(\tau,\pm\mu_v)\left\langle\delta(\Omega-\Omega_0)\delta(\Omega-\Omega^v_\pm)\right\rangle . \quad (8.200)\end{aligned}$$

We note that the last term in this equation is nonzero for the measurement of the transmitted radiance in the direction $\Omega^v_+ = \Omega_0$ only.

Substituting $\boldsymbol{\Psi}_\omega(\tau,\Omega)$ given by (8.191) into (8.182), we obtain for the single-scattering albedo WF:

$$\begin{aligned}\mathcal{V}_\omega(\tau,\varpi_v) &= [\boldsymbol{J}_{ms}-\omega(\tau)B(\tau)\boldsymbol{E}_1]^T\boldsymbol{I}^*_{d\pm}\\ &+ d^*(\tau,\pm\mu_v)[\boldsymbol{J}_{ms}(\tau,\Omega^v_\pm)-\omega(\tau)B(\tau)\boldsymbol{E}_1]^T\boldsymbol{E}_i , \quad (8.201)\end{aligned}$$

where $\boldsymbol{J}_{ms}(\Omega,\tau)$ is

$$\boldsymbol{J}_{ms}(\Omega,\tau) = \boldsymbol{J}_m(\Omega,\tau) + \boldsymbol{J}_s(\Omega,\tau) . \quad (8.202)$$

8.9.4 Using the formal solution of the direct VRTE for the weighting function derivation

We have obtained in previous sections the different expressions for the weighting functions starting from the representation of the measured functional Φ as the scalar product of the instrument response function, $\boldsymbol{R}(\varpi_v;\varpi)$, and the intensity vector, $\boldsymbol{I}(\varpi)$. However, there is an another way to derive weighting functions for optical and surface parameters, namely, starting from the formal solution of the linearized VRTE. In the scalar case it has been suggested by Ustinov [29].

To demonstrate this and find a relationship between these two approaches, we rewrite the linearized VRTE as given by (8.115) in the following form:

$$\mathbf{L}\delta\boldsymbol{I} = v_p(\tau)\boldsymbol{\Psi}_p(\tau,\Omega) , \quad (8.203)$$

assuming for simplicity that the variation of the intensity field is caused by the variation of a certain parameter $p(\tau)$. Taking into account that (8.203) is written in the generalized form, we rewrite at first this equation in the standard form (see section 8.4) as follows:

$$\mu\frac{\mathrm{d}}{\mathrm{d}\tau}\delta\boldsymbol{I}(\tau,\Omega) = -\delta\boldsymbol{I}(\tau,\Omega) + \delta\boldsymbol{J}(\tau,\Omega) + v_p(\tau)\boldsymbol{\Psi}_p(\tau,\Omega) , \quad (8.204)$$

$$\delta\boldsymbol{I}(0,\Omega) = \mathbf{0},\ \mu>0 , \quad (8.205)$$

$$\delta\boldsymbol{I}(\tau_0,\Omega) = \frac{A}{\pi}\int\limits_{\Omega_+}\mathbf{M}(\Omega,\Omega')\delta\boldsymbol{I}(\tau_0,\Omega')\mu'\mathrm{d}\Omega',\ \mu<0 , \quad (8.206)$$

where the variation of the multiple scattering source function $\delta\boldsymbol{J}$ is defined as

$$\delta\boldsymbol{J}(\tau,\Omega) \;=\; \frac{\omega(\tau)}{4\pi}\int\limits_{4\pi}\mathbf{Z}(\tau,\Omega,\Omega')\delta\boldsymbol{I}(\tau,\Omega')\mathrm{d}\Omega' \,. \tag{8.207}$$

Let us consider the reflected radiation. Then inserting $\Omega=\Omega^v_- \equiv \{-\mu_v,\phi_v\}$ into (8.204), we can derive the first-order inhomogeneous differential equation and the appropriate boundary condition for the variation of the upward radiation as follows:

$$-\mu_v\frac{\mathrm{d}}{\mathrm{d}\tau}\delta\boldsymbol{I}(\tau,\Omega^v_-) \;=\; -\delta\boldsymbol{I}(\tau,\Omega^v_-)+\delta\boldsymbol{J}(\tau,\Omega^v_-)+\upsilon_p(\tau)\boldsymbol{\Psi}_p(\tau,\Omega^v_-)\,, \tag{8.208}$$

$$\delta\boldsymbol{I}(\tau_0,\Omega^v_-) \;=\; \frac{A}{\pi}\int\limits_{\Omega_+}\mathbf{M}(\Omega^v_-,\Omega)\delta\boldsymbol{I}(\tau_0,\Omega)\mu\mathrm{d}\Omega \,. \tag{8.209}$$

The solution of such kinds of equations is well known (see [2,11] for details). In our case the formal solution of this equation at the optical depth $\tau=\tau_v$ can be written as follows:

$$\begin{aligned}\delta\boldsymbol{I}(\tau_v,\Omega^v_-) \;&=\; \frac{1}{\mu_v}\int\limits_{\tau_v}^{\tau_0}\Big[\delta\boldsymbol{J}(\tau,\Omega^v_-)+\upsilon_p(\tau)\boldsymbol{\Psi}_p(\tau,\Omega^v_-)\Big]\mathrm{e}^{-(\tau-\tau_v)/\mu_v}\mathrm{d}\tau \\ &+\; \frac{A}{\pi}\mathrm{e}^{-(\tau_0-\tau_v)/\mu_v}\int\limits_{\Omega_+}\mathbf{M}(\Omega^v_-,\Omega)\delta\boldsymbol{I}(\tau_0,\Omega)\mu\mathrm{d}\Omega \,.\end{aligned} \tag{8.210}$$

Assuming that the measured functional, Φ, is the ith component of the intensity vector at the optical depth τ_v in the direction Ω^v_- and substituting into (8.116) the ideal response function as $\boldsymbol{R}(\varpi;\varpi_v)=\delta(\tau-\tau_v)\delta(\Omega-\Omega^v_-)\boldsymbol{E}_i$, we have

$$\delta\Phi(\varpi_v)=\boldsymbol{E}_i^T\delta\boldsymbol{I}(\tau_v,\Omega^v_-)\,, \tag{8.211}$$

where the right-hand side should be treated as a scalar product in the Euclid space of dimension four.

Substituting further $\delta\boldsymbol{I}(\tau_v,\Omega^v_-)$ as given by (8.210) into (8.211) and taking into account that $\delta\boldsymbol{J}(\tau,\Omega^v_-)$ is given by (8.207), we obtain

$$\begin{aligned}\delta\Phi(\varpi_v) \;&=\; \frac{\omega(\tau)}{4\pi\mu_v}\int\limits_{\tau_v}^{\tau_0}\int\limits_{4\pi}\boldsymbol{E}_i^T\mathbf{Z}(\Omega^v_-,\Omega)\delta\boldsymbol{I}(\tau,\Omega)\mathrm{e}^{-(\tau-\tau_v)/\mu_v}\mathrm{d}\tau\mathrm{d}\Omega \\ &+\; \frac{A}{\pi}\mathrm{e}^{-(\tau_0-\tau_v)/\mu_v}\int\limits_{\Omega_+}\boldsymbol{E}_i^T\mathbf{M}(\Omega^v_-,\Omega)\delta\boldsymbol{I}(\tau_0,\Omega)\mu\mathrm{d}\Omega \\ &+\; \frac{1}{\mu_v}\int\limits_{\tau_v}^{\tau_0}\boldsymbol{E}_i^T\boldsymbol{\Psi}_p(\tau,\Omega^v_-)\mathrm{e}^{-(\tau-\tau_v)/\mu_v}\upsilon_p(\tau)\mathrm{d}\tau \,.\end{aligned} \tag{8.212}$$

In order to simplify this equation we introduce two following functions, namely, $\boldsymbol{R}_e^*(\tau,\Omega)$ and $\boldsymbol{R}_b^*(\tau,\Omega)$ as:

$$\boldsymbol{R}_e^*(\tau,\Omega) = \frac{\omega(\tau)}{4\pi\mu_v}\Theta(\tau-\tau_v)\mathrm{e}^{-(\tau-\tau_v)/\mu_v}\mathbf{Z}^T(\Omega_-^v,\Omega)\boldsymbol{E}_i \ , \tag{8.213}$$

where the function $\Theta(\tau-\tau_v)$ is introduced to extend the lower integration limit in the integral over τ in the first term of (8.212) from $\tau=\tau_v$ to $\tau=0$,

$$\boldsymbol{R}_b^*(\tau,\Omega) = \frac{A}{\pi}\mathrm{e}^{-(\tau_0-\tau_v)/\mu_v}\delta(\tau-\tau_0)\mu\Theta(\mu)\mathbf{M}^T(\Omega_-^v,\Omega)\boldsymbol{E}_i \ , \tag{8.214}$$

where the function $\Theta(\mu)$ is introduced to extend the lower integration limit in the integral over μ in the second term of (8.212) from $\mu=0$ to $\mu=-1$.

Substituting these functions into (8.212), we obtain

$$\begin{aligned}\delta\Phi(\varpi_v) &= \int_0^{\tau_0}\int_{4\pi}\Big[\boldsymbol{R}_e^{*T}(\tau,\Omega)+\boldsymbol{R}_b^{*T}(\tau,\Omega)\Big]\delta\boldsymbol{I}(\tau,\Omega)\mathrm{d}\tau\mathrm{d}\Omega \\ &+ \int_0^{\tau_0} d^*(\tau,-\mu_v)\boldsymbol{E}_i^T\boldsymbol{\Psi}_p(\tau,\Omega_-^v)v_p(\tau)\mathrm{d}\tau \ ,\end{aligned} \tag{8.215}$$

where $d^*(\tau,-\mu_v)$ is given by (8.162).

According to the definition (8.63) the first term in (8.215) is the scalar product of the functions $\boldsymbol{R}_e^*+\boldsymbol{R}_b^*$ and $\delta\boldsymbol{I}$. Thereby, we can write the variation of the measured functional, $\delta\Phi$, in the following form:

$$\delta\Phi(\varpi_v) = (\boldsymbol{R}_e^*+\boldsymbol{R}_b^*,\delta\boldsymbol{I}) + \int_0^{\tau_0} d^*(\tau,-\mu_v)\boldsymbol{E}_i^T\boldsymbol{\Psi}_p(\tau,\Omega_-^v)v_p(\tau)\mathrm{d}\tau \ , \tag{8.216}$$

where according to (8.213) and (8.214)

$$\begin{aligned}\boldsymbol{R}_e^*+\boldsymbol{R}_b^* &= \frac{\omega(\tau)}{4\pi}d^*(\tau,-\mu_v)\mathbf{Z}^T(\Omega_-^v,\Omega)\boldsymbol{E}_i \\ &+ \psi_b(\tau,\mu)\frac{A}{\pi}\mathrm{e}^{-(\tau_0-\tau_v)/\mu_v}\mathbf{M}^T(\Omega_-^v,\Omega)\boldsymbol{E}_i\end{aligned} \tag{8.217}$$

and $\psi_b(\tau,\mu)=\delta(\tau-\tau_0)\mu\Theta(\mu)$ as given by (8.56).

Comparing (8.216) and (8.116), we see that we have found using the formal solution of the radiative transfer equation yet another expression for the variation of the measured functional, $\delta\Phi(\varpi_v)$. The last term in (8.216) is linear to the variation of the given parameter $v_p(\tau)$. To evaluate the scalar product in (8.216) containing unknown variation $\delta\boldsymbol{I}$ we use the same technique as in section 8.7. Substituting $\boldsymbol{R}_e^*+\boldsymbol{R}_b^*$ instead of $\boldsymbol{R}$ into the right-hand side of the adjoint VRTE

written in the generalized form as given by (8.117), we obtain the following equation:

$$\mathbf{L}^* \boldsymbol{I}^* = \boldsymbol{R}_e^* + \boldsymbol{R}_b^* \, . \tag{8.218}$$

Then, using the adjoint approach, the scalar product $(\boldsymbol{R}_e^* + \boldsymbol{R}_b^*, \delta \boldsymbol{I})$ can be written by analogy to (8.118) as follows:

$$(\boldsymbol{R}_e^* + \boldsymbol{R}_b^*, \delta \boldsymbol{I}) = (\boldsymbol{I}^*, \delta \boldsymbol{S}) \ , \tag{8.219}$$

where $\delta \boldsymbol{S}$ is the right-hand side of the linearized VRTE given by (8.203).

Substituting now the scalar product $(\boldsymbol{R}_e^* + \boldsymbol{R}_b^*, \delta \boldsymbol{I})$ according to (8.219) into (8.216) and taking into account that in our case $\delta \boldsymbol{S} = v_p(\tau) \boldsymbol{\Psi}_p$, see (8.203), we obtain

$$\delta \Phi(\varpi_v) = (v_p(\tau) \boldsymbol{\Psi}_p, \boldsymbol{I}^*) + \int_0^{\tau_0} d^*(\tau, -\mu_v) \boldsymbol{E}_i^T \boldsymbol{\Psi}_p(\tau, \Omega_-^v) v_p(\tau) \mathrm{d}\tau \, . \tag{8.220}$$

The final expression for the weighting function derived employing the formal solution of the linearized VRTE is obtained using the short notation for the integral over Ω as given by (8.119):

$$\mathcal{V}_p(\tau, \varpi_v) = \left\langle \boldsymbol{\Psi}_p^T \boldsymbol{I}^* \right\rangle + d^*(\tau, -\mu_v) \boldsymbol{\Psi}_p^T(\tau, \Omega_-^v) \boldsymbol{E}_i \, . \tag{8.221}$$

Comparing the expression for the WF given by (8.221) with the TD representation given by (8.180), we see that the WF derived using the formal solution of the linearized direct VRTE is equivalent to the WF in the TD representation if the solution of (8.218) is equal to the solution of the adjoint VRTE which has been obtained for the diffuse component of the adjoint intensity as given by (8.171), i.e., $I^* \equiv I_{d-}^*$. Comparing right-hand sides of adjoint VRTEs (8.218) and (8.171) as given by (8.217) and by (8.166), (8.167), respectively, we obtain

$$\boldsymbol{R}_e^*(\tau, \Omega) + \boldsymbol{R}_b^*(\tau, \Omega) = \boldsymbol{W}_{e-}(\tau, \Omega) + \psi_b(\tau, \mu) \boldsymbol{W}_{b-}(\Omega) \, . \tag{8.222}$$

Thereby, (8.218) is the equation for the diffuse component of the adjoint intensity and (8.221) is the WF in the TD representation.

Thus, we have established that the WF derived using the formal solution of the linearized VRTE is the same as the WF in the TD representation. We note that this equivalence is found using the formal solution of the VRTE for the total forward intensity. Employing the same approach to the formal solution of the VRTE for the diffuse component of the forward intensity vector, it can be found that the WF derived using the formal solution in this case is equivalent to the WF in the DD representation.

Concluding, we can state that the weighting functions can be presented in the most general case using the total forward and total adjoint intensities ac-

cording to the TT representation as given by (8.121). Other representations of the weighting functions can be found as well:

— substituting the total forward intensity as a sum of the diffuse and direct component we get to the DT representation as as given by (8.194);
— substituting the total adjoint intensity as a sum of the diffuse and direct component we get to the TD representation as as given by (8.180);
— substituting both forward and adjoint intensities as a sum of the diffuse and direct component we get to DD representation as given by (8.195).

It is very important to choose appropriate representation both for the application of the weighting functions calculation with the existing numerical solution of the direct and adjoint VRTEs and for a comparison of the weighting functions derived by different authors.

8.10 Comparison with previous results

In this section we compare our expressions for the weighting functions with results which can be found in the literature. Taking into account the fact that the weighting functions of some authors have been derived neglecting polarization and azimuthal dependence of the forward and the adjoint intensity, we need to rewrite our expressions to exclude these effects.

To rewrite our expressions without polarization effects we will use the following transformation:

— forward and adjoint intensity

$$\boldsymbol{I}(\tau,\Omega) \implies I(\tau,\Omega)\,, \tag{8.223}$$

$$\boldsymbol{I}^*(\tau,\Omega) \implies I^*(\tau,\Omega)\,, \tag{8.224}$$

where $I(\tau,\Omega)$ and $I^*(\tau,\Omega)$ are the first components of the corresponding vectors;

— phase matrix

$$\mathbf{Z}(\tau,\Omega,\Omega') \Longrightarrow P_{11}(\tau,\Omega,\Omega')\,, \tag{8.225}$$

where $P_{11}(\tau,\Omega,\Omega')$ is the first element of the scattering matrix, $\mathbf{P}(\tau,\cos\beta)$, as given by (8.36);

— source function

$$\boldsymbol{J}(\tau,\Omega) \Longrightarrow J(\tau,\Omega) = \frac{\omega(\tau)}{4\pi}\int\limits_{4\pi} P_{11}(\tau,\Omega,\Omega')I(\tau,\Omega')\mathrm{d}\Omega'\,, \tag{8.226}$$

— scalar product

$$\int\limits_0^{\tau_0}\int\limits_{4\pi} \boldsymbol{f}^T(\tau,\Omega)\boldsymbol{g}(\tau,\Omega)\mathrm{d}\tau\mathrm{d}\Omega \Longrightarrow \int\limits_0^{\tau_0}\int\limits_{4\pi} f(\tau,\Omega)g(\tau,\Omega)\mathrm{d}\tau\mathrm{d}\Omega\,, \tag{8.227}$$

where $f(\tau,\Omega)$ and $g(\tau,\Omega)$ are the first components of the corresponding vectors.

To rewrite further our expressions neglecting azimuthal dependence of the forward and adjoint intensities we will use the following transformation:

— forward and adjoint intensity

$$I(\tau,\Omega) \implies I(\tau,\mu)\ , \tag{8.228}$$
$$I^*(\tau,\Omega) \implies I^*(\tau,\mu)\ , \tag{8.229}$$

where $I(\tau,\mu)$ and $I^*(\tau,\mu)$ are azimuthal averaged forward and adjoint intensities;

— phase matrix

$$P_{11}(\tau,\Omega,\Omega') \Longrightarrow p(\tau,\mu,\mu')\ , \tag{8.230}$$

where $p(\tau,\mu,\mu')$ is the phase function;

— source function

$$J(\tau,\Omega) \Longrightarrow J(\tau,\mu) = \frac{\omega(\tau)}{2}\int\limits_{-1}^{1} p(\tau,\mu,\mu')I(\tau,\mu')\mathrm{d}\mu'\ , \tag{8.231}$$

— scalar product

$$\int\limits_0^{\tau_0}\int\limits_{4\pi} f(\tau,\Omega)g(\tau,\Omega)\mathrm{d}\tau\mathrm{d}\Omega \Longrightarrow \int\limits_0^{\tau_0}\int\limits_{-1}^{1} f(\tau,\mu)g(\tau,\mu)\mathrm{d}\tau\mathrm{d}\mu\ . \tag{8.232}$$

Using these transformations we can easily rewrite our results for a non-polarized and azimuthal independent radiation. We note that numerical applications of the derived expressions without polarization require the forward and adjoint intensity to be solutions of the appropriate scalar RTEs.

Extinction coefficient weighting function comparison

An expression for the extinction coefficient weighting function has been presented by Ustinov [30] in the thermal spectral range neglecting polarization effects and assuming azimuthal independent intensity. In this case one can assume that there is no external source of the radiation. This assumption is reasonable in the thermal infrared spectral range for wavelength above $\sim 4\mu$ and has been used in [30]. We note that in this case the forward total and diffuse intensity coincide.

We start from the comparison of the extinction coefficient weighting function in the TT representation. Neglecting polarization and azimuthal dependence, our expression for the extinction coefficient weighting function in the TT representation as given by (8.123) can be written as follows:

$$\mathcal{V}_e(\tau,\varpi_v) = \int\limits_{-1}^{1}\left[J(\tau,\mu) + Q(\tau) - I(\tau,\mu)\right] I^*(\tau,\mu)\mathrm{d}\mu\ , \tag{8.233}$$

where $I(\tau,\mu)$ and $I^*(\tau,\mu)$ are azimuthal averaged scalar forward and adjoint intensity, respectively, and $Q(\tau)$ is the first element of the vector $\boldsymbol{Q}(\tau)$ given by (8.35). Introducing the scalar source function, $S_e(\tau,\mu)$, as follows:

$$\begin{aligned} S_e(\tau,\mu) &= J(\tau,\mu) + Q(\tau) \\ &= \frac{\omega}{2}\int\limits_{-1}^{1} p(\tau,\mu,\mu')I(\tau,\mu')\mathrm{d}\mu' + (1-\omega(\tau))B(\tau)\ , \end{aligned} \tag{8.234}$$

where $p(\tau,\mu,\mu')$ is the phase function, we obtain

$$\mathcal{V}_e(\tau,\varpi_v) = \int\limits_{-1}^{1}\left[S_e(\tau,\mu) - I(\tau,\mu)\right] I^*(\tau,\mu)\mathrm{d}\mu\ . \tag{8.235}$$

We note that our extinction coefficient WF is given for the relative variation of the corresponding parameter, i.e., $\delta\sigma_e(\tau)/\sigma_e(\tau)$ and the optical depth, τ, is used as a vertical coordinate in contrast to the geometrical height, z, employed in [30]. Thereby, for the direct comparison of results we need to rewrite expression (8.235) using the altitude z as a vertical coordinate. It can be done employing the following equality:

$$\mathcal{V}_e(\tau,\varpi_v)\frac{\delta\sigma_e(\tau)}{\sigma_e(\tau)}\mathrm{d}\tau = \mathcal{V}_e(z,\varpi_v)\delta\sigma_e(z)\mathrm{d}z\ . \tag{8.236}$$

Thus, using as a vertical coordinate the altitude instead of the optical depth, we obtain the WF in the same form as given by (8.235) but for the absolute variation of the extinction coefficient.

Taking into account the fact that the phase function used in our derivation is normalized by one as given by (8.37) and not by the single-scattering albedo, we conclude that the expression obtained is in agreement with the formula (43) derived in [30]

Another expression for the extinction coefficient weighting function at the top of a medium has been derived by Ustinov [30] using the formal solution of the linearized RTE (also referred to as integration of the source function). To compare our results in this case we note that, as has been proved in the previous section, the usage of the formal solution is equivalent to the TD representation of the weighting functions. Thus, substituting into (8.235) the total adjoint intensity as a sum of the diffuse and direct component, namely,

$$I^*(\tau,\mu) = I^*_d(\tau,\mu) + \frac{1}{\mu_v}\delta(\mu+\mu_v)\mathrm{e}^{-\tau/\mu_v}\ , \tag{8.237}$$

where the direct component of the adjoint intensity is used according to (8.162) and τ_v is set to zero for the reflected radiance at the top of the medium, we obtain

$$\mathcal{V}_e(\tau,\varpi_v) = \int_{-1}^{1} [S_e(\tau,\mu) - I(\tau,\mu)]\, I_d^*(\tau,\varpi_v)\mathrm{d}\mu + \frac{1}{\mu_v}\,[S_e(\tau,-\mu_v) - I(\tau,-\mu_v)]\,\mathrm{e}^{-\tau/\mu_v}\ . \tag{8.238}$$

Taking into account the fact that $I(\tau,-\mu_v)\mathrm{e}^{-\tau/\mu_v}$ is the same as the intermediate radiance, $r(\tau,\mu)$, given by (5) in [30], we conclude that our expression coincides with formula (98) derived by Ustinov [30].

Single scattering albedo weighting function comparison

An expression for the single-scattering albedo weighting function has been derived by Rozanov and Kokhanovsky [26] neglecting polarization and thermal emission. The corresponding weighting function was used for the calculation of the average number of photon-scattering events. Taking into account the fact that in the cited paper the linearized form of the direct RTE for the diffuse forward intensity has been used to derive the single-scattering albedo WF, the corresponding expression derived in the DD representation needs to be selected for the comparison.

Equation (8.201) can be rewritten under these assumptions as follows:

$$\mathcal{V}_\omega(\tau,\varpi_v) = \langle J_{ms} I_d^* \rangle + d^*(\tau,-\mu_v) J_{ms}(\tau,-\mu_v)\ , \tag{8.239}$$

where J_{ms} is given by (8.202) and we have restricted ourselves to the case of the reflected radiance.

If we define, following [26]:

$$S_e^r(\tau) = d^*(\tau,-\mu_v) J_{ms}(\tau,-\mu_v)\ , \tag{8.240}$$

$$S_e(\tau,\mu) = J_{ms}(\tau,\mu)\ , \tag{8.241}$$

we have the following expression:

$$\mathcal{V}_\omega(\tau,\varpi_v) = \langle S_e I_d^* \rangle + S_e^r(\tau)\ , \tag{8.242}$$

which is fully equivalent to (35) presented in [26].

Absorption coefficient weighting function comparison

The weighting function for the absolute variation of the ozone number density has recently been used by Hasekamp and Landgraf [8] in the UV-spectral range. The thermal emission has been neglected by authors. The weighting function is formulated for the total forward and total adjoint intensity. Thereby, the weighting function for the absolute variation of the number density, $\delta n(\tau)$, in the TT representation as given by (8.132) has to be used in the comparison.

Dividing the right-hand side of (8.132) by $n(\tau)$, setting $B(\tau) = 0$ and $1-\omega(\tau) = \sigma_a(\tau)/\sigma_e(\tau)$ where $\sigma_a(\tau)$ is an absorption coefficient, we obtain

$$\mathcal{V}_n(\tau, \varpi_v) = -\frac{\sigma_a(\tau)}{\sigma_e(\tau)n(\tau)} \left\langle \boldsymbol{I}^T \boldsymbol{I}^* \right\rangle . \tag{8.243}$$

As pointed out above, $\mathcal{V}_n(\tau, \varpi_v)$ describes the contribution of the number density variation in the infinitesimal layer $\mathrm{d}\tau$. For practical calculations a layer averaged weighting function is usually employed:

$$\bar{\mathcal{V}}_n(\tau_k, \varpi_v) = \int\limits_{\tau_{k-1}}^{\tau_k} \mathcal{V}_n(\tau, \varpi_v)\mathrm{d}\tau , \tag{8.244}$$

where τ_{k-1} and τ_k denote the optical depth of the upper and lower boundary of the kth layer. Substituting in this equation $\mathcal{V}_n$ according to (8.243) and changing variable τ to z, we have

$$\bar{\mathcal{V}}_n(z_k, \varpi_v) = -\sigma(z_k) \int\limits_{z_k}^{z_{k-1}} \left\langle \boldsymbol{I}^T \boldsymbol{I}^* \right\rangle \mathrm{d}z , \tag{8.245}$$

where we have assumed, following [8], that the cross-section, $\sigma(z)$, is constant within the kth layer and $\sigma_a(z) = \sigma(z)n(z)$. The derived expression is fully equivalent to the formula (49) reported in [8].

Albedo weighting function comparison

The surface albedo weighting function for the Lambertian reflection has been derived in the scalar case neglecting thermal emission by Box *et al.* [4] and used by Landgraf *et al.* [14] in the analysis of the ozone profile retrieval.

In the case of the Lambertian surface the expression for the albedo WF as given by (8.139) can be simplified. Indeed, the reflection matrix $\mathbf{M}$ as given by (8.41) has only one nonzero element, $M_{11} = 1$, the vector $\boldsymbol{F}(\Omega)$ as given by (8.136) is independent of the Ω and has only one nonzero component as well. Therefore, $\boldsymbol{F}(\Omega)$ can be written as follows:

$$\boldsymbol{F}(\Omega) = [F, 0, 0, 0]^T , \tag{8.246}$$

where F is the downward flux density at the ground level for the forward intensity:

$$F = \int\limits_{\Omega_+} I(\tau_0, \Omega)\mu \mathrm{d}\Omega . \tag{8.247}$$

Substituting (8.246) into expression for the albedo weighting function given by (8.139), we obtain

$$\mathcal{V}_A(\varpi_v) = \frac{A}{\pi} F F^* , \tag{8.248}$$

where F^* is the upward flux for the adjoint intensity $I^*(\tau_0, \Omega)$ as given by (8.143). Thus, $\mathcal{V}_A(\varpi_v)$ given by (8.248) is the surface albedo weighting function for the relative variation of the albedo, $\delta A/A$, in the case of the Lambertian surface. Dividing the right-hand side of this expression by A, we rewrite the albedo weighting function for the absolute variation of the surface albedo, δA, as follows:

$$\mathcal{V}_A(\varpi_v) = \frac{1}{\pi} F F^* \ . \tag{8.249}$$

The expression (8.249) corresponds to the surface albedo weighting function presented by Box *et al.* [4].

Surface emissivity weighting function comparison

An expression for the surface emissivity partial derivative neglecting polarization has been derived by Ustinov [30] in the thermal spectral range assuming that the forward and adjoint intensity are azimuthally independent. In the cited paper both the expression for the case of the total forward and adjoint intensity and the expression derived using the linearized form of the direct RTE (source function integration) can be found.

We start from the TT representation of the emissivity weighting function as given by (8.145). Neglecting azimuthal dependence of the adjoint intensity, the expression for F^* given by (8.143) should be rewritten as follows:

$$F^* = -2\pi \int_{-1}^{0} I^*(\tau_0, \mu)\mu \mathrm{d}\mu \ . \tag{8.250}$$

Neglecting polarization, azimuthal dependence of the forward intensity and assuming the Lambertian reflection, the expression for $\boldsymbol{F}(\Omega)$ as given by (8.136) should be replaced by

$$\boldsymbol{F}(\Omega) \Longrightarrow 2\pi \int_{0}^{1} I(\tau_0, \mu)\mu \mathrm{d}\mu \ . \tag{8.251}$$

Substituting further (8.251) into (8.145) and taking into account (8.232), we obtain

$$\mathcal{V}_\epsilon(\varpi_v) = -\epsilon B(T_s) F^* + 2\epsilon F^* \int_{0}^{1} I(\tau_0, \mu)\mu \mathrm{d}\mu \ . \tag{8.252}$$

This is the weighting function for the relative variation of the surface emissivity in the case of the Lambertian surface reflection neglecting polarization and assuming azimuthal independence of the forward and adjoint intensities. Taking into account the fact that in [30] the expression for the weighting function is given for the absolute variation of the emissivity, i.e., $\delta\epsilon$, we need to rewrite (8.252) to

have the weighting function for the absolute variation of the surface emissivity. Dividing the right-hand side of (8.252) by ϵ and substituting F^* according to (8.250), we obtain

$$\mathcal{V}_\epsilon(\varpi_v) = -\int_{-1}^{0} I^*(\tau_0,\mu)\mu \mathrm{d}\mu \left(B_s - 2\int_0^1 I(\tau_0,\mu)\mu \mathrm{d}\mu \right) , \tag{8.253}$$

where $B_s \equiv B(T_s)$. Expression (8.253) is equivalent in this case to the formula (59) presented in [30].

Replacing the total adjoint intensity, $I^*(\tau_0,\mu)$, in this equation by the sum of the diffuse and the direct adjoint components as given by (8.237), the following expression in the TD representation is obtained:

$$\mathcal{V}_\epsilon(\varpi_v) = -\left(\int_{-1}^{0} I_d^*(\tau_0,\mu)\mu \mathrm{d}\mu - \mathrm{e}^{-\tau_0/\mu_v} \right) \left(B_s - 2\int_0^1 I(\tau_0,\mu)\mu \mathrm{d}\mu \right) . \tag{8.254}$$

The derived expression is equivalent to the formula (118) given by Ustinov [30] for the emissivity weighting function obtained using the source function integration approach.

8.11 Conclusion

The measurements of the radiation after its interaction with a medium such as, for example, a planetary atmosphere contain a huge amount of information about various optical and surface parameters. Surface parameters such as the surface albedo are considered as scalar parameters whereas optical parameters such as, for example, the extinction coefficient are considered as parameter functions depending on the vertical coordinate. The estimation of a certain parameter from the measured radiation field characteristics is a subject of the inverse theory which is well developed in the case of a linear relationship between measured values and parameters to be retrieved. We have assumed in our discussion that such a linear relationship can be introduced employing the expansion of the intensity vector in the Taylor series in the case of scalar parameters or in the functional Taylor series in the case of parameter functions, respectively.

In this case the partial or variational derivative of the intensity vector with respect to the given parameter provides the desired linear relationship between the variation of the intensity vector and the variation of a certain surface or optical parameter, respectively. We have demonstrated that the weighting function can be found as a convolution of the partial or variational derivative with an instrument response function. In the case of the ideal instrument response function the weighting function coincides with the partial or variational derivative.

In order to derive an analytical expression for the variational and partial derivative we proposed alternatively to the Taylor expansion representation of the linear relationship between the variation of the measured functional and

the variation of the optical and surface parameters. We have shown that such a linear relationship can be found applying the linear perturbation theory to the direct radiative transfer equation written in the generalized form and the adjoint approach. Following this way we have formulated the generalized form of the direct and adjoint radiative transfer operators.

Introducing the radiative transfer operator and boundary condition operators we have rewritten the standard representation of the radiative transfer equation in the operator form. This form describes a specific boundary value problem consisting of three independent operator equations. We have demonstrated that the boundary value problem can be written in the form of a single-operator equation which is called the generalized form of the direct VRTE.

The direct VRTE written in the generalized form provides the generalized form of the direct radiative transfer operator comprising all operations with the intensity including boundary conditions. We have demonstrated that the direct radiative transfer operator written in the generalized form has an adjoint operator satisfying the Lagrange identity independently of the specific form of the boundary conditions for the forward intensity. The derived adjoint operator contains, in analogy with the generalized form of the direct operator, all operations with the adjoint intensity field including boundary conditions and is referred to as the generalized form of the adjoint radiative transfer operator.

Aploying linear perturbation theory to the direct radiative transfer equation written in the generalized form, we have derived the generalized expression for the partial and variational derivative. In particular, we have presented expressions for the variational derivatives of the intensity vector with respect to such optical parameters, as extinction, scattering and absorption coefficients, single-scattering albedo and phase matrix. The expressions for the partial derivatives with respect to the main surface parameters such as surface albedo and surface emissivity are presented as well.

The general expressions derived for the partial and variational derivatives contain the total forward and the total adjoint intensities. However, for practical purposes it is more convenient to have a representation for the variational derivative containing the diffuse forward and diffuse adjoint intensities. Thereby, we have demonstrated that appropriate expression can be easily found substituting the total forward as well as the total adjoint intensities as a sum of the diffuse and the direct component, respectively, into the general expression for the partial and variational derivative. Moreover, we have demonstrated that applying the formal solution (source function integration) of the direct radiative transfer equation to the derivation of the partial and variational derivative is equivalent to the generalized expression written for the diffuse adjoint intensity.

It is very important to choose an appropriate representation for the partial and variational derivative, both for the application with the existing numerical solution of the direct and adjoint VRTEs and, especially, for a comparison of derivatives derived by different authors. Such a comparison of the partial and variational derivatives derived by other authors with those presented here shows that they are fully equivalent with each other after employing appropriate simplifications. In particular, we have demonstrated that, neglecting thermal

emission in our expression for the variational derivative, we obtain the expression for the variational derivative with respect to the absorption coefficient as used by Hasekamp and Landgraf [8], and neglecting polarization and thermal emission we get the variational derivative with respect to the single-scattering albedo as derived by Rozanov and Kokhanovsky [26], neglecting polarization and azimuthal dependence of the forward and adjoint intensities we obtain the variational derivative with respect to the extinction coefficient as presented by Ustinov [30].

Although we have not given here any examples of the numerical calculations of the partial and variational derivatives, we note that in the scalar case the appropriate expressions are implemented in the software package SCIATRAN 2.0 [27] which can be used for the simultaneous calculation both of the reflected and transmitted intensity and of derivatives for the main optical and surface parameters. SCIATRAN 2.0 is freely available for non-commercial use at the website www.iup.physik.uni-bremen.de/sciatran.

Acknowledgments

The author is grateful to A. V. Rozanov and A. A. Kokhanovsky for the useful discussions. He thanks E.A. Ustinov for useful advices which helped to improve the manuscript. Parts of this work have been funded by the German Ministry of Education and Research BMBF (grant 07UFE12/8) and the German Aerospace Center DLR (grant 50EE0027).

Appendix A: Derivation of $t(\tau, \mu)$ and $b(\tau, \mu)$

The function $t(\tau, \mu)$ can be found requiring the direct VRTE written in the generalized form as given by (8.52) to result in the same solution for the transmitted intensity as the direct VRTE given by (8.33). Thereby, we find at first the solution of the direct VRTE for the transmitted radiance. For simplicity we rewrite (8.33) as follows:

$$\mu \frac{\mathrm{d}\boldsymbol{I}(\tau, \Omega)}{\mathrm{d}\tau} = -\boldsymbol{I}(\tau, \Omega) + \boldsymbol{S}_e(\tau, \Omega)\,, \tag{8.255}$$

where the source function, $\boldsymbol{S}_e(\tau, \Omega)$, is defined as

$$\boldsymbol{S}_e(\tau, \Omega) = \boldsymbol{J}(\tau, \Omega) + \boldsymbol{Q}(\tau, \Omega)\,, \tag{8.256}$$

and the boundary conditions are given according to (8.38) and (8.39).

For further discussion it is worth noticing that in (8.255) $\mu \in [-1, 1]$, $\phi \in [0, 2\pi]$ and $\tau \in [0, \tau_0]$. Inserting $\mu = +\mu$ into (8.255), we can derive the differential equation and the appropriate boundary condition for the downward radiation as follows:

$$\mu \frac{\mathrm{d}\boldsymbol{I}(\tau, \Omega_+)}{\mathrm{d}\tau} = -\boldsymbol{I}(\tau, \Omega_+) + \boldsymbol{S}_e(\tau, \Omega_+)\,, \tag{8.257}$$

$$\boldsymbol{I}(0, \Omega_+) = \boldsymbol{S}_t(\Omega_+)\,, \tag{8.258}$$

where $\boldsymbol{S}_t(\Omega_+)$ is given by (8.50), $\mu \in [0,1]$ and Ω_+ defines the set of variable $\{\mu, \phi\}$. This equation is the first-order ordinary inhomogeneous differential equation, describing the propagation of the transmitted light. The formal solution of this equation is well known (see [2, 11] for details) and can be written in the following form:

$$\boldsymbol{I}(\tau, \Omega_+) = \frac{1}{\mu} \int_0^\tau \boldsymbol{S}_e(\tau', \Omega_+) \mathrm{e}^{-(\tau-\tau')/\mu} \mathrm{d}\tau' + \boldsymbol{C}_t(\Omega_+) \mathrm{e}^{-\tau/\mu} \,. \tag{8.259}$$

Here the integration constant $\boldsymbol{C}_t(\Omega_+)$ is found setting $\tau = 0$ in (8.259) and then employing the corresponding boundary condition:

$$\boldsymbol{C}_t(\Omega_+) \;=\; \boldsymbol{S}_t(\Omega_+) \,. \tag{8.260}$$

Thus, the solution of the direct VRTE for the transmitted radiance satisfying the upper boundary condition as given by (8.258) is found as follows:

$$\boldsymbol{I}(\tau, \Omega_+) = \frac{1}{\mu} \int_0^\tau \boldsymbol{S}_e(\tau', \Omega_+) \mathrm{e}^{-(\tau-\tau')/\mu} \mathrm{d}\tau' + \boldsymbol{S}_t(\Omega_+) \mathrm{e}^{-\tau/\mu} \,. \tag{8.261}$$

Let us now find the solution of (8.52) for the transmitted intensity vector as well. Substituting the operator $\mathbf{L}_e$ given by (8.42) into (8.52), we have

$$\begin{aligned} &\mu \frac{\mathrm{d}\boldsymbol{I}(\tau, \Omega)}{\mathrm{d}\tau} + t(\tau, \mu)\Theta(\mu)\mathbf{L}_t \boldsymbol{I} + b(\tau, \mu)\Theta(-\mu)\mathbf{L}_b \boldsymbol{I} = -\boldsymbol{I}(\tau, \Omega) \\ &+\boldsymbol{S}_e(\tau, \Omega) + t(\tau, \mu)\Theta(\mu)\boldsymbol{S}_t(\Omega) + b(\tau, \mu)\Theta(-\mu)\boldsymbol{S}_b(\Omega) \,, \end{aligned} \tag{8.262}$$

where the source function $\boldsymbol{S}_e$ is used according to (8.256). Setting $\mu = +\mu$ in this equation, we obtain

$$\begin{aligned} \mu \frac{\mathrm{d}\boldsymbol{I}(\tau, \Omega_+)}{d\tau} + t(\tau, \mu)\mathbf{L}_t \boldsymbol{I} \;&=\; -\boldsymbol{I}(\tau, \Omega_+) \\ &+\; \boldsymbol{S}_e(\tau, \Omega_+) + t(\tau, \mu)\boldsymbol{S}_t(\Omega_+) \,, \end{aligned} \tag{8.263}$$

where $\mu \in [0,1]$ and, thus, the function $\Theta(\mu)$ can be omitted.

Let us assume that the solution of this equation can be found simularly to (8.257) in the following form:

$$\begin{aligned} \boldsymbol{I}'(\tau, \Omega_+) \;&=\; \frac{1}{\mu} \int_0^\tau \Big[\boldsymbol{S}_e(\tau', \Omega_+) + t(\tau', \mu)\boldsymbol{S}_t(\Omega_+) \Big] \mathrm{e}^{-(\tau-\tau')/\mu} \mathrm{d}\tau' \\ &+\; \boldsymbol{C}'_t(\Omega_+) \mathrm{e}^{-\tau/\mu} \,, \end{aligned} \tag{8.264}$$

where $\boldsymbol{C}'_t(\Omega_+)$ is the integration constant. Simularly to $\boldsymbol{I}(\tau, \Omega_+)$ given by (8.259), $\boldsymbol{I}'(\tau, \Omega_+)$ is the solution of the following equation:

$$\mu \frac{\mathrm{d}\boldsymbol{I}'(\tau, \Omega_+)}{\mathrm{d}\tau} = -\boldsymbol{I}'(\tau, \Omega_+) + \boldsymbol{S}_e(\tau, \Omega_+) + t(\tau, \mu)\boldsymbol{S}_t(\Omega_+) \,. \tag{8.265}$$

Thus, $\boldsymbol{I}'(\tau,\Omega_+)$ is a solution of (8.263) if

$$t(\tau,\mu)\mathbf{L}_t\boldsymbol{I}' = \mathbf{0}\,. \tag{8.266}$$

Substituting the operator $\mathbf{L}_t$ given by (8.44) into (8.266), we obtain

$$\begin{aligned} t(\tau,\mu)\mathbf{L}_t\boldsymbol{I}' &= t(\tau,\mu)\int\limits_0^{\tau_0}\delta(\tau)\boldsymbol{I}'(\tau,\Omega_+)\mathrm{d}\tau \\ &= t(\tau,\mu)\boldsymbol{C}_t'(\Omega_+) = \mathbf{0} \implies \boldsymbol{C}_t'(\Omega_+) = \mathbf{0}\,. \end{aligned} \tag{8.267}$$

Thus, the solution of (8.264) is found as follows:

$$\boldsymbol{I}'(\tau,\Omega_+) = \frac{1}{\mu}\int\limits_0^{\tau}\Big[\boldsymbol{S}_e(\tau',\Omega_+) + t(\tau',\mu)\boldsymbol{S}_t(\Omega_+)\Big]\mathrm{e}^{-(\tau-\tau')/\mu}\mathrm{d}\tau'\,. \tag{8.268}$$

Requiring now that $\boldsymbol{I}'(\tau,\Omega_+)$ should be equal to $\boldsymbol{I}(\tau,\Omega_+)$ given by (8.261), we have

$$\frac{1}{\mu}\int\limits_0^{\tau} t(\tau',\mu)\boldsymbol{S}_t(\Omega_+)\mathrm{e}^{-(\tau-\tau')/\mu}\mathrm{d}\tau' = \boldsymbol{S}_t(\Omega_+)\mathrm{e}^{-\tau/\mu}\,. \tag{8.269}$$

This equation is satisfied if the function $t(\tau,\mu)$ is chosen as follows:

$$t(\tau,\mu) = \mu\delta(\tau)\,. \tag{8.270}$$

Thus, the function $t(\tau,\mu)$ is determined.

To find the function $b(\tau,\mu)$ we should repeat the derivation used above for the reflected radiance. The result is as follows:

$$b(\tau,\mu) = -\mu\delta(\tau-\tau_0)\,. \tag{8.271}$$

Appendix B: Adjoint modified differential operator

To simplify our consideration we will use the following notation for the integral over Ω:

$$\int\limits_{4\pi}\boldsymbol{f}^T(\tau,\Omega)\boldsymbol{g}(\tau,\Omega)\mathrm{d}\Omega \;\equiv\; \big\langle\boldsymbol{f}^T(\tau,\Omega)\boldsymbol{g}(\tau,\Omega)\big\rangle\,. \tag{8.272}$$

First, we rewrite terms containing operators $\mathbf{L}_t$ and $\mathbf{L}_b$ in the scalar product given by (8.69). We note that according to the definition of operators $\mathbf{L}_t$ and $\mathbf{L}_b$ given by (8.44) and (8.45) we have

$$\mathbf{L}_t \boldsymbol{I} \;=\; \int_0^{\tau_0} \delta(\tau)\boldsymbol{I}(\tau,\Omega)\mathrm{d}\tau \;=\; \boldsymbol{I}(0,\Omega)\,, \tag{8.273}$$

$$\begin{aligned}\mathbf{L}_b \boldsymbol{I} \;&=\; \int_0^{\tau_0} \delta(\tau-\tau_0)\left(\boldsymbol{I}(\tau,\Omega) - \frac{A}{\pi}\int_{4\pi}\lambda(\mu')\mathbf{M}(\Omega,\Omega')\boldsymbol{I}(\tau,\Omega')\mathrm{d}\Omega'\right)\mathrm{d}\tau \\ &=\; \boldsymbol{I}(\tau_0,\Omega) - \frac{A}{\pi}\big\langle\lambda(\mu')\mathbf{M}(\Omega,\Omega')\boldsymbol{I}(\tau_0,\Omega')\big\rangle\,.\end{aligned} \tag{8.274}$$

Substituting $\psi_t(\tau,\mu)$ and $\psi_b(\tau,-\mu)$ given by (8.55) and (8.56), introducing the auxiliary function $\lambda(\mu) = \mu\Theta(\mu)$ and taking into account (8.273) and (8.274), we obtain

$$(\boldsymbol{I}^*, \psi_t(\tau,\mu)\mathbf{L}_t\boldsymbol{I}) \;=\; \big\langle\lambda(\mu)\boldsymbol{I}^{*T}(0,\Omega)\boldsymbol{I}(0,\Omega)\big\rangle\,, \tag{8.275}$$

$$(\boldsymbol{I}^*, \psi_b(\tau,-\mu)\mathbf{L}_b\boldsymbol{I}) \;=\; \big\langle\lambda(-\mu)\boldsymbol{I}^{*T}(\tau_0,\Omega)\boldsymbol{I}(\tau_0,\Omega)\big\rangle \;-\; T_A\,, \tag{8.276}$$

where the term T_A is defined as follows:

$$T_A = \;\frac{A}{\pi}\Big\langle\lambda(-\mu)\big\langle\lambda(\mu')\boldsymbol{I}^{*T}(\tau_0,\Omega)\mathbf{M}(\Omega,\Omega')\boldsymbol{I}(\tau_0,\Omega')\big\rangle\Big\rangle\,. \tag{8.277}$$

Employing further (8.64), (8.275) and (8.276), the scalar product P given by (8.69) can be written in the form

$$\begin{aligned}P \;&=\; -\left(\mu\frac{\mathrm{d}\boldsymbol{I}^*}{\mathrm{d}\tau},\boldsymbol{I}\right) + R \;+\big\langle\lambda(\mu)\boldsymbol{I}^{*T}(0,\Omega)\boldsymbol{I}(0,\Omega)\big\rangle \\ &\quad+\big\langle\lambda(-\mu)\boldsymbol{I}^{*T}(\tau_0,\Omega)\boldsymbol{I}(\tau_0,\Omega)\big\rangle \;-\; T_A\,.\end{aligned} \tag{8.278}$$

Rewriting (8.65) for R using the notation given by (8.272) as follows:

$$R = \big\langle\mu\boldsymbol{I}^{*T}(\tau_0,\Omega)\boldsymbol{I}(\tau_0,\Omega)\big\rangle - \big\langle\mu\boldsymbol{I}^{*T}(0,\Omega)\boldsymbol{I}(0,\Omega)\big\rangle\,, \tag{8.279}$$

and then substituting it into (8.278), taking into account that $\lambda(\mu)-\mu = \lambda(-\mu)$ and $\lambda(-\mu)+\mu = \lambda(\mu)$, we have

$$\begin{aligned}P \;&=\; -\left(\mu\frac{\mathrm{d}\boldsymbol{I}^*}{\mathrm{d}\tau},\boldsymbol{I}\right) + \big\langle\lambda(-\mu)\boldsymbol{I}^{*T}(0,\Omega)\boldsymbol{I}(0,\Omega)\big\rangle \\ &\quad+\big\langle\lambda(\mu)\boldsymbol{I}^{*T}(\tau_0,\Omega)\boldsymbol{I}(\tau_0,\Omega)\big\rangle - T_A\,.\end{aligned} \tag{8.280}$$

Taking into account that

$$\boldsymbol{I}^{*T}(\tau_0,\Omega)\mathbf{M}(\Omega,\Omega')\boldsymbol{I}(\tau_0,\Omega') = \big[\mathbf{M}^T(\Omega,\Omega')\boldsymbol{I}^*(\tau_0,\Omega)\big]^T\boldsymbol{I}(\tau_0,\Omega')\,, \tag{8.281}$$

changing the integration order over Ω and Ω' and replacing $\Omega \leftrightarrow \Omega'$, the term T_A given by (8.277) can be rewritten as follows:

$$T_A \;=\; \frac{A}{\pi}\Big\langle\lambda(\mu)\big\langle\lambda(-\mu')\boldsymbol{I}^T(\tau_0,\Omega)\mathbf{M}^T(\Omega',\Omega)\boldsymbol{I}^*(\tau_0,\Omega')\big\rangle\Big\rangle\,. \tag{8.282}$$

Combining last two terms into (8.280), we obtain

$$P = -\left(\mu\frac{\mathrm{d}\boldsymbol{I}^*}{\mathrm{d}\tau},\boldsymbol{I}\right) + \left\langle\lambda(-\mu)\boldsymbol{I}^{*T}(0,\Omega)\boldsymbol{I}(0,\Omega)\right\rangle + \left\langle\lambda(\mu)\boldsymbol{I}^T(\tau_0,\Omega)\left[\boldsymbol{I}^*(\tau_0,\Omega) - \frac{A}{\pi}\left\langle\lambda(-\mu)\mathbf{M}^T(\Omega',\Omega)\boldsymbol{I}^*(\tau_0,\Omega')\right\rangle\right]\right\rangle . \tag{8.283}$$

This equation is the desired representation for the scalar product P. To complete we should only rewrite last three terms in (8.283) in the form of the scalar product as well.

Let us define by analogy with operators, $\mathbf{L}_t$ and $\mathbf{L}_b$, two other operators, $\mathbf{L}_t^*$ and $\mathbf{L}_b^*$, operating on the adjoint intensity $\boldsymbol{I}^*(\tau,\Omega)$ giving it values on the upper and lower boundaries as follows:

$$\mathbf{L}_t^* = \int_0^{\tau_0}\mathrm{d}\tau\delta(\tau)\otimes , \tag{8.284}$$

$$\mathbf{L}_b^* = \int_0^{\tau_0}\mathrm{d}\tau\delta(\tau-\tau_0)\left[\otimes - \frac{A}{\pi}\int_{4\pi}\mathrm{d}\Omega\lambda(-\mu)\mathbf{M}^T(\Omega',\Omega)\otimes\right] . \tag{8.285}$$

Substituting (8.284) and (8.285) into (8.283), we obtain

$$P = -\left(\mu\frac{dI^*}{d\tau},I\right) + \left\langle\lambda(-\mu)I(0,\mu)L_t^*I^*\right\rangle + \left\langle\lambda(\mu)I(\tau_0,\mu)L_b^*I^*\right\rangle . \tag{8.286}$$

Employing functions $\psi_t(\tau,\mu)$ and $\psi_b(\tau,\mu)$, defined by (8.55) and (8.56), the scalar product P can be rewritten as

$$P = \left(I, -\mu\frac{dI^*}{d\tau} + \psi_t(\tau,-\mu)L_t^*I^* + \psi_b(\tau,\mu)L_b^*I^*\right) = (I, D^*I^*) . \tag{8.287}$$

Thus, the Lagrange identity is satisfied and the adjoint operator for the modified first-order differential operator D is

$$D^* = -\mu\frac{\mathrm{d}}{\mathrm{d}\tau} + \psi_t(\tau,-\mu)L_t^* + \psi_b(\tau,\mu)L_b^* . \tag{8.288}$$

References

1. G. I. Bell, S. Glasstone: *Nuclear Reactor Theory*, Van Nostrand Reinholt, New York 1970.
2. R. Bellman: *Introduction to matrix Analysis*, McGraw-Hill, New York, 1960.
3. M. A. Box, S. A. W. Gerstl, C. Simmer: Application of the adjoint formulation to the calculation of atmospheric radiative effects, *Beitr. Phys. Atmosph.* **61**, 303–311 (1988).

4. M. A. Box, S. A. W. Gerstl, C. Simmer: Computation of atmospheric radiative effects via perturbation theory, *Beitr. Phys. Atmosph.* **62**, 193–199 (1989).
5. M. A. Box: Radiative perturbation theory: a review. *Environmental Modelling and Software* **17**, 95–106 (2002).
6. S. Chandrasekhar: *Radiative transfer*, Oxford University Press, London, 1950.
7. E. S. Chalhoub, R. D. M. Garcia: The equivalence between two techniques of angular interpolation for the discrete-ordinates method, *JQSRT* **64**, 517–535 (2000).
8. O. P. Hasekamp, J. Landgraf: A linearized vector radiative transfer model for atmospheric trace gas retrieval, *JQSRT* **75**, 221–238 (2002).
9. J. W. Hovenier, C. Van der Mee, H. Domke: *Transfer of Polarized Light in Planetary Atmospheres. Basic Concepts and Practical Methods*, Kluwer, Dordrecht, 2004.
10. H. C. van de Hulst: *Multiple Light Scattering: Tables, Formulas, and Applications*, Vol. 1, Academic Press, New York, 1980.
11. A. Ishimaru: *Wave Propagation and Scattering in Random Media*, Vol. 1, *Single Scattering and Transport Theory*, Academic Press, New York, 1978.
12. A. A. Kokhanovsky: *Polarization Optics of Random Media*, Praxis Publishing, Chichester UK, 2003.
13. G. A. Korn, T. M. Korn: *Mathematical Handbook for Scientists and Engineers*, McGraw-Hill, New York, 1968.
14. J. Landgraf, O. P. Hasekamp, M. A. Box, T. Trautmann: A linearized radiative transfer model for ozone profile retrieval using the analytical forward-adjoint perturbation theory approach, *JGR* **106**, D21 (2001).
15. K. N. Liou: *An Introduction to Atmospheric Radiation*, Academic Press, New York, 1980.
16. *Radiative Transfer in Scattering and Absorbing Atmospheres*, edited by J. Lenoble, A. Deepak Publishing, Hampton, VA, 1985.
17. G. I. Marchuk: Equation for the value of information from weather satellites and formulation of inverse problems, *Cosmic Res.* (2), 394–409 (1964).
18. G. I. Marchuk: *Adjoint Equations and Analysis of Complex Systems*, Kluwer, Amsterdam, 1995.
19. Q. Min, L. E. Harrison: An adjoint formulation of the radiative transfer method, *JGR* **101**, D1, 1635–1640 (1996).
20. I. N. Polonsky, M. A. Box: General perturbation technique for the calculation of radiative effects in scattering and absorbing media, *JOSA A* **19**, Issue 11, 2281 (2002).
21. I. N. Polonsky, M. A. Box, A. B. Davis: Radiative transfer through inhomogeneous turbid media: implementation of the adjoint perturbation approach at the first order, *JQSRT* **78**, 85–98 (2003).
22. G. C. Pomraning: *Linear Kinetic Theory and Particle Transport in Stochastic Mixtures*, World Scientific, Singapore, 1991.
23. Yi Qin, D. L. B. Jupp, M. A. Box: Extension of the discrete-ordinate algorithm and efficient radiative transfer calculation, *JQSRT* **74**, 767–781 (2002).
24. C. D. Rodgers: *Inverse Methods for Atmospheric Sounding: Theory and Practice*, World Scientific, Singapore, 2000.
25. V. V. Rozanov, T. Kurosu, J. P. Burrows: Retrieval of atmospheric constituents in the UV-visible: a new quasi-analytical approach for the calculation of weighting functions, *JQSRT* **60**, 277–299 (1998).
26. V. V. Rozanov, A. A. Kokhanovsky: The average number of photon scattering events in vertically inhomogeneous atmospheres, *JQSRT* **96**, 11–33 (2005).

27. A. Rozanov, V. Rozanov, M. Buchwitz, A. Kokhanovsky, J.P. Burrows: SCIATRAN 2.0 – A new radiative transfer model for geophysical applications in the 175–2400 nm spectral region, *JASR*, doi:10.1016/j.asr.2005.03.012.
28. E. A. Ustinov: Adjoint sensitivity analysis of radiative transfer equation: temperature and gas mixing ratio weighting functions for remote sensing of scattering atmospheres in thermal IR, *JQSRT* **68**, 195–211 (2001).
29. E. A. Ustinov: Adjoint sensitivity analysis of radiative transfer equation: 2. Applications to retrievals of temperature in scattering atmospheres in thermal IR. *JQSRT* **73**, 29–40 (2002).
30. E. A. Ustinov: Atmospheric weighting functions and surface partial derivatives for remote sensing of scattering planetary atmospheres in thermal spectral region: general adjoint approach, *JQSRT* **92**, 351–371 (2005).
31. V. Volterra: *Theory of Functionals and of Integral and Integro-differential Equations*, Dover, New York, 1959.

Part III

Applications

9 Light scattering in combustion

Alan R. Jones

9.1 Introduction

Combustion very often involves two-phase flow. This takes the form of a gas containing fuel and/or combustion products. Mostly, the fuel is either a liquid spray or pulverised coal, though other solids may be present such as biological waste (biomass) and even sewerage. The products are very commonly soot, but also ash and char. Flames are also used in the manufacture of particles such as carbon black and pigments, and recently there has been growing interest in the production of nanoparticles.

In research to understand combustion processes and in industry to monitor combustor performance it is necessary to be able to measure the rates of conversion of the fuel and of formation of the products. The mass flow rate of particulate matter is also an important consideration, both in performance and in emissions control.

Flames and combustion products are very hostile environments. The temperatures involved are normally well in excess of 1000°C. This, combined with the high flow rates and bombardment by particles, is damaging to any probes that are inserted into the gas stream. This is one of the reasons why optical techniques have been developed into powerful tools for combustion diagnostics. Apart from the windows necessary in some cases, all the optical components are external to the combustion system. In addition, electromagnetic radiation at moderate intensities does not significantly interfere with the object under study, unlike, for example, the insertion of a probe.

The interaction of radiation with solid particles or liquid drops is covered under the generic term 'scattering'. The nature of the interaction depends upon the particle size, shape, structure, concentration and refractive index. In principle, therefore, scattering can be used to measure all of these variables. The nature of the scattering process can be a simple rebound not involving a change in frequency, other than Doppler shift. This is elastic scattering. Alternatively, there may be frequency shifts due to absorption and re-emission or due to nonlinear effects. This is inelastic scattering. This chapter will be restricted to elastic scattering and recent developments in this area will be reviewed.

Although the environment cannot damage a beam of light, there are some considerations when applying optics to combustion systems. The light will interact with the gas. In most cases, for the gases typically found in combustion systems and for visible wavelengths, it is the temperature gradients that are problematic because they cause deflections of the light that may lead to uncertainty in the position and size of the measurement space and spreading of the incident beam. There may also be a loss of intensity due to scattering out of the beam before it reaches the measurement point. A further difficulty in industrial combustors is that access may be limited and often only one port is available. Fogging of windows is also an important problem that will affect transmission of the light in and out of the combustor, leading not only to a loss of intensity but also to false results. For this reason, methods that do not rely on absolute intensity are to be preferred. Another problem is the presence of thermal radiation. This occurs at all wavelengths and can create difficulty in separating out the scattered signal.

Radiative emission from flames is influenced by scattering, and the presence of particulates can control heat transfer. The emission of radiation by particles can also be employed to measure temperature, common methods being total radiation and optical pyrometry and multi-colour methods. However, radiative emission is beyond the scope of this chapter. Further information can be found, for example, in Hottel and Sarofim (1967) and Modest (2003).

The emphasis here is to review recent work on the use of light scattering for diagnostics of particles relevant to flames and combustion. The author has written two earlier reviews (Jones, 1993, 1999) to which the reader is referred. This chapter will concentrate on developments since 1999. Reference to earlier work will be made only where necessary for reasons of clarity. In addition the review will concentrate on developments in techniques, and will not discuss results unless they are of a particularly fundamental nature.

9.2 Soot and other nanoparticles

When small particles formed in flames, such as soot, are sampled and viewed under an electron microscope they usually appear as branched chain agglomerates. Examples can be seen in Fig. 9.1. The aggregate is made up of a number of primary particles. For soot, the size of the primary particles is typically of the order 30–60 nm and the aggregates are up to 500 nm. The properties of the aggregates that we would like to measure include the sizes of the primary particles and the aggregates, both as functions of size and position. We would also like to follow the formation of the primary particles and the aggregation process, ultimately leading to smoke formation.

Apart from soot a number of other small particle types can be formed in flames. There is now a growing interest in the manufacture and uses of nanoparticles, and flames are a common source (Pratsinis, 1998; Wooldridge, 1998)

Before we can analyse the results of experimental measurements we need a theoretical basis to describe the scattering process. The importance of correctly

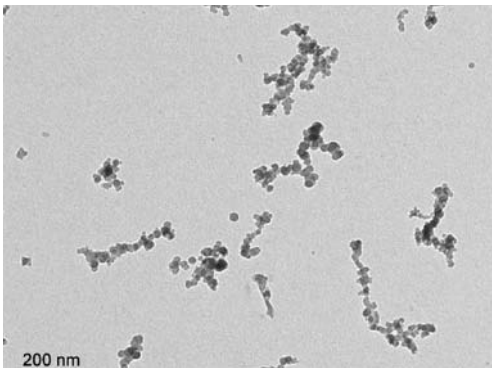

(a)

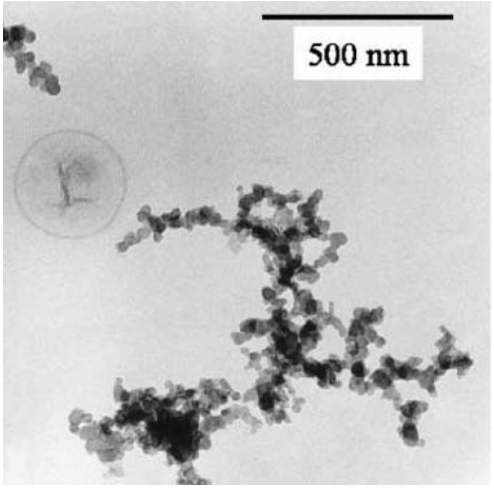

(b)

Fig. 9.1. Typical examples of soot aggregates sampled from flames. (a) Taken from Tian *et al.* (2004). (b) Taken from Wentzel *et al.* (2003).

treating aggregates has been demonstrated by Quinten *et al.* (2001). They compared scattering by aggregates with that of equal volume spheres in optical particle counters, which infer particle size from a measurement of scattered intensity. They demonstrated that scattered intensity increases due to irregularity caused by agglomeration. Models based on equal volume spheres with a variety of effective medium approximations failed to represent the experimental results.

In the case of aggregates of small particles there are two fundamental approaches. The first of these is full interactive scattering. Here there is a rigorous

theory (e.g. Xu, 1997; Xu and Gustafson, 2001; Saija *et al.*, 2003), but it is very complicated and very computer-intensive.

Because the monomers are so small they can be treated as Rayleigh scatterers and this leads to the coupled dipole method (e.g. Purcell and Pennypacker, 1973; Mulholland and Mountain, 1999; Xu and Gustafson, 1999; Shu and Charalampopoulos, 2000a). This is less complicated, but still involves the solution of $3N$ simultaneous equations, where N is the number of monomers in the aggregate. The advantage of the rigorous theories is that they will predict polarisation properties of the aggregates, as well as being accurate. The main disadvantage is that the position of every particle must be known. This is not possible even for one agglomerate, let alone a group of aggregates. Theorists get around this problem by simulating the aggregation process so that the positions are known.

A simpler approach arises from the observation that the aggregates are usually tenuous by nature. This leads to the prospect that the incident wave may propagate undisturbed through the structure, and that the Rayleigh–Gans–Debye (RGD) approximation may be applied. Where this is suitable the primary particles may be considered to scatter independently. The resulting analysis is then much more straightforward.

The positions of the primary particles cannot be predicted in any one aggregate, and all aggregates are different from each other. Overall the positions may be considered to be random. This suggests a statistical method, which leads to the concept of a correlation function. This is quite easily applied in the RGD model using the fractal approach; the so-called Rayleigh–Gans–Debye–fractal-aggregate (RGD-FA) model. Excellent reviews of this method have been given by Sorensen (2001) and Bushell *et al.* (2002).

Wang and Sorensen (2002) found good agreement between RGD theory and experiment for fractal aggregates. The materials used were TiO_2 ($m = 2.61$) and SiO_2 ($m = 1.46$). The primary particle size was of the order of 20 nm with about 150 per cluster. Van-Hulle *et al.* (2002a) examined the validity of the RGD-FA approach by comparison of theoretical results from the rigorous multisphere model using translation vectors (Xu, 1997) and the coupled dipole method. For scattering at 90° the two approximations were in reasonable agreement but disagreed with the rigorous solution. All three were in good agreement for the absorption and extinction coefficients, but RGD-FA was low for the scattering cross-section. di Stasio (2002b) has also queried whether the RGD-FA method obeys the optical theorem. Evidently these questions require further study.

In the RGD method the scattering is described in terms of the scattering wave vector $\boldsymbol{q}$, which has the magnitude

$$q = \frac{4\pi}{\lambda} \sin \frac{\theta}{2}$$

where θ is the angle between the incident and scattered directions. For a set of N scatterers the intensity becomes

$$I(q) = \left| \sum_{n=1}^{N} \mathrm{e}^{i\boldsymbol{q}\cdot\boldsymbol{r}_n} \right|^2 = \sum_{n=1}^{N} \sum_{m=1}^{N} \mathrm{e}^{i\boldsymbol{q}\cdot(\boldsymbol{r}_n - \boldsymbol{r}_m)}$$

where $\boldsymbol{r}_n$ is the position of the nth particle. This may also be written

$$I(q) = F(q)S(q)$$

where $F(q)$ describes the scattering by individual particles and $S(q)$ is the structure function. For N independent Rayleigh particles $F(q) \propto N^2$ and so

$$S(q) \propto \frac{1}{N^2} \sum_{n=1}^{N} \sum_{m=1}^{N} \mathrm{e}^{i\boldsymbol{q}\cdot(\boldsymbol{r}_n - \boldsymbol{r}_m)}$$

A powerful method of overcoming the lack of knowledge of the positions of the individual particles is to describe the agglomerates as fractal structures. These are defined by

$$N = K \left(\frac{R_\mathrm{g}}{a_\mathrm{p}} \right)^{D_\mathrm{f}}$$

where R_g is the radius of gyration, a_p is the radius of the primary particles and N is the number of primary particles in the agglomerate. K is a constant prefactor and D_f is the dimension. For infinite cylinders $D_\mathrm{f} = 1$, for flat discs $D_\mathrm{f} = 2$ and for spheres $D_\mathrm{f} = 3$. However, for these structures D_f is not found to be an integer, rather it is some fraction; hence the term 'fractal dimension'. For a soot agglomerate D_f is typically about 1.8.

The RGD approximation works reasonably well for $D_\mathrm{f} < 2$. For $D_\mathrm{f} > 2$ the agglomerate is too dense and the aggregate is better described by rigorous theory. As D_f approaches 3, Mie theory may be used.

It is worth noting here that the agglomerate is not a genuine fractal. For that, the properties should be independent of scale. Clearly, this is not so for the aggregate. If the scale is very small then individual primary particles play the most significant role. If the scale is very large it can be outside the limits of the actual aggregate. The correlation function has to be multiplied by a cut-off function to allow for this. Sorensen (2001) discusses this theory in detail.

The outcome of the analysis is that there are three regimes:

1. The Guinier regime ($qR_\mathrm{g} \ll 1$) where scattering is dominated by the large scale of the agglomerate. Here

$$S(q) = 1 - \frac{1}{3}(qR_\mathrm{g})^2$$

   A plot of $I(q)$ against q^2 will yield the radius of gyration.
2. The power law regime ($qR_\mathrm{g} \gg 1$) where interactive scattering and the structure of the agglomerate are important. Here

$$S(q) \propto (qR_\mathrm{g})^{-D_\mathrm{f}}$$

   A plot of $\ln[I(q)]$ against q will yield the fractal dimension.

3. For extremely large values of qR_g there is a third regime, sometimes known as the Porod regime, where scattering is dominated by the individual Rayleigh sized primary particles. Here

$$S(q) \propto q^{-4}$$

Thus, we can see that the measurement of scattered intensity against angle can yield both the radius of gyration of the agglomerate and the fractal dimension.

Fig. 9.2 shows the variation of these for soot as a function of height in a flame as measured by di Stasio (2001) and di Stasio *et al.* (2002). It can be seen that initially R_g is small and D_f is large, about 25 nm and 2.55 respectively. This is the region where the primary particles are either still separate or in the very early stages of agglomeration. Since for a sphere $D_f = 3$, we would expect a high value here. As agglomeration progresses R_g increases and D_f becomes smaller, eventually arriving at about 380 nm for R_g and 1.2 for D_f. In this case the agglomerates are similar to straight chains, as in Fig. 9.1(a). However, the agglomerate then begins to change shape. R_g falls to about 160 nm before further growth occurs taking it up to approximately 280 nm. At the same time the fractal dimension rises to almost 1.9. At this stage the agglomerate resembles that seen in Fig. 9.1(b). The reason for this restructuring is not clear, but the possibilities are discussed by the authors. Sorensen *et al.* (2003) and Kim *et al.* (2004) point to the possible formation of super-aggregates with fractal dimension as high as 2.6. They speculate that these may be formed by percolation of smaller aggregates with fractal dimension of 1.8, or by restructuring due to tenuous agglomerates subjected to shear flow.

Close to the burner it would be expected that individual soot monomers would form, and it would be of interest to detect the actual onset of agglomeration. A possible technique has been suggested by di Stasio (2002b) who claims that reciprocity is violated for very small agglomerates of about two particles. The author shows results that imply that at a certain height above the burner the ratio of cross-polarised intensities (I_{HV}/I_{VH}) can rise as high as six at a scattering angle of 120°. Higher up the burner, where the agglomerates are larger, the ratio returns to one and reciprocity is satisfied. However, reciprocity is such a well-established principle that the proposal should be treated with some caution[1].

Of course, the numbers suggested by Fig. 9.2 are not universal. The sizes and residence times will depend to some extent upon the fuel and the nature of the burner. However, the variation in size is not large and the fractal dimension is found to be reasonably universal. Also, the same kind of variation is found in the manufacture of other nanoparticles. As an example Fig. 9.3 shows results for

[1]It is worth noting that for larger agglomerates Shu and Charalampopoulos (2000a) state that previously reported violations of reciprocity arise from inappropriate orientation averaging. It is not sufficient to average only over angular orientations of the aggregate, but rotation about the axis must also be taken into account.

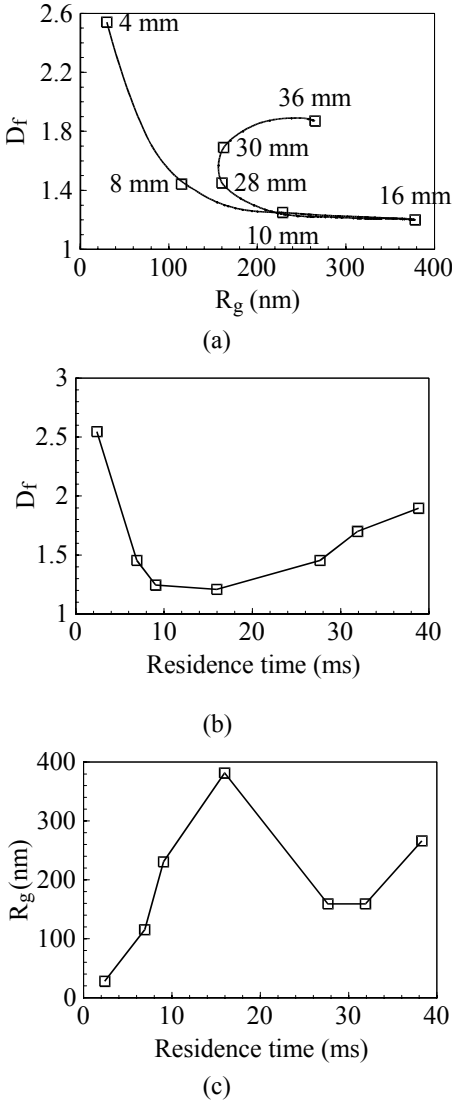

Fig. 9.2. Variation of radius of gyration and fractal dimension with (a) height in a flame (after di Stasio, 2001) and (b) and (c) residence time (after di Stasio *et al.* (2002a).

aluminium oxide formed in a flame obtained by Xing *et al.* (1999). In contrast to this, Kim and Choi (2003) found no evidence of rearrangement or sintering for silica particles formed in a flame.

It will be noted that the measurement of R_g and D_f is not a complete description of the aggregate. For this the size of the primary particles is needed and the number of particles in the aggregate. These could either be measured

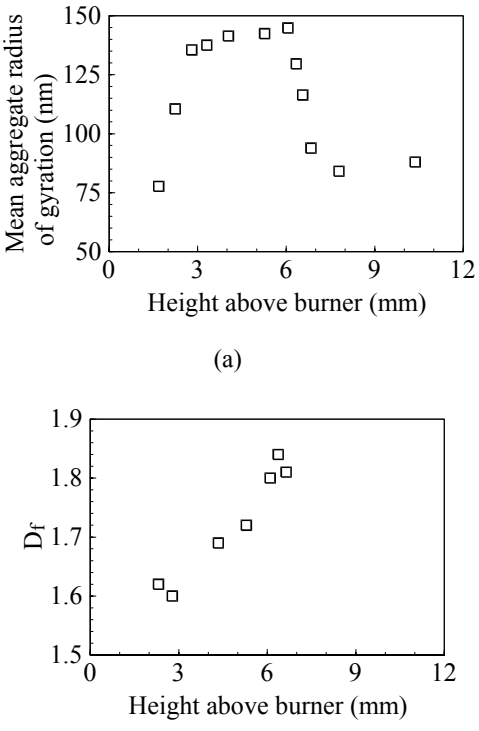

Fig. 9.3. Variation of the radius of gyration and fractal dimension for Al_2O_3 formed in a flame as a function of height above the burner (after Xing *et al.*, 1999).

independently, or one could be deduced from the other if the prefactor were known. Hu *et al.* (2003) used a combination of electron microscopy and laser extinction techniques and obtained $D_f = 1.74 \pm 0.11$ and $K = 2.2 \pm 0.4$. Brasil *et al.* (2000) commented that the fractal dimension is reasonably well understood with quoted values between 1.4 and 1.86, but that the prefactor can vary widely with quoted values between 1.05 and 3.5. They made an analysis with simulated aggregates with refractive indices typical of soot and alumina, which suggested a conclusive result. They found a fractal dimension of 1.82 and a prefactor of 1.27 independently of aggregate size and composition. However, they noted that experiments have yielded a dimension greater than 2. They suggested that this might be due in part to sintering and to polydispersity of the monomers.

Mulholland and Mountain (1999) performed calculations using a coupled electric and magnetic dipoles method, and concluded that there is a correlation between polarisation ratio

$$P = \frac{I_{\mathrm{HH}}(90^\circ)}{I_{\mathrm{VV}}(90^\circ)}$$

and the size of the primary particles. For a fixed number of particles in the agglomerate, their result is shown is shown in Fig. 9.4. It can be seen that there is an increasing trend, which for a point detector is linear. As the receiving aperture increases the linearity is corrupted. Krishnan *et al.* (2001) showed results for a range of measurements of polarisation ratio against primary particle size, as seen in Fig. 9.5. Again there is an increasing trend. In addition it will be observed that the ratios are higher for overfire soot with 260–552 particles per agglomerate than for underfire soot with 30–80 particles. This can be interpreted with aid of Fig. 9.6, taken from Mulholland and Mountain (1999). The polarisation ratio is predicted to increase or decrease with increasing number of particles depending upon the value of x_p. For small particles with $x_p < 0.2$ there is, indeed, a tendency to decrease.

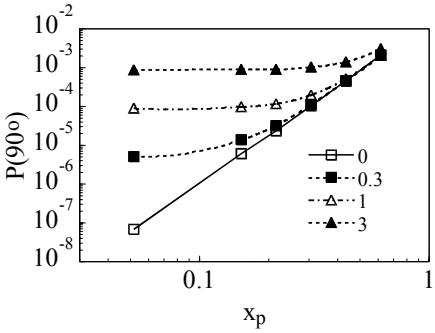

Fig. 9.4. Polarisation ratio versus size parameter of primary spheres for a range of detector acceptance angles in degrees (after Mulholland and Mountain, 1999).

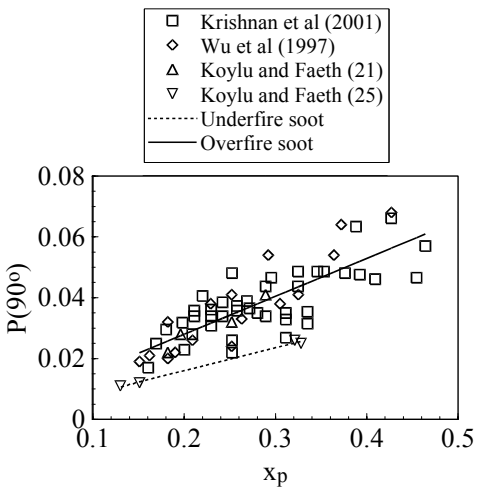

Fig. 9.5. Measurements of the polarisation ratio for various fuels as a function of the size parameter of the primary spheres (after Krishnan *et al.*, 2001).

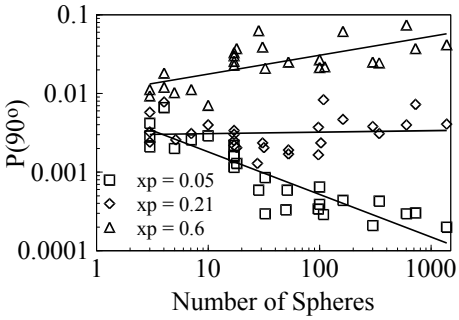

Fig. 9.6. Effects of primary size parameter and number of spheres in an agglomerate on the polarisation ratio for a detector acceptance angle of 2° (after Mulholland and Mountain, 1999).

Two methods for obtaining the primary particle size were proposed by di Stasio (2000). The first was also a linear relationship between the polarisation ratio and the primary particle size. This is illustrated in Fig. 9.7, but it is apparent that the negative gradient is in disagreement with the results presented in Fig. 9.5. The reason for this is again lies in the fact that the number of particles in the agglomerates and the primary particle size were both increasing with time.

Since for an isolated Rayleigh sized sphere I_{VV} is independent of angle; the angular variation is due to the structure function $S(q)$. The Fourier transform of the scattering pattern of I_{VV} is then the auto-correlation function, $G(r)$, of the aggregate structure. di Stasio's (2000) second method was to note that in the Porod regime the first peak in $G(r)$ corresponded to the primary particle diameter. The second peak corresponded to twice this diameter. An example of this function as measured by di Stasio (2000) is seen in Fig. 9.8. This technique has the advantage that the positions of the peaks are independent of the num-

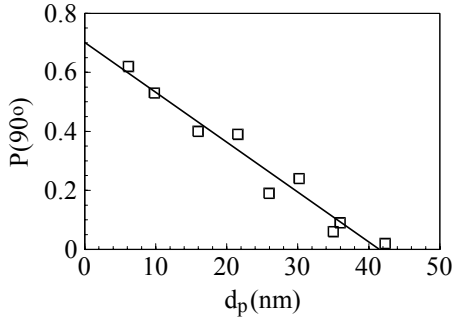

Fig. 9.7. Measured polarisation ratio versus primary particle size as obtained by scanning electron microscopy at corresponding heights above a Bunsen burner in an ethylene–air diffusion flame (after di Stasio, 2000).

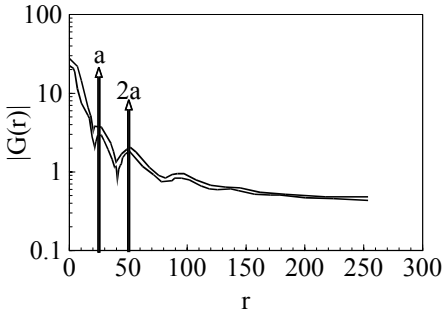

Fig. 9.8. Example of a density-density function $|G(r)|$ of fractal soot aggregates obtained by Fourier transformation of the measured structure function $S(q)$. The two lines represent the upper and lower envelopes of a rapidly oscillating curve (after di Stasio, 2000).

ber of particles, though that does affect the ratio of their heights. The author makes the point that the method may be limited by the need to ensure that q is sufficiently large (wavelength is sufficiently small) to ensure that the Porod regime is achieved.

Mulholland and Mountain (1999) suggested that the number of particles in an agglomerate could be obtained from the extinction cross-section provided that the primary particle size is known. di Stasio *et al.* (2002a) was able to infer this number from a measurement of the ratio of scattered intensities at 20° and 90°.

Krishnan *et al.* (2000, 2001) made measurements on sooting flames from both gaseous and liquid fuels. They based their analysis on RGD-FA but assumed a prefactor of 8.5, which is probably too high. Nonetheless, the fractal dimension was universally approximately 1.8 in general agreement with other authors. Some of their results are summarised in Table 9.1. From measurements of both

Table 9.1. A summary of some structure properties of overfire soot agglomerates (after Krishnan *et al.*, 2000).

Fuel	d_p (nm)	$\overline{N}$	D_f
Gas fuelled flames:			
Acetylene	47	417	1.79
Ethylene	32	467	1.80
Propylene	41	460	1.79
Butadiene	42	—	1.79
Liquid fuelled flames:			
Benzene	50	552	1.77
Cyclohexane	37	—	1.80
Toluene	51	526	1.79
n-Heptane	35	260	1.79

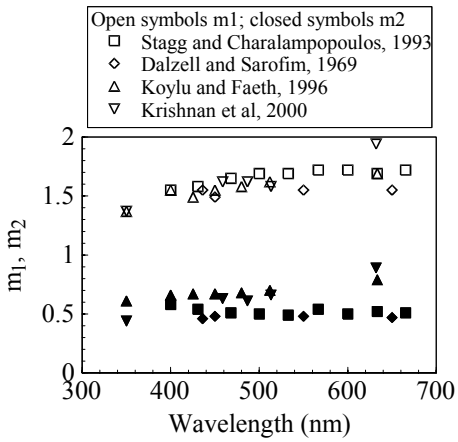

Fig. 9.9. Measurements of the real (m_1) and imaginary (m_2) parts of the refractive index of soot as reported by Krishnan *et al.* (2000).

scattered intensity and extinction coefficient they were able to determine both the functions

$$F(m) = \left|\frac{m^2-1}{m^2+2}\right|^2 \quad \text{and} \quad E(m) = \text{Im}\left(\frac{m^2-1}{m^2+2}\right)$$

so that in principle both the real and imaginary parts of the refractive index, m, could be established. The refractive index function for absorption $E(m)$ agreed with previous authors, but the scattering function $F(m)$ only agreed up to 550 nm, but then rose faster. Their results for refractive index are seen in Fig. 9.9. The measured values vary between approximately 1.4–i0.4 at 350 nm wavelength and 2–i0.9 at 660 nm.

Van-Hulle *et al.* (2002b) examined soot refractive index in turbulent methane flames with either air or oxygen. Soot sizes were obtained from sampling and then RGD theory applied to calculate the optical properties of fractal aggregates for comparison with measurement. Both extinction and $I_{\text{VV}}(90°)$ were measured at a wavelength of 632.8 nm and an inversion technique used to find the complex refractive index. Within experimental error the refractive index was independent of oxidiser and height above the burner and was 2–i0.5. Changing the morphological parameters was found to have important consequences on the predicted refractive index. A sensitivity analysis found that the fractal dimension is the most important variable overall, whereas d_{p} and K only influence the imaginary part. Their results are in reasonable agreement with the calculated value of 1.9–i0.55 of Lee and Tien (1981) and of the reflectance technique of 1.94–i0.64 of Mullins and Williams (1987). They also agree with the real part of 1.99–i0.89 given by Krishnan *et al.* (2000) but not with the imaginary part.

It is worth pointing out that the actual refractive index of soot is a function of a number of parameters. It will vary with carbon to hydrogen ratio in the soot, and this will depend upon the original fuel and oxidant combination and the age

of the soot in the flame. Examples of the variation that may be expected occur in the work of Charalampopoulos *et al.* (1989), Chang and Charalampopoulos (1990) and Vaglieco *et al.* (1990).

Charalampopoulos and Shu (2003) made experimental measurements on the fractal aggregates of Fe_2O_3 formed in a CO–air diffusion flame. Scattering, extinction and asymmetry were used and the measurements were combined with an exact light-scattering theory to yield the complex refractive index, the primary particle size parameter, the aspect ratio, and the number density and volume fractions of the chainlike aggregates under flame conditions. The effective complex refractive index was 1.96–i0.2. The corresponding primary particle size was found to be 48 nm and the aggregate aspect ratio was in the range of 6–7. The authors also provided an interesting discussion of the inversion procedure used to obtain the required data.

Apart from the variation of scattered intensity with angle, the other important variables are the scattering and extinction cross-sections. This is partly because they can indicate the absolute scattered intensity and because of the commonly used sizing method based on spectral extinction. In addition, however, the cross-sections are important to radiative heat transfer calculations. The optical properties of smoke are also critical to visibility and the design of escape routes and appropriate emergency lighting. Snegirev *et al.* (2001) were interested in the response of light scattering smoke detectors, and concluded that neglecting coagulation underestimated their response times. An example of the influence of fractal dimension on extinction is shown in Fig. 9.10. This indicates that the well-known peak in specific cross-section for spheres is not present for fractal agglomerates, and that the extinction increases with fractal dimension.[2] For a range of gaseous and liquid fuels, Krishnan *et al.* (2000) measured the dimensionless extinction coefficient defined by

$$\kappa_{\text{ext}} = -\lambda \ln(I/I_0)/(Lf_{\text{v}})$$

in the overfire region of flames and found it to be 8.5 almost independently of wavelength. However, Zhu *et al.* (2000) measured the dimensionless extinction coefficient at two wavelengths for soot from acetylene and ethene. For acetylene at a wavelength of 632.8 nm they found 8.1 and at 856 nm they obtained 8.8. The equivalent values for ethene were 9.7 and 9.4. For JP-8 soot Zhu *et al.* (2004) obtained values in the range 9.8 to 10.0 in the wavelength range 633 to 1565 nm. Widmann *et al.* (2003) demonstrated that the dimensionless extinction coefficient also depends on the fuel/air ratio, as seen in Fig. 9.11. It is worth noting that for most of these reports error values of at least ±0.5 were given.

[2]There is no evidence to doubt this calculation. However, it is slightly worrying that for fractal dimensions greater than 2 fractal theory may not be applicable (Berry and Percival, 1986; Farias *et al.*, 1995, 1996) and it is suggested that Mie theory may be appropriate. In Fig. 9.10 all the fractal calculations are higher than the Mie theory result and are increasing with fractal dimension. In support, it is noted that the Mie theory was applied to a volume equivalent sphere (not an actual sphere), and that the results are broadly in agreement with those of Dobbins *et al.* (1994).

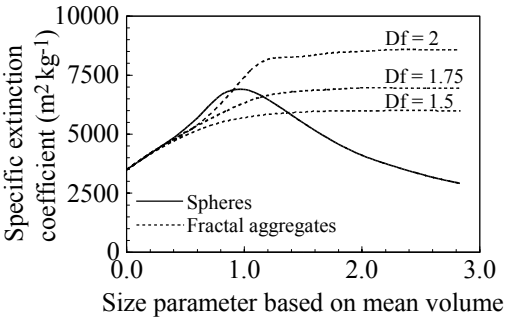

Fig. 9.10. Calculated specific extinction coefficient as a function of fractal dimension (after Snegirev *et al.*, 2001.

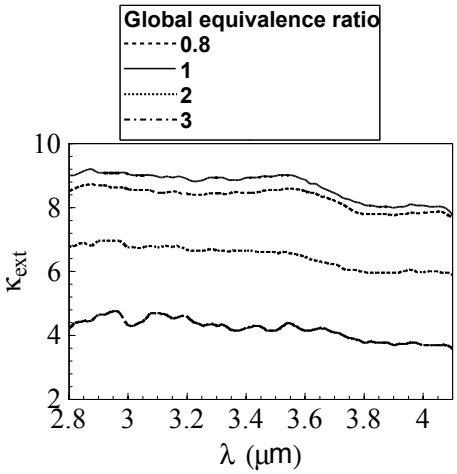

Fig. 9.11. Dimensionless extinction coefficient of soot agglomerates as a function of global equivalence ratio (after Widmann *et al.*, 2003). Only the mean curves are shown here; there is a variation of up to ±0.5 shown in the original. The sequence top to bottom is 1.0, 0.8, 2.0 and 3.0.

Mulholland and Croarkin (2000) quoted the mass specific extinction coefficient, which is given by

$$K_{\mathrm{m}} = -\ln(I/I_0)/(L\rho f_{\mathrm{v}})$$

to be $8.8 \pm 1.1\,\mathrm{m}^2\,\mathrm{g}^{-1}$ when averaged over 29 soots. Their interest was in fire research, and they commented that this nearly universal value means that the mass concentration of smoke can be inferred from extinction measurements. Mulholland *et al.* (2000) have described the design of a smoke concentration meter based on these principles.

Detailed calculations using a rigorous numerical method have been undertaken for fractal aggregates of soot by Klusek *et al.* (2003). Model clusters were derived to suit a chosen fractal dimension and extensive calculations of the scat-

tering matrix were performed. It was found that S_{12} and S_{34} are more sensitive to fractal properties than S_{11}. Detailed calculations were also discussed by Riefler *et al.* (2004) who used the T-matrix method. Models clusters were averaged both over orientation and over different clusters (configurational averaging). It was concluded that configurational averaging generally gives a superior fit to the measurements. They also emphasised that, while the T-matrix method is exact and superior to the RGD approach, it is much more consuming of time and effort.

Menguc and Manickavasagam (1998) also performed detailed calculations on simulated fractal aggregates. They investigated all the elements of the scattering matrix for soot with $D_\mathrm{f} = 1.8$, but with a prefactor of 5.8 which is rather large. They observed various interesting features of the various elements, and suggested that inversion procedures may be developed based on a library of calculated values. In particular they note that N and dp may be obtained from the angular variation of S_{11} provided that the complex refractive index is known. They also pointed to the sensitivity of S_{12} to fractal dimension and S_{34} to N almost independently of d_p.

In the studies described above it was tacitly assumed that all the primary particles were of the same size. An important question to be asked surrounds the possibility that the particles and agglomerates both have a range of sizes and what effect this may have. A detailed discussion of this has been given in the review by Sorensen (2001). Earlier, Sorensen and Wang (1999) examined agglomerates with large qR_g and looked at the effect of polydispersity on the constant in $S(q) \approx C(qR_\mathrm{g})^{-D_\mathrm{f}}$. Ideally $C = 1$, but polydispersity can have significant effects. Various equations have been proposed for this large size region and these authors explored which are the most suitable. C is dependent on the choice of cut-off function: The sharper the cut-off, the smaller the value of C. Thus it is required to find the most suitable cut-off function, and previous work has suggested that for polysdisperse aggregates a gaussian function is best. This suggests that $C = 1.0 \pm 0.05$ for D_f in the range 1.7 to 2.1. From RGD theory the authors find that

$$S_\mathrm{eff} = \begin{cases} 1 & qR_\mathrm{g,z} \ll 1 \\ C\dfrac{M_1}{M_2}\left(\dfrac{M_{2+2/D_\mathrm{f}}}{M_2}\right)^{D_\mathrm{f}/2} (qR_\mathrm{g,z})^{-D_\mathrm{f}} & qR_\mathrm{g,z} \gg 1 \end{cases}$$

where M_n is the nth moment of the distribution

$$M_\mathrm{i} = \int N^\mathrm{i} n(N)\,\mathrm{d}N$$

N is the number of primary particles in the aggregate and $n(N)$ is the number distribution function. $R_\mathrm{g,z}$ is an average of R_g weighted by the second moment of the distribution. They performed experiments on two aerosols: TiO_2 ($D_\mathrm{f} = 1.7$) and polystyrene ($D_\mathrm{f} = 2.15$). Defining

$$C_\mathrm{M} = \frac{M_1}{M_2}\left(\frac{M_{2+2/D_\mathrm{f}}}{M_2}\right)^{D_\mathrm{f}/2}$$

they found C_{M} in the range 1.53 to 1.71 for TiO_2 and in the range 2.6 to 3.6 for polystyrene. There is evidence that C_{M} increases as the width of the size distribution increases.

For chain-like aggregates with less than 20 primary particles having size parameter less than 40 and refractive index in the range 1.8 to 2.2, Charalampopoulos and Shu (2002) found that polydispersity of the primary particle size is more important than that of the number of particles per aggregate. The assumption of monodispersity tends to underestimate the real and imaginary components of the refractive index and the number of particles in the aggregate. If the standard deviation of the distribution is greater than 0.1 the effects of polydispersity must be included in any inversion procedure. The effects of polydispersity of number can be neglected if the standard deviation of this distribution is less than 0.6, otherwise the assumption of monodispersity will underestimate the real component of the refractive index but overestimate the imaginary part.

The models used in the RGD-FA calculations normally assume that the individual primary particles are just touching. However, micrographs of soot suggest that there is overlap. This is probably caused by particles colliding and fresh soot growing over the resulting combination. Brasil *et al.* (2001) looked at this and allowed for overlapping by means of a penetration coefficient.

$$C_{\mathrm{p}} = (d_{\mathrm{p}} - d_{ij})/d_{\mathrm{p}}$$

where d_{p} is the primary particle size and d_{ij} is the distance between two touching particles. If $C_{\mathrm{p}} = 0$ the primary particles are in point contact whereas $C_{\mathrm{p}} = 1$ indicates total sintering; i.e., every couple of neighbours are merged into a single particle. As a result of their modelling they suggest a fractal prefractor given by

$$K = 1.3 \exp(2.2C_{\mathrm{p}})$$

Markel and Shalaev (2001) also deal with overlapping by proposing a renormalisation procedure that retains the radius of rotation and the total volume. This takes the form

$$\begin{aligned} d'_{\mathrm{p}} &= d_{\mathrm{p}}(\xi/2)^{D_{\mathrm{f}}/(3-D_{\mathrm{f}})} \\ N' &= N(2/\xi)^{3D_{\mathrm{f}}/(3-D_{\mathrm{f}})} \\ l' &= \xi d_{\mathrm{p}} \end{aligned}$$

where l' is the distance between particle centres. ξ is an impact parameter equivalent to $C_{\mathrm{p}} + 1$ in the above, so that $1 < \xi < 2$. Calculations suggest that the best value for ξ in real clusters is between 1.61 and 1.69. With these changes the authors claim that the coupled dipole method can be used as normal.

Elongated particles in a flowing fluid with velocity gradients will have a tendency to align in the flow (Cerf and Scheraga, 1952). Studies on the scattering by aligned aggregates have been made by Botet and Rannou (2003), using a cluster–cluster model and the coupled dipole method. The results were averaged over 128 different generated aggregates. The influence of alignment is to introduce optical form anisotropy. For small aggregates the anisotropy was very

pronounced, but it vanished in the limit of large aggregates. The polarisation falls off because it arises from interactive scattering between the dipoles. Only dipoles within a distance of about 30 monomer radii can interact. For larger aggregates there are a number of such zones which are random with respect to each other, thus resulting in isotropy.

It is a tacit assumption of the RGD-FA that the primary particles are small enough to be in the Rayleigh scattering range. If they are not, then Mie theory may have to be used. Lambert *et al.* (2000) and Thill *et al.* (2000) discuss some of the consequences of this, including the need to allow for multiple scattering within the aggregate. They propose a mean field approach to deal with this involving an equivalent refractive index.

As mentioned above, in the early stages of the flame the primary particles have not had sufficient time to form agglomerates. In this case, methods are required for measurements on individual very small particles. In principle the easiest method from a theoretical point of view is Rayleigh scattering, but here the scattering polar diagram is independent of size. It is then necessary to infer the size from a combination of absolute scattered intensity (with its attendant problems) with an extinction measurement (van de Hulst, 1957).

An alternative method is dynamic light scattering, which is synonymous with photon correlation spectroscopy. Essentially this determines the Doppler frequency shifts associated with the random motion of the particles. In turn this is a function of the diffusion coefficient and the size. Since the frequency shift is due to a mechanical process, the method has the advantage that it is independent of refractive index. Lack of knowledge of this parameter is a problem for a number of optical particle sizing methods.

Usually the frequency shifts are not measured directly but are implied through their influence on the autocorrelation function. This has been briefly reviewed by Jones (1993, 1999). The correlation function takes the form

$$S(\tau) \propto \exp\left(-2q^2 D\tau - v^2\tau^2/w_0^2\right)$$

where τ is the time delay and D is the diffusion coefficient. The second term in the brackets is due to the Doppler ambiguity caused by the finite transit time across the laser beam of width w_0 by a particle with velocity v. For particles suspended in a gas, Lamprecht *et al.* (1999) suggest that

$$D = \frac{3}{8\rho a^2}\left(\frac{mk_\mathrm{b}T}{2\pi}\right)^{1/2}$$

provided that the particles are not too large. Here a is the hydrodynamic radius, ρ is the gas density, m is the average mass, k_b is Boltzmann's constant and T is the temperature. For larger particles when the concentration is not too high the Cunningham equation

$$D = \frac{k_\mathrm{b}T}{6\pi\eta a}\left(1 + \frac{L}{a}\left[\alpha + \beta\exp\left(-\frac{\gamma a}{L}\right)\right]\right)$$

may be used, where η is the gas viscosity, L is the mean free path and $\alpha = 0.864$, $\beta = 0.29$, $\gamma = 1.25$. When L approaches zero, this equation reduces to the Stokes–Einstein formula.

Cecere *et al.* (2003) used dynamic light scattering to measure the size distribution of nanoparticles produced in the non-sooting zone of ethylene/air premixed flames. The particle sizes range from 2 to 30 nm. Also, by combining *ex situ* results and the *in situ* scattering and extinction measurements in the ultraviolet, the complex refractive index of the nanoparticles was determined. The sizes obtained from DLS were independent of refractive index, and the refractive index was obtained from the ratio between extinction and vertical–vertical scattering.

However, they assumed that the real part of the refractive index was known from previous work, and obtained for the imaginary part 0.09.

Recently, Kroner *et al.* (2003) have compared static and dynamic light scattering and concluded that static scattering is better as it does not rely on *a priori* knowledge about the flame from diffusion measurements. They note that the derivation of the Stokes–Einstein formula from the basic dynamical equations of viscous flow depends on the following assumptions and comment on their applicability.

(1) Incompressibility of the medium: the compressibility of the medium starts to have effects only at velocities comparable to the speed of sound in the medium.
(2) Infinite extent of the medium: the conditions of infinite extent are never observed in practice.
(3) Very small rate of movement: Stokes law is only valid for low Reynolds numbers. (The errors are proportional to Re: At $Re = 0.1$ the difference is about 1.7%.)
(4) Constant rate of movement: this is valid for laminar flow, but not for turbulent.
(5) Rigidity of the particles: soot particles are not flexible.
(6) Absence of slipping at the particles surface: the Stokes–Einstein-relation requires that there is no velocity step at the surface of the sphere, a thin layer of medium at the surface must be fixed to the particle.

Not all of them are perfectly fulfilled, and requirement (6) is the most severe. It is not valid for measurements in gaseous media, and the Stokes–Einstein equation must be expanded by the Cunningham coefficient. They conclude that, because of all the uncertainties associated with the dynamic method, Guinier plots (as in RGD-FA) are preferable for the determination of the radius of gyration.

A method of sizing for small absorbing particles that has received considerable attention of late is laser-induced incandescence (LII). The concept here is that the absorption of a pulse of radiation from a high power laser causes heating of the particles and thermal emission. The properties are deduced from the temporal profile of the emission, and, in particular, after the pulse the rate

of cooling is observed. This rate is inversely proportional to the mass of the particles and thus the size may be obtained. The concept originated with Melton (1984), and a recent mathematical model has been given by Michelsen (2003). The first measurements based on the temporal profile appear to be due to Will *et al.* (1995). The method has become a widely used diagnostic for the investigation of soot in combustion systems, ranging from fundamental burners to practical devices such as diesel engines.

Useful comments on the method have been given by Axelsson *et al.* (2000) and Witze *et al.* (2001). Unique features of the technique are its apparent simplicity and excellent sensitivity, estimated to be better than one part per trillion ($2\,\mu m\,m^{-3}$) (Wainner *et al.*, 1999). Studies have shown good agreement between the LII signal and soot volume fraction in flames and combustion exhausts.

Witze *et al.* (2001) comment that a number of conditions need to be satisfied for the detected LII signal to be proportional to the soot volume fraction.

(1) The probed soot should consist of single or loosely aggregated primary particles that are small compared to the wavelengths of the laser excitation and the collected LII signal (such that absorption and emission occur in the Rayleigh limit).
(2) The peak particle temperatures reached during the laser pulse are relatively insensitive to the particle diameter.
(3) The soot particle mass evaporation is either negligible or largely independent of particle diameter.
(4) The detected LII signal is dominated by thermal emission occurring during laser excitation or shortly thereafter, so that size-dependent conductance cooling does not influence the signal.

Some information supporting the validity of (1) has been obtained by transmission electron microscopy grid sampling and analysis of soot in various environments, and some data demonstrating the necessity of (4) have been reported. However, little information has been gathered relative to (2) and (3).

Because the temperatures achieved by the particles can be very high (as much as 4000 to 4500 K) evaporation can be a serious problem. Also, laser ablation of soot particles can cause apparent plateaux in the signals. Signal integration times and data collection starting times are important variables. Starting measurements after the end of the laser pulse is used to eliminate problems of scattered light and fluorescence by polycyclic aromatic species. However, this slightly biases the result towards slower cooling larger particles. This can be minimised by the use of short detection times (25–100 ns). A long wave cut-off filter may be used to eliminate C_2 fluorescence from the LII signal, though a laser wavelength can be chosen to avoid this fluorescence: 532 nm or 1.06 μm are common. The choice of detection wavelength is more complicated. Long wavelengths make detection less sensitive to particle size, but short wavelengths reduce interference from flame emission.

Lehre *et al.* (2003a, 2003b) made studies on sooting flames with known properties with the specific aim of improving the mathematical model of the process.

They note that it is well established that heat loss due to radiation is a second-order effect in LII models. Further, at temperatures below 3300 K particle–gas heat transfer is the dominant cooling process. At later times after the laser pulse and during LII experiments with low laser power densities, soot evaporation can be neglected.

Measurements by Witze *et al.* (2001) suggested that there might be problems due to convective losses and thermal annealing (graphitisation). Significant evaporation loss occurs for incident power densities above $0.2\,\mathrm{J\,cm^{-2}}$.

Axelsson *et al.* (2000) combined LII with scattering-extinction measurements. Fig. 9.12 compares results by the two techniques. There is good agreement up to about 12 mm above the burner, but then the two methods drift apart. Scattering-extinction suggests that the particles continue to grow, but LII implies that the sizes tend to become constant. The authors comment that problems with scattering-extinction include variation of refractive index and polydispersity. LII can have problems with input values to the mathematical model, changes in morphology and evaporation. However, they conclude that the major differences above 15 mm are due to aggregation.

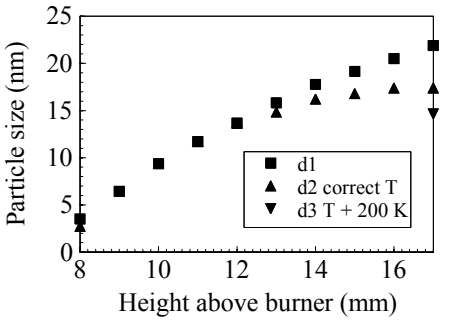

Fig. 9.12. Particle size at various heights above a burner (after Axelsson *et al.*, 2000). d1 is measured using a scattering-extinction method, while d2 and d3 are obtained using LII. The flame temperatures were measured using coherent anti-Stokes Raman spectroscopy (CARS). The point d3 illustrates the influence of varying the temperature on the LII result.

The possibility of measuring polydispersity using time resolved LII has been explored by Dankers and Leipertz (2004), using a method based on deviations from the exponential in regions where the heat loss is governed by conduction. The deviation is due to the fact that small particles have faster temperature decay than larger ones.

Snelling *et al.* (2004) deliberately kept laser power densities low to restrict soot particle temperatures to below 3500 K so that complications due to vaporisation could be avoided. To further ensure this, soot particle temperatures were measured by optical three-wavelength pyrometry. Particle sizes were obtained by sampling and electron microscopy. The fractal nature of the aggregates was

allowed for by modifying the heat transfer model by using an effective projected area equivalent diameter given by

$$d_{\mathrm{a}} = \left(\frac{N}{K}\right)^{1/2D_{\mathrm{f}}} d_{\mathrm{p}}$$

where K and D_{f} are the area pre-factor and fractal dimension. From their results they found $E(m) = 0.395$ without dispersion and 0.42 with linear dispersion, which are somewhat higher than previous authors. For example, Krishnan *et al.* (2000) reported $E(m)$ to be in the range 0.24 to 0.28 across the visible spectrum, broadly in agreement with other published values.

Another interesting technique that may prove very sensitive at low particle volume fractions is cavity ringdown (CRD) (O'Keefe and Deacon, 1988). In this a laser pulse is launched into a cavity formed by two mirrors that contains a cloud of absorbing particles. The distance between the mirrors is large in comparison to the pulse length, so that the pulse may be considered to travel back and forth many times leaking a little intensity every time it hits a mirror. On each pass there is some loss of intensity due to scattering and absorption, the consequence of which is that the pulse decays in time in a manner determined by the extinction coefficient of the particles. The CRD technique measures a characteristic exponential decay of the signal, a reference being obtained in the absence of the flame. The soot volume fraction, f_{v}, is obtained from the decay rate with the flame on, given by

$$\frac{k_{\mathrm{ext}} f_{\mathrm{v}} L}{\lambda} = \left(\frac{1}{c\tau} - 1 + R\right)$$

where $K_{\mathrm{ext}} = k_{\mathrm{ext}} f_{\mathrm{v}}/\lambda$ and l is the spacing between the cavity mirrors of reflectivity R. L is the path length in the flame, c is the speed of light and τ is the time constant of the exponential decay.

A discussion of some aspects of CRD has been given by van der Wal and Ticich (1999), who were interested in its use for the calibration of LII, which is strongly dependent on experimental conditions and details of the mathematical model. Commonly used calibration methods include extinction measurement and gravimetric sampling, but these are not effective at low soot volume fractions. Potentially CRD can measure down to one part in 10^9. Also, in CRD the laser power densities are much less than those observed to cause soot evaporation: typically $0.25\,\mathrm{J\,cm^{-2}}$ at 532 nm and $5\,\mathrm{J\,cm^{-2}}$ at 1.06 μm. Another advantage of CRD is that it yields integration over path length directly. A disadvantage is that it will not give spatially resolved results, though it gives good spatial resolution in two dimensions. It suffers similar problems to LII in the presence of scattering by large aggregates and fluorescence.

Moreau *et al.* (2004) combined LII and ringdown spectroscopy to examine soot and fluorescence of polyaromatic hydrocarbons (PAH). At 1.064 μm there is no PAH fluorescence, whereas at 532 nm both exist. They were able measure soot volume fractions down to 5 ppb.

Finally, it was noted above in passing that multicolour methods were employed to measure soot temperatures. The radiative emission by particles depends upon the emissivity of the cloud and the temperature. To determine these two unknowns, Hottel and Broughton (1932) devised a technique in which the radiation was measured at two wavelengths. Since that time the method has been widely used in a variety of ways. For two recent studies, the reader is referred to Jenkins and Hanson (2001) and Cignoli *et al.* (2001). The former authors compared absorption and emission at two wavelengths 830 and 1300 nm. The sources were modulated diode lasers. Using their method they reduced the error compared to normal two-colour pyrometry from ±50 K to ±20 K. The method is most suitable for soot volume fractions greater than 10^{-7}. Cignoli *et al.* (2001) imaged a flame onto a CCD camera at two wavelengths and were able to produce two-dimensional images of the temperature field.

9.3 Liquid fuel sprays and pulverised fuel (PF)

Both liquid and solid fuels (coal) are commonly burned in the form of small drops or particles. This is to increase the surface per unit mass, and, so, the evaporation and burning rates. For liquids, it is needed to understand the atomisation process and to follow the behaviour of the spray as a function of time and space. To this end, it is necessary to measure drop sizes and concentration (for evaporation and combustion rates) and velocity (for mass throughput). The spatial distribution of the drops is also important, as this will influence the way in which the fuel vapour mixes with available oxidant.

Among the practical problems that may be encountered are high concentration and particle shape. The former will influence whether a light beam can penetrate the spray, and can result in multiple and interactive scattering. Shape is a factor because most instruments assume that the particles are spherical. Also, the shape of the drops may affect the combustion process.

Optically the drops in a spray or PF cloud are mostly medium to large in size. This fact influences the techniques that can be used. The two most common are methods based on laser diffraction and those based on laser Doppler anemometry (LDA). A powerful version of the latter is phase Doppler anemometry (PDA).

The simple principle behind the diffraction method lies in the Airy equation

$$\sin\theta = \frac{1.22\lambda}{d}$$

where d is the particle diameter and θ is the angle of the first minimum in the diffraction pattern. There has been an extensive literature on this technique, including direct inversion to find the size distribution, the use of Mie theory to avoid error due to the diffraction approximation, the influence of shape and refractive index and the limits to particle concentration and corrections for multiple scattering. Several commercial instruments are available that make use of this fundamentally simple concept. A brief review was given by Jones (1993) with a later update (Jones, 1999).

There are two important limits to diffraction particle sizing. The method essentially assumes single scattering and so there is an upper limit to concentration before multiple scattering sets in. This is usually thought to be for transmissivities of the spray of less than 50%. Also, diffraction is an integral method and requires a minimum number of particles to achieve a sensible result for the size distribution. This is usually thought to be the concentration below which the transmissivity of the spray is more than 90%. Otherwise, integration over a long time may yield a result but this is not always satisfactory.

A number of studies have been conducted on ways to deal with high concentrations. Examples include the work of Cao *et al.* (1991) who divided the scattering volume into a series of thin, single scattering slices and calculated the progress of light through the system. They claimed to be able to extend the applicability of the diffraction method down to transmissivities of the order of 10%. Hirleman (1988) used a statistical approach to predict small angle scattering through a dense system.

More recently, Kokhanovsky and Weichert (2001a) have reviewed a number of small angle multiple scattering solutions and concluded that they are essentially all the same. Their paper provides a good discussion of the derivation of small angle solutions from the radiative transfer equation. On the basis of an azimuthally independent phase function, they obtain

$$I(\tau,\theta) = C\,\mathrm{e}^{-\tau}\int_0^1 \left[\exp\left(\frac{\tau g(z)}{2}\right) - 1\right] J_0(bz)z\,\mathrm{d}z$$

where $b = 2x\theta$, $C = \left[(2x^2)/\pi\right] I_0$, $x = \pi D/\lambda$, τ is the optical depth or turbidity and

$$g(z) = \frac{2}{\pi}\left[\arccos(z) - z(1-z^2)^{1/2}\right] \qquad z \le 1$$

For monodisperse particles they find that the size can be obtained from

$$d = \frac{\lambda h(\tau)}{2\pi\theta_0}$$

where $h(\tau) = 3.23614 + 0.0768\tau + 0.00937\tau^2$. The angle θ_0 is where the relative intensity falls to 0.5. The result is applicable for turbidities up to 6.5; that is transmissivities down to 0.15%. The authors also suggest an analytical solution for polydispersions with a gamma function size distribution. This equation has been proved experimentally by Kokhanovsky *et al.* (2001b).

Two novel diffraction instruments have been described by Gianinoni *et al.* (2003): one for very high concentrations and one for very low. In the former case the design incorporated an insertion probe with an optical configuration that made it suitable for the characterisation of high concentration particle laden flows (e.g. for pulverised coal downstream of the grinding mills) in the size range 3–300 μm. The authors noted that for high concentrations there are the following requirements:

(1) The measuring probe outer diameter must be minimised to reduce its invasiveness.

(2) The test region should be sufficiently short to prevent multiple scattering, but large enough to let the particles pass through without modifying their trajectories.
(3) The optical windows must be kept clean.

The most crucial requirement is the first one since the multi-element array sensor that collects the scattered light cannot be miniaturised without worsening its technical specifications. The minimisation of probe diameter was achieved by utilising an innovative optical scheme based on the use of a selfoc rod lens, originally developed for endoscopic applications. This lens collects the scattered light from the test region and brings it to the detector positioned far from the scattering volume outside the duct. The optical scheme of the probe is illustrated in Fig. 9.13.

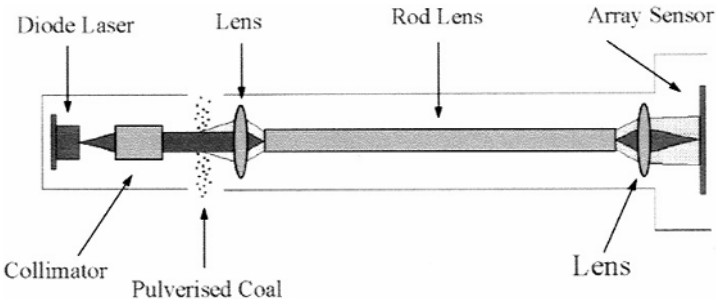

Fig. 9.13. Optical scheme of the probe developed for monitoring high concentration particle laden flows (Gianinoni *et al.*, 2003).

For low concentrations the scattered intensity is weak and particles on windows and lenses may make a significant contribution to the light received. To minimise this problem the authors reduced the number of optical components and used a converging illuminating beam focused onto a stop blade on the lens. The optical system is seen in Fig. 9.14. In this way, particles on the lens surface are no longer directly illuminated by the laser beam and do not generate undesired scattered light contributions. The authors recognise that this convergent system means that the received scattering pattern is no longer independent of the positions of the particles and discuss means of dealing with this problem. Their design enabled operation at extinction values as small as 10^{-5} in the size range 0.9–90 μm.

A deceptively simple method of measuring particle size is to measure the scattered intensity. It is expected that this will increase with volume for Rayleigh-sized particles and with area for larger particles. This is the basic principle lying behind particle counters, for example. Brief reviews of intensity measuring instruments were included in the papers by Jones (1993, 1999).

In practice, there are a number of problems with intensity measurement. First, being absolute, calibration is needed against some standard source. Also

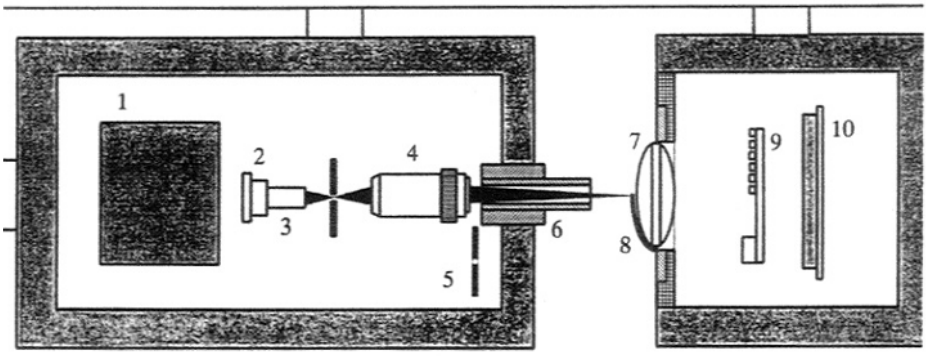

1 = Electronic box
2 = Laser Diode
3 = Selfoc Lens
4 = Microscope Objective
5 = Calibration Pin-hole
6 = Protective Pipe
7 = Collecting Lens
8 = Metallic Shell
9 = Annular Array Sensor
10 = Preamplification Card

Fig. 9.14. The measuring head of the particle sizer for low particle concentrations regimes (Gianinoni *et al.*, 2003).

the actual measured value is proportional to the strength of the illuminating light beam, so this needs constant monitoring. In combustion systems problems arise due to coating of input and output windows which changes the illumination and the transmission of the scattered light. Extinction losses along the optical paths are problematic for the same reason. Finally, there is a difficulty with the gaussian intensity profiles of laser beams since the illumination will depend upon which part of the beam the particle passes through.

With these considerations in mind it is preferable to use relative measurements as in the methods discussed below. Nonetheless, considerable effort has been devoted to particle counting devices and work continues. For example, Umhauer *et al.* (2000) have devised an instrument to enable sizing of particles in hot gases up to 1000°C. Uniform illumination of the test space is achieved by the use of a high-pressure xenon lamp as the light source. The use of a broadband source also overcomes fluctuations in the scattered intensity due to detailed variations with size and wavelength and also minor shape effects. The instrument also features a new scattering volume definition control system obtained using two masks with square apertures projected to have images vertical to each other. Protection against heat and dust precipitation is provided by having a long working distance.

A novel method of avoiding the problems associated with the gaussian profile by making use of it has been proposed by Castagner and Jones (2004). In this technique a prism was used to divide the incident beam into two parallel

gaussian beams with orthogonal polarisations. The amplitudes of the two intensities and the relative delay between them are indicative of the particle direction and velocity. Having obtained the direction of travel of a particle, its size can then obtained from the scattered intensity using Mie theory and a calibration with particles of known size. A main advantage of the method is its simplicity and lack of need of alignment. One difficulty with the method arose with non-spherical particles that cause cross-polarisation in the scattered light. This led to cross-talk between the two measured intensities. To avoid this, it was suggested that the same technique might be employed using two wavelengths instead of polarisations.

The use of LDA for particle sizing began with the papers by Farmer (1972, 1974) and Fristrom *et al.* (1973). It was recognised that an obstacle with circular cross-section traversing the interference pattern formed by two crossed laser beams would generate scattered light that oscillated in time. The frequency of this oscillation would give the velocity of the particle. However, the visibility of this signal varied depending upon the particle size and became zero for certain specific sizes. Various authors pursued this method, but it was found to suffer a number of disadvantages. The most significant of these was there are a series of zeros and the size measurement was not unique. Eventually the technique was supplanted by phase Doppler anemometry (PDA).

PDA was proposed by Durst and Zaré (1975) and came into prominence following the work of Bachalo and Houser (1984) and Saffman *et al.* (1984). In this technique the oscillatory signal is measured at a number (most usually three) of closely spaced angles, normally at about 30° (forward) or 150° (backward) out of the plane formed by the two laser beams. The phase difference between the observed oscillations is then found to have a linear dependence on particle size. Multiple angles are used to overcome the problem distinguishing phase changes greater than 2π and, thus, increase the dynamic range, typically 0.5 to 3000 μm at concentrations up to 10^{12} particles per cubic metre.

A possible way of eliminating the phase uncertainty and the need for a third detector was suggested by Onofri *et al.* (2002) in which they use multiple laser beams producing a range of spatial frequencies in the test space. To eliminate complexity of the resulting fringes the authors restricted their experiments to two overlapping fringe patterns between which interference was suppressed. This was achieved either by introducing an additional path length into one beam pair that was greater than the coherence length, or by cross-polarising the two beam pairs relative to each other.

The diffraction method makes a measurement over a volume containing the scatterers and results in a spatial average. However, PDA is a particle counting method and yields a temporal average. Thus, determination of velocity is also necessary to correct the measured size distribution. In addition, the accuracy of the measured distribution depends upon collecting a sufficient number of measurements to be statistically significant. This will be of particular importance in low concentration flows, as pointed out by Widmann *et al.* (2001a). It is then necessary to compromise between collecting a large number of samples for adequate statistics and practical data acquisition times. They investigated

the effect of insufficient sample statistics on the calculated probe area, and the resultant uncertainty in the volume flux measurement. From a range of experimental results they were able to propose corrections that resulted in statistically significant improvements.

A further problem is that there can be a trajectory error. This is because the effective size of the gaussian test space grows as the particle size increases. At the outer limits of the test space the low illumination is compensated by the higher scattered intensity. This problem is discussed, for example, by Xu and Tropea (1994), Hardalupas and Taylor (1994) and Albrecht *et al.* (1996). Zaidi *et al.* (1998) found that PDA, owing to the trajectory error, consistently gave larger drop sizes compared to those measured by the diffraction technique. Other trajectory problems associated with large particles have been tackled by Tropea *et al.* (1996) who devised a dual mode PDA, which used two orthogonal PDA beam pairs to better define the test space. More recently, Aisa *et al.* (2002) discussed the application to particles with three-directional paths. They commented that accurate measurements could be achieved if an integral method of calculation over the effective probe volume and an efficient autocalibration process are employed.

Strakey *et al.* (2000) have also examined methods of reducing many of the measurement errors. In particular, they mention the use of combined phase and scattered intensity validation methods and discuss the importance of the ratios of the angular spacing of the detectors. They also note that the use of small test space volumes can greatly improve measurement reliability in dense sprays for which multiple particle occurrences in the probe volume will affect the measurement.

The shape of the test space is generally spheroidal. Thus the size of this volume will depend upon the direction of the particle's trajectory, as noted by Yu and Rasmuson (1999). They developed a mathematical description of this effect and showed it may introduce very large errors. In the case of complex 3-D flows the projected area variation leads to a direction bias in the determination of time-averaged values of the flow. They proposed a system employing three colours, two producing independent LDA test volumes and one simply acting to define the centre of the volume. They then found that errors could be made very small.

In addition to the trajectory error there is also a slit effect, which arises from the use of a slit in the receiving optics to define the length of the measuring volume. This has been discussed by Zaidi *et al.* (1998), who pointed out that this can cause great error because for particles passing along certain trajectories the corresponding length of the measuring volume can be much longer than expected.

Problems due to particle refractive index and variations in temperature in the test space have been examined by Schneider and Hirleman (1994) and Köser and Wriedt (1996). The influence of nonspherical particle shape has been investigated by Doicu *et al.* (1996), who found that for spheroids with an eccentricity of only 0.05 there would be a phase error of 5%.

A unique new design for a PDA instrument has been described by Blondel *et al.* (2001). They note that the use of PDA in industrial environments is limited by the need for two optical access points. To overcome this they describe a monoblock instrument suitable for diesel fuel sprays that will operate with only one window, and is also compact and inexpensive. They discuss three feasible configurations, each with specific advantages and limitations:

(i) Collection in the Alexander's dark band. In this case only reflected light is collected. The measurement is then insensitive to the refractive index of the particle, but the amount of collected light is the smallest among the three possible configurations. The distance between the probe volume and the lens is also the smallest: about equal to the lens diameter.
(ii) Collection of light at the rainbow angle. Here the refractive index must be known for proper processing, but the signals are the most intense among the three configurations. However, this configuration can only be used when the particle diameter is smaller than the beam diameter. The working distance is equal to about 1.5 times the lens diameter.
(iii) Far backward collection. In this situation scattering can be dominated by three contributions depending on the particle location in the control volume: externally reflected light, internally reflected light with an impact parameter close to the edge of the particle or internally reflected light with an impact parameter close to the particle centre. The authors selected this configuration, mainly because it allows the use a large working distance: about 2–3 times the lens diameter. However, it does have the disadvantage that the different scattering modes have to be discriminated.

The design of the instrument is illustrated in Fig. 9.15. The incident beams were focused by a lens of 2 cm diameter with a focal length of 60 mm. The beam waist diameter was then as small as 40 μm and the scattering angle was 165°. These values were chosen to optimise the instrument for measurements inside a car engine.

A similar scheme for making LDA measurements in the backward direction has been proposed by Tillwick *et al.* (1999). Here the single lens both transmits and receives, but the detectors are on the periphery of the lens.

Another proposal for enabling PDA measurements at a single angle has come from Yokoi *et al.* (2001). In their technique, light scattered by a moving particle is divided into two rays that are detected with different polarisation angles to transmit dominantly reflected or refracted rays. To explore the optimum polarisation condition, they numerically investigated the phase–diameter properties in relation to polarisation angles by using the geometrical optics approximation and generalised Lorenz–Mie theory. They performed experiments with polystyrene and glass particles to verify the usefulness of the proposed method. They claim to be able to size particles up to 50 μm, but the absorption along the refracted ray must be extremely low to avoid unbalanced intensities.

An interesting situation arises when the drops are much larger than the diameter of the laser beams and the test space. In this case the drop scatters two pulses as it passes – a so-called 'dual burst'. The reason for this is that there

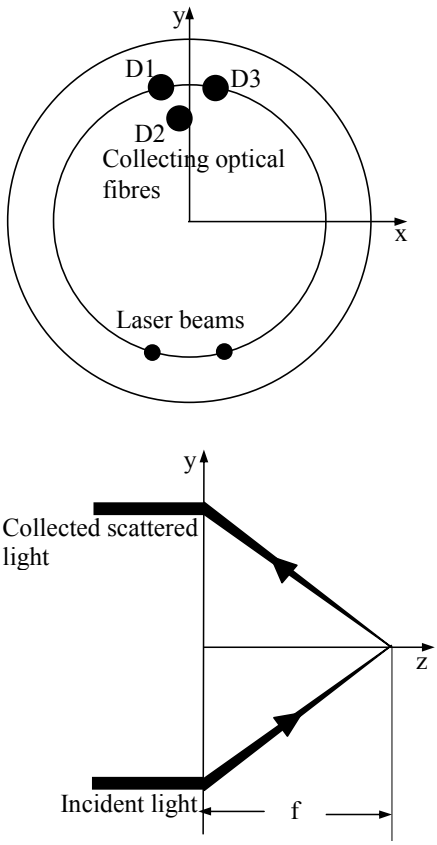

Fig. 9.15. Schematic diagram showing the geometry of the monoblock backward PDA. The top picture shows the positions of the incident laser beams and of the scattered light collecting optical fibres relative to the projecting lens. The lower picture shows the incident laser beams being brought together at the focus of the lens and of the collected scattered light originating from that point (after Blondel *et al.*, 2001).

are effectively two ray paths, as suggested by Fig. 9.16. One ray is reflected by the surface of the drop and the other is refracted through. This was originally noted by Onofri *et al.* (1996a, 1996b), who showed that, for a known particle size, the refractive index could be measured from the delay between the two pulses. Further, if the drop is absorbing the extent of absorption can be obtained from their relative heights. Thus the full complex refractive index could be obtained.

Of course, the loss of light along the refracted ray may not be caused by absorption but due to scattering or extinction loss. Thus, Onofri *et al.* (1999) proposed that the concentration of small inclusions within a drop may be determined using the dual burst technique, the properties of the main drops being obtained from reflected phase and frequency. They noted that the ratio of the refracted to the reflected signal amplitudes changes significantly with particle

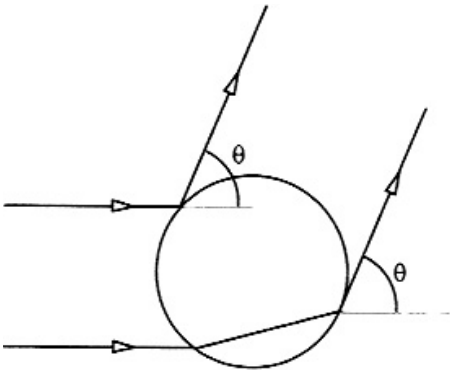

Fig. 9.16. Ray diagram illustrating the principle of the generation of two pulses by a spherical particle passing through a narrow laser beam (after Onofri *et al.*, 1996a, 1996b).

location perpendicular to the expected main direction. This is a trajectory effect that needs to be corrected for, and they discuss means of correction of this based on a gaussian laser beam. At low internal concentrations simple Beer-type transmission may be used. However, at higher concentrations multiple scattering occurs and a Monte Carlo model was applied. They performed experiments on cylindrical jets to prove the method, there being no confirmation for spherical drops.

Widmann *et al.* (2001b) have commented that the presence of burst splitting will lead to false counting of particle number and, hence, to incorrect determination of particle flux. They presented several techniques to identify the occurrence of burst splitting events, and discussed the impact of such events on the measurements. They confirmed the significance to flux measurements, but found that that the impact on size and velocity distributions was much weaker.

Damaschke *et al.* (2002a) have proposed a similar method to burst splitting to enable particle sizing in the backscatter direction at angles greater than 140°. Because of the different path lengths between the reflected and refracted rays there is a time delay between the two pulses that is proportional to the particle size. The two pulses can be separated when the particle size is rather greater than the width of the incident laser beam. Generally, the separation of the fractional signals in time will be determined by the particle size, the relative refractive index, the particle shape, and the particle velocity. Even for spheres it is necessary to know the velocity to extract the size. This can be achieved by using two laser beams in a LDA arrangement so that the velocity can be measured from the signal modulation frequency.

When it is desirable to measure the sizes of inclusions inside drops (as in a liquid containing fuel particles or soot, for example) there may be confusion caused by the presence of bubbles. Thus it is necessary to have a means to distinguish between these. Naqwi and Durst (1991) noted that the relationships between phase and size for refraction and reflection indicate that a change in

the relative refractive index around the value of unity will change the sign of the phase shift. A recent paper by Ziema *et al.* (2001) proposes a method based on this observation in which the interference fringes in the test space are made to move using Bragg cells. Separate LDA optics detect the direction of motion and velocity of the particles or bubbles. The PDA detector then monitors the sign of the phase shift.

It was mentioned above that even quite small deviations from spherical shape could result in significant errors when using PDA (Doicu *et al.*, 1996). For sizing and characterisation of solid particles, such as coal, it must be recognised that they are rarely, if ever, spherical. A modification to PDA that is capable of measuring velocity, size and shape is shadow Doppler velocimetry (SDV). In this, the particle passes through the fringes formed by two laser beams as in regular LDV and an offset detector measures the velocity from the frequency of the signal in the usual way. In addition, however, an extra lens images the particle onto a plane where a linear array detector is situated. As the shadow image of the particle crosses this detector the array gives the length of cross-section. The shape of the cross-section is then determined after the whole particle has traversed the array. A diagrammatic representation of the equipment is seen in Fig. 9.17.

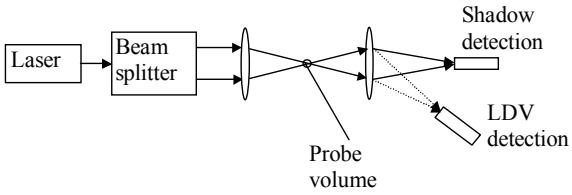

Fig. 9.17. Diagram illustrating an optical layout for shadow laser Doppler measurements (after Doicu *et al.*, 1996).

SDV was originally developed by Hardalupas *et al.* (1994) and Morikita *et al.* (1995). Concern over the influence of particles in out of focus planes on size determination (Jones *et al.*, 2002) led to a detailed analysis for two incident gaussian beams by Ren *et al.* (2003). From an extensive series of numerical computations, the behaviour of a shadow Doppler velocimeter was simulated, including the location of the image as a function of the angle between the two incident beams.

Morikita *et al.* (1995) pointed out that SDV could potentially be used to measure some extra properties of particles, such as the trajectory angle in a plane perpendicular to the optical axis. This information is especially important when precise particle shape reconstruction and flux measurements are required. However, Matsuura *et al.* (2004) state that the accuracy of the trajectory angle measurement by normal SDV is not sufficient for particles passing near the centre of the probe volume, with respect to the direction parallel to the optical axis. These authors replaced the single line array detector with two parallel

arrays of optical fibres. With a known separation of the two arrays and the measured shift of particle position can be established. In addition, stereoscopic SDV was developed by installing the arrays separately in two independent SDV optical systems. This provided stereoscopic views of the particles and enabled measurement of the trajectory angle in a plane parallel to the two laser beams, which is important for accurate particle flux estimation (Morikita *et al.*, 1997).

Rheims *et al.* (1999) proposed a system similar to shadow Doppler, except that the particle was not imaged onto the detector. In their set-up the line scan sensor covers an off-axis angular range from 30° to 60°. It is arranged in this position for two reasons: the intensity of scattered light is at maximum, and the scattered light shows distinct modulations with a clear variation with particle size. The authors provide examples of sizing homogeneous spheres and those containing emulsions.

A major advantage of LDV and PDA is that there is very good spatial resolution. However, this implies that measurements need to be made at a large number of different sites in order to obtain a spatial distribution of properties of a spray. A way to partially avoid this problem while retaining good spatial resolution in one dimension is to use a laser sheet as the illuminating source. It is then only necessary to move the sheet along one axis in the spray.

The laser sheet is formed by the use of cylindrical lenses, one of the earliest descriptions of its use being by Long *et al.* (1979). Conventional light scattering measurements can be made out of the sheet, but to obtain results over the body of a spray it has become common to observe images of the particles, either directly or by inference. Evidently the image is limited by the quality of the optical arrangement, so the method will be most suitable to particles above some minimum size.

The image of an opaque particle can be recorded directly and image analysis software can be used to retrieve the size. In principle the same is true for a transparent drop, but in that case the situation is complicated by the presence of glare spots. These arise from a reflection from the drop surface and from one refracted path through the liquid; rather in the way that dual Doppler bursts are produced for very narrow beams. These bright spots will dominate an image but can also be used for sizing. For a given scattering angle and a spherical drop the spots will always appear at the same angular position on the surface and, so, their separation is proportional to diameter. Alternatively, the image can be deliberately recorded in an out-of-focus plane. In this case the glare spots act as point sources and interfere at the detector. The fringe separation is then inversely proportional to the diameter of the drop. Fig. 9.18, after the work of Maeda *et al.* (2002), shows how the two planes may be recorded.

Burke *et al.* (2003) have described a holographic technique that is a mixture of both approaches. They state that larger droplets are best analysed at the image plane where the glare spots are recorded. However, smaller droplets are easier to analyse in the out-of-focus method and the fringe patterns are recorded. Photographic techniques allow only one of these planes to be chosen and are therefore not suitable for a range of drop sizes, whereas holography allows recording in

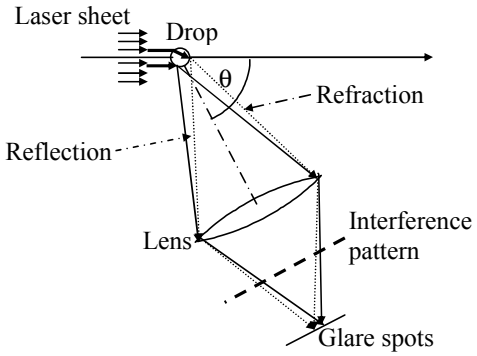

Fig. 9.18. Diagram showing the optical layout for either imaging the glare spots from a transparent sphere, or their interference pattern (after Maeda *et al.*, 2002).

depth. Unfortunately holography often suffers from low sensitivity, and in this work this problem was overcome using digital recording and analysis.

Early work on the interferometric method was reported by Roth *et al.* (1991) who gave an analysis for the angular fringe spacing on the form

$$\delta = \frac{2\lambda}{d} \frac{1}{\cos\frac{\theta}{2} + \frac{m \sin\frac{\theta}{2}}{\sqrt{m^2 + 1 - 2m\cos\frac{\theta}{2}}}}$$

where θ is the scattering angle, d is the diameter of the drop, m is the refractive index and δ is the angular fringe spacing. Later, for a scattering angle of 90°, Golombok *et al.* (1998) derived the approximate form

$$\delta \simeq \frac{2\lambda}{d} \frac{m}{m+1}$$

The full equation and the quality of the approximation were compared with Mie theory by Mounaim-Rousselle and Pajot (1999). The result is seen in Fig. 9.19. The authors claim that the significance of refractive index is small, especially at large particle sizes.

Maeda *et al.* (2002) and Kawaguchi *et al.* (2002) refer to the interferometric method as 'interferometric laser imaging for droplet sizing', or ILIDS. They note that conventional ILIDS, which observes a circular image with fringes, has difficulties at high concentration in evaluating the fringe spacing accurately owing to overlapping of the circular images. They propose a modification in which the circular images are optically compressed using cylindrical lenses. They then have the form of linear images that are horizontally defocused and vertically focused keeping the information of the location and the size of droplets. Damaschke *et al.* (2002a) derived limits on concentration to avoid overlapping images in ILIDS. They expressed their result in terms of an overlap probability coefficient as a function of number density and the parameters of the optical system.

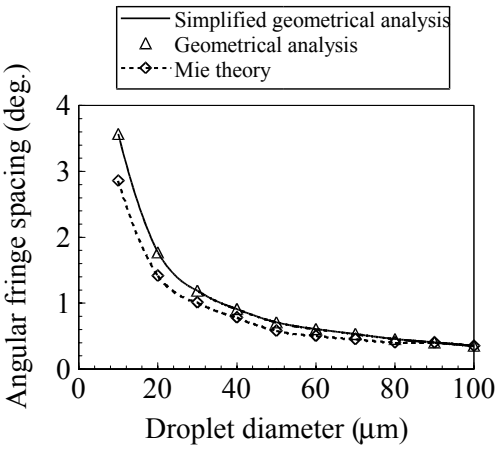

Fig. 9.19. Comparison of various calculations of the fringe spacing due to transparent drops of iso-octane as a function of drop size. The refractive index of the drops is 1.39 and the illuminating wavelength is 0.532 μm (after Mounaim-Rousselle and Pajot, 1999).

A variation on imaging was originally described by Wang and Tichenor (1991) that involved imaging particles onto a variable frequency grating. For a certain particle size roughly equal to the grating spacing the signal fell to a minimum. Velocity can also be determined. Card and Jones (2003a) developed the method by using a laser sheet that was trimmed to have a 'top hat' intensity profile both to provide uniform illumination and to restrict the depth of field. The predicted response was obtained by a Fourier analysis of a circle crossing the square wave grating, and comparison with experiment is shown in Fig. 9.20. Using this method irregular particles down to approximately 3.8 μm could be sized, the restriction being mainly due to the limited resolution of the optical system. The method was successful for certain particle types that were rough or irregular, partly absorbing or translucent. It was not successful for transparent spheres that display glare spots in the image, or other particles that produce localised regions of high brightness.

A technique showing promise is planar fluorescence imaging, which was originally suggested by Yeh *et al.* (1993). The fundamental principle behind this is that while scattered intensity is proportional to the area of the particle ($I_{\mathrm{sca}} = K_1 d^2$) the fluorescence intensity depends upon the volume ($I_{\mathrm{fl}} = K_2 d^3$). For a size distribution the average squared and cubed diameters are found and the ratio is

$$\frac{I_{\mathrm{fl}}}{I_{\mathrm{sca}}} = \frac{K_2 \overline{d^3}}{K_1 \overline{d^2}} = K_3 d_{32}$$

so that the Sauter mean diameter is measured directly. Evidently, K_1 depends upon the refractive index of the drop while K_2 is a function of the particular fluorescent dye used and its concentration. The presence of the dye may influence the refractive index of the drop if the concentration is too large, so some care

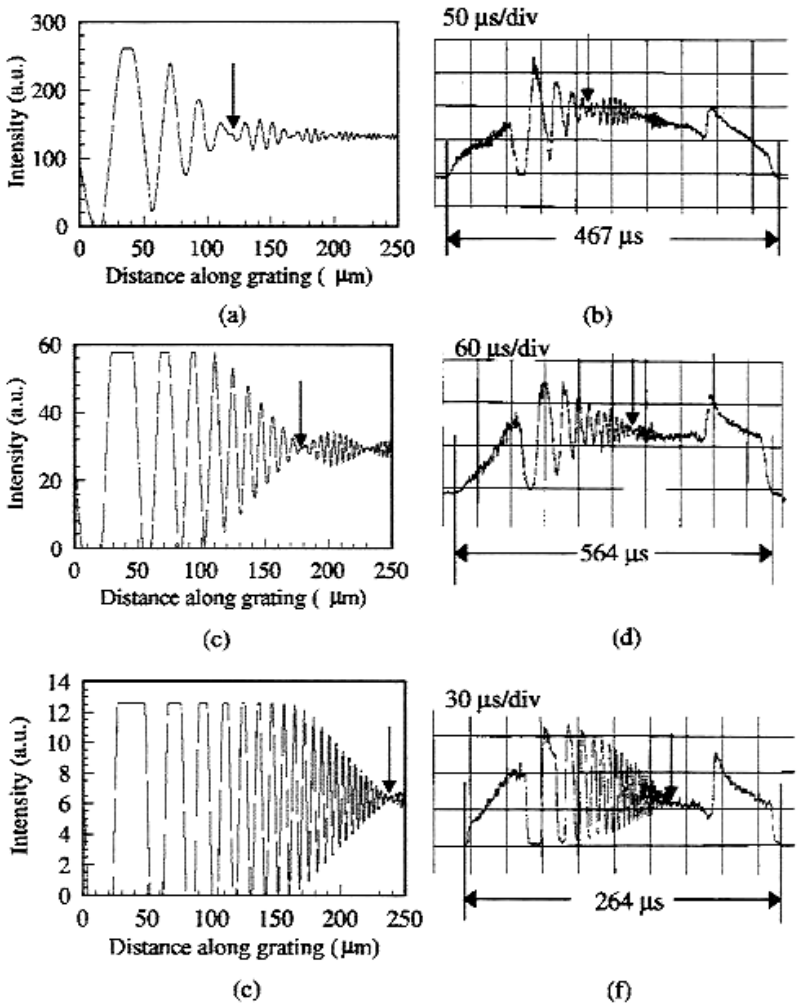

Fig. 9.20. Comparisons of theoretical predictions (a, c, e) and experiments (b, d, f) for spheres (circles) crossing a variable square wave grating. The arrows indicate the positions of the first minima (Card and Jones, 2003a).

is required. While, in principle, the functions for K_1 and K_2 can be calculated, other complications mean that calibration is required to find K_3. PDA has been used for this purpose.

Using this technique, Le Gal *et al.* (1999) produced laser sheet images of the distribution of Sauter mean diameter in a cross-section of a spray. Further, Jermy and Greenhalgh (2000) found that they could successfully measure size in a spray that was too dense for PDA. The uncertainty of the measured drop sizes was estimated at $\pm 7\%$, neglecting multiple scattering. However, it was acknowledged that multiple scattering was a large source of uncertainty.

An iterative correction scheme to allow for multiple scattering based on the Beer–Lambert law was proposed by Abu-Gharbieh *et al.* (2000). Jermy and Allen (2002) also explored the potential influence of multiple scattering using a Monte–Carlo photon transport model for transmission from the laser sheet through a half cone representing the rest of the spray. Up to 50% of the photons may be multiply scattered, but because forward scattering dominates for large particles the image is little affected. For smaller or absorbing particles the effects are more serious.

Domann and Hardalupas (2001) and Domann *et al.* (2002) have examined fluorescence intensity distributions within droplets both by geometrical optics and Mie theory. The nature of the internal structure was verified by experimental observations. A quantitative comparison of volume integrated energy results showed that for the investigated range of absorptivity Mie theory calculations lead to results that are ≈30% higher than in the geometrical optics case. Surface waves were identified as the cause for the discrepancies between the two as they cause high energy density in the rim region of the droplet images. However, the two methods gave good agreement on the general relationship between the volume and fluorescence intensity, as can be seen in Fig. 9.21. In both cases the fluorescent signal varies as $d^{2.96}$ so that the difference between Mie theory and geometrical optics can be corrected by a simple constant.

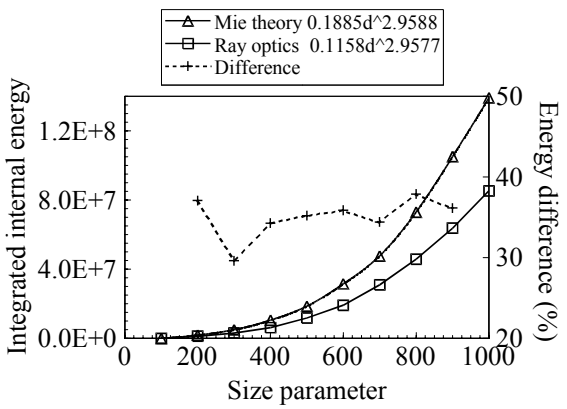

Fig. 9.21. Relationship between the volume and fluorescence intensity from a laser irradiated drop based both on Mie theory and ray optics. The refractive index of the drops is 1.333–i10^{-5} (after Domann *et al.*, 2002).

Measurements on heated water drops containing rhodamine 6G were made by Duwel *et al.* (2004) which showed that after some initial variation due to oxygen penetration, the fluorescence remained constant. This suggested that the signal is independent of drop size during evaporation and that the dye totally accumulates within the drop. In consequence, they concluded that this dye could not be used for size measurement. However, the ratio of Mie to fluorescence signal

is very sensitive to small changes in the drop surface. Potentially this could yield important information about evaporation and spray break up.

Boedec and Simoens (2001) made simultaneous measurements of velocity of droplets and ambient gas in the case of two-phase flow mixing. The basic principle of separation was to seed the ambient gas with micrometre particles and to add fluorescent dye to the liquid. The velocities were obtained using particle image velocimetry (PIV), while the fluorescence yielded the Sauter mean diameter.

An overview of fluorescence techniques in combustion systems with particular relevance to gas turbines has been provided by McDonel and Samuelsen (2000). In spray-fired systems there is a need to discriminate between phases in order to study fuel–air mixing. Numerous methods have been developed to provide information on the liquid drops, as are reviewed in this chapter. The measurement of fuel–air mixing in sprays is complicated by the need to discriminate the vapour from the liquid droplet phase. One strategy for measuring the vapour concentration in the presence of droplets is the use of light extinction. By using absorption lines at 3.39 μm for hydrocarbons in conjunction with a non-absorbing wavelength (e.g. 0.6328 μm) the vapour concentration along a line of sight can be deduced. Since the droplets scatter both wavelengths, but only the 3.39 μm wavelength is absorbed by vapour, the relative transmission of the two wavelengths yields the amount of extinction due to the presence of the vapour alone. However, there is evidence that this method may be limited to dilute sprays. Some of the practical difficulties in the application of (laser induced fluorescence) LIF in fuel–air sprays are discussed by de Sercey *et al.* (2002).

Apart from size, the refractive index of the drops in a spray is of interest. This is partly to identify the constitution of the liquid, but also to determine the temperature of the drop from the known variation of refractive index (Roth *et al.*, 1990). A technique that has been employed in this context for large drops is measurement at the rainbow angle. According to ray optics the angle at which the rainbow occurs is independent of size, which removes this variable. In addition the intensity of the scattered light is high at the rainbow. These properties make the rainbow method sound very attractive.

In reality the rainbow is only independent of size for diameters in excess of 60 μm (Massoli *et al.*, 1993). Also, a serious drawback in flames is that a temperature gradient is likely to exist within a fuel drop that will affect the rainbow position and can lead to very significant errors (Schneider *et al.*, 1993). However, Anders *et al.* (1996) using a geometric optics analysis suggested that if the surface temperature was known independently, then the rainbow could be used to measure the internal temperature gradient.

van Beeck *et al.* (2003) state that rainbow measurements on water sprays yield sizes between the normal mean and Sauter mean diameters (as measured by PDA) and temperatures correct to within a few degrees. Apart from temperature gradients, they have pointed to two other problems, namely droplet asphericity and a ripple structure that strongly perturbs the rainbow interference pattern from which one deduces the droplet's parameters. They resolved these last two difficulties by the use of global rainbow thermometry (GRT),

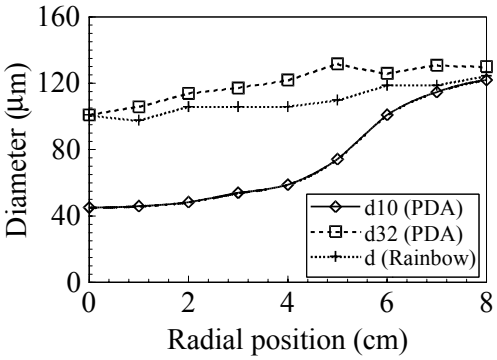

Fig. 9.22. Comparison of the mean size of drops in a fan-shaped water spray obtained from rainbow measurements with mean sizes obtained using PDA (after van Beeck *et al.*, 2003).

which was originally proposed by van Beeck *et al.* (1999). In their technique the rainbows scattered by a volume of the spray containing many drops are recorded simultaneously. In this way the high frequency ripple structures that are superimposed on the Airy fringes are averaged out owing to the size distribution, as are the effects of individual drop asphericity owing to random orientation. Their analysis is based on the angular positions of the inflection points about the main rainbow peak. Temperature is deduced from the first inflection, which is found to be very close to the geometric rainbow angle. The mean size is found from the separation between this and the second inflection. They find that the mean size obeys the equation

$$d_{\text{rainbow}} = 531.6\lambda \left(\theta_{\text{inf2}} - \theta_{\text{inf1}}\right)^{-3/2}$$

A comparison with PDA measurements is shown in Fig. 9.22.

Hom and Chigier (2002) agree that it is necessary to measure the average over many drops. For single drops less than 30 μm errors in measured water temperature can be almost ±18.8°C at 50°C and ±8.3°C for ethanol at any temperature. For larger particles this is reduced to ±5.7°C for water at 50°C and ±2.5°C for ethanol at any temperature. van Beeck *et al.* (2001) found that the temperature derivation from inflection points appears to be independent of spray dispersion, and reported preliminary measurements in a heated water spray. The accuracy of the temperature measurement by global rainbow thermometry was also shown to be a few degrees Celsius.

The potential for the use of the rainbow for absorption spectroscopy was explored by Card and Jones (2003b). By using a CCD camera and a xenon lamp light source, two-dimensional records were made of intensity against angle and wavelength for water sprays containing food dyes. The absorbance (A) is defined by $I = I_0 10^{-A}$ where I is the transmitted intensity and I_0 is the intensity in the absence of absorption. Provided that $m_2 \ll m_1$, where m_1 and m_2 are the real

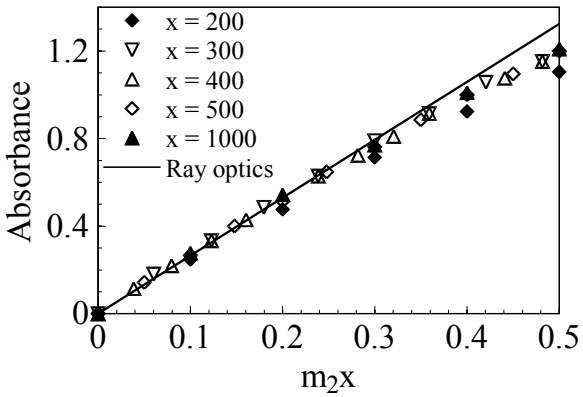

Fig. 9.23. Comparison between the ray optics prediction of absorbance at the rainbow and Mie theory for a range of size parameters, with $m_1 = 1.33$ (after Card and Jones, 2003b).

and imaginary parts of the complex refractive index, geometric optics analysis gives

$$A = \frac{16}{2.303 m_1} \sqrt{\frac{m_1^2 - 1}{3}} m_2 x$$

which is a simple linear function of the size parameter (x) and m_2. Comparisons with Mie theory, as in Fig. 9.23, show that the response is linear for $m_2 x < 0.3$. Drop sizes were estimated from the separation of the first and second rainbow peaks. Qualitatively the agreement between the theoretical predictions and the observed spectra was excellent. Quantitatively recovered values of m_2 were reasonable, though there were some discrepancies that were yet to be explained and accurate sizing is a crucial factor.

Some considerations for the future of spray diagnostics have been reviewed by Bachalo (2000).

In the combustion of coal the size and flux of particles is important, but so is their nature. As coal burns away it will form chars and ash. The latter is a particularly important product because it is non-combustible, is produced in large quantities, can have very significant effects on radiative heat transfer and causes slagging of furnace surfaces. Thus ash production needs to be monitored. Its composition is also important. If it contains too much unburned carbon this is a sign of poor combustion efficiency. Further, ash is either sold for the manufacture of concrete or is buried. In both cases the carbon content has important consequences.

An optical method for measuring the mass fraction of carbon in fly-ash was developed by Ouazzane *et al.* (2002). In this technique the particle cloud is illuminated with a polarised laser beam, but owing to the irregular shape of the particles the scattered light is partially depolarised. The extent of depolarisation depends upon the absorptivity of the particle. If the absorptivity is more then the depolarisation is less, because less light can penetrate, thus reducing the internal

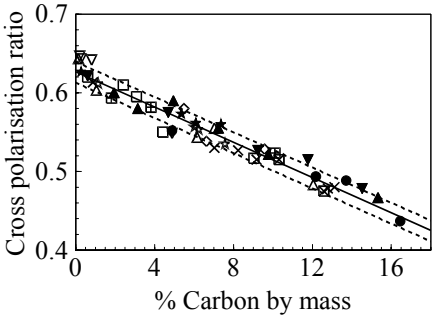

Fig. 9.24. Measurements of the residual carbon in fly ash from a range of coals by means of the cross-polarisation ratio in scattered light. The solid line is a linear least squares fit to the data, and the broken lines are plus and minus one standard deviation (after Ouazzane *et al.*, 2002).

reflections. Measurements on ashes from a wide range of coals demonstrated that there was a linear relationship between depolarisation and carbon mass fraction, as seen in Fig. 9.24.

9.4 Numerical inversion

There is a very large body of literature on the theory of direct inversion of light scattering data to yield particle size distribution. This is really beyond the scope of this chapter, especially as there is a whole journal (*Inverse Problems*) devoted to the subject. However, for the benefit of readers who may wish to pursue the subject, some of the more recent studies are referenced here.

A brief review emphasising biological particles has been provided by Popovici *et al.* (1999). They suggest that for quasi-monodisperse systems the Phillips–Twomey method is probably best, but for true polydisperse systems they preferred a combined Chahine–linear programming method.

The problem of overcoming the difficulties due to weak signals in noise and multiple scattering in dynamic light scattering systems has been studied by Buttgereit *et al.* (2001). Two scattering experiments are performed simultaneously in a three-dimensional geometry in such a way that the two scattering vectors and scattering volumes are the same, but the corresponding wave vectors do not coincide. Correlation measurements are then made at various points in the scattering pattern. Ruf *et al.* (2000) also consider noise in DLS experiments.

Inversion of diffraction measurements as in the Malvern analyser with semicircular photo-detectors is discussed by Wang *et al.* (2001). Their method begins with a guess at the size distribution represented as an N-dimensional point. The next guess is the projection of this point onto a hyperplane defined by the energy received by the next ring on the detector. The solution is represented by the point where all the hyperplanes intersect. A number of iterations of this method may

be required, but it always converges. A cut-off is determined simply by when the log of the residual error falls below a certain value. They claim that the method is stable and reliable and has good performance in the presence of noise.

A number of studies consider genetic or evolutionary programming to invert multi-wavelength extinction spectra. The method described by Lienert *et al.* (2001) searches for lognormal size distribution parameters whose calculated extinctions best fit the data. They show that, even in the case of a single lognormal distribution, many different distributions can fit the same set of extinction data unless the misfit is reduced below typical measurement error levels. In the case of a bimodal distribution, they find many dissimilar size distributions that fit the data to within 1% at six wavelengths. To recover the original bimodal distribution satisfactorily, they found that extinctions at 10 wavelengths must be fitted to within 0.5%. Li and Wilkinson (2001) discuss the retrieval of size distribution both for known and unknown refractive indices. Ye *et al.* (1999a, 1999b) conclude that genetic algorithms are superior to Monte Carlo inversion methods. Hodgson (2001) applied genetic algorithms to multimodal distributions of spheres, and Hodgson (2000) extended the technique to the determination the complex refractive index as well as size.

Li *et al.* (2004) examined light scattering by irregular particles based on the modified Wentzel–Kramers–Brillouin (WKB) and equisphere (EPS) methods and their potential to address the inverse-scattering problem by means of a spectral analysis of the total scattering cross-section of arbitrarily shaped particles. They concluded that, while EPS may be slightly better for some shapes, the modified WKB is better overall. An advantage of the two approximations is that they can easily be linearised for inversion schemes.

An inversion scheme for chain-like aggregates has been given by Shu and Charalampopoulos (2000b). The method entails the selection of suitable scattering quantities and their optimal measurement angles. The authors describe a rigorous interactive theory for chains of particles and stress the importance of correct orientation averaging.

A popular area for study is the application of neural networks to inversion. While these techniques take a long time to train, they are very rapid otherwise. Among the studies in this area are those by Wang *et al.* (1999) and Li *et al.* (2002)

Other methods include adaptive numerical filtering (Hespel and Delfour, 2000) and analytical inversion of the anomalous diffraction approximation (Franssens *et al.*, 2000)

9.5 Inclusions

In many situations there exist liquid drops containing solid particles or smaller immiscible drops. The combustion of slurries and emulsified fuels has received some attention, but one of the main areas of concern is the presence of inclusions in atmospheric aerosol. The latter may be particulates of soot, ash (either from

combustion or volcanic sources), soil or sand. The nature of these aerosols has influence on radiative transfer in the atmosphere and, thus, on climate.

Some prospects for the measurement of inclusions have been mentioned above. For optically large particles there are two glare spots, one from direct reflection from the surface and one from internal refraction. The ratio of these two intensities can be used to indicate the internal extinction losses. It has been proposed that the dual burst PDA method can be used for the same purpose, and proposals were made to discriminate between bubbles and solid particles (Naqwi and Durst, 1991; Onofri *et al.*, 1999; Ziema *et al.*, 2001).

Possible methods to measure the size of the host drop and the concentration of the inclusions based on polar diagrams have been suggested by Wriedt and Schuh (2002). Light scattering simulations showed significant changes in the scattered intensity distribution for drops with different inclusion concentrations, as can be seen in Fig. 9.25. Their evaluation reduced to only two parameters, namely angular fringe spacing and the slope in the angular scattering domain 30–70°. The fringe spacing can be used to find the size of the host particle for concentrations below 1%.

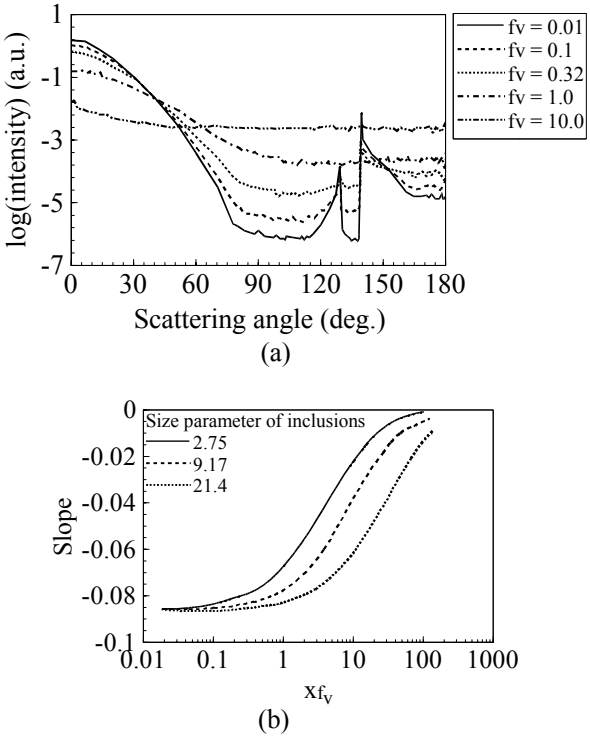

Fig. 9.25. Influence of the presence of inclusions on light scattering by drops. (a) Polar diagram as a function of volume fraction. $x_{\text{host}} = 460$, $x_{\text{inc}} = 2.75$, $m_{\text{host}} = 1.334$, $m_{\text{inc}} = 1.6$. (b) Slope of the scattered intensity in the angular range 30° to 70° for $280 < x_{\text{host}} < 1670$ (after Wriedt and Schuh, 2002).

For diagnostic and radiative transfer purposes the important parameters are the polar diagram (phase function), albedo and turbidity. For complicated compound materials a simple approach has been to derive an equivalent refractive index and perform the calculations using Mie theory. There are a number of models, perhaps the most common being the Maxwell–Garnett and Bruggeman equations.

The simple Maxwell–Garnett theory assumes that the inclusions are vanishingly small. Lakhtia and Vikram (1993) have proposed an equation that allows for finite particle size and volume fraction

$$m_{\mathrm{eq}} = m_{\mathrm{host}} \sqrt{\frac{1 + \dfrac{2\alpha f_{\mathrm{v}}}{3}}{1 - \dfrac{\alpha f_{\mathrm{v}}}{3}}}$$

where

$$\alpha = \frac{(m_{\mathrm{inc}}/m_{\mathrm{host}})^2 - 1}{1 - \left[(m_{\mathrm{inc}}/m_{\mathrm{host}})^2 - 1\right]\left[\frac{2}{3}(1 - im_{\mathrm{host}}x)\mathrm{e}^{ikm_{\mathrm{host}}x} - 1\right]}$$

Subscripts 'host' and 'inc' refer to the surrounding medium and the inclusions respectively. The authors claim that this equation is applicable for $|m_j x| \leq \pi/5$ where j is either 'host' or 'inc', and for $0 \leq f_{\mathrm{v}} \leq 0.2$.

An approximate formula based on the geometrical optics approximation was developed by Sharma and Jones (2000) for scattering by a sphere with highly absorbing randomly distributed inclusions. It was assumed that the rays propagated unperturbed in the weakly absorbing host medium, but on hitting an inclusion they were completely absorbed. In this model the real part of the equivalent refractive index is the same as that of the host medium, but the imaginary component becomes

$$m_{2,\mathrm{eq}} = \frac{3f_{\mathrm{v}}}{8x} + (1 - f_{\mathrm{v}})m_2$$

The equation was compared for dispersions of coal in water against calculations using a program developed by Mishchenko and Macke (1997) based on a Monte Carlo approach. This demonstrated that the approximation would be useful for predicting the absorption efficiency, asymmetry parameter and albedo of the sphere, as suggested by Fig. 9.26.

In a later study (Sharma and Jones, 2003) the approximation was extended to allow for absorption in the host medium together with an empirical term that allowed for finite particle size. Here

$$m_{2,\mathrm{eq}} = \frac{3f_{\mathrm{v}}}{8x} + \frac{1}{25f_{\mathrm{v}}(1 + x)}(1 - f_{\mathrm{v}})m_2$$

Doicu and Wriedt (2001) performed more rigorous calculations for the equivalent refractive index of a sphere with spherical inclusions using a recursive T-matrix method. They calculated angular scattering and then used least squares to compare the results with scattering by a homogeneous sphere with equivalent refractive index. Some comparisons with the approximate formula of Sharma and

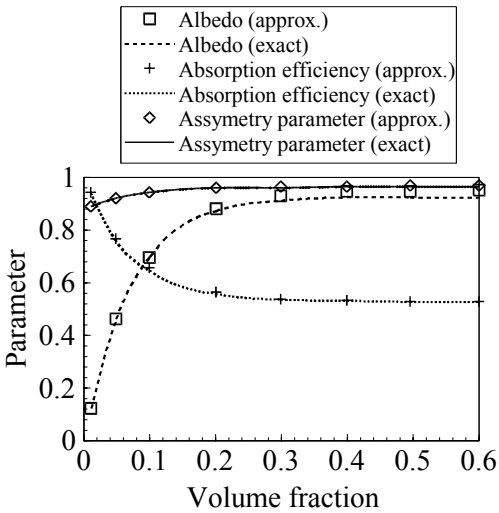

Fig. 9.26. Comparison of the albedo, absorption efficiency and asymmetry parameter for water drops containing absorbing inclusions between the approximate theory of Sharma and Jones (2000) and the exact theory of Mishchenko and Macke (1997). $d_{\text{host}} = 100\,\mu\text{m}$, $d_{\text{inc}} = 10\,\mu\text{m}$, $\lambda = 1\,\mu\text{m}$, $m_{\text{inc}} = 1.7\text{–i}0.04$ (after Sharma and Jones, 2000).

Table 9.2. Equivalent refractive index for different volume fractions (after Doicu and Wriedt, 2001). The parameters used in the calculation were $x_{\text{host}} = 500$, $x_{\text{inc}} = 25$, $m_{\text{host}} = 1.33$ and $m_{\text{inc}} = 1.28\text{–i}0.04$.

Volume fraction of inclusions	0.025	0.05	0.075	0.1
Equivalent refractive index	1.34–i0.000385	1.35–i0.000765	1.35–i0.00112	1.35–i0.00138
Refractive index from approximate formula	1.33–i0.000375	1.33–i0.000750	1.33–i0.00112	1.33–i0.00150

Jones (2000) are seen in Table 9.2. They concluded that the equivalent refractive index method is most accurate when the inclusions and the volume concentration are small and the difference between the two refractive indices is also small. At larger values the fit is much poorer and this questions the existence of a suitable solution.

The case of agglomerated soot in water was tackled by Markel and Shalaev (1999). One of their main conclusions was that the absorption of the agglomerates is enhanced. They defined the enhancement factor (G) as the ratio of the absorption cross section of carbon particles inside the water droplet and in vacuum. Fig. 9.27 shows the enhancement factor against fractal dimension. G is of the order 16 for $D_{\text{f}} = 1.8$. Markel (2002) also found that enhancement

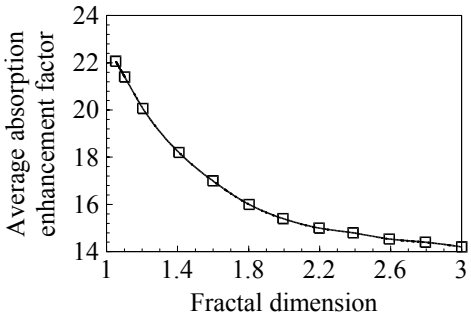

Fig. 9.27. Average enhancement of absorption due to soot in water drops ($10 < x_{\text{host}} < 1000$) as a function of the fractal dimension of the soot aggregates (after Markel and Shalaev, 1999).

factors are mostly of the order 10, but can be in excess of 10 000 at scattering resonances.

9.6 Conclusions

The literature on light scattering, even when restricted to the years after 1999, is very extensive. This chapter has concentrated on experimental methods of relevance to studies in combustion. Thus much of the recent experimental work has been omitted, and all of the theoretical studies. Even so, it can be seen from this restricted review that the field remains very active and lively.

It is probably true that the simple measurement of the size of homogeneous spheres has been very well covered over the years, and a number of excellent commercial instruments are available. As far as these spheres are concerned the remaining problems relate to measurements in difficult circumstances. Combustion is a case in point, since it presents hostile environments of high temperatures (and often high pressures) in fast-flowing dusty gases. Also, in industrial combustors such as furnaces, turbines and internal combustion engines optical access is limited.

Beyond homogeneous spheres the field remains open and active. The areas that have been covered in this chapter have included heterogeneous spheres. This relates to mixed fuels such as coal–water slurries and oil–water emulsions, and to atmospheric aerosols containing inclusions. Beyond that there remains the whole field of nonspherical particles, including the chain agglomerates that are such a feature of studies on soot and nanoparticles. In addition, there is the question of characterising particles through their refractive index and composition, examples being the measurement of temperature and quantification of residual carbon in fly-ash.

An important aspect of combustion is control because of its implications to efficiency and emissions, and thus to the environment. This has not been covered in this chapter, but evidently optical techniques play an important role.

For further information, the review by Docquier and Candel (2002) may be consulted. It gives a general review of control techniques, including a discussion of sensors.

In summary, therefore, light scattering is still an active and evolving field of study. Numerous exciting developments may be expected in the years to come.

9.7 Symbols

A	Absorbance
a	Radius of particle
a_{p}	Radius of primary particle
c	Speed of light *in vacuo*
D	Diffusion coefficient
D_{f}	Fractal dimension
d	Diameter of particle
d_{a}	Projected area equivalent diameter
d_{ij}	Distance between touching particles in an agglomerate
d_{p}	Diameter of primary particle
d_{10}	Mean diameter
d_{32}	Sauter mean diameter
$F(q)$	Scattering function for individual particles
f_{v}	Volume fraction
G	Enhancement factor
I	Intensity
I_0	Incident intensity
I_{HH}	Horizontal polarisation scattered and incident
I_{HV}	Horizontal polarisation scattered and vertical incident
I_{VH}	Vertical polarisation scattered and horizontal incident
I_{VV}	Vertical polarisation scattered and incident
K	Premultiplier in fractal description of agglomerates
K_{ext}	Extinction coefficient
$k = 2\pi/\lambda$	Wavenumber
k_{b}	Boltzmann's constant
L	Path length
l	Cavity mirror spacing
$m = m_1 - im_2$	Complex refractive index
m_{eq}	Equivalent refractive index
N	Number of particles
$\overline{N}$	Average number of particles in agglomerate
PF	Pulverised fuel
R_{g}	Radius of gyration
q	Amplitude of scattering wave vector
$\boldsymbol{q}$	Scattering wave vector
R	Reflectivity
Re	Reynolds number

$\boldsymbol{r}$	Position vector
S_{mn}	Elements of the scattering matrix
$S(q)$	Structure function in RGD theory
$S(\tau)$	Correlation function
T	Temperature
v	Velocity
w_0	Laser gaussian beamwidth
$x = \pi d/\lambda$	Particle size parameter
δ	Angular fringe spacing
θ	Scattering angle
λ	Wavelength
ρ	Density
τ	Time delay; time constant; turbidity

References

Abu-Gharbieh, R., Persson, J. L., Forsth, M., Rosen, A., Karlstrom, A. and Gustavsson, T. (2000) *Appl. Optics* **39** 1260–1267.

Aisa, L., Garcia, J. A., Cerecedo, L. M., Palacin, I. G. and Calvo, E. (2002) *Int. J. Multiph. Flow* **28** 301–324.

Albrecht, H. E., Borys, M. and Wenzel, M. (1996) *Part. Part. Syst. Char.* **13** 18–26.

Anders, K., Roth, N. and Frohn, A. (1996) *Part. Part. Syst. Char.* **13** 125–129.

Axelsson, B., Collin, R. and Bengtsson, P. E. (2000) *Appl. Optics* **39** 3683–3690.

Bachalo, W. D. (2000) *Atom. Sprays* **10** 439–474.

Bachalo, W. D. and Houser, M. J. (1984) *Opt. Eng.* **23** 583–590.

Berry, M. V. and Percival, I. C. (1986) *Optical Acta* **33** 577–591.

Blondel, D., Bultynck, H., Gouesbet, G. and Gréhan, G. (2001) *Part. Part. Syst. Charact.* **18** 79–90.

Boedec, T. and Simoens, S. (2001) *Exp. Fluids* **31** 506–518.

Botet, R. and Rannou, P. (2003) *J. Quant. Spectrosc. Radiat. Transf.* **79** 569–576.

Brasil, A. M., Farias, T. L. and Carvalho, M. G. (2000) *Aerosol Sci. Technol.* **33** 440–454.

Brasil, A. M., Farias, T. L., Carvalho, M. G. and Koylu, U. O. (2001) *J. Aerosol. Sci.* **32** 489–508.

Burke, J., Hess, C. F. and Kebbel, V. (2003) *Part. Part. Syst. Charact.* **20** 183–192.

Bushell, G. C., Yan, Y. D., Woodfield, D., Raper, J., Amal, R. (2002) *Adv. Colloid Interface Sci.* **95** 1–50.

Buttgereit, R., Roths, T., Honerkamp, J. and Aberle, L. B. (2001) *Phys. Rev. E* **6404** art. no. 041404.

Cao, J., Brown, D. J. and Rennie, A. G. (1991) *J. Inst Energy* **64** 26–30.

Card, J. B. A. and Jones, A. R. (2003a) *Part. Part. Syst. Charact.* **20** 259–266.

Card, J. B. A. and Jones, A. R. (2003b) *J. Phys. D-Appl. Phys.* **36** 236–243.

Castagner, J. L. and Jones, A. R. (2004) *Part. Part. Syst. Charact.* **21** 5–14.

Cecere, D., Bruno, A., Minutolo, P. and d'Alessio, A. (2003) *Synth. Met.* **139** 653–656.

Cerf, R. and Scheraga, H. A. (1952) *Chem Rev.* **51** 185–261.

Chang, H and Charalampopoulos, T. T. (1990) *Proc. Roy. Soc.* **A430** 577–591.

Charalampopoulos, T. T., Chang, H. and Stagg, B. (1989) *Fuel* **68** 1173–1179.

Charalampopoulos, T. T. and Shu, G. C. (2002) *Appl. Optics* **41** 723–733.

Charalampopoulos, T. T. and Shu, G. (2003) *Appl. Optics* **42** 3957–3969.
Cignoli, F., De Iuliis, S., Manta, V. and Zizak, G. (2001) *Appl. Optics* **40** 5370–5378.
Dalzell, W. H. and Sarofim, A. F. (1969) *ASME J. Heat Transfer* **91** 100–104.
Dankers, S. and Leipertz, A. (2004) *Appl. Optics* **43** 3726–3731.
Damaschke, N., Nobach, H. and Tropea, C. (2002a) *Exp. Fluids* **32** 143–152.
Damaschke, N., Nobach, H., Semidetnov, N. and Tropea, C. (2002b) *Appl. Optics* **41** 5713–5727.
de Sercey, G., Heikal, M., Gold, M., Begg, S., Wood, R., Awcock, G. and Laguitton, O. (2002) *Proc. Inst. Mech. Eng. Part C-J. Eng. Mech. Eng. Sci.* **216** 1017–1029.
di Stasio, S. (2000) *Appl. Phys. B-Lasers Opt.* **70** 635–643.
di Stasio, S. (2001) *J. Aerosol. Sci.* **32** 509–524.
di Stasio, S., Konstandopoulos, A. G. and Kostoglou, M. (2002a) *J. Colloid Interface Sci.* **247** 33–46.
di Stasio, S. (2002b) *J. Quant. Spectrosc. Radiat. Transf.* **73** 423–432.
Dobbins, R. A., Mulholland, G. W. and Bryner, N. P. (1994) *Atmos. Envir.* **28** 889–897.
Docquier, N. and Candel, S. (2002) *Prog. Energy Combust. Sci.* **28** 107–150.
Doicu, A., Schabel, S. and Ebert, F. (1996) *Part. Part. Syst. Char.* **13** 79–88.
Doicu, A. and Wriedt, T. (2001) *J. Opt. A-Pure Appl. Opt.* **3** 204–209.
Domann, R. and Hardalupas, Y. (2001) *Appl. Optics* **40** 3586–3597.
Domann, R., Hardalupas, Y., and Jones, A. R. (2002) *Meas. Sci. Technol.* **13** 280–291.
Durst, F. and Zaré, M. (1975) *Proc LDA Symp.*, Copenhagen, pp. 403–429.
Duwel, I., Schorr, J., Wolfrum, J. and Schulz, C. (2004) *Appl. Phys. B-Lasers Opt.* **78** 127–131.
Farias, T. L., Carvalho, M. G. and Koylu, U. O. (1995) *Trans. ASME-J. Heat Trans.* **117** 152–159.
Farias, T. L., Koylu, U. O. and Carvalho, M. G. (1996) *Appl. Optics* **35** 6560–6567.
Farmer, W. M. (1972) *Appl. Optics* **11** 2603–2612.
Farmer, W. M. (1974) *Appl. Optics* **13** 610–622.
Franssens, G., de Maziere, M. and Fonteyn, D. (2000) *Appl. Optics* **39** 4214–4231.
Fristrom, R. M., Jones, A. R., Schwar, M. J. R. and Weinberg, F. J. (1973) *Proc. 7th Faraday Symposium*, Chemical Society, London, pp. 183–197.
Gianinoni, I., Golinelli, E., Melzi, G., Musazzi, S., Perini, U. and Trespidi, F. (2003) *Opt. Lasers Eng.* **39** 141–154.
Golombok, M., Morin, V. and Mounaim-Rousselle, C. (1998) *J. Phys. D* **31** L59–L62.
Hardalupas, Y. and Taylor, A. M. K. P. (1994) *Exp. Fluids* **17** 253–258.
Hardalupas Y., Hishida K., Maeda M., Morikita H., Taylor A. M. K. P., and Whitelaw J. H. (1994) *Appl. Opt.* **33** 8417–8426.
Hespel, L. and Delfour, A. (2000) *Appl. Optics* **39** 6897–6917.
Hirleman, E. D. (1988) *Optical Particle Sizing: Theory and Practice* (G. Gouesbet and G. Grehan, eds.), Plenum Press, New York, pp. 135–146.
Hodgson, R. J. W. (2000) *J. Colloid Interface Sci.* **229** 399–406.
Hodgson, R. J. W. (2001) *J. Colloid Interface Sci.* **240** 412–418.
Hom, J. and Chigier, N. (2002) *Appl. Optics* **41** 1899–1907.
Hottel, H. C. and Broughton, F. P. (1932) *Ind. Engng. Chem. (Analyt. Edn.)* **4** 166–175.
Hottel, H. C. and Sarofim, A. F. (1967) *Radiative Transfer*, McGraw-Hill, New York.
Hu, B., Yang, B. and Koylu, U. O. (2003) *Combust. Flame* **134** 93–106.
Jenkins, T. P. and Hanson, R. K. (2001) *Combust. Flame* **126** 1669–1679.
Jermy, M. C. and Greenhalgh, D. A. (2000) *Appl. Phys. B-Lasers Opt.* **71** 703–710.
Jermy, M. C. and Allen, A. (2002) *Appl. Optics* **41** 4188–4196.

Jones, A. R. (1993) Light scattering for particle characterisation in *Instrumentation for flows with combustion* (A. M. K. P. Taylor, ed.), Academic Press, London, pp. 323–404.
Jones, A. R. (1999) *Prog. Energy Comb. Sci.* **25** 1–53.
Jones A. R., Parasram N. T. and Taylor A. M. K. P. (2002) *Meas. Sci. Technol.* **13** 317–330.
Kawaguchi, T., Akasaka, Y. and Maeda, M. (2002) *Meas. Sci. Technol.* **13** 308–316.
Kim, H. W. and Choi, M. (2003) *J. Aerosol. Sci.* **34** 1633–1645.
Kim, W., Sorensen, C. M. and Chakrabarti, A. (2004) *Langmuir* **20** 3969–3973.
Klusek, C., Manickavasagam, S. and Menguc, M. P. (2003) *J. Quant. Spectrosc. Radiat. Transf.* **79** 839–859.
Kokhanovsky, A. A. and Weichert, R. (2001a) *Appl. Optics* **40** 1507–1513.
Kokhanovsky, A. A., Weichert, R., Heuer, M. and Witt, W. (2001b) *Appl. Optics* **40** 2595–2600.
Köser, O. and Wriedt, T. (1996) *Appl. Optics* **35** 2537–2543.
Koylu, U. O. and Faeth, G. M. (1994a) *ASME J. Heat Transf.-Trans. ASME* **116** 152–159.
Koylu, U. O. and Faeth, G. M. (1994b) *ASME J. Heat Transf.-Trans. ASME* **116** 971–979.
Koylu, U. O. and Faeth, G. M. (1996) *ASME J. Heat Transf.-Trans. ASME* **118** 415–421.
Krishnan, S. S., Lin, K. C. and Faeth, G. M. (2000) *J. Heat Transf.-Trans. ASME* **122** 517–524.
Krishnan, S. S., Lin, K. C. and Faeth, G. M. (2001) *J. Heat Transf.-Trans. ASME* **123** 331–339.
Kroner, G., Fuchs, H., Tatschl, R. and Glatter, O. (2003) *Part. Part. Syst. Charact.* **20** 111–123.
Lakhtia, A. and Vikram, C. S. (1993) *Opt. Eng.* **32** 1996–1998.
Lambert, S., Thill, A., Ginestet, P., Audic, J. M. and Bottero, J. Y. (2000) *J. Colloid Interface Sci.* **228** 379–385.
Lamprecht, A., Eimer, W. and Kohse-Hoinghaus, K. (1999) *Combust. Flame* **118** 140–150.
Lee S. C. and Tien C. L. (1981) *18th Symp. on Combustion*, The Combustion Institute, pp. 1159–1166.
Le Gal, P., Farrugia, N. and Greenhalgh, D. A. (1999) *Opt. Laser Technol.* **31** 75–83.
Lehre, T., Jungfleisch, B., Suntz, R. and Bockhorn, H. (2003a) *Appl. Optics* **42** 2021–2030.
Lehre, T., Bockhorn, H., Jungfleisch, B. and Suntz, R. (2003b) *Chemosphere* **51** 1055–1061.
Li, M. Z. and Wilkinson, D. (2001) *Chem. Eng. Sci.* **56** 3045–3052.
Li, M. Z., Wilkinson, D. and Schrodl, M. (2002) *AICHE J.* **48** 2492–2498.
Li, X., Chen, Z. G., Gong, J. M., Taflove, A. and Backman, V. (2004) *Opt. Lett.* **29** 1239–1241.
Lienert, B. R., Porter, J. N. and Sharma, S. K. (2001) *Appl. Optics* **40** 3476–3482.
Long, M. B., Webber, B. F. and Chang, R. K. (1979) *Appl. Phys. Lett.* **34** 22–24.
Maeda, M., Akasaka, Y. and Kawaguchi, T. (2002) *Exp. Fluids* **33** 125–134.
Markel, V. A. and Shalaev, V. M. (1999) *J. Quant. Spectrosc. Radiat. Transf.* **63** 321–339.
Markel, V. A. and Shalaev, V. M. (2001) *J. Opt. Soc. Am. A-Opt. Image Sci. Vis.* **18** 1112–1121.

Markel, V. A. (2002) *J. Quant. Spectrosc. Radiat. Transf.* **72** 765–774.
Massoli, P., Beretta, F., d'Alessio, A. and Lazzaro, M. (1993) *Appl. Optics* **32** 3295–3301.
Matsuura, K., Komaki, M., Ueyama, K. and Hironaga, K. (2004) *Exp. Fluids* **36** 11–22.
McDonell, V. G. and Samuelsen, G. S. (2000) *Meas. Sci. Technol.* **11** 870–886.
Melton, L. A. (1984) *Appl. Opt.* **23** 2201–2208.
Menguc, M. P and Manickavasagam, S. (1998) *Int. J. Eng. Sci.* **36** 1569–1593.
Michelsen, H. A. (2003) *J. Chem. Phys.* **118** 7012–7045.
Mishchenko, M. I. and Macke, A. (1997) *J. Quant. Spectrosc. Radiat. Transfer* **57** 767–794.
Modest, A. F. (2003) *Radiative Heat Transfer*, 2nd edn., Academic Press, London.
Moreau, C. S., Therssen, E., Mercier, X., Pauwels, J. F. and Desgroux, P. (2004) *Appl. Phys. B-Lasers Opt.* **78** 485–492.
Morikita H., Hishida K. and Maeda M. (1995) *Developments in Laser Techniques and Applications to Fluid Mechanics*, Springer, Berlin, pp. 354–375.
Morikita H., Prassas I. and Taylor A. M. K. P. (1997) *Developments in Laser Techniques and Applications to Fluid Mechanics* (Adrian, R. J. *et al.*, eds), Springer, Berlin, pp. 233–258.
Mounaim-Rousselle, C. and Pajot, O. (1999) *Part. Part. Syst. Charact.* **16** 160–168.
Mulholland, G. W. and Croarkin, C. (2000) *Fire Mater.* **24** 227–230.
Mulholland, G. W. and Mountain, R. D. (1999) *Combust. Flame* **119** 56–68.
Mulholland, G. W., Johnson, E. L., Fernandez, M. G. and Shear, D. A. (2000) *Fire Mater.* **24** 231–243.
Mullins J. and Williams A. (1987) *Fuel* **66** 277–280.
Naqwi, A. and Durst, F. (1991) *Part. Part. Syst. Char.* **8** 245–258.
O'Keefe, A. and Deacon, D. A. G. (1988) *Rev. Sci. Instrum.* **59** 2544–2551.
Onofri, F., Blondel, D., Gréhan, G. and Gouesbet, G. (1996a) *Part. Part. Syst. Char.* **13** 104–111.
Onofri, F., Girasole, T., Gréhan, G., Gouesbet, G., Brenn, G., Domnik, J. and Tropea, C. (1996b) *Part. Part. Syst. Char.* **13** 112–124.
Onofri, F., Bergougnoux, L., Firpo, J. L. and Misguich-Ripault, J. (1999) *Appl. Optics* **38** 4681–4690.
Onofri, F., Lenoble, A. and Radev, S. (2002) *Appl. Optics* **41** 3590–3600.
Ouazzane, A. K., Castagner, J. L., Jones, A. R. and Ellahi, S. (2002) *Fuel* **81** 1907–1911.
Popovici, M. A., Mincu, N. and Popovici, A. (1999) *Math. Biosci.* **157** 321–344.
Pratsinis, S. E. (1998) *Prog. Energy Combust. Sci.* **24** 197–219.
Purcell, E. M. and Pennypacker, C. R. (1973) *Astrophys. J.* **186** 705–714.
Quinten, M., Friehmelt, R. and Ebert, K. F. (2001) *J. Aerosol. Sci.* **32** 63–72.
Ren, K. F., Girasole, T., Taylor, A. M. K. P., Gouesbet, G. and Grehan, G. (2003) *Opt. Commun.* **220** 269–280.
Rheims, J., Wriedt, T. and Bauckhage, K. (1999) *Meas. Sci. Technol.* **10** 68–75.
Riefler, N., di Stasio, S. and Wriedt, T. (2004) *J. Quant. Spectrosc. Radiat. Transf.* **89** 323–342.
Roth, N., Anders, K. and Frohn. A. (1990) *Proc. 2nd Inter. Conf. Optical Particle Sizing*, Arizona State University, Tempe, AZ, pp. 306–315.
Roth, N., Anders, K. and Frohn. A. (1991) *Appl. Opt.* **30** 4960–4965.
Ruf, H., Gould, B. J. and Haase, W. (2000) *Langmuir* **16** 471–480.
Saffman, M., Buchhave, P. and Tanger, H. (1984) *Laser Anemometry in Fluid Mechanics – II* (R.J. Adrian, D. F. G. Durão, F. Durst, H. Mishina and J. H. Whitelaw, eds), LADOAN, Lisbon, pp. 85–104.

Saija, R., Iati, M. A., Denti, P., Borghese, F., Giusto, A., Sindoni, O. I. (2003) *Appl. Optics* **42** 2785–2793.
Schneider, M., Hirleman, E. D., Salaheen, H., Chowdhury, D. Q. and Hill, S. C. (1993) *Proc. 3rd Inter. Conf. Optical Particle Sizing*, Keio University, Yokohama, Japan, pp. 323–326.
Schneider, M. and Hirleman, E. D. (1994) *Appl. Optics* **33** 2379–2388.
Sharma, S. K. and Jones, A. R. (2000) *J. Phys. D-Appl. Phys.* **33** 584–588.
Sharma, S. K. and Jones, A. R. (2003) *J. Quant. Spectrosc. Radiat. Transf.* **79** 1051–1060.
Shu, G. C. and Charalampopoulos, T. T. (2000a) *Appl. Optics* **39** 5827–5833.
Shu, G. C. and Charalampopoulos, T. T. (2000b) *Appl. Optics* **39** 6713–6724.
Snegirev, A. Y., Makhviladze, G. M. and Roberts, J. P. (2001) *Fire Saf. J.* **36** 73–95.
Snelling, D. R., Liu, F. S., Smallwood, G. J. and Gulder, O. L. (2004) *Combust. Flame* **136** 180–190.
Sorensen, C. M. and Wang, G. M. (1999) *Phys. Rev. E* **60** 7143–7148.
Sorensen, C. M. (2001) *Aerosol Sci. Technol.* **35** 648–687.
Sorensen, C. M., Kim, W., Fry, D., Shi, D. and Chakrabarti, A. (2003) *Langmuir* **19** 7560–7563.
Stagg, B. J. and Charalampopoulos, T. T. (1993) *Combust. Flame* **94** 381–396.
Strakey, P. A., Talley, D. G., Sankar, S. V. and Bachalo, W. D. (2000) *Appl. Optics* **39** 3875–3886.
Thill, A., Lambert, S., Moustier, S., Ginestet, P., Audic, J. M. and Bottero, J. Y. (2000) *J. Colloid Interface Sci.* **228** 386–392.
Tian, K., Liu, F. S., Thomson, K. A., Snelling, D. R., Smallwood, G. J., Wang, D. S. (2004) *Combust. Flame* **138** 195–198.
Tillwick, J., Uhlenwinkel, V. and Bauckhage, K. (1999) *Int. J. Heat Fluid Flow* **20** 530–537.
Tropea, C., Xu, T. H., Onofri, F., Gréhan, G., Hangen, P. and Stieglmeier, M. (1996) *Part. Part. Syst. Char.* **13** 165–170.
Umhauer, H., Berbner, S. and Hemmer, G. (2000) *Part. Part. Syst. Charact.* **17** 3–15.
Vaglieco, B. M., Beretta, F. and d'Alessio, A. (1990) *Comb. Flame* **79** 259–271.
van Beeck, J. P. A. J., Giannoulis, D., Zimmer, L. and Riethmuller, M. L. (1999) *Opt. Lett.* **24** 1696–1698.
van Beeck, J. P. A. J., Zimmer, L. and Riethmuller, M. L. (2001) *Part. Part. Syst. Charact.* **18** 196–204.
van Beeck, J. P. A. J., Grosges, T. and De Giorgi, M. G. (2003) *Appl. Optics* **42** 4016–4022.
van de Hulst, H. C. (1957) *Light Scattering by Small Particles*, Chapman and Hall, London.
van der Wal, R. L. and Ticich, T. M. (1999) *Appl. Optics* **38** 1444–1451.
Van-Hulle, P., Weill, M. E., Talbaut, M. and Coppalle, A. (2002a) *Part. Part. Syst. Charact.* **19** 47–57.
Van-Hulle, P., Talbaut, M., Weill, M., Coppalle, A. (2002b) *Meas. Sci. Technol.* **13** 375–382.
Wainner, R. T., Seitzman, J. M. and Martin, S. R. (1999) *AIAA J.* **37** 738–743.
Wang, G. M. and Sorensen, C. M. (2002) *Appl. Optics* **41** 4645–4651.
Wang, J. C. F. and Tichenor, D. A. (1991) *Appl. Opt.* **20**, 1367–1373.
Wang, J. P., Xie, S. Z., Zhang, Y. M. and Li, W. (2001) *Appl. Optics* **40** 3937–3945.
Wang, Z., Ulanowski, Z. and Kaye, P. H. (1999) *Neural Comput. Appl.* **8** 177–186.

Wentzel, M., Gorzawski, H., Naumann, K. H., Saathoff, H., and Weinbruch, S. (2003) *J. Aerosol. Sci.* **34** 1347–1370.
Widmann, J. F., Presser, C. and Leigh, S. D. (2001) *Atom. Sprays* **11** 711–733.
Widmann, J. F., Presser, C. and Leigh, S. D. (2001) *Meas. Sci. Technol.* **12** 1180–1190.
Widmann, J., Yang, J. C., Smith, T. J., Manzello, S. L. and Mulholland, G. W. (2003) *Combust. Flame* **134** 119–129.
Will, S., Schraml, S. and Leipertz, A. (1995) *Opt. Lett.* **22** 2342–2344.
Witze, P. O., Hochgreb, S., Kayes, D., Michelsen, H. A. and Shaddix, C. R. (2001) *Appl. Optics* **40** 2443–2452.
Wooldridge, M. S. (1998) *Prog. Energy Combust. Sci.* **24**, 63–87.
Wriedt, T. and Schuh, R. (2002) *Meas. Sci. Technol.* **13** 276–279.
Wu, J.-S., Krishnan, S. S. and Faeth, G. M. (1997) *J. Heat Transf.-Trans. ASME* **119** 230–237.
Xing, Y. C., Koylu, U. O., Rosner, D. E. (1999) *Appl. Optics* **38** 2686–2697.
Xu, T. H. and Tropea, C. (1994) *Meas. Sci. Tech.* **5** 969–975.
Xu, Y. L. (1997) *Appl. Opt.* **36** 9496–9508.
Xu, Y. L., Gustafson, B. A. S. (1999) *Astrophys. J.* **513** 894–909.
Xu, Y. L., Gustafson, B. A. S. (2001) *J. Quant. Spectrosc. Radiat. Transf.* **70** 395–419.
Ye, M., Wang, S. M. and Xu, Y. Q. (1999a) *Powder Technol.* **104** 80–83.
Ye, M., Wang, S. M., Lu, Y., Hu, T., Zhu, Z. and Xu, Y. Q. (1999b) *Appl. Optics* **38** 2677–2685.
Yeh, C.-N., Kamimoto, T., Kobori, S. and Kosaka, H. (1993) *Trans. JSME* 93-0134, 308.
Yokoi, N., Aizu, Y. and Mishina, H. (2001) *Appl. Optics* **40** 1049–1064.
Yu, Z. and Rasmuson, A. C. (1999) *Exp. Fluids* **27** 189–198.
Zaidi, S. H., Altunbas, A. and Azzopardi, B. J. (1998) *Chem. Eng. J.* **71** 135–143.
Zhu, J. Y., Choi, M. Y., Mulholland, G. W. and Gritzo, L. A. (2000) *Int. J. Heat Mass Transf.* **43** 3299–3303.
Zhu, J. Y., Irrera, A., Choi, M. Y., Mulholland, G. W., Suo-Anttila, J. and Gritzo, L. A. (2004) *Int. J. Heat Mass Transf.* **47** 3643–3648.
Ziema, M., Melling, A., Brenn, G. and Durst, F. (2001) *Exp. Fluids* **30** 426–433.

10 Absorption and scattering of light in natural waters

Vladimir I. Haltrin

10.1 Introduction

In this chapter we restrict ourselves to the problems of absorptionabsorption [1–13], elastic [1, 4, 5, 10, 14–22] and inelastic Raman [23–44] scattering of light, and fluorescence [45–62] in natural waters. Owing to the lack of clear and simple numerical procedures that connect scattering with easily measurable environmental parameters, scattering by air bubbles in water [63–65], Brillouin scattering [37, 66–69], and amplification of forward scattering by water turbulence [70, 71] are omitted from consideration. All conclusions of this chapter will be obtained mostly from analysis of experimental data with some additions derived from theory and from analysis of numerical computations. We will discuss in detail two basic inherent optical properties of natural water, the absorption coefficient, a, the angular scattering coefficient, β, and inelastic parameters of Raman scattering and fluorescence that are included as input parameters in a scalar radiative transfer equation:

$$\left[\frac{1}{v}\frac{\partial}{\partial t} + \mathbf{n}\nabla + c(\lambda, \boldsymbol{x})\right] L(\lambda, \boldsymbol{x}, \Omega) = Q^E(\lambda, \boldsymbol{x}, \Omega) + Q^I(\lambda, \boldsymbol{x}, \Omega), \tag{10.1}$$

here $L(\lambda, \boldsymbol{x}, \Omega)$ is a total radiance of light in water that depends on spatial coordinates $\mathbf{r}$ and time t (here $\boldsymbol{x} = (\mathbf{r}, t)$ is a combination of spatial coordinates and time), and solid angle $\Omega = \Omega(\theta, \varphi)$; v is the speed of light in water; $\mathbf{n}$ is a unit vector in the direction of propagation of light; λ is a wavelength of light; $c(\lambda, \boldsymbol{x})$ is an attenuation (or extinction) coefficient which is a sum of absorption a and beam scattering b coefficients,

$$c(\lambda, \boldsymbol{x}) = a(\lambda, \boldsymbol{x}) + b(\lambda, \boldsymbol{x}), \tag{10.2}$$

with the scattering coefficient expressed through the angular elastic scattering coefficient $\beta(\lambda, \boldsymbol{x}, \cos\vartheta)$ as follows:

$$b(\lambda, \boldsymbol{x}) = \int_{4\pi} \mathrm{d}\Omega' \beta(\lambda, \boldsymbol{x}, \cos\vartheta) \equiv 2\pi \int_0^\pi \beta(\lambda, \boldsymbol{x}, \cos\vartheta) \sin\vartheta \, \mathrm{d}\vartheta, \tag{10.3}$$

where $\cos\vartheta = \mathbf{nn}'$, $\mathbf{n}'$ is a unit vector in the direction of initial propagation of light.

The right part of eq. (10.1) consists of two source parts, elastic Q^E and inelastic Q^I.

The elastic source

$$Q^E(\lambda, \mathbf{r}, \Omega) = \int_{4\pi} \mathrm{d}\Omega' \beta(\lambda, \mathbf{r}, \cos\vartheta) L(\lambda, \mathbf{r}, \Omega'), \tag{10.4}$$

describes elastic scattering of light, *i.e.* scattering without change in wavelength.

The inelastic source

$$Q^I(\lambda, \boldsymbol{x}, \Omega) = \sum_{j=R,C,Y} \int_{\lambda'<\lambda} \mathrm{d}\lambda' \int_{4\pi} \mathrm{d}\Omega' \sigma^j(\lambda', \lambda, \boldsymbol{x}, \cos\vartheta) L(\lambda, \boldsymbol{x}, \Omega'), \tag{10.5}$$

describes an input of energy to wavelength λ from lower wavelengths λ' due to inelastic processes of Raman scattering, red fluorescence by chlorophyll, and blue fluorescence by yellow substance. Here σ^j $(j = R, C, Y)$ corresponds to Raman scattering, and chlorophyll and yellow substance emission coefficients. We ignore here anti–Stokes (blue–shifted) components that are significantly weaker than Stokes (red–shifted) components.

The previous eqs (10.1)–(10.5) introduce the following basic inherent optical properties of water:

$a(\lambda, \boldsymbol{x})$ – absorption coefficient;
$\beta(\lambda, \boldsymbol{x}, \cos\vartheta)$ – elastic angular scattering coefficient (or volume scattering function);
$\sigma^R(\lambda', \lambda, \cos\vartheta)$ – Raman scattering differential emission coefficient;
$\sigma^C(\lambda', \lambda, \boldsymbol{x}, \cos\vartheta)$ – chlorophyll fluorescence differential emission coefficient;
$\sigma^Y(\lambda', \lambda, \boldsymbol{x}, \cos\vartheta)$ – yellow substance fluorescence differential emission coefficient.

The dependence on $\boldsymbol{x}$ of all these inherent properties (except Raman scattering emission coefficient) is due to their dependence on concentrations of dissolved and suspended matter in water. Knowledge of these five basic inherent properties is enough to solve any scalar radiative transfer problem in a body of water.

Let us introduce additional four auxiliary inherent optical properties that are widely used in optics of natural waters:

elastic light scattering phase function,

$$p(\lambda, \boldsymbol{x}, \cos\vartheta) = \frac{\beta(\lambda, \boldsymbol{x}, \cos\vartheta)}{b(\lambda, \boldsymbol{x})}, \tag{10.6}$$

$$2\pi \int_0^\pi p(\lambda, \boldsymbol{x}, \cos\vartheta) \sin\vartheta \, \mathrm{d}\vartheta = 1; \tag{10.7}$$

single–scattering albedo (= probability of elastic scattering),

$$\omega_0 = \frac{b}{c} \equiv \frac{b}{a+b}; \tag{10.8}$$

backscattering coefficient,

$$b_B(\lambda, \boldsymbol{x}) = 2\pi \int_{\pi/2}^{\pi} \beta(\lambda, \boldsymbol{x}, \cos\vartheta) \sin\vartheta \, \mathrm{d}\vartheta; \tag{10.9}$$

probability of backscattering, or ratio of backscattering to scattering

$$B(\lambda, \boldsymbol{x}) = \frac{b_B(\lambda, \boldsymbol{x})}{b(\lambda, \boldsymbol{x})} = 2\pi \int_{\pi/2}^{\pi} p(\lambda, \boldsymbol{x} \cos\vartheta) \sin\vartheta \, \mathrm{d}\vartheta; \tag{10.10}$$

and Gordon's parameter,

$$x_G = \frac{b_B}{a+b_B} \equiv \frac{B\omega_0}{1-\omega_0+B\omega_0}. \tag{10.11}$$

Parameters ω_0, B, and x_G are dimensionless and vary in the following range for any possible type of absorbing and scattering media in natural water:

$$0 \le \omega_0 \le 1, \quad 0 \le B \le 0.5, \quad 0 \le x_G \le 1. \tag{10.12}$$

Solutions to eq. (10.1) are the basis of deriving various apparent optical properties such as diffuse attenuation coefficient, diffuse reflection coefficient, remote sensing reflection coefficient, average cosines over radiance distribution L, lidar equation, and others. In the following sections we consider inherent optical properties of natural, and mostly oceanic, water, in detail.

10.2 Absorption of light in natural water

Natural oceanic, marine or lake water consists of water molecules and impurities dissolved and suspended in water. Absorption of light occurs in water molecules, molecules of yellow substance, also known as 'Gelbstoff', dissolved organic matter (DOM), or colored dissolved organic matter (CDOM), and different kinds of chlorophyll molecules that present in phytoplankton cells that grow in natural waters. The composition of natural water is very complex and varies from region to region. In this section we restrict ourselves to a simplistic model that takes into account four major ingredients of absorption: pure water, two components of yellow substance and an average type of chlorophyll. In this approximation the absorption coefficient of natural water at wavelength of light λ at any fixed depth can be written as:

$$a(\lambda) = a_W(\lambda) + 0.06 a_C^0(\lambda) C^{0.65} + a_F^0 C_F \exp(-k_F\lambda) + a_H^0 C_H \exp(-k_H\lambda), \tag{10.13}$$

here a_W is an absorption coefficient of pure water in m^{-1}; a_C^0 is a specific absorption coefficient of chlorophyll in 1/m, and C is dimensionless concentra-

tion of chlorophyll, $C = C_C/C_0$, where C_C is a concentration of chlorophyll in mg/m^3, and $C_0 = 1\,\mathrm{mg/m^3}$. The absorption by yellow substance or DOM is split into two parts: absorption by fulvic acid and absorption by humic acid. Both components of DOM, fulvic and humic acids, have similar optical properties with different absorption and fluorescence coefficients. For typical marine water the composition of fulvic and humic acids is, approximately, constant with $\zeta = C_H/(C_F + C_H) = 0.1$. By introducing the total concentration of DOM

$$C_Y = C_F + C_H, \tag{10.14}$$

we can rewrite eq. (10.13) in the following simplified form:

$$a(\lambda) = a_W(\lambda) + 0.06a_C^0(\lambda)C^{0.65} + a_Y^0 C_Y \exp(-k_Y\lambda). \tag{10.15}$$

The numerical values of a_W and a_C^0 are given in Table 10.1, and coefficients a_j^0 and k_j for $j = F, H, Y$ are given in Table 10.2. The spectral behavior of all absorption components is shown in Fig. 10.1.

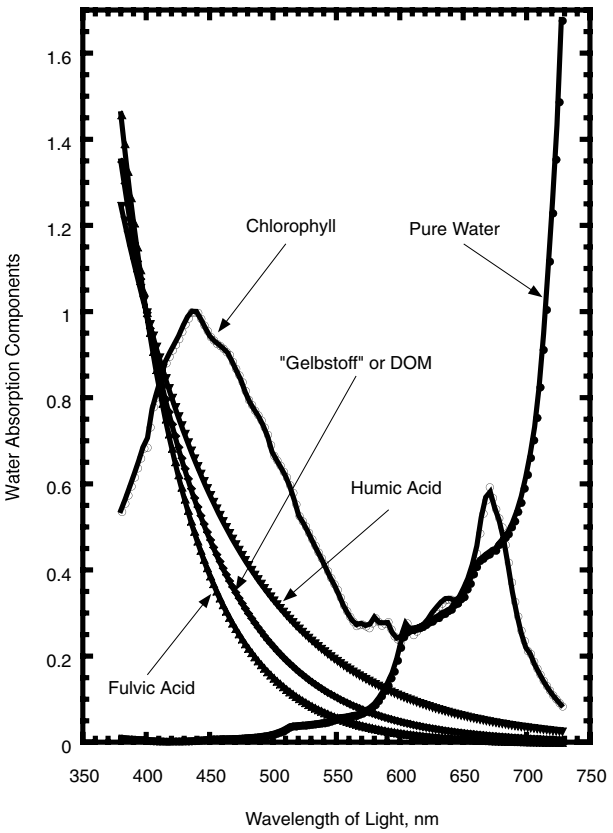

Fig. 10.1. The components of absorption of light in natural water

Table 10.1. Spectral absorption coefficient of pure water and specific spectral absorption coefficient of chlorophyll [8, 9]

λ, nm	a_w, m^{-1},	a_C^0, m^{-1}	λ, nm	a_w, m^{-1}	a_C^0, m^{-1}	λ, nm	a_w, m^{-1}	a_C^0, m^{-1}
380.0	0.01137	0.538	497.5	0.01910	0.693	615.0	0.26780	0.268
382.5	0.01044	0.557	500.0	0.02040	0.668	617.5	0.27070	0.272
385.0	0.00941	0.576	502.5	0.02280	0.657	620.0	0.27550	0.276
387.5	0.00917	0.597	505.0	0.02560	0.645	622.5	0.28100	0.287
390.0	0.00851	0.618	507.5	0.02800	0.631	625.0	0.28340	0.299
392.5	0.00829	0.639	510.0	0.03250	0.618	627.5	0.29040	0.308
395.0	0.00813	0.662	512.5	0.03720	0.600	630.0	0.29160	0.317
397.5	0.00775	0.685	515.0	0.03960	0.582	632.5	0.29950	0.325
400.0	0.00663	0.687	517.5	0.03990	0.555	635.0	0.30120	0.333
402.5	0.00579	0.734	520.0	0.04090	0.528	637.5	0.30770	0.334
405.0	0.00530	0.781	522.5	0.04160	0.516	640.0	0.31080	0.334
407.5	0.00503	0.804	525.0	0.04170	0.504	642.5	0.32200	0.330
410.0	0.00473	0.828	527.5	0.04280	0.489	645.0	0.32500	0.326
412.5	0.00452	0.855	530.0	0.04340	0.474	647.5	0.33500	0.341
415.0	0.00444	0.883	532.5	0.04470	0.459	650.0	0.34000	0.356
417.5	0.00442	0.898	535.0	0.04520	0.444	652.5	0.35800	0.372
420.0	0.00454	0.913	537.5	0.04660	0.430	655.0	0.37100	0.389
422.5	0.00474	0.926	540.0	0.04740	0.416	657.5	0.39300	0.415
425.0	0.00478	0.939	542.5	0.04890	0.400	660.0	0.41000	0.441
427.5	0.00482	0.956	545.0	0.05110	0.384	662.5	0.42400	0.488
430.0	0.00495	0.973	547.5	0.05370	0.370	665.0	0.42900	0.534
432.5	0.00504	0.987	550.0	0.05650	0.357	667.5	0.43600	0.565
435.0	0.00530	1.001	552.5	0.05930	0.339	670.0	0.43900	0.595
437.5	0.00580	1.000	555.0	0.05960	0.321	672.5	0.44800	0.570
440.0	0.00635	1.000	557.5	0.06060	0.307	675.0	0.44800	0.544
442.5	0.00696	0.986	560.0	0.06190	0.294	677.5	0.46100	0.523
445.0	0.00751	0.971	562.5	0.06400	0.283	680.0	0.46500	0.502
447.5	0.00830	0.958	565.0	0.06420	0.273	682.5	0.47800	0.461
450.0	0.00922	0.944	567.5	0.06720	0.275	685.0	0.48600	0.420
452.5	0.00969	0.936	570.0	0.06950	0.276	687.5	0.50200	0.374
455.0	0.00962	0.928	572.5	0.07330	0.272	690.0	0.51600	0.329
457.5	0.00957	0.923	575.0	0.07720	0.268	692.5	0.53800	0.295
460.0	0.00979	0.917	577.5	0.08360	0.279	695.0	0.55900	0.262
462.5	0.01005	0.909	580.0	0.08960	0.291	697.5	0.59200	0.238
465.0	0.01011	0.902	582.5	0.09890	0.282	700.0	0.62400	0.215
467.5	0.01020	0.886	585.0	0.11000	0.274	702.5	0.66300	0.208
470.0	0.01060	0.870	587.5	0.12200	0.278	705.0	0.70400	0.190
472.5	0.01090	0.855	590.0	0.13510	0.282	707.5	0.75600	0.174
475.0	0.01140	0.839	592.5	0.15160	0.265	710.0	0.82700	0.160
477.5	0.01210	0.819	595.0	0.16720	0.249	712.5	0.91400	0.146
480.0	0.01270	0.798	597.5	0.19250	0.242	715.0	1.00700	0.134
482.5	0.01310	0.786	600.0	0.22240	0.236	717.5	1.11900	0.123
485.0	0.01360	0.773	602.5	0.24700	0.258	720.0	1.23100	0.112
487.5	0.01440	0.762	605.0	0.25770	0.279	722.5	1.35600	0.103
490.0	0.01500	0.750	607.5	0.26290	0.266	725.0	1.48900	0.094
492.5	0.01620	0.734	610.0	0.26440	0.252	727.5	1.67800	0.086
495.0	0.01730	0.717	612.5	0.26650	0.260			

Table 10.2. Parameters of yellow substance ('Gelbstoff' or DOM) absorption [2]

$j \to$	$F(\zeta = 0)$	$H(\zeta = 1)$	$Y(\zeta = 0.01)$	$Y(\zeta = 0.025)$	$Y(\zeta = 0.05)$	$Y(\zeta = 0.1)$
a_j^0, $\mathrm{m}^2\,\mathrm{mg}$	35.959	18.828	14.547	8.5472	6.2777	5.6797
k_j, nm^{-1}	0.0189	0.011 05	0.016 58	0.014 96	0.013 69	0.012 62

10.3 Elastic scattering of light in natural water

The light propagating in natural water elastically scatters on density fluctuations of water molecules (Rayleigh scattering) and any kind of physical inhomogeneity that is larger than the water molecule (Mie scattering). Such inhomogeneities consist of any kind of suspended organic and terrigenic living or dead particles. Terrigenic particles consist of small fractions of mineral origin that can be found in any region of open ocean as well as in coastal areas of seas and in lakes; shallow coastal areas also contain terrigenic fractions related to clays and suspended quartz particles. Organic particles consist of living particles such as bacteria [72–74], zooplankton and phytoplankton, and dead particles such as detritus and zooplankton feces with predominant abundance of phytoplankton cells. In this paragraph we consider Rayleigh scattering by pure water, and experimentally measured volume scattering functions.

The elastic angular scattering coefficient and total elastic scattering coefficient can be expressed as a sum of coefficients due to water molecules and particular matter that consists of phytoplankton cells, detritus, bacteria, suspended terrigenic particles of mineral origin, suspended clay particles, quartz particles, etc.,

$$\beta(\lambda, \cos\vartheta) = \beta_W(\lambda, \cos\vartheta) + \beta_P(\lambda, \cos\vartheta), \quad b(\lambda) = b_W(\lambda) + b_P(\lambda). \tag{10.16}$$

The particulate part depends on the concentration of suspended particles and will be presented here in the tabular form of experimentally measured data and in the form of experimentally derived optical models.

10.3.1 Rayleigh scattering in pure water

According to Morel [15] the pure water angular scattering coefficient may be represented as:

$$\beta_W(\lambda, \vartheta) = b_W(\lambda) p_W(\cos\vartheta), \tag{10.17}$$

where

$$b_W(\lambda) = (0.001\,458\,4\,\mathrm{m}^{-1}) \left(\frac{550}{\lambda}\right)^{4.34}, \tag{10.18}$$

is a total natural base scattering coefficient of pure marine water with average salinity, temperature $T = 20°\mathrm{C}$, and depolarization factor $\delta = 0.09$. The wavelength λ in eq. (10.18) is in nm.

The normalized according to eq. (10.7) phase function of scattering of pure water that takes into account the depolarization effects with $\delta = 0.09$ is:

$$p_W(\cos\vartheta) = 0.062\,253\,2 + 0.051\,972\,8\cos^2\vartheta \tag{10.19}$$

10.3.2 Petzold experimental volume scattering functions

For almost three decades of the last century the experimental database of 15 angular scattering coefficients (ASC) β published by Petzold [75] was used by ocean optics scientific community. These VSF have been measured with the angular scattering meter with maximum sensitivity centered at 515 nm and with the half-width of sensitivity about 60 nm. The waters that were used to measure these angular scattering coefficients were taken in the coastal areas of the Pacific Ocean near the shares of Southern California. The ranges of variability of integral inherent optical properties were: $0.093\,\mathrm{m}^{-1} \le c \le 2.19\,\mathrm{m}^{-1}$; $0.008\,\mathrm{m}^{-1} \le b \le 1.824\,\mathrm{m}^{-1}$; $0.082\,\mathrm{m}^{-1} \le a \le 0.764\,\mathrm{m}^{-1}$; $0.091 \le \omega_0 \le 0.906$; $0.013 \le B \le 0.146$. The actual values of Petzold angular scattering coefficients with corresponding inherent optical properties are given in Tables 10.3 and 10.4.

10.3.3 Mankovsky experimental volume scattering functions

More recently another 41 volume scattering functions with associated attenuation and beam scattering coefficients that have been measured in natural waters of the Atlantic, Indian and Southern Oceans, the Mediterranean and Black Seas, and Lake Baikal were published by Mankovsky and Haltrin [76, 77]. These phase functions have been measured with a nephelometer (an angular scattering meter) that has a maximum of sensitivity at 520 nm with the half-width of sensitivity band about 40 nm. The ranges of variability of integral inherent optical properties were: $0.115\,\mathrm{m}^{-1} \le c \le 1.105\,\mathrm{m}^{-1}$; $0.000\,143\,\mathrm{m}^{-1} \le b \le 0.0103\,\mathrm{m}^{-1}$; $0.021\,\mathrm{m}^{-1} \le a \le 0.163\,\mathrm{m}^{-1}$; $0.435 \le \omega_0 \le 0.867$; $0.0078 \le B \le 0.037$. The angular scattering coefficients and corresponding inherent optical properties are given in Tables 10.5 and 10.6.

10.3.4 Lee experimental volume scattering functions

During the period between 2000 and 2004 more than a thousand high-resolution angular light scattering coefficients of marine water have been measured with the polar nephelometer that was developed and assembled by Michael E. Lee. The maximum intensity of this nephelometer was centered at 550 nm. The complete set of technical parameters of this probe was published in Haltrin *et al.*, [78] and Lee and Lewis [79]. The modified version of this nephelometer that has the ability to measure angular scattering coefficients at six wavelengths (443, 490, 510, 555, 590, and 620 nm) was developed and tested in 2003 by M. E. Lee in waters of Mobile Bay in the Gulf of Mexico. Some of the results of these measurements are presented in this section.

The measurements of more than 60 angular scattering coefficients [80] have been accomplished in 2000 in coastal waters near the shores of New Jersey in

Table 10.3a. Petzold [75] total angular scattering functions in m^{-1} $ster^{-1}$ (cases 1-8)

angle, °	β_{01}	β_{02}	β_{03}	β_{04}	β_{05}	β_{06}	β_{07}	β_{08}
0.1	355.78	53.182	75.181	871.25	653.290	2689.7	3262.0	2215.3
0.169	153.72	28.464	39.059	387.01	290.350	1396.9	1609.8	1039.7
0.338	50.739	12.465	16.446	132.49	99.4720	585.05	618.23	395.09
0.573	20.348	5.9045	7.3639	57.757	43.2250	283.71	307.91	184.58
1.72	2.9015	1.0191	1.1855	8.1372	6.29410	49.063	54.684	34.040
5.73	2.9564e-01	1.1347e-01	1.2633e-01	7.3434e-01	6.32420e-01	5.1290	5.9699	4.3004
10	9.9395e-02	4.1620e-02	4.4602e-02	2.4154e-01	2.15540e-01	1.7321	2.1107	1.4749
15	4.7716e-02	2.0375e-02	2.0871e-02	1.0703e-01	9.28280e-02	7.7653e-01	9.0405e-01	5.9012e-01
20	2.6227e-02	1.0990e-02	1.1988e-02	5.4145e-02	4.42680e-02	3.9389e-01	4.4523e-01	2.9443e-01
25	1.5466e-02	6.1656e-03	7.0743e-03	3.0441e-02	2.39000e-02	2.4745e-01	2.7335e-01	1.6615e-01
30	9.7519e-03	3.8877e-03	4.2671e-03	1.7026e-02	1.44500e-02	1.3752e-01	1.6128e-01	1.0204e-01
40	4.6734e-03	1.8991e-03	1.9990e-03	7.2160e-03	6.01400e-03	6.8674e-02	7.9133e-02	4.8882e-02
50	2.3972e-03	1.0196e-03	1.0695e-03	3.8094e-03	2.99340e-03	3.7004e-02	4.3884e-02	2.5982e-02
60	1.4785e-03	6.0280e-04	6.4576e-04	2.1547e-03	1.73660e-03	2.1594e-02	2.5483e-02	1.4840e-02
70	9.9904e-04	4.0688e-04	4.3685e-04	1.3769e-03	1.09400e-03	1.4017e-02	1.6550e-02	9.6046e-03
80	7.0735e-04	3.0191e-04	3.0890e-04	9.3400e-04	7.23760e-04	9.7490e-03	1.1239e-02	6.7265e-03
90	5.3652e-04	2.4593e-04	2.4592e-04	7.1848e-04	5.24120e-04	7.2413e-03	8.4110e-03	4.8646e-03
100	4.6757e-04	2.2394e-04	2.1893e-04	5.7577e-04	4.36260e-04	5.6499e-03	6.6940e-03	3.9923e-03
110	4.4657e-04	2.2393e-04	2.1892e-04	5.1384e-04	4.07270e-04	4.7480e-03	5.8912e-03	3.4458e-03
120	4.2656e-04	2.3392e-04	2.2891e-04	4.9379e-04	3.97230e-04	4.3681e-03	5.5491e-03	3.1757e-03
130	4.3649e-04	2.6290e-04	2.5689e-04	5.1058e-04	4.07100e-04	4.1531e-03	5.1541e-03	2.8847e-03
140	4.3638e-04	2.7488e-04	2.7486e-04	5.7309e-04	4.45820e-04	3.9046e-03	4.8223e-03	2.8087e-03
150	4.8909e-04	3.0882e-04	3.0180e-04	6.6212e-04	5.23190e-04	4.1061e-03	4.6344e-03	2.9532e-03
160	5.7340e-04	3.6268e-04	3.4665e-04	8.0075e-04	6.66510e-04	4.6227e-03	5.1417e-03	3.3427e-03
170	7.5441e-04	4.6710e-04	4.6697e-04	1.2964e-03	9.39270e-04	5.8137e-03	5.5497e-03	3.5323e-03
a, m^{-1}	0.082	0.114	0.122	0.195	0.179	0.337	0.366	0.125
b, m^{-1}	0.117	0.037	0.043	0.275	0.219	1.583	1.824	1.205
b_B, m^{-1}	0.002 92	0.001 63	0.001 63	0.003 85	0.002 85	0.0301	0.0365	0.0212
$\omega_0 = b/c$	0.588	0.247	0.258	0.585	0.551	0.824	0.833	0.906
$B = b_B/b$	0.025	0.044	0.038	0.014	0.013	0.019	0.020	0.018

Table 10.3b. Petzold [75] total angular scattering functions in m^{-1} $ster^{-1}$ (cases 9-15)

angle, °	β_{09}	β_{10}	β_{11}	β_{12}	β_{13}	β_{14}	β_{15}
0.1	2.3282	179.35	199.01	1356.7	843.35	185.95	1.8806
0.169	1.6820	133.13	144.74	873.28	440.53	92.305	—
0.338	1.0948	74.022	78.744	429.80	186.82	36.595	0.47797
0.573	6.9716e-01	44.265	46.846	230.23	83.938	15.455	—
1.72	1.8949e-01	14.547	15.277	47.846	12.466	2.4432	7.6815e-02
5.73	3.0964e-02	2.8018	3.0244	4.7692	1.2830	2.4749e-01	—
10	1.2294e-02	9.1763e-01	9.5995e-01	1.4783	4.4257e-01	7.5584e-02	1.1095e-02
15	5.9282e-03	3.2706e-01	3.5423e-01	5.3683e-01	1.7070e-01	3.3611e-02	7.3780e-03
20	3.2493e-03	1.6484e-01	1.6867e-01	2.9776e-01	9.8342e-02	1.9562e-02	4.6391e-03
25	1.8397e-03	8.6398e-02	8.5362e-02	1.6590e-01	5.1004e-02	1.0484e-02	2.1897e-03
30	1.1498e-03	5.2544e-02	5.1529e-02	1.0681e-01	3.5173e-02	6.7314e-03	1.1299e-03
40	5.2494e-04	2.1259e-02	2.1947e-02	5.2872e-02	1.6021e-02	2.8472e-03	5.8194e-04
50	3.1297e-04	1.1337e-02	1.0936e-02	2.6257e-02	8.3755e-03	1.5787e-03	3.6297e-04
60	2.2398e-04	6.0804e-03	5.8599e-03	1.4335e-02	4.7229e-03	9.0335e-04	2.6098e-04
70	1.8299e-04	3.7631e-03	3.4636e-03	8.9651e-03	2.8505e-03	5.8462e-04	2.0999e-04
80	1.6099e-04	2.4595e-03	2.4291e-03	5.9897e-03	1.9039e-03	4.1874e-04	1.8899e-04
90	1.4699e-04	1.8223e-03	1.8916e-03	4.4557e-03	1.4554e-03	3.3579e-04	1.6499e-04
100	1.4399e-04	1.5633e-03	1.5630e-03	3.3661e-03	1.1862e-03	2.9282e-04	1.5899e-04
110	1.5399e-04	1.4136e-03	1.4631e-03	2.9983e-03	1.0764e-03	2.8581e-04	1.6499e-04
120	1.6599e-04	1.4231e-03	1.3929e-03	2.8275e-03	1.0053e-03	2.9579e-04	1.7599e-04
130	1.8398e-04	1.4420e-03	1.4416e-03	2.7146e-03	9.7299e-04	3.0875e-04	2.0198e-04
140	1.9698e-04	1.5398e-03	1.4499e-03	2.7076e-03	9.7220e-04	3.2668e-04	2.2598e-04
150	2.1597e-04	1.6656e-03	1.5657e-03	2.7242e-03	1.0035e-03	3.6154e-04	2.5097e-04
160	2.5794e-04	1.7669e-03	1.7459e-03	2.9776e-03	1.1587e-03	4.0822e-04	2.6995e-04
170	3.2384e-04	2.4399e-03	2.2033e-03	3.3589e-03	1.4491e-03	4.9891e-04	3.5085e-04
a, m^{-1}	0.093	0.138	0.764	0.196	0.188	0.093	0.085
b, m^{-1}	0.009	0.547	0.576	1.284	0.407	0.081	0.008
b_B, m^{-1}	0.00107	0.00984	0.00979	0.0193	0.00692	0.00203	0.00117
$\omega_0 = b/c$	0.093	0.798	0.430	0.867	0.685	0.463	0.091
$B = b_B/b$	0.119	0.018	0.017	0.015	0.017	0.025	0.146

Table 10.4. Additional inherent optical properties to 15 Petzold angular scattering coefficients [75]. Maximal values of these properties are printed in bold and minimum values are printed in bold italic

#	c, m^{-1}	b, m^{-1}	a, m^{-1}	b_B, m^{-1}	$\omega_0 = b/c$	$B = b_B/b$	$x_G = b_B/(a+b_B)$	$\beta(140^\circ)$, $m^{-1}\,ster^{-1}$	$p(140^\circ)$, $ster^{-1}$
1	0.199	0.117	***0.082***	0.002 925	0.588	0.025	0.034 442	0.000 436 38	0.003 729 7
2	0.151	0.037	0.114	0.001 628	0.247	0.044	0.014 080	0.000 274 88	0.007 429 2
3	0.165	0.043	0.122	0.001 634	0.258	0.038	0.013 216	0.000 274 86	0.006 392 1
4	0.470	0.275	0.195	0.003 850	0.585	0.014	0.019 361	0.000 573 09	0.002 084 0
5	0.398	0.219	0.179	0.002 847	0.551	***0.013***	0.015 656	0.000 445 82	***0.002 035 7***
6	1.920	1.583	0.337	0.030 077	0.824	0.019	0.081 936	0.003 904 60	0.002 466 6
7	**2.190**	**1.824**	0.366	**0.036 480**	0.833	0.020	0.090 638	**0.004 822 30**	0.002 643 8
8	1.330	1.205	0.125	0.021 690	**0.906**	0.018	**0.147 860**	0.002 808 70	0.002 330 9
9	0.102	0.009	0.093	***0.001 071***	0.093	0.119	***0.011 385***	***0.000 196 98***	0.021 887 0
10	0.685	0.547	0.138	0.009 846	0.798	0.018	0.066 596	0.001 539 80	0.002 815 0
11	1.340	0.576	0.764	0.009 792	0.430	0.017	0.012 655	0.001 449 90	0.002 517 2
12	1.480	1.284	0.196	0.019 260	0.867	0.015	0.089 473	0.002 707 60	0.002 108 7
13	0.595	0.407	0.188	0.006 919	0.685	0.017	0.035 497	0.000 972 20	0.002 388 7
14	0.174	0.081	0.093	0.002 025	0.463	0.025	0.021 310	0.000 326 68	0.004 033 1
15	***0.093***	***0.008***	0.085	0.001 168	***0.091***	**0.146**	0.013 555	0.000 225 98	**0.028 247 0**

Table 10.5a. Mankovsky [76, 77] seawater angular scattering coefficients in $m^{-1}\,ster^{-1}$ (cases 1–7). Values in parentheses represent extrapolated and interpolated values

ang, °	β_{01}	β_{02}	β_{03}	β_{04}	β_{05}	β_{06}	β_{07}
(0.25)	146.29	56.691	32.871	57.838	23.036	43.313	22.265
(0.75)	85.333	36.418	20.961	28.243	12.411	32.249	16.673
(1.25)	50.982	23.884	13.640	14.313	6.9058	24.278	12.630
(1.50)	39.757	19.490	11.090	10.333	5.2133	21.150	11.041
(1.75)	31.197	15.985	9.0618	7.5304	3.9675	18.476	9.6787
2.0	24.267	13.032	7.3285	5.4327	2.9855	16.033	8.4143
(2.5)	15.621	9.0974	5.0994	3.0833	1.8362	12.520	6.6300
(3.5)	6.7564	4.6102	2.5452	1.0684	0.73573	7.7413	4.1669
(4.5)	3.2175	2.5352	1.3792	0.43005	0.33529	4.9982	2.7404
(5.5)	1.6866	1.5136	0.81155	0.20106	0.17387	3.3707	1.8863
(6.5)	0.97323	0.98088	0.51822	0.10915	0.10257	2.3742	1.3587
7.5	0.47634	0.55965	0.26786	0.45490E-01	0.45490E-01	1.5063	0.84706
12.5	0.12809	0.22260	0.84628E-01	0.19387E-01	0.19387E-01	0.47590	0.28676
(15.0)	0.97480E-01	0.14754	0.64404E-01	0.14925E-01	0.14925E-01	0.31183	0.17944
17.5	0.74185E-01	0.97795E-01	0.49013E-01	0.11490E-01	0.11490E-01	0.20432	0.11228
22.5	0.29855E-01	0.49547E-01	0.23715E-01	0.71617E-02	0.76739E-02	0.12735	0.73285E-01
27.5	0.21214E-01	0.32856E-01	0.13697E-01	0.42327E-02	0.47491E-02	0.62606E-01	0.44322E-01
(30.0)	0.16388E-01	0.23416E-01	0.10340E-01	0.37112E-02	0.39311E-02	0.53029E-01	0.31953E-01
32.5	0.12659E-01	0.16688E-01	0.78058E-02	0.32540E-02	0.32540E-02	0.44918E-01	0.23036E-01
37.5	0.96965E-02	0.14342E-01	0.43313E-02	0.22213E-02	0.22213E-02	0.21708E-01	0.13385E-01
42.5	0.36468E-02	0.76193E-02	0.39987E-02	0.15557E-02	0.17455E-02	0.21474E-01	0.87481E-02
(45.0)	0.29574E-02	0.59692E-02	0.29917E-02	0.13675E-02	0.13993E-02	0.13518E-01	0.71765E-02
47.5	0.23978E-02	0.46754E-02	0.22378E-02	0.12018E-02	0.11215E-02	0.85078E-02	0.58859E-02
52.5	0.17853E-02	0.32487E-02	0.16282E-02	0.89478E-03	0.89478E-03	0.59117E-02	0.43824E-02
57.5	0.12252E-02	0.24446E-02	0.13747E-02	0.70504E-03	0.70504E-03	0.43473E-02	0.30776E-02
62.5	0.93350E-03	0.16987E-02	0.10236E-02	0.51300E-03	0.57559E-03	0.34683E-02	0.21385E-02
67.5	0.64242E-03	0.15410E-02	0.10661E-02	0.47623E-03	0.47623E-03	0.24993E-02	0.20788E-02
72.5	0.55159E-03	0.11524E-02	0.77914E-03	0.39050E-03	0.39050E-03	0.17849E-02	0.14178E-02
77.5	0.44855E-03	0.89498E-03	0.56470E-03	0.35630E-03	0.35630E-03	0.15915E-02	0.11267E-02
82.5	0.39675E-03	0.90890E-03	0.49948E-03	0.28088E-03	0.28088E-03	0.13757E-02	0.11442E-02
87.5	0.36460E-03	0.69473E-03	0.57785E-03	0.25812E-03	0.28302E-03	0.13862E-02	0.91583E-03
(90.0)	0.37309E-03	0.61918E-03	0.49753E-03	0.25663E-03	0.28139E-03	0.12213E-02	0.91583E-03
92.5	0.38178E-03	0.55184E-03	0.42837E-03	0.25516E-03	0.27978E-03	0.10760E-02	0.91583E-03
97.5	0.36184E-03	0.62880E-03	0.40599E-03	0.27702E-03	0.27702E-03	0.99659E-03	0.99659E-03
102.5	0.33252E-03	0.57785E-03	0.37309E-03	0.27153E-03	0.27153E-03	0.98133E-03	0.67892E-03
107.5	0.34803E-03	0.60481E-03	0.38161E-03	0.26462E-03	0.29690E-03	0.10271E-02	0.79729E-03
112.5	0.39611E-03	0.54678E-03	0.34500E-03	0.28630E-03	0.28630E-03	0.97233E-03	0.68836E-03
117.5	0.34683E-03	0.54969E-03	0.43663E-03	0.31413E-03	0.31413E-03	0.91225E-03	0.70813E-03
122.5	0.41516E-03	0.62837E-03	0.42483E-03	0.33282E-03	0.33282E-03	0.90827E-03	0.72147E-03
127.5	0.46959E-03	0.64821E-03	0.45890E-03	0.34891E-03	0.34891E-03	0.10040E-02	0.91562E-03
132.5	0.54931E-03	0.63069E-03	0.48957E-03	0.40347E-03	0.35960E-03	0.10711E-02	0.91162E-03
137.5	0.59145E-03	0.69489E-03	0.50340E-03	0.40918E-03	0.45911E-03	0.11013E-02	0.10278E-02
(140)	0.64695E-03	0.74153E-03	0.50035E-03	0.43718E-03	0.46214E-03	0.11203E-02	0.11243E-02
142.5	0.70245E-03	0.78816E-03	0.49730E-03	0.46517E-03	0.46517E-03	0.11392E-02	0.12207E-02
147.5	0.74545E-03	0.85589E-03	0.55261E-03	0.48800E-03	0.48800E-03	0.12371E-02	0.10775E-02
152.5	0.70245E-03	0.82531E-03	0.36026E-03	0.53532E-03	0.53532E-03	0.13385E-02	0.12207E-02
157.5	0.96609E-03	0.11092E-02	0.50701E-03	0.58886E-03	0.58886E-03	0.20184E-02	0.13336E-02
162.5	0.10723E-02	0.11758E-02	0.56275E-03	0.57586E-03	0.61704E-03	0.20432E-02	0.15860E-02

Table 10.5b. Mankovsky [76, 77] seawater angular scattering coefficients in m^{-1} $ster^{-1}$ (cases 8–14). Values in parentheses represent extrapolated and interpolated values.

ang, °	β_{08}	β_{09}	β_{10}	β_{11}	β_{12}	β_{13}	β_{14}
(0.25)	105.37	53.545	42.026	163.01	93.372	46.485	51.345
(0.75)	64.926	30.684	21.848	104.76	57.308	28.213	31.941
(1.25)	40.928	18.023	11.787	68.741	35.910	17.523	20.315
(1.50)	32.765	13.961	8.7804	56.133	28.656	13.929	16.335
(1.75)	26.382	10.890	6.6026	46.049	23.026	11.137	13.209
2.0	21.136	8.4143	4.9547	37.602	18.417	8.8112	10.593
(2.5)	14.240	5.3817	2.9670	26.074	12.366	5.8919	7.2180
(3.5)	6.7720	2.3121	1.1634	13.098	5.8373	2.7329	3.4840
(4.5)	3.5238	1.1074	0.52944	7.0993	3.0284	1.3901	1.8370
(5.5)	2.0064	0.59104	0.27952	4.1612	1.7227	0.77535	1.0581
(6.5)	1.2497	0.35157	0.17128	2.6255	1.0721	0.47424	0.66580
7.5	0.70456	0.16901	0.92879E-01	1.5784	0.58643	0.23330	0.35311
12.50	0.28023	0.59926E-01	0.87502E-01	0.58508	0.24390	0.70397E-01	0.12519
(15.0)	0.19450	0.42074E-01	0.47744E-01	0.45626	0.18587	0.47748E-01	0.86887E-01
17.5	0.13499	0.29540E-01	0.24571E-01	0.35499	0.14132	0.32386E-01	0.60306E-01
22.5	0.62376E-01	0.15672E-01	0.13336E-01	0.19734	0.55618E-01	0.18839E-01	0.31265E-01
27.5	0.30663E-01	0.10392E-01	0.86420E-02	0.96876E-01	0.27939E-01	0.10390E-01	0.14676E-01
(30.0)	0.24804E-01	0.84065E-02	0.67533E-02	0.74854E-01	0.22091E-01	0.88009E-02	0.11469E-01
32.5	0.20064E-01	0.68001E-02	0.52773E-02	0.57838E-01	0.17467E-01	0.74547E-02	0.89626E-02
37.5	0.14676E-01	0.41373E-02	0.37733E-02	0.40385E-01	0.11123E-01	0.41368E-02	0.59795E-02
42.5	0.98156E-02	0.34827E-02	0.27034E-02	0.34058E-01	0.79839E-02	0.31038E-02	0.41870E-02
(45.0)	0.88291E-02	0.27920E-02	0.21425E-02	0.28590E-01	0.65496E-02	0.24596E-02	0.35146E-02
47.5	0.79399E-02	0.22383E-02	0.16975E-02	0.24000E-01	0.53730E-02	0.19492E-02	0.29502E-02
52.5	0.64821E-02	0.18269E-02	0.13235E-02	0.14495E-01	0.40852E-02	0.17048E-02	0.20974E-02
57.5	0.42483E-02	0.14071E-02	0.10674E-02	0.12538E-01	0.30776E-02	0.14068E-02	0.16529E-02
62.5	0.30911E-02	0.11226E-02	0.10003E-02	0.85156E-02	0.22398E-02	0.11224E-02	0.12593E-02
67.5	0.25575E-02	0.10421E-02	0.88678E-03	0.60009E-02	0.18976E-02	0.10419E-02	0.10419E-02
72.5	0.19571E-02	0.79747E-03	0.59104E-03	0.39014E-02	0.12625E-02	0.79732E-03	0.91545E-03
77.5	0.15553E-02	0.71091E-03	0.60508E-03	0.35663E-02	0.12948E-02	0.81620E-03	0.81620E-03
82.5	0.11709E-02	0.61449E-03	0.48811E-03	0.25016E-02	0.11434E-02	0.61445E-03	0.72191E-03
87.5	0.98133E-03	0.52701E-03	0.49183E-03	0.23026E-02	0.10285E-02	0.61916E-03	0.61916E-03
(90.0)	0.89498E-03	0.51798E-03	0.48341E-03	0.21243E-02	0.94889E-03	0.56144E-03	0.56144E-03
92.5	0.81624E-03	0.50911E-03	0.47513E-03	0.19598E-02	0.87542E-03	0.50910E-03	0.50910E-03
97.5	0.79162E-03	0.57348E-03	0.45553E-03	0.18976E-02	0.84765E-03	0.57343E-03	0.57343E-03
102.5	0.76176E-03	0.46432E-03	0.30677E-03	0.18290E-02	0.81699E-03	0.46430E-03	0.46430E-03
107.5	0.64806E-03	0.43323E-03	0.28616E-03	0.14833E-02	0.77842E-03	0.43315E-03	0.50890E-03
112.5	0.68836E-03	0.40079E-03	0.37395E-03	0.16528E-02	0.73827E-03	0.37396E-03	0.40071E-03
117.5	0.64583E-03	0.43173E-03	0.34286E-03	0.17387E-02	0.77663E-03	0.43166E-03	0.43166E-03
122.5	0.67331E-03	0.38754E-03	0.32985E-03	0.15784E-02	0.99590E-03	0.45524E-03	0.45524E-03
127.5	0.72730E-03	0.40431E-03	0.34412E-03	0.14165E-02	0.89375E-03	0.46418E-03	0.46418E-03
132.5	0.70765E-03	0.46764E-03	0.35466E-03	0.15143E-02	0.91246E-03	0.35469E-03	0.46757E-03
137.5	0.69489E-03	0.39987E-03	0.39987E-03	0.15930E-02	0.89581E-03	0.39985E-03	0.46978E-03
(140)	0.76971E-03	0.42159E-03	0.39749E-03	0.16004E-02	0.95511E-03	0.36805E-03	0.48357E-03
142.5	0.84453E-03	0.44332E-03	0.39511E-03	0.16077E-02	0.10144E-02	0.33625E-03	0.49735E-03
147.5	0.74545E-03	0.48141E-03	0.40965E-03	0.17467E-02	0.98224E-03	0.36512E-03	0.48132E-03
152.5	0.86420E-03	0.52085E-03	0.48598E-03	0.18459E-02	0.88352E-03	0.48598E-03	0.48598E-03
157.5	0.96609E-03	0.66852E-03	0.58212E-03	0.23726E-02	0.94453E-03	0.44163E-03	0.58218E-03
162.5	0.91267E-03	0.75930E-03	0.69233E-03	0.21888E-02	0.11226E-02	0.57591E-03	0.69240E-03

Table 10.5c. Mankovsky [76, 77] seawater angular scattering coefficients in $m^{-1}\,ster^{-1}$ (cases 15–21). Values in parentheses represent extrapolated and interpolated values

ang, °	β_{15}	β_{16}	β_{17}	β_{18}	β_{19}	β_{20}	β_{21}
(0.25)	30.802	41.392	30.303	29.081	34.223	29.211	78.944
(0.75)	16.977	22.554	19.393	17.419	22.874	18.136	44.589
(1.25)	9.6529	12.675	12.667	10.699	15.537	11.509	25.892
(1.50)	7.3643	9.6121	10.316	8.4637	12.882	9.2443	19.936
(1.75)	5.6622	7.3460	8.4441	6.7377	10.724	7.4656	15.457
2.0	4.3156	5.5595	6.8397	5.3093	8.8112	5.9571	11.886
(2.5)	2.6967	3.4345	4.7748	3.5294	6.3388	4.0636	7.5090
(3.5)	1.1185	1.3884	2.3978	1.6270	3.3267	1.9498	3.1594
(4.5)	0.52549	0.63503	1.3063	0.82909	1.8622	1.0212	1.4849
(5.5)	0.27963	0.32862	0.77216	0.46705	1.1117	0.58376	0.77958
(6.5)	0.16854	0.19240	0.49517	0.29084	0.70792	0.36426	0.45720
7.5	0.80894E-01	0.88698E-01	0.25581	0.14385	0.35311	0.17698	0.22280
12.5	0.39587E-01	0.36104E-01	0.80826E-01	0.53401E-01	0.75431E-01	0.50998E-01	0.80826E-01
(15.0)	0.27794E-01	0.28116E-01	0.58071E-01	0.37928E-01	0.53574E-01	0.38811E-01	0.52961E-01
17.5	0.19515E-01	0.21896E-01	0.41721E-01	0.26938E-01	0.38050E-01	0.29536E-01	0.34702E-01
22.5	0.12163E-01	0.10841E-01	0.24835E-01	0.17581E-01	0.21138E-01	0.17581E-01	0.17581E-01
27.5	0.70246E-02	0.94759E-02	0.14676E-01	0.94759E-02	0.94759E-02	0.10390E-01	0.94759E-02
(30.0)	0.57481E-02	0.70717E-02	0.10953E-01	0.75775E-02	0.80265E-02	0.88009E-02	0.75775E-02
32.5	0.47036E-02	0.52776E-02	0.81740E-02	0.60594E-02	0.67988E-02	0.74547E-02	0.60594E-02
37.5	0.31381E-02	0.37728E-02	0.59795E-02	0.35210E-02	0.47497E-02	0.47497E-02	0.37728E-02
42.5	0.23545E-02	0.23545E-02	0.34826E-02	0.31038E-02	0.34826E-02	0.34826E-02	0.23545E-02
(45.0)	0.19993E-02	0.21423E-02	0.34346E-02	0.24596E-02	0.27917E-02	0.29914E-02	0.19993E-02
47.5	0.16976E-02	0.19492E-02	0.33872E-02	0.19492E-02	0.22379E-02	0.25695E-02	0.16976E-02
52.5	0.13234E-02	0.15548E-02	0.18268E-02	0.18268E-02	0.17048E-02	0.18268E-02	0.15548E-02
57.5	0.10672E-02	0.11974E-02	0.18124E-02	0.16529E-02	0.18124E-02	0.16529E-02	0.14068E-02
62.5	0.10003E-02	0.11224E-02	0.17384E-02	0.12593E-02	0.14796E-02	0.12593E-02	0.85142E-03
67.5	0.77238E-03	0.88681E-03	0.15411E-02	0.11690E-02	0.13117E-02	0.10419E-02	0.77238E-03
72.5	0.59106E-03	0.69444E-03	0.10756E-02	0.91545E-03	0.10756E-02	0.91545E-03	0.59106E-03
77.5	0.51499E-03	0.60506E-03	0.93712E-03	0.71088E-03	0.71088E-03	0.71088E-03	0.51499E-03
82.5	0.52298E-03	0.52298E-03	0.82886E-03	0.61445E-03	0.61445E-03	0.52298E-03	0.52298E-03
87.5	0.49181E-03	0.52699E-03	0.72745E-03	0.52699E-03	0.52699E-03	0.52699E-03	0.49181E-03
(90.0)	0.48339E-03	0.51797E-03	0.65963E-03	0.56144E-03	0.56144E-03	0.56144E-03	0.40673E-03
92.5	0.47512E-03	0.50910E-03	0.59814E-03	0.59814E-03	0.59814E-03	0.59814E-03	0.33636E-03
97.5	0.45550E-03	0.48807E-03	0.48807E-03	0.57343E-03	0.67373E-03	0.48807E-03	0.45550E-03
102.5	0.46430E-03	0.46430E-03	0.43331E-03	0.64091E-03	0.46430E-03	0.46430E-03	0.43331E-03
107.5	0.40424E-03	0.43315E-03	0.40424E-03	0.43315E-03	0.43315E-03	0.43315E-03	0.40424E-03
112.5	0.40071E-03	0.37396E-03	0.40071E-03	0.47079E-03	0.55313E-03	0.47079E-03	0.37396E-03
117.5	0.36740E-03	0.43166E-03	0.43166E-03	0.58230E-03	0.50716E-03	0.36740E-03	0.36740E-03
122.5	0.38748E-03	0.45524E-03	0.45524E-03	0.60013E-03	0.45524E-03	0.45524E-03	0.38748E-03
127.5	0.40428E-03	0.46418E-03	0.40428E-03	0.62616E-03	0.40428E-03	0.46418E-03	0.40428E-03
132.5	0.40724E-03	0.40724E-03	0.40724E-03	0.46757E-03	0.46757E-03	0.40724E-03	0.35469E-03
137.5	0.39985E-03	0.39985E-03	0.39985E-03	0.46978E-03	0.46978E-03	0.39985E-03	0.39985E-03
(140.0)	0.42156E-03	0.44860E-03	0.44860E-03	0.48357E-03	0.45652E-03	0.42156E-03	0.39746E-03
142.5	0.44326E-03	0.49735E-03	0.49735E-03	0.49735E-03	0.44326E-03	0.44326E-03	0.39506E-03
147.5	0.40967E-03	0.56550E-03	0.56550E-03	0.48132E-03	0.40967E-03	0.48132E-03	0.48132E-03
152.5	0.44322E-03	0.59789E-03	0.48598E-03	0.52074E-03	0.44322E-03	0.52074E-03	0.44322E-03
157.5	0.38464E-03	0.66843E-03	0.38464E-03	0.86110E-03	0.58218E-03	0.76746E-03	0.50706E-03
162.5	0.51328E-03	0.87168E-03	0.57591E-03	0.64619E-03	0.64619E-03	0.97804E-03	0.64619E-03

Table 10.6. Additional inherent optical properties to 21 Mankovsky angular scattering coefficients [76, 77]. Maximal values of these properties are printed in bold and minimum values are printed in bold italic

#	c, m^{-1}	b, m^{-1}	a, m^{-1}	b_B, m^{-1}	$\omega_0 = b/c$	$B = b_B/b$	$x_G = b_B/(a+b_B)$	$\beta(140^\circ)$, $m^{-1}\,ster^{-1}$	$p(140^\circ)$, $ster^{-1}$
1	0.557 23	0.409 86	0.147 37	0.001 312 4	0.735 53	***0.007 813***	0.021 266	0.646 949E-03	***0.157 846E-02***
2	0.402 95	0.299 34	0.103 61	0.001 280 1	0.742 87	0.014 286	0.039 638	0.741 526E-03	0.247 720E-02
3	0.276 31	0.156 58	0.119 73	0.000 437 8	0.566 68	0.017 857	0.022 820	0.500 350E-03	0.319 549E-02
4	0.161 18	0.105 92	0.055 26	0.000 238 7	0.657 15	0.021 277	0.039 185	0.437 178E-03	0.412 743E-02
5	0.142 76	***0.062 17***	0.080 59	***0.000 143 2***	***0.435 49***	**0.037 037**	0.027 778	0.462 142E-03	**0.743 351E-02**
6	0.626 30	0.518 08	0.108 22	0.003 676 9	0.827 21	0.013 699	0.061 545	0.112 028E-02	0.216 238E-02
7	0.435 19	0.290 13	0.145 06	0.001 717 9	0.666 67	0.020 408	0.039 217	0.112 427E-02	0.387 505E-02
8	0.584 86	0.467 42	0.117 44	0.002 206 9	0.799 20	0.010 101	0.038 649	0.769 710E-03	0.164 672E-02
9	0.237 17	0.168 09	0.069 08	0.000 504 5	0.708 73	0.017 857	0.041 641	0.421 593E-03	0.250 814E-02
10	0.168 09	0.115 13	0.052 96	0.000 294 6	0.684 93	0.022 222	0.046 082	0.397 488E-03	0.345 251E-02
11	**1.105 20**	**0.941 76**	**0.163 44**	**0.010 313 0**	0.852 12	0.011 628	0.062 795	**0.160 037E-02**	0.169 934E-02
12	0.559 56	0.409 86	0.149 70	0.002 239 7	0.732 47	0.013 333	0.035 218	0.955 112E-03	0.233 034E-02
13	0.207 23	0.179 60	0.027 63	0.000 508 8	**0.866 67**	0.015 773	0.092 993	***0.368 051E-03***	0.204 928E-02
14	0.267 10	0.230 26	0.036 84	0.000 714 5	0.862 07	0.013 477	0.077 691	0.483 568E-03	0.210 009E-02
15	***0.115 13***	0.092 10	0.023 03	0.000 243 0	0.799 97	0.028 653	0.102 807	0.421 558E-03	0.457 718E-02
16	0.231 17	0.115 13	0.116 04	0.000 358 2	0.498 03	0.027 027	0.026 115	0.448 601E-03	0.389 647E-02
17	0.216 44	0.158 88	0.057 56	0.000 458 9	0.734 06	0.018 180	0.047 784	0.448 601E-03	0.282 352E-02
18	0.156 58	0.117 43	0.039 15	0.000 417 8	0.749 97	0.030 300	0.083 313	0.483 568E-03	0.411 792E-02
19	0.223 35	0.191 11	0.032 24	0.000 611 8	0.855 65	0.016 750	0.090 321	0.456 524E-03	0.238 880E-02
20	0.151 97	0.131 25	***0.020 72***	0.000 416 0	0.863 66	0.024 150	**0.132 680**	0.421 558E-03	0.321 187E-02
21	0.354 00	0.225 37	0.128 63	0.000 591 3	0.636 64	0.011 642	***0.019 991***	0.397 456E-03	0.176 357E-02

the Atlantic Ocean. The unique feature of this *in situ* experiment is that it was made in coastal waters with the largest range of variability of beam scattering coefficient known in the history of ocean optics ($0.37\,\mathrm{m}^{-1} \le b \le 9.3\,\mathrm{m}^{-1}$). The variability range of the probability of scattering was: $0.0058 \le B \le 0.0328$. The values of angular scattering coefficients have been measured at 590 scattering angles between 0.6 and 177.3 degrees. The values of these VSF for a subset of scattering angles with corresponding values of b, b_B, and B are given in Table 10.7.

10.3.5 Relationships between integral properties of experimental light scattering phase functions

Analysis of a massive database of experimental light scattering phase functions allows us to specify certain relationships between integral and angular properties of phase functions that determine their shape [81]. These parameters, presented in the decreasing order of importance, are:

$B \equiv b_B/b = 2\pi \int_{\pi/2}^{\pi} p(\lambda, \boldsymbol{x}, \cos\vartheta) \sin\vartheta \,\mathrm{d}\vartheta$ — the probability of backscattering;
$p(140^\circ)$ — the value of the phase function at 140°.
$\overline{\cos\vartheta} = 2\pi \int_0^{\pi} p(\cos\vartheta) \cos\vartheta \sin\vartheta \,\mathrm{d}\vartheta$ — the average cosine over phase function;
$\overline{\cos^2\vartheta} = 2\pi \int_0^{\pi} p(\cos\vartheta) \cos^2\vartheta \sin\vartheta \,\mathrm{d}\vartheta$ — the average square of cosine over phase function.

The probability of backscattering $B = b_B/b$ is defined by eq. (10.10). It is usually correlated with the total beam scattering coefficient [82]:

$$B = [0.5 b_W + 0.006\,18(b - b_W) + 0.003\,22(b - b_W)^2]/b, \quad r^2 = 0.88, \quad (10.20)$$

with the scattering coefficient of pure water b_W given by eq. (10.18). Relationship (10.20) is derived for typical oceanic waters, that include a total of 101 Petzold, Mankovsky and LEO-2000 measurements, it is valid for $\lambda \approx 500 \div 560\,\mathrm{nm}$ and $0.008\,\mathrm{m}^{-1} \le b \le 9.3\,\mathrm{m}^{-1}$.

The value of the phase function in the vicinity of 140° is correlated extremely well with the probability of backscattering. According to Haltrin *et al.* [82] the relationship based on more than 1000 phase functions, that include 15 Petzold [75], 41 Mankovsky [76, 77, 83], and about a thousand Lee [80] phase functions, is

$$B \equiv b_B/b = 2\pi\chi p(140^\circ), \quad b_B = 2\pi\chi\beta(140^\circ), \quad \chi = 1.15, \quad r^2 = 0.999, \quad (10.21)$$

with the phase function p normalized according to eq. (10.7). The similar relationship for scattering at angle 120° was proposed earlier by Oishi [84] and eq. (10.21) with $\chi = 1.08$ is used currently in the backscattering probe HydroScat by Hoby Labs [85].

Table 10.7a. Total angular scattering coefficients in $m^{-1}\,ster^{-1}$ measured at LEO-15 experiment in 2000 [80]

ang, $^\circ$	β_{58}	β_{59}	β_{60}	β_{57}	β_{51}	β_{16}	β_{19}
0.6	95.11	136.0	133.2	188.2	220.8	316.6	249.0
0.9	41.52	54.52	59.76	85.03	113.7	158.3	139.7
1.5	18.04	23.80	30.02	37.98	58.07	92.80	80.58
2.4	8.245	10.11	14.17	17.68	32.21	41.36	48.67
3.3	4.946	5.592	8.461	11.11	22.18	24.02	29.05
4.5	2.807	3.073	5.158	6.510	14.03	13.23	16.60
6.0	1.511	1.526	2.520	3.448	8.071	8.027	10.50
7.5	0.8835	0.8883	1.434	2.002	5.116	5.439	5.536
9.3	0.5038	0.5042	0.7735	1.048	2.931	2.796	3.120
11.4	0.2705	0.2622	0.3921	0.5267	1.517	1.594	1.727
13.5	0.1854	0.1789	0.2651	0.3763	1.042	1.150	1.162
15.6	0.1262	0.1218	0.1943	0.2550	0.7690	0.8176	0.8477
18.3	0.8264E-01	0.8177E-01	0.1287	0.1662	0.5058	0.5255	0.5498
21.0	0.6169E-01	0.6075E-01	0.9067E-01	0.1150	0.3556	0.3798	0.4029
23.7	0.4778E-01	0.4598E-01	0.6614E-01	0.8348E-01	0.2630	0.2835	0.2946
27.0	0.3321E-01	0.3248E-01	0.4682E-01	0.5951E-01	0.1849	0.1921	0.2010
30.0	0.2450E-01	0.2419E-01	0.3269E-01	0.4155E-01	0.1340	0.1447	0.1473
30.3	0.2395E-01	0.2358E-01	0.3187E-01	0.4032E-01	0.1303	0.1401	0.1440
33.6	0.1751E-01	0.1740E-01	0.2190E-01	0.2996E-01	0.9331E-01	0.1010	0.1062
37.2	0.1274E-01	0.1290E-01	0.1594E-01	0.2121E-01	0.6791E-01	0.7170E-01	0.7784E-01
41.1	0.9146E-02	0.9367E-02	0.1152E-01	0.1509E-01	0.4988E-01	0.5340E-01	0.5448E-01
45.0	0.6827E-02	0.6585E-02	0.8006E-02	0.1121E-01	0.3706E-01	0.4014E-01	0.4020E-01
49.2	0.4957E-02	0.4996E-02	0.5854E-02	0.7808E-02	0.2729E-01	0.2881E-01	0.3157E-01
53.4	0.3910E-02	0.3869E-02	0.4280E-02	0.5657E-02	0.2060E-01	0.2131E-01	0.2450E-01
57.9	0.3078E-02	0.3003E-02	0.3224E-02	0.4281E-02	0.1545E-01	0.1591E-01	0.1792E-01
63.0	0.2204E-02	0.2257E-02	0.2298E-02	0.3448E-02	0.1222E-01	0.1249E-01	0.1381E-01
67.8	0.1791E-02	0.1764E-02	0.1809E-02	0.2634E-02	0.9182E-02	0.9762E-02	0.1031E-01
72.9	0.1456E-02	0.1414E-02	0.1421E-02	0.2054E-02	0.7690E-02	0.8008E-02	0.8132E-02
78.0	0.1237E-02	0.1158E-02	0.1139E-02	0.1609E-02	0.6294E-02	0.6479E-02	0.6938E-02
83.4	0.1010E-02	0.9475E-03	0.9108E-03	0.1389E-02	0.5357E-02	0.5452E-02	0.5678E-02
90.0	0.8379E-03	0.8083E-03	0.7897E-03	0.1139E-02	0.4335E-02	0.4472E-02	0.4855E-02
95.4	0.7642E-03	0.7271E-03	0.6799E-03	0.1034E-02	0.3664E-02	0.4107E-02	0.4268E-02
101.1	0.7182E-03	0.6785E-03	0.5881E-03	0.9497E-03	0.3221E-02	0.3610E-02	0.3692E-02
107.4	0.6520E-03	0.6303E-03	0.5463E-03	0.8842E-03	0.3034E-02	0.3277E-02	0.3406E-02
113.7	0.6550E-03	0.5965E-03	0.5326E-03	0.8701E-03	0.2735E-02	0.3247E-02	0.3208E-02
120.0	0.6098E-03	0.6089E-03	0.5314E-03	0.8158E-03	0.2630E-02	0.3123E-02	0.3215E-02
127.2	0.6141E-03	0.5992E-03	0.5217E-03	0.7899E-03	0.2588E-02	0.2861E-02	0.3128E-02
127.5	0.6112E-03	0.5965E-03	0.5241E-03	0.7881E-03	0.2576E-02	0.2901E-02	0.3157E-02
134.1	0.6226E-03	0.6061E-03	0.5302E-03	0.7899E-03	0.2547E-02	0.2745E-02	0.2994E-02
148.5	0.6625E-03	0.6465E-03	0.6004E-03	0.7990E-03	0.2697E-02	0.2874E-02	0.3035E-02
140.0	0.6303E-03	0.6160E-03	0.5505E-03	0.7678E-03	0.2622E-02	0.2798E-02	0.2996E-02
156.0	0.7034E-03	0.6912E-03	0.6568E-03	0.8348E-03	0.2910E-02	0.3123E-02	0.3367E-02
163.8	0.8958E-03	0.8484E-03	0.9067E-03	0.1113E-02	0.3647E-02	0.3977E-02	0.4076E-02
172.2	0.1715E-02	0.1523E-02	0.1903E-02	0.2063E-02	0.5175E-02	0.6585E-02	0.6843E-02
177.3	0.5324E-02	0.4213E-02	0.5302E-02	0.4683E-02	0.8452E-02	0.1580E-01	0.1262E-01
b, m^{-1}	0.3796	0.4341	0.5807	0.7823	1.631	1.822	2.012
b_B, m^{-1}	0.004352	0.004059	0.003930	0.005482	0.01879	0.02025	0.02234
$B = b_B/b$	0.01147	0.009349	0.006768	0.007007	0.01152	0.01111	0.01110

Table 10.7b. Total angular scattering coefficients in $m^{-1}\,ster^{-1}$ measured at LEO-15 experiment in 2000 [80]

ang, °	β_{34}	β_{53}	β_{33}	β_{56}	β_{27}	β_{42}	β_3
0.6	565.9	358.1	531.2	413.7	677.1	638.6	643.7
0.9	254.5	181.6	235.7	210.2	335.5	320.8	309.5
1.5	107.3	98.63	108.2	117.7	185.2	157.8	158.7
2.4	47.72	50.47	53.24	63.93	76.50	69.06	83.31
3.3	25.93	32.66	30.08	44.44	43.02	39.38	40.99
4.5	13.39	19.01	16.49	26.35	21.61	19.29	22.07
6.0	6.618	11.38	10.10	13.27	11.26	10.43	12.49
7.5	4.053	6.792	6.099	8.142	6.378	6.490	7.494
9.3	2.425	4.018	3.840	4.718	3.449	4.133	4.663
11.4	1.321	2.094	2.215	2.436	1.865	2.467	2.629
13.5	0.9544	1.265	1.601	1.555	1.308	1.829	1.962
15.6	0.6978	0.9290	1.154	1.032	0.9433	1.470	1.408
18.3	0.4642	0.5862	0.7435	0.6588	0.5980	0.9914	0.9925
21.0	0.3394	0.4121	0.5374	0.4537	0.4322	0.7590	0.7704
23.7	0.2557	0.2904	0.3956	0.3249	0.3263	0.5933	0.5884
27.0	0.1835	0.1968	0.2687	0.2222	0.2232	0.4133	0.4195
30.0	0.1386	0.1426	0.1987	0.1643	0.1606	0.3186	0.3309
30.3	0.1358	0.1387	0.1933	0.1610	0.1555	0.3099	0.3226
33.6	0.1027	0.1007	0.1446	0.1185	0.1150	0.2329	0.2499
37.2	0.7581E-01	0.7499E-01	0.1062	0.8664E-01	0.8427E-01	0.1796	0.1935
41.1	0.5751E-01	0.5598E-01	0.7839E-01	0.6306E-01	0.6481E-01	0.1365	0.1468
45.0	0.4423E-01	0.4286E-01	0.5865E-01	0.4653E-01	0.4794E-01	0.1062	0.1145
49.2	0.3402E-01	0.3013E-01	0.4308E-01	0.3410E-01	0.3433E-01	0.8208E-01	0.9010E-01
53.4	0.2623E-01	0.2323E-01	0.3260E-01	0.2569E-01	0.2568E-01	0.6520E-01	0.7026E-01
57.9	0.1994E-01	0.1778E-01	0.2451E-01	0.1922E-01	0.2012E-01	0.5096E-01	0.5659E-01
63.0	0.1509E-01	0.1318E-01	0.1920E-01	0.1475E-01	0.1458E-01	0.3911E-01	0.4273E-01
67.8	0.1215E-01	0.1040E-01	0.1501E-01	0.1134E-01	0.1163E-01	0.3071E-01	0.3465E-01
72.9	0.1009E-01	0.8223E-02	0.1192E-01	0.8969E-02	0.9113E-02	0.2479E-01	0.2791E-01
78.0	0.8313E-02	0.6715E-02	0.1010E-01	0.7307E-02	0.7123E-02	0.2033E-01	0.2370E-01
83.4	0.6962E-02	0.5445E-02	0.8134E-02	0.5858E-02	0.6091E-02	0.1668E-01	0.1949E-01
90.0	0.5926E-02	0.4345E-02	0.6596E-02	0.4696E-02	0.4816E-02	0.1368E-01	0.1647E-01
95.4	0.5126E-02	0.3855E-02	0.5852E-02	0.4053E-02	0.4204E-02	0.1203E-01	0.1482E-01
101.1	0.4696E-02	0.3468E-02	0.5167E-02	0.3604E-02	0.3554E-02	0.1092E-01	0.1320E-01
107.4	0.4323E-02	0.3090E-02	0.4606E-02	0.3249E-02	0.3489E-02	0.9711E-02	0.1238E-01
113.7	0.3997E-02	0.3105E-02	0.4398E-02	0.3131E-02	0.3196E-02	0.9359E-02	0.1169E-01
120.0	0.3808E-02	0.2729E-02	0.4039E-02	0.3004E-02	0.3039E-02	0.8897E-02	0.1098E-01
127.2	0.3765E-02	0.2723E-02	0.3920E-02	0.2984E-02	0.3074E-02	0.8735E-02	0.1056E-01
127.5	0.3773E-02	0.2742E-02	0.3911E-02	0.2916E-02	0.3109E-02	0.8755E-02	0.1054E-01
134.1	0.3679E-02	0.2686E-02	0.4039E-02	0.2943E-02	0.2997E-02	0.8775E-02	0.1061E-01
148.5	0.3906E-02	0.2938E-02	0.4162E-02	0.3117E-02	0.3109E-02	0.9252E-02	0.1081E-01
140.0	0.3722E-02	0.2825E-02	0.4108E-02	0.2925E-02	0.3027E-02	0.8863E-02	0.1059E-01
156.0	0.3988E-02	0.3133E-02	0.4338E-02	0.3402E-02	0.3324E-02	0.9644E-02	0.1098E-01
163.8	0.4642E-02	0.4131E-02	0.5239E-02	0.4653E-02	0.4006E-02	0.1080E-01	0.1204E-01
172.2	0.6291E-02	0.7727E-02	0.7133E-02	0.9094E-02	0.6319E-02	0.1391E-01	0.1454E-01
177.3	0.8684E-02	0.1503E-01	0.1080E-01	0.1814E-01	0.1137E-01	0.2204E-01	0.1598E-01
b, m^{-1}	2.102	2.256	2.495	2.739	3.009	3.296	3.533
b_B, m^{-1}	0.02657	0.02020	0.02869	0.02078	0.02167	0.06251	0.07637
$B = b_B/b$	0.01264	0.008952	0.01150	0.007587	0.007203	0.01896	0.02162

Table 10.7c. Total angular scattering coefficients in $m^{-1}\,ster^{-1}$ measured at LEO-15 experiment in 2000 [80]

ang, °	β_{37}	β_4	β_{47}	β_{46}	β_{45}	β_{41}	β_{48}
0.6	688.0	802.8	899.9	966.8	952.4	815.5	107.1
0.9	373.8	389.6	440.7	506.2	512.7	421.1	588.6
1.5	213.1	183.5	188.4	200.1	208.9	219.5	310.3
2.4	104.9	79.92	83.40	91.90	85.87	100.3	155.2
3.3	61.04	40.89	43.17	45.01	53.07	60.45	93.51
4.5	31.59	21.91	23.18	23.51	24.54	32.99	54.30
6.0	15.54	12.04	12.06	12.77	13.06	17.92	29.91
7.5	9.049	7.774	7.856	8.557	8.069	11.39	19.45
9.3	5.053	4.804	5.072	5.424	5.246	7.201	12.56
11.4	2.544	2.683	3.070	3.179	3.168	4.309	7.868
13.5	1.635	2.045	2.340	2.428	2.437	3.261	6.121
15.6	1.137	1.526	1.771	1.834	1.819	2.451	4.763
18.3	0.7221	1.046	1.286	1.310	1.330	1.752	3.498
21.0	0.4984	0.8140	1.024	1.060	1.064	1.382	2.811
23.7	0.3553	0.6377	0.8057	0.8362	0.8548	1.085	2.207
27.0	0.2441	0.4652	0.5918	0.6185	0.6192	0.7824	1.625
30.0	0.1748	0.3553	0.4669	0.4823	0.4930	0.6158	1.273
30.3	0.1704	0.3449	0.4583	0.4681	0.4829	0.6004	1.244
33.6	0.1226	0.2622	0.3583	0.3692	0.3809	0.4639	0.9657
37.2	0.8822E-01	0.2073	0.2839	0.2926	0.3019	0.3593	0.7531
41.1	0.6377E-01	0.1584	0.2250	0.2384	0.2437	0.2776	0.5927
45.0	0.4694E-01	0.1264	0.1833	0.1894	0.1931	0.2195	0.4719
49.2	0.3424E-01	0.9764E-01	0.1446	0.1543	0.1538	0.1724	0.3697
53.4	0.2562E-01	0.7738E-01	0.1189	0.1234	0.1282	0.1385	0.2977
57.9	0.1917E-01	0.6118E-01	0.9754E-01	0.1012	0.1049	0.1108	0.2403
63.0	0.1405E-01	0.4793E-01	0.7712E-01	0.8041E-01	0.8182E-01	0.8559E-01	0.1866
67.8	0.1124E-01	0.3860E-01	0.6341E-01	0.6597E-01	0.6727E-01	0.6861E-01	0.1516
72.9	0.9007E-02	0.3088E-01	0.5202E-01	0.5474E-01	0.5519E-01	0.5552E-01	0.1216
78.0	0.7355E-02	0.2616E-01	0.4277E-01	0.4491E-01	0.4601E-01	0.4523E-01	0.9927E-01
83.4	0.6118E-02	0.2176E-01	0.3583E-01	0.3761E-01	0.3880E-01	0.3779E-01	0.8257E-01
90.0	0.4927E-02	0.1810E-01	0.2973E-01	0.3143E-01	0.3212E-01	0.3122E-01	0.6727E-01
95.4	0.4291E-02	0.1620E-01	0.2625E-01	0.2763E-01	0.2804E-01	0.2732E-01	0.5913E-01
101.1	0.3851E-02	0.1471E-01	0.2334E-01	0.2462E-01	0.2534E-01	0.2480E-01	0.5331E-01
107.4	0.3448E-02	0.1342E-01	0.2129E-01	0.2240E-01	0.2285E-01	0.2220E-01	0.4796E-01
113.7	0.3152E-02	0.1284E-01	0.2005E-01	0.2067E-01	0.2118E-01	0.2106E-01	0.4548E-01
120.0	0.3066E-02	0.1238E-01	0.1906E-01	0.2039E-01	0.2022E-01	0.2020E-01	0.4324E-01
127.2	0.2976E-02	0.1193E-01	0.1863E-01	0.1920E-01	0.1967E-01	0.1979E-01	0.4215E-01
127.5	0.2983E-02	0.1193E-01	0.1859E-01	0.1916E-01	0.1958E-01	0.1974E-01	0.4215E-01
134.1	0.2948E-02	0.1158E-01	0.1829E-01	0.1956E-01	0.1958E-01	0.1988E-01	0.4196E-01
148.5	0.3116E-02	0.1190E-01	0.1876E-01	0.1969E-01	0.2036E-01	0.2039E-01	0.4294E-01
140.0	0.2989E-02	0.1165E-01	0.1833E-01	0.1902E-01	0.1954E-01	0.1997E-01	0.4209E-01
156.0	0.3354E-02	0.1224E-01	0.1911E-01	0.1997E-01	0.2055E-01	0.2096E-01	0.4374E-01
163.8	0.4194E-02	0.1323E-01	0.2043E-01	0.2100E-01	0.2157E-01	0.2231E-01	0.4333E-01
172.2	0.7089E-02	0.1595E-01	0.2313E-01	0.2428E-01	0.2420E-01	0.2418E-01	0.3714E-01
177.3	0.8822E-02	0.1856E-01	0.3517E-01	0.3920E-01	0.3646E-01	0.3771E-01	0.4496E-01
b, m^{-1}	3.720	3.797	4.386	4.650	4.668	5.367	9.263
b_B, m^{-1}	0.02164	0.08509	0.1330	0.1400	0.1435	0.1420	0.3034
$B = b_B/b$	0.005818	0.02241	0.03032	0.03011	0.03074	0.02646	0.03276

The best relationship between average cosine and probability of backscattering is given by Haltrin [86]:

$$\overline{\cos(\vartheta)} = 2\frac{1-2B}{2+B}, \quad r^2 = 0.999, \tag{10.22}$$

This relationship is derived from experimental data by Timofeyeva [87–89], corrected to match theoretical asymptotics for isotropic ($B = 0.5$, $\overline{\cos(\vartheta)} = 0$) and delta-shaped scattering ($B = 0$, $\overline{\cos(\vartheta)} = 1$), and later successfully tested with the available database of more than 1000 experimental phase functions.

The second physically correct relationship derived by Haltrin [86] from Timofeyeva's [87–89] data,

$$\overline{\cos^2(\vartheta)} = \frac{6-7B}{3(2+B)}, \quad r^2 = 0.999, \tag{10.23}$$

did not pass as well as eq. (10.21) the applicability test on a set of newly measured phase functions. Instead, some alternative regionally dependent 'non-physical' regressional relationship

$$\overline{\cos^2(\vartheta)} = 0.985\,\overline{\cos(\vartheta)}, \quad r^2 = 0.996, \tag{10.24}$$

was proposed [80].

10.4 Raman scattering of light in natural water

The model of Raman scattering is presented here according to Haltrin and Kattawar [30] with corrections by Gordon [28], Faris and Copeland [27], and Bartlett *et al.* [23]. The frequency redistribution is derived from the works by Walrafen [42, 43]. To be consistent with the elastic scattering and absorption models the Raman scattering model is presented in a wavelength representation.

The wavelength distribution of the Raman scattering coefficient is:

$$\sigma^R(\lambda', \lambda, \cos\vartheta) = b^R(\lambda', \lambda) f^R(\lambda', \lambda) p_R(\lambda', \lambda, \cos\vartheta), \tag{10.25}$$

$$\left.\begin{aligned} b^R(\lambda', \lambda) &= b_0^R \frac{v^4}{(v_i^2 - v'^2)^2} \equiv b_0^R \left[\frac{\lambda_i^2 \lambda'^2}{\lambda^2(\lambda'^2 - \lambda_i^2)}\right]^2, \\ b_0^R &= 0.018\,\mathrm{m}^{-1}, \quad v_i = 88.000\,\mathrm{cm}^{-1}, \quad \lambda_i \simeq 113.636\,\mathrm{nm}, \end{aligned}\right\} \tag{10.26}$$

here $b^R(\lambda', \lambda)$ is a total Raman scattering coefficient, λ' and λ (in nanometers) are wavelengths of excitation and emission, $\nu' = k_\nu/\lambda'$, and $\nu = k_\nu/\lambda$ are excitation and emission wave numbers (both in inverse centimeters), $k_\nu = 1 \equiv 10^7\,\mathrm{nm/cm}$, ν_i and λ_i are frequency and wavelength of intermediate resonance [27], p_R is a Raman angular scattering phase function [28, 90]:

$$p_R(\lambda', \lambda, \cos\vartheta) = \frac{3}{4\pi[3 + \gamma(\nu_S)]}[1 + \gamma(\nu_S)\cos^2\vartheta], \tag{10.27}$$

$$\gamma(\nu_S) = \frac{1-\rho(\nu_S)}{1+3\rho(\nu_S)}, \quad \nu_S = \nu' - \nu \equiv \frac{k_\nu(\lambda-\lambda')}{\lambda\lambda'} \tag{10.27a}$$

p_R is normalized according to eq. (10.7), $\rho(\nu_S)$ is the Raman depolarization ratio, and

$$f^R(\lambda',\lambda) = -\frac{\mathrm{d}\nu'}{\mathrm{d}\lambda'}\sigma^R_\nu(\nu',\nu) = \frac{\nu'^2}{k_\nu} f^R_\nu(\nu',\nu), \tag{10.28}$$

$$\int f^R_\nu(\nu',\nu)\,\mathrm{d}\nu' \equiv \int f^R_\nu(\nu',\nu)\,\mathrm{d}\nu \equiv \int f^R_\nu(\nu_S)\,\mathrm{d}\nu_S = 1, \tag{10.28a}$$

is the frequency redistribution of Raman-scattered light. The Raman depolarization ratio $\rho(\nu_S)$ is given in Table 10.8 and shown with $\gamma(\nu_S)$ in Fig. 10.2.

The Raman scattering frequency redistribution is represented according to the data of Walrafen [42, 43], namely:

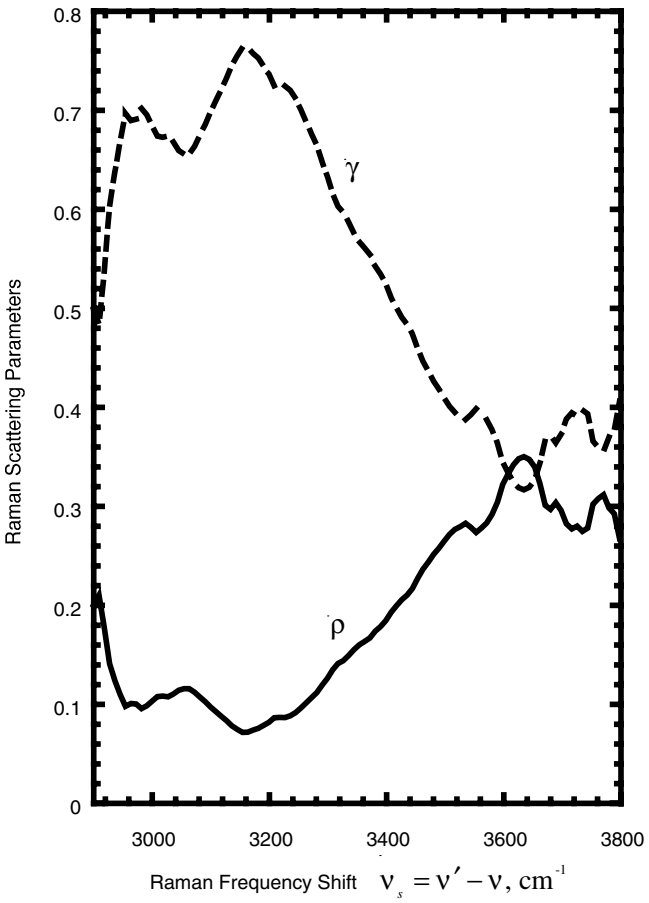

Fig. 10.2. Raman scattering parameters as a function of frequency shift

Table 10.8. Raman depolarization ratio $\rho(\nu_S)$ and parameter $\gamma(\nu_S)$; ν_S in cm^{-1}

ν_S	ρ	γ	ν_S	ρ	γ	ν_S	ρ	γ	ν_S	ρ	γ
2900.0	0.20052	0.49919	3125.8	0.084249	0.73099	3350.7	0.15928	0.56888	3575.8	0.28748	0.38257
2905.2	0.20846	0.48699	3130.1	0.081258	0.73867	3355.0	0.16076	0.56618	3580.1	0.29194	0.37747
2910.4	0.20945	0.48549	3135.3	0.078762	0.74517	3360.2	0.16274	0.56259	3585.4	0.29740	0.37131
2915.5	0.19552	0.50706	3140.4	0.076763	0.75042	3365.4	0.16471	0.55905	3590.6	0.30732	0.36040
2920.6	0.16073	0.56624	3145.6	0.074764	0.75573	3370.6	0.16669	0.55551	3595.8	0.31924	0.34773
2925.7	0.14382	0.59812	3150.8	0.072268	0.76243	3375.8	0.17016	0.54939	3600.2	0.32469	0.34209
2930.8	0.13586	0.61392	3155.1	0.071762	0.76380	3380.1	0.17363	0.54335	3605.4	0.33064	0.33604
2935.1	0.12641	0.63339	3160.3	0.071750	0.76383	3385.3	0.17660	0.53824	3610.6	0.33610	0.33058
2940.2	0.11745	0.65260	3165.5	0.072236	0.76252	3390.5	0.17907	0.53404	3615.8	0.34155	0.32522
2945.4	0.10999	0.66920	3170.7	0.073715	0.75854	3395.7	0.18253	0.52822	3620.1	0.34452	0.32233
2950.5	0.099046	0.69457	3175.9	0.075194	0.75459	3400.0	0.18551	0.52327	3625.3	0.34799	0.31899
2955.7	0.098538	0.69578	3180.2	0.075682	0.75329	3405.2	0.19146	0.51356	3630.5	0.35245	0.31475
2960.0	0.10250	0.68642	3185.4	0.076664	0.75068	3410.4	0.19492	0.50801	3635.7	0.34946	0.31759
2965.2	0.10050	0.69113	3190.6	0.079137	0.74419	3415.6	0.19889	0.50174	3640.8	0.34597	0.32093
2970.4	0.10049	0.69115	3195.7	0.081610	0.73776	3420.8	0.20236	0.49633	3645.2	0.34844	0.31856
2975.6	0.10048	0.69117	3200.1	0.082097	0.73651	3425.2	0.20533	0.49175	3650.3	0.34495	0.32192
2980.7	0.095998	0.70187	3205.3	0.085067	0.72891	3430.4	0.20830	0.48723	3655.5	0.33351	0.33316
2985.1	0.096485	0.70070	3210.5	0.087540	0.72267	3435.6	0.21077	0.48350	3660.6	0.32605	0.34070
2990.3	0.098461	0.69596	3215.6	0.087032	0.72395	3440.8	0.21374	0.47907	3665.7	0.30964	0.35790
2995.4	0.099941	0.69245	3220.8	0.086524	0.72523	3445.1	0.21820	0.47250	3670.0	0.30218	0.36601
3000.6	0.10390	0.68316	3225.1	0.086514	0.72525	3450.3	0.22465	0.46319	3675.2	0.29769	0.37099
3005.8	0.10787	0.67401	3230.3	0.087496	0.72278	3455.5	0.22961	0.45617	3680.4	0.29719	0.37155
3010.2	0.10786	0.67404	3235.5	0.088479	0.72032	3460.7	0.23506	0.44860	3685.6	0.30016	0.36824
3015.3	0.10834	0.67294	3240.7	0.089958	0.71664	3465.0	0.23903	0.44317	3690.8	0.30561	0.36226
3020.5	0.10833	0.67296	3245.0	0.091936	0.71176	3470.2	0.24299	0.43784	3695.1	0.30013	0.36828
3025.7	0.10782	0.67413	3250.2	0.094409	0.70571	3475.4	0.24745	0.43192	3700.2	0.29267	0.37664
3030.0	0.10781	0.67415	3255.4	0.097379	0.69855	3480.6	0.25191	0.42608	3705.4	0.28471	0.38578
3035.2	0.10979	0.66965	3260.6	0.10035	0.69148	3485.8	0.25637	0.42034	3710.5	0.27824	0.39339
3040.4	0.11574	0.65636	3265.8	0.10332	0.68451	3490.2	0.25835	0.41782	3715.7	0.27723	0.39459
3045.6	0.11424	0.65968	3270.1	0.10579	0.67878	3495.4	0.26182	0.41344	3720.0	0.27822	0.39341
3050.8	0.11473	0.65859	3275.3	0.10876	0.67198	3500.6	0.26727	0.40666	3725.2	0.28019	0.39108
3055.1	0.11621	0.65532	3280.5	0.11173	0.66528	3505.8	0.27074	0.40241	3730.4	0.27770	0.39403
3060.3	0.11669	0.65427	3285.7	0.11570	0.65645	3510.1	0.27321	0.39942	3735.5	0.27371	0.39881
3065.5	0.11519	0.65757	3290.1	0.11966	0.64779	3515.3	0.27618	0.39585	3740.7	0.26823	0.40548
3070.6	0.11319	0.66201	3295.3	0.12363	0.63927	3520.5	0.27866	0.39289	3745.1	0.28512	0.38531
3075.8	0.11069	0.66762	3300.5	0.12759	0.63091	3525.7	0.27964	0.39173	3750.3	0.30101	0.36730
3080.1	0.10820	0.67326	3305.7	0.13255	0.62065	3530.0	0.28062	0.39057	3755.5	0.30398	0.36404
3085.3	0.10521	0.68012	3310.9	0.13800	0.60962	3535.2	0.28310	0.38766	3760.7	0.30744	0.36027
3090.5	0.10271	0.68593	3315.2	0.14048	0.60468	3540.4	0.28159	0.38943	3765.1	0.31041	0.35707
3095.6	0.099222	0.69415	3320.4	0.14245	0.60080	3545.5	0.27761	0.39414	3770.3	0.31189	0.35549
3100.8	0.096727	0.70011	3325.6	0.14393	0.59790	3550.7	0.27412	0.39832	3775.4	0.30542	0.36247
3105.1	0.094729	0.70494	3330.8	0.14690	0.59214	3555.0	0.27411	0.39833	3780.6	0.29696	0.37181
3110.3	0.091737	0.71225	3335.1	0.14938	0.58739	3560.2	0.27708	0.39477	3785.7	0.29049	0.37912
3115.5	0.089241	0.71842	3340.3	0.15235	0.58176	3565.4	0.28055	0.39066	3790.0	0.29297	0.37630
3120.6	0.086745	0.72467	3345.5	0.15631	0.57436	3570.6	0.28302	0.38775	3797.7	0.26761	0.40624

$$f_\nu^R(\nu',\nu) = k^R \sum_{i=1}^{4} \alpha_i \exp\left[-\frac{(\nu'-\nu-\Delta\nu_i)^2}{2\sigma_i^2}\right],$$
$$f_\nu^R(\nu_S) = k^R \sum_{i=1}^{4} \alpha_i \exp\left[-\frac{(\nu_S-\Delta\nu_i)^2}{2\sigma_i^2}\right], \tag{10.29}$$

where

$$k^R = \left(\sqrt{2\pi}\sum_{i=1}^{4}\alpha_i\sigma_i\right)^{-1} = 5.152\cdot 10^{-3}\,\text{cm}.$$

Values of α_i, $\Delta\nu_i$, and σ_i are given in Table 10.9. The Raman scattering model presented here coincides with the Haltrin and Kattawar [30] model if we neglect $\nu^2 \simeq 4\times 10^8\,\text{cm}^{-2}$ in eq. (10.26) in comparison with $\nu_i^2 \approx 7.7\times 10^9\,\text{cm}^{-2}$ and set γ in eq. (10.27) to be equal to 0.6.

Table 10.9. Raman frequency distribution parameters [30]

i	α_i	$\Delta\nu_i$, cm^{-1}	σ_i, cm^{-1}
1	0.41	3250	89.179
2	0.39	3425	74.317
3	0.10	3530	59.453
4	0.10	3625	59.453

10.5 Chlorophyll fluorescence in natural water

The chlorophyll or red fluorescence is represented according to Gordon [48] in the interpretation of Haltrin and Kattawar [30]:

$$\sigma^C(\lambda',\lambda,\cos\gamma) \equiv \sigma^C(\lambda',\lambda) = a_C^0(\lambda')C_C\eta^C(\lambda',\lambda), \tag{10.30}$$

$$\eta^C(\lambda',\lambda) = \begin{cases} \dfrac{\eta_0^C}{4\pi}\dfrac{\lambda'}{\lambda_{0F}}\dfrac{1}{\sqrt{2\pi\sigma^2}}\exp\left[-\dfrac{(\lambda-\lambda_{0F})^2}{2\sigma^2}\right], & 370\,\text{nm}\le\lambda'\le 690\,\text{nm} \\ 0, & \text{elsewhere,} \end{cases} \tag{10.31}$$

here $\eta_0^C \simeq 0.05$ (an average value by Kiefer [51]), $\lambda_{0F} \simeq 683\,\text{nm}$, $\sigma = 10.6\,\text{nm}$.

10.6 Yellow substance (Gelbstoff, DOM or CDOM) fluorescence in natural water

The most advanced yellow substance fluorescence model was proposed by Hawes *et al.* [49]. According to this model, the yellow substance components fluorescence emission coefficient can be expressed as follows:

$$\chi^j(\lambda',\lambda) = a_j(\lambda')\eta^j(\lambda',\lambda) \equiv a_j^0\exp(-k_j\lambda')\eta^j(\lambda',\lambda), \quad j=F,H, \tag{10.32}$$

with the coefficients a_j^0 and k_j given in Table 10.2, and the spectral fluorescence efficiency function η^j represented by the following empirical equation:

$$\eta^j(\lambda', \lambda) = A_0^j(\lambda') \exp\left\{ - \left[\frac{1/\lambda - A_1^j/\lambda' - B_1^j}{0.6(A_2^j/\lambda' + B_2^j)} \right]^2 \right\}, \quad j = F, H, \tag{10.33}$$

with the coefficients $A_0^j(\lambda')$, A_1^j, A_2^j, B_1^j, B_2^j given in Table 10.10a and 10.10b. This model is more advanced than the model for chlorophyll fluorescence because the predominant part of yellow substance or DOM is dissolved in water and the yellow substance is easier to process experimentally than the chlorophyll which is imbedded into living phytoplanktonic cells [1].

Table 10.10a. Parameters for fluorescence model $\eta(\lambda_x, \lambda_m)$ of fulvic and humic acids [49]

	λ_x, nm	Fulvic acid				Humic acid				
		FA7	FA8	FA9	FA11	HA1	HA2	HA4	HA6	HA8
$A_0(\lambda_x)$	310	5.18	4.48	5.21	5.09	2.49	2.78	4.83	5.77	3.61
$\times 10^5$	330	6.34	5.67	6.57	6.27	2.68	3.13	5.11	6.86	4.01
	350	8.00	7.23	7.93	7.93	2.95	3.73	5.94	7.27	0.46
	370	9.89	9.26	9.93	9.76	3.34	4.42	7.20	8.37	5.48
	390	9.39	9.06	**9.93**	8.72	2.77	4.03	6.53	7.08	5.06
	410	10.48	9.22	9.47	7.93	2.26	3.91	6.41	7.80	5.05
	430	12.59	10.14	10.21	8.15	2.63	4.41	7.66	8.90	5.66
	450	13.48	9.90	10.08	7.75	2.72	4.52	7.55	9.30	5.70
	470	13.61	9.70	10.11	7.70	2.65	4.75	7.88	8.41	5.32
	490	9.27	7.90	8.34	5.98	2.20	4.29	6.81	6.68	4.42
A_1		0.470	0.389	0.466	0.471	0.304	0.379	0.346	0.447	0.356
$B_1 \times 10^4$		8.077	10.073	8.340	8.204	12.169	10.043	10.891	8.594	10.694
A_2		0.407	0.386	0.386	0.386	0.591	0.362	0.411	0.417	0.406
$B_2 \times 10^4$		−4.57	−4.20	−4.13	−4.20	−9.39	−3.17	−4.60	−4.64	−4.42
r^2		0.987	0.989	0.975	0.991	0.712	0.985	0.985	0.985	0.986

Table 10.10b. FA and HA fluorescence sample information [49]

Sample name	Location	Sample date	Sample volume, liters	Extraction Method	Total Mass extracted (mg)
HA1	Peru upwelling (El Niño)	—	—	XAD2	—
HA2	Gulf of Mexico, outside Loop Cur.	—	—	XAD2	—
HA4	Gulf of Mexico, mouth of Tampa Bay	12 October 1989	26	XAD2	0.156
HA6	Gulf of Mexico, mid-West Florida shelf	4 March, 1990	55	XAD2	0.65
FA7	Gulf of Mexico, mid-West Florida shelf	4 March, 1990	32	C18	12.66
FA8, HA8	Gulf of Mexico, mouth of Tampa Bay	5 March, 1990	20	C18	2.24, 0.42
FA9	North Atlantic, 60°N 20°W	24 May 1991	55	C18	19.06
FA11	North Atlantic, 60°N 20°W	20 August 1991	55	C18	6.99

10.7 Diffuse reflection coefficient

The diffuse reflection coefficient (DRC), or diffuse reflectance (DR), or albedo of the sea just below the sea surface, is defined as a ratio of upward to downward irradiance at the level just below the sea surface. It is a very important apparent optical property and constituent part of the remote sensing coefficient [91, 92] that is used to extract information from remotely measured optical images of the ocean. As an apparent optical property it depends not only on inherent optical properties but also on conditions of illumination just below the sea surface. The theory and experiments show that DRC depends only on two inherent optical properties, the absorption coefficient, a, and the backscattering coefficient, b_B, that is derived from the angular scattering coefficient. Dependence on other properties (or moments) of angular scattering coefficient is weak and can be neglected. The diffuse reflection coefficient of open ocean illuminated by diffuse light can be written in a very simple way:

$$R = k\frac{b_B}{a}, \quad R = k\frac{b_B}{a + b_B}. \tag{10.34}$$

The second variant in eqs (10.34) is preferable because it does not give infinite values for R at $a = 0$. According to Morel and Prieur [93] for open ocean water $k = 1/3$. Equations (10.34) are widely used to describe DRC of the ocean. The

big shortcoming of eqs (10.34) is that they do not satisfy physical conditions that restrict values of diffuse reflection coefficient:

$$0 \le R \le 1. \tag{10.35}$$

At zero backscattering $b_B = 0$ the DRC should be equal to zero (no light returns from the water depth), and at zero absorption $a = 0$ DRC should by equal to 1 (all light is eventually reflected back). Both eqs (10.34) only satisfy the first condition, but do not satisfy the second one. At zero absorption value the first equation gives infinity, and the second one gives $k < 1$. This means that eqs (10.34) are only rough approximations. The theoretical analysis shows that they are good only for rather small values of Gordon's parameter:

$$x_G = \frac{b_B}{a + b_B} < 0.1, \quad \text{or} \quad a > 9b_B. \tag{10.36}$$

In addition to theoretical considerations there is experimental data by Timofeyeva [107] who measured the DRC in a wide range of Gordon's parameter (see Table 10.11). The measurements have been made in marine waters for smaller values of x_G and in artificially created absorbing and scattering substances for higher values of x_G. These data together with the DRC computed with different equations are shown in Fig. 10.3. Some authors try to improve eqs (10.34) by representing DRC with a series over b_B/a or x_G, but this method is useless for $x_G > 0.9$. According to Gate [95], asymptotics of the DRC for x_G close to one described by the following equation:

$$R = \frac{\sqrt{6x_G} - 2\sqrt{1 - x_G}}{\sqrt{6x_G} + 2\sqrt{1 - x_G}} \equiv \frac{1 - \sqrt{2a/(3b_B)}}{1 + \sqrt{2a/(3b_B)}} \equiv \frac{\sqrt{3b_B/(2a)} - 1}{\sqrt{3b_B/(2a)} + 1}, \quad 1 - x_G < 0.1. \tag{10.37}$$

It is clear that this dependence could not be described by any power series for small x_G or small ratios b_B/a.

Table 10.11. Downward and upward average cosines and diffuse reflectance as a function of average cosine over radiance distribution according to *in situ* and modeling experiments by V. A. Timofeyeva [107]

$\overline{\mu}$	$\overline{\mu}_d$	$\overline{\mu}_u$	R_∞
0.1	0.5249	0.4831	0.671
0.2	0.5525	0.4545	0.443
0.3	0.5834	0.4202	0.283
0.4	0.6184	0.3745	0.171
0.5	0.6566	0.3311	0.095
0.6	0.7008	0.3003	0.048
0.7	0.7536	0.2857	0.0207
0.8	0.8217	0.3610	0.0082
0.9	0.9033	0.6849	0.0016

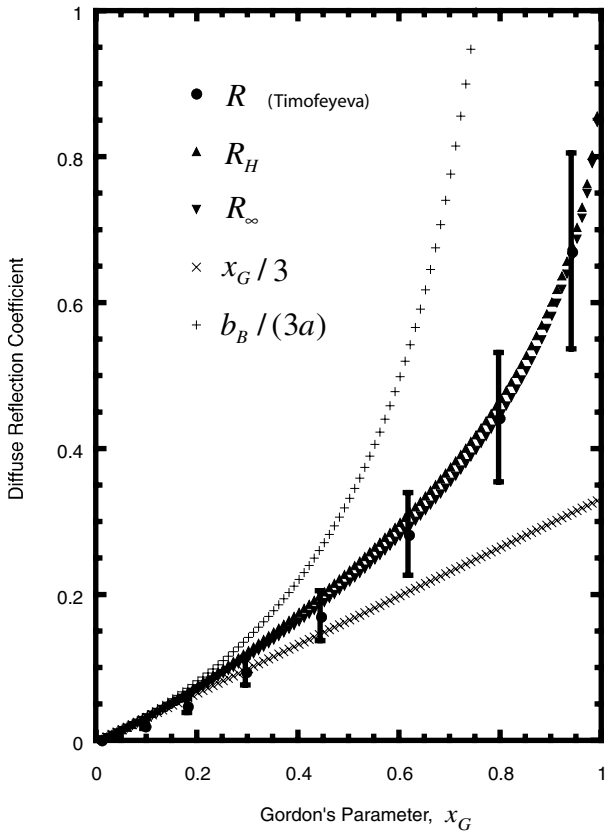

Fig. 10.3. Diffuse reflection coefficient of natural water basin according to experiment, and to linear, and nonlinear theories

Fortunately, there are several equations available in the literature that satisfy physical condition (10.35) and give good approximation to the DRC of the seawater basin with arbitrary values of optical properties.

The first such equation was proposed by Haltrin [96]:

$$R = \frac{1-\overline{\mu}_H}{1+\overline{\mu}_H}\left(\sqrt{1+\overline{\mu}_H^2}-\overline{\mu}_H\right)^2, \tag{10.38}$$

$$\overline{\mu}_H = \sqrt{\frac{a}{a+(4+2\sqrt{2})b_B}} \equiv \sqrt{\frac{1-x_G}{1+(3+2\sqrt{2})x_G}}. \tag{10.39}$$

It was derived as a result of the exact solution of the radiative transfer equation in the asymptotic regime ($cz \gg 1$, where z is a physical depth in m^{-1}) with the phase function approximated as:

$$p_H(\cos\vartheta) = \frac{1}{4\pi}\left[2g\delta(1-\cos\vartheta) + \frac{1-g}{\sqrt{2(1-\cos\vartheta)}}\right], \tag{10.40}$$

here δ is a Dirac's delta function, and $g = 1 - (2 + \sqrt{2})B$ is an average cosine over phase function p_H, with $B = b_B/b$ being a probability of backscattering (see eq. (10.10)).

The exact solution of the RTE in the asymptotic regime with the phase function (40) is given by the following equation:

$$L_\infty(z,\theta) = \frac{L_0(1-\overline{\mu}_H^2)\exp(-az/\overline{\mu}_H)}{(1+\overline{\mu}_H^2 - 2\overline{\mu}_H\cos\theta)^{3/2}}, \tag{10.41}$$

where L_0 is determined by the boundary conditions, and $\overline{\mu}_H$ is given by eq. (10.39). The shape of radiance distribution (10.41) is a Henyey–Greenstein function [97].

Another analytic equation was proposed in the framework of the self-consistent approximation to the RTE [98, 99]:

$$R = R_\infty = \left(\frac{1-\overline{\mu}}{1+\overline{\mu}}\right)^2, \tag{10.42}$$

with the average cosine $\overline{\mu}$ over radiance distribution in the asymptotic regime given by

$$\overline{\mu} = \sqrt{\frac{a}{a+3b_B+\sqrt{b_B(4a+9b_B)}}} \equiv \sqrt{\frac{1-x_G}{1+2x_G+\sqrt{x_G(4+5x_G)}}}. \tag{10.43}$$

Equations (10.42) and (10.43) give almost the same values for R as eqs (10.38) and (10.39) (see Fig. 10.3), but they can be generalized to the cases of finite water depth and combined illumination of water surface by the light of the sun and the sky.

Equations (10.42) and (10.43) and (10.38) and (10.39) seem more complex than simple linear eqs (10.34). But they are good for any value of Gordon's parameter x_G (or for any arbitrary pair of values a and b_B: $0 \le a \le \infty$, $0 \le b_B \le \infty$), and satisfy all physical conditions outline above, while eqs (10.34) fail for values of $x_G > 0.1$. The question arises, is it worth to use more complex expressions instead of the very simple linear expressions (10.34)? The answer can be obtained from the analysis of frequency distribution of Gordon's parameter values in natural waters. Extensive *in situ* measurements show that in the following three cases: (a) waters of the open ocean, (b) clear inland water basins, like Lake Baikal, and (c) biologically stable waters of marine coastal areas and certain lakes Gordon's coefficient $x_G < 0.1$ and simple linear equations (10.34) can be used without inflicting unacceptable error. At the same time certain inland waters, coastal ocean waters, and even whole seas contain large number of scattering particles such as detritus with low absorption which results in much higher values of Gordon's parameter. Fig. 10.4 shows a frequency distribution (histogram) of Gordon's parameter in the Yellow Sea [100]. It shows that about 50% of all values of x_G exceed the critical value of 0.1 and some values of this parameter are as large as 0.9. It means that for the Yellow Sea water types we should use the nonlinear equations given above.

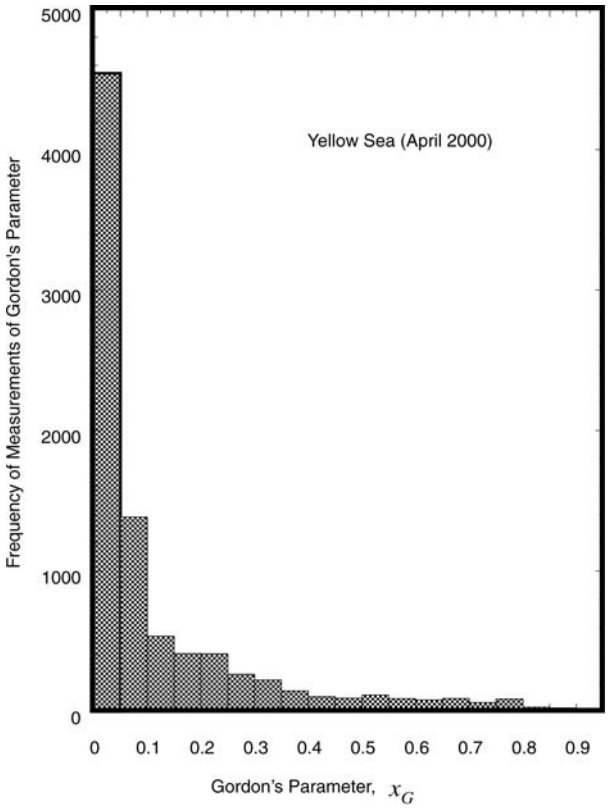

Fig. 10.4. Frequency distribution of measured Gordon's parameter in waters of Yellow Sea

Another reason to use the nonlinear approach is that it can be generalized to the case of shallow water depth and to the case that takes into account the combined illumination of water surface by the direct light of the sun and the diffuse light of the sky.

10.8 Diffuse reflection coefficient of a water basin illuminated by direct solar light and diffuse light of the sky

The diffuse reflection coefficient of water illuminated by the light of the sun and the sky was considered by several authors. Here we restrict ourselves to the solution that is valid for all optical water types and validated with experimental data [101].

The DRC of the water body illuminated by the light of the sun and the sky is a linear combination of DRC for diffuse illumination R_∞ and the DRC

for directed illumination R_s with the weight determined by the ratio of direct irradiance to the diffuse irradiance just below the water surface, q_w:

$$R = \frac{R_\infty + q_w R_s}{1 + q_w}, \tag{10.44}$$

with R_∞ given by eq. (10.42) and

$$R_s \equiv \frac{(1-\overline{\mu})^2}{1 + \overline{\mu}\mu_s(4 - \overline{\mu}^2)}, \tag{10.45}$$

where $\overline{\mu}$ is an average cosine of the radiance distribution in the asymptotic regime and is expressed through absorption and backscattering coefficients by eq. (10.43), and μ_s is a cosine of the direction of solar rays just below the sea surface:

$$\mu_s = \sqrt{1 - \left(\frac{\sin Z_s}{n_w}\right)^2} \geq \sqrt{1 - 1/n_w^2} \approx 0.6656; \tag{10.46}$$

here Z_S is the solar zenith angle, and n_w is the water refractive index.

The ratio of direct irradiance to the diffuse irradiance just below the water surface q_w can be expressed through the similar ratio measured just above the water surface q_a through the following expression [91]:

$$q_w = \frac{(1-f)T_\downarrow^S q_a}{f(1-A_f) + (1-f)(1-q_a)T_\downarrow^D + a_q T_\downarrow^S}, \tag{10.47}$$

here A_f is a foam albedo, f is a fraction of the water surface covered by white caps that can be estimated from the wind speed u using the following empirical equation [91]:

$$f = \begin{cases} 1.2 \cdot 10^{-5}\, u^{3.3}, & u \leq 9\,\mathrm{m\,s^{-1}}, \\ 1.2 \cdot 10^{-5}\, u^{3.3}(0.221u - 0.99), & u > 9\,\mathrm{m\,s^{-1}}. \end{cases} \tag{10.48}$$

The transmittance of direct solar light penetrated to water depth through the wind roughened surface was computed for different wind speeds and solar zenith angles using Monte Carlo modeling of the water surface from an experimentally derived spectrum of wind waves with the results converted to the following equation [91]:

$$T_\downarrow^S(Z_S, u) = 1 - a_0(u) - R_F^0(Z_S)\left\{a_1(u) + R_F^0(Z_S)\left[a_2(u) + a_3(u)R_F^0(Z_S)\right]\right\}, \tag{10.49}$$

where R_F^0 is a Fresnel reflection coefficient of unpolarized light by flat water surface:

$$R_F^0(Z_S) = \frac{1}{2}\left[\left(\frac{\cos Z_S - \sqrt{n_w^2 - \sin^2 Z_S}}{\cos Z_S + \sqrt{n_w^2 - \sin^2 Z_S}}\right)^2 + \left(\frac{n_w^2 \cos Z_S - \sqrt{n_w^2 - \sin^2 Z_S}}{n_w^2 \cos Z_S + \sqrt{n_w^2 - \sin^2 Z_S}}\right)^2\right], \tag{10.50}$$

and coefficients a_0 through a_3 expressed through the wind speed u (in $\mathrm{m\,s^{-1}}$):

$$a_0(u) = 0.001(6.944\,831 - 1.912\,076\,u + 0.036\,584\,33\,u^2), \quad (10.51)$$

$$a_1(u) = 0.743\,136\,8 + 0.067\,978\,7\,u - 0.000\,717\,1\,u^2, \quad (10.52)$$

$$a_2(u) = 0.565\,026\,2 + 0.006\,150\,2\,u - 0.023\,981\,0\,u^2 + 0.001\,069\,5\,u^3, \quad (10.53)$$

$$a_3(u) = -0.412\,808\,3 - 0.127\,103\,7\,u + 0.28\,390\,7\,u^2 - 0.001\,170\,6\,u^3. \quad (10.54)$$

Transmission by diffuse light $T_{\downarrow}^{D}$ is obtained by averaging eq. (10.49) over the sky radiance distribution. For Lambertian sky we have the following equation for diffuse transmittance [91]:

$$T_{\downarrow}^{D}(u) = 1.367 \times 10^{-5}(46.434 - u)(1410 + 20.6u + u^2), \quad 0 \le u < 12\,\mathrm{m\,s^{-1}}. \quad (10.55)$$

For overcast sky (cardioid distribution [4]) we have the following equation for diffuse transmittance [91]:

$$T_{\downarrow}^{D}(u) = 6.123{\times}10^{-6}(59.3{-}u)(2564{+}33.74u{+}u^2), \quad 0 \le u < 12\,\mathrm{m\,s^{-1}}. \quad (10.56)$$

The ratio of direct irradiance to the diffuse irradiance just above the water surface is a function of atmospheric optical properties and can be evaluated using the following equation taken from reference [91]:

$$q_a = \left(1 + \frac{B_a \tau_a}{\cos Z_S}\right) \exp\left(-\frac{\tau_a}{\cos Z_S}\right), \quad (10.57)$$

where B_a is a probability of backscattering in atmosphere, and τ_a is a total atmospheric optical thickness.

Equation (10.44) for diffuse reflectance coefficient R, with values of, a, b_B, and q_w measured experimentally, was tested by E. I. Afonin [102] using *in situ* measurements in the waters of Black Sea during the whole light day. The difference between predicted and measured values of R was in the range of 5%.

10.9 Diffuse reflection coefficient of shallow water body illuminated by diffuse light

The diffuse reflection coefficient of a shallow water basin should take into account not only multiple scattering of light inside the water, but multiple reflection of light from the bottom and the surface. For coastal waters it is very important that the model used to derive the DRC is valid not only for arbitrary depth but also for any arbitrary value of inherent optical property thus covering very clear and very turbid shallow water bodies.

According to reference [99] the diffuse reflection coefficient of shallow water with the bottom depth z_B and bottom albedo A_B could be expressed as:

$$R = \frac{R_\infty(1 - A_B R_0) + (A_B - R_\infty)e^{-\alpha_R z_B}}{(1 - A_B R_0) + (A_B - R_\infty)R_0 e^{-\alpha_R z_B}}, \quad (10.58)$$

with

$$R_0 = \left(\frac{2+\overline{\mu}}{2-\overline{\mu}}\right) R_\infty, \quad \alpha_R = 2\overline{\mu}(a+b_B), \tag{10.59}$$

and R_∞ and $\overline{\mu}$ are given, respectively, by eqs (10.42) and (10.43).

Equation (10.58) satisfies all limiting conditions implied by the correct physics of light scattering:

$$R\big|_{z_B\to\infty} \equiv R\big|_{A_B=R_\infty}, \quad R\big|_{z_B=0} = A_B, \quad R\big|_{x_G=0} = 0, \quad R\big|_{x_G=1} = 1. \tag{10.60}$$

Equation (10.58) can be used in algorithms to restore water depth and bottom albedo from remotely measured multispectral optical images of water basins in the cases when the combined nature of the illumination of water surface could be neglected.

10.10 Diffuse attenuation coefficient

Downward and upward diffuse attenuation coefficients of light at depth z are defined as follows:

$$k_d(z) = -\frac{1}{E_d(z)}\frac{\mathrm{d}E_d(z)}{\mathrm{d}z}, \quad k_u(z) = -\frac{1}{E_u(z)}\frac{\mathrm{d}E_u(z)}{\mathrm{d}z}, \tag{10.61}$$

where E_d and E_u are downward and upward irradiances. In the framework of self-consistent approximation diffuse attenuation coefficients for optically deep water can be written as follows [101]:

$$k_d(z) = \alpha_\infty \frac{1 + q_w\left\{\mu_0\varepsilon(z)/\mu_s + hR_s[(2+\overline{\mu}) + 1/\mu_s]Y_s(z)\right\}}{1 + q_w\left\{\varepsilon(z) + hR_s[(2+\overline{\mu}) + 1/\mu_s]F_s(z)\right\}}, \tag{10.62}$$

$$k_u(z) = \alpha_\infty \frac{R_\infty + q_w R_s\left\{\mu_0\varepsilon(z)/\mu_s + h[(2-\overline{\mu}) - 1/\mu_s]Y_s(z)\right\}}{R_\infty + q_w R_s\left\{\varepsilon(z) + h[(2-\overline{\mu}) - 1/\mu_s]F_s(z)\right\}}, \tag{10.63}$$

where

$$\alpha_\infty = \sqrt{4a(a+2b_B) + \overline{\mu}^2 b_B^2} - \overline{\mu}(a+b_B), \tag{10.64}$$

$$Y_s(z) = \begin{cases} \mu_0\mu_s\frac{1-\varepsilon(z)}{\mu_0-\mu_s} - \mu_0\varepsilon(z), & \mu_s \neq \mu_0, \\ \alpha z - \mu_0, & \mu_s = \mu_0, \end{cases} \tag{10.65}$$

$$F_s(z) = \begin{cases} \left(1 - \exp\left[-\alpha z\left(\frac{1}{\mu_s} - \frac{1}{\mu_0}\right)\right]\right) \Big/ \left(\frac{1}{\mu_s} - \frac{1}{\mu_0}\right), & \mu_s \neq \mu_0, \\ \alpha z, & \mu_s = \mu_0, \end{cases} \tag{10.66}$$

$$\alpha = a + 2b_B, \quad \mu_0 = \frac{1+\overline{\mu}^2}{\overline{\mu}(3-\overline{\mu}^2)}, \quad h = \frac{(1+\overline{\mu})^2}{2(1+\overline{\mu}^2)}, \tag{10.67}$$

$$\varepsilon(z) = \exp\left[-\alpha z\left(\frac{1}{\mu_s} - \frac{1}{\mu_0}\right)\right], \tag{10.68}$$

with parameters R_∞, $\overline{\mu}$, R_s and q_w defined, accordingly, by eqs (10.42), (10.43), (10.45), and (10.47).

At large optical depths both k_d and k_u converge to the diffuse attenuation coefficient in asymptotic regime that is given by Gershun's equation:

$$k_d(z), \quad k_u(z)\big|_{cz\to\infty} \Rightarrow k_\infty, \quad k_\infty = a/\overline{\mu}. \tag{10.69}$$

10.11 Optical models of scattering and absorption of light in natural water

10.11.1 The Kopelevich physical model of elastic scattering

The physical model of elastic scattering was proposed by Kopelevich [94, 103]. The original model also included an absorption part that is now obsolete. The scattering part satisfies contemporary criteria for all parts of marine water bodies excluding shallow coastal areas contaminated with clay and sand particles raised from the bottom. The model was based on the results of *in situ* measurements of inherent optical properties and particle size distributions over during several decades by the Shirshov Institute of Oceanology in the Pacific, Indian and Atlantic Oceans.

The angular scattering coefficient in this model consists of three parts: the angular scattering coefficient of pure water, the angular scattering coefficient of small particles, and the angular scattering coefficient of large particles. The angular scattering coefficients of particles have been derived by the solution of the inverse problem to derive particle size distributions using water samples taken in various regions of the World Ocean. Then angular scattering coefficients were calculated using Mie scattering approach.

The large fraction represents organic particles of phytoplankton and detritus with the density $\rho_L = 1\,\mathrm{g\,cm^{-3}}$ and relative to water refractive index $n_L = 1.03$. The size distribution for the large particle fraction was found to be Junge distribution r^{-v} for $1.3\,\mu\mathrm{m} \le r \le 13\,\mu\mathrm{m}$ with $v = 3$. The small fraction represents terrigenic particles with density $\rho_L = 2\,\mathrm{g\,cm^{-3}}$ and relative refractive index $n_S = 1.15$ [10]. The size distribution for the small particle fraction was found to be represented by three Junge distributions: the Junge distribution with $v = 2.5$ for $0.01\,\mu\mathrm{m} \le r \le 0.05\,\mu\mathrm{m}$, the Junge distribution with $v = 3.5$ for $0.05\,\mu\mathrm{m} \le r \le 0.1\,\mu\mathrm{m}$, and the Junge distribution with $v = 4.5$ for $0.1\,\mu\mathrm{m} \le r \le 1.3\,\mu\mathrm{m}$. The model is represented by the following equation:

$$\beta(\lambda,\vartheta) = \beta_W(\lambda,\vartheta) + \left(\frac{550}{\lambda}\right)^{0.3} \beta_L^K(\vartheta) v_L + \left(\frac{550}{\lambda}\right)^{1.7} \beta_S^K(\vartheta) v_S, \tag{10.70}$$

with the pure water angular scattering coefficient $\beta_w(\lambda,\vartheta)$ computed using eq. (10.17), and the angular scattering coefficients of large $\beta_L^K(\vartheta)$ and small $\beta_S^K(\vartheta)$ particles for $\lambda = 550\,\mathrm{nm}$ given in Table 10.12. The volume concentrations v_L and v_S are given in $\mathrm{cm^3\,m^{-3}}$. To convert them to the conventional concentrations the following relationships are used:

$$C_S = \rho_S v_S, \quad C_L = \rho_L v_L. \tag{10.71}$$

Table 10.12. Components of physical model of light scattering by sea water by O. V. Kopelevich [94] in $m^{-1}\,ster^{-1}$; small fraction of suspended matter β_S; large fraction of suspended matter β_L (the volume concentration of each component is $1\,cm^3\,m^{-3}$)

angle, °	β_S^K	β_L^K	angle, °	β_S^K	β_L^K
0	5.3	140	45	$9.8 \cdot 10^{-2}$	$6.2 \cdot 10^{-4}$
0.5	5.3	98	60	$4.1 \cdot 10^{-2}$	$3.8 \cdot 10^{-4}$
1	5.2	46	75	$2.0 \cdot 10^{-2}$	$2.0 \cdot 10^{-4}$
1.5	5.2	26	90	$1.2 \cdot 10^{-2}$	$6.3 \cdot 10^{-4}$
2	5.1	15	105	$8.6 \cdot 10^{-3}$	$4.4 \cdot 10^{-5}$
4	4.6	3.6	120	$7.4 \cdot 10^{-3}$	$2.9 \cdot 10^{-5}$
6	3.9	1.1	135	$7.4 \cdot 10^{-3}$	$2.0 \cdot 10^{-5}$
10	2.5	0.2	150	$7.5 \cdot 10^{-3}$	$2.0 \cdot 10^{-5}$
15	1.3	0.05	180	$8.1 \cdot 10^{-3}$	$7.0 \cdot 10^{-5}$
30	0.29	0.0028	b, m^{-1}	1.34	0.312

This model gives very good predictions of the angular scattering coefficient for open oceanic waters and for clean biologically stable waters with no clay or sand particles suspended by the water movement.

10.11.2 Chlorophyll-based model of elastic scattering and absorption

This model was proposed by Haltrin [104]. The scattering part of this model is based on a modified version of the Kopelevich [72, 103] elastic scattering model; the absorption part of the model is taken from works by Pope and Fry [8], Prieur and Sathyendranath [9], Morel [105], and Carder *et al.* [2]. The absorption coefficient in this model is represented as follows:

$$a(\lambda) = a_W(\lambda) + 0.06 a_C^0(\lambda)\left(C_C/C_C^0\right)^{0.602} + a_H^0 C_H \exp(-k_H\lambda) + a_F^0 C_F \exp(-k_F\lambda), \tag{10.72}$$

with $C_C^0 = 1\,mg\,m^{-3}$, $a_W(\lambda)$, $a_C^0(\lambda)$, a_H^0, a_F^0, k_H, and k_F identical to the values given above in section 10.2. The elastic angular scattering coefficient was a modification of Kopelevich's model given by eq. (10.70):

$$\beta(\lambda,\vartheta) = \beta_W(\lambda,\vartheta) + \left(\frac{400}{\lambda}\right)^{1.7} \frac{\beta_S(\vartheta)}{\rho_S} C_S + \left(\frac{400}{\lambda}\right)^{0.3} \frac{\beta_L(\vartheta)}{\rho_L} C_L, \tag{10.73}$$

$$\left.\begin{aligned} \beta_S(\vartheta) &= (5.5870\,m^2\,cm^{-3}\,sr^{-1}) \exp\left(\sum_{n=1}^{5} s_n \vartheta^{3n/4}\right), \\ \beta_L(\vartheta) &= (190.027\,m^2\,cm^{-3}\,sr^{-1}) \exp\left(\sum_{n=1}^{5} l_n \vartheta^{3n/4}\right), \end{aligned}\right\} \tag{10.74}$$

Table 10.13. The coefficients to eqs (10.74) for two basic phase functions and [104]

n	1	2	3	4	5
s_n	$-2.957\,089 \cdot 10^{-2}$	$-2.782\,943 \cdot 10^{-2}$	$1.255\,406 \cdot 10^{-2}$	$-2.155\,880 \cdot 10^{-2}$	$1.356\,632 \cdot 10^{-2}$
l_n	$-1.604\,327$	$8.157\,686 \cdot 10^{-2}$	$-2.150\,389 \cdot 10^{-3}$	$2.419\,323 \cdot 10^{-5}$	$-6.578\,550 \cdot 10^{-8}$

where ϑ is the scattering angle in degrees. The coefficients s_n and l_n in eq. (10.74) are given in Table 10.13.

The model given by eqs (10.72)–(10.74) depends on five different concentrations of dissolved and suspended matter, C_C, C_H, C_F, C_S, and C_L. Using several experimentally derived regressions and with the use of optimization procedure the number of independent concentrations was reduced to one – the concentration of chlorophyll C_C in $\mathrm{mg\,m^{-3}}$. The other four concentrations of dissolved and suspended matter are expressed through the chlorophyll concentration:

$$\left.\begin{aligned} C_H &= 0.19334\, C_C \exp\left[0.12343\left(C_C/C_C^0\right)\right], \\ C_F &= 1.74098\, C_C \exp\left[0.12327\left(C_C/C_C^0\right)\right], \\ C_S &= 0.01739(\mathrm{g/mg}) C_C \exp\left[0.11631\left(C_C/C_C^0\right)\right], \\ C_L &= 0.76284(\mathrm{g/mg}) C_C \exp\left[0.03092\left(C_C/C_C^0\right)\right], \end{aligned}\right\} \tag{10.75}$$

This chlorophyll-based model represents a modification and extension of the Kopelevich model and, like the Kopelevich model, is valid for open ocean and biologically stable coastal waters. The model that covers more turbid waters should include more scattering components related, for instance, to clays and suspended sand.

10.11.3 Empirical model of inherent optical properties

The empirical model of inherent optical properties was proposed by Haltrin [106]. It makes it possible to restore an angular scattering coefficient, diffuse reflection and diffuse attenuation coefficients, and also total, upward and downward average cosines over the radiance distribution of diffuse light through the absorption and attenuation coefficients at one fixed wavelength close to 520 nm. This model is based on experimental measurements by Petzold [75] and Timofeyeva [107]. It was tested using independent measurements of the complete set of inherent properties by Mankovsky [76, 77] and showed good agreement between measured and predicted results.

Given, that we know the values of absorption and attenuation coefficients (a and c) measured, for example, with the AC-9 probe by WetLabs, we can estimate all other optical properties using the following procedure:

(1) We compute a beam scattering coefficient b and a single-scattering albedo (probability of elastic scattering) ω_0 through a and c:

$$b = c - a, \quad \omega_0 = b/c. \tag{10.76}$$

(2) A total average cosine is computed through the single-scattering albedo using the following equation:

$$\overline{\mu} = y\{2.617\,839\,8 + y[-4.602\,418 + y(9.004\,06 + y\{-14.599\,94 + y[14.839\,09 + y(-8.117\,954 + 1.859\,322\,2y)]\})]\}, \quad y = \sqrt{1-\omega_0}. \tag{10.77}$$

(2) We compute upward and downward average cosines using the following equations:

$$\overline{\mu}_d = \frac{1-\overline{\mu}(1-\overline{\mu})^2\left\{0.0326+\overline{\mu}^2\left[0.1661+\overline{\mu}^2(0.7785+0.0228\overline{\mu}^2)\right]\right\}}{2-\overline{\mu}}, \tag{10.78}$$

$$\overline{\mu}_u = \frac{1-0.987\overline{\mu}(1-\overline{\mu})^2\exp\left(\overline{\mu}^2\left\{8.4423+\left[-15.6605+\overline{\mu}^2(21.882-11.2257\overline{\mu}^2)\right]\right\}\right)}{2-\overline{\mu}}, \tag{10.79}$$

(3) We compute the backscattering probability, B, and the backscattering coefficient, b_B, as follows:

$$B = \frac{(1-\omega_0)(1-\overline{\mu}^2)^2}{2\omega_0\overline{\mu}^2(3-\overline{\mu}^2)}, \quad b_B = bB. \tag{10.80}$$

(4) We compute the diffuse reflection coefficient using values of the average cosines:

$$R_\infty = \frac{1-\overline{\mu}/\overline{\mu}_d}{1+\overline{\mu}/\overline{\mu}_u}, \tag{10.81}$$

(5) We compute the diffuse attenuation coefficient using Geshun's equation:

$$\overline{k} = \frac{a}{\overline{\mu}} \equiv c\frac{1-\omega_0}{\overline{\mu}}, \tag{10.82}$$

(6) And, finally, we compute the angular scattering coefficient using the following equation:

$$\beta(\vartheta) = l_0^{-1}\exp\left[q\left(1+\sum_{n=1}^{5}k_n\vartheta^{\frac{n}{2}}\right)\right], \tag{10.83}$$

here ϑ is a scattering angle in radians, $l_0 = 1\,\mathrm{m}$. Coefficients q and k_n ($n = 1,\ldots,5$) are given by the following regressions:

$$\left.\begin{aligned} q &= 2.598 + 5.932\sqrt{l_0 b}(2.992 + l_0 b) - 16.722 l_0 b,\\ k_1 &= 5.2077\omega_0 - 8.9924,\\ k_2 &= 17.59 - 10.886\omega_0,\\ k_3 &= 13.098\omega_0 - 19.863,\\ k_4 &= 10.636 - 7.386\omega_0,\\ k_5 &= 1.515\omega_0 - 2.087. \end{aligned}\right\} \tag{10.84}$$

The FORTRAN code that implements this model is published in reference [108].

10.12 Conclusion

The simplified model presented here of absorption, elastic and Raman scattering, and fluorescence is written as a practical tool – to model radiative transfer in real natural waters using either the radiative transfer approach [109] given by eq. (10.1) or the numerical approach based on Monte Carlo or discrete ordinates (Hydrolight [74]). There are certain aspects of scattering, such as Brillouin scattering, scattering by air bubbles, and scattering by turbulent fluctuations of natural water, that are omitted from this chapter because there is not sufficient material in the literature to cover them quantitatively. Other more developed areas are given in a detail that allows for reasonable representative optical modeling of deep and shallow waters with wind-roughened surface.

References

1. Bricaud, A., and A. Morel, 1986, Light attenuation and scattering by phytoplanktonic cells: a theoretical modeling, *Appl. Optics,* **25**, 571–580.
2. Carder, K. L., Stewart R. G., Harvey, G. R., and Ortner P. B., 1989, Marine humic and fulvic acids: their effects on remote sensing of ocean chlorophyll, *Limnol. Oceanogr.*, **34**, 68–81.
3. Hoepfner, N., and S. Sathyendranath, 1992, Bio-optical characteristics of coastal waters: absorption spectra of phytoplankton and pigment distribution in the western North Atlantic, *Limnol. Oceanogr.*, **37**, 1660–1679.
4. Jerlov, N. G., 1976, *Marine Optics*, Elsevier, Amsterdam.
5. Mobley, C. D., 1994, *Light and Water*, (Academic Press, San Diego, CA).
6. Morel, A., 1988, Optical modeling of the upper ocean in relation to its biogenous matter content (Case I waters), *J. Geophys Res.*, **93C**, 749–810.
7. Morel, A., 2001, Bio-optical properties of oceanic waters: A reappraisal, *J. Geophys. Res.*, **106C**, 7163–7180.
8. Pope, R. M., and E. S. Fry, 1997, Absorption spectrum (380–700 nm) of pure water: II. Integrating cavity measurements, *Appl. Optics*, **36**, 8710–8723.
9. Prieur, L., and S. Sathyendranath, 1981, An optical classification of coastal and oceanic waters based on the specific spectral absorption curves of phytoplankton pigments, dissolved organic matter, and other particulate materials, *Limnol. Oceanogr.*, **26**, 671–689.
10. Shifrin, K. S., 1988, *Physical Optics of Ocean Water*, American Institute of Physics, New York.
11. Smith, R. C., and K. S. Baker, 1981, Optical Properties of Clearest Natural Waters, *Appl. Opt.*, **20**, 177–184.
12. Stramski, D., A. Bricaud, and A. Morel, 2001, Modeling of the inherent optical properties of the ocean based on the detailed composition of the planktonic community, *Appl. Optics*, **40**, 2929–2945.
13. Stramski, D., and C. D. Mobley, 1997, Effect of microbial particles in oceanic optics: a database of single-particle optical properties, *Limnol. Oceanogr.*, **42**, 538–549.
14. Babin, M., A. Morel, V. Fournier-Sicre, F. Fell, and D. Stramsky, 2003, Light scattering properties of marine particles in coastal and open ocean waters as related to the particle mass concentration, *Limnol. Oceanogr.*, **48**, 843–859.

15. Morel, A., 1974, Optical properties of pure water and pure sea water, Chapter 1, pp. 1–24, in *Optical Aspects of Oceanography*, eds. N. G. Jerlov, and E. Steemann Nielsen, Academic Press, London.
16. Morel, A., and H. Loisel, 1998, Apparent optical properties of oceanic water: dependence on the molecular scattering contribution, *Appl. Optics*, **37**, 4765–4776.
17. Stramski, D., and D. A. Kiefer, 1991, Light scattering by microorganisms in the open ocean, *Prog. Oceanog.*, **28**, 343–383.
18. Subramaniam, A., E. J. Carpenter, and P. G. Falkowski, 1999, Bio-optical properties of the marine diazotrophic cyanobacteria *Trichodesmium* spp. II. A reflectance model for remote sensing, *Limnol. Oceanogr.*, **44**, 618–627.
19. Subramaniam, A., E. J. Carpenter, D. Karentz, and P. G. Falkowski, 1999, Bio-optical properties of the marine diazotrophic cyanobacteria *Trichodesmium* spp. I. Absorption and photosynthetic action spectra, *Limnol. Oceanogr.*, **44**, 608–617.
20. Ulloa, O., S. Sathyendranath, T. Platt, and R. A. Quiñones, 1992, Light scattering by marine heterotopic bacteria, *J. Geophys. Res.*, **97 C**, 9619–9629.
21. Voss, K. J., W. M. Balch, and K. A. Kilpatrick, 1998, Scattering and attenuation properties of *Emiliania huxleyi* cells and their detached coccoliths, *Limnol. Oceanogr.*, **43**, 870–876.
22. Waltham, C., J. Boyle, B. Ramey, and J. Smit, 1994, Light scattering and absorption caused by bacterial activity in water, *Appl. Optics*, **33**, 7536–7540.
23. Bartlett, J. S. , K. J. Voss, S. Sathyendranath, and A. Vodacek, 1998, Raman scattering by pure water and seawater, *Appl. Optics,* **37**, 3324–3332.
24. Bartlett, J. S., 1997, A comparison of models of sea-surface reflectance incorporating Raman scattering by water, in *Ocean Optics XIII: SPIE,* 2963, S. G. Ackleson and R. Frouin (eds), Bellingham, WA, pp. 592–596.
25. Berwald, J., D. Stramski, C. D. Mobley, and D. Kiefer, 1998, Effect of Raman scattering on the average cosine and diffuse attenuation coefficient of irradiance in the ocean, *Limnol. Oceanogr.*, **43**, 564–576.
26. Desidero, R. A., 2000, Application of the Raman scattering coefficient of water to calculations in marine optics, *Appl. Optics*, **39**, 1893–1894.
27. Faris, G. W., and R. A. Copeland, 1997, Wavelength dependence of the Raman cross section for liquid water, *Appl. Optics*, **36**, 2686–2688.
28. Gordon, H. R., 1999, Contribution of Raman scattering to water-leaving radiance: a reexamination, *Appl. Opt.*, **38**, 3166–3174.
29. Haltrin, V. I., and G. W. Kattawar, 1991 Effects of Raman scattering and fluorescence on apparent optical properties of seawater, Report, Department of Physics, Texas A&M University, College Station, TX.
30. Haltrin, V. I., and G. W. Kattawar, 1993, Self-consistent solutions to the equation of transfer with elastic and inelastic scattering in oceanic optics: I. Model, *Appl. Optics*, **32**, 5356–5367.
31. Haltrin, V. I., G. W. Kattawar and A. D. Weidemann, 1997, Modeling of elastic and inelastic scattering effects in oceanic optics, in *Ocean Optics XIII, SPIE,* 2963, S. G. Ackleson and R. Frouin (eds), Bellingham, WA, pp. 597–602.
32. Hu, C., and K. J. Voss, 1997, *In situ* measurements of Raman scattering in clear ocean water, *Appl. Optics*, **36**, 6962–6967.
33. Kattawar, G. W., and Xin Xu, 1992, Filling-in of Fraunhofer Lines in the Ocean by Raman Scattering, *Appl. Optics*, **31**, 6491–6500.
34. Marshall, B. R., and R. C. Smith, 1990, Raman Scattering and in-water ocean optical properties, *Appl. Optics*, **29**, 71–84.

35. Romanov, N. P., and V. S. Shuklin, 1975, Raman scattering cross section of liquid water, *Opt. Spectrosc.*, **38**, 646–648.
36. Schrötter, H. W., and H. W. Klöckner, 1979, Raman scattering cross-sections in gases and liquids, (pp. 123–166, in *Raman Spectroscopy of Gases and Liquids*, ed. A. Weber, Springer Verlag, Berlin.
37. Shen, Y. R., and N. Blombergen, 1965, Theory of simulated Brillouin and Raman scattering, *Phys. Rev. A*, **137**, 1787–1805.
38. Stavn, R. H., 1993, The effects of Raman scattering across the visible spectrum in clear ocean water: A Monte-Carlo Study, *Appl. Optics*, **32**, 6853–6863.
39. Stavn, R. H., and A. D. Weidemann, 1988, Optical modeling of clear ocean light fields: Raman scattering effects, *Appl. Optics*, **27**, 4002–4011.
40. Stavn, R. H., and A. D. Weidemann, 1992, Raman scattering in oceanic optics: quantitative assessment of internal radiant emission, *Appl. Optics*, **31**, 1294–1303.
41. Sugihara, S., M. Kishino, and N. Okami, 1984, Contribution of Raman scattering to upward irradiance in the sea, *J. Ocean. Soc. of Japan*, **40**, 397–403.
42. Walrafen, G. E., 1967, Raman spectral studies of the effects of temperature on water structure,, *J. Chem. Phys.*, **47**, 114–126.
43. Walrafen, G. E., 1969, Continuum model of water – an erroneous interpretation, *J. Chem. Phys.*, **50**, 567–569.
44. Waters, K. J., 1995, Effects of Raman scattering on the water-leaving radiance, *J. Geophys. Res.*, **100C**, 13151–13161.
45. Aiken, J., 1989, Investigation of various fluorescence phenomena, Report, Plymouth Marine Laboratory, Plymouth, UK, pp. 1–38.
46. Dirks, R. W. J., and D. Spitzer, 1987, On the radiative transfer in the sea, including fluorescence and stratification effects, *Limnol. Oceanogr.*, **32**, 942–953.
47. Dirks, R. W. J., and D. Spitzer, 1987, Solar radiance distribution in deep natural waters including fluorescence effects, *Appl. Optics*, **26**, 2427–2430.
48. Gordon, H. R., 1979, Diffuse reflectance of the ocean: the theory of its augmentation by chlorophyll *a* fluorescence at 685 nm, *Appl. Opt.*, **18**, 1161–1166.
49. Hawes, S. K., Carder, K. L., and Harvey, G. R. 1992, Quantum fluorescence efficiencies of fulvic and humic acids: effect on ocean color and fluorometric detection, *Ocean Optics XI*, *Proceedings of SPIE*, 1750, pp. 212–223.
50. Kattawar, G. W., and J. C. Vastano, 1982, Exact 1-D solution to the problem of chlorophyll fluorescence from the ocean, *Appl. Optics*, **21**, 2489–2492.
51. Kiefer, D. A., 1973, Fluorescence properties of natural phytoplankton populations, *Mar. Biol.*, **22**, 263–269.
52. Kiefer, D. A., W. S. Chamberlin, and C. R. Booth, 1989, Natural fluorescence of chlorophyll *a*: relationship to photosynthesis and chlorophyll concentration in the western South Pacific gyre, *Limnol. Oceanogr.*, **34**, 868–881.
53. Maritorena, S., A. Morel, and B. Gentili, 2000, Determination of the fluorescence quantum yield by oceanic phytoplankton in their natural habitat, *Appl. Optics*, **39**, 6725–6737.
54. Neville, R. A., and J. F. R. Gower, 1977, Passive remote sensing of phytoplankton via chlorophyll a fluorescence, *J. Geophys Res.*, **82**, 3487–3493.
55. Peacock, T. B., K. L. Carder, C. O. Davis, and R. G. Steward, 1990, Effects of fluorescence and water Raman scattering on models of remote sensing reflectance, *Ocean Optics X*, *Proceedings of SPIE*, 1302, pp. 303–319.
56. Preisendorfer, R. W., 1988, Theory of fluorescent irradiance fields in natural waters, *J. Geophys. Res.*, **93**, 10 831–10 855.

57. Slovacek, R., P. Hannan, 1977, *In vivo* fluorescence determination of phytoplankton chlorophyll *a*, *Limnol. Oceanogr.*, **22**, 919–925.
58. Spitzer, D., and R. W. J. Dirks, 1985, Contamination of the reflectance of natural waters by solar-induced fluorescence of dissolved organic matter, *Appl. Optics*, **24**, 444–445.
59. Traganza, E. D., 1969, Fluorescence excitation and emission spectra of dissolved organic matter in sea water, *Bulletin of Marine Science*, **19**, 897–904.
60. Trees, C., 1990, Frequency shifting of light by fluorescence, Technical Memorandum No. 0005–90, pp. 1–9, SDSU Foundation, Center for Hydro-Optics and Remote Sensing, San Diego, CA.
61. Vodacek, A., 1992, An explanation of the spectral variation in freshwater CDOM fluorescence, *Limnol. Oceanogr.*, **37**, 1808–1813.
62. Vodacek, A., S. A. Green, and N. V. Blough, 1994, An experimental model of the solar stimulated fluorescence of chromophoric dissolved organic matter, *Limnol. Oceanogr.*, **39**, 1–11.
63. Terrill, E. J., W. K. Melville, and D. Stramski, 2001, Bubble entrainment and their influence on optical scattering in the upper ocean, *J. Geophys. Res.*, **106C**, 16 815–16 823.
64. Zhang, X., M. Lewis, and B. Johnson, 1998, Influence of bubbles on scattering of light in the ocean, *Appl. Optics*, **37**, 6525–6536.
65. Zhang, X., M. Lewis, M. Lee, B. Johnson, and G. Korotaev, 2002, The volume scattering function of natural bubble populations, *Limnol. Oceanogr.*, **47**, 1273–1282.
66. Cummings, H. Z., and R. W. Gammon, 1966, Rayleigh and Brillouin scattering in liquids: the Landau–Placzek ratio, *J. Chem. Phys.*, **44**, 2785–2797.
67. Goldblatt, N., 1969, Stimulated Brillouin scattering, *Appl. Optics*, **8**, 1559–1566.
68. Joelson, B., and G. Kattawar, 1996, Multiple scattering effects on the remote sensing of the speed of sound in the ocean by Brillouin scattering, *Appl. Optics*, **35**, 2693–2701.
69. O'Connor, C. L., and J. P. Schlupf, 1967, Brillouin scattering in water: the Landau–Placzek ratio, *J. Chem. Phys.*, **47**, 31–38.
70. Bogucki, D. J., J. A. Domaradzki, D. Stramski, and J. R. Zaneveld, 1998, Comparison of near-forward light scattering on oceanic turbulence and particles, *Appl. Optics,* **37**, 4669–4677.
71. Bogucki, D. J., J. A. Domaradzki, R. E. Ecke, and C. R. Truman, 2004, Light scattering on oceanic turbulence, *Appl. Optics,* **43**, 5662–5668.
72. Kopelevich, O. V., V. V. Rodionov, and T. P. Stupakova, 1987, Effect of bacteria on optical characteristics of ocean water, *Oceanology*, **27**, 696–700.
73. Mobley, C. D., and D. Stramski, 1997, Effect of microbial particles in oceanic optics: methodology for radiative transfer modeling and example simulations, *Limnol. Oceanogr.*, **42**, 550–560.
74. Mobley, C. D., and L. K. Sundman, 2000, *Hydrolight 4.1 User Guide,* Sequoia Scientific, Inc., Redmond, WA.
75. Petzold, T. J., 1972, Volume scattering functions for selected ocean waters, SIO Ref. 72–78, Scripps Institute of Oceanography, Visibility Laboratory, San Diego, CA.
76. Mankovsky, V. I., and V. I. Haltrin, 2002, Phase functions of light scattering measured in waters of World Ocean and Lake Baykal, – *2002 IEEE International Geoscience and Remote Sensing Symposium and the 24th Canadian Symposium on Remote Sensing Proceedings on CD ROM*, June 24–28, 2002, Toronto, Canada.

Library of Congress Number: 2002 105858, Paper # I2E09_1759. Also published in *Geoscience and Remote Sensing Symposium*, 2002 IEEE International, IEEE 2002; softcover, 2002: ISBN 0-7803-7536-X; Product No.: CH37380-TBR.

77. Mankovsky, V. I., and V. I. Haltrin, 2003, Light scattering phase functions measured in waters of Mediterranean Sea, *OCEANS 2002 MTS-IEEE Proceedings*, Vol. 4, IEEE Catalog Number: 02CH37362C, ISBN: 0-7803-7535-1, pp. 2368–2373, Biloxi, Mississipi, USA, October 29–31, 2002 (CD-ROM). Also published in *OCEANS, 2002 MTS/ IEEE Conference & Exhibition Proceedings*, ISBN 0-7803-7534-3, IEEE Product no. CH37362-TBR (2003).
78. Haltrin, V. I. , M. E. Lee, and O. V. Martynov, 1996, Polar nephelometer for sea truth measurements, pp. 444–450, in *Proceedings of the Second International Airborne Remote Sensing Conference and Exhibition*, Vol. II, San Francisco, CA, (Published by ERIM: ISSN 1076–7924, 1996).
79. Lee, M. E. and M. Lewis, 2003, A new method for the measurement of the optical volume scattering function in the upper ocean, *J. Atmos. Ocean. Technol.*, **20**, 563–571.
80. Lee, M. E., V. I. Haltrin, E. B. Shybanov, and A. D. Weidemann, 2003, Light scattering phase functions of turbid coastal waters measured in LEO-15 experiment in 2000, in *OCEANS 2003 MTS-IEEE Conference Proceedings on CD-ROM*, pp. 2835–2841, San Diego, California, September 22–26, 2003. ISBN: 0-933957-31-9, Holland Enterprises, Escondido, CA.
81. Haltrin, V. I., M. E. Lee, E. B. Shybanov, R. A. Arnone, A. D. Weidemann, V. I. Mankovsky, W. S. Pegau, and S. D. Ladner, 2002, Relationship between backscattering and beam scattering coefficients derived from new measurements of light scattering phase functions, *Ocean Optics XVI CD-ROM*, November 18–22, 2002, Santa Fe, New Mexico, USA. Prepared by the Office of Naval Research, USA.
82. Haltrin, V. I., M. E. Lee, V. I. Mankovsky, E. B. Shybanov, and A. D. Weidemann, 2003, Integral properties of angular light scattering coefficient measured in various natural waters, pp. 252–257 in *Proceedings of the II International Conference Current Problems in Optics of Natural Waters*, ONW'2003, eds Iosif Levin and Gary Gilbert, St. Petersburg, Russia.
83. Haltrin, V. I., 1997, Theoretical and empirical phase functions for Monte Carlo calculations of light scattering in seawater, pp. 509–518 in *Proceedings of the Fourth International Conference Remote Sensing for Marine and Coastal Environments*, Environmental Research Institute of Michigan, Ann Arbor, MI.
84. Oishi, T., 1990, Significant relationship between the backward scattering coefficient of sea water and the scatterance at 120°, *Appl. Optics*, **29**, 4658–4665.
85. Maffione, R. A. and D. R. Dana, 1997, Instruments and methods for measuring the backwardscattering coefficient of ocean waters, *Appl. Optics*, **36**, 6057–6067.
86. Haltrin, V. I., 2002, One-parameter two-term Henyey–Greenstein phase function of light scattering in seawater, *Appl. Optics*, **41**, 1022–1028.
87. Timofeyeva, V. A., 1975, Brightness in the depth regime in a turbid medium illuminated by normally incident rays, *Izvestiya USSR AS, Atmos. Ocean Physics*, **11**, 259–260.
88. Timofeyeva, V. A., 1978, Relationship between light-field parameters and between scattering phase function characteristics of turbid media, including seawater, *Izvestiya USSR AS, Atmos. Ocean Physics*, **14**, 843–848.
89. Timofeyeva, V. A., 1979, Determination of light-field parameters in the depth regime from irradiance measurements, *Izvestiya USSR AS, Atmos. Ocean Physics*, **15**, 774 -776.

90. Ge, Y., H. R. Gordon, and K. J. Voss, 1993, Simulations of inelastic-scattering contributions to the irradiance field in the ocean: variation in Fraunhofer line depths, *Appl. Optics*, **32**, 4028–4036.
91. Haltrin, V. I., 2004, The nature of optical remote sensing coefficient, in *Remote Sensing and Modeling of Ecosystems for Sustainability*, eds by Wei Gao and David R. Shaw, *Proceedings of SPIE,* 5544, pp. 364–371.
92. Lee, Z. , K. L. Carder, S. K. Hawes, R. G. Steward, T. G. Peacock, and C. O. Davis, 1992, Interpretation of high spectral resolution remote sensing reflectance, in *Optics of Air–Sea Interface: Theory and Measurement,* ed. L. Estep, *Proceedings of SPIE*, 1749, pp. 49–64.
93. Morel, A., and L. Prieur, 1977, Analysis of variations in ocean color, *Limnol. Oceanogr.*, **22**, 709–722.
94. Kopelevich, O. V., 1983, Small–parameter model of optical properties of seawater, pp. 208–234 in *Ocean Optics*, Vol. 1: *Physical Ocean Optics*, ed. A. S. Monin, Nauka, Moscow (in Russian).
95. Gate, L. F., 1974, Comparison of the photon diffusion model and Kubelka–Munk equation with the exact solution of the radiative transfer equation, *Appl. Optics*, **13**, 236–238.
96. Haltrin, V. I., 1988, Exact solution of the characteristic equation for transfer in the anisotropically scattering and absorbing medium, *Appl. Optics*, **27**, 599–602.
97. Henyey, L. C., and J. L. Greenstein, 1941, Diffuse radiation in the galaxy, *Astrophys. J.*, **93**, 70–83.
98. Haltrin, V. I. (*aka* V. I. Khalturin), 1985, The self-consistent two-flow approximation of the transport theory of radiation, *Izvestiya USSR AS, Atmos. and Ocean Physics,* **21**, 589–597.
99. Haltrin, V. I., 1998, Self-consistent approach to the solution of the light transfer problem for irradiances in marine waters with arbitrary turbidity, depth and surface illumination: I. Case of absorption and elastic scattering, *Appl. Optics*, **37**, 3773–3784.
100. Haltrin, V. I., and S. C. Gallegos, 2003, About nonlinear dependence of remote sensing and diffuse reflection coefficients on Gordon's parameter, pp. 363–369, in '*Proceedings of the II International Conference Current Problems in Optics of Natural Waters*,' ONW'2003, eds Iosif Levin and Gary Gilbert, St. Petersburg, Russia, 2003.
101. Haltrin, V. I., 1998, Apparent optical properties of the sea illuminated by Sun and sky: case of the optically deep sea, *Appl. Optics*, **37**, 8336–8340.
102. Afonin, E. I., V. L. Vladimirov, B. Piesick, V. A. Urdenko, and G. Zimmermann, 1985, Ship- and coast-borne investigations of optical properties of medium and parameters of light field of the atmosphere–ocean system, (in Russian), pp. 197–198 in Chapter 6 in *Optical Remote Sensing of the Sea and Influence of the Atmosphere*, The Institute for Space Research, Academy of Sciences of The German Democratic Republic, Berlin.
103. Kopelevich, O. V., and O. A. Gushchin, 1978, Statistical and physical models of the light scattering properties of sea water, *Izvestiya USSR AS, Atmos. Ocean Physics*, **14**, 680–684.
104. Haltrin, V. I., 1999, Chlorophyll based model of seawater optical properties, *Applied Optics*, **38**, 6826–6832.
105. Morel, A., 1980, In-water and remote measurement of ocean color, *Boundary–Layer Meteorol.*, **18**, 177–201.

106. Haltrin, V. I., 2000, Empirical algorithms to restore a complete set of inherent optical properties of seawater using any two of these properties, *Canadian J. Remote Sensing*, **26**, 440–445.
107. Timofeyeva, V. A., 1972, Relation between the optical coefficients in turbid media, *Izvestiya USSR AS, Atmos. Ocean Physics*, **8**, 654–656.
108. Haltrin, V. I., 1999, Empirical algorithms to restore a complete set of inherent optical properties of seawater, in *Proceedings of the Fourth International Airborne Remote Sensing Conference and Exhibition/21st Canadian Symposium on Remote Sensing*, 21–24 June 1999, Ottawa, Ontario, Canada, ISSN 1076–7924, Published by ERIM International, Inc., Ann Arbor, MI.
109. Zege E. P., A. P. Ivanov, and I. L. Katsev, 1991, *Image Transfer through a Scattering Medium*, Springer Verlag, New York.

Appendix: Notation and definitions

A. A. Kokhanovsky

The problem of notation is considered to be of a secondary importance in scientific research. However, it is easier to understand results obtained, if consistent notation is used in various papers on the optics of light scattering media. Currently, this is not the case. In particular, oceanic and atmospheric optics communities use, for example, different notations for such basic local optical characteristics of a light scattering medium as the extinction, scattering, and absorption coefficients.

This book has a multidisciplinary character. Therefore, there is a need to summarize some of the notation used in this book by various authors, reflecting, of course, the use of corresponding symbols in their particular research field. Corresponding notations, together with those preferred by this author, are given in Table A1.

Table A.1. Selected notations for local optical characteristics of turbid media used in this volume

Author	Absorption, scattering, and extinction coefficients	Absorption, scattering, and extinction cross-sections	Absorption, scattering, and extinction efficiency factors	Phase function	Phase matrix	Single-scattering albedo
Yang and Liou	—	$\sigma_{abs}, \sigma_{sca}, \sigma_{ext}$	$Q_{abs}, Q_{sca}, Q_{ext}$	P_{11}	P	$\tilde{\omega}_0$
Sharma	σ_{ext}	—	$Q_{abs}, Q_{sca}, Q_{ext}$	p	—	—
Farafonov and Il'in	—	$C_{abs}, C_{sca}, C_{ext}$	$Q_{abs}, Q_{sca}, Q_{ext}$	—	—	—
Borovoi	—	$\sigma_a, \sigma_s, \sigma_e$	—	p	P	—
Kokhanovsky	$K_{abs}, K_{sca}, K_{ext}$	—	—	p	—	ω_0
Gorodnichev, Kuzovlev, and Rogozkin	σ_a, σ, σ_{tot}	—	—	—	d	—
Haltrin	a, b, c	—	—	p	—	ω_0
Editor's preferred notation	$K_{abs}, K_{sca}, K_{ext}$	$C_{abs}, C_{sca}, C_{ext}$	$Q_{abs}, Q_{sca}, Q_{ext}$	p	P	ω_0

Let us illustrate the difference between efficiency factors, cross-sections, and coefficients. For this we will consider direct light transmittance through a scattering medium with spherical particles of the same radius a. It is assumed the volumetric concentration of particles is small and spherical scatterers are randomly distributed.

It follows that the direct light intensity $I(z)$ at the depth z (counted from the boundary of a scattering layer ($z = 0$)) is given by the following equation:

$$I(z) = I(z = 0) \exp(-K_{ext} z). \tag{A.1}$$

The extinction coefficient K_{ext} is measured in inverse meters. It can be expressed via the extinction cross-section of a single particle C_{ext}:

$$K_{ext} = NC_{ext}, \tag{A.2}$$

where N is the number of particles in unit volume measured in m^{-3}. Therefore, C_{ext} is measured in m^2. It is useful to introduce the dimensionless extinction efficiency factor

$$Q_{ext} = \frac{C_{ext}}{\pi a^2}. \tag{A.3}$$

Similar definitions are valid also for absorption and scattering processes. It follows for the single scattering albedo: $\omega_0 = K_{sca}/K_{ext}$. Also we can introduce the probability of photon absorption: $\beta = 1 - \omega_0$.

For polydispersions of spherical or randomly oriented nonspherical particles, C_{ext} in eq. (A.2) must be substituted by the average value of the extinction cross section for the ensemble of scatterers.

The probability of photon scattering in a given direction θ counted from the direction of propagation is characterized by the phase function $p(\theta)$. Different normalizations of the phase function are used. Astrophysicists and atmospheric scientists prefer to use the following normalization:

$$\int_{4\pi} p(\Omega) \frac{d\Omega}{4\pi} = 1, \tag{A.4}$$

where Ω is the solid angle. It follows from this definition for the isotropic scattering (p does not depend on Ω): $p \equiv 1$. Equation (A1) is simplified, for example, for the case of spherical or randomly oriented nonspherical particles:

$$\frac{1}{2} \int_0^\pi p(\theta) \sin\theta \, \mathrm{d}\theta = 1. \tag{A.5}$$

The notion of the average cosine of scattering angle g is also often used in papers dealing with light scattering. This parameter is defined as:

$$g = \frac{1}{2} \int_0^\pi p(\theta) \cos\theta \sin\theta \, \mathrm{d}\theta. \tag{A.6}$$

Clearly, it follows that $g = 0$ for isotropic scattering ($p = 1$). Therefore, g is often called the asymmetry parameter. It vanishes for symmetric scattering (e.g., for

the symmetric with respect to the angle $\theta = \pi/2$ Rayleigh phase function $p(\theta) = 0.75(1+\cos^2\theta)$). One can also introduce the symmetry parameter $q = 1-g$. This parameter is equal to one for isotropic scattering. However, it is close to zero for highly extended in the forward direction phase functions. An important role in light scattering media optics belongs to yet another two parameters. They are the transport extinction coefficient

$$K_{tr} = (1-g)K_{ext} \equiv qK_{ext} \tag{A.7}$$

and the similarity parameter

$$s = \sqrt{\frac{1-\omega_0}{1-g\omega_0}}. \tag{A.8}$$

One can write for the case of weakly absorbing light scattering media: $s \approx \sqrt{\beta/q}$. It is interesting that the absorption, A, of light by a semi-infinite weakly absorbing light scattering medium is determined mostly by the parameter s. Such media having the same values of s but possibly different values of β and q have close values of A.

Turning to the case of the analysis of the polarized scattered light, we note that the 4×4 scattering matrix $\hat{F}(\theta)$ relates the Stokes vectors $\boldsymbol{S}(I, Q, U, V)$ of scattered light with the Stokes vector $\boldsymbol{S}_0(I_0, Q_0, U_0, V_0)$ of incident light:

$$\boldsymbol{S} = (kr)^{-2}\hat{F}(\theta)\boldsymbol{S}_0, \tag{A.9}$$

where r is the distance to the observation point and $k = 2\pi/\lambda$, λ is the wavelength. This matrix is defined with respect to the scattering plane, which holds directions of incident and scattering beams.

It follows from eq. (A.9) for the intensity of scattered light:

$$I = (kr)^{-2}F_{11}(\theta)I_0, \tag{A.10}$$

where we assumed that the incident light is unpolarized. The total flux of the scattered light Φ_{sca} is given by the integral:

$$\Phi_{sca} = \int_{4\pi} I(\Omega)r^2 \,\mathrm{d}\Omega. \tag{A.11}$$

Therefore, we have, for example, for a single spherical particle:

$$\Phi_{sca} = 2\pi k^{-2} I_0 \int_0^{\pi} F_{11}(\theta)\sin\theta \,\mathrm{d}\theta, \tag{A.12}$$

where we performed integration with respect to the azimuth angle. Now we take into account that $C_{sca} = \Phi_{sca}/I_0$ by definition. This means that

$$C_{sca} = 2\pi k^{-2} \int_0^{\pi} F_{11}(\theta)\sin\theta \,\mathrm{d}\theta \tag{A.13}$$

and, therefore,

$$\frac{1}{2}\int_0^\pi P_{11}(\theta)\sin\theta\,\mathrm{d}\theta = 1, \tag{A.14}$$

where

$$P_{11}(\theta) = \frac{4\pi F_{11}(\theta)}{k^2 C_{sca}}. \tag{A.15}$$

Both functions ($F_{11}(\theta)$ and $P_{11}(\theta)$) describe the angular distribution of scattered light. In particular, F_{11} is related to van de Hulst's dimensionless Mie intensities i_1 and i_2 with the following equation: $F_{11} = (i_1 + i_2)/2$. Also one can introduce the differential scattering cross-section $C_{sca}(\theta) = k^{-2}F_{11}(\theta) \equiv (i_1 + i_2)/2k^2$ which is yet another way to describe the angular distribution of scattered light. We underline that the combination $v(\theta) = N\langle C_{sca}(\theta)\rangle$ is called the volume scattering function. Here brackets mean averaging with respect to the particle size/shape distributions.

The use of $P_{11}(\theta)$ is more convenient in theoretical studies because its normalization condition coincides with that given by eq. (A.5). Therefore, we can call $P_{11}(\theta)$ the phase function and also introduce the phase matrix

$$\hat{P}(\theta) = \frac{4\pi\hat{F}(\theta)}{k^2 C_{sca}}. \tag{A.16}$$

The first element of this matrix coincides with the phase function. In applied light scattering optics studies the normalized phase matrix is often used: $\hat{p}(\theta) \equiv \hat{P}(\theta)/P_{11}$. We can also introduce the normalized scattering matrix $\hat{f}(\theta) = \hat{F}(\theta)/F_{11}(\theta)$. Clearly it follows that matrices $\hat{f}$ and $\hat{p}$ coincide.

For polydispersed media, one must use average values of C_{sca} and $\hat{F}(\theta)$ in eq. (A.16).

Index

LIGHT SCATTERING REVIEWS

Editor: Alexander A. Kokhanovsky

Institute of Environmental Physics
University of Bremen, Otto Hahn Allee 1, D-28334 Bremen, Germany
Publisher: Springer-Praxis

Description: Light Scattering Reviews aims to familiarize research community with recent advances in the light scattering media optics (LSMO). Covering a much wider field than the usual specialist journals, this publication allows the reader to see his particular interest related to LSMO as a whole. Because of the breadth and depth of its approach to subjects of current interest, Light Scattering Reviews is an important vehicle of information gathering for instructors, students, research scientists and private industries concerned with LSMO issues.

Light Scattering Reviews – the publication medium for review articles in light scattering media optics.

Authors benefits: no restriction on the length of your review, rapid publication in the form of a book, no page charges, free copy of the book , one page of color free, payment of US$ 200 upon publication of your article, worldwide distribution of your review through many indexing and abstracting services, easy online submission (camera-ready copy is not required).

Submission: Prospective authors must contact Editor specifying the title and providing a short Abstract of the paper (bookman@praxis-publishing.co.uk).

Audience: All research scientists involved in applications of light scattering techniques

Printing: Mercedes-Druck, Berlin
Binding: Stein + Lehmann, Berlin